AFRL-PR-WP-TR-2005-2023

ADVANCED INTEGRATED FUEL/COMBUSTION SYSTEMS

S. Zabarnick, J.S. Ervin, M.J. DeWitt, D.R. Ballal, K.E. Binns, T.F. Williams, and S. Stouffer

University of Dayton Research Institute
300 College Park
Dayton, OH 45469-0110

JANUARY 2004

Final Report for 29 September 1997 – 31 December 2003

STINFO FINAL REPORT

PROPULSION DIRECTORATE
AIR FORCE RESEARCH LABORATORY
AIR FORCE MATERIEL COMMAND
WRIGHT-PATTERSON AIR FORCE BASE, OH 45433-7251

NOTICE

Using Government drawings, specifications, or other data included in this document for any purpose other than Government procurement does not in any way obligate the U.S. Government. The fact that the Government formulated or supplied the drawings, specifications, or other data does not license the holder or any other person or corporation; or convey any rights or permission to manufacture, use, or sell any patented invention that may relate to them.

This report has been reviewed and is releasable to the National Technical Information Service (NTIS). It will be available to the general public, including foreign nationals.

THIS TECHNICAL REPORT HAS BEEN REVIEWED AND IS APPROVED FOR PUBLICATION.

_____//s//_____
ROBERT W. MORRIS JR.
Manager, High Heat Sink Fuels Technologies
Fuels Branch
Turbine Engine Division
Propulsion Directorate

_____//s//_____
WILLIAM E. HARRISON III
Chief, Fuels Branch
Turbine Engine Divison
Propulsion Directorate

_____//s//_____
JEFFREY M. STRICKER
Chief Engineer
Turbine Engine Division
Propulsion Directorate

This report is published in the interest of scientific and technical information exchange and does not constitute approval or disapproval of its ideas or findings.

REPORT DOCUMENTATION PAGE

Form Approved
OMB No. 0704-0188

1. REPORT DATE *(DD-MM-YY)*	2. REPORT TYPE	3. DATES COVERED *(From - To)*
January 2004	Final	9/29/97 – 12/31/03

4. TITLE AND SUBTITLE
ADVANCED INTEGRATED FUEL/COMBUSTION SYSTEMS

5a. CONTRACT NUMBER
F33615-97-C-2719

5b. GRANT NUMBER

5c. PROGRAM ELEMENT NUMBER
62203F

6. AUTHOR(S)
S. Zabarnick, J.S. Ervin, M.J. DeWitt, D.R. Ballal, K.E. Binns, T.F. Williams, and S. Stouffer

5d. PROJECT NUMBER
3048

5e. TASK NUMBER
04

5f. WORK UNIT NUMBER
AM

7. PERFORMING ORGANIZATION NAME(S) AND ADDRESS(ES)
University of Dayton Research Institute
300 College Park
Dayton, OH 45469-0110

8. PERFORMING ORGANIZATION REPORT NUMBER
UDR-TR-2004-00007

9. SPONSORING/MONITORING AGENCY NAME(S) AND ADDRESS(ES)
Propulsion Directorate
Air Force Research Laboratory
Air Force Materiel Command
Wright-Patterson AFB, OH 45433-7251

10. SPONSORING/MONITORING AGENCY ACRONYM(S)
AFRL/PRTG

11. SPONSORING/MONITORING AGENCY REPORT NUMBER(S)
AFRL-PR-WP-TR-2005-2023

12. DISTRIBUTION/AVAILABILITY STATEMENT
Approved for public release; distribution is unlimited.

13. SUPPLEMENTARY NOTES
Report contains color. The appendices contain a number of journal articles and conference papers, resulting from Department of the Air Force contract number F33615-97-C-2719. Appendices M, P, S, V, and W are declared works of the U.S. Government and are not subject to copyright protection in the United States. The other appendices are copyrighted. The United States has for itself and others acting on its behalf an unlimited, paid-up, nonexclusive, irrevocable worldwide license. Any other form of use is subject to copyright restrictions.

14. ABSTRACT

This report is a compilation of highlights of research accomplishments completed under Contract No. F33615-97-C-2719, "Advanced Integrated Fuel/Combustion Systems," with the Air Force Research Laboratory, Propulsion Directorate, Turbine Engine Division. This report covers work performed during the period September 29, 1997 to December 31, 2003. Research efforts covered a wide range of topics toward development of advanced fuels and combustion systems. These efforts included High Heat Sink Fuels Studies, Low Temperature Fuel Studies, Fuel Modeling and Simulation, Particulate Emission Abatement Studies, and Well-Stirred Reactor Combustion Studies.

15. SUBJECT TERMS
Jet Fuel, JP-8, JP-8+100, Fuel Additives, Autoxidation, Thermal Stability, Deposition, Fuel Systems, Particulates, Combustion, Turbine Engines, Fuel, High Heat Sink Fuel, Low Temperature Fuel, Combustion Emissions, Emissions

16. SECURITY CLASSIFICATION OF:			17. LIMITATION OF ABSTRACT:	18. NUMBER OF PAGES	19a. NAME OF RESPONSIBLE PERSON (Monitor) / 19b. TELEPHONE NUMBER *(Include Area Code)*
a. REPORT	b. ABSTRACT	c. THIS PAGE			
Unclassified	Unclassified	Unclassified	SAR	314	Robert Morris (937) 255-3527

Standard Form 298 (Rev. 8-98)
Prescribed by ANSI Std. Z39-18

TABLE OF CONTENTS

LIST OF FIGURES

This Page Intentionally Left Blank

PREFACE

This final report was submitted by the University of Dayton Research Institute (UDRI) under Contract No. F33615-97-C-2719, sponsored by the U.S. Air Force Research Laboratory, Propulsion Directorate, Wright-Patterson AFB, OH. Mr. Robert W. Morris, Jr. of AFRL/PRTG was the Contract Monitor and Dr. Dilip R. Ballal of the Energy & Environmental Engineering Division of UDRI, was the Principal Investigator. This report covers work performed during the period September 29, 1997 to December 31, 2003.

The authors would like to acknowledge the support and encouragement of Mr. Bill Harrison, Dr. Tim Edwards, Mr. Bob Morris, Mr. Edwin Corporan, Ms. Pattie Pearce, and Ms. Cindy Obringer of the AFRL Fuels Branch and Dr. Mel Roquemore, Dr. Robert Hancock, and Dr. Joe Zelina of the AFRL Combustion Branch.

This Page Intentionally Left Blank

1. SUMMARY

This report is a compilation of highlights of research accomplishments completed under Contract No. F33615-97-C-2719, "Advanced Integrated Fuel/Combustion Systems," with the Air Force Research Laboratory, Propulsion Directorate, Turbine Engine Division. This report covers work performed during the period September 29, 1997 to December 31, 2003. Research efforts covered a wide range of topics toward development of advanced fuels and combustion systems. These efforts included High Heat Sink Fuels Studies, Low Temperature Fuel Studies, Fuel Modeling and Simulation, Particulate Emission Abatement Studies, and Well Stirred Reactor Combustion Studies.

This Page Intentionally Left Blank

2. INTRODUCTION

The University of Dayton is pleased to submit this final report to the Air Force Research Laboratory, Propulsion Directorate (AFRL/PR) under Contract No. F33615-97-C-2719, "Advanced Integrated Fuel/Combustion Systems." The goal of this program was to extend the technology base for development, validation, and fielding of high heat sink fuels, fire-safe fuel system components, novel low-emissions combustor designs, and optimum fuel/combustion system integration for use in 21st century aircraft and missile systems. An additional objective was to establish an experimental and theoretical database needed to understand fundamental processes associated with fuel development, hot fuel system components, low-emissions combustion, and fire suppression technologies. Such fundamental knowledge is necessary to validate and refine computer models for designing future high performance aircraft fuels, fuel system components, combustors, and turbines. This program was comprised of four parts: Part I, Fuel Research and Development; Part II, High Temperature and Pressure Fire-Safe Fuel System Components; Part III, Combustion Research and Development; and Part IV, Integrated Fuel/Combustion System Development and Demonstration. Research efforts covered a wide range of topics toward development of advanced fuels and combustion systems. These efforts included High Heat Sink Fuels Studies, Low Temperature Fuel Studies, Fuel Modeling and Simulation, Particulate Emission Abatement Studies, and Well Stirred Reactor Combustion Studies.

Here we highlight the research accomplishments during the program; provide a list of publications, presentations, honors, and awards; and provide copies of publications that show the most important research successes achieved during the research period.

This Page Intentionally Left Blank

3. HIGHLIGHTS OF FUEL STUDIES

3.1 High Heat Sink Fuel Studies

Jet fuel is not only the propellant, but also the primary coolant for many aircraft engines. With the development of next-generation propulsion systems, both the maximum heat flux and the overall bulk temperature that the fuel will experience will be significantly increased as compared to current standards. This poses a significant problem since current fuels can begin oxidize at temperatures as low as 140°C. This oxidation can result in the formation of undesirable carbonaceous deposits in both the fuel transfer and injection systems that can lead to increased maintenance as well as possible mechanical failure of the aircraft. Although it is possible to use specialty fuels that are less prone to deposit formation, it is not an economically desirable approach. Therefore, efforts are underway to develop additives, that when added at low concentrations to conventional jet fuels, enhance the thermal stability of the fuel. Here we report on our accomplishments toward the development of improved high temperature fuels and additives.

We explored novel test methods and additive methodologies for creation of a JP-8+225 fuel (Zabarnick, 2000). This work is built upon our previous success in development of JP-8+100. The increased temperatures and resulting increased oxygen consumption at JP-8+225 conditions is extremely challenging for development of test methods. Previous batch reactors, such as the ICOT system, cannot be used because the fuel will boil at these temperatures. We explored the use of the quartz crystal microbalance (QCM) system at elevated temperatures with oxygen injection after heat-up. The QCM experiments showed the efficacy in using high concentration of detergent and/or dispersant species for decreasing bulk and surface deposition. These higher concentrations are required due to the greater amount of polar and particulates produced at higher oxygen consumption levels.

We studied the possible use of pipeline drag reducing additives in jet fuel (Wohlwend et al., 2000). The use of drag reducing additives may be necessary due to the prediction that pipelines dedicated to jet fuels will be at 40% over-capacity in the next ten years. Additives provide a relatively inexpensive alternative to building more pipeline capacity. These additives are routinely used in various oil products including kerosene and gasoline. However in order to gain approval, drag reducing additives need to undergo appropriate testing to demonstrate that they do not cause deleterious impact to aircraft system components. In this work, we studied the effect of Baker Flo-XS drag reducing additive on the thermal stability of jet fuel in various test devices. It was found that the additive had no negative effect on thermal stability in neat fuel or in fuel containing the JP-8+100 additive package.

We developed methods for the evaluation of antioxidants for use in fuel using oxygen monitoring in the quartz crystal microbalance and chromatographic oxygen measurements in the near isothermal flowing test rig (Zabarnick et al., 1998). The ability of an antioxidant to delay oxygen consumption was chosen as a measure of performance. Various hindered phenol and amine antioxidants were evaluated.

We studied various aspects of jet fuel oxidation behavior, including the correlation between oxidation and deposition, the temperature dependence of oxidation and deposition, and studies of peroxy radical intercepting antioxidants and metal deactivator additives (Zabarnick and Whitacre, 1998). These studies showed a strong correlation between oxygen consumption and deposition, demonstrating the direct relationship between these phenomena. Temperature studies showed that while oxidation rate increases with temperature, surface deposition peaks at an intermediate temperature. In studies of jet fuel antioxidants, we found that rapid increases in oxidation rate occur upon consumption of these species. The antioxidant appears to be consumed by peroxy radicals. In studies of metal deactivator additives (MDA), we found that MDA is consumed during thermal stressing, and this consumption results in large increases in oxidation rate of metal containing fuels.

We explored the use of silylation agents as jet fuel additives for reducing oxidative deposition (Zabarnick et al., 1999). Silylation agents have the ability to react with the heteroatomic species, such as phenols, which have been implicated in deposit-producing mechanisms. Thus, they have the potential to chemically transform these species into relatively innocuous silylated products. In this work, we studied the effect that silylation agents have on jet fuel oxidation and deposition. We showed that these additives result in an increased oxidation rate and substantially reduced deposition. The increased oxidation rate is due to the removal of these heteroatomic species, which can act as antioxidants by intercepting peroxy radicals. The results showed that silylation agents may be useful as jet fuel additives for preventing oxidative deposition in advanced aircraft fuel systems, including endothermic fuel systems. Silylation agents have also been proven useful in helping to identify fuel components, particularly those detrimental to fuel thermal stability.

We explored the use of hydroperoxide decomposing species for inhibiting oxidation in jet fuel (Zabarnick and Mick, 1999). We found that hydroperoxide decomposing species, such as alkyl sulfides, do not slow or delay oxidation in hydrocarbon solvents at 140°C. However, when phenolic species are also present, such as those naturally occurring in fuel or by addition of hindered phenols, substantial delays in oxidation were observed. We used a pseudo-detailed chemical kinetic mechanism to provide insight into the oxidation process. The combination of hydroperoxide decomposer and hindered phenol can substantially inhibit oxidation of fuel under the conditions studied.

An isothermal oxidation apparatus (IOA) was modified to include an oxygen sensor so that both oxidation and deposition data can be measured for jet fuels that are thermally stressed (Grinstead and Zabarnick, 1999). This modification is useful for comparing the relative oxidation rates of jet fuels and fuels blended with additives. Antioxidants were evaluated in this apparatus by comparing the delay in the onset of oxidation at a given temperature in a fast oxidizing fuel. Other additive types, such as dispersants, were evaluated by their ability to reduce deposition.

We investigated the thermal oxidative stability of prototype coal-derived jet fuels in collaboration with the Energy Institute at The Pennsylvania State University (Badger et al., 2002). We found that these fuels exhibited oxidation characteristics that were similar to hydrotreated petroleum-derived fuels. There was no strong correlation between the makeup of the feedstocks and the oxidative stability. The fuels exhibited a wide range of deposit production, with the vast majority demonstrating good to excellent thermal oxidative stability. It was noted

that many of these fuels produced relatively dark colored deposits. These dark deposits could result in issues with using visual tube ratings in JFTOT testing of coal-derived fuels.

We demonstrated the utility of solid-phase extraction (SPE) techniques for the analysis of polar species in jet fuel (Zabarnick et al., 2002). SPE was used to separate and preconcentrate the polar fuel species. Elution of these species with a polar solvent and subsequent analysis by gas chromatography with mass spectrometric detection can provide information on the polar species present. In addition, the ability to follow the formation and/or removal of the species during thermal-oxidative exposure is invaluable in understanding the autoxidative mechanism that results in the formation of insolubles and deposits.

We conducted a variety of tests in the Extended Duration Thermal Stability Test (EDTST) system. The primary testing was conducted for evaluating JP-8+100 additive candidates. Other testing included the following:

1. Evaluation of copper effects on thermal stability for JP-8 fuels (Dieterle and Binns, 1998; Binns and Dieterle, 1999).
2. Evaluation of the effects of reduced oxygen on fuel thermal stability (Dieterle and Binns, 1998; Binns and Dieterle, 1998).
3. Evaluation of thermal stability effects of JP-8+100LT additives.
4. Evaluation of thermal stability effects of drag reducer additives (Wohlwend et al., 2000; Biddle et al., 2002; Wohlwend, 2000).
5. Evaluation of copper effects on the thermal stability of JP-5 fuels (Binns et al., 2001).
6. Thermal stability evaluation of JP-7 fuel to establish baseline data for JP-8+225 fuels (Binns and Dieterle, 1999).

A summary of the significant results of this EDTST testing are as follows:

1. Copper (250 ppb) resulted in doubling the deposition in the JP-8 fuels tested. The JP-8 +100 additive (Betz 8Q462) resulted in ten times lower deposition in the same fuel and copper level.
2. Tests of JP-8 fuel with the Betz 8Q462 additive at reduced oxygen levels (5%) resulted in higher deposition than with oxygen saturated fuel.
3. Another additive has passed the EDTST test for JP-8+100 additives. It will undergo further tests including: materials, full-scale engine, and aircraft evaluations.

We conducted a variety of tests in the Advanced Reduced Scale Fuel System Simulator (ARSFSS). The primary testing was for the evaluation of promising JP-8+100 additive candidates. The candidates evaluated had previously passed the screening tests of other smaller test systems or devices. The simulator was also extensively upgraded to provide a capability to evaluate air/fuel heat exchangers. The Northrop Grumman Corporation (under another USAF contract) designed and fabricated a subsystem for providing high temperature nitrogen to heat exchangers. An airflow and temperature control system was also provided. This subsystem was assembled in an enclosed compartment that was mounted on top of the engine compartment of the ARSFSS.

Testing conducted in the ARSFSS included the following:

1. Evaluation of JP-8+100 additive candidates (Morris et al., 2002).
2. Evaluation of the thermal stability effects of drag reducer additives (Wohlwend et al., 2000; Biddle et al., 2002; Wohlwend, 2000).
3. Evaluation of a unique air/fuel heat exchanger provided by the Northrop Grumman Corporation (Tibbs, 1998).
4. Hysteresis checks of valves for various EDTST tests.

A summary of the significant results of this testing are as follows:

1. A second additive has passed the ARSFSS test for JP-8+100 additives. It will undergo further tests including materials, full-scale engine, and aircraft evaluations.
2. A small-scale air/fuel heat exchanger successfully completed 325 aircraft mission cycles (approximately 600 hours) of testing. The heat exchanger experienced no mechanical or fuel related problems.

We patented a series of new additive combinations for inhibiting oxidation and peroxide formation in hydrocarbon liquids, such as jet fuels (Heneghan et al., 2002). This combination of a peroxy radical inhibiting species and a peroxide decomposing species results in extremely long oxidation delays. The additive combination works synergistically to slow oxidation beyond that obtained with the current state-of-the-art antioxidant techniques. This new additive combination could be useful to slow fuel degradation in storage or to improve thermal stability aboard aircraft.

USAF Captain Jeff Thornburg performed his AFIT M.S. thesis research in collaboration with UDRI using the System for Thermal Diagnostic Studies (STDS) (Thornburg, 1999). He instrumented the metal reactor with thermocouples to model the temperature profile in the reactor as a function of axial distance. He used this information to model how n-decane heats up and cracks in a thermal reactor. Based on the data he obtained in conducting these experiments, he changed the system design by adding forced convection (air stirring) to the reactor cavity. This changed the temperature profile so that the reactor was isothermal for 80-90% of the reactor length depending on the flow rate of liquid reactants used. Initial data for products of n-decane pyrolysis were obtained.

The System for Thermal Diagnostic Studies (STDS) was designed and constructed for examining short residence time (less than 5 seconds) high temperature (up to 700°C) thermal stress on small quantities of fuels. The system is used to screen the liquid or supercritical phase thermal stability of candidate fuels. For example, rocket fuels with strained ring energy are often not stable at temperatures above 300°C. This system was used to rank these fuels and additives to determine their stability (Striebich and Rubey, 1998). It was also used to study the formation of cyclic compounds and watch the growth of these compounds to form aromatics and eventually heavier compounds and/or carbonaceous material (Maurice and Striebich, 1998; Maurice et al., 1999; Wohlwend et al., 2001; Striebich et al., 1999).

The STDS was used to rank the supercritical phase thermal stability of rocket fuel candidates submitted by Edwards AFB (Wohlwend et al., 2001; Striebich and Lawrence, 2003). More than 10 candidate materials were evaluated in this study including quadricyclane, BCP, RP-1, RG-1, proprietary mixtures, JP-10 and others. The thermal stability of many strained ring compounds is relatively low (e.g., quadricyclane degrades at 300°C) and therefore may not be appropriate for use as coolants. Bicyclopropylidene was examined in more detail with regard to its thermal degradation products and mechanisms proposed for its degradation.

At temperatures above 400°C and at fuel system pressures, JP-8 and Jet A jet fuels exist as supercritical fluids. Fuel nozzles operating under conventional aircraft (subcritical) conditions atomize liquid fuel streams into droplets. The physical injection and mixing mechanisms associated with a nozzle operating under supercritical conditions are very different from those occurring under subcritical conditions. We have studied the flow of fuel at supercritical conditions through a simple nozzle into a region that is also at supercritical conditions (Doungthip et al., 2002; Ervin et al., 2000a). Schlieren images of supercritical jet fuel exiting a simple nozzle into an optical chamber were obtained in this work. In additional, computational fluid dynamics simulations of the flow were performed using *n*-decane as a surrogate fuel which has a critical temperature and pressure similar to the pseudo critical temperature and pressure of the jet fuel sample used in the experiments. The results of the computational fluid dynamics simulations and the measurements obtained from the recorded images showed that *n*-decane is a reasonable surrogate for Jet A fuel for predictions of the spreading angle and jet penetration length. In addition, the measurements and computations showed that jet penetration and spreading angle are dependent on the fuel exit temperature and mass flow rate. Lastly, we found that the penetration depth of a supercritical jet into the optical chamber is less than that for a subcritical jet with the same fuel mass flow rate and pressure conditions.

Within the JP-8+225 additive development program, we established the use of the ECAT Flow Reactor System for both performing fundamental studies and screening potential base fuels and chemical additives (DeWitt et al., 2002; DeWitt and Zabarnick, 2002) The currently qualified JP-8+100 additive package (Betz 8Q462) was used as the basis of comparison for all additive and fuel studies. The ECAT system had previously been used to evaluate the ability of additives to inhibit pyrolytic deposition of jet fuels, which is substantially different than the reaction conditions for the JP-8+225 regime. Therefore, modifications were made to the reactor system and operating methodology to accommodate the required experimental conditions; the primary requirement was complete consumption of the dissolved oxygen within the reaction zone. This system is currently the smallest flow reactor system at the AFRL/PRTG facility that can be used to perform experimental studies under a JP-8+225 reaction condition.

We investigated the use of antioxidant chemistry for use within JP-8+225 thermal stability additive packages. This approach has been extremely effective at inhibiting fuel deposition during partial oxygen consumption. We found that the use of antioxidants actually increased the rate of deposition under a complete oxygen consumption regime, as shown in Figure 1. This figure shows results for testing conducted on the ECAT with a neat JP-8 (POSF-3804) and the JP-8 with 500 mg/L of BHT. BHT is a hindered phenol which is typically used to delay oxidation during fuel storage; it is also used as a component in the JP-8+100 package. The addition of BHT significantly increased the overall total and maximum peak deposition during

testing. This result supported previous hypotheses that species formed via the reaction of the antioxidants participate or promote fuel deposition (Heneghan and Zabarnick, 1994) This type of dependence indicated that it may be necessary to remove antioxidants (or maintain at extremely low concentration) in JP-8+225 thermal stability additive packages.

We conducted preliminary testing of the use of peroxide decomposing species under a JP-8+225 condition, since the combination of these with antioxidants showed synergism which significantly reduced the relative rate of oxidation and deposition (Zabarnick and Mick, 1999). Figure 2 shows results of testing conducted with neat JP-8 (POSF-3804), the JP-8+100 additive package (256 mg/L), and JP-8+100 with 200 mg/L of triphenylphosphine (TPP), which is known to decompose peroxides. The addition of TPP further reduced the peak deposition relative to the JP-8+100, but also shifted the onset of deposition to lower temperatures. In addition, there was an increase in surface deposition at temperatures where significant reaction would not be expected. This behavior was opposite the result that would be expected if the combination of the TPP with an antioxidant (BHT in the JP-8+100) delayed the rate of oxygen consumption. It was proposed that the addition of the TPP either increased the overall oxidation rate within this reaction regime (e.g., earlier on-set of deposition) or the TPP chemically and/or physically interacted with the reaction wall tubing. The latter could result in the “in-situ” passivation of the tubing surface rendering significantly lower deposition for longer reaction times. An important result from this testing was that alternate chemistries can be used to improve thermal stability characteristics beyond that of the JP-8+100 additive package.

We studied the use of dispersants and detergents to inhibit surface and bulk deposit formation under JP-8+225 conditions This type of functionality is included in the current JP-8+100 package (JP-8+100 includes the GE-Betz dispersant 8Q405 at a concentration of 100 mg/L) (Heneghan et al., 1996). It was believed that it may be necessary to further exploit these characteristics due to the limited application of antioxidant chemistries under a JP-8+225 condition, as previously discussed. Figure 3 shows results of testing conducted on the ECAT with neat JP-8 (POSF-3804), JP-8+100 (256 mg/L), and JP-8 with 1,000 mg/L of the 8Q405 dispersant. By increasing the dispersant concentration by a factor of 10 (relative to the JP-8+100), the neat JP-8 surface deposition was reduced below that of the JP-8+100. This demonstrated that beneficial reductions in deposition are achieved by increasing the dispersant concentration. Additional benefits may possibly be realized via the inclusion of species that selectively interact with material surfaces and further prevent surface adhesion (e.g., metal deactivators).

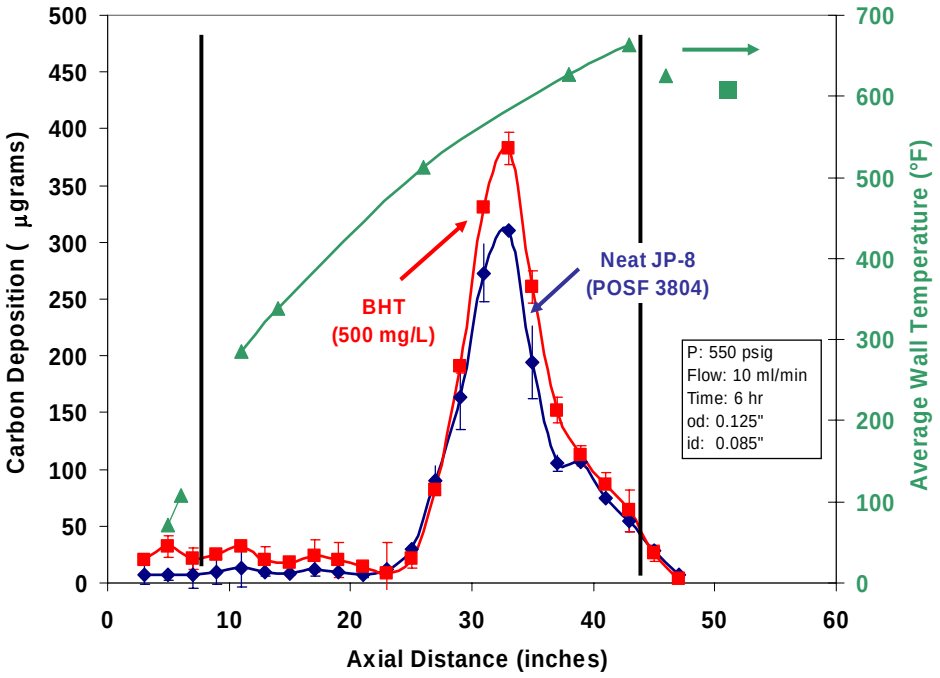

Figure 1. Measured carbon deposition and average wall temperature as a function of position for testing conducted with a neat JP-8 (POSF-3804) and JP-8 with 500 mg/L BHT in the ECAT Flow Reactor System.

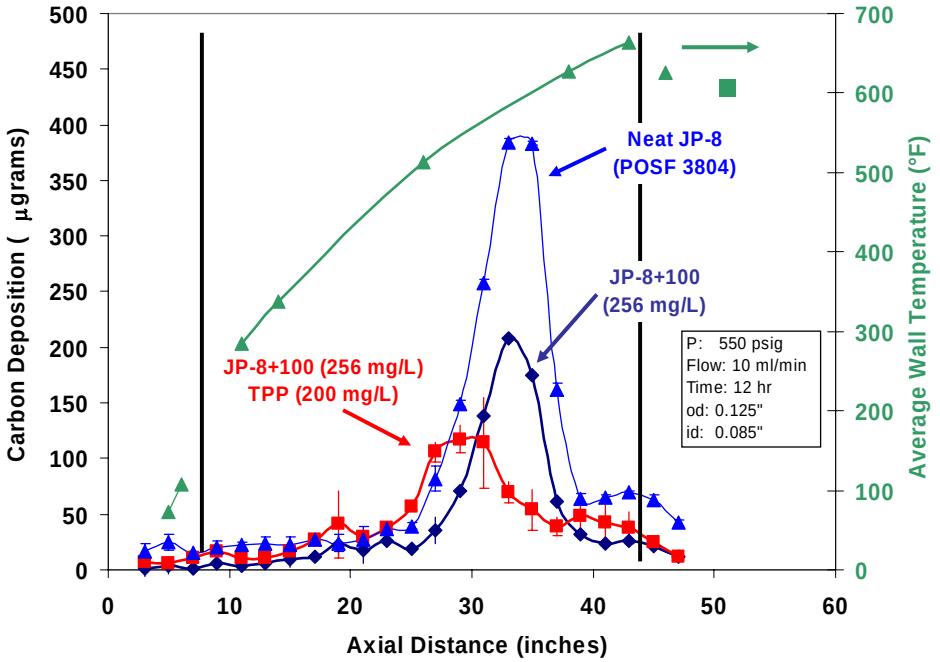

Figure 2. Measured carbon deposition and average wall temperature as a function of position for testing conducted with a neat JP-8 (POSF-3804), the JP-8+100 additive package (256 mg/L), and JP-8+100 with 200 mg/L triphenylphosphine in the ECAT Flow Reactor System.

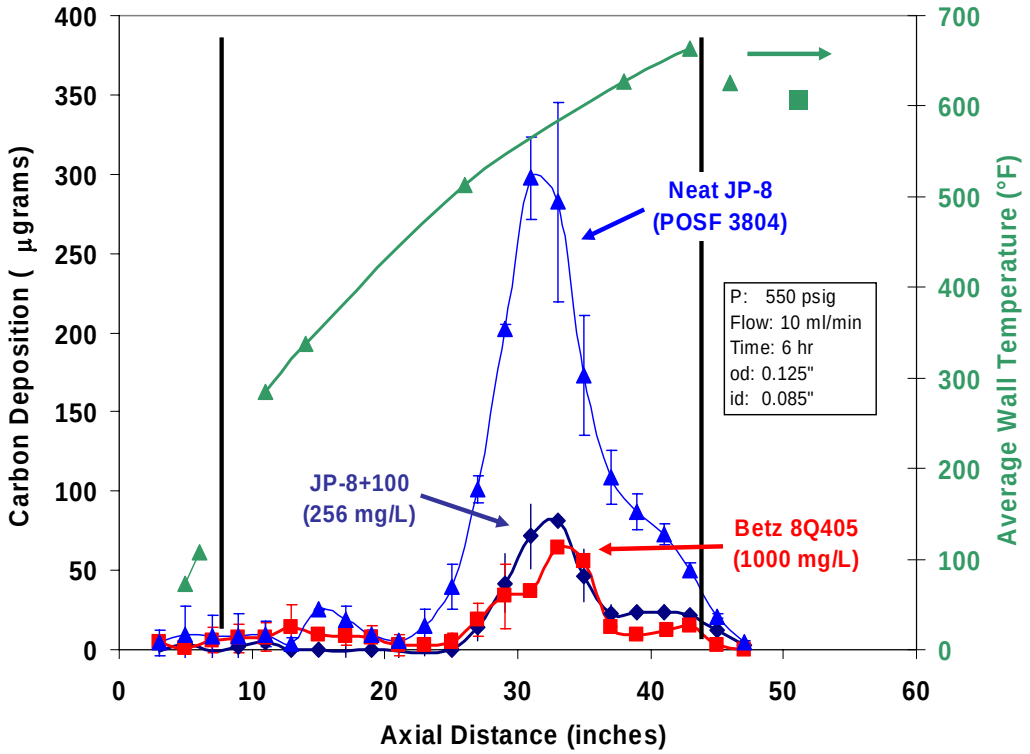

Figure 3. Measured carbon deposition and average wall temperature as a function of position for testing conducted with a neat JP-8 (POSF-3804), JP-8+100 (256 mg/L), and JP-8 with 1000 mg/L Betz 8Q405 dispersant in the ECAT Flow Reactor System.

We conducted studies on the ECAT to investigate the effect of the base fuel chemical composition on the overall thermal stability under a JP-8+225 condition. Specifically, the thermal stability characteristics of fuels that were produced synthetically via Fischer-Tropsch (FT) chemistry were evaluated due to their potential production for future applications. Figure 4 shows results of testing conducted on the ECAT with a neat JP-8 (POSF-3804), a neat JP-7 (POSF-3327), a 50/50 blend of a JP-5 with an S5 fuel produced by Syntroleum (POSF-4409), a 50/50 blend of a Jet-A with a FT fuel produced by Sasol (POSF-4285), and a FT fuel produced by NETL (POSF-4303). on for future applications. The JP-7, blends of synthetic fuels, and the pure FT fuel all showed significantly improved thermal stability characteristics as compared to the neat JP-8 fuel. These differences indicate that there are certain chemical functionalities within the JP-8 fuel that promote unfavorable deposition chemistry that are not contained in the other fuels. Identifying these species will assist in deconvoluting the complicated processes of fuel oxidation and deposition chemistry and assist in developing viable thermal stability strategies for JP-8+225 conditions. These studies also demonstrated the potential benefits of using (or blending) synthetically produced fuels with JP-8 to obtain enhanced thermal stability characteristics.

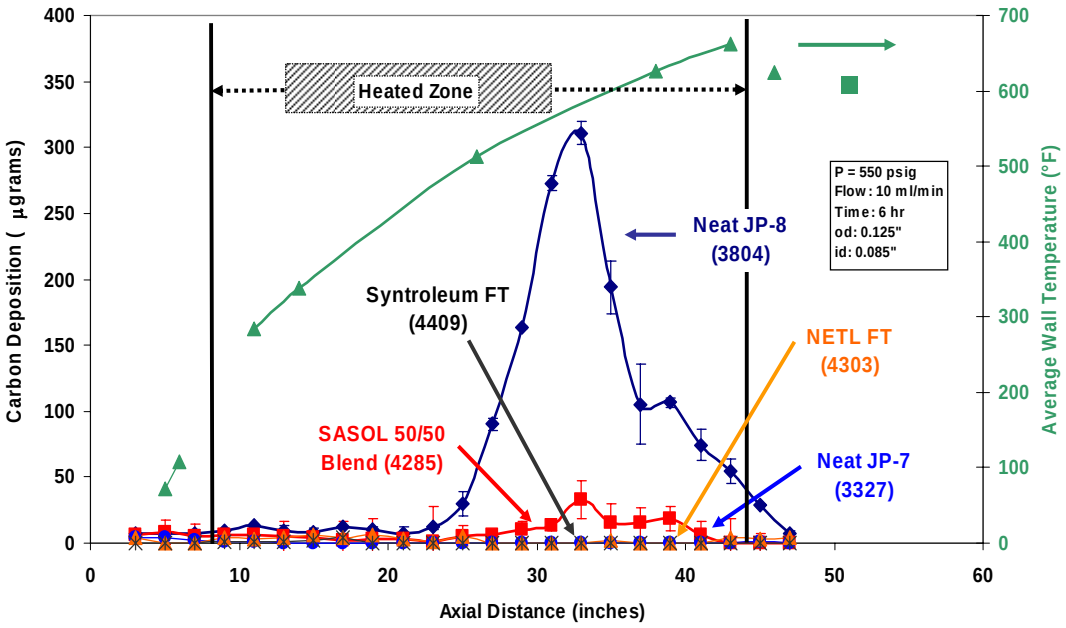

Figure 4. Measured carbon deposition and average wall temperature as a function of position for testing conducted with neat JP-8 (POSF-3804), neat JP-7 (POSF-3327), a 50/50 blend of a JP-5 with a S5 fuel produced by Syntroleum (POSF 4409), a 50/50 blend of a Jet-A with a FT fuel produced by Sasol (POSF-4285), and a FT fuel produced by NETL (POSF 4303) in the ECAT Flow Reactor System.

We investigated the use of non-additive (e.g., “engineering”) approaches to improve heat sink capabilities of fuels. The use of these engineering approaches is particularly attractive since it could be possible to use currently available fuel and additive technologies without the undesirable degradation of the fuel. We performed experimental studies to investigate the use of surface coatings to inhibit the formation of carbonaceous surface deposits, particularly during the initial stages of deposition (Ervin et al., 2003). One specific coating treatment involved the chemical vapor deposition of a proprietary silica-based layer that has a thickness of approximately 10,000Å (Silcosteel, produced by Restek). Studies using surface coatings showed a shift in the onset of deposition with minimal deposition within the reaction zone. Since there is still complete oxygen consumption in the reaction zone, these results indicated the deposit precursors that are formed may undergo alternate reaction pathways rather than adsorbing on tubing surfaces. Since the silica layer is not believed to contribute significant resistance to heat transfer (e.g., the surface and bulk fuel temperatures are not affected), these results also showed that the treatment reduced the catalytic oxidation of the parent fuel and inhibited surface chemisorption or physisorption. These explanations are supported by previous observations of untreated stainless steel surfaces promoting catalytic oxidation and deposition pathways. Overall, the use of surface treatments could be beneficial for reducing the initial and subsequent rates of surface deposition within various systems. Possible implementations of this technology could be treatment of all surfaces in the fuel system or in a specific unit designed to selectively consume the dissolved oxygen.

We performed feasibility testing to evaluate the use of currently available thermal stability additives with potential engineering strategies since it may be necessary to combine these methods to achieve required heat sink capabilities for future applications. Specifically, long-duration testing using the JP-8+100 additive package, inert surface treatments, and deoxygenation of the parent fuel, was conducted. Figure 5 shows the total surface deposition for long-duration studies conducted using the Phoenix Rig Flow Reactor System. Tests were conducted using a neat JP-8 (POSF-3804), a neat JP-7 (POSF-3327), and the JP-8+100 with silcosteel-treated reaction tubing and deoxygenation of the parent fuel. The deoxygenation of the JP-8+100 was accomplished via nitrogen sparging of the fuel reservoir (Ervin and Williams, 1996). The reaction conditions were specified to ensure complete oxygen consumption within the reaction zone. The neat JP-8 test was stopped after 71 hours due to excessive deposition that plugged the reaction tubing. With the addition of the JP-8+100 additive package, inert surface treatment, and deoxygenation, the neat JP-8 deposition was reduced by over a factor of 50 for an extended reaction time of 200 hours (to the level of the neat JP-7). This result demonstrated that JP-8 type fuels can achieve JP-7 thermal stability characteristics using currently available additive chemistries together with viable engineering strategies. Significant advancements must be made to implement effective engineering strategies on-board future aircraft and missile applications; however, this study demonstrated that enhanced thermal stability characteristics can be achieved. In addition, this result indicates that the combination of thermal stability additives and engineering approaches may be required to achieve the ambitious goals that are needed for future applications.

We performed studies to investigate the use of the High Reynolds Number Thermal Stability (HiReTS) Tester produced by Stanhope-Seta for use as a preliminary screening device within our JP-8+225 thermal stability program (DeWitt et al., 2003). The HiReTS is designed to evaluate the thermal stability of JP-8 fuels under standard temperature conditions We attempted to adapt the operating protocol to accommodate a JP-8+225 condition (i.e., complete consumption of dissolved oxygen in reaction zone). This included significantly increasing the operating wall temperature and fuel residence time as compared to the standard conditions. We found that general trends in the thermal stability of the fuels/additives tested were consistent with those observed in the ECAT, with the exception of testing with antioxidants. These decreased the surface deposition on the HiReTS but increased them in the ECAT. This result indicated that there was only partial oxygen consumption within the reaction zone for the HiReTS while there was complete consumption on the ECAT. The partial oxygen consumption hypothesis was verified via the use of computational fluid dynamic modeling. Since it is imperative that preliminary evaluation be performed under conditions where consistent experimental trends are observed, the current HiReTS can most likely not be used as a primary development/screening instrument within our JP-8+225 program. Therefore, we will continue to design and develop a system that provides optimal performance for the experimental regime of interest.

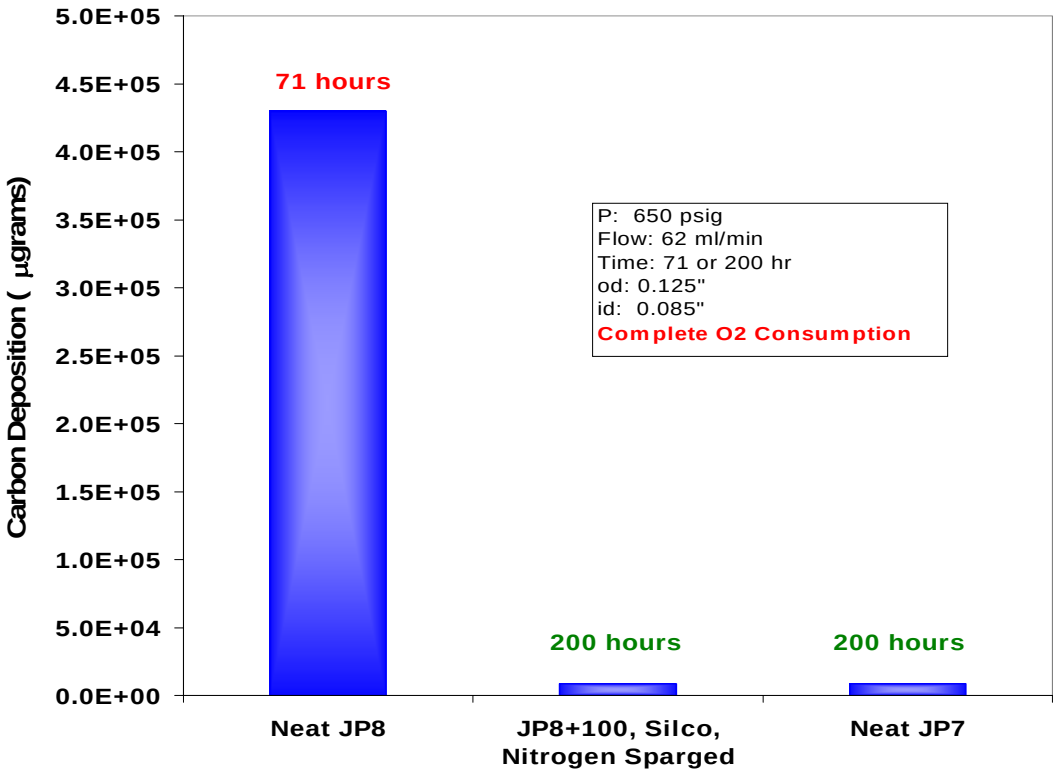

Figure 5. Total carbon deposition for long-duration testing in the Phoenix Rig Flow Reactor System with a neat JP-8 (POSF-3804), a neat JP-7 (POSF-3327), and JP-8+100 with silcosteel reaction tubing and deoxygenation.

3.2 Low Temperature Fuel Studies

Aircraft operation at high altitude can subject jet fuel to extremely low temperature conditions. At such temperatures, fuels have an increased viscosity which limits the ability of the fuel to flow and, at the lowest temperatures, may result in partial solidification of the fuel due to freezing. JPTS is a specialty fuel that has excellent thermal-oxidative stability characteristics and a low freeze-point temperature. Unfortunately, JPTS costs roughly three times as much as the more readily available JP-8 fuel. In addition, replacement of JPTS with JP-8 has important logistical advantages. Thus, it would be advantageous to have a JP-8 fuel that has thermal-oxidative and low-temperature characteristics that are similar to those of JPTS. The JP-8+100 additive package that has been developed previously provides JP-8 fuels with low surface deposition characteristics. However, enhancement of the low-temperature behavior of JP-8 has not been addressed. Our research has considered the potential of developing low-temperature additives for JP-8+100 fuel which provide the same performance as JPTS (Ervin et al., 1999; Ervin et al., 2001). Currently, jet fuel low temperature properties are defined by specification of freeze point and viscosity. The use of the cold flow additives requires a new approach in that the fuels may no longer be a single-phase liquid but could potentially be a liquid phase with a second dispersed solid phase of small crystals. Fundamental laboratory experiments were performed in parallel with additive screening tests in order to increase our understanding of how newly developed low-temperature additives work. In addition, we began the development of

computational models to assist our understanding of both fundamental experiments and screening tests.

Studies were conducted to investigate the use of urea treatment for improving the low temperature properties of jet fuel (Zabarnick and Widmor, 2002). In particular, we utilized differential scanning calorimetry (DSC), cold-stage microscopy, and ASTM freeze, cloud, and pour-point testing to characterize the changes in the fuel that occur upon urea treatment. We also used gas chromatography (GC) to study both the qualitative and quantitative changes that occur in the chemical constituents of the fuel. These studies show that urea treatment in the presence of an activator species, such as methanol, is quite selective and effective at removing long chain n-alkanes. The resulting fuel shows a substantial decrease in crystal formation observed via DSC and cold-stage microscopy. The fuel also displays a significant reduction in the measured pour and cloud points. Some of the practical issues in using urea treatment for jet fuel are also discussed.

As a part of our low-temperature studies, we developed a unique low-temperature optical cell for the visualization of fuel freezing (Atkins and Ervin, 2001). JPTS, kerosene, Jet A, and additized Jet A samples were cooled below their freeze point temperatures in the rectangular, optical cell. Images and temperature measurements recorded during the solidification process provided information on crystal habit, crystallization behavior, and the influence of the buoyancy-driven flow on freezing. As a part of this research, the *n*-alkane compositions of the fuel samples were determined. The Jet A sample contained the smallest total *n*-alkane mass. The cooling of JPTS resulted in the lowest wax volume, while the cooling of kerosene yielded the greatest wax volume. The JPTS and kerosene samples exhibited similar crystallization behavior and crystal habits during cooling. Low-temperature additives were found to modify the crystal habit of the Jet A fuel, making the crystals more likely to flow relative to those of the neat fuel.

Differential scanning calorimetry (DSC) was used to study the freezing of jet fuel and the effect of cold flow improving additives (Zabarnick and Widmor, 2001). We found that the cooling (freezing) exotherm is a more useful diagnostic tool for this purpose than the heating (melting) endotherm. Jet fuels (Jet A, JP-8, and Jet A-1) display a strong exotherm upon cooling between -45 and -60°C. By the study of mixtures composed of classes of jet fuel components (normal paraffins, isoparaffins, and aromatics), we found that the cooling exotherm is primarily due to the liquid-solid phase transition of the normal paraffins. Cold flow improving additives (e.g., pour point depressants) show only small effects on the DSC exotherm despite larger effects observed in cold flow devices. This indicates that these additives work primarily by affecting the habit of the n-alkane crystals. This change in crystal habit is supported by low-temperature microscopy studies.

We studied changes in jet fuel properties at low temperatures using the scanning Brookfield viscometer; pour, cloud, and freeze point measurements; and differential scanning calorimetry (DSC) (Zabarnick and Vangsness, 2002). We demonstrated how changes in viscosity correlate with other property measurements, such as cloud point. One goal of this work was to enable use of these measurements in predicting operability of fuel tanks and systems at low temperature. In addition, we were able to show that these measured properties change upon addition of additives that attempt to interfere with crystallization of the large normal alkanes present.

In studies of jet fuel freezing, we investigated the use of a thermodynamic phase equilibrium model to predict the freeze point temperatures of jet fuel samples (Widmor et al., 2002). This model uses the normal alkane distribution of the fuel sample as input and predicts the freeze point temperature, as well as the distribution of normal alkanes in the liquid and solid phases as a function of temperature. We found that the calculation is very sensitive to the binary interactions parameters used for the activity coefficient calculations. In particular, new techniques for determination of binary interaction parameters for the solid phase species need to be created for improved predictive capabilities for jet fuels.

To provide improved binary interaction parameters for thermodynamic phase equilibrium models of jet fuel crystallization, we investigated the use of molecular modeling techniques (Heltzel et al., 2002). Initially, conformational analysis molecular dynamics methods were used to estimate the interaction energies between normal alkane pairs. The use of molecular mechanics energy minimization of normal alkane crystals resulted in improved results. Future work to refine these techniques will result in improved ability to predict jet fuel low temperature behavior versus temperature.

Differential scanning calorimetry (DSC) was used to detect phase transitions in the cooling of jet fuels (Widmor et al., 2003). In addition, the DSC demonstrated differences in the low-temperature characteristics of two Jet A fuel samples and a JPTS fuel. By varying the cooling rate over a large range, the effect of supercooling on crystallization within jet fuel was shown to be important. In addition, correlations for liquid-to-solid phase-change kinetics were developed. The DSC can be used to develop kinetic models of fuel crystal formation and growth and can provide specific heat measurements. We found that both kinetic growth models and specific heat measurements are important for the development of engineering computational fluid dynamics models of fuel freezing. The cold-stage microscope provided information concerning crystal morphology that varies with cooling rate and can also be used in future numerical simulations that involve multiphase flows.

We developed a new and simple experimental technique to screen cold fuel additives rapidly (CAST – Cold fuel Additive Screening Test). The CAST system consists of twelve 500 mL flasks. The flasks are connected in pairs by a 1/4" tube, one flask is open to atmosphere while the second flask is sealed, and connected to an external vacuum source. A type-“T" thermocouple monitors the fuel temperature near the bottom of the flask. The CAST assembly is placed in an environmental chamber and adjusted to the test temperature. Application of vacuum pulls the additized fuel from one flask to the other. The measured flow rate and final mass transferred, ranks the additives as to their ability to reduced holdup (i.e., fuel that is solidified to a point that it will not transfer) and their flow characteristics at the test temperature. This screening technique has greatly accelerated the additive evaluation process and has successfully ranked several hundred additives and additive/fuel combinations.

We designed and built a small glass simulator that can replicate the temperature conditions found in a wing section. The simulator allows for visualization of the effects of low temperatures on fuels under static and flowing conditions. The simulator permits separate temperature control of the top, bottom, and sidewall surfaces, as well as, the bulk fuel inlet (during flow testing). A removable insert, that models a wing’s flow passage geometry, has been instrumented with a

thermocouple rake to allow for studies of flow blockage due to fuel crystallization at very low temperatures (Figure 6). Experiments with JP-8 and JPTS show not only a difference in crystallization temperature, but also crystal structure (Figure 7). Studies of fuel crystallization (i.e., fuel freezing), with and without an ullage, show a significant reduction in the amount of crystallization do to the thermal barrier produced by the air gap. Dye injection tests have also shown the changes in flow patterns due to the variations in density and viscosity at different temperatures. The small-scale glass wing simulator fills the gap between large tank simulators and bench-top experiments for CFD model validation.

3.3 Development of Fuel Analysis Techniques

Improved fuel analysis techniques are required to enable progress in every area of fuels research including high heat sink fuel and additive development, improved low temperature fuel development, and field problems studies. Here we highlight some of our more important accomplishments in the development of new advanced fuels analysis techniques.

The quantitative analysis of phenolic and amine-containing petroleum additives can be challenging. One such compound, N,N'-disalicylidene-1,2-propanediamine, a common metal deactivator additive (MDA) inhibits fuel oxidation catalyzed by metals both in the fuel and on surfaces. The ability to measure the concentration of MDA in storage stability tests, thermal-stressing studies, and field samples is important. Quantitating low concentrations of MDA can be difficult because of surface adsorptivity due to the phenol and amine functional groups. We described the shortcomings of direct-injection gas chromatography-mass spectrometry to quantitate MDA as well as a solution to the analytical problem using the common silylation agent BSA to derivatize the MDA (Striebich et al., 2000a). The silylation technique is suitable for the determination of MDA concentrations in aviation fuel samples and suggests that the MDA may be readily determined in other petroleum products with a lower detection limit for MDA of 0.5 mg/L. Measurements conducted in heated batch reactors indicated that the MDA concentration is reduced as hydrocarbon fuels are stressed. In addition, only free or available MDA is measured by this technique, not MDA that is complexed with metals.

We pursued the development of microbore column gas chromatography techniques for use in screening jet fuel quality (Rozenzhak et al., 2002; Striebich, 2002; Motsinger and Striebich, 2003). By using short 0.10 mm ID capillary columns, the speed of analysis was lowered to less than five minutes with adequate resolution to distinguish many of the important peaks (e.g., n-alkanes). By performing these analyses fast with FID and flame photometric detection, we were able to develop correlations of GC compositional data to flash point, freeze point, sulfur content, and simulated distillation (all four specification properties of interest). A dedicated GC was purchased for this project, modified, and shipped to screen fuels in a forward operating location. Correlations to GC data allowed us to predict four specification tests accurately in about five minutes.

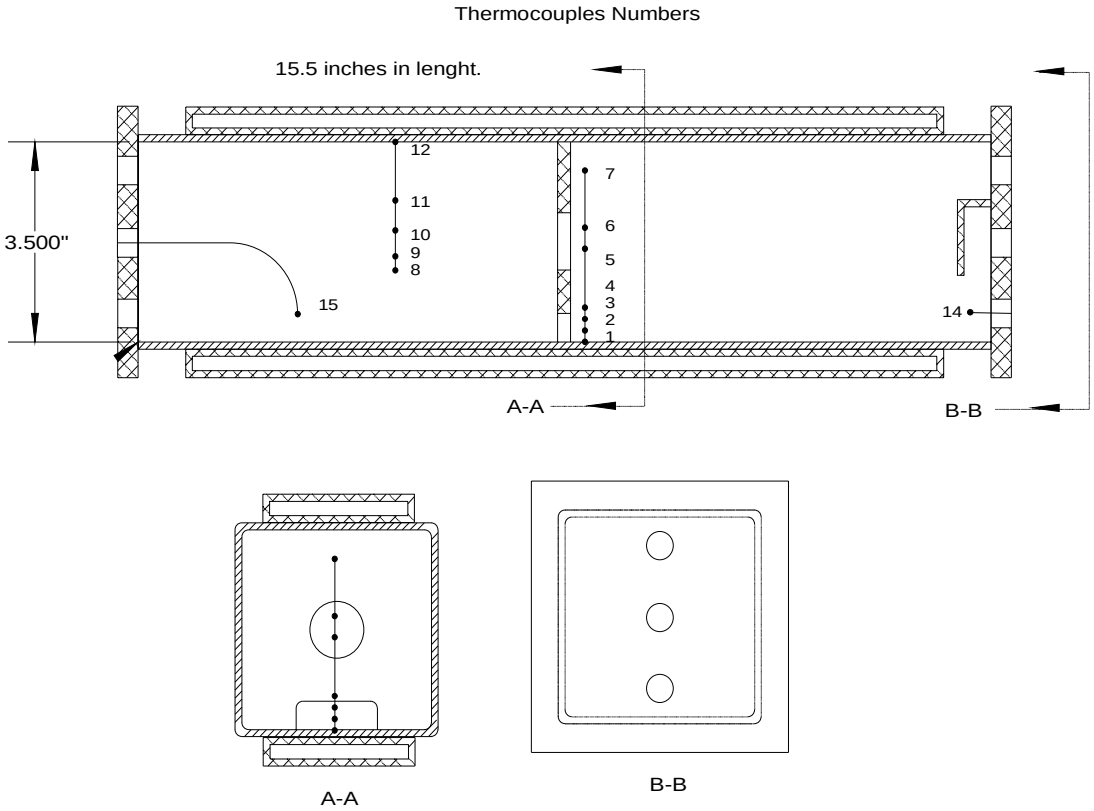

Figure 6. Upper drawing shows the glass wing simulator design. Bottom picture shows a standard test: fuel crystals blocking the bottom slot and covering the top portion of the wing. Test parameters: Fuel JP-8 3804, Flow 240 ml/m, Side Walls at –47°C, Top & Bottom at –60°C.

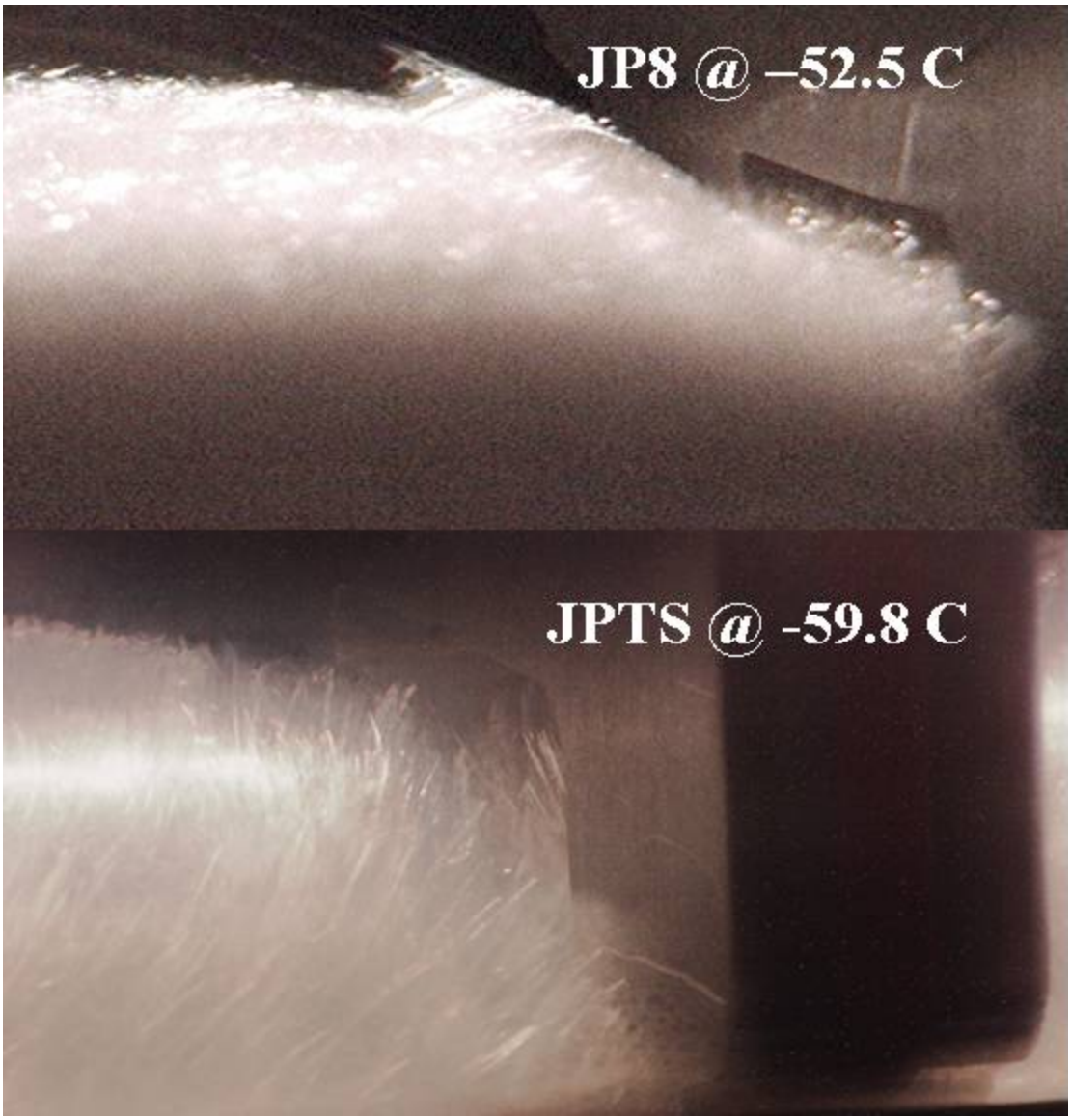

Figure 7. Comparison of fuels at point where blockage of flow slot occurs, fuel temperature measured in front of slot. Test parameters: Fuel JP-8 3804 and JPTS, Flow 120 ml/m, Side Walls at –47°C, Top & Bottom at –60°C.

Multi-dimensional gas chromatography with mass spectrometric detection (MDGC-MS) is currently being developed at UDRI under EPA funding. However, applications of MDGC were performed in the current program for complex mixtures such as solid-phase extraction (SPE) samples, jet fuel mixtures, and synthetic fuels (e.g., Fischer-Tropsch liquids). We examined some of these samples and developed a polarity separation for alkanes, aromatics, and polars (Contreras and Striebich, 2003). We also used this technique to identify components in polar fractions which were of interest: phenols, anilines, BHT, etc. We will be upgrading the MDGC setup to include a Time of Flight Mass Spectrometer which will allow us to conduct fast GC separations with MS identification of peaks in one minute or less.

We developed analysis techniques for polar species in jet fuel by HPLC. We showed that, for most fuels studied, a direct relationship exists between the amount of polar species present in the unstressed jet fuel and the amount of surface deposit the fuel forms upon thermal stressing (Balster et al., 2002). Also, by coupling the HPLC polar species technique with GC-MS, we were able to show that the majority of the polar species present in neat fuel are phenols, but that nitrogen species such as anilines, indoles, and pyridines also exist in significant amounts in some neat fuels. These results are important for our overall understanding and, eventually, prediction of thermal stability behavior in jet fuel.

We developed techniques for sulfur analysis using GC-MS, GC-AED and multidimensional GC-MS, as well as HPLC and SPE sample prep followed by these techniques (Link et al., 2002a; Link et al., 2002b; Link et al., 2003). These techniques were developed in anticipation of the changes in jet fuel quality with the advent of FT liquids. FT liquids will be very low in sulfur but may be blended with sulfur containing fuels. We want to understand which sulfur compounds are important in thermal stability, lubricity, and combustion efficiency. We analyzed fuels via GC-AED before and after stressing on several thermal stability devices. We also examined saturate, aromatic, and diaromatic fractions for sulfur containing compounds, to determine where the bulk of the sulfur compounds may be contained. We also developed a technique for determination of reactive and inert sulfur compounds in fuels.

The measurement of dissolved water in jet fuel was examined using GC-TCD analysis (Anderson et al., 1997; Rubey et al., 1998). This technique is fairly simple, as it requires only a thick phase GC column and a modulating TC detector. Fuels can be injected neat at high split ratios to accurately measure dissolved water. Applications included the analysis of water for fuel containing the current JP-8+100 additive (a detergent/dispersant). The water concentration of the fuels with this powerful additive did increase significantly due to the ability of the additive to disperse polar compounds (such as water) within the fuel matrix.

Polars species in jet fuel are related to thermal instability, and are thus important to measure and identify. Polar compounds can be extracted from fuel by solid phase extraction or HPLC for analysis. SPE using silica gel cartridges and alumina cartridges have been used to collect different fractions depending on the polarity of the compounds being removed (Zabarnick et al., 2002). These normal phase media were eluted with toluene and/or methanol to obtain polarity fractions, each of which contain different compounds. Some examples of compounds isolated thus far are: MDA, alkyl phenols, anilines, carbazoles, moderately polar sulfur compounds, multi-ring aromatics, and BHT.

We did a limited amount of work characterizing emissions and stressed mixtures from other contractors and consultants, such as TDA and ISSI (Wickham et al., 1998; Jones et al., 1999). We examined a number of mixtures of decane, decomposed in a high temperature, high pressure system to evaluate the change in structure of decane to alkane/alkene mixtures, and then to cyclized products (cyclohexane/cyclohexene), and finally to aromatic compounds such as benzene and naphthalene. This category of work also included the analysis of the disappearance of n-paraffins from Norpar as a function of pressure at supercritical conditions.

3.4 Fuel Modeling and Simulation

The development of improved modeling and simulation enables more efficient use of fuel in air vehicles. In addition, improved models can increase our understanding of the fundamental chemistry and physics that are involved in operation of complex fuel systems. Here we highlight our important accomplishments in science and engineering modeling and simulation towards the development of improved fuel, fuel additives, and fuel systems.

We developed a unique pseudo-detailed chemical kinetic mechanism for modeling of jet fuel oxidation (Zabarnick, 1998). This included chemistry of peroxy radical inhibiting antioxidants and hydroperoxide decomposing species. The model has the potential to be able to differentiate between these two types of oxidation slowing species. In addition, the model predicts that the presence of these types of species result in a synergistic slowing of oxygen consumption. The model showed good agreement with the oxidation behavior observed in laboratory experiments. The model predicted increases in oxygen consumption rate upon consumption of antioxidant species, in good agreement with experiments.

We combined pseudo-detailed chemical kinetic mechanisms of jet fuel oxidation with computational fluid dynamic techniques to explore prediction of jet fuel oxidation in complex flow systems (Ervin and Zabarnick, 1998). Dissolved oxygen and hydroperoxide measurements were calculated and compared with measurements in isothermal and non-isothermal flow devices. These were performed for two different fuel types and the calculations showed reasonable agreement over a range of fuel temperatures and flow rates.

For purposes of aircraft design, it is important to understand and predict jet fuel oxidation and the resulting surface deposition. Detailed multi-dimensional numerical simulations are useful in understanding interactions between the fluid dynamics and fuel chemistry. Unfortunately, the detailed simulation of an entire fuel system is impractical. One-dimensional and lumped parameter models of fluid dynamics and chemistry can provide the simultaneous simulation of all components which comprise a complex fuel system. We developed a simplified one-dimensional model of jet fuel oxidation and surface deposition within cylindrical passages (Ervin et al., 2000b). Both global and pseudo-detailed chemical kinetic mechanisms were used to model fuel oxidation, while a global chemistry model alone was used to model surface deposition. Dissolved O_2 concentration profiles and surface deposition rates were calculated for nearly isothermal and non-isothermal flow conditions. Our simulated dissolved O_2 concentrations and surface deposition rates agreed reasonably well with measurements over a wide range of temperature and flow conditions. Our new model is computationally inexpensive and represents a practical alternative to detailed multi-dimensional calculations of the flow in cylindrical passages.

We developed a methodology for using a pseudo-detailed chemical kinetic model for predicting jet fuel oxidation and deposition behavior in actual fuel systems (Balster et al., 2003). The model utilizes a chemical kinetic mechanism that represents jet fuel as a collection of species classes that have important functions in jet fuel oxidation and deposition processes. The influence of heteroatomic species classes (i.e., molecules containing oxygen, nitrogen, or sulfur) on these processes was emphasized. Particular attention was paid to two of the important heteroatomic

species classes in jet fuel: peroxy radical inhibiting species (represented by AH in the model) and peroxide decomposing species (represented by SH in the model). The mechanisms by which AH and SH are believed to influence jet fuel oxidation and deposition behavior were discussed. In addition, methods were discussed for quantitating AH and SH. Quantitative values of AH and SH will ultimately be used as inputs for the chemical kinetic model. The variation of the initial concentrations of AH and SH in the model is expected to capture many of the unique differences among jet fuel samples, in terms of their oxidation and deposition behavior. The reasons AH and SH are important to jet fuel behavior, as well as the identities of species which could comprise AH and SH in jet fuel, were also explored. It was also shown that the oxidation and deposition behavior of several jet fuel-like liquids and several actual jet fuels can be successfully modeled by utilizing this methodology.

Using the images and temperature measurements obtained from the fabrication of the low-temperature optical cell, we initiated the development of a computational fluid dynamics model to simulate the freezing of jet fuel in a buoyancy-driven flow (Atkins and Ervin, 2003). The objective of this research was to improve the understanding of the interactions between the flow and the phase change dynamics which would ultimately be used to assist the development of advanced thermal management tools or in the study of low-temperature additives. The proposed model incorporated DSC measurements of the specific heat of individual fuel samples along with measured values of the viscosity. Images and surface temperatures were recorded during the solidification process. The images recorded during solidification tracked the advancing freezing front and, thus, the influence of the buoyancy-driven flow. In addition, it was observed that the additized Jet A fuel developed a population of suspended particles that was much greater than that of the neat Jet A fuel. We have demonstrated that our newly created model can predict the shape and volume of the solidifying fuel.

Global reaction mechanisms have been used routinely in the simulation of thermal-oxidative jet fuel degradation. These mechanisms are many times calibrated using one set of conditions, such as flow rate and temperature. New conditions are then calculated by extrapolation using the global expressions. Inspection of the origin of global oxidation rate constants reveals that for systems that undergo autocatalysis or auto inhibition, a simple overall global activation energy and reaction order are not good descriptors of the reaction process (Ervin and Heneghan, 1998). Furthermore, pseudo-detailed chemical kinetic modeling of a fuel that experiences autocatalysis shows that the observed reaction order for oxygen consumption varies with the initial dissolved oxygen concentration, extent of reaction, and temperature. Thus, a simple global rate expression used to describe dissolved oxygen consumption in an autoaccelerating system is insufficient to allow extrapolation to different temperature or time regimes.

The enormous complexity of an aircraft fuel system precludes simultaneous detailed CFD simulation of all system components. As an alternative approach, system level modeling views the flow through most components as having spatially lumped properties. Multi-dimensional effects are typically approximated by friction factors and heat transfer coefficients. We have developed system components for the commercially available software, EASY5 (Engineering Analysis System 5, Boeing Corp.), to predict the transient system behavior of the Advanced Reduced Scale Fuel System Simulator (ARSFSS) and the Phoenix Rig. Fluid properties such as density, viscosity, thermal conductivity, enthalpy, and specific heat were calculated by linking

FORTRAN property subroutines with EASY5 (Acosta, 1995). These subroutines provided the physical and thermodynamic properties of hydrocarbon mixtures as a function of composition, temperature, and pressure. Steady-state and transient simulations of the ARSFSS were performed. In addition, pressure and temperature controllers and the resulting system dynamics of the Phoenix Rig were simulated. Reasonable agreement was found between the measurements and predictions. We found EASY5 to be a reasonable design tool, which can simulate complex fuel systems for purposes of thermal management. For improved predictive capabilities, we believe that more sophisticated pump models need to be developed for EASY5.

3.5 Particulate Emission Abatement Studies

Over the past five years, we made significant efforts to develop methodologies to assist in the abatement of particulate and gaseous emissions from turbine engine combustors. These included developing experimental and analytical capabilities to measure and quantitate particulate and gaseous emissions, developing research combustion platforms for performing detailed studies, and evaluating both base fuels and chemical additives for their potential to reduce particulate matter production. Overall, these efforts have improved the understanding of the mechanisms by which particulate matter is produced and have also established extensive experimental capabilities at the AFRL/PRTG facility.

We developed robust methodologies for collecting and quantifying particulate emissions from a range of combustion sources. This included the development of techniques employing particulate sampling probes for the collection and conditioning of combustion emissions. We evaluated various sampling probe designs and methodologies and determined the most favorable sampling approach. We constructed analytical instrumentation carts for quantifying both solid particulate and gaseous emissions. This included a cart capable of quantifying particulate number density, particle size distribution and mass concentration emissions using a condensation nuclei counter, differential mobility analyzer and a tapered element oscillating microbalance, respectively. This system allows for quantitative analysis of three major particulate matter indices Very few laboratories have the ability to perform these various measurements simultaneously. We also constructed a cart capable of quantifying major and minor gaseous emission using a Fourier Transform Infrared (FTIR) analyzer, a total hydrocarbon (THC) analyzer and an oxygen analyzer. The gaseous emission cart was successfully used both in-house and in-field (Barksdale AFB, October 2003) for quantifying gaseous emissions on a wide range of combustion platforms. We designed and fabricated a sampling system for acquiring solid particulate samples via flow-through filtration; the samples subsequently undergo numerous types of analytical techniques which provide a wide range of information. These techniques that we developed and used include the calculation of the overall smoke number, mass quantification via gravimetric measurement, mass quantification via temperature programmed oxidation (which also provides quantitative information about the chemical nature of the particulate sample), and chemical and morphological analysis (Stouffer et al., 2002; Reich et al., 2003).

We performed preliminary calculations and established an experimental protocol for calculating the radiative heat flux of soot particles within a combustor (Ballal et al., 2003). This work will allow correlations between the external particulate emissions and the radiative heat flux within a combustor to be established, subsequently allowing for feasible estimations of the latter without

the necessity of complex in-situ measurement techniques. This will significantly assist in the development of methodologies for reducing incipient particulate production within the primary and secondary combustion zones of a combustor. This decrease will allow for increased combustion operating efficiencies and fuel economy with reduced emissions on both current and future aircraft and missile applications.

We established the use of a T63-A-700 turboshaft helicopter engine located in the Engine Environment Research Facility (EERF) in the Propulsion Directorate at WPAFB for the research and development of methodologies to reduce gaseous and particulate emissions from aviation combustors. The research efforts were primarily focused on improving the understanding of the chemical and physical factors by which particulate matter emissions are produced and identifying the major parameters that affect this complicated process. This included detailed studies investigating the effect of the chemical and physical composition of the fuel, the effect of blending fuels and solvents with standard JP-8 type fuels, and the effect of model and proprietary chemical additives on the overall particulate production. These studies have provided a strong basis for developing and evaluating viable technologies to reduce particulate and gaseous emissions from both legacy and future aircraft and missile systems.

We investigated the effect of chemical and physical composition of various base fuels on particulate matter production using the T63 engine (Corporan et al., 2003). Fuels with varying aromatic, cycloparaffin, iso-paraffin, and normal paraffin levels were evaluated and compared to typical JP-8 fuels. The fuels studies included methylcyclohexane, a semi-synthetic jet fuel, two high naphthenic experimental fuels, and three Exxsol solvents. The effect of blending the solvents with JP-8 on the particulate emissions was also assessed. Results showed a general trend of reduced particulate production and smaller diameter particles for fuels having higher hydrogen-to-carbon (H/C) ratio and lower aromatic concentration. However, for several fuels with approximately the same H/C ratio (neat or blended), significant differences in particulate concentration were observed. This indicated that other chemical properties of the fuel impact the production of soot. The aromatic content was shown to have a significant effect on particle size distribution, likely due to the increased concentration of soot precursors and increased rates of particle nucleation and surface growth. When paraffinic solvents were blended with JP-8, significant reductions in emissions were observed. This presents a promising option for reducing PM emissions via the use of biological or Fischer-Tropsch (FT) derived ultra-clean fuels. The impact of the bulk physical properties of the fuel on particulate emissions were found to be negligible compared to the chemical effects. Significant differences in performance between straight and branched paraffins suggested that intermediates formed from the branched species are larger contributors to molecular growth and polyaromatic hydrocarbon (PAH) formation than those of normal paraffins. Overall, these findings provided insight into the fuel properties that impact PM emissions, which will assist in the development of fuel additives for reducing particulate emissions from turbine engine combustors.

The performance of fuel additive candidates to mitigate soot particulate emissions was assessed in a T63 helicopter engine (Corporan et al., 2002; Corporan et al., 2004). Seventeen additives, including commercial compounds to reduce emissions in internal combustion engines, diesel cetane improvers, and experimental/proprietary additives, were evaluated. The additives were individually injected into the main JP-8 fuel feed using a syringe pump, and evaluated at a

minimum of three concentration levels. This approach allowed for the instantaneous addition and removal of the chemical additives from the main fuel flow, which allowed for the investigation of whether the effect of an additive is immediate (e.g., directly affects the combustion process) or time-dependent (e.g., “cleans” the fuel injector/combustor). The engine was operated at two conditions, idle and cruise, to investigate the additive interactions at different power settings and equivalence ratios. Results indicated that the diesel cetane improvers and commercial smoke abatement additives tested had minimal impact on particulate emissions of the T63 turboshaft engine. One proprietary additive was shown to reduce particulate number density (PND) by up to 67% at the relatively high concentration of 3,000 mg/L. These benefits were only observed at the cruise condition, which may provide insight into the mechanisms by which the additive suppressed the formation or enhanced the oxidation of the soot particles. Test results with blends of JP-8 and Norpar-13 (normal paraffins) showed significant reductions in particulate emissions for both the idle and cruise conditions, demonstrating the potential environmental benefits of using blends of clean (low aromatic and low sulfur) fuels with JP-8. In addition, analysis of the collected soot particles showed that Norpar-13 significantly reduced the concentration of PAH in the samples. The thermal stability JP-8+100 additive was shown to be ineffective in the T63, even at concentrations up to 40 times the recommended value. Additive companies were informed about the performance of their additives, and several provided additional formulations for future evaluation.

We constructed a swirl-stabilized single-nozzle atmospheric CFM-56 combustion system at the AFRL/PRTG facility that was used within our emission reduction program. The primary goal of developing this combustor platform was to assist in deconvoluting the complicated chemical and physical processes that control particulate matter and soot production. A major complication of the system is the ability to precisely and independently control the overall air and fuel flow rates to the combustor, which allows for studies over a wide range of effective equivalence ratios. Accordingly, it is possible to operate the combustor under both fuel-lean and fuel-rich conditions, allowing for detailed information about the effect of combustor operating condition to be obtained. Three of the walls of the combustion chamber are comprised of quartz windows for optical access to the primary combustion zone, which allows laser/camera measurements (e.g., in-situ) to be made. Accordingly, both in-situ (e.g., temperature, soot volume fraction, hydroxyl radical concentration) and ex-situ measurements can be made during experimental studies. By coupling the in-situ (within the primary zone) and ex-situ (combustor exit) measurements, increased understanding about the soot particulate inception and growth can be obtained. This will lead to advancements in the development of PM-reducing additives while simultaneously improving the combustor operating efficiency.

We used the CFM-56 atmospheric combustor to investigate the effect of pressure, temperature, and transport processes on the effectiveness of the various chemical additives previously tested on the T63 engine. The majority of the candidates showed similar results on both combustion platforms, but some conflicting results were obtained. For example, the proprietary additive that reduced PND by 67% on the T63 actually increased the PND on the atmospheric combustor. Though the cause of this discrepancy is under investigation, the conflicting trends are believed to be due to the major differences in the combustion platforms. These include the lack of secondary dilution air and expansion through a turbine section on the atmospheric rig, which could promote

downstream oxidation/consumption of the particulate matter. The former capability is planned to be implemented on the CFM-56 for future combustion studies.

We made facility improvements to allow fuel composition studies to be performed using the atmospheric combustion platform. These studies will complement those previously conducted on the T63; however, in-situ measurements will be performed on the CFM-56. This work will significantly contribute to improving the understanding of the process by which specific fuel constituents affect the production of particulate matter. The major modifications include the design and fabrication of a high-pressure fuel delivery system that can be used to efficiently study numerous fuels with minimal complexity. Overall, the fabrication and implementation of the atmospheric combustion assembly at the AFRL/PRTG facility has provided a valuable platform for the continuing research and development of methodologies for reducing particulate and gaseous emissions from combustion sources. Enhanced capabilities will continue to be implemented onto this system.

Ballal and Harrison (2001) studied a time scale approach to particulate formation and growth. In this investigation, time scales of fuel combustion were calculated for a gas turbine combustor burning JP-8 fuel. The time scales ranged between 4.5 μs (elementary chemical reactions) to 10 ms (jet fuel thermal stressed oxidation time). Between these two extremes of time scales can be found time scales of ignition (60 μs) and microscale turbulent mixing (67 μs). These time scales were used in the fundamental analysis of particulate formation and growth.

An embryonic stage of particle formation is nuclei formation. The theory of homogeneous nucleation predicted the formation of stable nuclei in the size range 1.6 to 3 nm dia. containing 30 to 140 molecules, respectively. As stable nuclei concentration increases, they collide and coalesce to form larger primary particles. Calculations predicted a primary particle size of 71 nm. Primary particles grow as a result of two key processes: heterogeneous chemical reaction condensation and turbulent coagulation. For the turbulent Kolmogoroff micro-scale convection time of 67 μs in a typical gas turbine combustor, the rate of heterogeneous chemical reactions increased the primary particle size 13 percent to 80 nm diameter and turbulent coagulation grew it further 17 percent to a 94 nm diameter particle. In a combustion process, soot oxidation decreases measured particle size down to 50 nm in diameter. Thus, it remains to relate the predicted particulate formation and growth to the measured particulate size and emissions index (g/kg of fuel) from gas turbine engines and also to determine how jet fuel additives work to decrease the particulate size and number density.

3.6 Other Fuel Studies

A significant effort was conducted to understand the formation of “Apple Jelly,” a viscous liquid which contaminates sump areas in both aircraft and ground equipment. The concentrations of DIEGME and water were measured in several suspected apple jelly cases and found to be consistently between 40 and 50% of each. By analyzing the water filter cartridges used in fuel delivery systems, we found that the sodium agar used to absorb water from fuel may be dissolved by water/diegme solutions of the concentrations found and the agar transported downstream and perhaps even into the aircraft. These findings were important since they were

first reported occurrence of the solubility of the water-absorbing cartridge in the DIEGME water solutions.

The phenomenon of elastomer swell was studied from the viewpoint of chemical analysis of the material in jet fuel absorbed into polymers (Froning et al., 2003). Five materials used in aircraft o-rings were subjected to JP-5 and synthetic FT liquids which contained no aromatics compounds. The o-rings were tested by both ASTM tests and thermal desorption GC-MS which was able to selectively extract the compounds within the o-ring, presumably the compounds which made the o-rings swell. The analysis of the data indicated a marked increase in aromatic concentration within the o-ring matrix, as well as a very large increase (factor of 20-50) in polar compound concentrations such as DIEGME. The goal of this work is to understand the swelling of elastomers such that FT liquids, with no aromatics or polar compounds, can be additized to swell elastomers so that these fuels may be used as drop-in replacements for JP-5 or JP-8.

Filters containing soot were collected from combustion devices such as the Well Stirred Reactor and T-63 combustors. A small (less than 2 mg) sample of the filter was removed and subjected to high temperature desorption in the injector of a Saturn 2000 GC-MS (Blevins et al., 2003; Stouffer et al., 2002). The materials contained on the filter and possibly adsorbed to the soot was desorbed thermally and collected onto a GC column. PAH’s were quantified using standard mixtures and reported to help evaluate the ability of additives to influence the formation of aromatic compounds and soot in combustion devices.

4. HIGHLIGHTS OF COMBUSTION STUDIES

The impetus for the combustion research was provided by the two goals identified in the Air Force Contract No. F33615-97-C-2719 namely: Part II: Fire-Safety of Advanced Fuel Systems and Part III: Combustion Performance and Particulate Emissions. The following technical tasks were performed to meet these goals:

4.1 Stabilization Mechanism of a Jet Diffusion Flame
4.2 Suppression of a Bluff-Body Stabilized Flame
4.3 Ignition Studies of JP-8 and Jet A Fuel
4.4 Well Stirred Reactor Studies

Highlights of results obtained and the relevant publications are described below.

4.1 Stabilization Mechanism of a Jet Diffusion Flame

We completed fundamental research on the attachment mechanisms of diffusion flames. This has produced a unified view of the stabilization mechanism of methane diffusion flames, including jet and porous flat-plate flame. Takahashi et al. (1998) and Takahashi and Katta (2000) have described this attachment mechanism that stabilizes the flame and the chemical kinetic structure of the flame reaction kernel respectively.

Takahashi et al. (1998) used two-color particle image velocimetry to measure the velocity field in the stabilizing region of jet diffusion flames under near-lifting conditions. Computations were performed using a time dependent, implicit, third-order accurate numerical model. These calculations demonstrated that highest reactivity spot (reaction kernel) with peak rates of heat release, oxygen consumption, and water vapor production was formed in the relatively low-temperature (<1600 K) flame base as a result of back-diffusion of radical species against the incoming oxidizing flow. This reaction kernel provides a stationary ignition source and sustained stable combustion for incoming reactants, thus holding the trailing diffusion flame in the oxidizing stream.

Takahashi and Katta (2000) numerically analyzed the detailed structure of the stabilizing region of an axisymmetric laminar methane jet diffusion flame. Again, computations were performed using a time-dependent, implicit, third-order accurate numerical scheme with buoyancy effects and using two different C_2-chemistry models. These computations were compared with the previous data using a C_1-chemistry model. The results were nearly identical for all kinetic models except that the C_1-chemistry model over-predicted the methyl-radical and formaldehyde concentrations on the fuel side of the flame and that the standoff distance of the flame base from the burner rim varied. The standoff distance was sensitive to the $CH_3 + H + (M) \rightarrow CH_4 + (M)$ reaction. The highest reactivity spot (reaction kernel) was formed in the relatively low-temperature (<1600K) flame base, where the $CH_3 + O \rightarrow CH_2O + H$ reaction predominantly contributed to the heat release, providing a stationary ignition source to incoming reactants and thereby stabilizing the trailing diffusion flame.

Such fundamental results provided valuable information when considering the suppression and extinction mechanism of bluff body-stabilized diffusion flames.

4.2 Suppression of a Bluff-Body Stabilized Flame

We studied the mechanism of stabilization and suppression of a nonpremixed flame formed behind a backward-facing step in a small wind tunnel by impulsively injecting a gaseous fire-extinguishing agent (bromotrifluoromethane) into the airflow. Methane issued from a porous plate downstream of the step to simulate a pool fire in the aircraft engine nacelle. As the mean air velocity was increased, Takahashi et al. (2001) observed two distinct flame stabilization and suppression regimes: rim-attached wrinkled laminar flame and wake-stabilized turbulent flame. In both regimes, as the agent injection period was increased at a fixed mean air velocity, the critical agent mole fraction at suppression decreased. In the rim-attached flame regime, the total agent mass at suppression was nearly constant at a fixed air velocity nearly independent of the agent mole fraction, injection period and step height. In the wake-stabilized flame regime, the turbulent mixing process of the agent into the recirculation zone behind the step essentially determined the critical agent mole fraction dependence on the injection period. The total agent mass required for suppression increased with the mean air velocity and then leveled off to a level proportional to the step height as the transition from the rim-attached to wake-stabilized flame regime occurred.

Therefore, the suppression of step-stabilized flames occurs under the extinction condition of relatively low strain-rate diffusion flame. Furthermore, Takahashi (1999) has shown that the suppression data trend can be predicted by a theoretical expression using the measured characteristic mixing time.

4.3 Ignition Studies of JP-8 and Jet A Fuel

Jet fuels form deposits, which may be electrically conductive, on surfaces within fuel tanks. These surfaces include electrical terminal strips. If these terminals are shorted to a 120 volt source within the airplane, the surrounding conductive films may be exposed to 177 peak volts. While it is not normally possible to obtain a spark at less than 200 volts, a surface conductive deposit may be vaporized and initiate an arc between terminals. An arc, or plasma, will have very low resistance and will dissipate all of the available energy until it is extinguished. A project was carried out to determine the likelihood of this type of ignition happening under operational condition. A hot plate heated a covered Pyrex vessel, (d = 400 mm, h = 200 mm), containing 50 mL of Jet A fuel. Specially fabricated igniters were suspended within the container in contact with the fuel vapors. A high-speed video camera was used to provide a visual record while a digital recording oscilloscope was used to record electrical events.

Obringer et al. (2000) documented results of 22 ignition tests, using carbon filament igniters, at temperatures from 132 to147°F, after a 5 minute equilibration period, showed that a flammable atmosphere could be formed repeatedly. A total of 10 discharges were attempted through conductive deposits on a terminal strip recovered from an aircraft fuel tank. In all cases no arcs were observed, no current surges were recorded, and all current paths were ‘open’ after the test was completed.

4.4 Well Stirred Reactor Studies

The well-stirred reactor (WSR) facility was redesigned to improve durability, repeatability, and reliability. The improved WSR design is based on an Inconel jet ring which was installed between two spring-loaded ceramic reactor sections. Various ceramic materials (silicon carbide, zirconia oxide, and fused silica) were used depending on the desired experiment. The new design allows the fast detection of thermal-mechanical cracking problems and rapid replacement and re-assembly of ceramic reactor parts. The well-stirred reactor can be operated on a range of gaseous and liquid fuels. Liquid fuels are pre-vaporized in an improved vaporizer designed to safely vaporize rich mixtures of liquid fuels in air. The design of the improved WSR has been transitioned to another federal laboratory (NIST) and became operational there in August 2003.

The major focus of the research in the well-stirred reactor facility has been in the area of particulate formation and mitigation for gaseous and liquid fuels in support of the SERDP program. Soot formation was evaluated by use of the smoke number from samples collected on paper filters and from carbon mass measurements made using the temperature programmed oxidation technique from quartz filters. In studies of ethylene with ethanol additive (Stouffer et al., 2002; Reich et al., 2003) it has been shown that formation of soot is highly dependent on temperature in the well-stirred reactor. Comparison of temperature programmed oxidation results with filter mass measurements and GC-MS analysis confirm the validity of using the oxidation method to determine carbon mass and give qualitative indications of the types of carbon containing species present in the soot samples (organic or carbonaceous).

This Page Intentionally Left Blank

5. REFERENCES

V. Acosta, "Aircraft Fuel System Modeling Using EASY5," M.S. Thesis, University of Dayton, 1998.

S.D. Anderson, W.A. Rubey, and R.C. Striebich, "Measurement of Dissolved and Total Water Content in Advanced Turbine Engine Fuels with a Gas-Liquid Chromatographic Technique," Proceedings of 6th (Int.) Conference on Stability & Handling of Liquid Fuels, Vol. 1, pp. 103-112, 1997.

D.L. Atkins, and J.S. Ervin, "Freezing of Jet Fuel within a Buoyancy-Driven Flow in a Rectangular Optical Cell," *Energy and Fuels*, Vol. 15, pp. 1233-1240, 2001.

D.L. Atkins and J.S. Ervin, "Simulation of the Freezing of Jet Fuel," Proceedings of NATO AVT Symposium on Advanced Flow Management, Part B. Heat Transfer and Cooling in Propulsion and Power Systems, Loen, Norway, Paper 21, 2003.

M.W. Badger, S. Zabarnick, and G.R. Wilson, "Selection of Prototype Thermally Stable Jet Fuels. 2. Quartz Crystal Microbalance Tests for Thermal-Oxidative Stability," *Prepr.-Am. Chem. Soc., Div Pet. Chem.*, Vol. 47, pp. 170-173, 2002.

D. R. Ballal and W. E. Harrison III, "A Time Scale Approach to Understanding Jet Fuel Combustion and Particulate Formation and Growth," AIAA 2001-1085, 2001.

D.R. Ballal, M.J. DeWitt, E. Corporan, and W.E. Harrison III, "Particulate Loading and Radiation in Gas Turbine Combustors," *AIAA 2003-0337*, 2003.

L.M.T. Balster, S. Zabarnick, and R.C. Striebich, "Predicting the Fouling Tendency of a Thermally Stressed Jet Fuel by High Performance Liquid Chromatography (HPLC) Analysis," *Prepr.-Am. Chem. Soc., Div Pet. Chem.*, Vol. 47, pp. 161-164, 2002.

L.M. Balster, S. Zabarnick, J.S. Ervin, R.C. Striebich, M.J. De Witt, and T. Doungthip, "Predicting the Thermal Stability of Jet Fuel: Analytical Techniques Toward Model Validation," *Proceedings of the 8th International Conference on Stability and Handling of Liquid Fuels*, 2003, in press.

T. Biddle, E. Strobel, D. Minus, S. Zabarnick, L. Balster, and E. Binns, "Thermal Stability Tests Performed on Refined Power II Flow Improver," Presented at the CRC Aviation Fuels Meeting, Alexandria, VA, May 2002.

K.E. Binns, G. Dieterle, and D. Davis, "Extended Duration Thermal Stability Tests of Copper Doped JP-5," UDR-TR-2001-00022, February 2001.

L.G. Blevins, K.A. Jensen, R.A. Ristau, N.Y.C. Yang, C.W.Frayne, R.C. Striebich, M.J. DeWitt, S.D. Stouffer, E.J. Lee, R.A. Fletcher, J.M. Oran, J.M. Conny, G. W. Mulholland, "Soot Inception in a Well Stirred Reactor," Proceedings of the Third Joint Meeting of the US Sections, The Combustion Institute, 2003.

J. W. Blust, D. R. Ballal, and G. J. Sturgess, "Fuel Effects on Lean Blowout and Emissions from a Well-Stirred Reactor," *AIAA Journal of Propulsion and Power*, Vol. 15, pp. 216-223, 1999.

J. Contreras and R.C. Striebich, "Determinations of Polar Components in Aviation Fuels Using Multidimensional Gas Chromatography (MDGC-MS)," poster presentation at the AIAA 100th Anniversary of Flight, Dayton, Ohio, July 2003.

E. Corporan, L.Q. Maurice, D.K. Minus, R.C. Striebich, and S. Zabarnick, "Thermal Stability and Heat Sink Assessment of a Russian Fuel," Proceedings of JANNAF Combustion Subcommittee, Airbreathing Propulsion Subcommittee and Propulsion Systems Hazards Subcommittee Joint Conference, Cocoa Beach, FL, October 1999.

E. Corporan, M.J. DeWitt, and M. Wagner, "Evaluation of Soot Particulate Mitigation Additives in a T63 Engine," *Proceedings of the International Conference on Air Quality III, Arlington, VA*, 2002.

E. Corporan, M.J. DeWitt, O. Monroig, J. Everhart, and M. Wagner, "Effect of Fuel Character on the Emissions of a T63 Engine," *Proceedings of the 8th International Conference on Stability & Handling of Liquid Fuels*, 2003.

E. Corporan, M.J. DeWitt, and M. Wagner, "Evaluation of Soot Particulate Mitigation Additives in a T63 Engine," *Fuel Processing Technology (accepted for publication)*, 2004.

M.J. DeWitt, and S. Zabarnick, "Development and Evaluation of Additives to Inhibit Oxidative Deposition of Jet Fuels," *Prepr.-Am. Chem. Soc., Div Pet. Chem.,* Vol. 47, pp. 183-186, 2002.

M.J. DeWitt, S. Zabarnick, and D. Brooks, "Development and Evaluation of Additives to Inhibit Oxidative Deposition of Jet Fuels at Elevated Temperatures," *Presented at CRC Aviation Meeting, Washington, D.C.,* April 2002.

M.J. DeWitt, L. Shafer, and S. Zabarnick, "Development of Methodologies to Minimize the Oxidative Deposits of Jet Fuels," *Presented at the CRC Aviation Fuels Meeting, Alexandria, VA*, April 2003.

G.L. Dieterle and K.E. Binns, "Evaluation of JP-8+100 Additives in Large Laboratory Test Systems," AIAA Paper No. 98-3531, 34th AIAA/ASME/SAE/ASEE Joint Propulsion Conference and Exhibit, Cleveland, OH, July 1998.

T. Doungthip, J. S. Ervin, T. F. Williams, and J. Bento, "Studies of Injection of Jet Fuel at Supercritical Conditions," *Ind. Eng. Chem. Res.,* Vol. 41, pp. 5856-5866, 2002.

J.S. Ervin and S.P. Heneghan, "The Meaning of Activation Energy and Reaction Order in Autoaccelerating Systems," *J. Eng. Gas Turbines Power,* Vol. 120, pp. 468-473, 1998.

J.S. Ervin and T.F. Williams, "Dissolved Oxygen Concentration and Jet Fuel Deposition," *Ind. Eng. Chem. Res.,* Vol. 35, pp. 899-904, 1996.

J. S. Ervin and S. Zabarnick, "Computational Fluid Dynamics Simulation of Jet Fuel Oxidation Incorporating Pseudo-Detailed Chemical Kinetics," *Energy and Fuels*, Vol. 12, pp. 344-352, 1998.

J.S. Ervin, S. Zabarnick, K.E. Binns, G. Dieterle, D. Davis, and C. Obringer, "Investigation of the Use of JP-8+100 with Cold Flow Enhancer Additives as a Low-Cost Replacement for JPTS," *Energy Fuels*, Vol. 13, pp. 1246-1251, 1999.

J.S. Ervin, T.F. Williams, J. Bento, and T. Doungthip, "Studies of Jet Fuel Thermal Stability and Flow Characteristics within a Nozzle Under Supercritical Conditions," *Prepr.-Am. Chem. Soc., Div Pet. Chem.*, Vol. 45, pp. 538-541, 2000a.

J.S. Ervin, S. Zabarnick, and T.F. Williams, "One-Dimensional Simulations of Jet Fuel Thermal-Oxidative Degradation and Deposit Formation Within Cylindrical Passages," *Trans. ASME J. of Energy Res. Tech.*, Vol. 122, pp. 229-238, 2000b

J.S. Ervin, S. Zabarnick, M. Vangsness, G. Dieterle, K.E. Binns, and C.A. Obringer, 2001, "Evaluation of Cold Flow Additives for Use in JP-8+100," AIAA, 2001-3709.

J.S. Ervin, T.A. Ward, T.F. Williams and J. Bento, "Surface Deposition within Treated and Untreated Stainless Steel Tubes Resulting from Thermal-Oxidative and Pyrolytic Degradation of Jet Fuel," *Energy Fuels*, Vol. 17, pp. 577-586, 2003.

K. Froning, G. Garcia, J. Graham, and R. Striebich, D. Minus, "Interactions of Elastomers with Aviation Turbine Fuel," Poster presentation AIChE National Meeting, San Francisco, CA, October 2003.

B. Grinstead and S. Zabarnick, "Studies of Jet Fuel Thermal Stability, Oxidation, and Additives Using an Isothermal Oxidation Apparatus Equipped with Oxygen Sensor," Energy and Fuels, Vol. 13, pp. 756-760, 1999.

S.P. Heneghan and S. Zabarnick, "Oxidation of Jet Fuels and the Formation of Deposits," *Fuel*, Vol. 73, pp. 35-43, 1994.

S.P. Heneghan, S. Zabarnick, D.R. Ballal and W.E. Harrison, "JP-8+100: Development of a Thermally Stable Jet Fuel," *J. Energy Res. Tech.*, Vol. 118, pp. 170-179, 1996.

S.P. Heneghan, S. Zabarnick, and M.S. Mick, U.S. Patent 6,475,252B1, "Stabilizing Additive for the Prevention of Oxidation and Peroxide Formation," 2002.

A. Heltzel, S. Zabarnick, and J.S. Ervin, unpublished results, 2002.

E.G. Jones, L.M. Balster, W.J. Balster, R.C. Striebich, "Effect of Pressure on Supercritical Pyrolysis of n-Paraffins", *Prepr.-Am. Chem. Soc., Div Pet. Chem.*, Vol. 44, pp. 394-397, 1999.

D.D. Link, J.P. Baltrus, K.S. Rothenberger, P. Zandhuis, D. Minus, and R.C. Striebich, "Rapid Determination of Total Sulfur in Fuels using Gas Chromatography with Atomic Emissions Detection," *Journal of Chromatographic Science*, Vol. 40, pp. 500-504, 2002a.

D.D. Link, D.K. Minus, R.C. Striebich, K.S. Rothenberger, and J.P. Baltrus, "The Analysis of Total Sulfur and Speciated Sulfur Compounds in Aviation Turbine Fuel," *Prepr.-Am. Chem. Soc., Div Pet. Chem.*, Vol. 47, pp. 212-215, 2002b.

D.D. Link, J.P. Baltrus, K.S. Rothenberger, P. Zandhuis, D.K. Minus, and R.C. Striebich, "Class- and Structure-Specific Separation, Analysis, and Identification Techniques for the Characterization of the Sulfur Components of JP-8 Aviation Fuel," *Energy and Fuels*, Vol. 17, pp. 1292-1302, 2003.

L.Q. Maurice and R.C. Striebich, "Cyclic Species Formation in the Fuel Systems of High-Speed Vehicles," *Prepr.-Am. Chem. Soc., Div Pet. Chem.*, Vol. 43, pp. 423-427, 1998.

L.Q. Maurice, E. Corporan, W.E. Harrison, D. Minus, R. Mantz, T. Edwards, R.C. Striebich, S. Sidhu, J. Graham, B. Hitch, D. Wickham, and M. Karpur, "Controlled Chemically Reacting Fuels: A New Beginning," Proceedings of the 14th Intl. Symp. on Airbreathing Engines, Florence , Italy, 1999.

R.W. Morris, D. Minus, S. Zabarnick, L. Balster, K. E. Binns, G. Dieterle, and T. Biddle, "Protocol of Test Methods for Evaluating High Heat Sink Fuel Thermal Stability Additives for Aviation Turbine Fuel: JP-8+100," Technical Report No. AFRL-PR-WP-TR-2002-2037, Propulsion Directorate, Air Force Research Laboratory, 2002.

M. Motsinger and R.C. Striebich, "Aviation Fuel Quality Predictions using Gas Chromatography," poster presentation at the AIAA 100th Anniversary of Flight, Dayton, Ohio, July 2003.

C. Obringer, M. D. Vangsness, and D. R. Ballal, "Ignition of Jet-A Fuel Vapor by the Breakdown of Aircraft Fuel Gauge Terminal Strip Deposits," NTSB Technical Report 2000-1, January 2000.

R.F. Reich, S.D. Stouffer, V.R. Katta, H.T. Mayfield, C.W. Frayne, and J. Zelina, "Particulate Matter and Polycyclic Aromatic Hydrocarbon Determination Using a Well-Stirred Reactor," *AIAA 2003-0664*, 2003.

S.M. Rozenzhak, R.C. Striebich, and C.E. Bunker, "Development of a High-Speed Jet-Fuel Diagnostic System Using Gas Chromatography and Principal Component Analysis," *Prepr.-Am. Chem. Soc., Div Pet. Chem.*, Vol. 47, pp. 227-230, 2002.

W.A. Rubey, R.C. Striebich, and S.D. Anderson, "Various Instrumental Aspects of Analyzing Water in Jet Fuel by Gas-Liquid Chromatography," *Prepr.-Am. Chem. Soc., Div Pet. Chem.*, Vol. 43, pp. 471-474, 1998.

S.D. Stouffer, R.C. Striebich, C.W. Frayne, and J. Zelina, "Combustion Particulates Mitigation Investigation Using a Well-Stirred Reactor," *AIAA 2002-3723*, 2002.

R.C. Striebich, "Fast Gas Chromatography for Middle-Distillate Aviation Turbine Fuels," *Prepr.-Am. Chem. Soc., Div Pet. Chem.*, Vol. 47, pp. 219-222, 2002.

R.C. Striebich and J. Lawrence, "Thermal Decomposition of High Energy Density Materials at High Pressure and Temperature," *Journal of Analytical and Applied Pyrolysis*, Vol. 70, pp. 339-352, 2003.

R.C. Striebich and W.A. Rubey, "High-Pressure High Temperature Pyrolysis Reactions in the Condensed Phase with In-Line Chemical Analysis," *Prepr.-Am. Chem. Soc., Div Pet. Chem.*, Vol. 43, pp. 378-381, 1998.

R.C. Striebich, L.Q. Maurice, T. Edwards, "Formation of Cyclic Compounds in Cracking Reactions for Hydrocarbon-fueled High Speed Vehicles, IGTI Paper No. 99-GT-136, International Gas Turbine and Aeroengine Congress and Exhibition, Indianapolis IN, June 1999.

R.C. Striebich, B. Grinstead, and S. Zabarnick, "Quantitation of Metal Deactivator Additive by Derivatization and Gas Chromatography-Mass Spectrometry," *Journal of Chromatographic Science*, Vol. 38, pp. 393-398, 2000a.

R.C. Striebich, S. Zabarnick, and J. Lawrence, "Analysis and Thermal Testing of a Russian Coolant Material," Final Report for Subcontract with Johns Hopkins University, PO Number R9904553, 2000b.

F. Takahashi, "Suppression and Characterization of Bluff-Body Stabilized Flames," UDRI Report No. UDR-TR-1999-00088, November 1999.

F. Takahashi and V. R. Katta, "Chemical Kinetic Structure of the Reaction Kernel of Methane Jet Diffusion Flames," Combustion Science and Technology, Vol. 155, pp. 243-279, 2000.

F. Takahashi, W. J. Schmoll, and V. R. Katta, "Attachment Mechanisms of Diffusion Flames," *Proceedings of 27th Symposium (Int.) on Combustion*, The Combustion Institute, pp. 675-684, 1998.

F. Takahashi, W. J. Schmoll, E. Strader, and V. M. Belovich, "Suppression Behavior of Obstruction-Stabilized Pool Flames," Combustion Science and Technology. Vol 163, pp. 107-130, 2001.

G.B. Tibbs, "Test Results of the Northrup Grumman Corporation Turbine Engine Bleed Air/Fuel Heat Exchanger after 165 Hours of Operation with JP-8+100 Fuel, AIAA Paper No. 985559, 34th 1998 World Aviation Conference, Anaheim, CA, September 1998.

J. Thornburg, "Simulations of Flowing Supercritical n-Decane," MS Thesis, Air Force Institute of Technology, 1999.

D.T. Wickham, J.V. Atria, J.R. Engel, B.D. Hitch, M.E. Karpuk, R.C. Striebich, "Formation of Carbonaceous Deposits in a Model Jet Fuel under Pyrolysis Conditions," *Prepr.-Am. Chem. Soc., Div Pet. Chem.*, Vol. 43, pp. 428-432, 1998.

N. Widmor, J. S. Ervin, and S. Zabarnick, "Properties of Jet Fuels At Low Temperature and the Effect of Additives," *Prepr.-Am. Chem. Soc., Div Pet. Chem.*, Vol. 47, pp. 239-242, 2002.

N. Widmor, J.S. Ervin, M. Vangsness, and S. Zabarnick, "Studies of Jet Fuel Freezing by Differential Scanning Calorimetry and Cold-Stage Microscopy," *J. Eng. Gas Turbines Power*, Vol. 125, pp. 34-39, 2003.

K. Wohlwend, "Testing of Baker Flo-XS Pipeline Drag-Reducing Additive" Technical Report No. AFRL-PR-WP-TR-2001-2060, Propulsion Directorate, Air Force Research Laboratory, 2000.

K. Wohlwend, S. Zabarnick, K.E. Binns, and B. Grinstead, "Thermal Stability Testing of the Baker Flo-XS Pipeline Drag Reducing Additive," *Prepr.-Am. Chem. Soc., Div Pet. Chem.*, Vol. 45, pp. 501-504, 2000.

K. Wohlwend, L.Q. Maurice, T. Edwards, R.C. Striebich, M. Vangsness, and A.S. Hill, "Thermal Stability of Energetic Hydrocarbon Fuels for Use in Combined Cycle Engines," *J. of Propulsion & Power*, Vol. 17, pp. 1258-1262, 2001.

S. Zabarnick, "Pseudo-Detailed Chemical Kinetic Modeling of Antioxidant Chemistry for Jet Fuel Applications," *Energy and Fuels*, Vol. 12, pp. 547-553, 1998.

S. Zabarnick, "Investigation of Fuel Additives for a JP-8+225 Jet Fuel Using the Quartz Crystal Microbalance," *Prepr.-Am. Chem. Soc., Div Pet. Chem.*, Vol. 45, pp. 501-504, 2000.

S. Zabarnick and M.S. Mick, "Inhibition of Jet Fuel Oxidation by Addition of Hydroperoxide Decomposing Species," *Industrial & Engineering Chemistry Research*, Vol. 38, pp. 3557-3563, 1999.

S. Zabarnick, and M. Vangsness, "Properties of Jet Fuels At Low Temperature and the Effect of Additives," *Prepr.-Am. Chem. Soc., Div Pet. Chem.*, Vol. 47, pp. 243-246, 2002.

S. Zabarnick and S.D. Whitacre, "Aspects of Jet Fuel Oxidation," *Transactions of ASME, Journal of Engineering for Gas Turbines and Power*, Vol. 120, pp. 519-525, 1998.

S. Zabarnick and N. Widmor, "Studies of Jet Fuel Freezing by Differential Scanning Calorimetry," *Energy and Fuels*, Vol. 15, pp. 1447-1453, 2001

S. Zabarnick, and N. Widmor, "Studies of Urea Treatment on the Low Temperature Properties of Jet Fuel," *Energy and Fuels*, Vol. 16, pp. 1565-1570, 2002.

S. Zabarnick, E.G. Jones, S. Anderson, "The Measurement of Antioxidant Performance in Aviation Turbine Fuel Using the Quartz Crystal Microbalance and Near Isothermal Flowing Test Rig," *Proceedings of the 6th International Conference on Stability & Handling of Liquid Fuels*, Ed. H. N. Giles, US Department of Energy, Washington DC, Vol. 1, p. 989, 1998.

S. Zabarnick, M.S. Mick, R.C. Striebich, and R.R. Grinstead, "Model Studies of Silylation Agents as Thermal-Oxidative Jet Fuel Additives," *Energy and Fuels*, Vol. 13, pp. 154-159, 1999.

S. Zabarnick, R.C. Striebich, K. Straley, and L.M.T. Balster, "Solid-Phase Extraction Analysis of Polar Species in Jet Fuel," *Prepr.-Am. Chem. Soc., Div Pet. Chem.*, Vol. 47, pp. 223-226, 2002.

APPENDICES

A. The Effects of Dissolved Oxygen Concentration, Fractional Oxygen Consumption, and Additives on JP-8 Thermal Stability

The Effects of Dissolved Oxygen Concentration, Fractional Oxygen Consumption, and Additives on JP-8 Thermal Stability

J. S. Ervin

T. F. Williams

S. P. Heneghan

S. Zabarnick

University of Dayton, Dayton, OH 45469-0210

Since dissolved oxygen participates in fuel deposit formation, knowledge of the effects of dissolved oxygen concentration on fuel thermal stability is critical for fuel system design. In this work, the combined effects of dissolved oxygen availability and additives on jet fuel thermal stability are studied. Experiments with JP-8 jet fuel were conducted in a three-part heat exchanger that simulated a complex thermal and flow environment. The dissolved oxygen content at the flow inlet was varied, and deposition was studied under conditions of either fractional or complete oxygen consumption. The effects of a thermal stability additive package were also studied. An intriguing result found with JP-8 fuels is an increase in deposits formed in heated regions for decreased oxygen consumption, but inverse behavior with the additive package.

Introduction

Most high-performance aircraft rely on jet fuel circulation for cooling. Unfortunately, heated fuel reacts with small concentrations of dissolved oxygen gas to form oxidized products and deposits that can block fuel lines, foul close-tolerance valves, and deteriorate sealing materials (Hazlett, 1991; Ervin et al., 1996). On certain military jets, the fuel tanks are vented to the ambient air. At high altitudes, the ambient pressure and temperature are reduced significantly, resulting in a diminished concentration of dissolved oxygen. In addition, as a fire-preventative measure, an on-board inert gas generating system (OBIGGS) may be used to reduce the oxygen level in the fuel tank ullage space and, ultimately, in the liquid fuel. A fundamental understanding of the effect of low dissolved oxygen concentration and oxygen consumption on thermal stability (thermal stability refers to the deposit forming tendency of the fuel) is essential for aircraft design.

There is a general concensus that reducing the dissolved oxygen decreases the resulting deposition (Baker et al., 1983; Taylor, 1979). This has been observed in the case of complete oxygen consumption (Zabarnick et al., 1996; Heneghan et al., 1995) for both static and flowing tests. Few studies have considered the effects of fractional oxygen consumption on deposition. In previous works (Bradley et al., 1974; Taylor, 1974, 1976; Taylor and Frankenfeld, 1978; Frankenfeld and Taylor, 1980), the effects of intermediate levels of dissolved oxygen (20 to 40 ppm, mass basis) on surface fouling were not studied in detail. This regime of available oxygen is particularly important for aircraft that make use of OBIGGS or have vented fuel tanks. Further, the flow conditions and temperature fields were not well defined. More recent works (Heneghan et al., 1995; Jones et al., 1995) have studied the formation of jet fuel deposits under conditions of complete consumption of the dissolved oxygen at relatively high temperatures. Under these conditions, the mass of deposits increased as the mass of oxygen consumed increased. In contrast, under conditions of incomplete consumption of the available oxygen, Ervin et al. (1996) in a flowing test and Zabarnick et al. (1996) in a static test have found that decreasing the oxygen availability does not necessarily result in reduced deposition. Moreover, in aircraft, high fuel flow rates often result in circumstances in which the dissolved oxygen is not completely consumed (Harrison et al., 1993).

Additives can sometimes be used in small quantities to improve the deposition characteristics of the jet fuel (Zabarnick and Grinstead, 1994). However, additives are not always effective in reducing fouling. The relationship between fuel oxidation and deposit formation is extremely complex, and the ways in which additives affect this relationship are unclear. Moreover, the effects of thermal stability additives on deposition for fuel oxygen concentrations below that of normal air saturation are unknown.

In this work, experiments were conducted using a three-part heat exchanger, which simulated a complex thermal and flow environment approaching that of an aircraft. Different dissolved oxygen concentrations at the flow inlet determined the amount of available dissolved oxygen within the bulk flow. The objectives of these experiments were:

1. To study fouling produced by JP-8 jet fuel under conditions of partial oxygen consumption.
2. To study the effect of a thermal stability additive package on deposition under conditions of partial oxygen consumption.
3. To study deposition produced by JP-8 fuel with different inlet dissolved oxygen concentrations under conditions in which the available bulk oxygen is entirely depleted.

Experimental

In the experimental apparatus described in detail in Heneghan et al. (1993) (Fig. 1), fuel at ambient temperature is pumped from a preconditioning tank into the heated sections, which are at a pressure of 2.48 MPa. At this pressure level, the fuel remains as a liquid everywhere within the system. In the preconditioning tank, nitrogen and oxygen are bubbled through the fuel to control the amount of dissolved oxygen which enters the test section. Dissolved oxygen concentrations at the inlet can be varied from the air-saturation concentration of 70 ppm to as

Contributed by the International Gas Turbine Institute and presented at the 41st International Gas Turbine and Aeroengine Congress and Exhibition, Birmingham, United Kingdom, June 10–13, 1996. Manuscript received at ASME Headquarters February 1996. Paper No. 96-GT-132. Associate Technical Editor: J. N. Shinn.

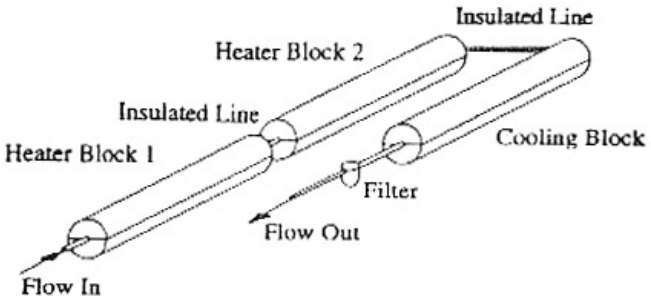

Fig. 1 Flow rig

low as 1 ppm. Bulk dissolved oxygen levels are measured online at the flow inlet and at a location within each insulated tube section by means of a Hewlett Packard 5890 Series II gas chromatograph (Rubey et al., 1992). After passing through two heated sections, the fuel flows into the cooled section, then is collected in a waste reservoir.

Two heated copper blocks (46 cm long with a 7.6 cm diameter) envelop the 316 stainless-steel tubing (180 cm long by 2.16 mm ID by 3.18 mm OD) through which the fuel passes. In the experiments performed here, the deposits remained thin (on the order of microns) and, as a result, did not appreciably affect the heat transfer or fluid motion. Thus, the temperatures were essentially steady. The tubing between the heated blocks is insulated. A third copper block (46 cm long with a 7.6 cm diameter), which has internal passages through which chilled water flows, provided cooling of the tube. Calibrated type K thermocouples (20 gage) are welded to the outer surface of the stainless-steel tubing to provide the outer tube wall temperatures with an uncertainty of ±2°C. The stainless steel tubes (ASTM grade A269/A213) have a surface roughness (arithmetic average) of 8 to 15 μin. and are cleaned with Blue Gold alkaline solution in an ultrasonic bath, rinsed with deionized water, and dried with flowing laboratory-grade nitrogen gas prior to use.

Table 1 lists characteristics of neat F2980, F2827, and F3119, the straight run base fuels used in this study. These Jet A fuels were acquired from different sources to avoid biasing the results. Jet A base fuels that contain compounds in the amounts (military specification MIL T-83133) listed in Table 2 are referred to as JP 8 fuels. Table 3 lists additives that comprise the thermal stability additive package used, which is also being considered for use by the U.S. Air Force (Anderson et al., 1994). Here, JP-8 fuel containing the additive package is referred to as JP-8A.

In the present experiments, the volumetric flow rate was selected to be either 16 ml/min or 62 ml/min. The flow was laminar at the entrance of the first heated block for both flow rates, and Reynolds numbers (Re_D) based on the tube diameter and bulk temperature are listed in Table 4 for the exit of the second heated block. Steady temperature and velocity distributions within the fuel were obtained by the finite difference solution of the Navier–Stokes, turbulent energy, and enthalpy equations. Fluid motion inside the tube was assumed to be axisymmetric, and a cylindrical coordinate system was used (Katta and Roquemore, 1993). The density of the fuel changes significantly with temperature, which gives rise to considerable buoyancy force on the fuel near the tube wall. It is believed that the buoyancy forces normal to the forced flow direction increased the heat and mass transport, rendering the flow turbulent (Katta et al., 1995). Thus, turbulent simulations yielded bulk temperatures that approximated the measured values more accurately than did the laminar computations. Turbulent flow is normally encountered in the fuel systems of military aircraft.

The extent of oxidation depends on both the residence time and the temperature field. Dissolved oxygen is more readily consumed under conditions of high temperature and long residence times. Although the available dissolved oxygen is not completely consumed in aircraft fuel systems (Harrison et al., 1993), thermal stability studies of flowing jet fuel are generally performed under conditions of complete oxygen consumption (Henegban et al., 1993; Jones et al., 1995). Thus, two categories of experiment were performed for purposes of comparison. In the first, the available dissolved oxygen was partially consumed. In the second, it was entirely depleted. For the first category, a block temperature of 270°C and a volumetric flow rate of 62 ml/min were used since these conditions resulted in little oxidation. The partial oxidation tests were conducted in 24 hour periods to obtain sufficient accumulation of deposits. In experiments performed with fractional oxygen consumption, both JP-8 and JP 8A fuel were used. In the experiments in which the dissolved oxygen was entirely consumed, the flow rate was 16 ml/min, the block temperature was either 300°C or 270°C, and the test period was six hours. In addition, JP-8 fuel alone was used. The dissolved oxygen concentrations provided at the flow rig inlet for all experiments are listed in Table 4. (The nominal dissolved oxygen concentration for air-saturated fuels here is 70 ppm; 30 ppm is representative of conditions that may be produced by an OBIGGS.)

At the termination of an experiment, the tubes were removed from the system, drained, and rinsed with hexane. They were then dried by flowing filtered nitrogen gas through them. Finally, they were sliced into 50 mm segments and heated in a vacuum oven at 120°C for one hour. Since the deposits are comprised largely of carbon, carbon measurements provide an indication of the axially distributed mass of deposits. A Leco (RC-412) multiphase carbon analyzer determined the mass of carbon in each tube segment; the reproducibility in the determination of the carbon mass is on the order of ±5 percent, determined by sequential tests performed within one week using fuel from the same batch.

Results and Discussion

In subsequent figures, the mass of carbon obtained from carbon burnoff measurements is ratioed by the inner surface area of the tube. The wall temperature distribution, given by polyno-

Nomenclature

$A^{\cdot}$ = antioxidant radical
AH = antioxidant species
$AO_2^{\cdot}$ = antioxidant peroxy radical
ASTM = American Society for Testing and Materials
BHT = butylated-hydroxy-toluene
D = tube diameter, m
FXXXX = U.S. Air Force naming scheme for neat Jet A fuels
JP-8A = JP-8 with BHT, MDA, and 8Q405
JP-8 = Jet A fuel with additives given by military specification MIL-T-83133
MDA = proprietary metal deactivator
OBIGGS = on-board inert gas generation system
O_2 = dissolved oxygen
PH = phenol molecule
$R^{\cdot}$ = hydrocarbon alkyl radical species
Re_D = Reynolds number = VD/ν
$RO_2^{\cdot}$ = peroxy radical
RH = hydrocarbon compound representing bulk fuel
$ROOH$ = hydroperoxide
V = mean velocity, m/s
8Q405 = Betz Corporation proprietary dispersant
ν = kinematic viscosity, m^2/s

Table 1 Neat fuel properties

fuel (Jet A)	sulfur mass %	aromatics volume %	JFTOT breakpoint (C)
F2980	0.1	17.0	288
F3119	0.1	18.0	285
F2827	<0.05	19.0	282

mial fits of the measured values, and the computed bulk temperature distribution are provided for reference. As the test section is horizontal, Taylor instabilities (Katta et al., 1995) yield an essentially turbulent flow at a flow rate of 16 ml/min. At 62 ml/min, the buoyancy force is less significant, and the flow undergoes a reverse transition to laminar flow (Katta et al., 1995). The complex dynamics of the flow at 62 ml/min are believed to be highly three dimensional and, hence, were not captured by the numerical simulation since the mathematical formulation was based on the assumption that the flow is axisymmetric. Thus, the bulk temperatures computed for 16 ml/min agree well with the measured values, but those computed for 62 ml/min lie above the measured temperatures within the heated sections and are used to show qualitative trends. As the fuel passes through the cooling block at 62 ml/min, the flow becomes more turbulent, and the computed and measured bulk temperatures become closer in agreement.

Partial Consumption of Dissolved Oxygen. In Fig. 2, the surface density of carbon deposited on the inner surface of the tube is expressed as a function of the axial distance through the two heated tube segments and the cooling block. Figure 2 shows three peaks, labeled A, B, and C, in the carbon deposit profiles obtained for both (F2980) JP-8 and JP-8A fuels under conditions of partial consumption of the bulk oxygen. Within the unheated segment between *A* and *B*, the deposition declines as the wall temperature decreases. Deposition then increases near 50 cm as the wall temperature approaches 270°C. Between *B* and *C*, near 100 cm, another decline occurs in the deposition profiles due to the fuel entering the unheated tube segment between the second heated block and the cooled block. Although the measured bulk temperature (200°C) at 100 cm is greater than that (160°C) at 50 cm, the deposition still falls to low levels. Figure 2 shows that the deposition in heated sections more closely follows the wall temperature than the bulk fuel temperature. The dependence of the deposition on wall temperature within heated sections was also observed in experiments with F2827 (Fig. 3) and F3119 (not shown). This dependence is plausible because in heated regions the stainless-steel wall is the location of maximum radial temperature and, thus, fuel oxidation rate. In addition, the wall is the location of minimum velocity and greater residence time than at the center of the tube. Further, the stainless-steel may be responsible for potential catalytic activity, such as the decomposition of hydroperoxides formed in the fuel autoxidation process.

At location C of Fig. 2, the wall temperature is a minimum, yet the level of deposition for JP-8 (and JP-8A) is of the same order as that at *A* and *B* where the temperature is greater. Increased deposition in cooled regions downstream of heated sections has been previously observed (Heneghan et al., 1995). The deposition mechanisms within the cooled tube are believed to be different from those in heated locations for several reasons. Chemical differences between fouling with JP-8 in the heated and cooled sections have been measured by means of X-ray photoelectron spectroscopy, and morphological differences have been detected by scanning electron microscopy (Ervin et al., 1996). Furthermore, the oxygen consumption within the cooled tube was immeasurably small, in contrast to that measured in the heated sections (Tables 5 and 6), which contain locations *A* and *B*. Lastly, experiments (Ervin et al., 1996) have shown that significantly more deposits are formed in the cooled section with higher cooling rates. Thus, deposits are believed to accumulate within the cooled section as a result of oxidized fuel products becoming less soluble at lower temperatures. The formation of deposits in cooled regions has particular import to the development of recirculating fuel systems. Recirculation systems will use ram air heat exchangers to cool the fuel prior to returning it to the fuel tanks. These heat exchangers would

Table 2 Properties of JP-8 additives

additive name	additive classification	type of compound	concn (mg/L)
DiEGME	icing inhibitor	diethylene-glycol -monomethyl-ether	25
DuPont Stadis 450	static dissipator	proprietary	2
DCI-4A	corrosion inhibitor/ lubricity enhancer	proprietary	9

Table 3 Properties of thermal stability additives

additive name	additive classification	type of compound	concn (mg/L)
BHT	antioxidant	butylated hydroxy-toluene	25
8Q405	detergent-dispersant	proprietary	100
MDA	metal deactivator	N,N'-disalicylidene-1,2-propanediamine	2

Table 4 Experiments performed

JP-8 fuel	thermal stability additives	flow rate (ml/min)	testing period (hrs)	heated block temp. (C)	inlet O_2 concn. (ppm)	Re_D exit heated block 2
partial O_2 consumption						
F2980	no	62	24	270	70,30, 6.1	2500
F2980	yes	62	24	270	70,30	2500
F2827	no	62	24	270	70,30	2500
F2827	yes	62	24	270	70,30	2500
F3119	no	62	24	270	70,30	2500
F3119	yes	62	24	270	70,30	2500
complete O_2 consumption						
F3119	no	16	6	300	70,30, 19	950
F3119	no	16	6	270	70,30, 19	850

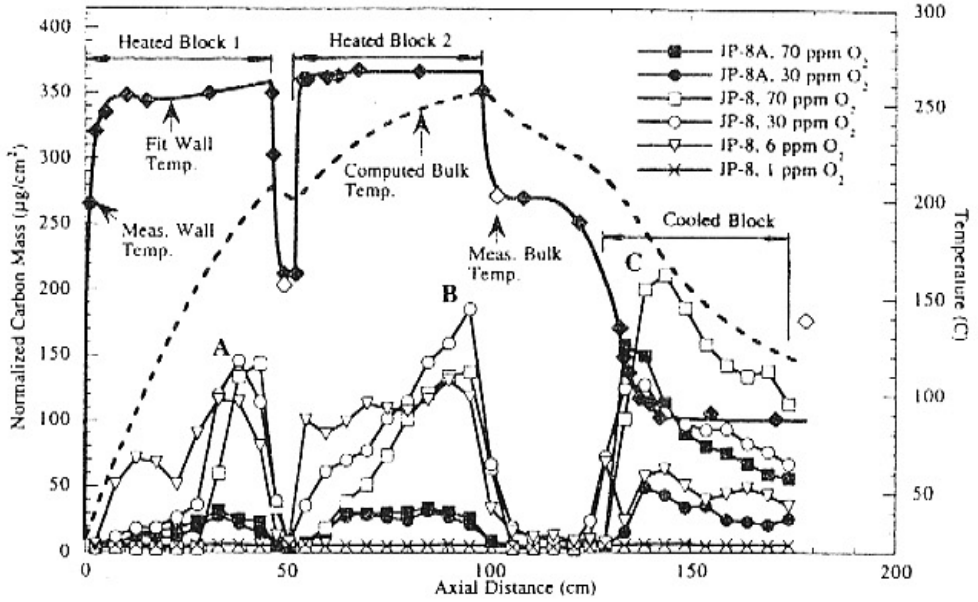

Fig. 2 Tube deposit and temperature profiles: partial O_2 consumption for fuel F2980, 62 ml/min, and 24 h

likely collect deposits similar to those found here in the cooled tube.

Figure 2 shows that the deposit profiles formed from JP-8 fuel are influenced by the inlet dissolved oxygen concentration. At locations *A* and *B*, the measured deposition for JP-8 fuel is greater for a dissolved oxygen concentration of 30 ppm than that obtained with air-saturated fuel. Similarly, greater deposition was observed with a dissolved oxygen concentration of 30 ppm rather than with 70 ppm for both F2827 (Fig. 3) and F3119 (not shown). Figure 2 shows that at a dissolved oxygen concentration of six ppm, the JP-8 fuel deposits at locations *A* and *B* are even greater than those that occur with higher dissolved oxygen concentrations and occur earlier in the tube. In Fig. 2, when the dissolved inlet oxygen is further lowered to 1 ppm, there is little deposition. Likewise, Tables 5 and 6 show that, with decreasing inlet oxygen concentrations for JP-8 (F2980 and F2827), the total mass of deposits formed in the heated sections approaches a maximum and then falls with lower oxygen concentrations.

The JP-8 deposit profiles of F2980 (Fig. 2), F2827 (Fig. 3), and F3119 (not shown) in the first heated section (between 0 and 49 cm) for dissolved oxygen concentrations less than 70 ppm rise above background levels near the tube entrance, well upstream of that for air-saturated conditions. In this region of the tube, as the initially thin thermal boundary layer develops near the heated wall, the radial temperature gradient is large at the wall but decreases with increasing axial distance. In the second heated section (between 55 and 99 cm) following the insulated tube, the thermal boundary layer again develops. The deposit profiles for initial dissolved oxygen concentrations below 70 ppm again rise at locations upstream of the point where the deposit profile for initially air-saturated fuel rises. In a flow-

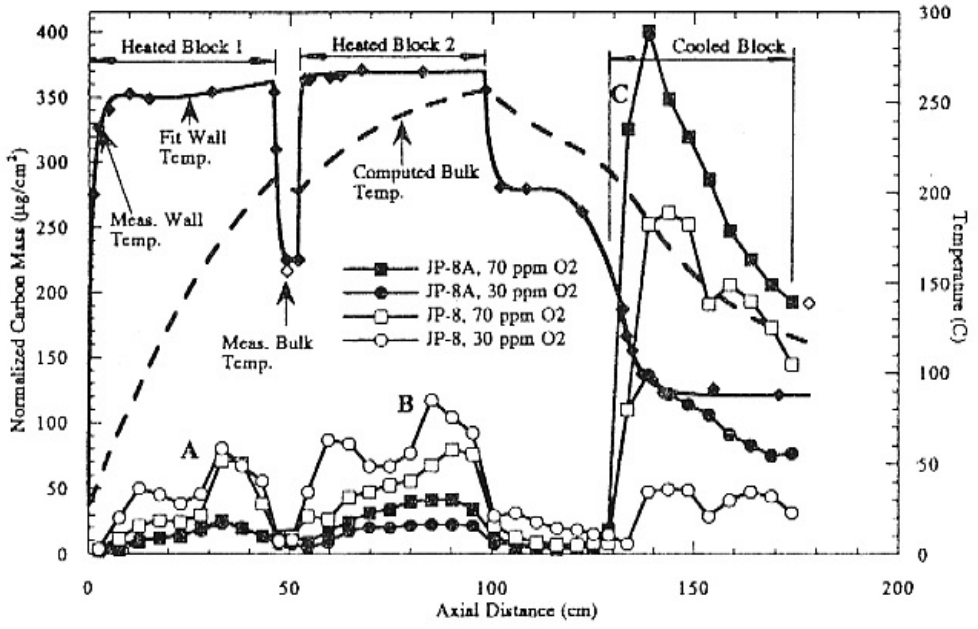

Fig. 3 Tube deposit and temperature profiles: partial O_2 consumption for fuel F2827, 62 ml/min, and 24 h

Table 5 Carbon deposits and consumed dissolved O_2 for partial consumption conditions and fuel F2980

inlet O_2 concn. (ppm)	O_2 consumed heated block 1 (ppm)	O_2 consumed heated block 2 (ppm)	total O_2 consumed (ppm)	deposits-heated blocks (µg)	deposits-cooled block (µg)
JP-8					
70	5	11	16	4057	4774
30	4	6	10	5800	2976
6	1	3	4	6007	1400
1	0.7	0.3	1	482	183
JP-8A					
70	5	6	11	1366	2909
30	5	6	11	1177	923

ing system, the oxygen consumption is controlled by both the kinetics of oxidation and the species transport. The fuel near the wall is heated at a faster rate and for a greater residence time than fuel passing through the center of the tube. In experiments using a quartz crystal microbalance, Zabarnick et al. (1996) observed an increasing fuel oxidation rate occurring at low dissolved oxygen concentrations. However, this observation is not consistent with the consumed oxygen values given in Tables 5 and 6.

At location *C* of Fig. 2, deposition for the JP-8 fuel is greatest for the inlet oxygen concentration of 70 ppm. Lower inlet levels of dissolved oxygen resulted in lower levels of deposits in the cooled tube (between 95 cm and the exit). The relationship between inlet oxygen concentration and the mass of deposits formed in the cooled section is quite different from that in the heated sections; that is, the deposition in the cooled section declines with decreasing inlet oxygen concentrations. Similar trends in deposition for JP-8 without additives are also observed for F-2827 (Fig. 3) and F-3119 (not shown). In addition, these observations support the previously described concept of a mechanism different from that of the heated sections, acting in the cooled section.

Additives and Partial Consumption of Dissolved Oxygen. Figure 2 shows deposit distributions resulting from stressed JP-8A (F-2980). Within the heated sections, the magnitude of deposit accumulation is significantly reduced in comparison to that formed from JP-8 for all inlet dissolved oxygen concentrations. Further, the level of deposition in the heated sections resulting from JP-8A now seems to follow the inlet oxygen concentration. Similar results were obtained with F2827 (Fig. 3) and F3119 (not shown). In addition as the inlet dissolved oxygen concentrations increased, Figs. 2 and 3 show that JP-8A, like JP-8, yielded more deposits in the cooled tube. In contrast to the deposition behavior of the JP-8 fuels described previously, Figs. 2 and 3 show that the deposit profiles of the JP-8A fuels rise above background levels at the entrance of the first and second heated blocks at nearly the same location, regardless of inlet dissolved oxygen concentration. Previous work (Zabarnick and Grinstead, 1994) has demonstrated that the additive package can significantly delay the oxidation process.

The addition of thermal stability additives complicates the understanding of the relation between deposition and oxidation for JP-8A because the thermal stability additives can change the chemical mechanisms of deposit formation. For example, Table 5 for fuel F2980 shows that for an inlet dissolved oxygen concentration of 30 ppm, JP-8 and JP-8A consumed similar amounts of oxygen. However, JP-8A formed significantly less deposits. These trends in oxidation and deposition were also found with F3119. Although (F2827) JP-8 and JP-8A consumed nearly the same mass of oxygen for each inlet dissolved oxygen concentration (Table 6), JP-8A formed more deposits in the cooled section than did JP-8. Thus, the thermal stability additive package affected deposition in the cooled tube with F2827 differently from that observed with F2890 and F3119.

Complete Consumption of Dissolved Oxygen. In military aircraft, jet fuel is recirculated through the fuel system and exposed to a variety of temperatures. These temperatures change continuously during a mission while the aircraft manuevers. Thus, an understanding of the effect of temperature on jet fuel thermal stability is essential to the design of jet fuels systems. In experiments performed under conditions of complete consumption of the bulk dissolved oxygen, the heated block temperature was varied while monitoring deposition and oxidation.

Figures 4(*a*) and 4(*b*) show deposition profiles for JP-8 fuel (F3119) resulting from different heated block temperatures, and the measured tube wall temperatures and computed bulk temperatures are given for reference. Within the heated or insulated tube, the deposition may fall to very low levels for two reasons. The first is that the dissolved oxygen is fully consumed and, thus, there is no more fuel oxidation. The second reason is that the temperature is low, and oxidation proceeds at a very slow rate (as shown in Figs. 2 and 3 between locations *A* and *B*). In Fig. 4(*a*), at a nominal block temperature of 300°C, the oxygen is fully consumed within the first heated block (Table 7). Thus, there is little deposition in the insulated tube and the second heated block. In the first heated block, deposition and oxidation follow each other except near the entrance of the first heated block (before 10 cm), where an inlet dissolved oxygen concentration of 19 ppm produces the greatest mass of deposits. In the cooled block there is little deposition. Figure 4(*b*) shows that a dissolved oxygen concentration of 19 ppm, the lowest level of dissolved oxygen, results in the greatest mass of deposits within the first heated section for block temperatures of 270°C. Interestingly, the dissolved oxygen is completely consumed within the first heated block for oxygen concentrations of 70 and 30 ppm. However, for an inlet dissolved oxygen concentration of 19 ppm, the bulk dissolved oxygen is not entirely consumed there (Table 7). Thus, Fig. 4 shows that even under conditions of partial oxygen consumption, greater deposition may occur with dissolved oxygen concentrations below that of normal air saturation. Similar to the fouling observed under conditions of partial oxygen consumption (Figs. 2 and 3), there are now obvious peaks in the deposition occurring in

Table 6 Carbon deposits and consumed dissolved O_2 for partial consumption conditions and fuel F2827

inlet O_2 concn. (ppm)	O_2 consumed heated block 1 (ppm)	O_2 consumed heated block 2 (ppm)	total O_2 consumed (ppm)	deposits-heated blocks (µg)	deposits-cooled block (µg)
JP-8					
70	4	7	11	2986	6179
30	1	5	6	5727	2407
JP-8A					
70	5	6	11	1357	8827
30	3	5	8	976	3161

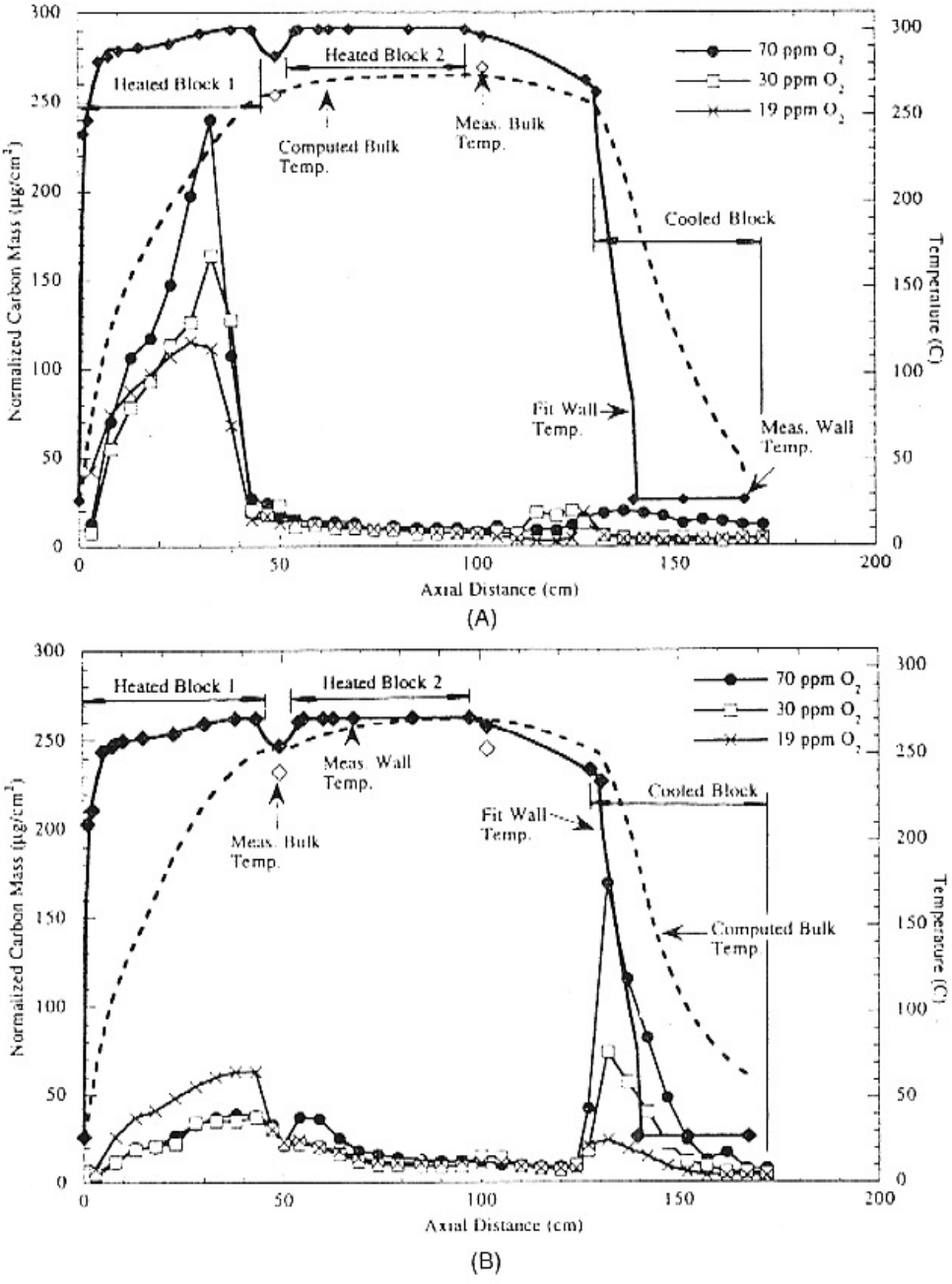

Fig. 4 Tube deposit and temperature profiles for complete O_2 consumption, JP-8 (F3119), and 16 ml/min: (*A*) 300°C block temperature; (*B*) 270°C block temperature

the cooled tube, and these peaks follow the inlet dissolved oxygen concentration.

Figure 4 shows that the heated block temperature affects the kind of oxidation products that are produced. The dissolved oxygen is consumed at a greater rate at the heated block temperature of 300°C than at the heated block temperature of 270°C. For example, Table 7 with 19 ppm dissolved oxygen and a block temperature of 300°C shows all dissolved oxygen is consumed within the first heated block. However at 270°C, 9 ppm is consumed within the second block. Although Table 7 does not show differences in oxidation rates between 270 and 300°C for the other dissolved oxygen concentrations, Heneghan et al. (1995) have observed that under conditions of complete oxygen consumption, greater temperatures result in greater rates of oxygen consumption. Furthermore, fewer solubles that deposit in cooled regions (Ervin et al., 1996) are produced with relatively high block temperatures. This has been observed previously (Heneghan et al., 1995) under conditions of complete oxygen consumption and different heated block temperatures.

An intriguing result found with JP-8 fuel is that increases in deposits in the heated sections may coincide with decreased oxygen consumption (Figs. 2–4). This observation is seemingly contrary to nearly all prior observations concerning the relation between deposit formation and oxygen consumption (Heneghan et al., 1995; Jones et al., 1995). Further, it conflicts with theories concerning the formation of deposits (Heneghan and Zabarnick, 1994; Hazlett, 1991). The mechanism proposed by Heneghan and Zabarnick (1994) for the autoxidation and antioxidant chemistry of jet fuels is:

Initiation Production of $R^{\cdot}$ (1)

Propagation $R^{\cdot} + O_2 \rightarrow RO_2^{\cdot}$ (2)

Table 7 Carbon deposits and dissolved O_2 consumption for complete consumption conditions, JP-8 (F3119)

inlet O_2 concn. (ppm)	O_2 consumed heated block 1 (ppm)	O_2 consumed heated block 2 (ppm)	total O_2 consumed (ppm)	deposits-heated blocks (μg)	deposits-cooled block (μg)
300 C					
70	70	0	70	3893	482
30	30	0	30	2974	139
19	19	0	19	2792	124
270 C					
70	70	0	70	1420	1673
30	30	0	30	1163	795
19	10	9	19	1837	302

$$RO_2^{\cdot} + RH \rightarrow RO_2H + R^{\cdot} \quad (3)$$

Termination $RO_2^{\cdot} + RO_2^{\cdot} \rightarrow$ Termination Products (4)

Transfer $RO_2^{\cdot} + AH \rightarrow RO_2H + A^{\cdot}$ (5)

$$AO_2^{\cdot} + RH \rightarrow AO_2H + R^{\cdot} \quad (6)$$

$$A^{\cdot} + O_2 \rightarrow AO_2^{\cdot} \quad (7)$$

$$AO_2^{\cdot} + AH \rightarrow AO_2H + A^{\cdot} \quad (8)$$

Deposition $AO_2^{\cdot} + AO_2^{\cdot} \rightarrow$ Deposit (9)

This mechanism is reconsidered in an attempt to explain the behavior observed here. Jet fuels are composed of hundreds of compounds. Thus, it is impractical to model the chemical changes of all components in the mixture. Here, the bulk fuel is modeled as a single hydrocarbon compound, *RH*. AH represents an antioxidant species, $R^{\cdot}$ is a hydrocarbon alkyl radical species, RO_2H is a hydroperoxide, O_2 represents the dissolved oxygen present in the fuel. In addition, $RO_2^{\cdot}$ is a peroxy radical, $A^{\cdot}$ is an antioxidant radical, and $AO_2^{\cdot}$ is an antioxidant peroxy radical. The first four reactions constitute a simplified autoxidation mechanism for hydrocarbons in the liquid phase, and the remaining reactions include the chemistry of an antioxidant molecule. Reaction (9) is responsible for the production of insoluble deposits. From the results of the current work, it is desirable for a mechanism to account for increases in deposits in heated sections that occur with decreased oxygen consumption. It should also account for the presence of soluble deposits which form in cooled regions. Hence, reactions (6) - (9) are replaced with the following reactions:

Equilibrium $A^{\cdot} + O_2 \leftrightarrow AO_2^{\cdot} \rightarrow$ Soluble Products (6′)

Deposition $A^{\cdot} + PH \rightarrow$ Deposit (7′)

Thus, it is proposed that reaction (6′) is an equilibrium reaction that leads to soluble products, and a competing reaction, (7′), leads to the formation of deposits in the heated regions. *PH* represents an unidentified molecule, but may be a phenol as Heneghan and Kauffman (1994) have shown a strong correlation between the formation of deposits in jet fuels and the presence of phenols. The equilibrium in reaction (6′) would be shifted to the right under large initial O_2 concentrations resulting in decreased deposits for each oxygen molecule consumed as shown in the heated regions of Figs. 2 and 3 and by Zabarnick et al. (1996). In addition, the equilibrium would be shifted to the left at high temperatures, causing increased deposition with temperature, a well-established trend (Hazlett, 1991). In future work, detailed computational kinetic modeling will be performed to verify the predicted behavior and establish values for the equilibrium constant in reaction (6′).

Conclusions

An understanding of the effect of the dissolved oxygen concentration on thermal stability is essential for the design of jet fuel systems. For this purpose, the dissolved oxygen concentration within the fuel at the inlet of a flowing system was varied. It was found that with JP-8 fuel under conditions of either partial or complete dissolved oxygen consumption there may be an increase in deposition for decreased inlet dissolved oxygen concentration. In addition, it was found that the thermal stability additive package improved the deposition characteristics of JP-8 fuel in the heated tube, but not necessarily in the cooled tube. From the results of this work, the following conclusions may be drawn:

- Deposit formation can be significantly affected by the upstream availability of the dissolved oxygen. Under certain conditions, more deposits can be produced with less dissolved oxygen. This is important for fuel system devices such as OBIGGS.
- Global chemistry models used in computational fluid dynamics computer codes to simulate jet fuel fouling do not presently account for the effects of dissolved oxygen availability observed here. A better understanding of the underlying chemical kinetics is needed for improved numerical simulation.
- Thermal stability tests are often conducted under conditions of high temperature and long residence time such that the influence of bulk dissolved oxygen availability on deposition is not observed. Thus, the testing of jet fuel thermal stability should be performed over a range of dissolved oxygen concentrations, residence times, and temperatures.

Acknowledgments

This work was supported by the U.S. Air Force, Fuels and Lubrication Division, Aero Propulsion and Power Directorate, Wright Laboratory, WPAFB, under Contract No. F33615-92-C-2207 (Technical Monitor: C. W. Frayne).

References

Anderson, S., Harrison, W., III, and Roquemore, W., 1994, "Development of Thermal Stability Additive Package for JP-8," *Proc. Fifth International Conference on the Handling and Stability of Liquid Fuels*, Rotterdam, Netherlands.

Baker, C. E., Bittker, D. A., Cohen, S. M. and Seng, G. T., 1983, NASA Tech Memorandum 83420.

Bradley, R., Bankhead, R., and Bucher, W., 1974, *High Temperature Hydrocarbon Fuels Research in an Advanced Aircraft Fuel System Simulator on Fuel AFFR-14 70*, (AFAPL-TR 73-95), Air Force Aero Propulsion Laboratory, Wright-Patterson Air Force Base, Ohio.

Ervin, J. S., Heneghan, S. P., Martel, C. R., and Williams, T. F., 1996, "Surface Effects on Deposits From Jet Fuels," ASME JOURNAL OF ENGINEERING FOR GAS TURBINES AND POWER, Vol. 118, pp. 278–285.

Frankenfeld, J. and Taylor, W., 1980, "Deposit Formation From Deoxygenated Hydrocarbons. 4. Studies in Pure Compound Systems," *Ind. Eng. Chem. Prod. Res. Dev.*, Vol. 19, p. 65.

Harrison, W., Binns, K., Anderson, S., and Morris, R., 1993, "High Heat Sink Fuels for Improved Aircraft Thermal Management," SAE Paper No. 111525.

Hazlett, R., 1991, *Thermal Oxidation Stability of Aviation Turbine Fuels*, American Society for Testing and Materials, Philadelphia, PA.

Heneghan, S., Martel, C., Williams, T., and Ballal, D., 1993, "Studies of Jet Fuel Thermal Stability in a Flowing System," ASME JOURNAL OF ENGINEERING FOR GAS TURBINES AND POWER, Vol. 115, p. 480.

Heneghan, S. P., and Zabarnick, S., 1994, "Oxidation of Jet Fuels and the Formation of Deposits," *Fuel*, Vol. 73, p. 35.

Heneghan, S. P., and Kauffman, R. E., 1994, "Analytic Tests and Their Relation to Jet Fuel Thermal Stability," *Proc. Fifth International Conference on the Stability and Handling of Liquid Fuels*, Rotterdam, Netherlands.

Heneghan, S., Martel, C., Williams, T., and Ballal, D., 1995, "Effects of Oxygen and Additives on the Thermal Stability of Jet Fuels," ASME JOURNAL OF ENGINEERING FOR GAS TURBINES AND POWER, Vol. 117, p. 120.

Jones, E. G., Balster, W. J., and Post, M. E., 1995, "Degradation of a Jet A Fuel in a Single Pass Heat Exchanger," ASME JOURNAL OF ENGINEERING FOR GAS TURBINES AND POWER, Vol. 117, p. 125.

Katta, V. R., and Roquemore, W. M., 1993, "Numerical Method for Simulating Fluid Dynamic and Heat Transfer Changes in Jet Engine Injector Feed-Arm Due to Fouling," *J. of Thermophysics and Heat Transfer*, Vol. 7, p. 651.

Katta, V. R., Blust, J., Williams, T. F., and Martel, C. R., 1995, "Role of Buoyancy in Fuel-Thermal Stability Studies," *J. of Thermophysics and Heat Transfer*, Vol. 9, p. 159.

Rubey, W., Striebich, R., Anderson, S., Tissandier, M., and Tirey, D., 1992, "In Line Gas Chromatographic Measurement of Trace Oxygen and Other Dissolved Gases in Flowing High Pressure Thermally Stressed Jet Fuel," *Symposium on Structure of Jet Fuels III*, American Chemical Society, Div. Petr. Chem., San Francisco, California.

Taylor, W., 1974, "Deposit Formation from Deoxygenated Hydrocarbons. I. General Features," *Ind. Eng. Chem. Prod. Res. Dev.*, Vol. 13, p. 133.

Taylor, W., 1976, "Deposit Formation From Deoxygenated Hydrocarbons. II. Effect of Trace Sulfur Compounds," *Ind. Eng. Chem. Prod. Res. Dev.*, Vol. 15, p. 64.

Taylor, W., and Frankenfeld, J., 1978, "Deposit Formation From Deoxygenated Hydrocarbons. 3. Effects of Trace Nitrogen and Oxygen Compounds," *Ind. Eng. Chem. Prod. Res. Dev.*, Vol. 17, p. 87.

Taylor, W. F., 1979, "Jet Fuel Thermal Stability," NASA TM-79231.

Zabarnick, S., and Grinstead, R., 1994, "Studies of Jet Fuel Additives Using the Quartz Crystal Microbalance and Pressure Monitoring at 140°C," *Ind. Eng. Chem. Res.*, Vol. 33, p. 2771.

Zabarnick, S., Zelesnik, P., and Grinstead, R., 1996, "Jet Fuel Deposition and Oxidation: Dilution, Materials, Oxygen, and Temperature Effects," ASME JOURNAL OF ENGINEERING FOR GAS TURBINES AND POWER, Vol. 118, pp. 271–277.

B. Aspects of Jet Fuel Oxidation

Aspects of Jet Fuel Oxidation

S. Zabarnick

S. D. Whitacre

University of Dayton Research Institute,
Aerospace Mechanics Division,
300 College Park/KL 463,
Dayton, OH 45469-0140

A quartz crystal microbalance (QCM)/Parr bomb system with a headspace oxygen sensor is used to measure oxidation and deposition during thermal oxidative stressing of jet fuel. The advantages of the oxygen sensor technique in monitoring fuel oxidation is demonstrated. Simultaneous measurement of deposition using the QCM shows a strong correlation between oxidation and deposition in jet fuels. Studies performed over the temperature range 140 to 180°C show that surface deposition peaks at an intermediate temperature, while bulk deposition increases with temperature. In studies of jet fuel antioxidants, we find that rapid increases in oxidation rate occur upon consumption of the antioxidant. The antioxidant appears to be consumed by reaction with alkylperoxy radicals. In studies of metal deactivator (MDA) additives, we find that MDA is consumed during thermal stressing, and this consumption results in large increases in the oxidation rate of metal containing fuels. Mechanisms of MDA consumption are hypothesized.

Introduction

Jet fuel undergoes oxidative chemistry upon being heated in the fuel systems of advanced military aircraft. Besides being heated by heat transfer from the hot turbine compressor air (or in the afterburner by combustor exhaust), the fuel is also heated while being used as a coolant for various engine and airframe components (Hazlett, 1991). It has been predicted that this coolant usage will become even more important in future advanced aircraft (Heneghan et al., 1996). Air saturated fuel typically contains ≈60 ppm (w/w) or 1.8×10^{-3} M of oxygen. This very small amount of oxygen can result in the formation of gums and deposits which are capable of impairing proper performance of the fuel system and grounding of the aircraft. In a flowing fuel system, the mass of deposits formed per volume of fuel is small, on the order of 1 μg/mL (≈1.2 ppm w/w) for complete oxygen consumption (Edwards, 1996); but, the volumes of fuel used in military aircraft are extremely large over the lifetime of an aircraft. Thus, the small amounts of deposits that form can build up over time, ultimately resulting in filter plugging, fouling of close tolerance valves, valve hysteresis, and other problems.

The amount of deposits which form on fuel systems components is a function of the bulk temperature history of the fuel, the fuel system surface temperatures, and the flow rates encountered. These parameters will vary continuously during a typical mission. The temperature history of the fuel will determine the extent of oxygen consumption. Also, each fuel sample will have quite different oxidative and deposit forming characteristics. Additional complications in understanding oxidation and deposition occur when safety systems are employed that attempt to lower the oxygen concentration of the fuel tank ullage, such as the on-board inert gas generating system (OBIGGS). It is believed that in present military aircraft fuel systems only a relatively small percentage (<10 percent) of the dissolved oxygen is consumed as the fuel flows from the tank to the fuel nozzle. Despite this fact, most jet fuel tests employed to date have used conditions where the dissolved oxygen is completely consumed to maximize these difficult to quantify deposits.

As military aircraft fuel system conditions are so complex, all test devices are simplifications of these real systems. Also, as thousands of hours of run time with many thousands of gallons of fuel are typical of the conditions to which real engine components are subjected, most test devices are operated in an accelerated mode. That is, one or more test parameters are adjusted to increase the deposition rate, and, therefore, decrease the test time and/or reduce the volume of fuel required. Accelerated conditions can entail higher temperatures or higher oxygen availabilities, or a combination of the two. Most flowing tests employ higher temperatures to yield measurable deposits in a reasonable time, while static (batch) tests usually employ higher oxygen availabilities. It is important to consider the difference in conditions between the laboratory test and the aircraft when evaluating the relevance of the tests. Thus, it is important to understand the effect that changes in these parameters have on oxidation and deposition. An understanding of the effect of changes in temperature and oxygen availability on oxidation and deposition is crucial. As the US Air Force and its contract researchers are presently involved in development of jet fuel additives to increase fuel thermal stability and allow increased aircraft fuel system temperatures (the JP-8 + 100 program), it is important to evaluate the effect of oxygen availability and temperature on additive behavior and effectiveness. To address these issues we utilize a test device which can simultaneously monitor both deposition and oxidation during the thermal stressing of a jet fuel. This device is a static reactor which uses a quartz crystal microbalance (QCM) for the in-situ measurement of deposition, and a polarographic oxygen sensor that is situated in the reactor headspace to monitor oxidation. Previously, we have demonstrated the usefulness of the quartz crystal microbalance (QCM) with a pressure monitoring technique for studying the deposition and oxidation of jet fuels (Zabarnick, 1994). The addition of the polarographic oxygen sensor allows more meaningful oxidation information, as it directly monitors the headspace oxygen concentration.

Experimental

The QCM/Parr bomb system has been previously described in detail, and will only be outlined briefly here (Zabarnick, 1994; Zabarnick and Grinstead, 1994). The Parr bomb is a 100 mL stainless-steel reactor. It is heated with a clamp-on band heater, and its temperature is controlled by a PID controller through a thermocouple immersed in the fuel. The reactor contains an *rf* feedthrough, through which the connection for the quartz crystal resonator is attached. The crystals are 2.54 cm in diameter, 0.33 mm thick, and have a nominal resonant frequency of 5 MHz. The crystals were acquired from Maxtek Inc. and are available in crystal electrode surfaces of gold, silver, platinum, and aluminum. For the studies reported here, gold crystal electrodes were used. The QCM measures deposition (i.e., an increase in mass) that occurs on overlapping sections of the two sided electrodes. Thus, the device responds to deposi-

Contributed by the International Gas Turbine Institute and presented at the International Gas Turbine and Aeroengine Congress and Exhibition, Orlando, FL, June 2–5, 1997. Manuscript received by the ASME Headquarters March 7, 1997. Paper No. 97-GT-219. Associate Technical Editor: H. A. Kidd.

Table 1 Properties of fuels studied

Fuel Number and Type	Total Sulfur (ppm)	Copper (ppb)
F-2827 (Jet A)	763	<5
F-2747 (Jet A-1)	37	<5
F-3119 (Jet A)	1000	7
F-3145 (JP-5)	not determined	285
F-3139 (Jet A)	not determined	not determined
Exxsol D-110 (solvent)	3	not determined

tion that occurs on the metal surface, and does not respond to deposition on the exposed quartz.

The device is also equipped with a pressure transducer (Sensotec) to measure the absolute headspace pressure and a polarographic oxygen sensor (Ingold) to measure the headspace oxygen concentration. Previous studies have demonstrated the value of determining the oxidation characteristics of fuels and fuels with additives. A personal computer is used to acquire data at one-minute intervals during the experimental run. The following data are recorded during a run: temperature, crystal frequency, headspace pressure, headspace oxygen concentration, and crystal damping voltage.

The reactor is charged with 60 mL of fuel, which is sparged with the appropriate gas for one hour before each test. The reactor is then sealed, and the heater is started. All runs in this study were performed at 140°C; heat-up time to this temperature is 40 ± 5 minutes. Most runs are conducted for 15 hours, after which the heater is turned off and the reactor allowed to cool. Surface mass measurements can only be determined during the constant temperature (±0.2°C) portion of an experimental run. The crystal frequency is converted to a surface mass measurement using the process described below.

For the temperature effect studies, a slightly different method was used to prevent significant oxygen consumption and deposition during the heat-up period. For these runs, the fuel is sparged with nitrogen for one hour to purge the fuel of dissolved oxygen. The reactor is then sealed and heated to temperature. Once the fuel has reached temperature, air or oxygen is added through the gas inlet line, and the headspace pressure is monitored to determine the amount added. This technique prevents significant oxidation from occurring during the heat-up period for higher temperature runs.

The theory that relates the measured frequency changes to surface mass has been presented in detail elsewhere (Martin et al., 1991). The frequency change of a crystal immersed in a liquid fuel can be due to two effects: the first results from changes in the surface mass density, and the second is due to changes in the liquid density and viscosity. At constant temperature and relatively small extents of chemical conversion, the liquid properties remain constant, and the frequency change can be related to surface deposition via the equation

$$\rho_s = -(2.21 \times 10^5 \text{ g/(cm}^2 s)) \frac{\Delta f}{f_0^2}, \qquad (1)$$

where f_0 is the unperturbed resonant frequency, Δf is the change in resonant frequency, and ρ_s is the surface mass density (mass/area). The reproducibility of the mass deposition measurements on fuels is limited to ±20 percent for the QCM technique. The fuels studied and some of their properties are listed in Table 1. The fuels were acquired from the Fuels and Lubricants Division of Wright Laboratory, Wright-Patterson AFB, Ohio, and are referred to by the Wright Lab assigned accession number.

Bulk fuel insolubles were measured gravimetrically. The cooled, post-test fuel was filtered with a pre-weighed 1 μm microfiber glass filter. The reactor was rinsed twice with 5 mL portions of hexane which were subsequently filtered. The filter was dried in a laboratory oven at 100°C for two hours to remove residual fuel. The hot filter was cooled in a desiccate chamber and then weighed to determine the bulk deposit mass.

BHT (2,6 di-tert-butyl-4-methylphenol) was quantified by gas chromatography-mass spectrometry (GC-MS). 500 μL fuel samples were withdrawn from the reactor through a GC septum and extracted with 500 μL of methanol. 2 μL samples of the methanol solution were injected into a Hewlett-Packard GC-MS operating in single-ion monitoring (SIM) mode. The mass spectrometer was set to follow the intensity of the 205 amu fragment ion and the 220 amu parent ion of BHT. Calibration curves were obtained by injecting standard solutions of BHT in methanol.

MDA was quantified by a procedure developed by Streibich (Streibich, 1996). 10 mL of fuel is passed through a silica gel solid phase extraction cartridge. The polar components, including MDA, are retained on the cartridge and subsequently eluted with methanol. The methanol is evaporated and the remaining condensate is dissolved in 200 μL of toluene. This toluene solution is injected into a GC/MS operated with base deactivated injector liner and column. Single ion monitoring of the 161 amu fragment ion and the 282 amu parent ion were used for quantitation.

Results and Discussion

Correlation Between Oxidation and Deposition—Oxygen Sensor Measurements. Previously we demonstrated the ability of the Parr bomb/QCM device to simultaneously measure deposition and oxidation (Zabarnick, 1994). This study used a pressure transducer to monitor the headspace pressure during the test. As oxygen is consumed in the fuel, the headspace oxygen diffuses into the fuel, resulting in a pressure drop in the headspace. While the pressure transducer technique is valuable for providing an indirect measure of oxidation, it has limitations. In particular, any changes in the volatility of the fuel during stressing will result in headspace pressure changes that cannot be separated from changes due to oxygen consumption. Thus, it was demonstrated that in a slow oxidizing fuel (F-2827) the production of volatiles was able to completely mask the pressure drop due to oxygen removal. Another disadvantage of the pressure technique is that the pressure at which oxygen is completely consumed is not known. Thus, the leveling off of the pressure is usually taken to indicate complete consumption, an assumption that is not always true. To provide a more quantitative measure of the oxidation process in the Parr bomb/QCM system we have modified the device to accept a polarographic oxygen sensor. While this sensor provides a headspace oxygen measurement only, it responds to the gaseous oxygen concentration and not to pressure changes due to volatiles, and has an easily calibrated zero oxygen level to allow determination of the point of complete oxygen consumption.

The advantages of the oxygen probe over the pressure transducer are demonstrated for two fuels in Fig. 1. Figure 1(*a*) shows the limitations of the pressure monitoring technique. Fuel F-2827 displays a flat pressure profile during the entire run despite generating a relatively large deposition of ≈4 μg/cm² during the 15 hour run. The oxygen sensor results in Fig. 1(*b*) show that oxygen is indeed consumed in the fuel, dropping from 33 to 24 percent during the run. Thus, ≈28 percent of the original oxygen is consumed. Figure 1(*b*) also demonstrates the correspondence between oxidation and deposition for this fuel. Both oxidation and deposition are relatively slow during the first three hours, increasing significantly at longer times. The deposition process continues for this fuel throughout the run, and the oxygen sensor profile shows that this is due to the presence of oxygen throughout the run. The different levels of noise in the deposition plots in the two F-2827 runs are due to experimental variations; the QCM is very sensitive to electromagnetic noise in the laboratory. Also shown in these plots are the deposition and oxidation profiles for fuel F-2747. The

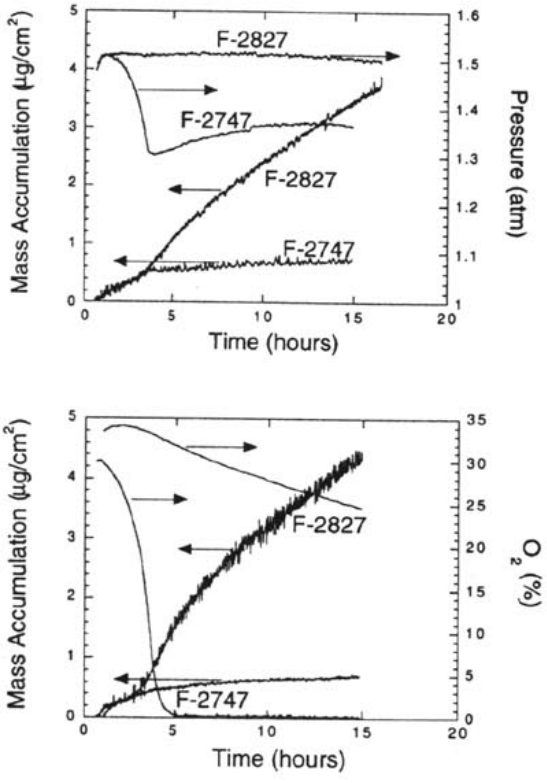

Fig. 1 Plots of mass accumulation and pressure (*a*, top) and percent oxygen (*b*, bottom) for fuel F-2827 and F-2747 at 140°C

pressure sensor profile in Fig. 1(*a*) shows a rapid decrease in pressure over the first 4 hours, with a slow rise in pressure at longer times. Previously, this slow rise in pressure was attributed to the production of volatiles during thermal stressing of the fuel (Zabarnick, 1994). Figure 1(*b*) shows that oxygen rapidly decays to zero over the first five hours of the run. The oxygen sensor measurements are not affected by the formation of volatile products. Most of the deposition of this fuel occurs during the oxygen decay, with only a slight rise in deposition at longer times. It is apparent that the oxygen sensor is able to provide quantitative information on the oxidation process without the limitations of the pressure monitoring technique.

This quantitative measure of the oxidation process allows a direct comparison of the deposit forming efficiency of the two fuels. After normalizing by the amount of oxygen consumed, we calculate that F-2827 is 22 times more efficient at producing deposition than fuel F-2747. Obviously, the quantitative information provided by the oxygen sensor overcomes the limitations of the pressure measurement technique, and yields crucial information for the interpretation of jet fuel thermal stability studies. Even more valuable information would result from in-situ measurement of the oxygen concentration in the liquid fuel. Unfortunately, the oxygen sensor is limited to temperatures below 60°C and is not able to handle the high temperatures encountered during the stressing of jet fuel. The oxygen sensor is also valuable for studies of jet fuel additives as demonstrated in the following studies.

The observed strong correspondence between oxidation and deposition has been observed in this system for a large variety of fuels and fuel/additive combinations. In general, it is found for a given fuel that deposition and oxidation occur concurrently. This is illustrated graphically in Fig. 2 for fuel F-3145 with 3.0 mg/L MDA added. Also shown in the figure is the very good agreement between the oxygen sensor and pressure measurements. The pressure measurement maximum and minimum have been normalized to the oxygen sensor measurements to allow comparison. The actual pressure varied over the range 1.2 to 1.4 atm. The figure shows that the fuel begins to deposit near six hours, and deposition levels off at 5.1 $\mu g/cm^2$ after 11 to 12 hours. Correspondingly, oxygen removal begins near six hours and is complete near 11 hours.

It is important to differentiate between the correspondence between oxidation and deposition for a given fuel as reported here, and the inverse relationship between oxidation rate and deposition over a range of fuels previously reported (Heneghan and Zabarnick, 1994). The present data shows that the oxidation process is responsible for deposition; for a given fuel, if we slow or delay oxidation by the addition of additives, we will slow or delay deposition. But, when one looks at a range of fuels with widely different oxidation rates, one finds that, in general, the fast oxidizing fuels are lower depositors than the slow oxidizing fuels. It was hypothesized that this is due to the presence of naturally occurring antioxidants in the slow oxidizing fuels; these naturally occurring antioxidants slow oxidation and increase deposition (Heneghan and Zabarnick, 1994).

Studies of the Temperature Dependence of Oxidation and Deposit Formation. Previously, we reported on the temperature dependence of jet fuel deposition and oxidation in the QCM system over the range 140 to 180°C (Zabarnick et al., 1996). We found that although the oxidation rate increases with temperature, final surface deposition displays a more complex temperature dependence. The two fuels studied showed a maximum efficiency for producing surface deposits near 150 to 160°C. Reduced deposition was noted at both higher and lower temperatures. These results contrasted sharply with most previous measurements, which report increasing deposition with temperature for the regime below 400°C (Hazlett, 1991). We hypothesized that the different temperature dependence of deposition was due to a difference in the regime of oxygen availability in these tests. Most previous work was performed on either static tests with unlimited oxygen availability or flowing heated tube tests with partial oxygen consumption. Both of these systems will have temperature dependencies of deposition that are controlled by the temperature dependence of the oxidation rate. Due to the unlimited oxygen availability conditions of the bubbling air/oxygen static flask tests, the increase in oxidation rate with temperature will result in an increase in deposition with temperature. In the case of the flowing heated tube tests, it is less obvious that the deposition rate will be controlled by the oxidation rate. These tests use relatively high temperatures and short residence times, which result in incomplete oxygen consumption. This relatively short reaction time along with possible laminar flow conditions results in oxygen consumption occurring near the tube wall surface, while the bulk fuel may

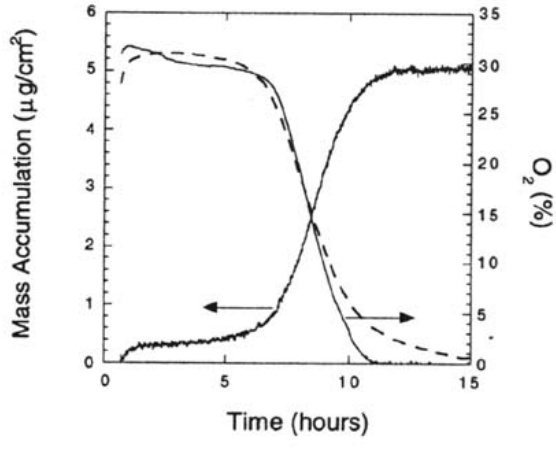

Fig. 2 Plots of mass accumulation, oxygen percent, and relative pressure (- - -) for fuel F-3145 with 3.0 mg/L MDA

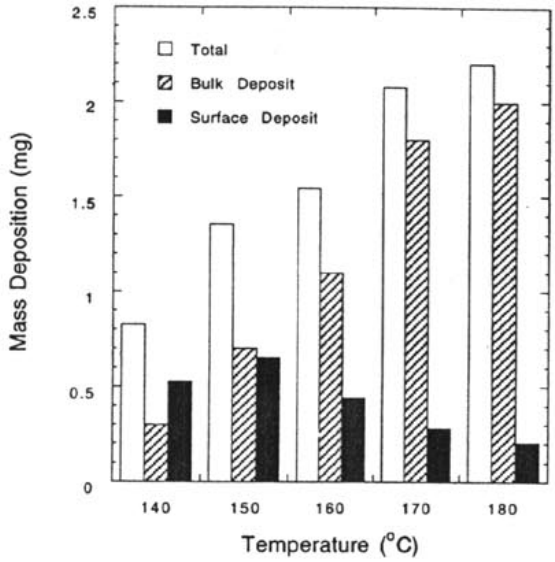

Fig. 3 Histogram of bulk, surface, and total insoluble mass versus temperature for fuel F-3119

not show significant oxygen consumption. Thus, the bulk fuel appears to be an unlimited supply of oxygen to the surface. Thus, the deposition rate at the surface reflects this nonvarying oxygen concentration in the bulk, and results in a similar temperature dependence of deposition as the bubbling static tests.

Recently, in agreement with our measurements, other workers have observed a decrease in surface deposition versus temperature over the range 155 to 225°C in a flowing heated tube (Jones and Balster, 1994). These experiments were conducted under very slow flow conditions, where complete oxygen consumption occurs within the tube. Thus, these experiments with limited oxygen and complete oxygen consumption more closely mimic the oxygen regime of our QCM experiments. The oxygen limited and complete or near-complete oxygen consumption conditions for most fuels tested in the QCM results in a final surface deposition amount that is independent of the oxidation rate. Rather, the final surface deposition is a measure of the efficiency of deposit production for a given amount of oxygen. Our previous study shows that near 150 to 160°C the efficiency of surface deposition is at a maximum, with less efficient production of surface deposits at both higher and lower temperatures.

To better understand the temperature dependence of deposit formation, we have developed a technique to measure the amount of bulk deposits, i.e., insoluble deposits that stay in the liquid fuel, but do not adhere to the reactor surfaces. These were measured gravimetrically by a technique described in the experimental section. Final surface and bulk deposit measurements were performed on fuel F-3119 with 125 mg/L of Betz 8Q406, a detergent/dispersant additive being considered for the US Air Force JP-8 + 100 program, over the temperature range 140 to 180°C. The results are shown in Fig. 3. To compare the final bulk deposit mass with the surface deposition, the areal mass density (the measured mass accumulation over the active surface area of the QCM electrode) was converted to total mass by multiplying by the calculated total surface area exposed to liquid fuel in the reactor. This surface area includes the inside of the reactor surface, the thermocouple, gas inlet tube, QCM crystal surface, and the QCM adapter. We calculate an estimated total surface area of 68 cm^2 for the reactor. The calculation of the total surface deposit uses the assumption that the areal mass density remains constant over the entire wetted surface of the reactor. This assumption is an oversimplification as we routinely observe greater deposition near the liquid/headspace interface in this reactor, but it allows a semiquantitative comparison of the bulk and surface deposits. The figure demonstrates that the surface deposition is a maximum at 150°C, decreasing at both higher and lower temperatures, in agreement with the previous observations on other fuels. Oxygen consumption was complete at all temperatures studied. The bulk deposition increases with temperature throughout the temperature range. As the bulk deposition is larger than the surface deposition at all temperatures but 140°C, the total deposition also increases with increasing temperature.

The data of Fig. 3 show that there appears to be a partitioning of deposits from the surface to the bulk with increasing temperature, although the increase in bulk deposit mass is much larger than the decrease in estimated surface deposit mass. As oxygen is completely consumed at all temperatures studied, these changes in bulk and surface deposition are due to changes in the chemistry of deposit formation with temperature. It is also possible that solubility differences with temperature can play a role in this partitioning. Jones and Balster (1994) measured bulk and surface deposition over the temperature range 155 to 225°C in a flowing rig with complete oxygen consumption. They reported a decrease in surface deposition with temperature, but noted no change in bulk deposition with temperature. It is important to note that Jones and Balster measured bulk deposits from particles collected on an in-line 0.45 μm filter downstream of the heated section. In the present work, the fuel remains at temperature for 15 hours, is allowed to cool for many hours, and is then subsequently filtered through a 1 μm filter. The technique used in the present study gives much more time for insoluble material to precipitate. These differences in methodology may account for the differences observed in the temperature dependence of the bulk deposits.

Studies of Peroxy Radical Intercepting Antioxidants. Peroxy radical intercepting antioxidants are widely used in the petroleum industry to slow the oxidation of petroleum distillates. Military jet fuels which are hydrotreated require the addition of antioxidants to prevent the formation of gums and peroxides during storage and handling. In addition, the US Air Force is considering the use of an antioxidant additive in the JP-8 + 100 thermal stability additive package. We have noted, in rapidly oxidizing fuels stressed at 140°C in the QCM system (Zabarnick and Grinstead, 1994), that the addition of an antioxidant additive can significantly delay oxidation and deposition. But, in such fast oxidizing fuels, the oxygen removal process will begin after some time.

This behavior is illustrated in Fig. 4 for a hydrocarbon solvent, Exxsol D-110. Exxsol D-110 is a dearomatized, narrow-cut aliphatic solvent with <1 percent aromatics and 3 ppm sulfur. As it is highly refined, it contains few naturally occurring antioxidants, and, therefore, oxidizes quite rapidly. The figure shows that complete oxygen consumption occurs in two hours at 140°C. As it contains few naturally occurring antioxidants, Exxsol D-110 is an ideal model fuel in which to study antioxidants. We have added the antioxidant BHT over the concentration range 4.2 to 50 mg/L, and measured the headspace oxygen concentration. Deposition is not reported as it is quite low for this solvent. The figure shows that as the concentration of added BHT is increased, the oxidation process is delayed. But, after the delay period, oxidation occurs at a very similar rate to the neat fuel. Chemical kinetic schemes can reproduce this delay in oxidation (Zabarnick, 1993); but, it is not clear why the oxidation rate increases at longer times. One possible explanation is that the antioxidant molecule is consumed during the slow oxidation time until it is reduced below some critical level, then the oxidation process can proceed. This explanation is supported by the concentration dependence of the oxygen curves of Fig. 4. The more antioxidant that is present the longer is the delay before rapid oxidation occurs. A second explanation is that oxidation products build up slowly during the slow oxida-

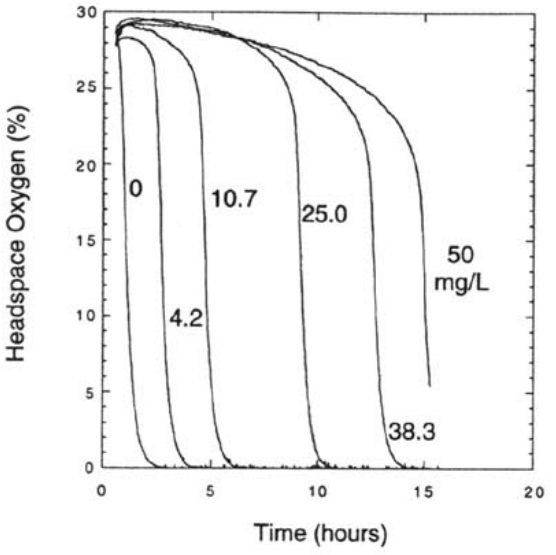

Fig. 4 Plots of headspace oxygen concentrations versus time for Exxsol D-110 at various concentrations of added BHT at 140°C

tion, and reach a critical level at which point they can help initiate faster oxidation.

To test the first theory, we have measured the concentration of BHT during a run by withdrawing 500 μL samples and performing the GC-MS analysis for BHT described in the experimental section. These experiments were performed in fuel F-3139, a fast oxidizing Jet A fuel. The results are shown in Fig. 5. The neat fuel consumes all of the headspace oxygen in three hours, and the addition of 25 mg/L of BHT delays the time of complete oxygen consumption out to seven hours. The figure shows that the BHT concentration decreases to near zero over the first 5 hours of the run. The oxidation rate increases when the BHT concentration begins to get quite low (<5 mg/L). Unfortunately, not enough data were taken during the 3 to 6 hour range to better determine the critical BHT concentration below which the oxidation rate increases. We believe that these BHT concentration measurements support the first explanation hypothesized above. Recently performed chemical kinetic modeling also supports the supposition that the consumption of the antioxidant will precipitate rapid oxidation (Zabarnick, 1998).

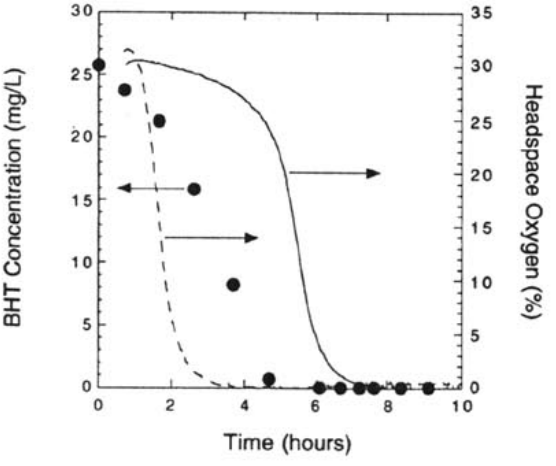

Fig. 5 Plots of BHT (●) and headspace oxygen concentrations versus time for fuel F-3139 neat (dashed line) and with 25 mg/L BHT (solid line) at 140°C

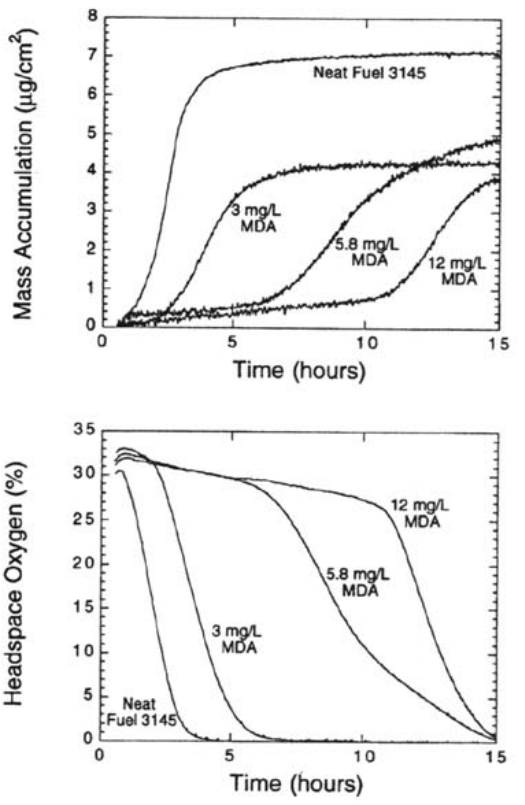

Fig. 6 Plots of mass accumulation (*a*, top) and percent oxygen (*b*, bottom) for fuel F-3145 at various concentrations of added MDA at 140°C

Presumably the antioxidant is being consumed by reaction with peroxy radicals in its role as a peroxy radical inhibitor.

Studies of Metal Deactivator Additives. Metal deactivator species have been used for many years in the petroleum industry to inhibit the catalytic effect of metals in petroleum distillates (Downing et al., 1939). These metals, and copper in particular, act to catalyze the autoxidation chemistry, thereby greatly increasing oxidation and deposition rates. This catalytic effect occurs at the part per billion level of dissolved metal. It was realized early on that the presence of these metals in petroleum distillates had the effect of greatly reducing the antioxidant capabilities of peroxy radical inhibiting antioxidant species. Thus, metal deactivator additives were developed as an inexpensive solution to suppressing the catalytic activity of the metals without removing them from the system. The metal deactivators, N,N′-disalicylidene-1,2-propanediamine and N,N′-disalicylidene-1,2-cyclohexanediamine, are optional additives in the JP-8 military specification (MIL-T-83133D). In the jet fuel community, the use of metal deactivators is controversial due to their possible over response in the JFTOT thermal stability fuel specification test (Clark, 1988).

Although originally designed to chelate metal ions in solution, it has been proposed that these metal deactivators may also act by surface passivation of exposed metal surfaces and as antioxidants by radical inhibition (Clark et al., 1990). To further explore the nature of metal deactivators as thermal stability additives we have performed a series of experiments in the QCM system. In these studies we use fuel F-3145, which has been doped with 285 ppb copper, and the metal deactivator, N,N′-disalicylidene-1,2-propanediamine, hereafter referred to simply as MDA. In Figs. 6(*a*) and 6(*b*) are shown plots of deposition and headspace oxygen at 140°C for fuel F-3145 neat and with 3.0, 5.8, and 12.0 mg/L added MDA. The neat fuel

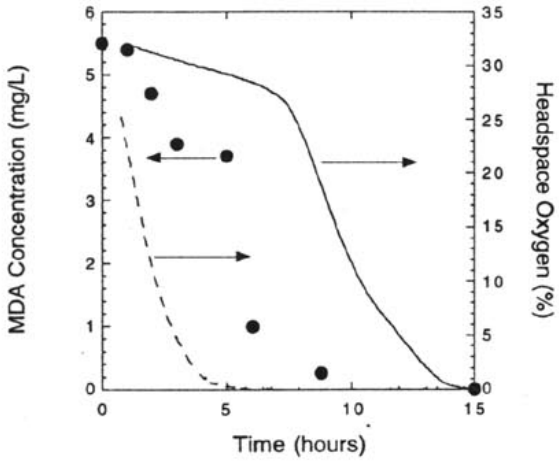

Fig. 7 Plots of MDA (●) and headspace oxygen (line) concentrations versus time for fuel F-3145 with 5.8 mg/L MDA at 140°C. Dashed line is oxygen profile for fuel F-3145 neat

produces deposition during the first four hours, after which the deposition levels. The oxygen sensor data show that oxidation occurs during this initial four hour period, and oxygen is completely consumed at five hours. The addition of MDA delays both the oxidation and deposition processes. Increasing amounts of MDA allow longer delays in oxidation and deposition. With 3 mg/L added MDA, these processes are delayed for one hour, with 5.8 mg/L the delay is five hours, and with 12 mg/L the delay is 10 hours. The final deposit amounts for all of the MDA concentrations are near 4 $\mu g/cm^2$, reduced from the 7 $\mu g/cm^2$ produced by the neat fuel.

As fuel F-3145 contains 285 ppb copper, a delay in the oxidation and deposition process is fully expected. Clark (1988) reported a chelation ratio for MDA:Cu of 1.1:1 mol/mol or 5:1 w/w. Thus, all of the copper can be complexed by the addition of approximately 1.1 mg/L MDA. Therefore, even the smallest amount of added MDA shown in Fig. 6, 3 mg/L, is enough to completely complex all of the copper in the fuel. If MDA acted only as a simple complexing agent of copper and was not depleted during the test, we would expect the oxidation and deposition results to be identical for these three concentrations of MDA, because addition of excess MDA (>1.1 mg/L) should have no effect on oxidation or deposition. Instead, we see that the oxidation delay is a function of the concentration of MDA.

The two previously reported secondary behaviors of MDA, surface passivation, and free radical inhibition may be able to yield the observed behavior. In addition, if MDA is consumed by chemical reaction, the observed behavior would be expected. To date, we are not aware of any previous reports of MDA consumption during thermal stressing of a fuel. To test this third mechanism we have measured the concentration of MDA present during an experimental run, and the results are shown in Fig. 7. A separate experimental run was used for each MDA concentration point shown in the figure, as the analysis required 10 mL of fuel. The figure shows that the MDA concentration drops during the entire run, resulting in an MDA concentration below the detection limit at 15 hours. The figure also shows that oxygen consumption is moderately slow until seven hours, after which the oxidation rate increases substantially. The time of rapid increase in the oxidation rate occurs when the MDA concentration drops below approximately 1 mg/L. This is close to the predicted concentration requirement (1.1 mg/L) for chelation of all of the copper as determined by the binding ratio. It would appear that when the MDA concentration falls below this level, unchelated copper becomes available to catalyze the initiation reactions, and, thereby, accelerates the oxidation process. These results clearly show that the consumption of MDA controls the time delays observed from MDA addition to fuel.

However, the mechanism by which MDA is depleted is uncertain. We are not aware of any MDA consumption reactions reported in the literature. Presumably, MDA could be removed by chemical reaction, complexation with reaction products, or adsorption to the reactor walls. MDA contains phenolic hydrogen atoms that may be amenable to attack by peroxy radicals. Complexation of acidic reaction products is also a possible pathway for MDA consumption.

Conclusions

This study has utilized the QCM/Parr bomb system with a headspace oxygen sensor to simultaneously measure oxidation and deposition during thermal oxidative stressing of jet fuel. We have demonstrated the advantages of the oxygen sensor over the pressure monitoring technique for following the oxidation process. In particular, the simultaneous in-situ measurements of headspace oxygen concentration and QCM deposition show the strong correlation between oxidation and deposition in jet fuels. In a given fuel, the slowing or delaying of oxidation will slow or delay deposition. We have shown that, over the temperature range 140 to 180°C, surface deposition peaks at an intermediate temperature, but bulk deposition increases with temperature. We conclude that the temperature dependence of deposition is a function of the oxygen availability of the system and the extent of oxygen conversion. We find that rapid increases in oxidation will occur upon consumption of an added antioxidant to a fast oxidizing fuel. The antioxidant appears to be consumed by reaction, presumably with alkylperoxy radicals. We find that MDA is consumed during thermal oxidative stressing, and this consumption results in large increases in the oxidation rate in metal containing fuel. Mechanisms for MDA consumption have been hypothesized. The consumption of antioxidants and MDA have important implications in the design of jet fuel thermal stability improving additive packages, particularly in the additive concentration optimization process.

Acknowledgments

This work was supported by the US Air Force, Propulsion Directorate, Air Force Research Laboratory, WPAFB under Contract Nos. F33615-92-C-2207 and F33615-97-C-2719 with Mr. Charles Frayne as technical monitor. We would like to thank Mr. Rich Streibich and Ms. Becky Grinstead for developing the BHT and MDA analysis techniques.

References

Clark, R. H., 1988, "The Role of a Metal Deactivator in Improving the Thermal Stability of Aviation Kerosenes," presented at the 3rd International Conference on the Stability and Handling of Liquid Fuels, London, UK.

Clark, R. H., Delargy, K. M., and Heins, R. J., 1990, "The Role of Metal Deactivator Additive in Improving the Thermal Stability of Aviation Kerosines: Additive Adsorption Studies," *Prepr.-Am. Chem. Soc., Div. Fuel Chem.*, Vol. 35, pp. 1223–1230.

Downing, F. B., Clark, R. G., and Pedersen, C. J., 1939, "Suppression of Metal Catalysts in Gasoline Gum Formation," *Oil & Gas J.*, Vol. 38, pp. 97–101.

Edwards, T., 1996, "Recent Research Results in Advanced Fuels," *Prepr.-Am. Chem. Soc., Div Pet. Chem.*, Vol. 41, pp. 481–487.

Hazlett, R. N., 1991, *Thermal Oxidation Stability of Aviation Turbine Fuels*, ASTM, Philadelphia, PA.

Heneghan, S. P., and Zabarnick, S., 1994, "Oxidation of Jet Fuels and the Formation of Deposits," *Fuel*, Vol. 73, pp. 35–43.

Heneghan, S. P., Zabarnick, S., Ballal, D. R., and Harrison, W. E., 1996, "JP-8+100: The Development of High Thermal Stability Jet Fuel," presented at the 34th Aerospace Sciences Meeting and Exhibit, Reno, NV.

Jones, E. G., and Balster, W. J., 1994, "Formation of Insolubles in a Jet-A Fuel: Temperature Effects," *Prepr.-Am. Chem. Soc., Div Pet. Chem.*, Vol. 39, pp. 78–81.

Martin, S. J., Granstaff, V. E., and Frye, G. C., 1991, "Characterization of a Quartz Crystal Microbalance with Simultaneous Mass and Liquid Loading," *Anal. Chem.*, Vol. 63, pp. 2272–2281.

Streibich, R., 1996, unpublished results, University of Dayton Research Institute, Dayton, OH.

Zabarnick, S., 1993, "Chemical Kinetic Modeling of Jet Fuel Autoxidation and Antioxidant Chemistry," *Ind. Eng. Chem. Res.*, Vol. 32, pp. 1012–1017.

Zabarnick, S., 1994, "Studies of Jet Fuel Thermal Stability and Oxidation Using a Quartz Crystal Microbalance and Pressure Measurements," *Ind. Eng. Chem. Res.*, Vol. 33, pp. 1348–1354.

Zabarnick, S., 1998, "Chemical Kinetic Modeling of Antioxidant Chemistry for Jet Fuel Applications," *Energy & Fuel*, in press.

Zabarnick, S., and Grinstead, R. R., 1994, "Studies of Jet Fuel Additives Using the Quartz Crystal Microbalance and Pressure Monitoring at 140 C," *Ind. Eng. Chem. Res.*, Vol. 33, pp. 2771–2777.

Zabarnick, S., Zelesnik, P., and Grinstead, R. R., 1996, "Jet Fuel Deposition and Oxidation: Dilution, Materials, Oxygen, and Temperature Effects," ASME JOURNAL OF ENGINEERING FOR GAS TURBINES AND POWER, Vol. 118, pp. 271–277.

C. The Meaning of Activation Energy and Reaction Order in Autoaccelerating Systems

The Meaning of Activation Energy and Reaction Order in Autoaccelerating Systems

J. S. Ervin

S. P. Heneghan

University of Dayton Research Institute,
300 College Park,
Dayton, OH 45469-0140

Global reaction mechanisms and rate constants are commonly used in computational fluid dynamics models that incorporate chemical reactions to study aviation fuel thermal and oxidative thermal stability. Often these models are calibrated using one set of conditions, such as flow rate and temperature. New conditions are then calculated by extrapolation using the global expressions. A close inspection of the origin of global oxidation rate constants reveals that in systems that undergo autocatalysis or auto inhibition, a simple overall global activation energy and reaction order are not good descriptors of the reaction process. Furthermore, pseudo-detailed chemical kinetic modeling of a fuel that experiences autocatalysis shows that the observed reaction order for oxygen consumption varies with initial oxygen concentration, extent of reaction, and temperature. Thus, a simple global rate expression used to describe oxygen consumption in an autoaccelerating system is insufficient to allow extrapolation to different temperature or time regimes.

Introduction

Jet fuel is circulated in military aircraft for cooling. In the presence of heat and dissolved oxygen, jet fuel degrades, forming surface deposits and fouling close-tolerance valves. In time, accumulated surface deposits impair engine performance by disrupting the normal fuel flow within fuel system components (Hazlett, 1991). Moreover, the fouling of close-tolerance valves may lead to catastrophic failure of the aircraft. Since the chemical reactions in which dissolved oxygen is consumed are intimately tied to the chemical and physical processes of fouling, a fundamental understanding of dissolved oxygen consumption is imperative for proper aircraft design.

For over five decades, the thermal-oxidative stability of jet fuels generally has been studied by experiment and empirical models (Martel, 1987). However, these empirical models lack generality and offer little fundamental insight into fouling processes. Numerical solutions of the Navier-Stokes, energy, and species conservation equations are more general and can be used to predict oxygen consumption and surface deposition for different flow geometries, flow rates, and temperatures. Since fuel oxidation and deposition processes are extremely complex, global-chemistry kinetics have been used in computational simulations (Krazinski et al., 1992; Chin et al., 1994; Katta et al., 1995; Ervin et al., 1996). The global-chemistry mechanisms used in computational fluid dynamics simulations generally employ the single overall reaction

$$\text{Fuel} + \text{O}_2 \rightarrow \text{Products} \tag{1}$$

to represent fuel autoxidation. Although fuel autoxidation involves a complex series of reactions, the underlying assumption of Eq. (1) is that the overall reaction of a mixture of compounds can be represented by one rate equation. This rate equation is comprised of a rate constant multiplied by concentrations with simple order dependence, such as in Eq. (2):

$$\mathbf{RR} = -\frac{d\text{O}_2}{dt} = k\text{O}_2^N. \tag{2}$$

It is further assumed that the rate constant, k, is defined by the product of an Arrhenius A-factor (or pre-exponential) and an activation energy, as in Eq. (3):

$$k = Ae^{(-E_a/RT)}. \tag{3}$$

In previous studies that used global models to represent oxygen consumption as a single reaction, it was found that use beyond the temperature calibration regime resulted in very poor predictions of the measured mass of carbon deposits accumulated along the length of heated tubes. This was largely due to inadequate prediction of the complex process of oxygen consumption (Chin et al., 1994). Since nearly all current engineering computational fluid dynamics models of fuel oxidation and deposition use global chemistry, the underlying assumptions of the global mechanisms should be carefully considered. The objective of this paper is to demonstrate that the concepts of a single global activation energy and a single global reaction order are not well-defined in a chain branching process. It will be shown later, using simple low temperature oxidation of hydrocarbons with decomposition of the product peroxide molecules, that the global parameter E_a of Eq. (3) and the observed reaction order are functions of the initial conditions, time, and temperature.

Autoxidation Mechanism

The reaction mechanism for the oxidation of hydrocarbons has long been the discussion of numerous articles (Mayo, 1968). The intention of this paper is not to establish that one mechanism is correct, but rather to show that the global kinetic rate expression is nontrivial for a given mechanism. To accomplish this, a simple chain autoxidation mechanism that includes autocatalysis by means of a unimolecular peroxide decomposition reaction was selected. The autoxidation mechanism used in the analysis that follows is given in Table 1.

Theoretical Description

The general approach will be to first describe the rate law (**RR**) for autoxidation in terms of concentrations, temperature, and rate constant parameters, and then to apply the appropriate operators to extract activation energy and order from the rate law. The appropriate operators for activation energy, E, and oxygen reaction order, N, are given in Eqs. (4) and (5). Thus,

Contributed by the International Gas Turbine Institute and presented at the International Gas Turbine and Aeroengine Congress and Exhibition, Orlando, FL, June 2–5, 1997. Manuscript received by the ASME Headquarters March 7, 1997. Paper No. 97-GT-224. Associate Technical Editor: H. A. Kidd.

Table 1 Autoxidation mechanism used in present analysis

	Reaction	Reaction No.
initiation	initiation of $R^{\bullet}$	(1)
propagation	$R^{\bullet} + O_2 \rightarrow RO_2^{\bullet}$	(2)
	$RO_2^{\bullet} + RH \rightarrow RO_2H + R^{\bullet}$	(3)
chain-transfer/ termination reactions	$RO_2^{\bullet} + AH \rightarrow RO_2H + A^{\bullet}$	(3t)
autocatalysis	$RO_2H \rightarrow RO^{\bullet} + OH^{\bullet}$	(u)

E and N (Wylie and Barrett, 1982) applied to **RR** (Eq. (2)) yield E_o and N, respectively.

$$E = \frac{RT^2}{\mathbf{RR}} \frac{\partial}{\partial T} \tag{4}$$

$$N = \frac{O_2}{\mathbf{RR}} \frac{\partial}{\partial O_2} \tag{5}$$

Rate Law Derivation. Heneghan and Zabarnick (1994) have shown that in a strongly terminated oxidation system, such as described here, the rate of oxidation can be given by Eq. (6).

$$\mathbf{RR} = \frac{-dO_2}{dt} = \frac{k_3 RH R_i}{k_{3t} AH} + R_i \tag{6}$$

With the assumption of a long chain length,

$$\frac{k_3 RH}{k_{3t} AH} \gg 1 \tag{7}$$

the rate of oxidation can be given approximately as

$$\mathbf{RR} = \frac{-dO_2}{dt} \approx \frac{k_3 RH R_i}{k_{3t} AH}. \tag{8}$$

Zabarnick (1993) showed that a unimolecular decomposition reaction was adequate to show the curvature in oxygen consumption profiles observed in the experiments of Jones (1995). Thus, the rate of initiation can be given by Eq. (9).

$$R_i = k_u(O_{2(0)} - O_{2(t)}) + B \tag{9}$$

$$B = k_1 O_{2(t)}^n \tag{10}$$

In Eq. (9), R_i is the rate of formation of radicals, k_u is the unimolecular process associated with the decomposition of the oxidation products, and B is the baseline initiation rate given by Eq. (10). These initiation reactions have been the subject of much theorizing, but, to date, there has been no consensus on their form. In this analysis, a general reaction process is used that involves oxygen to an unknown power. It is important to note that if there is no autoacceleration ($k_u = 0$), global kinetic parameters provide an excellent description of the oxidation rates, and the activation energy is a valid parameter for extrapolation to new temperatures. In addition, it should be noted that k_1 and k_u exhibit Arrhenius behavior with regard to temperature.

Inserting R_i and B (Eqs. (9) and (10)) into the time derivative of oxygen concentration (Eq. (8)) leads to Eq. (11).

$$\mathbf{RR} = k'(k_u \Delta O_2 + k_1 O_{2(t)}^n), \tag{11}$$

where $k' = (k_3 RH / k_{3t} AH)$, a unitless ratio, and ΔO_2 is $O_{2(0)} - O_{2(t)}$.

Activation Energy and Reaction Order. Applying the activation energy operator (Eq. (4)) to the global rate equation (Eq. (8)) yields the observed activation energy (E_o) in Eq. (12). This clearly shows that the activation energy is not a constant of the reaction process; it changes with dissolved oxygen concentration, and its rate of change varies with temperature.

$$E_o = E\mathbf{RR} = E_3 - E_{3t} + \frac{E_u k_u \Delta O_2 + E_1 k_1 O_{2(t)}^n}{k_u \Delta O_2 + k_1 O_{2(t)}^n} \tag{12}$$

The order operator can also be applied to the rate equation (Eq. (8)) to yield the observed order (N) of Eq. (13). The order of the reaction shows behavior similar to the activation energy in that it depends upon the progress of the reaction.

$$N = N\mathbf{RR} = \frac{-k_u O_{2(t)} + n k_1 O_{2(t)}^n}{k_u \Delta O_2 + k_1 O_{2(t)}^n} \tag{13}$$

Discussion

In general, the activation energy (Eq. (12)) for the process is the difference of the activation energy for propagation and termination plus the average of E_1 and E_u weighted by the corresponding rate of reaction (1) and reaction (u) of Table 1. At time zero ($O_{2(0)} = O_{2(t)}$), the acceleration reaction is not occurring, so that the average is E_1. As time progresses and O_2 decreases, ΔO_2 increases and the average approaches E_u. Therefore, the activation energy starts at $E_3 - E_{3t} + E_1$ and monotonically increases or decreases to $E_3 - E_{3t} + E_u$. (It is noted that if E_1 is equal to E_u, E_o remains constant.)

The order for the reaction is much more complicated. N is shown in Eq. (14) for time zero (also substituting B from Eq. (10)). This shows that the initial rate depends not only on the ratio of k_u, the acceleration rate, and baseline initiation rate B

Nomenclature

A = pre-exponential multiplier in rate constant expression
$A^{\bullet}$ = antioxidant radical
AH = antioxidant species
AO_2 = antioxidant peroxy radical
B = the baseline rate of radical formation
E = Arrhenius activation energy
E_o = observed activation energy
E = Arrhenius activation energy operator
I = initiator species
k = Arrhenius rate constant
M = molarity, moles/L
N = observed reaction order
n = oxygen reaction order of the initiation reactions
N = reaction order operator
$O_{2(t)}$ = dissolved oxygen concentration at time t
R = universal gas constant
$R^{\bullet}$ = alkyl radical species
R_i = rate of formation of radicals
RR = rate law for the loss of oxygen ($-dO_2/dt$)
RH = bulk hydrocarbon fuel
$RO^{\bullet}$ = alkoxy radical
$RO_2^{\bullet}$ = peroxy radical
RO_2H = hydroperoxide
R_{prime} = alkyl radical
SH = hydroperoxide decomposer
T = temperature
t = time
θ = the product 2.303RT

$(k_1 O_{2(0)}^n)$, but also on the initial value of the oxygen concentration $O_{2(0)}$. The ratio of k_u and B is evaluated using rates from Chin et al. (1994) in Eq. (15).

$$N = \frac{-k_u O_{2(0)}}{B} + n. \quad (14)$$

$$\log\left(\frac{k_u}{B}\right) = (14.8 - 40/\theta) - (11.3 - 35.8/\theta)$$

$$= 3.5 - 4.2/\theta \quad (15)$$

In Eq. (15), θ is defined as the product 2.303RT. Equations (14) and (15) show that N is -0.1 for n equal to zero at a normal air saturation concentration of oxygen ($O_{2(0)} = 1.8 \times 10^{-3}$ M, where M is molarity in moles/L) and at a temperature of 185°C. However, N approaches zero with decreasing temperature.

To support the previous analysis and to further demonstrate that the concept of a simple overall global reaction order is unclear for an autoaccelerating system, pseudo-detailed chemical kinetic modeling was performed using the mechanism of Table 2. The model is pseudo-detailed in the sense that the chemical kinetics of oxygen consumption are described using several reactions that represent the dominant chemistry, rather than hundreds of reactions as might be found in a detailed model. All rate parameters given in Table 2 are taken from Zabarnick (1996), who used this mechanism to successfully reproduce the chain mechanism that is responsible for oxygen consumption in hydrocarbon fuels. The initiation step (reaction 1 of Table 2) is assumed to occur by unimolecular decomposition of an initiating species, I. This is a simple representation of an inadequately understood initiation process, but it is used to begin the chain with a low production rate of $R^\bullet$ radicals (Zabarnick, 1993, 1996) that becomes negligible once the autoxidation chain begins. Thus, for reaction 1, a small Arrhenius A-factor of 0.001 s^{-1} was chosen along with an activation energy of zero. Using the parameters of Table 2, Zabarnick (1996) predicted oxygen concentrations that compared favorably with the near-isothermal experiments of Jones (1996) and with experiments in which the antioxidant concentration was varied (Zabarnick, 1996). In addition, a similar mechanism was used to predict dissolved oxygen consumption and hydroperoxide production in the nonisothermal flow studies of Ervin et al. (1997). The salient feature of the mechanism of Table 2 is that it permits alkyl hydroperoxide decomposition, and, thus, can be used to simulate autocatalysis.

Table 2 Reaction mechanism used for pseudo-detailed kinetic modeling (Zabarnick, 1996)

Reaction	Arrhenius A-factor (mol, L, and S)	Activation Energy (kcal/mol)	Reaction No.
$I \rightarrow R^\bullet$	0.001	0	(1)
$R^\bullet + O_2 \rightarrow RO_2^\bullet$	3×10^9	0	(2)
$RO_2^\bullet + RH \rightarrow R\,O_2H + R^\bullet$	3×10^9	12	(3)
$RO_2^\bullet + RO_2^\bullet \rightarrow$ termination	3×10^9	0	(4)
$RO_2^\bullet + AH \rightarrow R\,O_2H + A^\bullet$	3×10^9	5	(5)
$AO_2^\bullet + RH \rightarrow AO_2H + R^\bullet$	3×10^5	10	(6)
$A^\bullet + O_2 \rightarrow AO_2^\bullet$	3×10^9	0	(7)
$AO_2^\bullet + AH \rightarrow A\,O_2H + A^\bullet$	3×10^9	6	(8)
$AO_2^\bullet + AO_2^\bullet \rightarrow$ products	3×10^9	0	(9)
$R^\bullet + R^\bullet \rightarrow R_2$	3×10^9	0	(10)
$RO_2H \rightarrow RO^\bullet + {}^\bullet OH$	1×10^{15}	42	(11)
$RO^\bullet + RH \rightarrow ROH + R^\bullet$	3×10^9	10	(12)
$RO^\bullet \rightarrow R_{prime}^\bullet$ + carbonyl	1×10^{16}	15	(13)
${}^\bullet OH + RH \rightarrow H_2O + R^\bullet$	3×10^9	10	(14)
$RO^\bullet + RO^\bullet \rightarrow$ termination	3×10^9	0	(15)
$R_{prime}^\bullet + RH \rightarrow$ alkane $+ R^\bullet$	3×10^9	10	(16)
$RO_2H + SH \rightarrow$ products	3×10^9	0	(17)

With the assumption of an isothermal reacting system, the time-varying species concentrations were found numerically by a finite difference solution of the coupled ordinary differential equations that arise from the mechanism of Table 2. The following were input to the numerical code: the activation energies and pre-exponential multipliers of Table 2, concentrations (O_2, AH, RH, SH, and I) for each species at time zero, reaction temperature and time, and the grid resolution. Three different fractions (10, 50, and 100 percent) of the normal air saturation concentration (1.8×10^{-3} M at 25°C) estimated from tabulated jet fuel properties (Coordinating Research Council, 1983) were used as initial oxygen concentrations for each temperature of interest. The RH concentration was estimated from the molarity of liquid jet fuel (average molecular weight of 170 amu and a density of 0.684 g/cm^3 at 185°C, for example) in this temperature range (Coordinating Research Council, 1983), and a small I concentration (1.0×10^{-7} M) was used to initiate the chain. The temperatures chosen for the simulations were 185°C and 215°C. It is expected from the value of the activation energy associated with reaction 11 of Table 2 that the production rate of radicals by hydroperoxide decomposition will be much more significant at 215°C than at 185°C. Thus, the effects of autoacceleration are expected to be more substantial at the higher temperature. The computational grid was uniformly spaced in time using a maximum of 400 nodes, and the equations were solved sequentially in an iterative manner. More refined computational grids resulted in negligible changes in the computed values. The solution was considered to be converged when the computed residuals for the species decreased by six orders of magnitude. Using the rate parameters given in Zabarnick (1996), it was found that the numerical procedure described here could reproduce the oxygen profiles computed by Zabarnick (1996), who used an entirely different solution technique.

For completeness, two kinds of computations were performed: those for an inhibited system and those for a completely noninhibited system. For the inhibited system, the initial AH concentration was 2.3×10^{-4} M, which is a representative value for jet fuels (Zabarnick, 1993; Heneghan and Zabarnick, 1994). For the completely uninhibited case, which could represent autoxidation in a severely hydrotreated fuel, the AH concentration was set equal to 0 M. For simplicity, SH, the hydroperoxide decomposer, was assumed to be zero in all computations. Such simulations have been found to represent autoxidation well in a fuel that is low in heteroatomic species (Ervin et al., 1997). In the figures that follow, three different fractions (10, 50, and 100 percent) of the normal air saturation

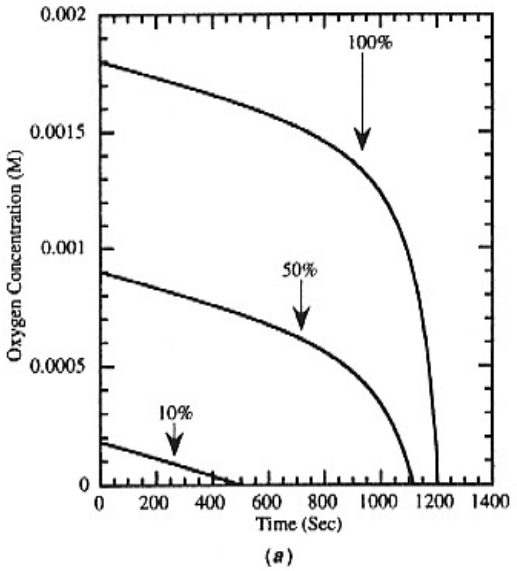

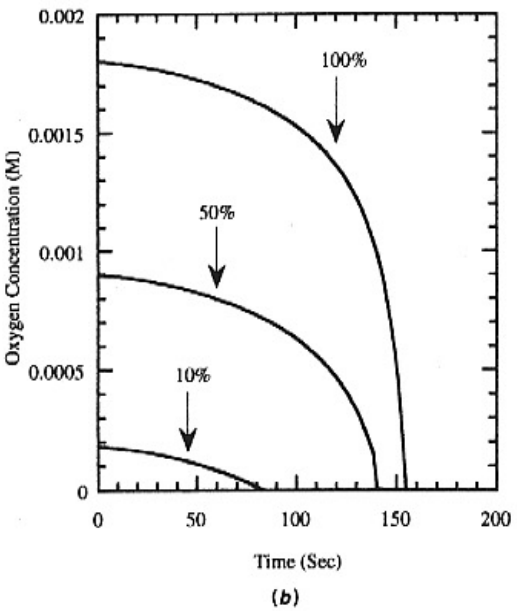

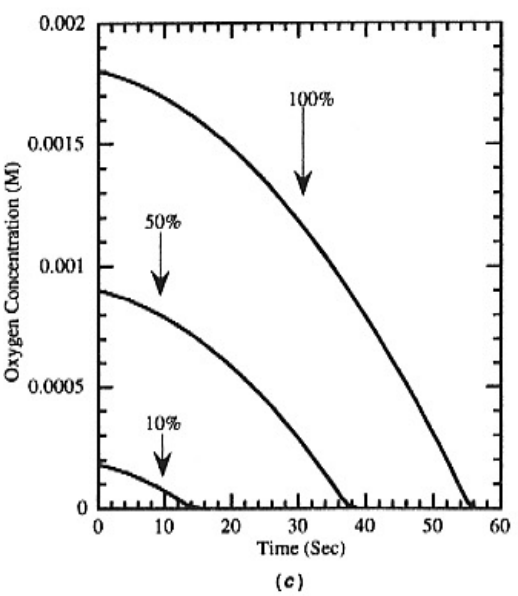

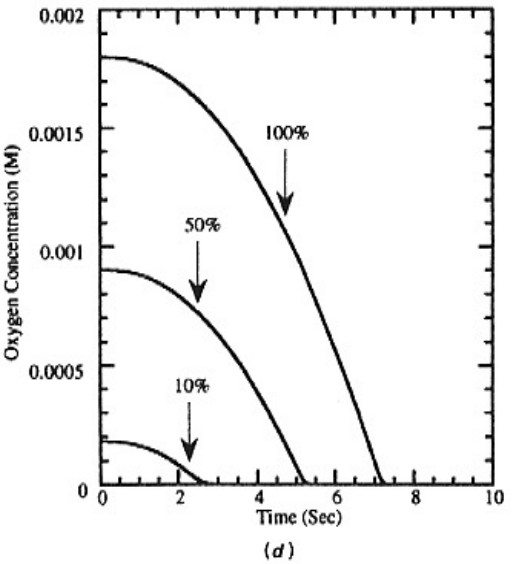

Fig. 1(*a*) Decay of oxygen concentration with time for different initial oxygen concentrations at 185°C & antioxidant concentration of 2.3 × 10^{-4} M; (*b*) decay of oxygen concentration with time for different initial oxygen concentrations at 215°C and antioxidant concentration of 2.3 × 10^{-4} M; (*c*) Decay of oxygen concentration with time for different initial oxygen concentrations at 185°C and antioxidant concentration of 0 M; and (*d*) decay of oxygen concentration with time for different initial oxygen concentrations at 215°C and antioxidant concentration of 0 M.

concentration are given as initial oxygen concentrations. Figures 1(*a*) through (*d*) show the computed decay profiles of dissolved oxygen concentration.

Figures 1(*a*) and 1(*b*) show the computed decay profiles of dissolved oxygen concentration for fuel with an initial antioxidant concentration of 2.3 × 10^{-4} M. As expected, as the temperature is increased from 185°C (Fig. 1(*a*)) to 215°C (Fig. 1(*b*)), the time required for complete depletion of the dissolved oxygen for each initial oxygen concentration decreases. The enhanced oxygen consumption rate with increasing temperature is primarily due to the temperature dependence of reactions 3 and 11 of Table 2. In this temperature range, the alkyl hydroperoxides produced in reaction 3 of Table 2 decompose, generating radi-

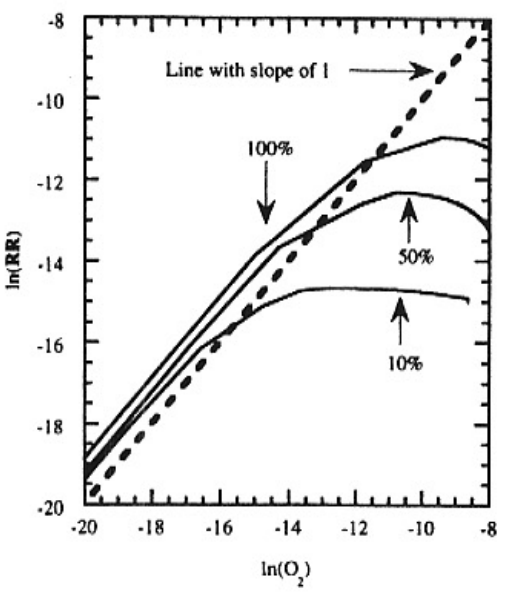

Fig. 2 Observed order plot for different initial oxygen concentrations. 185°C and antioxidant concentration of 2.3 × 10^{-4}M.

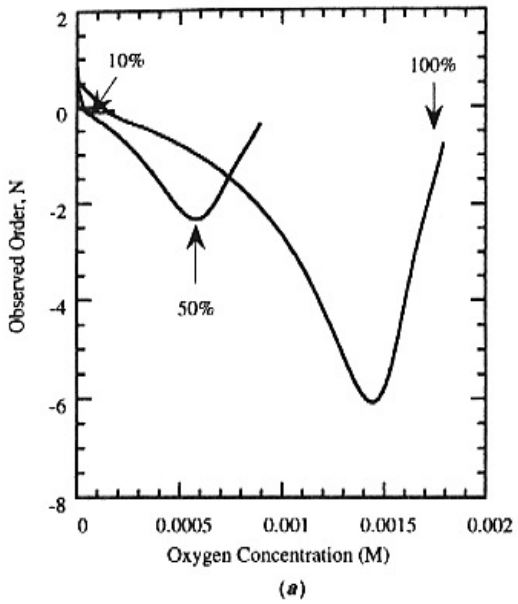

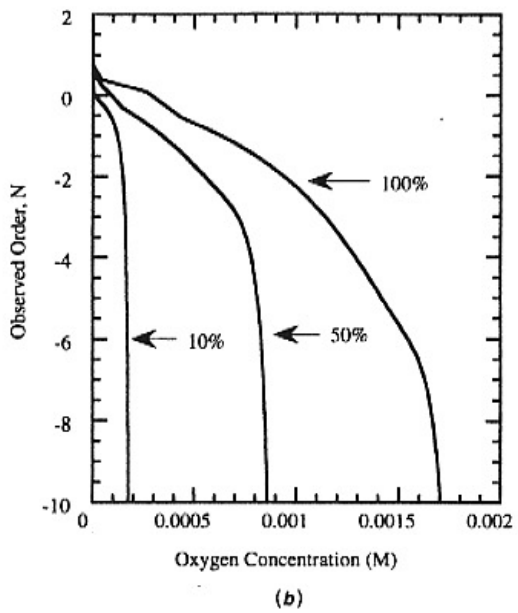

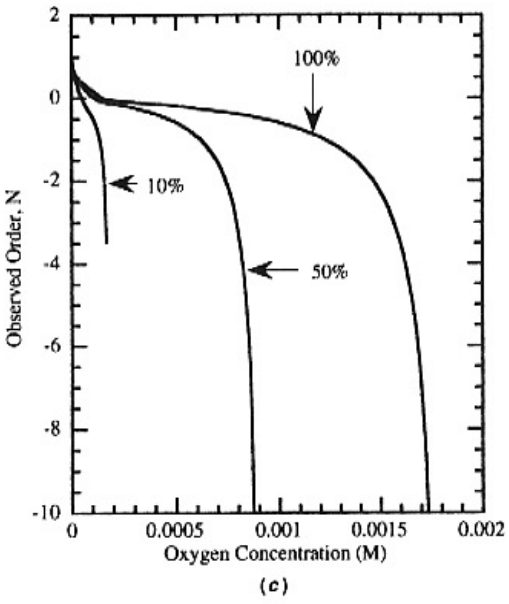

Fig. 3(*a*) Variation of *N* with oxygen consumption for different initial oxygen concentrations. 185°C and antioxidant concentration of 2.3×10^{-4} M; (*b*) Variation of *N* with oxygen consumption for different initial oxygen concentrations. 215°C and antioxidant concentration of 2.3×10^{-4} M; and (*c*) variation of *N* with oxygen consumption for different initial oxygen concentrations. 185°C and antioxidant concentration of 0 M.

cals (reaction 11) that greatly increase the rate of oxygen removal.

Figures 1(*c*) and 1(*d*) (fuel temperatures of 185°C and 215°C, respectively) show dissolved oxygen decay profiles resulting from a zero AH concentration. Given the same temperature and initial dissolved oxygen concentration, the dissolved oxygen is reacted at a significantly greater rate with the noninhibited system than with the presence of AH (Figures 1(*a*) and 1(*b*)). The decrease in oxygen decay rate associated with the fuel containing the antioxidant occurs because AH acts to interfere with the chain propagation. Again, as in Figures 1(*a*) and 1(*b*), as the temperature is increased from 185°C to 215°C, the time period required for complete oxygen removal decreases because the rate of alkyl hydroperoxide decomposition significantly increases as the temperature is increased. As observed by Zabarnick (1993) in numerical simulations and by Jones et al. (1995) in nearly isothermal flowing experiments, autocatalysis is characterized by curvature of the oxygen decay profile. Thus, at 185°C, the oxygen profile is nearly linear, and the nonlinearity increases at 215°C as the rate of alkyl hydroperoxide decomposition rises. Similarly, for the fuel containing antioxidants, the oxygen decay profile is nearly linear for much of the period before oxygen depletion at 185°C (Fig. 1(*a*)), and the nonlinearity increases at 215°C (Fig. 1(*b*)).

If an initial oxygen concentration is established and then followed in time by either experiment or computational simulation, a functional relationship between O_2 and time for a given set of conditions can be established. The rate (**RR**) can be calculated from the time derivative of the computed oxygen concentration, and the observed order can be found from the plot of ln (**RR**) versus ln (O_2). Values of ln (**RR**) for three different initial oxygen concentrations at a temperature of 185°C and AH concentration of 2.3×10^{-4} M are given in Fig. 2. Figure 2 shows that d ln (**RR**)/d ln (O_2), the observed order, changes continuously for each O_2 curve until the dissolved oxygen is significantly diminished. As the three curves converge, they are more linear with a slope that approaches unity. Thus, Fig. 2 shows that the observed order depends on both the initial and remaining dissolved oxygen concentrations.

More explicitly for the three different initial oxygen concentrations at 185°C, Fig. 3(*a*) gives values of N resulting from the calculation of d ln (**RR**)/d ln (O_2) as part of the finite difference computations. (These values of N may also be derived from Fig. 2 by taking tangents to the curves shown.) Figure 3(*a*) shows that N changes in a complicated manner with O_2 concentration which also decreases with time: N is a small negative number at time zero, and then approaches unity as the oxygen nears depletion. Thus, Fig. 3(*a*) reveals that a constant overall reaction order cannot represent the observed behavior of this autoaccelerating system. (In practice, the overall reaction order is some N selected at an arbitrary time that is often near time zero). Furthermore, Fig. 3(*a*) shows that N varies with the initial oxygen concentration. Figure 3(*b*) at a temperature of 215°C shows that N again is different for different initial oxygen concentrations and varies with the concentration of unreacted dissolved oxygen. At 215°C, where the hydroperoxide decomposition reactions become more important, N is initially a negative number and remains negative over much of the oxygen consumption history. For small oxygen concentrations, N becomes equal to unity. Thus, the behavior of N is very different from that observed at 185°C. Figures 3(*a*) and (*b*)

show that the observed reaction order depends strongly on temperature, initial oxygen concentration, and the extent of reaction.

Figure 3(*c*) shows that N changes with initial O_2 concentration and the extent of O_2 consumption for conditions in which the initial AH concentration is zero at a reaction temperature of 185°C. In Fig. 3(*c*), N is negative near time zero but approaches unity for dissolved oxygen concentrations that fall below 0.0001 M. For conditions of zero antioxidant and a temperature of 215°C (not shown), the computed N values were negative near time zero but approached unity for small dissolved oxygen concentrations in a manner similar to that observed at the lower temperature in Fig. 3(*c*). Figures 3(*a*), (*b*), and (*c*) show that the value for the overall reaction order is dependent on how the order is measured. Thus, to determine the order of the initiation reactions, it is insufficient to follow the rate and the oxygen concentration in time and extrapolate the observed N back to time zero.

For simplicity, some engineering computational fluid dynamics codes that use global chemistry assume an overall reaction order for oxygen consumption of unity (Krazinski et al., 1992). Others (Chin et al., 1994; Ervin et al., 1996) permit a step change in the global order. These models ignore the initiation region of the observed order curve (Fig. 3(*c*), for example) and assume that the overall reaction order is 0 until the O_2 is reduced to some arbitrary critical concentration. At this low concentration, the order is set equal to unity. For initial dissolved O_2 concentrations of 100 percent and 50 percent of normal air saturation, Fig. 3(*c*) (with zero initial AH) demonstrates that an overall zero order reaction over much of the oxygen profile at 185°C, with a change to an overall first order reaction, is a reasonable first approximation to the more detailed modeling. As the temperature is increased, the rate of peroxide decomposition will also increase, and the effects of autoacceleration on N are more significant. In addition, Fig. 3(*c*) shows that for small initial dissolved oxygen concentrations (here, on the order of 0.0001 M) that very little of the oxygen decay profile is characterized by an N of zero. Furthermore, with the nonzero antioxidant concentration for both temperatures (Figs. 3(*a*) and (*b*)), it is obvious that assuming either an overall constant first order reaction or a zero order reaction that then switches to a first order reaction will be different from the N given by the pseudo-detailed kinetic modeling. Thus, as the fuel is heated to greater temperatures, or if antioxidants are used, the explicit form for the global order will not be simple. Moreover, Figs. 3(*a*) through (*c*) suggest that the error in using a simple overall global expression for oxygen consumption may be large.

Conclusions

Analysis and numerical simulation of low temperature oxidation of a hydrocarbon fuel have been used to show that a single overall activation energy and observed order are functions of the initial conditions, time, and temperature. The activation energy and the reaction order both depend on the initial concentration of dissolved oxygen and the concentration remaining. Applying the operator for activation energy and reaction order to the rate law for a complicated (autoaccelerating) rate does not necessarily yield a simple activation energy or reaction order, as might be expected from a global reaction rate law. Consequently, the activation energy or the reaction order of such a reaction process are not well defined concepts, and referring to them in the classical manner is incorrect. Furthermore, using these concepts to extrapolate data in time or temperature will likely yield erroneous results. These findings have important implications for the use of simple global parameters in engineering computational fluid dynamics models that simulate autoaccelerating systems. Pseudo-detailed kinetic mechanisms for oxygen consumption (as in Table 2) have been found in previous works to predict reasonably well oxygen consumption measurements. As a practical consequence, pseudo-detailed global models may be used to represent autoxidation instead of a single, simplistic reaction that may fail to represent a complex series of reactions.

Acknowledgments

This work was supported by the US Air Force, Fuels and Lubrication Division, Aero Propulsion and Power Directorate, Wright Laboratory, WPAFB, under Contract No. F33615-92-C-2207 (Technical Monitor: C. W. Frayne). The authors acknowledge the many beneficial discussions with Dr. S. Zabarnick of the University of Dayton Research Institute.

References

Chin, L. P., Katta, V. R., and Heneghan, S. P., 1994, "Numerical Modeling of Jet Fuel Autoxidation in Flowing Systems," *ACS Preprints, Div. of Petroleum Chemistry,* Vol. 39, p. 19.

Coordinating Research Council, 1983, *Handbook of Aviation Fuel Properties,* Coordinating Research Council, Atlanta, GA.

Ervin, J. S., Williams, T. F., and Katta, V. R., 1996, "Global Kinetic Modeling of Aviation Fuel Fouling in Cooled Regions in a Flowing System," *Ind. Eng. Chem. Res.,* Vol. 35, p. 4028.

Ervin, J. S., Zabarnick, S., and Williams, T. F., 1997, "Modeling of Jet Fuel Oxidation at Low Temperatures," AIAA 97-0272, AIAA 35th Aerospace Sciences Meeting, Reno, NV, Jan. 1997.

Hazlett, R. N., 1991, *Thermal Oxidative Stability of Aviation Turbine Fuels,* ASTM, Philadelphia, PA.

Heneghan, S. P., and Zabarnick, S., 1994, "Oxidation of Jet Fuels and Formation of Deposits," *Fuel,* Vol. 73, p. 35.

Katta, V. R., Blust, J., Williams, T. F., and Martel, C. R., 1995, "Role of Buoyancy in Fuel-Thermal Stability Studies," *J. of Thermophysics and Heat Transfer,* Vol. 9, p. 159.

Krazinski, J. L., Vanka, S. P., Pearce, J. A., and Roquemore, W. M., 1992, "A Computational Fluid Dynamics Model for Jet Fuel Thermal Stability," ASME JOURNAL OF ENGINEERING FOR GAS TURBINE AND POWER, Vol. 114, p. 104.

Jones, E. G., Balster, W. J., and Post, M. E., 1995, "Thermal Degradation of Jet-A Fuel in a Single Pass Heat Exchanger," ASME JOURNAL OF ENGINEERING FOR GAS TURBINE AND POWER, Vol. 117, p. 125.

Jones, E. G., Balster, W. J., and Rubey, W. A., 1995, "Fouling of Stainless Steel and Silcosteel Surfaces During Aviation-Fuel Autoxidation," *ACS Preprints, Div. of Petroleum Chemistry,* Vol. 40, p. 660.

Jones, E. G., Balster, L. M., and Balster, W. J., 1996, "Thermal Stability of Jet A Fuel Blends," *Energy and Fuels,* Vol. 10, p. 509.

Martel, C. R., 1987, "Military Jet Fuels, 1944–1987," Air Force Wright Aeronautical Laboratory Technical Report AFWAL-TR-87-2062, Wright-Patterson Air Force Base, OH.

Mayo, F. R., 1968, "Free-Radical Autoxidations of Hydrocarbons," *Acc. Chem. Res.,* Vol. 1, p. 193.

Wylie, C., and Barrett, L., 1982, *Advanced Engineering Mathematics,* McGraw-Hill, New York.

Zabarnick, S., 1993, "Chemical Kinetic Modeling of Jet Fuel Autoxidation and Antioxidant Chemistry," *Ind. Eng. Chem. Res.,* Vol. 32, p. 1012.

Zabarnick, S., 1998, "Chemical Kinetic Modeling of Jet Fuel Autoxidation and Antioxidant Chemistry," *Energy and Fuels,* Vol. 12, p. 547.

D. Pseudo-Detailed Chemical Kinetic Modeling of Antioxidant Chemistry for Jet Fuel Applications

Pseudo-Detailed Chemical Kinetic Modeling of Antioxidant Chemistry for Jet Fuel Applications

Steven Zabarnick†

Aerospace Mechanics Division, University of Dayton Research Institute, 300 College Park, KL-463, Dayton, Ohio 45469-0140

Received September 2, 1997. Revised Manuscript Received February 13, 1998

Chemical kinetic modeling was used to simulate the autoxidation of jet fuel including the chemistry of peroxy radical inhibiting antioxidants and hydroperoxide decomposing species. Recent experimental measurements of oxygen concentration during autoxidation of model hydrocarbon solvents were used to "calibrate" the rate parameters of the mechanism. The model showed good agreement with oxygen profiles of static measurements at 140 °C. At this temperature, the model predicts large increases in oxidation rate upon peroxy radical inhibiting antioxidant consumption to below 1×10^{-5} M. At 185 °C we have shown that peroxy radical inhibiting antioxidants and hydroperoxide decomposers both slow and/or delay oxidation, but the resulting oxygen profiles display different characteristics. We have shown that comparison of these profiles with fuel blending and fuel dilution measurements has the potential to differentiate between the two types of oxidation-slowing species. The modeling predicts that the presence of both types of species in a fuel results in a synergistic behavior.

Introduction

Liquid hydrocarbons, and liquid hydrocarbon fuels such as jet fuel in particular, undergo a series of reactions in the presence of oxygen which together are often called "autoxidation." These reactions occur at moderate temperatures (∼100−300 °C) and produce oxygenated species, such as hydroperoxides, alcohols, ketones, aldehydes, and acids. Subsequent poorly understood reactions can produce particulates, gums, and solid deposits. In general, the production of these and other oxidized species is highly undesirable. For example, in lubricating oils the reaction with oxygen produces acids which are corrosive.[1] The production of gums in gasoline can cause injector/carburetor plugging, valve malfunctions, and piston and crankcase fouling.[2] In military supersonic aircraft, where jet fuel is used for cooling of lubricating oils and hydraulic fluids, the formation of deposits has been implicated in the fouling of injector nozzles, fuel manifolds, and main engine controls.[3]

Antioxidants have been used for many decades to slow and/or delay autoxidation. Indeed, the development of antioxidants has been so successful that they are used routinely in many industrial and consumer products, including foods and gasoline. There are many types of antioxidants that have been used in hydrocarbon liquids: hindered phenols, phenylenediamines, peroxide decomposers, and metal deactivators. It is believed that hindered phenols and phenylenediamines slow oxidation by intercepting the alkylperoxy free radicals that carry the autoxidation chain. Peroxide decomposers react with hydroperoxides and prevent their decomposition into free radicals. Metal deactivators complex with metal ions and prevent their catalysis of processes which form free radicals. Thus, each of these antioxidant types is thought to lower the concentration of free radicals by either preventing their formation or rapidly removing them after they are formed.

Although antioxidants are widely used and have proven very successful in preventing the formation of detrimental products, chemical kinetic modeling of the chemical mechanism of antioxidant action has received little attention. Fortunately, the primary reactions by which hindered phenol antioxidants intercept alkylperoxy radicals have been studied extensively. Previously, we have performed chemical kinetic modeling of antioxidant action for jet fuel applications.[4] This study was limited to relatively short reaction times before significant consumption of the antioxidant species occurred. Also, because of the lack of suitable experimental data, no comparison with laboratory measurements was included. Recent measurements of oxygen concentration during the autoxidation of jet fuel, jet fuel mixtures, and model jet fuel species have provided reasonable data for comparison with modeling.[5−8] In the present study we utilize these experimental data

† Telephone: (937) 255-3549. E-mail: steve@snake.appl.wpafb.af.mil.

(1) Murphy, C. M.; Ravner, H.; Smith, N. L. *Ind. Eng. Chem.* **1950**, *42*, 2479−2489.
(2) Walters, E. L.; Minor, H. B.; Yabroff, D. L. *Ind. Eng. Chem.* **1949**, *41*, 1723−1729.
(3) Hazlett, R. N. *Thermal Oxidation Stability of Aviation Turbine Fuels*; ASTM: Philadelphia, 1991.
(4) Zabarnick, S. *Ind. Eng. Chem. Res.* **1993**, *32*, 1012−1017.
(5) Jones, E. G.; Balster, L. M.; Balster, W. J. *Energy Fuels* **1996**, *10*, 509−515.
(6) Zabarnick, S.; Whitacre, S. D. Aspects of Jet Fuel Oxidation. *Proceedings of the 1997 ASME Turbo Expo Conference*; ASME: New York, 1997; Paper No. 97-GT-219.
(7) Zabarnick, S.; Zelesnik, P.; Grinstead, R. R. *J. Eng. Gas Turbines Power* **1996**, *118*, 271−277.
(8) Balster, L. J.; Balster, W. J.; Jones, E. G. *Energy Fuels* **1996**, *10*, 1176−1180.

S0887-0624(97)00157-6 CCC: $15.00
Published on Web 04/08/1998

Table 1. Reaction Mechanism for Chemical Kinetic Modeling

reaction	Arrhenius *A* factor (mol, L, s)	activation energy (kcal/mol)	reaction no.
$I \rightarrow R^{\bullet}$	1×10^{-3}	0.0	1
$R^{\bullet} + O_2 \rightarrow RO_2^{\bullet}$	3×10^{9}	0.0	2
$RO_2^{\bullet} + RH \rightarrow RO_2H + R^{\bullet}$	3×10^{9}	12.0	3
$RO_2^{\bullet} + RO_2^{\bullet} \rightarrow$ termination	3×10^{9}	0.0	4
$RO_2^{\bullet} + AH \rightarrow RO_2H + A^{\bullet}$	3×10^{9}	5.0	5
$AO_2^{\bullet} + RH \rightarrow AO_2H + R^{\bullet}$	3×10^{5}	10.0	6
$A^{\bullet} + O_2 \rightarrow AO_2^{\bullet}$	3×10^{9}	0.0	7
$AO_2^{\bullet} + AH \rightarrow AO_2H + A^{\bullet}$	3×10^{9}	6.0	8
$AO_2^{\bullet} + AO_2^{\bullet} \rightarrow$ products	3×10^{9}	0.0	9
$R^{\bullet} + R^{\bullet} \rightarrow R_2$	3×10^{9}	0.0	10
$RO_2H \rightarrow RO^{\bullet} + {}^{\bullet}OH$	1×10^{15}	42.0	11
$RO^{\bullet} + RH \rightarrow ROH + R^{\bullet}$	3×10^{9}	10.0	12
$RO^{\bullet} \rightarrow R_{prime}^{\bullet} +$ carbonyl	1×10^{16}	15.0	13
${}^{\bullet}OH + RH \rightarrow H_2O + R^{\bullet}$	3×10^{9}	10.0	14
$RO^{\bullet} + RO^{\bullet} \rightarrow RO^{\bullet}$ termination	3×10^{9}	0.0	15
$R_{prime}^{\bullet} + RH \rightarrow$ alkane $+ R^{\bullet}$	3×10^{9}	10.0	16
$RO_2H + SH \rightarrow$ products	3×10^{9}	0.0	17

for "calibration" of the kinetic parameters of the model. Also, we compare the predicted and measured oxygen profiles to provide insight into the antioxidant mechanism. In addition, we explore the type of behavior expected by the presence of peroxide-decomposing species. This study will also address relatively long reaction times, where the antioxidant species may become completely consumed.

Methodology

The methodology used in the chemical kinetic modeling reported here has been reported previously[4] and therefore will only be described briefly. The chemical kinetic modeling was performed using the modeling package REACT.[9] This is a relatively simple package that integrates the multiple differential equations that result from a detailed chemical kinetic mechanism and yields species concentrations as a function of time. This code does not solve the energy equation and therefore does not include energy production or removal due to chemical reaction. The following is input to the code: reaction mechanism with rate constants, initial concentrations for each species present in the mechanism, reaction time and time intervals for output, and various tolerances for the precision of the computation. The code outputs the individual species concentrations at each time interval.

Because jet fuels are mixtures of hundreds of chemical species, it is impractical to model the chemical changes of all components of the mixture. Instead we have chosen to model the bulk fuel as a single compound, RH. RH has the chemical properties of a straight-chain alkane, such as *n*-dodecane; this is a reasonable simplification as alkanes comprise a large proportion of a jet fuel mixture. This single compound "fuel" can also contain dissolved oxygen (O_2), an antioxidant species (AH), and a peroxide decomposer (SH). The reaction mechanism used in the present study is shown in Table 1. We refer to the mechanism as being "pseudo-detailed" as it has some of the characteristics of detailed reaction mechanisms, i.e., real chemistry with physically meaningful rate parameters, but is less simplified than the simple empirical modeling using one or two reactions that have been used in jet fuel modeling in the past. The mechanism is a modification of that used previously.[4] Modifications involve adjustment of rate parameters to better match experimental measurements and the inclusion of a "peroxide decomposer" species. These modifications will be detailed below.

In the previous modeling study,[4] we presented a reaction mechanism of jet fuel autoxidation and estimated rate parameters (Arrhenius "*A* factors" and activation energies) for these pseudo-elementary reactions. These are not true elementary reactions due to the modeling of all fuel species as a single species, RH. The rate constant parameters were estimated using a combination of techniques: comparison with measured rate constants and Benson style "thermochemical kinetics" analysis. Also, some of the rate parameters were adjusted and the effects of these changes were observed in the output. The rate constants, k, were estimated in Arrhenius form, i.e., $k = A \exp(E_a/RT)$; thus, an activation energy, E_a, and an Arrhenius "*A* factor" were estimated for each reaction. The mechanism used in the current study is a modified version of the previous mechanism. These modifications are based on comparisons of the calculated oxygen concentration time behavior with experimental measurements.

The mechanism has been described in detail previously[4] and will only be summarized here. In Table 1, $R^{\bullet}$ is a hydrocarbon alkyl radical species, RH represents the bulk fuel as a single hydrocarbon compound, AH is an antioxidant species (i.e., a species with an easily abstractable hydrogen atom, also referred to in the literature as an inhibitor), O_2 represents the dissolved oxygen present in the liquid fuel, SH is a peroxide decomposing species, and I is an initiator species. The alkyl radicals required to begin the autoxidation chain are produced by an initiation step, reaction 1. For simplicity we use a unimolecular decomposition of I into $R^{\bullet}$ radicals to represent the poorly understood initiation process. This is an obvious oversimplification of the poorly understood initiation process, but its inclusion is required to begin the chain with a very small production rate of $R^{\bullet}$ radicals. An activation energy of zero was chosen for simplicity, although it is most likely that the real initiation rate increases strongly with temperature. The *A* factor was chosen along with the initial I concentration to produce an initial $R^{\bullet}$ radical production rate that is large enough to start the autoxidation chain, yet small enough to remain an insignificant source of radicals once the chain has begun.

Reaction 2 converts these $R^{\bullet}$ radicals to alkylperoxy radicals, $RO_2^{\bullet}$, by reaction with dissolved O_2. This addition reaction is expected to have a near-zero activation energy, and thus proceeds very rapidly. In reaction 3, $RO_2^{\bullet}$ abstracts a hydrogen atom from a fuel molecule, generating a hydroperoxide, RO_2H, and another $R^{\bullet}$ radical, thus propagating the chain. At sufficiently high temperatures, the hydroperoxide will decompose to yield the additional radicals, $RO^{\bullet} + OH$ (reaction 11). These radicals then undergo additional reactions (reactions 12−16), forming alcohols, carbonyl compounds, water, and other species. If the concentration of $RO_2^{\bullet}$ radicals is sufficient, the termination reaction, reaction 4, can occur; this reaction can produce aldehydes, alcohols, and ketones and may regenerate oxygen by a disproportion-

(9) Whitbeck, M. *Tetrahedron Comput. Methodol.* **1990**, *3*, 497−505.

Table 2. Initial Concentrations of Species

species	initial concn (M)
I	1.0×10^{-7}
O_2	1.8×10^{-3}
RH	4.4
AH	varied, but typically 2.0×10^{-4}
SH	varied
all other species	0.0

ation pathway. For simplicity, we have chosen to disregard the subsequent reactions of the products of reaction 4. When the dissolved oxygen concentration becomes low, R• radicals predominate over RO_2• and these can self-terminate by reaction 10. When an antioxidant species, AH, is present, reactions 5−9 become important. Also, when a peroxide-decomposing species, SH, is present, reaction 17 may play an important role. The AH and SH reactions will be addressed in detail below.

The initial concentrations of each of the species present in the mechanism are also required input to the modeling code. These initial concentrations are listed in Table 2. The RH concentration was estimated from the room-temperature molarity of *n*-dodecane liquid (molecular weight of 170 amu and density of 0.752 g/cm^3). The dissolved oxygen concentration was estimated from the review of oxygen solubility by Battino et al.[10] and from a compilation of jet fuel properties.[11] From these papers we estimate the dissolved oxygen concentration at room temperature and one atmosphere air in jet fuels and hydrocarbons as ∼79 ppm (by weight). Therefore, we have used 1.8×10^{-3} M for the oxygen concentration. The antioxidant concentration, AH, was varied over a wide range in the calculation, so a typical value of 2.0×10^{-4} M was listed in the table. A very small concentration (1.0×10^{-7} M) of the initiator species, I, was included for the initial production of R• radicals required to get the chain mechanism started. The peroxide-decomposing species concentration was varied.

Calibration of the Model

A modified version of the previous mechanism was used in the present study.[4] To provide agreement with the measured oxidation rates, the rate constant parameters of reactions 1, 3, and 8 were adjusted. The oxygen concentration versus time data of Balster et al.[8] was used to "calibrate" the rate parameters in the absence of antioxidant species, AH. Balster et al. measured the oxygen concentration at the outlet of a tubular heat exchanger operated isothermally at 185 °C. These measurements were performed as a function of flow rate to provide various residence times in the heated tube. For the present modeling study, we are most interested in the results of Balster et al. on the oxidation of the paraffinic/cycloparaffinic solvent Exxsol D-80. Exxsol D-80 is a dearomatized, narrow-cut aliphatic solvent with <1% aromatics and 3 ppm total sulfur. As it is highly refined, it contains few naturally occurring antioxidants and therefore oxidizes quite rapidly. If we think of a real jet fuel as composed largely of relatively unreactive hydrocarbons with small amounts of reactive heteroatom species, then Exxsol D-80 closely resembles jet fuel without these other species. Thus, we used the measured oxidation rate of Exxsol D-80 to "calibrate" the model as follows. The reactants AH and SH were set to zero; this "shuts off" the antioxidant (reactions 5−9) and peroxide decomposition (reaction 17) parts of the mechanism. Thus we are modeling a highly purified fuel with few antioxidants or peroxide decomposers, which are usually heteroatomic species.

We adjusted the activation energy for reaction 3 until the calculated oxygen vs time data closely matched the measurements of Balster et al. for Exxsol D-80 at 185 °C. This occurs at an activation energy for reaction 3 of 12.0 kcal/mol. This value is higher than the 10.0 kcal/mol used in the previous study.[4] In the previous work, this activation energy was chosen based on an average of similar H-atom abstraction reactions in the literature. But, these activation energies vary over the range 8−14 kcal/mol. Thus, a value of 12.0 kcal/mol is still reasonable. Using this new value for E_a of reaction 3 yields complete oxygen removal in 1 min at 185 °C. As this reaction time is now much longer than in the previous modeling study, it was found necessary to lower the rate of initiation, i.e., the rate constant of reaction 1. The *A* factor of reaction 1 was decreased from the previous value of 1×10^{-1} to 1×10^{-3} s^{-1}. This was necessary because it is important that the initiation step produce a large enough R• radical production rate to start the autoxidation chain, yet small enough to remain an insignificant source of R• radicals once the chain has begun. Unusual O_2 versus time behavior was noted when the initiation rate was too fast.

The headspace oxygen concentration versus time data of Zabarnick and Whitacre[6] were used to calibrate the antioxidant section of the mechanism. This study measured the headspace oxygen concentration versus time for oxidation of Exxsol D-110 solvent at various BHT (2,6-di-*tert*-butyl-4-methylphenol) concentrations in a Parr reactor at 140 °C. Exxsol D-110 is very similar to Exxsol D-80, but with a lower volatility. It was found that good agreement with the experimental data at 25 mg/L (1.14×10^{-4} M) BHT could be obtained by adjusting the activation energy of reaction 8 from the previously used value of 5.0 kcal/mol to 6.0 kcal/mol. In the previous modeling study this value had been estimated based on analogous reactions.

Results and Discussion

Modeling of BHT Addition at 140 °C. Recent measurements of the antioxidant behavior of jet fuel, jet fuel mixtures, and model jet fuel species have shown a distinctive behavior of the oxidation profiles as the antioxidant concentration is varied.[6−8] An example of this behavior is shown in Figure 1 for the autoxidation of Exxsol D-110 with various levels of added BHT at 140 °C in a Parr bomb reactor.[6] It is apparent from the figure that increasing levels of added BHT result in increasing delays in the oxidation process. The oxidation behavior with added antioxidant is characterized by a slow initial oxidation followed by a sudden rapid increase in the oxidation rate. Zabarnick and Whitacre[6] followed the BHT concentration in time and observed a decrease in BHT during the initial slow oxidation. The

(10) Battino, R.; Rettich, T. R.; Tominaga, T. *J. Phys. Chem. Ref. Data* **1983**, *12*, 163−178.
(11) Coordinating Research Council. *Handbook of Aviation Fuel Properties*; 1983.

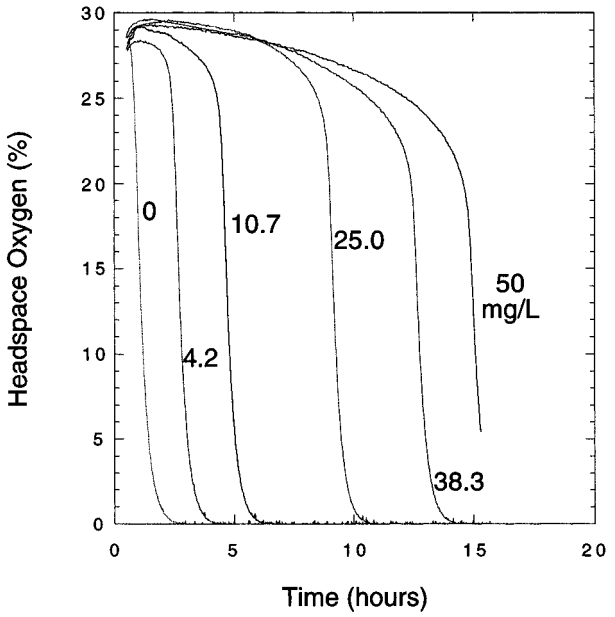

Figure 1. Plots of headspace oxygen concentrations versus time for Exxsol D-110 at various concentrations of added BHT at 140 °C in a Parr bomb/QCM system. Reprinted with permission from ref 6. Copyright 1997 American Society of Mechanical Engineers (ASME).

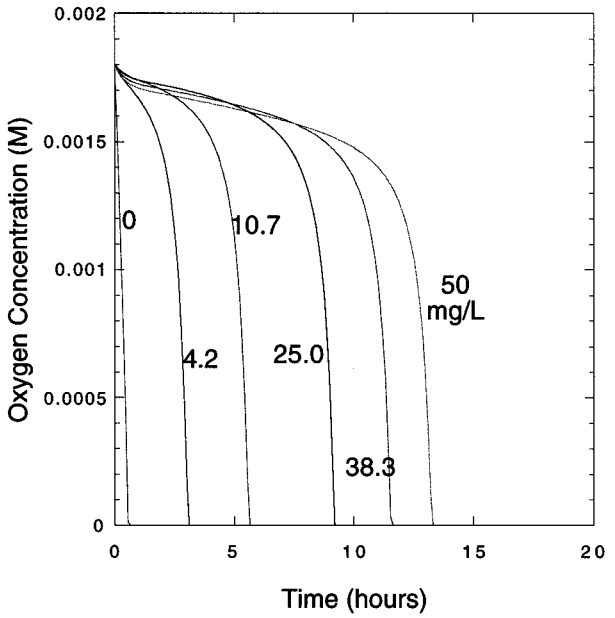

Figure 2. Plots of calculated oxygen concentration versus time at various concentrations of added antioxidant BHT at 140 °C.

change to an increased oxidation rate occurred when the BHT concentration became very low (<5 mg/L).

Previous chemical kinetic modeling of antioxidants in jet fuel concentrated on relatively short reaction times, where significant consumption of the antioxidant species had not occurred.[4] In the present work, we extend the modeling to longer times to determine if the model can predict and corroborate the sudden increase in oxidation rate upon antioxidant consumption. The results at various levels of added BHT antioxidant are shown in Figure 2. The figure shows plots of oxygen concentration versus time for modeling performed at 140 °C. The rate parameters of Table 1 were used and the concentration of the peroxide decomposing species, SH, was held at zero to turn off reaction 17. The plot shows that without added antioxidant the fuel oxidizes rapidly, completely consuming the available oxygen in less than 1 h. In the presence of added antioxidant there is an initial slow oxidation followed by a change to a more rapid loss of oxygen. As the antioxidant concentration is increased, the delay until the onset of rapid oxidation increases. This qualitative behavior is remarkably similar to the experimental measurements of Figure 1. As the antioxidant concentration is varied over the range 0−50 mg/L, the time at which the oxidation rate rapidly increases matches the measurements quite well. Note that a direct quantitative comparison between Figures 1 and 2 cannot be performed as the Parr bomb technique is complicated by the presence of headspace oxygen and diffusional effects.[12] Also the first 45 min to 1 h of the measurements in Figure 1 corresponds to the heat-up period of the reactor, and thus significant reaction does not occur during this time.

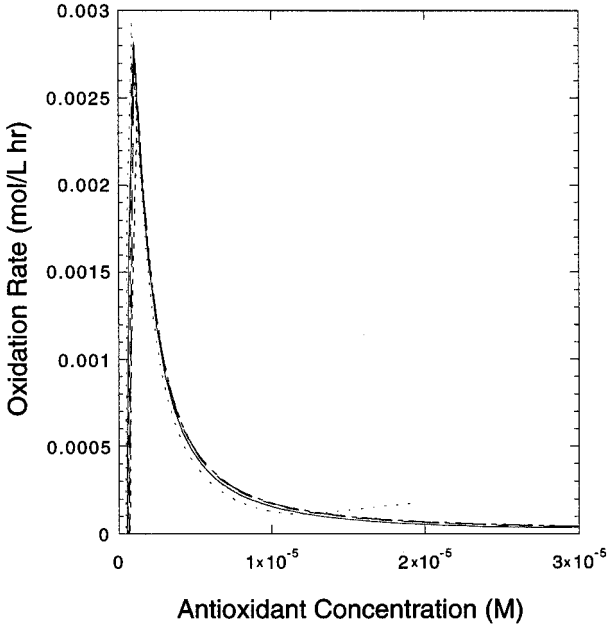

Figure 3. Plots of oxidation rate versus antioxidant concentration for chemical kinetic modeling at 140 °C.

In order to determine if antioxidant consumption is the cause of the sudden increase in oxidation rate during these runs, we have plotted oxidation rate versus antioxidant concentration for the five concentrations of AH modeled, in Figure 3. The figure shows that when the antioxidant concentration is high (i.e., at short times) the oxidation rate is low, but as the antioxidant is consumed and reduced below 1×10^{-5} M (2.2 mg/L using the molecular weight of BHT) there is a rapid increase in the oxidation rate. This increase in rate is independent of the starting antioxidant concentration. At even lower antioxidant concentrations the oxidation rate drops rapidly; this is due to complete oxygen consumption. This plot demonstrates that the model predicts the sudden change in oxidation rate seen in Figure 2 is due to consumption of the antioxidant.

Modeling of Autoxidation at 185 °C. Figure 4 shows results for the modeling at a temperature of 185 °C. Without antioxidant the fuel oxidizes rapidly, completely consuming the oxygen in 60 s. As at 140

(12) Zabarnick, S. *Ind. Eng. Chem. Res.* **1994**, *33*, 1348−1354.

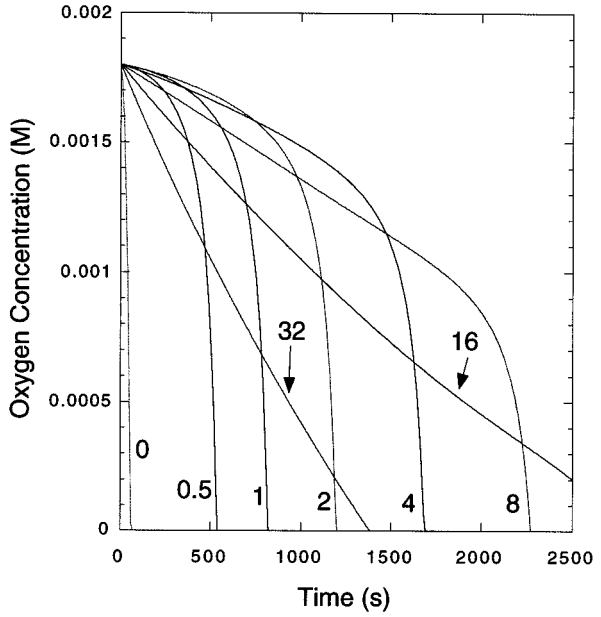

Figure 4. Plots of calculated oxygen concentration versus time for various concentrations of added antioxidant AH ($\times 10^{-4}$ M) at 185 °C.

°C, at relatively low concentrations of added antioxidant ($(0.5-8) \times 10^{-4}$ M) there is an initial slow oxidation followed by a change to a more rapid oxygen loss. The figure also shows predicted oxygen profiles at relatively high concentrations of added antioxidant, up to 3.2×10^{-3} M (704 mg/L based on the molecular weight of BHT). As the antioxidant concentration is increased above 8×10^{-4} M, the rate of the initial oxidation increases significantly, eroding the gains in slowing the oxidation at lower concentrations of antioxidant. This increase in oxidation rate with added antioxidant is similar to that observed in the blending of slow and fast oxidizing fuels.[8] These workers progressively diluted a slow oxidizing fuel with Exxsol D-80 and measured the oxidation profiles at 185 °C. They observed that as the fuel was diluted to a 1:1 fuel:solvent ratio, that oxidation slowed. Upon further dilution the oxidation rate increased. We have previously argued that the dilution of a slow oxidizing fuel, i.e., one which contains a significant quantity of naturally occurring antioxidants, is effectively the same as lowering the concentration of these antioxidants.[7] Thus, the present modeling predicts that at relatively high concentrations of antioxidant, increases in the oxidation rate will be observed relative to lower, more optimum levels. Indeed, the blending experiments showed such behavior, implying the slow oxidizing fuel contained a concentration of antioxidant greater than optimum. Thus, dilution slows oxidation until the optimum concentration is reached, and further dilution decreases the time to complete oxygen consumption due to a lower than optimum antioxidant concentration. This behavior, where there exists an optimum antioxidant concentration above and below which the oxidation rate increases, was also predicted by the previous modeling study.[4]

Figure 4 also shows that as the concentration of added antioxidant is varied over the range $(0.5-8) \times 10^{-4}$ M, the time at which complete oxygen consumption occurs appears to increase in approximately even increments as the antioxidant concentration is doubled. This behavior is remarkably similar to that observed in the blending of fuels.[8] Balster et al. observed an approximate even spacing in increasing oxygen consumption time as the dilution factor is doubled for the blending of a fast oxidizing fuel with a slow oxidizing fuel. This occurred over the range 2.5−20% of the slow oxidizing fuel. This agreement lends further support to the validity of the chemical kinetic model. It also supports the view that dilution of a slow oxidizing fuel with a fast oxidizing fuel is, in effect, a dilution of the naturally occurring antioxidants present in the slow oxidizing fuel.

The good qualitative agreement observed between the chemical kinetic model employed here and measurements of fuel and hydrocarbon oxidation provides evidence of the correctness of the assumptions in the mechanism. In particular, the interception of peroxy radicals by the antioxidant species, reaction 5, and subsequent antioxidant product chemistry are successful in reproducing both the observed slowing in oxidation at short times and the subsequent increase in oxidation rate at long times. On the other hand, Jones et al.[5] have hypothesized that the primary mechanism for the relatively slow autoxidations observed in some jet fuels is the reaction of hydroperoxides with sulfur species to produce nonradical products, reaction 17. We have shown above that the presence of peroxy radical inhibiting species can provide significant slowing of oxidation and the modeling of these reactions shows excellent qualitative agreement to the measured oxygen profiles. In order to explore the role that hydroperoxide decomposers may play in the autoxidation process, we will set the AH concentration to zero and vary the concentration of SH over the range $(0-2) \times 10^{-2}$ M for oxidation at 185 °C. As we do not know the identity or concentrations of the hydroperoxide decomposing species present in jet fuel, we cannot assign realistic rate parameters or concentrations. We have chosen to maximize the importance of this reaction to assess its potential effect on fuel oxidation. To maximize the importance of reaction 17, we have used a "fast" *A* factor and an activation energy of zero for the rate parameters of this reaction. The results are shown in Figure 5. The figure shows that over the range of SH concentrations $(2-200) \times 10^{-4}$ M, significant delays in oxidation are predicted. Complete oxygen consumption is delayed to 670 s upon addition of 2×10^{-3} M of SH. No further changes in oxidation are predicted at higher concentrations of SH. With increasing SH concentration, the oxygen profiles appear to approach a limiting oxygen profile which is near linear in time. This is due to hydroperoxide consumption via reaction 17 completely preventing unimolecular hydroperoxide decomposition via reaction 11.

Figure 5 also shows that as the peroxide decomposer concentration is varied over the range $(2-16) \times 10^{-4}$ M, the time for complete oxygen consumption is not evenly spaced as the additive concentration is doubled, as in the peroxy radical inhibitor case. To illustrate these differences, in Figure 6 we have plotted the time for complete oxygen consumption versus additive concentration for both types of additives. The plot shows the peroxy radical inhibiting additive displays a near-logarithmic consumption time versus additive concen-

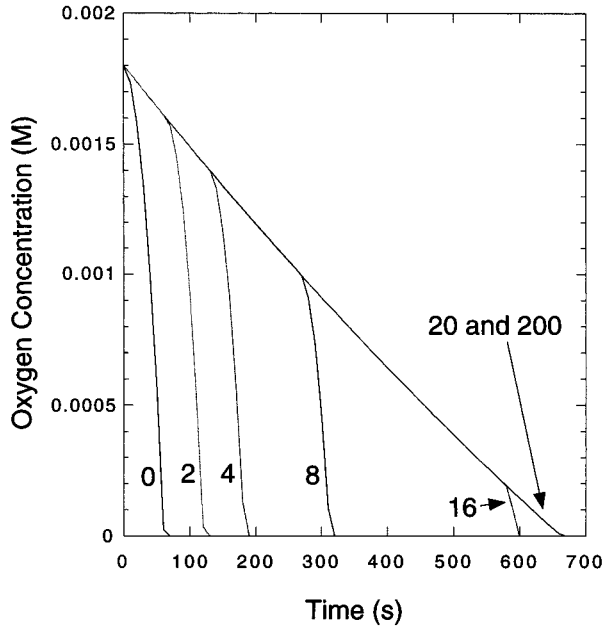

Figure 5. Plots of calculated oxygen concentration versus time for various concentrations of hydroperoxide decomposer SH ($\times 10^{-4}$) at 185 °C.

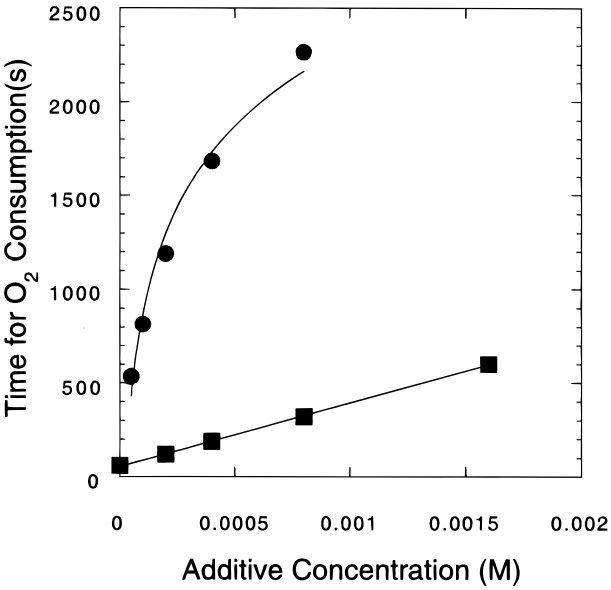

Figure 6. Plots of time for complete oxygen consumption versus additive concentration for the peroxy radical inhibiting antioxidant (●) and peroxide-decomposing additive (■) at 185 °C.

tration, while the peroxide decomposer yields a linear dependence. It is apparent that the chemical kinetic model predicts that addition of peroxy radical inhibitors and peroxide decomposers yield very different oxygen profiles as the additive concentration is varied.

Can we now use these modeled oxygen profiles to determine if the observed laboratory oxygen behavior during fuel/solvent blending[8] is due to a peroxy radical inhibitor or a peroxide decomposer? The behavior of the calculated oxygen profiles of Figure 5 with increasing peroxide decomposer, SH, is different from those observed with increasing peroxy radical interceptor, AH (Figure 4), in three respects. First, the delays observed, a maximum of 670 s, are significantly smaller than for the addition of AH. Second, as the SH concentration is doubled over the range $(2-16) \times 10^{-4}$ M, the time for complete oxygen consumption is not evenly spaced. And third, at large SH concentrations the oxidation profile reaches a limiting rate. In contrast, the measured oxygen profiles of fuel blends of Balster et al. have oxygen consumption times greater than 1500 s, show evenly spaced consumption times with a doubling of the AH concentration, and do not reach a limiting profile. It is apparent that the predicted effects of a peroxide decomposer addition on oxidation are not similar to the laboratory measurements of Balster et al., while the peroxy radical inhibition mechanism does represent the data well.

In a separate work, Jones et al.[5] studied the effects of blending two jet fuels, one of which (the slower oxidizing fuel) is the same fuel as in the Balster et al. study. This study reports maximum oxygen consumption times of 840 s and the oxygen profiles do reach a limiting value at blends approaching 100% of the slow oxidizing fuel. But as the slow oxidizing fuel is added to the fast oxidizing fuel, as the slow oxidizing fuel is doubled the time to complete oxygen consumption does appear to be evenly spaced. Thus, it would appear that in this study the oxygen decay behavior has some, but not all, of the characteristics of the peroxide decomposer mechanism. Unfortunately, this study is complicated by the probable presence of naturally occurring (and possibly refinery added) antioxidants in the relatively fast oxidizing fuel. The blending of these two fuels is not a true dilution of the antioxidant concentration of the slow oxidizing fuel because the fast oxidizing fuel contains these additional inhibitors. Balster et al. point out that dilution of a jet fuel which contains approximately 20% aromatics with another jet fuel of similar aromatic content is different from dilution with a solvent which is devoid of aromatics. They posit that the initiation rate is proportional to the aromatic content and attribute the differences in the two studies to these changes in aromatic content.

This modeling study shows that the fuel/solvent blending behavior matches the behavior predicted by the peroxy radical interception mechanism and is therefore the most likely mechanism for the observed oxygen profiles in these fuel blends. The fuel/fuel blending study exhibits behavior that has some of the characteristics of both the peroxy radical inhibition and hydroperoxide decomposition (reaction 17) mechanisms. As the slow oxidizing fuel is the same in the two studies, it is likely that the same oxidation slowing pathways are important in both studies. It must be emphasized that the mechanism used here is an oversimplification of the complex chemistry that occurs during the oxidation of real fuels. In particular, the peroxide decomposer reaction, reaction 17, is a simplification of a poorly understood mechanism in which oxidized sulfur species that are produced from the reaction may provide additional peroxide decomposition pathways.[13,14] Also, as jet fuel is a complex chemical mixture which likely contains both naturally occurring peroxy radical inhibitors and peroxide decomposer compounds, it is likely that both mechanisms occur in real fuels. To determine

(13) Holdsworth, J. D.; Scott, G.; Williams, D. *J. Chem. Soc.* **1964**, 4692−4699.
(14) Denison, G. H.; Condit, P. C. *Ind. Eng. Chem.* **1945**, *37*, 1102−1108.

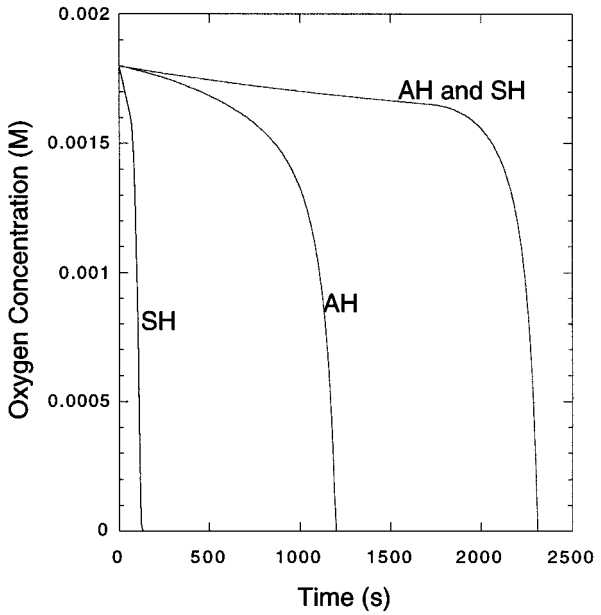

Figure 7. Plots of oxygen concentration versus time at 185 °C for AH and SH both at 1×10^{-4} M and each compound individually at 2×10^{-4} M.

the behavior predicted for the simultaneous occurrence of the two inhibition pathways we have modeled the case at 185 °C in which equal concentrations of the two compounds, AH and SH, are present at a concentration of 1×10^{-4} M. The results are shown in Figure 7, along with the predicted oxygen profiles in the presence of the individual compounds at 2×10^{-4} M. It is apparent from the figure that the model predicts the two compounds acting together display a synergistic effect on the oxidation profile. The oxidation rate is drastically slowed by the presence of both species, much more than would occur from just the sum of the two effects. Indeed, this type of synergism between peroxy radical inhibiting antioxidants and peroxide-decomposing species has been observed experimentally.[15] Apparently, the presence of the peroxide decomposer lowers the radical production rate enough to significantly slow the consumption of the peroxy radical inhibiting antioxidant. Thus, AH survives longer and the change to faster oxygen consumption occurs later. Another view is that the peroxy radical inhibiting antioxidant slows the production of hydroperoxides and thus the peroxide decomposer is able to survive longer. These processes occur simultaneously as both SH and AH are removed simultaneously during the run.

(15) Scott, G. *Chem. Ind.* **1963**, 271−281.

Conclusions

This study has used chemical kinetic modeling to simulate the autoxidation of jet fuel including the chemistry of peroxy radical inhibiting antioxidants and hydroperoxide-decomposing species. Recent experimental measurements of oxygen concentration during autoxidation of model hydrocarbon solvents were used to "calibrate" the rate parameters of the mechanism. The model shows good agreement for oxygen profiles of static measurements at 140 °C. At this temperature the model predicts large increases in oxidation rate upon peroxy radical inhibiting antioxidant consumption to below 1×10^{-5} M. At 185 °C we have shown that peroxy radical inhibiting antioxidants and hydroperoxide decomposers both slow and/or delay oxidation, but the resulting oxygen profiles display different characteristics. We have shown that comparison of these profiles with fuel blending measurements has the potential to differentiate between the two types of oxidation-slowing species. The modeling predicts that the presence of both types of species in a fuel results in a synergistic slowing in the oxidation rate.

Hopefully, future experimental measurements will allow refinements to this chemical kinetic mechanism. Measurements of relevant species, such as oxygen, hydroperoxides, and antioxidants during the autoxidation of fuel and/or model solvents will yield essential information for modeling the bulk chemistry. Inclusion of deposit/particulate formation and surface chemistry is also necessary. Future modeling should also include the chemistry expected when aromatic species are present. In the future, we hope to be able to use analytical tests for antioxidant and hydroperoxide decomposer species along with a future refined mechanism to allow the prediction of jet fuel oxidation characteristics. The present modeling shows that the antioxidant and hydroperoxide species present in the fuel have a substantial impact on the fuel oxidation behavior.

Acknowledgment. This work was supported by the U.S. Air Force, Fuels and Lubrication Division, Wright Laboratories, Wright-Patterson AFB, under contract Nos. F33615-92-C-2207 and F33615-97-C-2719 with Mr. Charles Frayne as technical monitor. The author would like to acknowledge Dr. Grant Jones (ISSI) for enlightening discussions.

EF970157L

E. Computational Fluid Dynamics Simulations of Jet Fuel Oxidation Incorporating Pseudo-Detailed Chemical Kinetics

Computational Fluid Dynamics Simulations of Jet Fuel Oxidation Incorporating Pseudo-Detailed Chemical Kinetics

J. S. Ervin* and S. Zabarnick

University of Dayton Research Institute, Dayton, Ohio 45469-0210

Received July 29, 1997

Military jet aircraft circulate fuel as a cooling medium. Upon heating, dissolved oxygen reacts with the fuel forming insoluble deposits which can block fuel lines and disrupt operation of close tolerance valves. Thus, an understanding of how dissolved oxygen reacts with the fuel is important to aircraft designers. A pseudo-detailed kinetics model which considers antioxidant chemistry was incorporated in a computational fluid dynamics code, and dissolved oxygen and hydroperoxide concentration profiles along a stainless steel tube were calculated for both nearly isothermal and nonisothermal flowing systems. Flowing experiments were performed with both a severely hydrotreated fuel and a straight-run fuel, and the predicted dissolved oxygen and hydroperoxide profiles agreed reasonably well with the measured profiles over a range of bulk fuel temperatures and flow conditions. The present model offers an improved understanding of jet fuel oxidation and antioxidant chemistry.

Introduction

Aviation fuel is circulated in military aircraft for cooling. In the presence of heat and dissolved O_2 at relatively low temperatures (120−300 °C), jet fuel degrades through a complex series of reactions forming surface deposits. Accumulated surface deposits impair engine performance by disrupting the normal fuel flow within fuel system components.[1] Moreover, the fouling of close-tolerance valves may lead to catastrophic failure. Since the chemical reactions in which dissolved O_2 is consumed are intimately tied to fouling processes, a fundamental understanding of dissolved O_2 removal is imperative for aircraft design.

For over five decades, the thermal and oxidative stabilities of aviation fuels have been studied by experiment, and the experimental results largely have been described using empirical relationships.[1] Computational solutions of the Navier−Stokes, energy, and species conservation equations are more general and can be used to predict O_2 consumption for different flow geometries, flow rates, and temperatures. Since fuel oxidation is complex, global-chemistry kinetics have been used in computational simulations.[2−5] The global chemistry mechanisms used in computational fluid dynamics simulations generally employ one reaction to represent fuel autoxidation:

$$\text{fuel} + O_2 \rightarrow \text{products} \quad (1)$$

Although fuel autoxidation involves a series of reactions, the underlying assumption of eq 1 is that the overall reaction of a mixture of compounds can be represented by one rate equation. This rate equation is composed of a rate constant multiplied by concentrations with simple order dependence, such as in eq 2. It

$$-\mathrm{d}[O_2]/\mathrm{d}t = k[\mathrm{RH}][O_2]^n \quad (2)$$

is further assumed that the rate constant, k, is defined by the product of an Arrhenius A factor and an activation energy term.

Some engineering computational fluid dynamics codes which use global chemistry assume an O_2 consumption reaction order of unity for simplicity.[2] Others permit a step change in the global order.[3,5] These models assume that the overall reaction order is zero until the dissolved O_2 is reduced to some arbitrary critical concentration. At this low concentration, the order is set equal to unity. However, with autoacceleration, or if naturally occurring antioxidants or antioxidant additives are present, the explicit form for the global order is not simple.[6]

In previous studies which made use of global chemistry to predict the mass of carbon deposits accumulated along the length of heated tubes, it has been found that global models employed much beyond the temperature calibration regime poorly predict measured deposit mass profiles.[3] One explanation for the poor prediction of most global models is that as the temperature is increased, the rate of hydroperoxide decomposition

* Corresponding author. E-mail: jervin@engr.udayton.edu.

(1) Hazlett, R. N. *Thermal Oxidative Stability of Aviation Turbine Fuels*; ASTM: Philadelphia, PA, 1991.

(2) Krazinski, J. L.; Vanka, S. P.; Pearce, J. A.; Roquemore, W. M. *ASME J. Eng. Gas Turb. Power.* **1992**, *114*, 104−110.

(3) Chin, L. P.; Katta V. R.; Heneghan, S. P. *Prepr.—Am. Chem. Soc., Div. Pet. Chem.* **1994**, *39*, 19−25.

(4) Katta, V. R.; Blust, J.; Williams, T. F.; Martel, C. R. *J. of Thermophys. Heat Transfer* **1995**, *9*, 159−168.

(5) Ervin, J. S.; Williams, T. F.; Katta, V. R. *Ind. Eng. Chem. Res.* **1996**, *35*, 4028−4032.

(6) Ervin, J. S.; Heneghan, S. P. The Meaning of Activation Energy and Reaction Order in Autoaccelerating Systems. Presented at the International Gas Turbine Institute Turbo Expo 97, Orlando, FL, June 1997. Paper 97-GT-224.

S0887-0624(97)00132-1 CCC: $15.00
Published on Web 02/04/1998

Table 1. Characteristics of F2747 and F2827 Jet Fuels

	F2747	F2827
fuel type	Jet A−1	Jet A
density at 25 °C (kg/m^3)	809.0	809.0
viscosity at 25 °C (kg m/s)	1.9×10^{-5}	1.9×10^{-5}
refinery treatment	hydrotreated	straight run
total sulfur (%)	0.004	0.079
mercaptan sulfur (%)	0.000	0.001
aromatics (vol %)	19	19
JFTOT breakpoint (°C)	332	266
copper (ppb)	<5	<5
iron (ppb)		8
zinc (ppb)	18	<5

increases, and the effects of the resulting increased oxidation rate on the observed order and dissolved O_2 concentration are more significant.[6] The new approach taken here is to model the oxidation of hydrocarbon fuels by means of pseudo-detailed chemical kinetic modeling. The model is pseudo-detailed in the sense that the chemical kinetics of O_2 consumption are described using several reactions which represent the dominant chemistry rather than using hundreds of reactions as might be found in a detailed model or a single oxidation reaction as found in previous studies. The current work is the first to model dissolved O_2 consumption and antioxidant chemistry in flowing aviation fuel using pseudo-detailed chemistry and computational fluid dynamics. The numerical model permits the study of the effects of naturally occurring antioxidants and antioxidant additives. It is highly desirable to have the capability to predict the effects of additives on fuels because experiments involving the additive testing of fuels are costly.

Two groups of antioxidants are considered. The first, denoted by AH, represents hindered phenols which slow oxidation by removing alkyl peroxy free radicals from the autoxidation chain.[1,7] Hydroperoxide decomposers, represented by SH, comprise the second group. SH is thought to be some sulfur (or other) species which provide alkyl hydroperoxide (ROOH) decomposition pathways as an alternative to unimolecular ROOH decomposition reactions.[7−9] The objective of this paper is to study jet fuel oxidation and the behavior of these two groups of antioxidants in flowing systems using computational fluid dynamics and pseudo-detailed chemical kinetic modeling.

Experimental Section

For model verification, experiments were conducted using a heat exchanger which simulated a complex thermal and flow environment approaching that of an aircraft. Profiles of dissolved O_2 and ROOH concentrations along the tube length for both a rapidly oxidizing hydrotreated fuel and a slowly oxidizing straight-run fuel were compared to numerical predictions which used a pseudo-detailed kinetic model. Table 1 lists characteristics of neat F2827 and F2747 jet fuels used in the experiments. F2827 produces relatively low hydroperoxide concentrations and oxidizes relatively slowly when heated in the presence of dissolved O_2. On the other hand, F2747, which has very low sulfur and naturally occurring antioxidant components and produces relatively high concentrations of ROOH, oxidizes relatively rapidly when oxidatively stressed. Based on the measurements of Striebich and Rubey,[10] the dissolved O_2 concentration (air saturated value) at the flow rig inlet was 65 ppm (w/w) for F2827 and 73 ppm for F2747.

Fuel at ambient temperature enters the heated tube[11] at a pressure of 2.48 MPa. At this pressure level, the fuel remains as a liquid everywhere within the system. Bulk dissolved O_2 levels were measured on-line at the flow inlet and exit by means of a modified gas chromatograph.[12] The ROOH concentrations of the aged fuel were measured by cyclic voltammetry techniques.[13]

A heated copper block envelopes the 316 stainless steel tubing (45.8 cm long by 2.16 mm i.d. by 3.18 mm o.d.) through which the fuel passes. Calibrated thermocouples (20 gage) are welded to the outer surface of the stainless steel tubing to provide the outer tube wall temperatures with an uncertainty of ±2 °C. The bulk fuel temperature at the exit of the heated tube was also measured, and the uncertainty in its measurement was ±10 °C. (The relatively large uncertainty in the location of the thermocouple within the heated tube contributed to the uncertainty in the bulk fuel temperature measurement.) The stainless steel tubes (ASTM grade A269/A213) have a surface roughness (arithmetic average) of 8−15 microinches and are cleaned with Blue Gold alkaline solution in an ultrasonic bath, rinsed with deionized water, and dried with flowing laboratory-grade nitrogen gas prior to use.

The tests conducted in the present apparatus are usually conducted under conditions of relatively high flow rates and temperatures. In the present work, with a volumetric flow rate of 16 mL/min, the flow was laminar at the entrance of the heated block but became turbulent. Buoyancy forces normal to the flow direction increased the heat and mass transport, rendering the flow turbulent.[4] The study of turbulent flow is important because it is normally encountered in the fuel systems of military aircraft.

Fluid dynamics and heat transfer strongly influence jet fuel oxidation, but the nature of this influence is not well understood.[1] For this reason, numerical simulations of dissolved O_2 consumption were performed for the present flow conditions as well as for the flow conditions reported by Jones et al.[8,14] in a near-isothermal flowing test rig (NIFTR). In contrast to the conditions of our apparatus, the NIFTR experiments are conducted at lower temperatures and flow rates in order to attain near-isothermal conditions in a minimum length of tube. In both experiments, the temperature of the copper block used to heat the tube and the flow rate are varied to produce different oxidation rates and residence times, respectively. Figure 1 shows calculated bulk fuel temperature and measured tube wall temperature profiles along the heated tube length for both the present experiments and the NIFTR experiments. The NIFTR experiments use a 81.3 cm long heated tube, whereas the current experiments use a 45.8 cm long heated tube. The maximum wall temperature for both experiments of Figure 1 is near 200 °C. Figure 1 shows that for a flow rate of 16 mL/min and a maximum tube wall temperature near 200 °C, the calculated bulk fuel temperature increases along the entire heated tube length, never reaching the wall temperature. Although not shown, similar experiments performed at greater wall temperatures were characterized by bulk temperature profiles which also never attained the wall temperature. In contrast, in the NIFTR for a flow rate of 0.125 mL/min, the fuel temperature reaches the tube wall temperature near the flow entrance.

(7) Zabarnick, S. *Energy Fuels*, submitted for publication.
(8) Jones, E. G.; Balster, L. M.; Balster, W. J. *Energy Fuels* **1996**, *10*, 509−515.
(9) Scott, G. *Chem. Ind.* **1963**, 271−281.
(10) Striebich, R.; Rubey, W. *Prepr.—Am. Chem. Soc., Div. Pet. Chem.* **1994**, *39*, 47−50.
(11) Heneghan, S. P.; Williams, T. F.; Martel, C.; Ballal, D. R. *ASME J. Eng. Gas Turb. Power* **1993**, *115*, 480−485.
(12) Rubey, W. A.; Striebich, R. C.; Tissandier, M. D.; Tirey, D. A.; Anderson, S. D. *J. Chromatogr. Sci.* **1995**, *33*, 433−437.
(13) Kauffman, R. E. *Prepr.—Am. Chem. Soc., Div. Pet. Chem.* **1994**, *39*, 42−46.
(14) Jones, E. G.; Balster, W. J.; Post, M. E. *ASME J. Eng. Gas Turb. Power* **1995**, *117*, 125−131.

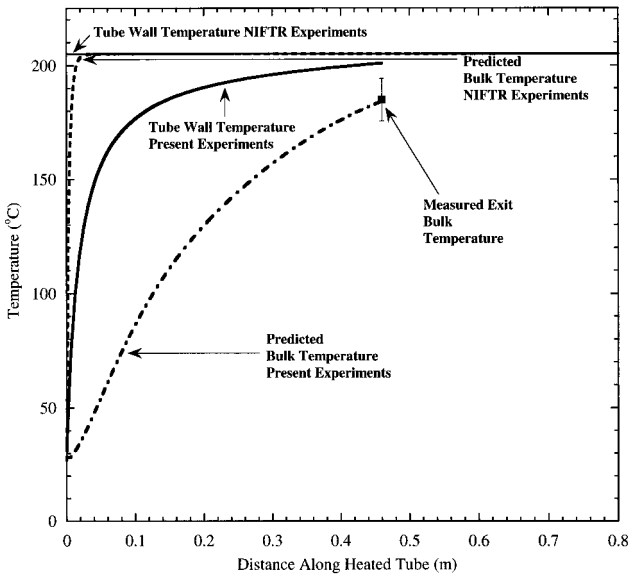

Figure 1. Bulk and tube wall temperature profiles along heated tube length. Present experiments (16 mL/min 0.46 m heated length) and NIFTR experiments[14] (0.125 mL/min 0.8 m heated length).

Table 2. Pseudo-Detailed Reaction Mechanism for Chemical Kinetic Modeling

reaction	Arrhenius A factor (mol, L, and s)	activation energy (kcal/mol)	reaction no.
$I \rightarrow R^{\bullet}$	1×10^{-10}	0	1
$R^{\bullet} + O_2 \rightarrow RO_2^{\bullet}$	3×10^{9}	0	2
$RO_2^{\bullet} + RH \rightarrow RO_2H + R^{\bullet}$	3×10^{9}	12	3
$RO_2^{\bullet} + RO_2^{\bullet} \rightarrow$ termination	3×10^{9}	0	4
$RO_2^{\bullet} + AH \rightarrow RO_2H + A^{\bullet}$	3×10^{9}	5	5
$AO_2^{\bullet} + RH \rightarrow AO_2H + R^{\bullet}$	3×10^{5}	10	6
$A^{\bullet} + O_2 \rightarrow AO_2^{\bullet}$	3×10^{9}	0	7
$AO_2^{\bullet} + AH \rightarrow AO_2H + A^{\bullet}$	3×10^{9}	6	8
$AO_2^{\bullet} + AO_2^{\bullet} \rightarrow$ products	3×10^{9}	0	9
$R^{\bullet} + R^{\bullet} \rightarrow R_2$	3×10^{9}	0	10
$RO_2H \rightarrow RO^{\bullet} + {}^{\bullet}OH$	1×10^{15}	37	11
$RO^{\bullet} + RH \rightarrow ROH + R^{\bullet}$	3×10^{9}	10	12
$RO^{\bullet} \rightarrow R_{prime}^{\bullet}$ + carbonyl	1×10^{16}	15	13
${}^{\bullet}OH + RH \rightarrow H_2O + R^{\bullet}$	3×10^{9}	10	14
$RO^{\bullet} + RO^{\bullet} \rightarrow$ termination	3×10^{9}	0	15
$R_{prime}^{\bullet} + RH \rightarrow$ alkane $+ R^{\bullet}$	3×10^{9}	10	16
$RO_2H + SH \rightarrow$ products	3×10^{9}	16	17

Numerical Simulations

Pseudo-detailed chemical kinetic modeling was performed using the mechanism of Table 2 which is based on the mechanism of Zabarnick.[7] It is extremely difficult, if not impossible, to model the multitude of compounds present in jet fuel. Thus, the fuel is represented by the single compound RH. The initiation step (reaction 1 of Table 2) is assumed to occur by unimolecular decomposition of an initiating species, I. Reaction 1 is a simple representation of complex process that initiates the autoxidation chain with a low production rate of $R^{\bullet}$ radicals.[7,15] Reactions 1−4 and reaction 10 represent a simple chain mechanism for the oxidation of a hydrocarbon fuel. Reactions 5−9 represent the antioxidant chemistry associated with AH, which is a species with an easily abstracted H atom. Reactions 11−16 are associated with ROOH decomposition which occurs at sufficiently high temperatures and is believed to play an important role in accelerated O_2 consumption.[9,15] Reaction 17 is used to model the effects of hydroperoxide-decomposing species (SH). Zabarnick[7,15] estimated the rate parameters (Arrhenius A factors and activation energies) for the pseudo-elementary reactions largely by comparison with measured rate constants and Benson-style "thermochemical kinetics" analysis.[16]

With the exception of three rate parameters, those listed in Table 2 are taken from Zabarnick[7] where a similar mechanism was used to study the antioxidant chemistry of hydrocarbon fuels in a nonflowing isothermal system. In the present study, the preexponential factor for the initiation reaction (reaction 1) is 1×10^{-10}, whereas in Zabarnick[7] this preexponential factor is given as 1×10^{-3}. A smaller preexponential factor is used here such that the production rate of $R^{\bullet}$ becomes negligible once the chain begins. In the current work, the activation energies of reactions 11 and 17 are different from those originally given in Zabarnick.[7] For reaction 11, Zabarnick[7] used an activation energy of 42 kcal/mol, which is a representative value for a homogeneous ROOH decomposition reaction. However, metals have long been suspected of being involved in catalytic decomposition of hydroperoxides.[1,8,9] Thus, in the presence of a metal surface and/or dissolved metals, it is reasonable for the activation energy for the ROOH decomposition reaction to be less than 42 kcal/mol. In the present work, the activation energy for reaction 11 was taken as 37 kcal/mol. This value provided predictions of O_2 consumption which agreed well with flowing experiments which used fuel F2747 over a large temperature range. Fuel F2747 has very low concentrations of AH and SH and is nearly a pure solvent. Thus, fuel F2747 was chosen for the "calibration" of the activation energy corresponding to reaction 11 because it is desirable to make the "calibrated" activation energy independent of the AH and SH concentrations. The activation energy for reaction 17 was chosen to be zero in Zabarnick.[7] In the present work, the activation energy for reaction 17 is selected to be 16 kcal/mol. It was observed here that an activation energy less than 16 kcal/mol removed ROOH too rapidly at lower temperatures for various concentrations of AH and SH. As a result, for activation energies less than 16 kcal/mol, the predicted dissolved O_2 concentration was nearly always greater than the measured concentration at the exit of the heated tube for the straight-run fuel (F2827). In the modeling performed here, it is assumed for simplicity that all fuels have the same initiating species concentration (I) of 4×10^{-8} mol/L. With the activation energies and preexponential factors of Table 2, it is then possible to define different fuels in terms of their initial AH and SH concentrations.

The species concentrations were found numerically by a finite difference solution[4,18] of the coupled equations that arise from the mechanism of Table 2 and the

(15) Zabarnick, S. *Ind. Eng. Chem. Res.* **1993**, *32*, 1012−1017.

(16) Benson, S. W. *Thermochemical Kinetics*; Wiley: New York, 1976.

(17) Heneghan, S. P.; Martel, C. M.; Williams, T. F.; and Ballal, D. R. *ASME J. Eng. Gas Turb. Power* **1995**, *117*, 120−124.

(18) Katta, V. R.; Jones, E. G.; Roquemore, W. M. Development of Global-Chemistry Model for Jet Fuel Thermal Stability Based on Observations from Static and Flowing Experiments. Presented at the 81st AGARD Symposium on Fuels and Combustion Technology for Advanced Aircraft Engines, Colliferro, Italy, May 1993; AGARD-CP-536; Paper No. 19.

Table 3. Initial Concentrations of Species

species	initial concentration (mol/L)
I	4.0×10^{-8}
RH	4.7
AH	varied, $(0-16.2) \times 10^{-4}$
SH	varied, $(0-16.2) \times 10^{-4}$
O_2	1.8×10^{-3}
remaining species	0

transport equations. The following were input to the numerical code: the activation energies and preexponential factors of Table 2, concentrations (O_2, AH, RH, SH, and I) for each species at the entrance of the heated tube, tube wall temperature profile, and the grid resolution. Individual jet fuel samples are known to possess a range of oxidation and deposition characteristics which results from varying source petroleum and refinery processing. To provide the range of oxidation properties that a fuel may possess, we have chosen to modify the antioxidant, AH, and hydroperoxide decomposer, SH, concentrations for individual fuel samples. In simulations of fuel oxidation, two kinds of computations were performed: those for a naturally inhibited system (F2827 fuel) and those for a relatively noninhibited system (F2747 fuel). For the inhibited fuel, AH and SH concentrations were chosen to match experimentally determined oxidation rates and measured hydroperoxide concentrations. The initial AH concentration was assumed to be 1.62×10^{-3} mol/L which is a reasonable value for jet fuels,[7] and the initial SH concentration was assumed to be 1.21×10^{-3} mol/L. For the completely uninhibited case, both the AH and SH concentrations were set equal to 0 mol/L. For both the severely hydrotreated fuel (F2747) and the straight-run fuel (F2827), an identical initial I concentration was used for simplicity. The normal air saturation concentration was used for the initial O_2 concentration. Table 3 summarizes the initial O_2, AH, SH, and I concentrations used in the simulations. The initial concentration for RH was estimated using the density of the jet fuel at 25 °C (809 kg/m^3)[19] and an average molecular weight for the fuel of 170 amu. Ultimately, this model will be most useful if an analytical chemistry test could be used to determine an "effective" AH and SH concentration for individual jet fuel samples. Thus, a measure of the "effective" AH and SH concentration could be measured in the laboratory and entered into the model to provide a method to predict the oxidation properties of the fuel over a range of temperature, residence times, and flow properties.

Results and Discussion

Simulations of Flowing Fuel F2747. Figure 2 shows measured and predicted fractions of remaining dissolved O_2 at the exit of the heated tube for F2747 fuel (zero AH and SH concentrations) flowing at 16 mL/min for different bulk temperatures. Figure 2 shows that as the temperature approaches 170 °C, the dissolved O_2 concentration decreases rapidly until near 210 °C where the O_2 is nearly depleted. This rapid increase in oxidation rate with increasing temperature has been observed previously[17] for similar flow conditions and different fuel types.

(19) Coordinating Research Council. *Handbook of Aviation Fuel Properties*; Coordinating Research Council: Atlanta, GA, 1983.

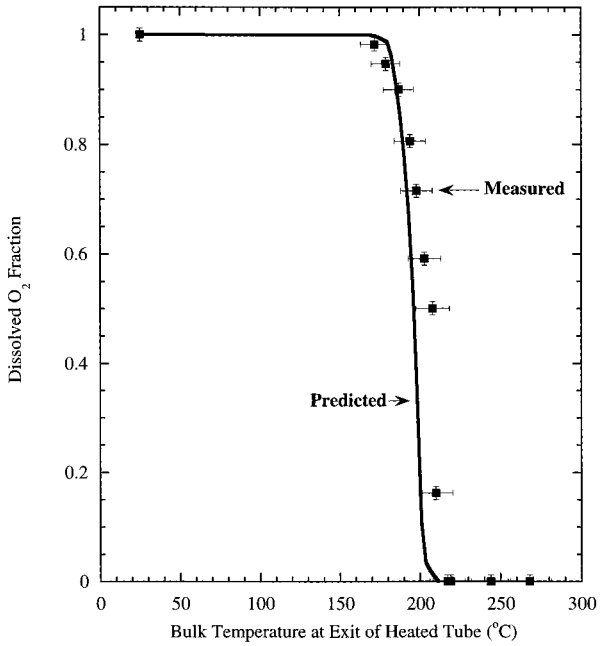

Figure 2. Dissolved O_2 concentration at heated tube exit (16 mL/min and F2747 fuel).

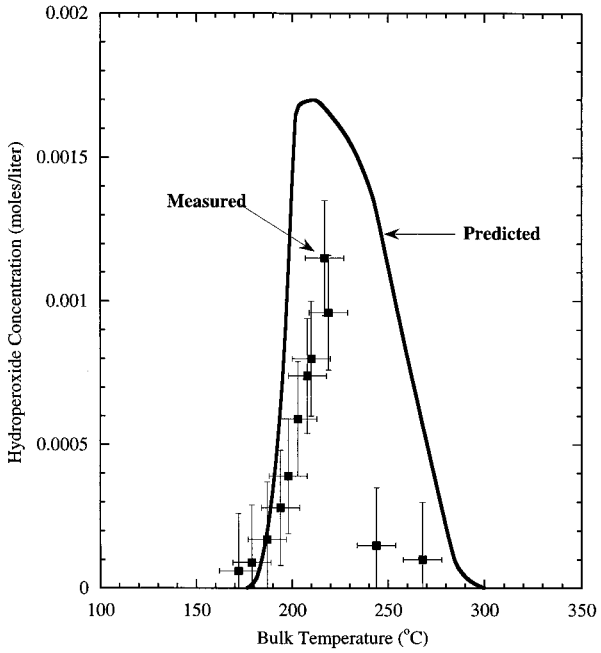

Figure 3. Hydroperoxide concentration at heated tube exit (16 mL/min and F2747 fuel).

The rate of ROOH decomposition has been shown to be important in understanding jet fuel oxidation.[1,9,15] Figure 3 shows measured and predicted ROOH concentrations at the heated tube exit for F2747 fuel for the same range of bulk temperatures described in Figure 2. Figure 3 shows a maximum in both the predicted and measured hydroperoxide concentrations at 210 °C, which is near the temperature associated with the dissolved O_2 depletion of Figure 2. In addition, the ROOH concentration of Figure 3 increases to levels near the initial dissolved O_2 concentration. This means that the initial dissolved O_2 concentration reacts nearly entirely to form ROOH. After the dissolved O_2 is fully consumed and as the bulk temperature continues to rise, ROOH decomposition by unimolecular reaction

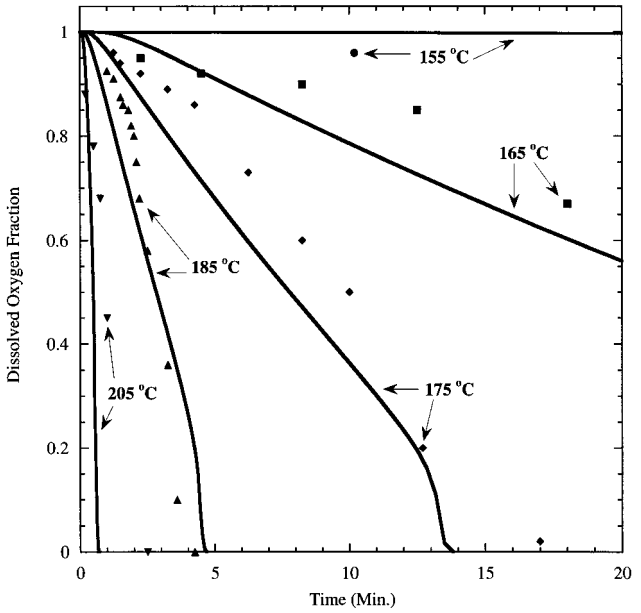

Figure 4. Predicted and measured[8,14] dissolved O_2 removal for nearly isothermal flow, (0.125 mL/min and F2827 fuel; curves represent predictions).

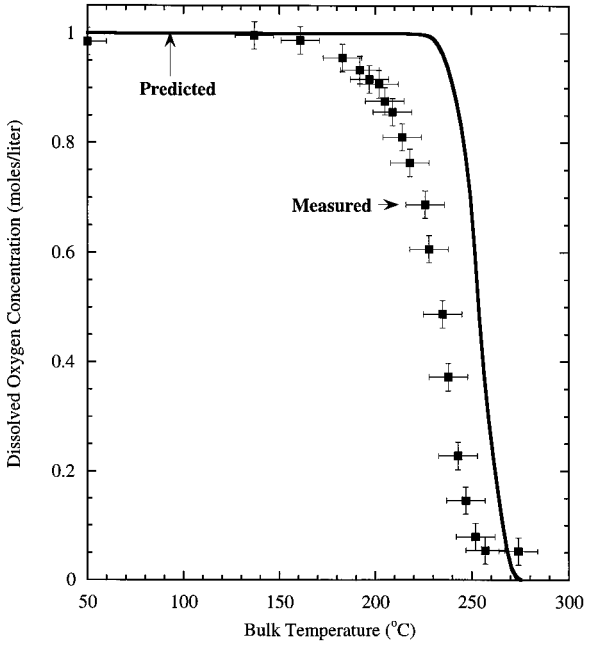

Figure 5. Predicted and measured dissolved O_2 concentration at heated tube exit (16 mL/min and F2827 fuel).

reaction 11 of Table 2) becomes increasingly significant. Figure 3 shows a relatively large maximum concentration of ROOH for fuel F2747 in contrast to the ROOH concentration produced with fuel F2827 (described later) for otherwise identical conditions. This was expected as the hydrotreating process removes heteroatomic species which may decompose hydroperoxides.

Simulations of Flowing Fuel F2827. Figure 4 shows predicted and measured dissolved O_2 fractions at the exit of a heated tube for fuel F2827 flowing at 0.125 mL/min (laminar flow) and for different constant wall temperatures. The experimental measurements[8,14] are for fuel F2827 passing through stainless steel tubes. Different tubes of varying lengths were used to obtain different residence times. At a constant mass flow rate, any position along the tube may be directly related to the reaction time through the average velocity which, in turn, can be found from the known inner tube diameter, mass flow rate, and fuel density. Thus, Figure 4 shows the dissolved O_2 fraction as a function of residence time. Figure 4 shows that as the tube wall temperature is increased, the reaction time required for complete O_2 depletion decreases. The initial AH and SH concentrations were adjusted to give an O_2 consumption history which followed the O_2 measurements at 185 °C. Oxygen consumption histories of F2827 at the other temperatures and in our experiments were then predicted reasonably well using these initial concentrations of AH and SH.

Figure 5 shows measured and predicted dissolved O_2 concentrations at the exit of a heated tube for fuel F2827 flowing at a rate of 16 mL/min. In contrast to the constant wall temperatures associated with Figure 4, the imposed wall temperatures corresponding to Figure 5 vary along the tube length. The bulk fuel temperature (275 °C) at which the O_2 is fully consumed is greater than that observed with fuel F2747 (210 °C) for similar flow conditions. This depletion of O_2 at the greater temperature for F2827 might be expected because F2827, unlike F2747, contains relatively large concentrations of AH and SH. After heating of the fuel, the ROOH concentrations measured for F2827 were much smaller than those produced with F2747. Measured hydroperoxide concentrations at the exit of the heated tube remained near or less than 0.000 03 mol/L over an exit bulk temperature range from 186 to 237 °C. These concentration measurements are near the detection limit of our instrumentation and, thus, have large uncertainties. Calculated ROOH concentrations at the exit of the heated tube lie in a range between 0 and 0.0004 mol/L with the maximum occurring with an exit bulk temperature of 260 °C.

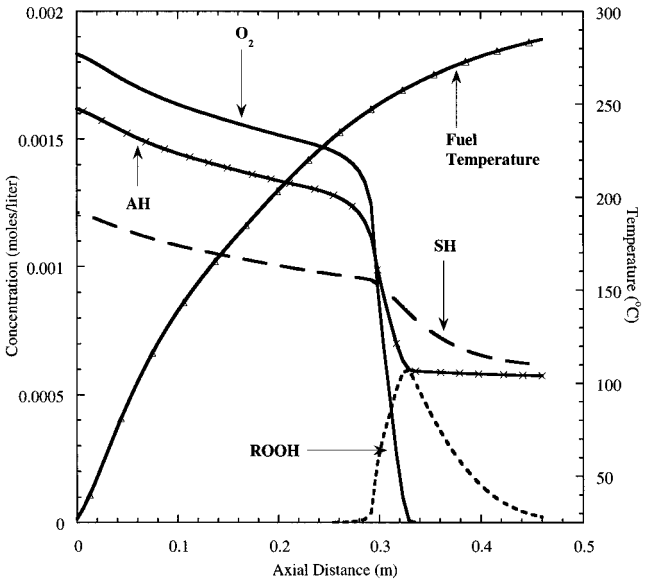

Figure 6. Calculated profiles of dissolved O_2, ROOH, AH, SH, and fuel temperature along heated tube (fuel F2827, 16 mL/min and 300 °C tube wall temperature).

Figure 6 shows the simulated consumption of dissolved O_2, AH, and SH together with the ROOH concentration for turbulent, nonisothermal flowing F2827 fuel at 300 °C maximum wall temperature. The O_2, AH,

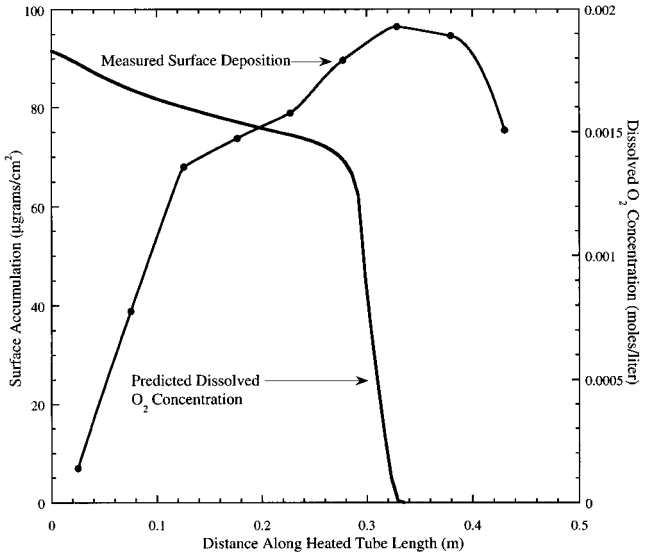

Figure 7. Surface deposition and fuel oxidation for fuel F2827 (16 mL/min and wall temperature of 300 °C).

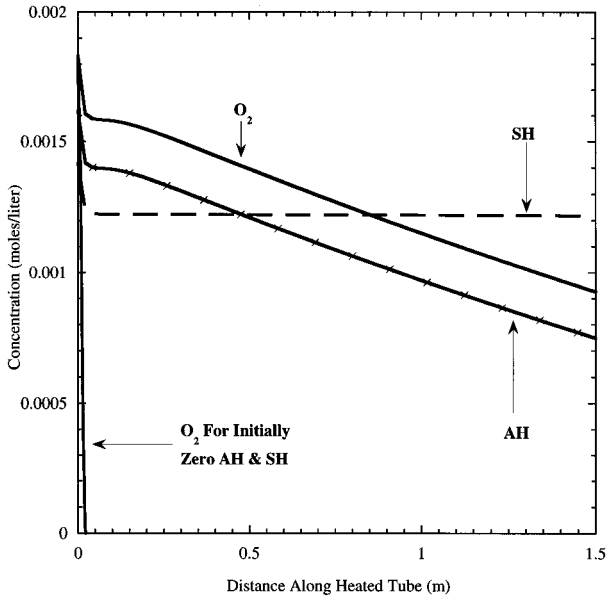

Figure 8. Calculated profiles of dissolved O_2, ROOH, AH, and SH along heated tube for F2827 (0.125 mL/min and 165 °C tube wall temperature).

and SH concentrations drop slowly until near 0.28 m, where there is increased O_2 consumption. As a result of increased fuel oxidation, the ROOH concentration begins to rise. Consequently, the rate of disappearance of SH increases due to the increase in the ROOH concentration. In addition at 0.28 m, the fuel temperature (251 °C) is relatively high which means that reaction 17, based on its activation energy, will proceed more readily than at lower temperatures. Beyond 0.28 m, the ROOH concentration profile rises rapidly to a maximum at a location of 0.33 m, which coincides with the location of O_2 depletion. There, $RO_2^\bullet$ is no longer produced by means of reaction 2. Later in the tube as the $RO_2^\bullet$ concentration decreases to zero (reactions 3 and 5), the AH concentration profile becomes flat because AH is no longer consumed (reaction 5). The ROOH concentration profile decays by both the unimolecular decomposition reaction (reaction 11) and the ROOH−SH decomposition reaction (reaction 17) beyond the location of 0.33 m. For the initial conditions of Figure 6, the acceleration in O_2 consumption is controlled by ROOH decomposition rather than by depletion of the antioxidants. Although occurring later in the tube, similar behavior in consumption profiles for O_2, AH, and SH was observed at lower wall temperatures of 270 and 265 °C.

The consumption of dissolved O_2 is intimately related to the formation of surface deposits, but the involved chemical and physical relationships are not understood. The study of these relationships is necessarily difficult in a flowing system because particles which foul heated surfaces are in all likelihood far removed in time from the autoxidation initiation reactions. Figure 7 shows surface deposit accumulation along the length of the heated tube for the flow conditions of the present experiments, and the predicted O_2 consumption along the tube length. (Here, the maximum tube wall temperature is 300 °C.) Figure 7 shows that the location of maximum deposition is near the location of O_2 depletion. Experiments in flowing systems[5,14] have demonstrated that the location of maximum surface deposit accumulation generally occurs near the location where most (if not all) the dissolved O_2 is consumed. In addition, Figure 7 shows that the surface deposit accumulation varies more gradually with distance along the tube than does the O_2 consumption. There are many possible explanations for the relatively gradual surface deposit accumulation. Some researchers[1] believe that surface deposits form within the bulk fuel and are transported to the wall. Transport of precursor particles to the wall would involve complex fluid dynamics, and the adhesion of particles to the surface would involve surface chemistry that is not understood. Others[18] believe that surface deposits form both as a result of nucleation at the metal surface and from the transport of precursor particles from the bulk of the heated fuel to the metal surface.

Temperature Effects. Using a flow rate of 16 mL/min and the heated copper block of the present experiments, the fuel temperature continuously rises along the tube. Thus, the interpretation of AH and SH concentration changes is complicated by the fact that the increasing temperature decreases the fuel density and increases the rates of reactions with high activation energies. Thus, to further explore the antioxidant chemistry associated with F2827 fuel, the more simple conditions of isothermal walls and laminar flow are used. Figures 8−10 show simulations of the consumption of dissolved O_2, AH, and SH together with the depletion of ROOH for F2827 fuel flowing at a rate of 0.125 mL/min and an imposed constant tube wall temperature. For reference, O_2 removal profiles are also shown for the situation where there are no initial antioxidants present in the fuel. Figure 8 (165 °C wall temperature) shows that the dissolved O_2 and AH profiles are essentially parallel along most of the tube length, indicating that AH and O_2 are consumed at nearly the same rate in this region of the tube. At this low temperature, the ROOH concentration is small and, thus, the SH concentration changes little, as suggested by reaction 17 of Table 2. As the temperature is increased to 175 °C (Figure 9), the O_2 and SH profiles are again parallel over much of the tube length, until the O_2 is depleted. At this location, the AH is no longer

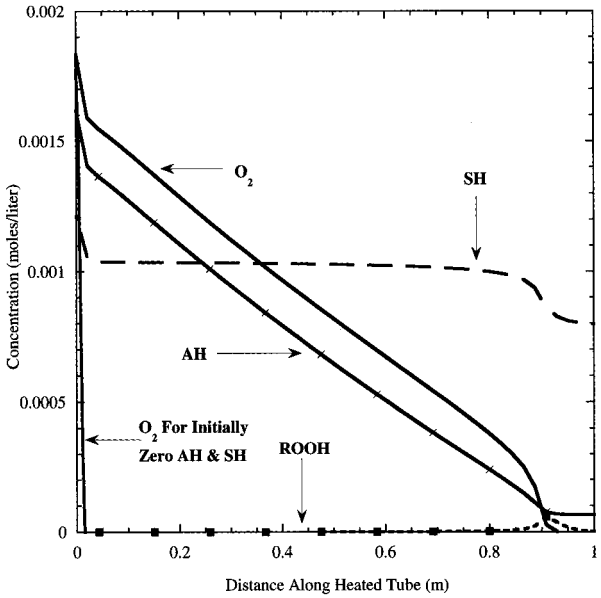

Figure 9. Calculated profiles of dissolved O_2, ROOH, AH, and SH along heated tube for fuel F2827 (0.125 mL/min 175 °C tube wall temperature).

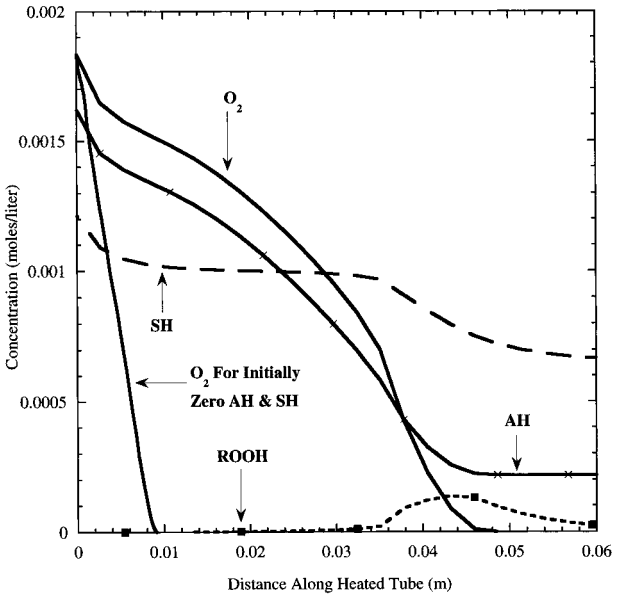

Figure 10. Calculated profiles of dissolved O_2, ROOH, AH, and SH along heated tube for fuel F2827 (0.125 mL/min and 205 °C tube wall temperature).

consumed, and the AH profile is horizontal. As the ROOH concentration approaches 0.0001 mol/L, SH is consumed at an accelerated rate by means of reaction 17 until the ROOH concentration is sufficiently decreased by both reactions 11 (unimolecular ROOH decomposition reaction) and 17 (SH−ROOH decomposition reaction). Once the available ROOH is consumed, Figure 9 shows that there is negligible consumption of SH. Figure 10 shows that with a wall temperature of 205 °C, the AH and O_2 profiles appear less linear than those observed at 165 and 175 °C. Again, as with the wall temperature of 175 °C of Figure 9, Figure 10 shows an increased rate of consumption of SH as the ROOH concentration approaches 0.0001 mol/L. As the tube wall temperature is increased from 165 to 205 °C, the location of dissolved O_2 depletion moves in the upstream direction.

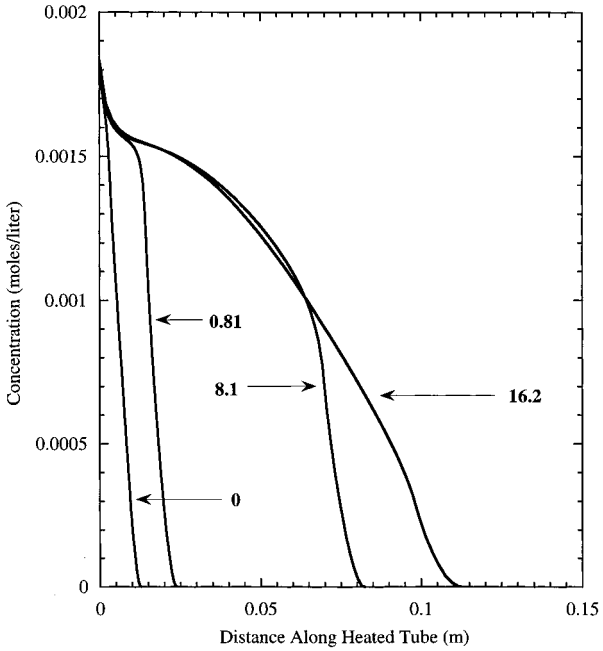

Figure 11. Calculated O_2 concentrations along heated tube for various inlet concentrations of AH ($\times 10^{-4}$ mo/L) in the absence of SH. Tube wall temperature was 185 °C and flow rate 0.125 mL/min.

Simulations of Flowing Fuel in Which the Concentration of AH or SH Is Individually Varied. As the proposed mechanism of Table 2 has been shown capable of predicting measurements of dissolved O_2 consumption for real fuels under conditions of laminar and turbulent flow over a wide temperature range, it is reasonable to use the mechanism to explore the effects of varying the initial concentration of one antioxidant while the initial concentration of the other is zero. For these simulations, it was decided to use the well-defined conditions of laminar flow with the tube walls held at constant temperature. Two tube wall temperatures (185 and 205 °C) and a flow rate of 0.125 mL/min were chosen.

For a constant wall temperature of 185 °C, Figure 11 shows the predicted O_2 consumption along the length of the heated tube for four different initial concentrations of AH and zero SH. In the initial portion of the heated tube (upstream of 0.0025 m), the O_2 concentration decreases because of changes in fuel density associated with heating. As the AH concentration at the entrance of the tube is varied from 0 to 16.2 $\times 10^{-4}$ mol/L, the location of dissolved O_2 depletion moves downstream. This downstream shift in the location of complete O_2 removal with increasing AH concentration demonstrates that the predicted oxidation rate decreases significantly with increasing AH. For the same initial AH concentrations of Figure 11 but at a higher wall temperature of 205 °C, Figure 12 shows that the locations of complete O_2 removal are upstream from those of Figure 11. As the temperature is increased, the rates of reactions which have nonzero activation energies tend to increase. Reactions (reactions 3, 6, 11, 12, 13, 14, and 16) which either directly or indirectly produce R$^\bullet$ and propagate the oxidation chain have greater rates at 205 °C. Thus, relative to 185 °C, there is increased oxidation prior to O_2 depletion at 205 °C.

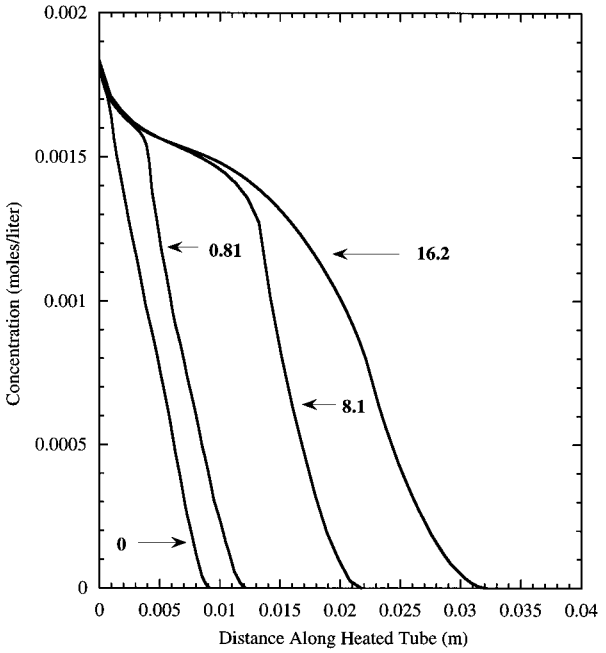

Figure 12. Calculated O_2 concentrations along heated tube for various inlet concentrations of AH ($\times 10^{-4}$ mol/L) in the absence of SH. Tube wall temperature was 205 °C and flow rate 0.125 mL/min.

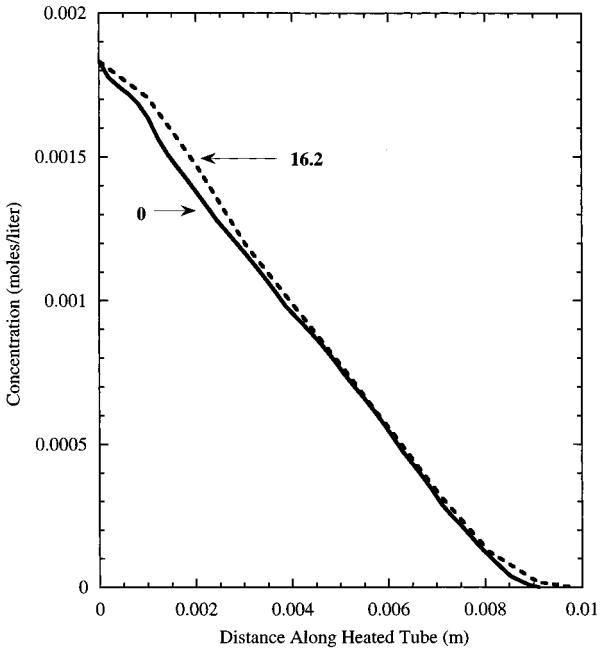

Figure 13. Calculated O_2 concentrations along heated tube for different inlet concentrations of SH ($\times 10^{-4}$ mol/L) in the absence of AH. Tube wall temperature was 205 °C and flow rate 0.125 mL/min.

Figure 13 shows O_2 consumption along the heated tube length for a wall temperature of 205 °C. Here the initial SH is varied between concentrations of either 0 or 16.2×10^{-4} mol/L in the absence of AH. As the initial SH concentration is increased above zero, the location of complete O_2 removal moves slightly further from the tube entrance. The profiles of dissolved oxygen removal corresponding to the nonzero inlet SH concentrations (0.81×10^{-4}, 8.1×10^{-4}, and 16.2×10^{-4} mol/L) essentially overlay each other. At a tube wall temperature of 185 °C (not shown), the dissolved oxygen profiles again nearly lie on each other, but the individual curves are less distinguishable near the tube inlet than those observed for an imposed wall temperature of 205 °C. For the same flow and temperature conditions, a comparison of Figures 12 and 13 reveals that SH is significantly less effective in delaying dissolved O_2 depletion for identical initial concentrations of SH and AH. Similarly, at a lower tube wall temperature of 185 °C and with the same initial concentrations of SH (not shown) and AH, AH is substantially more effective in delaying dissolved O_2 removal.

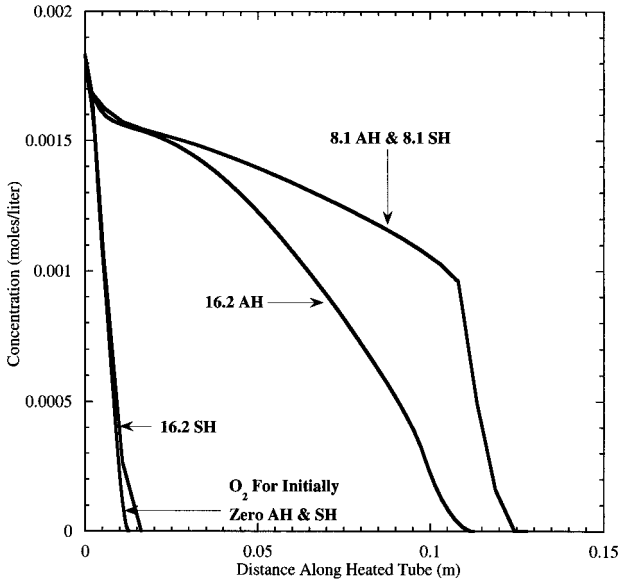

Figure 14. Demonstration of synergism between AH and SH antioxidants. Calculated O_2 profiles for different initial concentrations ($\times 10^{-4}$ mol/L) of AH and SH (0.125 mL/min and 185 °C wall temperature).

Synergistic Effects. Although the pseudo-detailed model presented here is an oversimplification of the complex chemistry that occurs during the oxidation of fuels, the model has been shown to correctly predict measured O_2 consumption and ROOH production and, as a consequence, may be used to further study the simultaneous presence of both AH and SH antioxidants. To this end, autoxidation under conditions of a constant wall temperature of either 185 or 205 °C and a flow rate of 0.125 mL/min has been modeled. Figure 14 shows that the presence of both AH and SH, each at a concentration of 8.1×10^{-4} mol/L and at a wall temperature of 185 °C, is much more effective in delaying O_2 consumption than that occurring from the sum of the two effects of the antioxidants acting individually. The synergism between peroxy radical inhibiting antioxidants and peroxide-decomposing species shown in Figure 14 and with a wall temperature of 205 °C (not shown) has been observed experimentally[9] and in an isothermal nonflowing model.[7]

Conclusions

The present study is the first to model dissolved O_2 consumption and antioxidant chemistry in flowing jet fuel using both pseudo-detailed chemistry and computational fluid dynamics. With this pseudo-detailed model, experimental measurements such as hydroperoxide measurements in addition to dissolved oxygen

measurements are used to characterize fuels over fairly wide temperature ranges. No assumption of a value for the overall reaction order for oxygen consumption needs to be made with the current model. Since pseudo-detailed kinetic modeling relies on rate parameters which are more physically realistic than simpler global parameters, it is believed that pseudo-detailed kinetic modeling offers more promise to extend current simulation capabilities to include the effects of fuel additives. Experiments were conducted using a heat exchanger which simulated a complex thermal and flow environment. Oxygen consumption and the production of hydroperoxides were measured for a rapidly oxidizing hydrotreated jet fuel and for a slower oxidizing straight-run jet fuel. The predictions from the numerical simulations compared well with the experimental measurements.

Acknowledgment. This work was supported by the U.S. Air Force, Fuels and Lubrication Division, Aero Propulsion and Power Directorate, Wright Laboratory, WPAFB, under Contract Nos. F33615-92-C-2207 and F33615-97-C-2719 (Technical Monitor: C. W. Frayne). The authors thank V. R. Katta of Innovative Scientific Solutions, Inc. for many helpful comments.

EF970132M

F. Investigation of the Use of JP-8+100 with Cold Flow Enhancer Additives as a Low-Cost Replacement for JPTS

Investigation of the Use of JP-8+100 with Cold Flow Enhancer Additives as a Low-Cost Replacement for JPTS

J. S. Ervin,* S. Zabarnick, E. Binns, G. Dieterle, and D. Davis

University of Dayton Research Institute, Dayton, Ohio 45469-0140

C. Obringer

Air Force Research Laboratory, Wright-Patterson Air Force Base, Ohio 45433-7103

Received July 20, 1999. Revised Manuscript Received September 28, 1999

Aircraft operation at high altitude can subject jet fuel to extremely low temperature conditions. At such temperatures, fuels have an increased viscosity which limits the ability of the fuel to flow and, at the lowest temperatures, may result in partial solidification of the fuel due to freezing. JPTS is a specialty fuel that has excellent thermal-oxidative stability characteristics and a low freeze-point temperature. Unfortunately, JPTS costs nearly three times as much as the more readily available JP-8 fuel. In addition, replacement of JPTS with JP-8 has important logistical advantages. Thus, it would be advantageous to have a JP-8 fuel that has thermal-oxidative and low-temperature characteristics that are similar to those of JPTS. The JP-8+100 additive package that has been developed previously provides JP-8 fuels with very low surface deposition characteristics. However, enhancement of the low-temperature behavior of JP-8 has not been addressed. The current work studies the potential of developing low-temperature additives for JP-8+100 fuel. One objective was to experimentally determine if a class of additives commonly used in diesel fuels, cold flow enhancers, could effectively be used in kerosene-based fuels, such as JP-8+100. The additives were blended with a representative JP-8+100 fuel. The resulting fuel blends were evaluated in a low-temperature (−73 °C) test facility. Both the amount of solidified fuel remaining in the tank after the flowing fuel had been drained (i.e., "hold-up") and the reduction in fuel flow rate from that at 21 °C were measured. Some of the additives significantly enhanced the cold flow characteristics. The best cold flow additive candidate was tested in two thermal stability test systems and showed no detrimental effect on deposit formation. These results suggest that an additive can enhance the low-temperature properties of JP-8+100 such that it can be used as a low-cost replacement for JPTS fuel.

Introduction

The operation of aircraft at high altitude can subject jet fuel to extremely low temperature conditions. At such low temperatures, fuels have an increased viscosity which limits the ability of the fuel to flow and, at the lowest temperatures, may result in partial solidification of the fuel due to freezing. JPTS is a specialty fuel developed by the U.S. Air Force for use in the U-2 aircraft, that has a low freeze-point temperature and excellent thermal-oxidative stability characteristics. Unfortunately, JPTS costs nearly three times as much as the more readily available primary U.S. Air Force jet fuel, JP-8. In addition, replacement of JPTS with JP-8 has important logistical advantages. Thus, it would be advantageous to have a JP-8 fuel that has thermal-oxidative and low-temperature characteristics that are similar to those of JPTS. The JP-8+100 additive package that has been developed previously provides JP-8 fuels with very low surface deposition characteristics.[1] (In this paper, fuels which contain the JP-8+100 additive package are referred to as JP-8+100 fuels.) However, enhancement of the low-temperature behavior of JP-8 has not been addressed. In addition, the Canadian Ministry of Defense has become interested in fuels which can be used in the extreme conditions encountered in Canada. With regard to commercial aircraft, there has been an increase in long-duration high-altitude transpolar and Siberian flights which expose the fuel to low temperatures.

In developing a fuel which has desirable low-temperature characteristics, it is important to understand the mechanisms involved in the freezing process. Nucleation, growth, and agglomeration (gelling) of paraffin crystals are phenomena which have important roles in the freezing process. As the temperature of a multicomponent hydrocarbon fuel decreases, the long-chain paraffins precipitate at higher temperatures than the other components.[2,3] When the forces of attraction among the paraffin molecules become more dominant than the

* Author to whom correspondence should be addressed. E-mail: jervin@engr.udayton.edu.

(1) Heneghan, S. P.; Zabarnick, S.; Ballal, D. R.; Harrison, W. E. *J. Energy Res. Tech.* **1996**, *118*, 170−179.

10.1021/ef9901600 CCC: $18.00
Published on Web 10/26/1999

paraffin-solvent interactions, a crystal nucleus forms that is comprised of a critical number of paraffin molecules.[4−6] Growth of the nucleus occurs as free paraffin molecules are attracted by molecular forces to locations on the nucleus where they fit into an ordered configuration. Growing crystals have ordered structures in which the molecular chains are aligned parallel to each other, and the terminal methyl groups belong to parallel planes which are perpendicular or oblique to the chain axis.[4]

Additives have been developed which modify paraffin crystal nucleation, growth, and agglomeration. Recent work has led to the development of certain "comb-type" polymers which have lateral groups that cocrystallize with paraffin molecules.[7] The comb teeth attach to the paraffins and increase their solubility. Thus, the increase in solubility reduces the temperature of nucleation. Some additives adsorb onto growing crystals and reduce the growth rate of crystal faces (ethylene−vinyl ester copolymers, ethylene−vinyl acetate copolymers, alkenyl succinic amides, and certain "comb-type" additives such as poly-alkyl acrylates and fumarate vinyl acetate copolymers), producing compact crystal shapes. As the additive competes for lattice sites on the crystal, protruding moieties prevent incorporation of more paraffin molecules.[4,7,8] In addition, agglomeration can sometimes be hindered by electrostatic repulsion under the influence of ionic groups.[4] Additives which individually affect nucleation, growth, or agglomeration are often used in combination to achieve a desired low-temperature behavior. For example, some diesel fuel additives which produce multitudes of paraffin nuclei are used in combination with other additives that arrest crystal growth. This is important because, if the paraffin crystals remain small and suspended in the liquid hydrocarbon, the fuel will still flow.

To study the effects of additives on the low-temperature behavior of jet fuel, different analytical techniques may be used. These techniques may be divided into three categories. The first involves the measurement of some property concerning the formation of paraffin crystals. Examples include measurement of the cloud-point temperature (ASTM D2500), freeze-point temperature (ASTM D2386), and the Shell Cloud/Pour Analysis.[9,10] The second category relies on the trapping of liquid fuel as solidified paraffins accumulate on cooled surfaces. This phenomenon is referred to as "hold-up" and is assessed by measurement of the pour-point temperature (ASTM D97), the Shell Cloud/Pour Analyzer, and the Shell Cold Flow Test.[9] Knowledge of the mass of solid fuel is important because in an aircraft the solid fuel is unavailable for combustion. The last group of analyses characterizes the fluidity of a fuel at low temperatures; tests of this type include the Cold Filter Plugging Point Test[9] and the Seta Point Test.[9,10] The fluidity of a fuel is important because difficulty in pumping fuel from the fuel tanks, can result in catastrophic consequences.

Table 1. Fuel Characteristics of Fuel F3219

aromatics	17% (vol)
total sulfur	321 ppm
freeze-point temperature	−46.8 °C
copper	$<5 \pm 5$ ppb
zinc	$<10 \pm 5$ ppb
iron	$<10 \pm 5$ ppb

Currently, the freeze-point temperature and viscosity (ASTM D445) are the two measures of low-temperature fluidity used for fuel specification. The freeze-point temperature is the temperature at which crystals disappear when a fuel sample is heated (in actuality this is a melting point), and has been considered a conservative measurement.[10] Viscosity is a measure of flow resistance but does not adequately address the fluidity of a two-phase fuel. Although freeze-point temperature and viscosity are used for fuel specifications, it is clear that these tests have limitations in representing the operability of a multiphase jet fuel at low temperatures.[10]

The low-temperature additives being considered for use with JP-8+100 do not arrest crystal nucleation, but rather, they inhibit crystal agglomeration and maintain crystal suspension in the liquid phase. Cold flow additives induce the formation of small needle-shaped crystals (10−100 μm) which have growth and agglomeration rates that are lower than those otherwise obtained without additives.[7,11] Moreover, needle-shaped crystals form aggregations on filter surfaces that are relatively permeable to fuel flow. In this study, the effect of low-temperature fuel additives on fluidity, tank hold-up, and thermal stability are considered. A two-phase flow operability test for evaluating additized fuels at temperatures below the fuel freeze point is developed. The effect of conventional and new low-temperature additives on fuel thermal stability is unknown. Thus, the additives were are also tested in two thermal stability test systems.

Experimental Section

Fuels. For the cold flow testing and the flowing thermal stability test, a Jet A fuel, F3219, with the properties given in Table 1 was selected. JP-8 additives (static dissipator additive, corrosion inhibitor, and fuel system icing inhibitor as specified in MIL-T-83133D) and JP-8+100 additives (256 mg/L BetzDearborn 8Q462 which consists of dispersant, antioxidant, and metal deactivator additives) were added to neat F3219 fuel. The JP-8+100 additives are intended to enhance the thermal stability of the fuel and are a proprietary mixture of additives. Samples of JP-8+100 fuel were blended with the candidate cold flow additives such that the additive concentration was 250 ppm. Fourteen proprietary low-temperature additive candidates (Table 2) provided by various manufacturers were used. All of these blends used the same base JP-8+100. For purposes of comparison, JP-8+100 and

(2) Van Winkle, T. L.; Hazlett, R. N.; Beal, E. J.; Mushrush, G. W. Liquid and Solid Phase Compositions in a Partially Frozen JP-5 Fuel Low in *n*-Alkanes, June 1984; Naval Research Laboratory Report 5357.
(3) Affens, W. A.; Hazlett, R. N. A Statistical Examination of the Effect of Composition on the Freezing Points of Hydrocarbon Mixtures, July 1983; Naval Research Laboratory Report 8692.
(4) Denis, J.; Durand, J. P. *Rev. Inst. Fr. Pet.* **1991**, *46*, 637−649.
(5) Walton, A. G. *Science* **1985**, *148*, 601−607.
(6) Turner, W. R. *Ind. Eng. Chem. Prod. Res. Dev.* **1971**, *10*, 238−260.
(7) Dunn, R. O.; Shockley, M. W.; Bagby, M. O. *J. Oil Chem. Soc.* **1996**, *73*, 1719−1728.
(8) Lewtas, K.; Tack, R. D.; Beiny, D. H. M.; Mullin, J. W. In *Advances in Industrial Crystallization*; Garside, J., Davy, R. J., Jones, A. G., Mullin, J. W., Eds.; Butterworth Heinemann: Boston, 1991; pp 166−179.
(9) Coordinating Research Council. Low-Temperature Behavior of Fuels in Simulated Aircraft Tanks, May 1983; Report No. 532.
(10) Brunton, G.; Willock; R. R.; Voisey, M. A. *Aeronaut. J.* **1982**, *86*, 313−319.
(11) Brown, G. I.; Lehmann, E. W.; Lewtas, K. Evolution of Diesel Fuel Cold Flow−The Next Frontier, 1989; SAE Paper No. 890031.

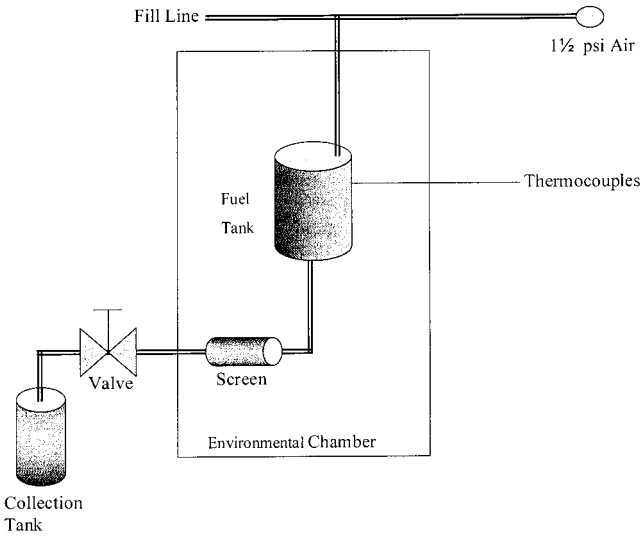

Figure 1. Apparatus for low-temperature flow reduction and hold-up experiments.

Table 2. Measurements of the Cloud-Point, Pour-Point, Freeze-Point Temperatures, and Viscosity for Fuels and Fuels with Cold Flow Additives

fuel/additive sample	cloud point (°C)	pour point (°C)	freeze point (°C)	viscosity (cSt) −40 °C
JP-8+100	−51.2	<−71	−46.8	10.6
JPTS F3657	−59.3	<−71	−54	6.5
3604	−52.2	−69	−45.7	10.7
3605	−51.3	<−71	−46.7	10.7
3607	−52	−68	−46.6	10.7
3608	−50.5	<−71	−47	10.8
3610	−51.7	<−71	−46.9	10.5
3611	−51.4	<−71	−46.3	10.5
3612	−51.2	−70	−46.5	10.6
3614	−47.7	<−71	−45.4	10.8
3615	−49	<−71	−46.8	10.8
3616	−51	<−71	−46.8	10.7
3617	−50.6	<−71	−46.9	10.8
3629	−52.9	<−71	−46.9	10.7
3630	−51.8	<−71	−46.7	10.8
3631	−51.3	<−71	−47.1	10.7

JPTS were used as baseline fuels. JPTS has a very low freeze-point temperature specification (−53 °C, MIL-DTL-25524E) and produces relatively little surface deposition when heated (i.e., high thermal stability).[12] In contrast JP-8 (−47 °C freeze point, MIL-T-83133D), has a higher freeze-point temperature and, for the same conditions, generally produces a greater mass of surface deposits than JPTS.[12] In the current experiments, two samples of JPTS (F2976 and F3657) originating from different sources were used. For the quartz crystal microbalance tests, two other jet fuels were selected: F3166 (Jet A) and F3497 (JP-8). F3166 and F3497 are fuels which have deposition characteristics which were deemed more suitable for these thermal stability tests, as explained in more detail below.

Low-Temperature Flow Reduction and Hold-Up Experiments. In this work, the fuel hold-up and the mass flow rate of fuel passing through a filter are measured for temperatures in the range −51 to −57 °C. This temperature range was selected because it brackets the JPTS freeze-point temperature specification, and preliminary tests demonstrated that crystal nucleation readily began there. Moreover, these temperatures represent severe conditions existing within an aircraft fuel wing tank. In the apparatus used for the evaluation of low-temperature additives (Figure 1), fuel passes from the tank (7.6 L) through stainless steel tubing (1.9 cm o.d. × 1.7 cm i.d.) which is in series with a screen and valve. The screen (8 mesh) is similar to fuel filtering media found in actual aircraft and is considered a likely location for flow blockage. The tank, fuel line, valve, and screen are contained within a chamber in which the temperature may be lowered to −73 °C. The fuel exits the cooled chamber and is collected in a vessel which resides on a scale outside the chamber. The scale is used to measure the mass of fuel flowing from the fuel tank and screen. Thus, a timer used in combination with the mass measurement provides an average mass flow rate of the fuel exiting the chamber. In addition, the fuel tank is pressurized with nitrogen such that the internal pressure of the tank was 10.5 kPa above the ambient pressure. This pressure difference is similar to that used for the pumping of fuel from wing tanks in aircraft.

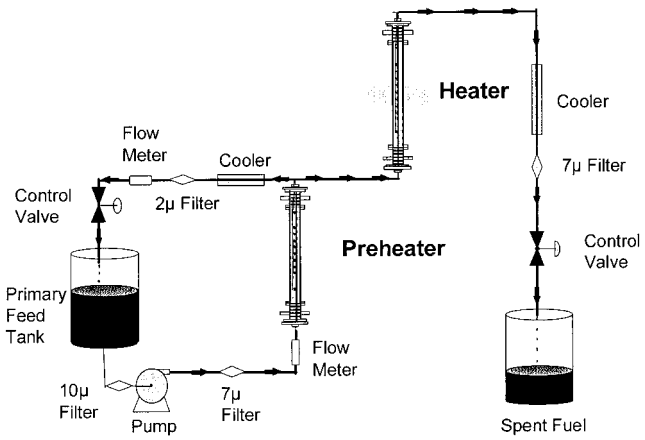

Figure 2. Flow system for heated tube experiments.

The bulk fuel temperatures within the fuel tank were measured by thermocouples (type T) at two locations within the tank and one location directly in the center of the screen. The thermocouple signals were recorded in time to provide estimates of the cooling rate of the fuel. The cooling rate is important because it affects the rate of crystal nucleation and growth. The chamber was set to the desired cooling temperature and the fuel allowed to cool for 16 h. The fuel in the tank was maintained at the desired steady-state temperature for at least 1 h before flow is permitted from the fuel tank. Differences in mass flow rate at a given temperature and source pressure provide an indication of the flow resistance through the tubes and the screen. Since the mass of fuel is known before initiating flow, the mass of fuel that solidifies within the tank (fuel hold-up) is determined from measurement of the mass of fuel collected in the collection vessel which resides outside of the cooling chamber. In addition, a boroscope was used to view the residual fuel within the fuel tank after the flowing fuel had drained.

Thermal Stability Experiments. It is important to know if the low-temperature additives would adversely affect high-temperature thermal stability. These additives usually consist of relatively high molecular weight polymers. These types of species have previously been implicated in increasing deposit formation in fuels. For this reason, two different thermal stability tests were used. In the first, the Extended Duration Thermal Stability Test (EDTST) shown in Figure 2, fuel flows through a heated tube at a rate of 3.8 L/h. The fuel entered the heated test section at a bulk temperature of 107 °C and exited at 188 °C while being subjected to a maximum wall temperature of 371 °C. These temperatures were chosen to be similar to severe conditions that might be encountered in actual aircraft. The tests were conducted for 48 h. Following the flow tests, the tubes were sliced into 5 cm segments for carbon burnoff analysis. Since the surface deposits are largely composed of carbon, the carbon burnoff measurements give

(12) Zabarnick, S. *Ind. Eng. Chem. Res.* **1994**, *33*, 2771−2777.

an indication of the mass of surface deposits that are formed. Details of the apparatus and test procedure are given in ref 13.

The second thermal stability test is the quartz-crystal microbalance/Parr bomb (QCM) system that has been described in detail previously.[12] The QCM system has been used extensively in our laboratory for evaluation of thermal stability additives and for fundamental studies of fuel oxidation and deposition. The batch reactor consists of a 100 mL stainless steel bomb that is heated with a clamp-on band heater. The fuel temperature is controlled by a PID controller via a thermocouple immersed in the fuel. The reactor contains a radio frequency feedthrough, through which the connection for the quartz crystal resonator is attached. The crystals are 2.54 cm in diameter, are 0.33 mm thick, and have a nominal resonant frequency of 5 MHz. For the studies reported here gold crystal electrodes were used. The QCM measures deposition (i.e., an increase in mass) which occurs on overlapping sections of the two-sided electrodes. The reactor is charged with 60 mL of fuel, which is sparged with air for 1 h before each test. The reactor is then sealed and the heater is started. All runs in this study were performed at 140 °C; heat-up time to this temperature is 40 ± 5 min. Most runs are conducted for 15 h, after which the heater is turned off and the reactor is allowed to cool. Surface mass measurements can only be determined during the constant temperature (±0.2 °C) portion of an experimental run. The crystal frequency is converted to a surface mass measurement using a process described previously.[12]

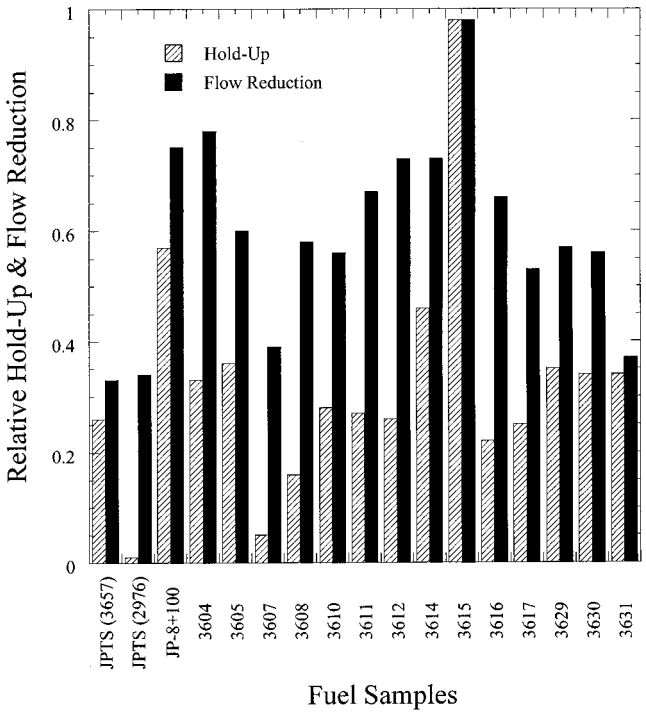

Figure 3. Hold-up and flow reduction for different fuel samples at −57 °C.

Results and Discussion

Three types of experiments were performed to study the relative effectiveness of cold flow additives blended with JP-8+100 in improving low-temperature fuel properties. The first involved conventional ASTM test methods for the determination of effects caused by the additives on the viscosity (D445), cloud-point temperature (D2500), pour-point temperature (D97), and the freeze-point temperature (D2386). The second kind measured hold-up and flow reduction to provide indications of changes in fuel characteristics at low temperatures. In the third type of experiment, two tests were used in which fuel was heated causing surface deposit formation from oxidation reactions. The objective of these thermal oxidative stability tests was to observe evidence of potential adverse effects of the low-temperature additives on the measured surface deposition.

ASTM Tests. Table 2 shows measured values of the freeze-point, cloud-point, and pour-point temperatures for each fuel sample. In addition, viscosity measurements are listed. In the table, JP-8+100 is the baseline fuel, and a JPTS fuel sample (F3657) is shown for purposes of comparison. The freeze-point and cloud-point temperatures are associated with the onset of paraffin crystal nucleation in the fuel. Since the present low-temperature additives do not arrest crystal nucleation, they should not change these properties. As expected, Table 2 shows that the additives have essentially no effect on the freeze-point and cloud-point temperatures. In addition, the viscosity measurements were performed at −40 °C, which is above the freeze-point temperature of all the fuels. Table 2 shows that the viscosity of the fuel containing the cold flow enhancers is the same as the baseline JP-8+100 fuel. It is known that cold flow enhancers affect crystal size and morphology, which in turn, may influence the fuel fluidity. Thus, it might be expected that the low-temperature additives would affect the pour-point temperature of the baseline JP-8+100. Unfortunately, the pour-point temperatures for nearly all the JP-8+100 based fuels were below the detection limits of the test. For additives 3604, 3607, and 3612, it appears that the cold flow additives increased the pour-point temperature. Generally, an increase in the pour-point temperature would not be considered desirable for low-temperature applications. However as shown below, this increase in pour-point temperature for additive 3607 does not correspond to an increase in the measured hold-up and flow reduction values above the baseline fuel in the experiments reported below. More work needs to be done to study the implications of this increase in pour-point temperature on fuel flowability. The table also shows that the JPTS fuel has a lower cloud-point temperature, freeze-point temperature, and viscosity than any of the additive candidate fuels. More work needs to be done to study the implications of these observations.

Low-Temperature Flow Reduction and Hold-Up Test. Figure 3 shows the measured relative hold-up and flow reduction for different fuel samples at −57 °C. For purposes of comparison, the measured average mass flow rate at the low temperature (−57 °C) is normalized by the measured mass flow rate of neat JP-8+100 fuel at ambient conditions (20 °C). Here, one minus the ratio of mass flow rates is defined as the flow reduction. The hold-up is given in the figure as a fraction of the mass of fuel originally contained within the fuel tank. The figure shows that the two JPTS samples have very similar flow reduction values near 0.34, which is sig-

(13) Dieterle, G. L.; Binns, K. E. Evaluation of JP-8+100 Additives in Large Laboratory Test Systems. 34th AIAA/ASME/SAE/ASEE Joint Propulsion Conference and Exhibit, Cleveland, OH, July 1998; AIAA Paper No. 98-3531.

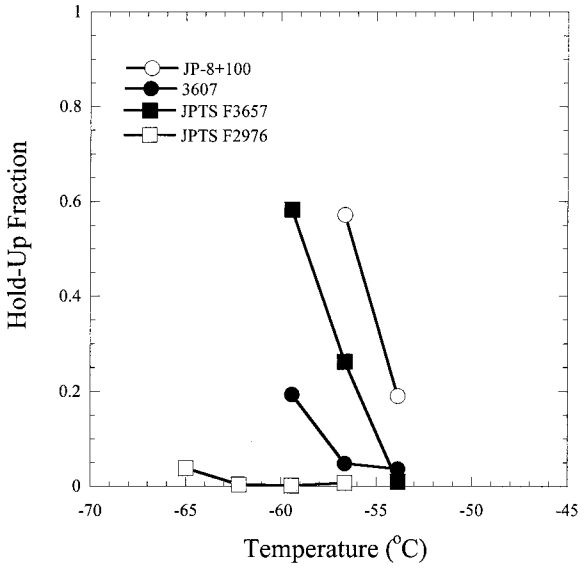

Figure 4. Effect of temperature on hold-up.

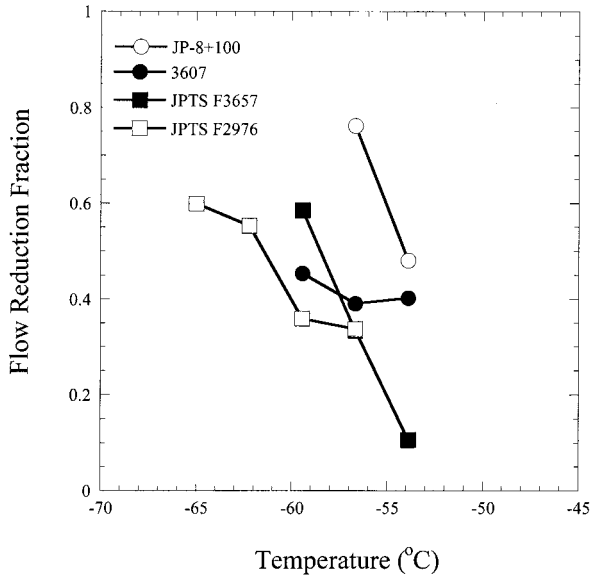

Figure 5. Effect of temperature on flow reduction.

nificantly lower than the JP-8+100 fuel. Presumably, the relative flow reduction observed for these fuels is due to plugging of the screen, fuel viscosity changes, and/or reductions in flow areas due to fuel freezing on internal surfaces. Although none of the fuel samples containing the cold flow enhancers have a flow reduction value below that of the JPTS fuels, additives 3631 and 3607 exhibit flow reductions that are similar to those of the JPTS fuels.

The data of Figure 3 shows that the two JPTS fuels have very different relative hold-up values, although both are significantly lower than the JP-8+100 fuel. This large variability in hold-up behavior of the JPTS samples is most likely due to a variability in the chemical species and their concentrations in the two fuels. Additive 3607 shows the best behavior in reducing hold-up with a result that is considerably better than that of the lesser performing JPTS sample (F3657). Many of the additives provide significant improvement in hold-up relative to the JP-8+100 fuel. Overall, with regard to measured values of hold-up and flow reduction for additives 3607 and 3631, Figure 3 shows that there is good potential for using JP-8+100 in combination with the cold flow enhancers as an alternative to JPTS.

We will now examine the effect of temperature on the measured hold-up and flow reduction for the JP-8+100 fuel with and without additive 3607, and for the two JPTS fuels. Generally, it is expected that values of fuel hold-up will increase as the temperature decreases below the freeze-point temperature. Figure 4 shows this increase in hold-up with declining temperature for four fuel samples. The figure shows that there are large differences in the hold-up fractions of the two JPTS fuels, F3657 and F2976, as the temperature decreases. Interestingly, additive 3607 has a lower hold-up value near −60 °C than does F3657 near −57 °C. Additive 3607 has hold-up values that are significantly less than those of JP-8+100 between −57 and −54 °C. Thus, the figure shows that the low-temperature additive 3607 is effective in reducing fuel hold-up for the JP-8+100 fuel over the range of temperatures tested.

With regard to flow reduction, Figure 5 shows that, as the temperature decreases, the flow reduction increases significantly for the JP-8+100 fuel. On the other hand, for additive 3607, the flow reduction changes little between −60 and −54 °C. In addition, within the temperature range −60 to −57 °C, the flow reduction obtained for additive 3607 is similar to that of the two JPTS samples. The figure shows that at some temperatures there are large differences in the flow reduction measured for the two JPTS fuels.

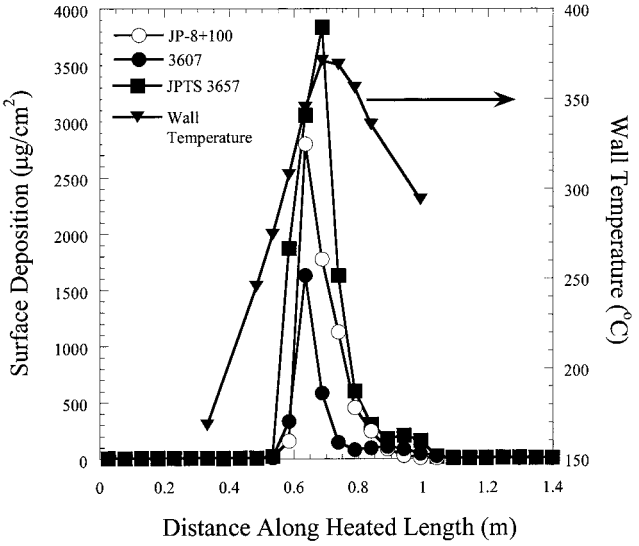

Figure 6. Surface deposition along heated tube for JP-8+100, JPTS, and 3607 fuel samples.

Thermal Stability Tests. As the effect of the cold flow additives on the thermal-oxidative stability of JP-8+100 is not known, we used two thermal stability tests to evaluate the effect of cold flow additive candidate 3607 on the deposit producing tendency of the JP-8+100 fuel.

In the first test, experiments were performed in the EDTST in which fuel passed through heated stainless steel tubes. Figure 6 shows the wall temperature along the tube length and the measured surface deposition for additive and fuel samples 3607, JP-8+100, and JPTS F3657. The mass accumulated at the tube wall is normalized by the original interior surface area of the

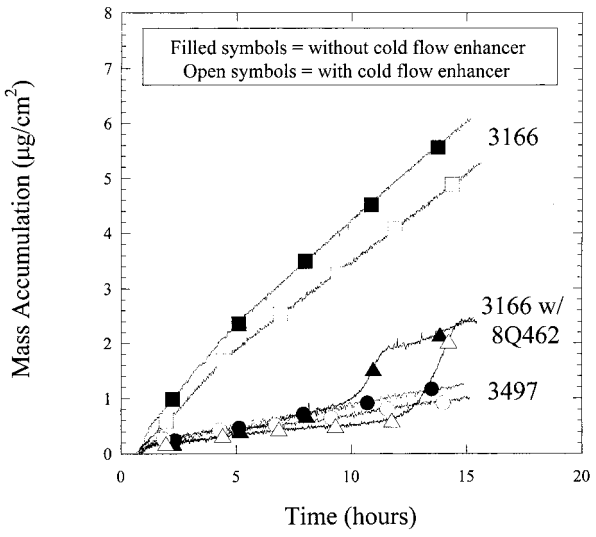

Figure 7. Plots of mass accumulation vs time in the QCM at 140 °C. Filled symbols are without the 3607 cold flow additive, open symbols are with the additive (■, fuel F3166; ▲, fuel F3166 with SPEC·AID 8Q462 thermal stability additive; ●, fuel F3497).

tube. The figure shows a peak in surface deposition near the center of the tube for each fuel. Similar peaks in deposition have been observed previously for similar flow and temperature conditions in which the dissolved oxygen has been fully consumed. Thus for the present flow and temperature conditions, it is believed that the dissolved oxygen is fully consumed. The smallest peak occurs for additive 3607. The figure shows that all three fuel/additive combinations result in similar surface deposition profiles. This deposition is greatly reduced from that of a JP-8 fuel without the JP-8+100 thermal stability additive package. Although this preliminary result is for a single flow and temperature condition, it indicates that there is no detrimental effect on thermal stability from the presence of the cold flow additive. To further explore this potential, more detailed work must be performed which uses different neat fuels, flow rates, and temperature conditions.

For the second thermal stability test, the QCM, we chose two different fuels than the F3219 fuel used for previous low-temperature and thermal stability tests. We chose a low thermal stability fuel, F3166, which yields significant deposition and a high thermal stability fuel, F3497, which yields very low deposition. We tested the low thermal stability fuel with and without the JP-8+100 additive package. In this way, we can test for possible detrimental effects of the cold flow additive on thermal stability in low depositing fuels, F3497 unadditized and F3166 with the JP-8+100 package, and also in a high depositing, fuel F3166 unadditized. The resulting plots of mass accumulation vs time are shown in Figure 7. The results show that both of the unadditized fuels, F3166 and F3497, show no change in deposition upon addition of the 3607 cold flow additive within the experimental reproducibility (±20%). Most importantly, the low depositing fuel, F3497, still produces very low deposition in the presence of the additive. The figure also shows that addition of the JP+8+100 additive package to the high depositing fuel, F3166, results in a significant reduction in deposition. Subsequent addition of the cold flow additive to the F3166/JP-8+100 combination results in a small delay in the time where deposition increases, but the final deposition is identical to the fuel combination without the cold flow additive.

The results of these two thermal stability tests in a range of fuels demonstrate that the cold flow additive (3607) at a concentration of 250 ppm has no significant detrimental effect on high-temperature thermal stability. As mentioned above, these tests were performed under a limited set of conditions but indicate that cold flow additives, such as the one tested, may be useful for addition to JP-8+100 fuel for use as a low-cost replacement for JPTS.

Conclusions

This work examined the potential of using cold flow enhancing additives for addition to JP-8+100 fuel for use as a low-cost replacement for JPTS fuel. Flow enhancing additives are commonly used in diesel fuels, but their effectiveness in kerosene-based fuels has not been fully explored. The additives were blended with a representative JP-8+100 fuel and evaluated in a low-temperature test facility. In these experiments, both the reduction in flow and the fuel hold-up were measured. Several cold flow additives provided significant enhancement of hold-up and flow reduction characteristics relative to those of unadditized JP-8+100. In addition, the use of one cold flow additive provided a fuel which appeared to have better hold-up characteristics than those of a JPTS sample. In addition, this additive had no detrimental effect on high-temperature thermal-oxidative stability. Thus, the results suggest that a potential cold flow additive can be used to enhance the low-temperature properties of JP-8+100 such that it can be used as a low-cost replacement for JPTS.

Additional work needs to be performed to address important issues before cold flow additives can be used in the field. Studies need to address the following areas of concern: additive/fuel system materials compatibility, evaluation of the temperatures to which such a fuel is subjected in high-altitude aircraft, studies of hold-up and fuel flow over an extended temperature range using various cooling rates, studies of additional fuel samples, additive concentration optimization studies, evaluation of fuel low-temperature flow behavior in actual fuel system components, evaluation of additional additive candidates, and additional thermal stability studies over a wide range of temperatures and flow rates.

Acknowledgment. This work was supported by the U.S. Air Force, Warner Robins Air Logistic Command, U-2 Special Programs Office, Robins Air Force Base, Warner Robins, Georgia, under Project No. 205 (Project Manager: Capt. Bernard Frank) and the U.S. Air Force Research Laboratory, Propulsion Directorate, Propulsion Sciences and Advanced Concepts Division, Wright-Patterson Air Force Base, Ohio, under Contract No. F33615-97-C-2719 (Technical Monitor: C. W. Frayne). Quality Assurance Specialist Michael Thiede performed the fuel analyses at the Aerospace Fuels Laboratory at Wright Patterson Air Force Base.

EF9901600

G. Studies of Jet Fuel Thermal Stability, Oxidation, and Additives Using an Isothermal Oxidation Apparatus Equipped with an Oxygen Sensor

Studies of Jet Fuel Thermal Stability, Oxidation, and Additives Using an Isothermal Oxidation Apparatus Equipped with an Oxygen Sensor

Becky Grinstead* and Steven Zabarnick

Aerospace Mechanics Division, University of Dayton Research Institute, 300 College Park, Dayton, Ohio 45469-0140

Received November 13, 1998. Revised Manuscript Received January 26, 1999

An isothermal oxidation apparatus (IOA) has been modified to include an oxygen sensor so that both oxidation and deposition data can be measured for jet fuels that are thermally stressed. This modification is useful for comparing the relative oxidation rates of jet fuels and fuels blended with additives. Antioxidants can be evaluated in this apparatus by comparing the delay in the onset of oxidation at a given temperature in a fast oxidizing fuel. Other additive types, such as dispersants, can be evaluated by their ability to reduce deposition.

Introduction

In military aircraft, jet fuel is used as both a coolant and a propellant. Future high-performance aircraft engines will produce more excess heat than current engines. Consequently, the jet fuel will be exposed to higher temperatures. When fuel is heated, it reacts with small amounts of dissolved oxygen to form soluble and insoluble oxidation products. Insoluble products (both bulk and surface deposits) pose a problem because they can clog fuel lines and foul close tolerance valves. Ultimately, the fouling caused by deposits could result in engine failure. To address this issue, the U.S. Air Force developed a program called JP-8+100.[1]

The primary goal of the JP-8+100 program is to increase the heat-sink capacity of JP-8 fuel by 100 °F (55 °C) using a thermal stability additive package. This corresponds to an increase in bulk fuel temperature at the nozzle from 163 to 218 °C. Thermal stability refers to the deposit-forming tendency of a fuel. It is generally accepted that dissolved oxygen initiates the deposition process in freshly refined fuels. Usually, over a range of fuels, an inverse relationship exists between thermal stability and oxidative stability—a fuel's tendency to oxidize. In other words, a fuel that oxidizes slowly is likely to form more deposits than a fuel that oxidizes rapidly.[2,3] An exception would be a highly refined hydrotreated fuel, which is required to have an antioxidant added at the refinery to prevent oxidation. This fuel would demonstrate low oxidation and low deposition until the antioxidant was consumed. To this end, many laboratory tests have been developed to investigate the thermal and oxidative stability of fuels. Because fuel in an aircraft experiences various temperatures, flow rates, and oxygen levels, laboratory tests must cover a wide range of conditions. In general, there are two types of laboratory tests: static and flowing.

In flowing tests, air-saturated fuel passes through a single-tube heat exchanger. The oxygen content is limited to that which is dissolved in the fuel, which is realistic; however, accelerated temperatures are usually needed to produce measurable deposits. Frequently, deposits are measured by carbon burnoff of the tube at the completion of the test. Due to the large amounts of fuel (many gallons) and relatively long test times (days) that may be required, many flowing tests are not practical for screening a large number of candidate additives. Rather, the flowing rigs are useful for testing a few promising additives and for studying jet fuel behavior at various flow rates, temperatures, and oxygen availabilities. The Phoenix rig is an example of a flowing test that has been used for additive testing and fundamental studies of jet fuel.[4]

In a static test, fuel is heated in the presence of air or oxygen in a flask or reactor. Generally, deposits are separated from the stressed fuel by filtration after suitable cooling and then measured gravimetrically. Static tests can be accelerated in time, temperature, and oxygen availability. For example, Kendall and Mills used a flask oxidation test to study the thermal stability of kerosines.[5] Static tests are useful for screening a large number of additives because test times are short (hours) and sample volumes are small (<100 mL). The Parr bomb/quartz crystal microbalance (QCM) system measures oxidation and deposition of jet fuel simultaneously in real time over a 15 h test run. The usefulness of the QCM in fundamental studies of jet fuel and as an additive screening tool has been demonstrated.[6]

(1) Heneghan, S. P.; Zabarnick, S.; Ballal, D. R.; Harrison, W. E., III *J. Energy Resour. Technol.* **1996**, *118*, 170−179.
(2) Heneghan, S. P.; Zabarnick, S. *Fuel* **1994**, *73*, 35−43.
(3) Hardy, D. R.; Beal, E. J.; Burnett, J. C. *Proc. 4th Int. Conf. Stability Handling Liq. Fuels* **1992**, 260−271.
(4) Heneghan, S. P.; Williams, T. F.; Martel, C. R.; Ballal, D. R. *J. Eng. Gas Turbines Power* **1993**, *115*, 480−486.
(5) Kendall, D. R.; Mills, J. S. *Ind. Eng. Chem. Prod. Res. Dev.* **1986**, *25*, 360−366.
(6) Zabarnick, S.; Grinstead, R. R. *Ind. Eng. Chem. Res.* **1994**, *33*, 2771−2777.

10.1021/ef980252+ CCC: $18.00
Published on Web 02/26/1999

Table 1. Identification of Additives Studied

additive	supplier	treat rate (mg/L) Fuel 3204	Fuel 3166	compound	percent active ingredient
BHT	Aldrich	25, 100	25	2,6-di-*tert*-butyl-4-methylphenol	100
AO-24	DuPont	25, 100		*N*,*N*′-di-*sec*-butyl-*p*-phenylenediamine	50
hexyl sulfide	Aldrich	3000			95
MDA	DuPont	22	2	*N*,*N*′-disalicylidene-1,2-propanediamine	73−75
SPEC•AID 8Q405	BetzDearborn		100	proprietary	proprietary
SPEC•AID 8Q462	BetzDearborn		256	SPEC•AID 8Q405/BHT/MDA	proprietary

This paper will discuss another static test used to evaluate jet fuels and jet fuel additives—an isothermal oxidation apparatus (IOA). For this study, the IOA has been modified to include an oxygen sensor. With the oxygen sensor, the oxidation rate is measured in real time over the 5 h test run. The amount of deposition is determined gravimetrically by filtration at the end of the run. This new technique will be used to study the behavior of jet fuels and jet fuel additives as well as the relationship between oxidation and deposition.

Experimental Section

All jet fuel samples were thermally stressed in an isothermal oxidation apparatus (IOA, Falex Corporation) that meets the criteria of ASTM 4871−88, "A Standard Guide for Universal Oxidation/Thermal Stability Test Apparatus".[7] In the IOA, fuel is heated in glass test tubes through which air is bubbled. The IOA includes a heater block containing several test wells, a temperature controller to maintain the heater block temperature, and flow meters to regulate the air flow to the jet fuel sample via a gas dispersion tube. The gas dispersion tubes are made of 1/4 in. o.d. glass with a hollow fritted cylinder at the tip. The fritted tip produces very fine bubbles of air, which helps the oxygen to become dissolved in the fuel rapidly by increasing the fuel/oxygen contact area. Past experiments without the fritted tip showed that the rate of oxidation in the fuel was limited by the ability of the oxygen to diffuse into the fuel from a large bubble. The 150 mL glass test cell is topped with a glass adapter that houses the Ingold dissolved oxygen sensor, which measures the headspace oxygen concentration. A condenser, which is supplied with 20 °C water via a refrigerated recirculation bath, fits on top of the adapter.

All tests were performed using the following procedure. A test run begins by calibrating the oxygen sensor in room temperature air to read 20.9%. Then, the test cell containing a 100 mL fuel sample is assembled with the adapter, oxygen sensor, condenser, and gas dispersion tube. The fuel is sparged with nitrogen until the oxygen sensor reads 0.0%. This prevents oxidation from occurring while the fuel is heating to the desired temperature. At this point, the entire test-tube assembly is placed in the heated test well. The fuel takes approximately 30 min to reach 180 °C. This temperature was chosen because it falls within the range of the +100 temperature increase and because moderate deposits can be produced within the 5 h test period. Next air is added at 10 L/h and data acquisition begins. The high flow rate rapidly saturates the fuel with air, so the reaction rate is not limited by the rate of oxygen introduction into the fuel. The fuel is cooled slightly, 2−3 °C, by this high flow rate, but the set-point temperature is returned within 15 min. After 1 min, the flow rate is adjusted to 1.3 L/h for the remainder of the test.

The temperature at the oxygen sensor remains fairly constant at 24 ± 1 °C. The output of the oxygen sensor is read by an Ingold dissolved oxygen microprocessor transmitter (model 4300) whose output is sent to a digital multimeter (Hewlett-Packard model 3478A) and recorded at 10 s intervals by a personal computer for 5 h. After 5 h, the air flow is stopped and the test tube assembly removed from the test well and allowed to cool overnight. The next day bulk deposits are collected on a preweighed 4.7 cm 1 μm glass microfiber filter (Whatman, EPM 2000) by vacuum filtration. Surface deposits on the test cell and the glass blower tube are not evaluated. The filter is rinsed with heptane and then dried in an oven at 110 °C for a minimum of 3 h. The filter is cooled in a desiccator and then weighed. The results are reported as milligrams of solid.

Table 2. Properties of Fuels Studied

fuel	type	total sulfur (ppm)	copper (ppb)	iron (ppb)
2962	JP-5	438		
2963	JP-5	438	98	60
2926	Jet A	524	<5	10
3166	Jet A	1200	<5	<5
3119	Jet A	1000	7	26
2827	Jet A	763	<5	8
3204	JP-5	0		

To generate reproducible oxidation results, a scrupulous cleaning technique for all the glassware was essential. Trace amounts of metals, surfactants, and other contaminants can alter the oxidation rate of a fuel. The following procedure, a modified version of a procedure developed by Kendall and Mills, was used to clean the glassware.[5] The test tubes were soaked in Citranox acid cleaner for 2 h, rinsed with distilled water, rinsed with acetone, soaked in 0.1 N methanolic potassium hydroxide for 2 h, rinsed again with distilled water, and then dried. The condenser was rinsed with heptane followed by acetone, while the adapter was washed with soapy water. New gas dispersion tubes are used for each run because attempts to clean and reuse them were not successful.

Additives for this study were received from various suppliers and are listed in Table 1. The fuels for this study were acquired from the Advanced Concepts and Propulsion Division of the Air Force Research Laboratories. Some properties of these fuels are listed in Table 2.

Results and Discussion

The oxygen data will be presented as the headspace oxygen in percent vs time. In Figure 1 the oxygen profiles of a fast and slow oxidizing fuel are shown. The headspace oxygen level goes from 0.0 to 20.9% in about 1 min for both fuels. This corresponds to the time that the air flow rate is 10 L/h. The headspace reading corresponds to the amount of oxygen that is not consumed by the fuel. So, for a fuel with a slow oxidation rate, the sensor will read close to 20.9%. A fast oxidizing fuel, on the other hand, consumes a large portion of the oxygen; therefore, the headspace reading will be low. Notice that both fuels also exhibit an approximately 20 min induction period—the early period during which the oxidation rate is relatively slow.

The total amount of oxygen consumed can be calculated by converting the headspace oxygen to consumed oxygen (20.9 minus the probe reading) then summing

(7) 1997 *Annual Book of ASTM Standards*, ASTM: Philadelphia, PA, 1997; Vol. 05.03, pp 175−178.

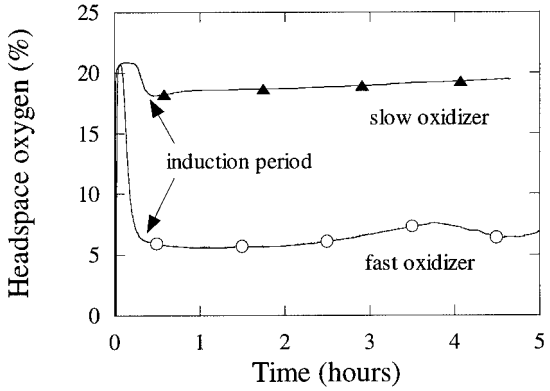

Figure 1. Headspace oxygen profiles for a fast and slowly oxidizing fuel.

Table 3. Deposition, Oxygen Consumption, and Deposition/Consumed Oxygen for Various Fuels

fuel	solids (mg)	O_2 consumed (mol × 10^{-2})	solids/O_2 consumed ((mg/mol) × 10^3)
2962	23.3	0.172	13.5
2963	48.4	1.58	3.06
2926	8.9	0.363	2.5
3166	13.6	0.500	2.72
3119	9.5	0.569	1.7
2827	16.7	1.15	1.45
3204	0	4.02	

the area under the curve after the 1 min high-flow aeration period. An air flow rate of 1.3 L/h of air corresponds to 2.0×10^{-4} mol of O_2/min. If the oxygen sensor reading is 20.9%, then the amount of oxygen consumed is 0. If the oxygen sensor reading is 0.0%, then the amount of oxygen consumed is 2.0×10^{-4} mol of O_2/min. The maximum amount of oxygen that could be consumed during a 5 h run would be 6.0×10^{-2} mol. For comparison, the QCM has about 4.5×10^{-4} mol of oxygen available in the headspace and in the fuel.[8] The QCM has less available oxygen because it is a closed system.

A group of fuels were evaluated for both deposition and oxidation characteristics in the IOA at 180 °C. The sulfur, copper, and iron content of each fuel is listed in Table 2. Sulfur-containing compounds are thought to play an important role in increasing deposition, and they have been implicated in slowing or delaying oxidation.[9] Fuel reacts with metal surfaces in transit, thereby acquiring dissolved metals. Dissolved metals copper and iron are noted for decreasing thermal stability.[10] The amount of solids collected on a 1 μm filter, the amount of oxygen consumed during the 5 h run, and the amount of deposition produced per mole of oxygen for this group of fuels are listed in Table 3.

As a general trend, a fuel that consumes oxygen slowly tends to produce deposits.[2] An example of this phenomenon is fuel 2962—it consumes the least amount of oxygen and it has one of the highest depositions of this group of fuels. Fuel 2963 is fuel 2962 that has been spiked with 98 ppb of copper. The copper causes an increase in oxygen consumed in this fuel by an order of magnitude, from 1.72×10^{-3} to 15.8×10^{-3} mol. This

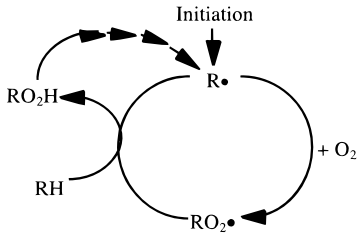

Figure 2. Autoxidation chain mechanism of jet fuel.

increase in oxidation rate also has the detrimental effect of increasing the deposition. This observation agrees with previous studies showing that copper is detrimental to thermal stability. The remedy for this type of fuel is usually an additive that will hold insoluble deposition products in solution by preventing agglomeration. An antioxidant is generally ineffective because the fuel already contains many natural antioxidants that contribute to its inherently slow oxidation rate.

On the other hand, fuel 3204 consumes oxygen rapidly but produces little deposits under these stressing conditions. Fuel 3204 contains very few naturally occurring antioxidants and the concentration of sulfur is low. An antioxidant will generally be beneficial for this type of fuel because it will be effective in delaying oxidation, thereby delaying any deposition that may occur. Although 3204 and 2962 represent extremes in this group of fuels, most fuels fall somewhere in between, in which the oxidation rate and deposition amount are both moderate.

It is apparent that the oxygen sensor can provide valuable information about the oxidation characteristics of a given fuel. In the following sections we will explore the use of this device in studying the behavior of potential jet fuel additives.

Antioxidant Behavior. A free radical, autoxidation chain mechanism has been proposed to describe fuel oxidation and deposition behavior.[2] Zabarnick modeled the autoxidation sequence and expanded it to include reactions that account for autoacceleration.[11,12] The classical autoxidation chain mechanism of jet fuel is shown in Figure 2. An initiation reaction results in the formation of an alkyl radical, R•. The alkyl radical reacts with dissolved oxygen, O_2, to form an alkylperoxy radical, RO_2•. The alkylperoxy radical, RO_2•, reacts with another fuel molecule, RH, to generate a hydroperoxide, RO_2H, and another alkyl radical, R•, thus propagating the chain mechanism. Autoacceleration occurs when the hydroperoxide decomposes to form two radicals: RO• and •OH. The multiple arrows indicate that these two radicals further react to contribute to the pool of alkyl radicals, R•.

Antioxidants are commonly used in hydrocarbon liquids to slow and/or delay autoxidation. For example, hindered phenols and phenylenediamines break the chain mechanism by intercepting the alkylperoxy radical, RO_2•.[13] Peroxide decomposers break down hydroperoxides by a nonradical pathway, thus preventing their decomposition into free radicals.[14] Metal deactivators complex with metal ions, preventing metal-cata-

(8) Zabarnick, S. *Ind. Eng. Chem. Res.* **1994**, *33* (5), 1348−1354.
(9) Kauffman, R. E. *J. Eng. Gas Turbines Power* **1997**, *119*, 322−327.
(10) *Handbook of Aviation Fuel Properties*; CRC Report No. 530, 1983; p 100.
(11) Zabarnick, S. *Ind. Eng. Chem. Res.* **1993**, *32*, 1012−1017.
(12) Zabarnick, S. *Energy Fuels* **1998**, *12*, 547−553.
(13) Pedersen, C. J. *Ind. Eng. Chem.* **1956**, *48*, 1881−1884.
(14) Denison, G. H., Jr.; Condit, P. C. *Ind. Eng. Chem.* **1945**, *37*, 1102−1108.

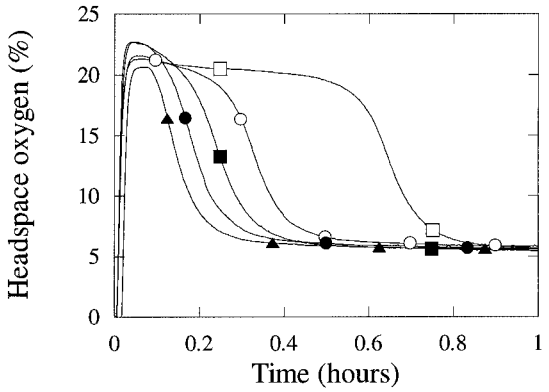

Figure 3. Fuel 3204 with no additives (▲), BHT at 25 mg/L (●), BHT at 100 mg/L (■), AO-24 at 25 mg/L (○), and AO-24 at 100 mg/L (□).

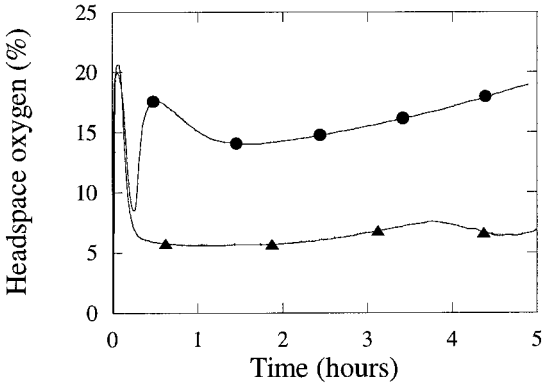

Figure 4. Fuel 3204 with no additives (▲), and hexylsulfide at 3000 mg/L (●).

lyzed reactions that produce free radicals. Each of these antioxidants lowers the concentration of free radicals either by preventing their formation or rapidly removing them after they have been formed. The aforementioned induction period is likely related to the time it takes a fuel to build up radical concentrations to a steady-state level.

To study the effect of the various types of antioxidants in our system, fuel 3204 was blended with the following additives: BHT (a hindered phenol), AO-24 (a phenylenediamine), hexylsulfide (a peroxide decomposer), and MDA (a metal deactivator). Fuel 3204 is a fast oxidizing JP-5 fuel that produces no deposits under these operating conditions. Therefore, any deposition and/or delays in oxidation due to an additive will be readily apparent.

Fuel 3204 blended with AO-24 or BHT displays progressively longer delays in oxidation with increasing antioxidant concentration as shown in Figure 3. Notice that BHT is not as effective at delaying oxidation as AO-24 at a given concentration. For example, 100 mg/L of BHT offers a 6 min delay while the same concentration of AO-24 gives a 36 min delay. One way antioxidants can be ranked is by the delay that they provide in a fast oxidizing fuel. This provides a way to compare the effectiveness of candidate antioxidants in jet fuel. This is a new capability for the IOA, since only deposition data was available before the oxygen sensor was installed. Both antioxidants extend the induction time, but the final oxidation rate remains the same. Zabarnick and Whitacre observed similar behavior for BHT in a fast oxidizing fuel stressed in the QCM.[15] They showed that BHT slowed the oxidation rate until it was consumed, then the autoxidation continued at a more rapid rate.

Condit and Denison have shown that alkylsulfides can decompose hydroperoxides to nonradical products during lubricating oil oxidation.[14] This results in a reduced oxidation rate in these oils. In Figure 4 we show the effect of hexyl sulfide (3000 mg/L) on the oxidation rate of fuel 3204. Note that this corresponds to approximately 0.06 wt % of sulfur, while the ASTM specification for JP-5 fuel allows a maximum of 0.4 wt %. The hexyl sulfide has no effect on the induction period but does change the final oxidation rate of fuel 3204. Since it is likely that radical and peroxide concentrations are building up during the induction period, it is expected that the hexyl sulfide would not have an effect during this time. However, after about 30 min, a much slower oxidation rate is observed when the hexyl sulfide is present. We calculate that the total oxygen consumption is reduced by approximately 70% due to the presence of the additive. This would support the premise that the hexyl sulfide is decomposing the hydroperoxides by a nonradical pathway, since a decrease in oxidation rate is observed. One can also conclude that the hydroperoxide decomposition strongly influences the overall oxidation rate for this fuel at this temperature.

The metal deactivator MDA had little effect on the oxidation of fuel 3204. A slight delay in the onset of oxidation is observed. This fuel has negligible levels of dissolved metals; thus, no effect would be expected. No measurable deposition was obtained for any of the runs with 3204 blended with antioxidants.

Additive Package Studies. It is convenient to evaluate antioxidants in a fast oxidizing fuel so that a delay in oxidation can be observed. However, fuels that oxidize rapidly often produce few deposits. Fuels that produce deposits are needed to study the ability of an additive to reduce deposition. For example, dispersants are used in some military fuels to prevent deposition by surrounding polar species and preventing them from agglomerating and/or reacting to form larger species that ultimately produce deposits. Fuel 3166 is a commercial Jet A fuel that oxidizes slowly and produces a moderate amount of deposits under these stressing conditions. This fuel was blended with a dispersant (SPEC•AID 8Q405), an antioxidant (BHT), a metal deactivator (MDA), and a package containing all three additives (SPEC•AID 8Q462). Headspace oxygen curves for fuel 3166 with and without additives are shown in Figures 5 and 6. The unadditized fuel shows the fastest oxidation rate initially (0.5−1.5 h). All fuel/additive combinations have slower oxidation rates throughout the run compared to the neat fuel, except for 3166 with SPEC•AID 8Q405 at longer times. The reason for this observation is not readily apparent.

Table 4 summarizes the amount of solids collected on a 1 μm filter, the amount of oxygen consumed during the 5 h run, and the deposition normalized to the amount of oxygen consumed for fuel 3166 blended with additives. The deposition per consumed oxygen of unadditized 3166, 3166 with MDA, and 3166 with BHT is 2.67 × 10^3, 2.1 × 10^3, and 2.3 × 10^3 mg/mol, respec-

(15) Zabarnick, S.; Whitacre, S. D. *J. Eng. Gas Turbines Power* **1998**, *120*, 519−525.

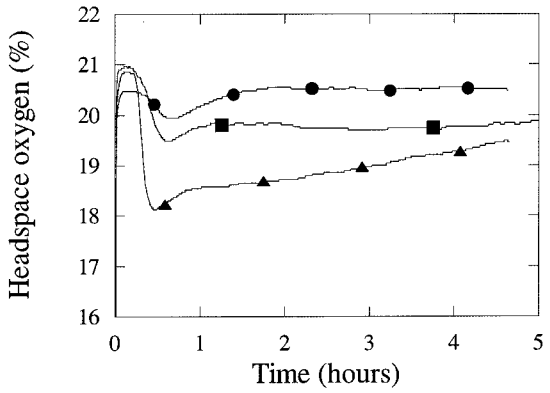

Figure 5. Fuel 3166 with no additives (▲), BHT (■), and MDA (●).

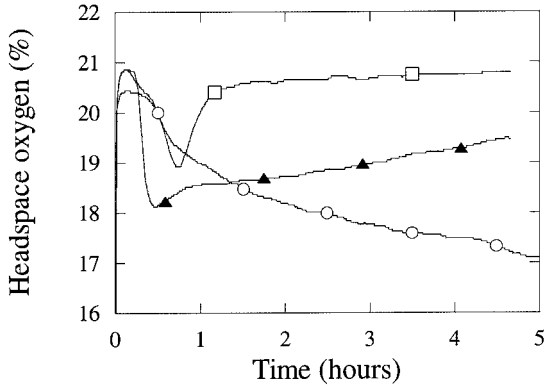

Figure 6. Fuel 3166 with no additives (▲), SPEC•AID 8Q405 (○), and SPEC•AID 8Q462 (□).

Table 4. Deposition, Oxygen Consumption, and Deposition/Consumed Oxygen for Fuel 3166 Additive Blends

fuel/additive blends	solids (mg)	oxygen consumed (mol × 10^{-3})	solids/O_2 consumed ((mg/mol) × 10^3)
3166	13.6	5.09	2.67
3166 with MDA	2.6	1.23	2.1
3166 with BHT	6.9	3.00	2.3
3116 with SPEC•AID 8Q405	4.3	6.68	0.64
3166 with SPEC•AID 8Q462	0.8	1.07	0.7

tively. Even though the amount of deposits and oxygen consumed are less when these two additives are present, the amount of solids produced per mole of oxygen consumed is about the same as the unadditized fuel. This indicates that the MDA and BHT are slowing the oxidation rate, which directly results in reduced deposition. Also of interest is that when MDA is present in fuel 3166, the amount of oxygen consumed decreases from 5.09 × 10^{-3} to 1.23 × 10^{-3} mol. This implies that dissolved metals play a significant role in the oxidation of this fuel since the metal deactivator has such a dramatic effect. Since the copper and iron contents of this fuel were each <5 ppb, it is likely that there are significant levels of other metals that catalyze the oxidation of fuel 3166. Another possibility is that MDA is acting in a way other than by chelation of dissolved metals. Compounds with an easily extractable hydrogen atom have antioxidant properties, and the MDA molecule has two easily abstractable phenolic hydrogen atoms.

On the other hand, the 3166 with SPEC•AID 8Q405 produces 0.64 × 10^3 mg of deposition per mole of oxygen consumed. The amount of oxygen consumed for this run is slightly greater than the neat fuel; however, the deposition is greatly reduced. This indicates that the dispersant, SPEC•AID 8Q405, reduces deposition independently of affecting the oxidation rate. This type of behavior is fully expected for a dispersant type of additive.

Fuel 3166 with the additive package SPEC•AID 8Q462 represents the best combination overall because the oxygen consumption and deposition are both minimized. SPEC•AID 8Q462 is currently being used in the field as an additive for JP-8+100 fuel with excellent results.[1] The additive package combines the separate actions of MDA and BHT which slow the oxidation and SPEC•AID 8Q405 which prevents deposition.

Conclusions

The IOA equipped with an oxygen sensor provides real-time data for the oxidation of jet fuels and jet fuels blended with additives in addition to deposition data at the end of the run. Antioxidant additives can be evaluated based on their ability to delay oxidation in a fast oxidizing fuel when the oxygen sensor is present. Also, the deposition produced per mole of oxygen consumed is used to evaluate additives based on their ability to reduce deposition and to understand how additives affect the deposition/oxidation mechanism in a particular fuel.

Acknowledgment. This work was supported by and performed at the U.S. Air Force Research Laboratories, Fuels and Lubrications Division, Wright-Patterson AFB, OH, under Contract Nos. F33615-92-C-2207 and F33613-97-2719 with Charles Frayne as technical monitor.

EF980252+

H. Inhibition of Jet Fuel Oxidation by Addition of Hydroperoxide-Decomposing Species

Inhibition of Jet Fuel Oxidation by Addition of Hydroperoxide-Decomposing Species

S. Zabarnick* and M. S. Mick

University of Dayton Research Institute, Aerospace Mechanics Division, 300 College Park, Dayton, Ohio 45469-0140

We have explored the use of hydroperoxide decomposing species for inhibiting oxidation in jet fuel. We find that hydroperoxide decomposing species, such as alkyl sulfides, do not slow or delay oxidation in hydrocarbon solvents at 140 °C. However, when phenolic species are also present, such as those naturally occurring in fuel or by addition of hindered phenols, substantial delays in oxidation are observed. We used a pseudo-detailed chemical kinetic mechanism to provide insight into the oxidation process. The combination of hydroperoxide decomposer and hindered phenol can substantially inhibit oxidation of fuel under the conditions studied here.

Introduction

The introduction of additives into petroleum liquids to improve properties or characteristics has been used successfully for many decades. Currently, additives which may be used in the U. S. Air Force primary jet fuel, JP-8, include icing inhibitors, corrosion inhibitors, antioxidants, metal deactivators, and static dissipators. Recently, the U. S. Air Force JP-8+100 program has developed an additive package which significantly increases the thermal stability (tendency to resist deposit formation) of the fuel, preventing the formation of deposits which result from fuel oxidation within aircraft fuel systems.[1,2] This additive package presently includes a dispersant, an antioxidant, and a metal deactivator. While a wide variety of additive types were investigated in the JP-8+100 program, the use of hydroperoxide decomposers to slow or delay oxidation has not received significant attention. Hydroperoxide-decomposing additives have been used in lubricants and polymers to decompose alkyl hydroperoxides formed during oxidation into nonradical products.[3] In the present study, we explore the role that hydroperoxide decomposers play in slowing or delaying autoxidation of jet fuel. We also study the synergism of these species with other additive types. In addition, pseudo-detailed chemical kinetic modeling was performed to provide insight into the chemical mechanism of additive behavior. We have also used the insights provided by these studies to help in understanding the various oxidation characteristics of fuels.

Experimental Section

Fuel oxidation and deposition characteristics were evaluated in the quartz crystal microbalance (QCM) Parr bomb system that has been described in detail previously.[4,5] Most fuel oxidation tests were run at 140 °C and 1 atm of air initial pressure. The reactor is heated with a clamp-on band heater, and its temperature is controlled by a PID controller via a thermocouple immersed in the fuel. The device is equipped with a pressure transducer (Sensotec) to measure the absolute headspace pressure and a polarographic oxygen sensor (Ingold) to measure the headspace oxygen concentration. The oxygen sensor and pressure gauge allow us to follow the oxidation process. As oxygen is consumed in the liquid, oxygen in the headspace diffuses into the liquid, resulting in a decrease in the headspace oxygen concentration. The reactor also contains a radio frequency feedthrough, through which the connection for the quartz crystal resonator is attached. The crystals are 2.54 cm in diameter and 0.33 mm thick and have a nominal resonant frequency of 5 MHz. The crystals were acquired from Maxtek Inc. and are available in crystal electrode surfaces of gold, silver, platinum, and aluminum. For the studies reported here gold crystal electrodes were used. The QCM measures deposition (i.e., an increase in mass) which occurs on overlapping sections of the two-sided electrodes. Thus, the device responds to deposition which occurs on the metal surface and does not respond to deposition on the exposed quartz. Deposition measurements for the additized fuels (Exxsol D110 and F-2747) will not be shown in this study because the fuels, and fuels with additives, produce very low levels of deposition ($<1.0\ \mu g/cm^2$).

A personal computer is used to acquire data at 1 min intervals during the experimental run. The following data are recorded during a run: temperature, crystal frequency, headspace pressure, headspace oxygen concentration, and crystal damping voltage. The reactor is charged with 60 mL of fuel, which is sparged with air for 1 h before each test. The reactor is then sealed, and the heater is started. All runs in this study were performed at 140 °C; heat-up time to this temperature is 40 ± 5 min. Most runs are conducted for 15 h, after which the heater is turned off and the reactor is allowed to cool. Surface mass measurements can only be determined during the constant temperature (±0.2 °C) portion of an experimental run. The crystal frequency is converted to a surface mass measurement using a process described previously.[5] Post-test analyses of hydroperoxide concentrations were performed using a cyclic voltammetry technique.[6] Fuels were acquired from the U. S. Air Force Research Laboratory, Propulsion Directorate. Exxsol D110 was acquired from Exxon. Some properties of the fuels studied are summarized in Table 1.

* Telephone: (937) 255-3549. Fax: (937) 252-9917. E-mail: zabarnic@saber.udayton.edu.

10.1021/ie990107z CCC: $18.00
Published on Web 07/08/1999

Table 1. Properties of Fuels Studied

fuel no. and designation	sulfur (ppm)	aromatics (vol %)	QCM deposition (μg/cm^2)	relative oxidation rate
Exxsol D110, solvent	3	<1	0.5	fast
F-2747, Jet A-1	37	19	0.9	moderate
F-2827, Jet A	763	19	3.0	slow

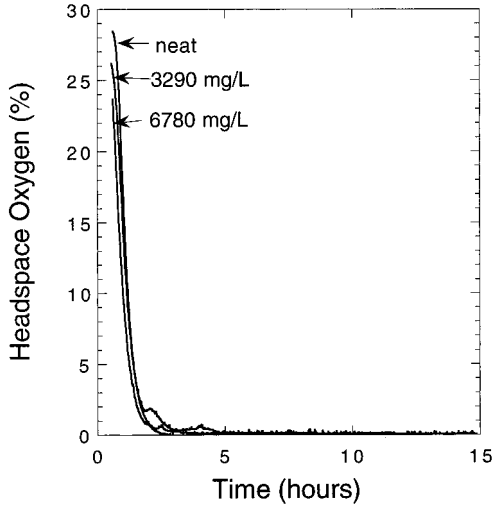

Figure 1. Headspace oxygen vs time for the oxidation of Exxsol D110 neat and with added hexyl sulfide.

Results and Discussion

Hydroperoxide Decomposer Experimental Study. The ability of hydroperoxide decomposing species to slow or delay oxidation of petroleum liquids has been explored in some detail previously. In particular, Denison and Condit[7,8] showed that alkyl sulfides and selenides provide substantial oxidation delays in the autoxidation of desulfurized lubricating oils. They showed that alkyl sulfides react with alkyl hydroperoxides via a nonradical pathway to produce a sulfoxide and an alcohol,

$$RSR + ROOH \rightarrow R_2S{=}O + ROH$$

The removal of these hydroperoxides via this nonradical process results in significant slowing of the hydrocarbon oxidation rate due to the prevention of their thermal decomposition into radicals, which may accelerate autoxidation.

To confirm these results we tested Exxsol D110, a dearomatized, low-sulfur hydrocarbon solvent, with various levels of added hexyl sulfide. The results for the neat solvent and two concentrations of hexyl sulfide are shown in Figure 1. The figure shows that even up to relatively high levels of added hexyl sulfide, no delay or slowing of oxidation was observed, in marked contrast to the results of Denison and Condit.

To further explore the cause for this discrepancy, we added hexyl sulfide to a hydrotreated jet fuel, F-2747. The results are shown in Figure 2. The figure shows that, in contrast to Exxsol D110, this Jet A-1 fuel displays substantial delays in oxidation upon addition of hexyl sulfide. What is it that is causing this difference in behavior between these two systems upon addition of hexyl sulfide? One clue is apparent when looking at the oxidation curves for the two neat fuels, shown in Figure 2. Under these conditions, fuel F-2747 oxidizes much more slowly, consuming the available oxygen in 4.5 h, than does Exxsol D110, which consumes the available oxygen in 2.5 h. It is apparent that there are naturally occurring or added species in the jet fuel that slow the oxidation relative to Exxsol D110. Can the presence of these species result in the substantial oxidation delays observed in the presence of hexyl sulfide? What are these species?

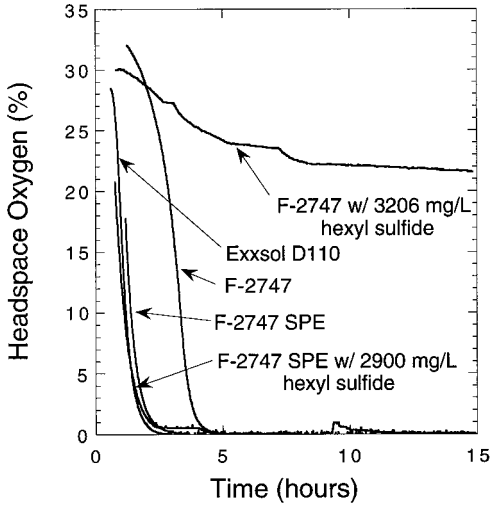

Figure 2. Headspace oxygen vs time for Exxsol D110, fuel F-2747, F-2747 with added hexyl sulfide, F-2747 SPE, and F-2747 SPE with added hexyl sulfide.

The JP-8 specification (MIL-T-83133D) requires an antioxidant to be added to hydrotreated fuel and offers the supplier the option of adding antioxidants to non-hydrotreated fuel. The Jet A-1 specification (D1655) does not require antioxidants but offers the refinery the option of adding one of four antioxidants. Thus, this Jet A-1 fuel may contain up to 24 mg/L of either phenylene diamine or hindered phenol antioxidants. In addition, naturally occurring antioxidants, such as phenols, sulfur, and nitrogen compounds, may be present in the fuel. We posit that the slower oxidation of the jet fuel versus Exxsol D110 observed in Figure 2 is due to the presence of antioxidants such as phenols. Two methods to test this supposition are (1) remove the antioxidants from F-2747 to observe if added hexyl sulfide still results in oxidation delays, and (2) add a phenolic species along with hexyl sulfide to a low-phenol solvent such as Exxsol D110.

To test the first method, we used silica gel solid-phase extraction (SPE) of the fuel to remove phenolic species. Previous work has shown that SPE is quite successful at removing phenolic species from hydrocarbon liquids.[9,10] Fuel F-2747 (60 mL) that was passed through a 1 g silica gel SPE cartridge was stressed for 15 h at 140 °C. The oxidation curve is shown in Figure 2. The resulting fuel oxidizes quite rapidly, yielding an oxidation curve that is identical to that of Exxsol D110. This further supports the supposition that phenolic species in fuel F-2747 are responsible for its slower oxidation than Exxsol D110. Also plotted in the figure is the oxidation curve for fuel F-2747 that was SPE treated and subsequently additized with 2900 mg/L hexyl sulfide. The curve shows that removing the phenolic species in F-2747 via SPE results in a fuel that no longer responds to the addition of hexyl sulfide. This evidence supports our supposition that the oxidation slowing observed upon addition of hexyl sulfide to jet fuel is due the concurrent presence of phenolic species.

To test the second method, we added 2,6-di-*tert*-butyl-4-methylphenol (also known as BHT or butylated hy-

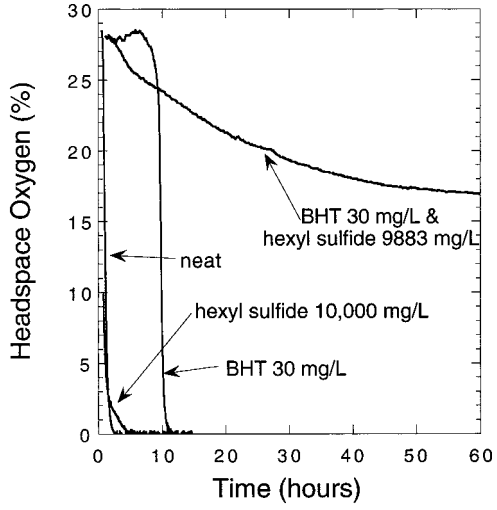

Figure 3. Headspace oxygen vs time for Exxsol D110 neat, with added BHT, with added hexyl sulfide, and with added BHT and hexyl sulfide.

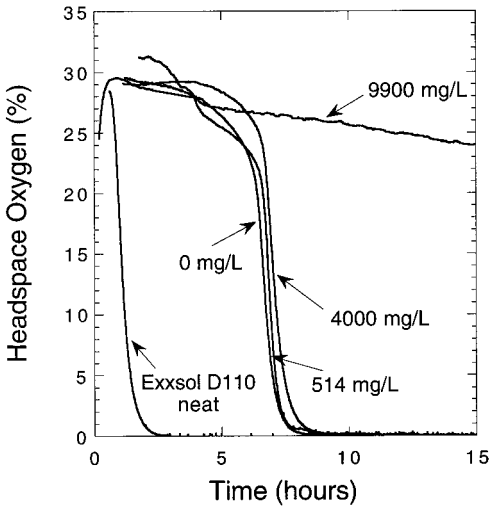

Figure 4. Headspace oxygen vs time for Exxsol D110 neat and with added BHT (25−30 mg/L) at various levels of added hexyl sulfide.

droxytoluene) with and without hexyl sulfide to Exxsol D110. The results are plotted in Figure 3. This figure shows that when 30 mg/L of BHT is added to Exxsol D110, there is a resulting 10 h delay before oxidation occurs. The initial slow oxidation during the first 10 h is due to the interception of alkylperoxy radicals by BHT. Previous work in our laboratory has shown that the subsequent rapid oxidation, which occurs here at 10 h, is due to the consumption of BHT below some critical concentration.[4] The most striking observation from Figure 3 is the extremely slow oxidation which occurs when both BHT and hexyl sulfide are present. This run was extended beyond the normal 15 h period. The plot shows that even after 60 h over 60% of the oxygen still remains.

This extremely slow oxidation observed when both BHT and hexyl sulfide are present is indicative of a synergistic slowing of oxidation since this oxidation delay is significantly greater than the sum of the individual additives. Synergism between various classes of antioxidants has been observed previously.[11] Pseudo-detailed chemical kinetic modeling performed in our laboratory has predicted the observed behavior between alkylperoxy radical-inhibiting antioxidants and hydroperoxide decomposing species.[12] We can now see that the slow oxidation with added alkyl sulfides observed by Condit and Denison in lubricating oils, but not observed here in neat Exxsol D110, is due to the presence of naturally occurring antioxidants in these lubricating oils, presumably alkylperoxy radical inhibitors such as phenols. We have shown that under our conditions alkyl sulfides alone do not slow/delay oxidation, but in the presence of inhibiting phenols, a substantial synergistic slowing of oxidation is observed.

To study the synergism between a hydroperoxide decomposer and a phenol in further detail, we thermally stressed Exxsol D110 at various concentrations of added BHT and hexyl sulfide. Figure 4 shows oxidation plots for Exxsol D110 with 25−30 mg/L BHT in which the hexyl sulfide concentration was varied over the range 0−9900 mg/L. Figure 5 shows oxidation plots for Exxsol D110 with 10,000 mg/L hexyl sulfide in which the BHT concentration was varied over the range 10−30 mg/L. Figure 4 shows that at hexyl sulfide concentrations at or below 4000 mg/L no synergistic slowing of the oxidation is observed. However, when the hexyl sulfide concentration is increased to 9900 mg/L, a substantial synergism is apparent. Figure 5 shows that at BHT concentrations at or below 17.5 mg/L no synergism is seen; however, at BHT concentrations of 20 mg/L and higher, this synergism becomes obvious. These figures show a rather sudden change to synergistic oxidation slowing as the BHT or hexyl sulfide concentration is increased by relatively small increments.

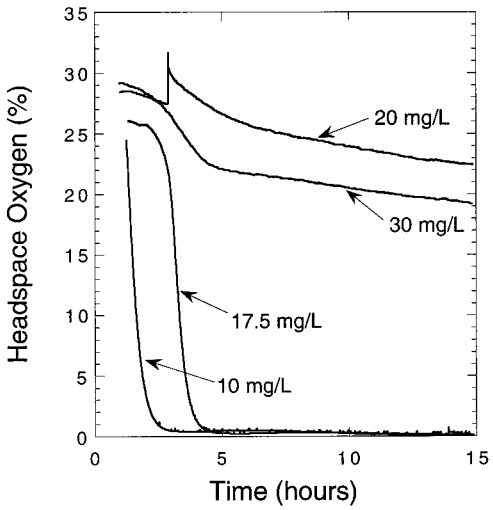

Figure 5. Headspace oxygen vs time for Exxsol D110 with 10,000 mg/L hexyl sulfide at various levels of added BHT.

Table 2. Peroxide Concentrations Measured in Post-stressed Fuel Samples

post-test fuel sample	peroxide concn (mmoles/L)
Exxsol D110	0.49 ± 0.10
Exxsol D110 w/25−30 mg/L BHT and 1400−3300 mg/L hexyl sulfide	0.20 ± 0.10
Exxsol D110 w/10,000 mg/L hexyl sulfide and 10−30 mg/L BHT	0.06 ± 0.10
F-2747	1.03 ± 0.10
F-2747 w/3206 mg/L hexyl sulfide	0.20 ± 0.10

Table 2 summarizes post-test hydroperoxide measurements performed in these fuels with various levels of BHT and hexyl sulfide. The table shows that the presence of hexyl sulfide, in both Exxsol D110 and fuel F-2747, does reduce the measured hydroperoxide concentration, confirming its effect as a hydroperoxide

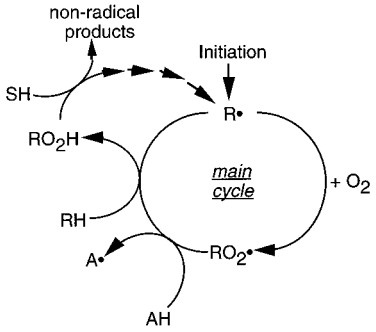

Figure 6. Autoxidation cycle showing interception of alkylperoxy radicals by peroxy radical-inhibiting antioxidants (AH) and interception of alkyl hydroperoxides by hydroperoxide decomposers (SH).

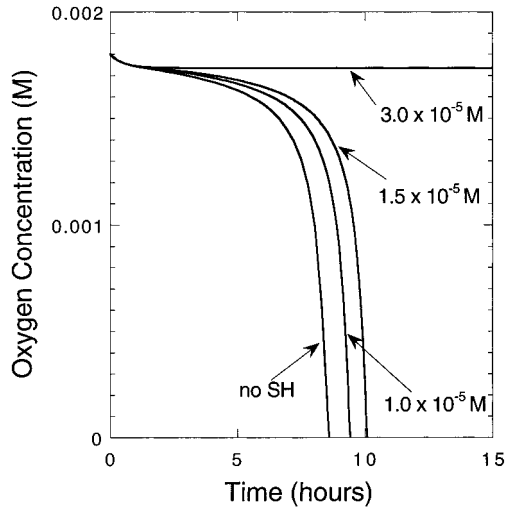

Figure 7. Calculated headspace oxygen concentration vs time for AH at 1.0×10^{-4} M at various SH levels.

decomposer. In Exxsol D110, higher levels of added hexyl sulfide result in somewhat lower hydroperoxide concentrations. These results support the conclusion that the addition of hexyl sulfide does result in the decomposition of alkyl hydroperoxides under these conditions.

Chemical Kinetic Modeling. To better understand the chemistry which occurs in this system, particularly the concentration dependence and synergism observed experimentally, we employed a pseudo-detailed chemical kinetic model of fuel autoxidation that was developed previously.[12] The complete mechanism with rate coefficients is shown in this previous publication. Figure 6 is a simplified schematic diagram of the main reactions in the autoxidation cycle used in the mechanism, including the interception of alkylperoxy radicals (RO_2•) by peroxy radical inhibiting antioxidants (AH, for which we employ BHT) and the interception of alkyl hydroperoxides by hydroperoxide decomposers (SH, for which we employ hexyl sulfide). In previous work, we demonstrated that the mechanism predicts a strong synergism between these two species in slowing/delaying oxidation at 185 °C.[12] For the present study, we have attempted to model the oxidation behavior at 140 °C by varying the concentrations of AH and SH independently in the presence of both species, as was shown experimentally in Figures 4 and 5.

The calculated oxidation plots are shown in Figures 7 and 8. In Figure 7, the AH concentration was held at 1.0×10^{-4} M while the SH concentration was varied

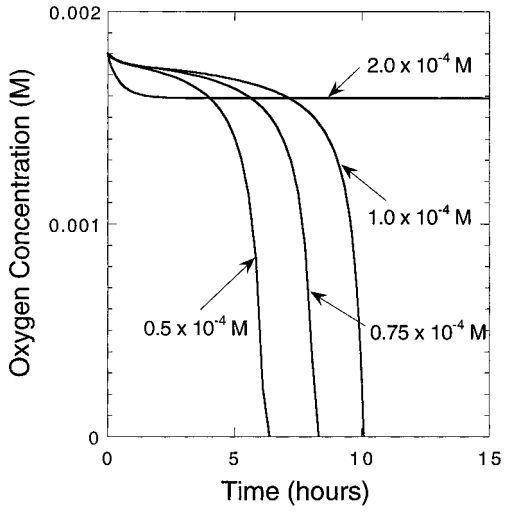

Figure 8. Calculated headspace oxygen concentration vs time for SH at 1.5×10^{-5} M at various AH levels.

over the range $1.0-3.0 \times 10^{-5}$ M. This level of BHT corresponds to 21.9 mg/L. The SH concentration used in the model does not directly correspond to a hexyl sulfide concentration as the peroxide decomposition rate parameters used in the model are not based on rate constant measurements, but rather, a "fast" rate constant was used to maximize the importance of this process.[12] This simplification of the ROOH + SH reaction is necessary as rate parameters are not known at 140 °C, and the identity of the many possible hydroperoxide compounds that may be present are not known. Thus, the SH concentrations used in the model appear low compared with the hexyl sulfide concentrations used in the experiments. The figure shows that as SH is added at $(1.0-1.5) \times 10^{-5}$ M only modest additional delays are observed in oxidation above that provided by the peroxy radical inhibitor, AH. However, once the SH concentration reaches 3.0×10^{-5} M, oxidation is nearly completely stopped for the entire 15 h period. This type of behavior is very similar to that observed in the experimental measurements of Figure 4. Note that a direct quantitative comparison between the experimental measurements and the calculated results cannot be performed as the Parr bomb technique is complicated by the presence of headspace oxygen and diffusional effects.[5] In Figure 8, the SH concentration was held at 1.5×10^{-5} M while the AH concentration was varied over the range $0.5-2.0 \times 10^{-4}$ M. The figure shows that while increasing AH over the range $0.5-1.0 \times 10^{-4}$ M does delay oxidation, a more substantial delay is observed when the AH concentration reaches 2.0×10^{-4} M. This behavior is quite similar to that observed experimentally in Figure 5.

Let us now explore the autoxidation cycle, shown in Figure 6, in more detail to attempt to understand the behavior that is observed experimentally. One interpretation of the data of Figure 1 is that the main autoxidation cycle, where fuel molecules (RH) are converted to hydroperoxides via peroxy radicals (RO_2), is fast relative to unimolecular hydroperoxide decomposition,

$$RO_2H \rightarrow RO + OH$$

where hydroperoxides decompose to yield radicals which may accelerate the overall oxidation process. Thus, addition of a hydroperoxide decomposer (SH) will have

little effect on slowing the overall oxidation rate, because unimolecular hydroperoxide decomposition is already slow relative to the overall oxidation process. This reasoning can also explain the observation that the presence of a peroxy radical inhibitor (AH) then allows oxidation delays to be observed upon addition of SH, as observed in Figure 3. This occurs because AH can slow the main cycle by intercepting peroxy radicals, thereby increasing the relative importance of hydroperoxide thermolysis to yield radicals which accelerate the overall oxidation. Thus, unimolecular hydroperoxide decomposition becomes more important relative to the overall oxidation rate, and slowing it by addition of hydroperoxide decomposers now results in a slowing of the overall oxidation rate. This reasoning then successfully explains the observation that the hydroperoxide decomposer is able to delay oxidation only in the presence of the peroxy radical inhibitor. This peroxy radical inhibitor can be added to the system, as in the case of BHT, or be naturally occurring, as in the case of a distillate fuel.

The modeling results show that, when both species are present, the presence of the peroxide decomposer lowers the radical production rate enough to significantly slow the consumption of the peroxy radical-inhibiting antioxidant. Thus, AH survives longer, and the change to faster oxygen consumption occurs later. Also, the presence of the peroxy radical inhibitor slows the main chain, which greatly slows the production of hydroperoxides. As the production of hydroperoxide is slowed, the consumption of hydroperoxide decomposer is reduced. Thus, the peroxy radical inhibitor and the hydroperoxide decomposer act together to prevent/delay the consumption of the other. In this way, consumption of both species is greatly slowed, and their combined effect in slowing oxidation of the fuel continues for extended periods. These mechanistic arguments help explain the synergism observed.

Other explanations for the observed synergism are also possible and cannot be excluded on the basis of the present data or analysis. Synergism can also occur if the peroxy radical inhibitor is able to prevent other radicals, such as peroxy radicals, from attacking the hydroperoxide decomposer. Also, the reaction of alkyl sulfides with peroxides may involve a more complex process than the simple bimolecular reaction considered here. Indeed, other workers have demonstrated that the combination of the reaction rate and order is a strong function of various parameters including solvent acidity and the structure of the hydroperoxide.[13,14]

Practical Implications. Let us now focus on the practical implications of using alkyl sulfide hydroperoxide decomposing species in jet fuels and other distillate fuels. We have shown that the addition of such species along with a peroxy radical inhibitor, such as BHT, can greatly slow or delay the autoxidation chain under the conditions studied. This significantly slowed oxidation can benefit fuel storage and handling in many ways. This combination of additives could provide reduced oxygen consumption and lower levels of hydroperoxides formed during fuel storage. Hydroperoxides formed in storage have been implicated in the degradation of elastomers used in fuel tank sealants and gaskets. Hydroperoxides formed during fuel recirculation in military aircraft contribute to a faster oxidation rate and resulting increased deposition on fuel system surfaces. We have not shown the potential reduction in deposition which can be observed upon delaying or slowing oxidation, as the fuels studied here (Exxsol D110 and F-2747) produce very low deposition levels.

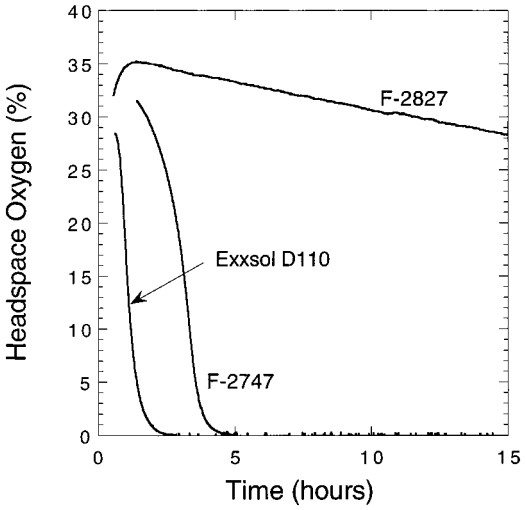

Figure 9. Headspace oxygen concentration vs time for three fuels with varying oxidation characteristics.

These benefits do not come without potential disadvantages. Hexyl sulfide levels of up to 10 g/L were required in many of the present experiments. This corresponds to the addition of ca. 0.2% sulfur to a fuel. The JP-8 specification (MIL-T-83133D) limits the total sulfur level to a maximum of 0.3%. Thus, the addition of this level of hexyl sulfide may create an off-specification fuel. The sulfur content of fuel is limited for a variety of reasons. The combustion emissions of oxidized sulfur compounds is undesirable for environmental reasons. The sulfur content is controlled to limit potential corrosion problems in the engine. Sulfur compounds are also known for promoting deposition in fuel systems. In addition to the desire to limit sulfur compounds in jet fuel, the issue of cost is another downside for the use of hexyl sulfide. The high concentrations needed would result in the additive combination being prohibitively expensive. These disadvantages indicate that alternative species will need to be found to allow the practical use of hydroperoxide decomposing species in jet fuel. Ideally, these species would contain no sulfur and would be effective at relatively low concentrations (<100 mg/L).

Interpretation of the Oxidation Characteristics of Fuels. We will now use the results obtained in this work to explore the various oxidation characteristics of fuel. The oxidation characteristics of fuels are primarily determined by the identity and concentration of various heteroatomic species that can occur naturally or be added during or after refinery processing. We have shown that these species cause a fuel to display characteristic oxidation behavior that reflects the presence of the type of species present. In Figure 9, the headspace oxygen curves for the oxidation of three fuels at 140 °C are plotted. These fuels display very different oxidation characteristics: Exxsol D110 consumes oxygen very rapidly, F-2747 consumes oxygen at a more moderate rate, and F-2827 consumes oxygen extremely slowly. We would like to use our understanding of the effects of peroxy radical inhibitors and peroxide decomposers to interpret the oxidation characteristics of these fuels. Exxsol D110 is a low-sulfur solvent that also contains very few phenolic compounds. Thus, it contains negligible levels of both peroxide-decomposing species and

peroxy radical-inhibiting species. Due to the lack of these species, it oxidizes quite rapidly. Fuel F-2747 exhibits delayed oxidation relative to Exxsol D110. F-2747 produces measurable amounts of peroxides upon oxidation, as shown in Table 2. Its oxidation characteristics and production of peroxides are indicative of a fuel whose oxidation is primarily controlled by peroxy radical inhibitors. The observation that SPE treatment of this fuel yields a fuel with the same oxidation characteristics as those of Exxsol D110 (see Figure 2) is additional evidence of the importance of peroxy radical inhibitors, as we know that SPE treatment provides substantial removal of phenolic species. Fuel F-2827 oxidizes much more slowly than the other two fuels. Our results indicate that such slow oxidation is probably due to the presence of both naturally occurring peroxy radical inhibitors and peroxide decomposers. Indeed, this fuel produces negligible quantities of peroxides upon oxidation.[15] The low level of peroxides produced indicates the presence of a peroxide-decomposing species, whereas our results show that the additional presence of a peroxy radical inhibiting species is required to obtain such a slow oxidation. We can see that the behavior of peroxy radical inhibitors and peroxide decomposers reported in this work has allowed us to better understand the oxidation characteristics of fuels.

Table 1 also includes the measured QCM deposition for each of these fuels. These QCM deposition measurements were performed at 140 °C for 15 h. The table shows that the tendency of a fuel to deposit is inversely related to its oxidation rate.[16] This is due to the fact that naturally occurring heteroatomic species act to slow oxidation while at the same time increase deposition. Our goal in designing additives and additive combinations is to slow oxidation without increasing the formation of bulk and surface deposits.

Future Work. In addition to the need to search for alternative hydroperoxide decomposer additives, the behavior of this class of additives needs to be studied over a range of temperatures. This is especially true for use in jet fuel, as it is subjected to a wide range of temperatures in its transport through aircraft/engine fuel systems. The temperature dependence of both the decomposer/hydroperoxide reaction, as well as the unimolecular hydroperoxide decomposition reaction, will result in this type of additive being effective only over a somewhat limited temperature range. At relatively low temperatures, unimolecular hydroperoxide decomposition (which generally has an activation energy of ca. 40 kcal/mol) will become slow enough to no longer contribute a significant number of radicals to effect the overall oxidation rate. Thus at low temperatures, hydroperoxide decomposing additives will not effect the oxidation rate. At relatively high temperatures, unimolecular hydroperoxide decomposition will become extremely fast, and peroxide-decomposing additives will be unable to intercept these species before they decompose into radicals. Thus at high temperatures, these additives will also be ineffective. It is important to study the temperature dependence to determine the effective temperature range.

Another interesting aspect of temperature is that as temperatures increase above 140 °C, the unimolecular peroxide decomposition will become increasingly important in determining the overall oxidation rate due to its large activation energy (ca. 40 kcal/mol) relative to the activation energy of the autoxidation propagation reaction (ca. 10−14 kcal/mol). Thus, as the temperature is raised above 140 °C, it is likely that the presence of an alkyl peroxy radical inhibitor may no longer be required for peroxide-decomposing additives to be effective. Preliminary experiments at higher temperatures (150−180 °C) support this hypothesis. In addition, the activation energy for the reaction between peroxides and alkyl sulfides is thought to be in the range 11−17 kcal/mol,[13,14] further increasing the effectiveness of these additives at temperatures above 140 °C. Future modeling studies should determine and employ more realistic rate parameters for the peroxide decomposer reaction. Future studies should also examine the effects of acid and oxygen catalyses and the nature of the solvent on peroxide-decomposer effectiveness.

Conclusions

We have explored the use of hydroperoxide decomposing species for inhibiting oxidation in jet fuel. We find that hydroperoxide decomposing species, such as alkyl sulfides, do not slow or delay oxidation in hydrocarbon solvents at 140 °C. However, when phenolic species are also present, such as those naturally occurring in fuel or by addition of hindered phenols, substantial delays in oxidation are observed. We used a pseudo-detailed chemical kinetic mechanism to provide insight into the oxidation process. The combination of hydroperoxide decomposer and hindered phenol can substantially inhibit oxidation of fuel under the conditions studied here.

Acknowledgment

This work was supported by the Propulsion Sciences and Advanced Concepts Division, Propulsion Directorate, Air Force Research Laboratory, U.S. Air Force, Wright-Patterson AFB, OH, under Contract No. F33615-97-C-2719 with Mr. Charles Frayne as technical monitor.

Literature Cited

(1) Heneghan, S. P.; Zabarnick, S.; Ballal, D. R.; Harrison, W. E. JP-8+100: Development of a Thermally Stable Jet Fuel. *J. Energy Res. Technol.* **1996**, *118*, 170.

(2) Zabarnick, S.; Grinstead, R. R. Studies of Jet Fuel Additives using the Quartz Crystal Microbalance and Pressure Monitoring at 140 °C. *Ind. Eng. Chem. Res.* **1994**, *33*, 2771.

(3) Ingold, K. U. Inhibition of the Autoxidation of Organic Substances in the Liquid Phase. *Chem. Rev.* **1961**, *61*, 563.

(4) Zabarnick, S.; Whitacre, S. D. Aspects of Jet Fuel Oxidation. *J. Eng. Gas Turbines Power* **1998**, *120*, 519.

(5) Zabarnick, S. Studies of Jet Fuel Thermal Stability and Oxidation Using a Quartz Crystal Microbalance and Pressure Measurements. *Ind. Eng. Chem. Res.* **1994**, *33*, 1348.

(6) Kauffman, R. E. Development of a Rapid, Portable Hydroperoxide Test for Jet Fuels. *Prepr.—Am. Chem. Soc., Div. Pet. Chem.* **1994**, *39*, 42.

(7) Denison, G. H.; Condit, P. C. Oxidation of Lubricating Oils, Mechanism of Sulfur Inhibition. *Ind. Eng. Chem.* **1945**, *37*, 1102.

(8) Denison, G. H.; Condit, P. C. Oxidation of Lubricating Oils, Dialkyl Selenides as Inhibitors. *Ind. Eng. Chem.* **1949**, *41*, 944.

(9) Schulz, W. D. Analysis of Jet Fuel Additives. *Prepr.—Am. Chem. Soc., Div. Petr. Chem.* **1992**, *37*, 477.

(10) Mick, M. S. Fundamental Studies of the Oxidation and Deposition of Jet Fuels. M.S. Thesis, University of Dayton, Dayton, OH, 1998.

(11) Scott, G. Antioxidants. *Chem. Ind.* **1963**, 271.

(12) Zabarnick, S. Pseudo-detailed Chemical Kinetic Modeling of Antioxidant Chemistry for Jet Fuel Applications. *Energy Fuels* **1998**, *12*, 547.

(13) Hargrave, K. R. Oxidation of Organic Sulphides. VI. Interaction of Hydroperoxides with Unsaturated Sulphides. *Proc. R. Soc. (London)* **1956**, *A235*, 55.

(14) Bateman, L.; Hargrave, K. R. Oxidation of Organic Sulphides. I. Interaction of Cyclohexyl Methyl Sulphide with Hydroperoxides in Alcohols. *Proc. R. Soc. (London)* **1954**, *A224*, 389.

(15) Jones, E. G.; Balster, L. M.; Balster, W. J. Thermal Stability of Jet-A Fuel Blends. *Energy Fuels* **1996**, *10*, 509.

(16) Heneghan, S. P.; Zabarnick, S. Oxidation of Jet Fuels and the Formation of Deposits. *Fuel* **1994**, *73*, 35.

Received for review February 12, 1999
Revised manuscript received April 30, 1999
Accepted May 20, 1999

IE990107Z

I. Model Studies of Silylation Agents as Thermal-Oxidative Jet Fuel Additives

Model Studies of Silylation Agents as Thermal-Oxidative Jet Fuel Additives

S. Zabarnick,* M. S. Mick, R. C. Striebich, and R. R. Grinstead

University of Dayton Research Institute, Aerospace Mechanics Division, 300 College Park, KL-463, Dayton, Ohio 45469-0140

Received June 29, 1998. Revised Manuscript Received September 15, 1998

In this study we explore the use of silylation agents as jet fuel additives for reducing oxidative deposition. Silylation agents have the ability to react with the heteroatomic species, such as phenols, which have been implicated in deposit-producing mechanisms. Thus, they have the potential to chemically transform these species into relatively innocuous silylated products. In this work we study the effect that silylation agents have on jet fuel oxidation and deposition. We show that these additives result in an increased oxidation rate and substantially reduced deposition. The increased oxidation rate is due to the removal of these heteroatomic species which can act as antioxidants by intercepting peroxy radicals. The results show that silylation agents may be useful as jet fuel additives for preventing oxidative deposition in advanced aircraft fuel systems, including endothermic fuel systems. Silylation agents have also been proven to be useful in identifying fuel components, particularly those detrimental to fuel thermal stability.

Introduction

Derivatization techniques are well-known methods to alter species structures to make them more amenable to chemical analysis. Silylation is one type of derivatization process, in which species which contain reactive hydrogen atoms are reacted with an appropriate agent, resulting in the conversion of these reactive hydrogen sites to relatively unreactive trimethylsilyl sites.[1] Silylation is widely practiced in chromatographic analysis to improve analytical quantitation and transport, increase detectability and volatility, and decrease surface interactions. In general, silylating agents are able to react with the active hydrogens in the following species: acids, alcohols, thiols, amines, amides, and enolizable ketones and aldehydes. A variety of agents are known, which vary in their reactivity, selectivity, side reactions, and character of reaction byproducts.

In advanced military aircraft, jet fuel is used as a coolant in addition to its use in propulsion. The resulting hot fuel reacts with dissolved oxygen, forming oxidized products. These oxidized products include gums and solid deposits which can coat fuel system surfaces, resulting in filter plugging, fouling of close tolerance valves, valve hysteresis, and other problems. Various chemical additives and additive combinations have been utilized to inhibit oxidation and/or reduce deposition. For example, the U.S. Air Force JP-8+100 additive package contains a dispersant, an antioxidant, and a metal deactivator.[2,3] It is generally agreed that the advanced military aircraft being presently conceived will have significantly higher heat loads that will be transferred to the fuel. These resulting higher fuel temperatures will result in substantially increased oxygen consumption and subsequent increased deposition.

The higher fuel system temperatures of advanced aircraft will result in complete or near complete oxygen consumption. Additives which delay oxidation, such as antioxidants, metal deactivators, and hydroperoxide decomposers, will be unable to provide significant benefits in reducing deposition under time/temperature conditions where dissolved oxygen consumption is certain. While dispersant additives may still be useful under these conditions, it is apparent that alternative additive techniques need to be explored.

In this study we explore the use of silylation agents as jet fuel additives for reducing oxidative deposition. Silylation agents have the ability to react with the heteroatomic species, such as phenols, which have been implicated in deposit-producing mechanisms.[4,5] Thus, they have the potential to chemically transform these species into relatively innocuous silylated products. In this work we study the effect that silylation agents have on jet fuel oxidation and deposition. We show that these additives result in an increased oxidation rate and substantially reduced deposition. The increased oxidation rate is due to the removal of these heteroatomic species, which can act as antioxidants by intercepting peroxy radicals. These results show that silylation agents may be useful as jet fuel additives for preventing oxidative deposition in advanced aircraft fuel systems, including endothermic fuel systems. Silylation agents may also prove to be useful in easing identification of

(1) Pierce, A. E. *Silylation of Organic Compounds*; Pierce Chemical Co.: Rockford, IL, 1968.
(2) Zabarnick, S.; Grinstead, R. R. *Ind. Eng. Chem. Res.* **1994**, *33*, 2771−2777.
(3) Heneghan, S. P.; Zabarnick, S.; Ballal, D. R.; Harrison, W. E. *J. Energy Res. Technol.* **1996**, *118*, 170−179.
(4) Heneghan, S. P.; Zabarnick, S. *Fuel* **1994**, *73*, 35−43.
(5) Kauffman, R. E. *J. Eng. Gas Turbines Power* **1997**, *119*, 322−327.

10.1021/ef980149k CCC: $18.00
Published on Web 11/06/1998

fuel components, particularly those detrimental to fuel thermal stability.

Experimental Section

Fuel oxidation and deposition characteristics were evaluated in the quartz crystal microbalance/Parr bomb system (QCM) which has been described in detail previously.[6,7] All fuel oxidation tests were run at 140 °C and 1 atm of air initial pressure. The 100 mL stainless steel batch reactor is heated with a clamp-on band heater, and its temperature is controlled by a PID controller through a thermocouple immersed in the fuel. The reactor contains an rf feedthrough, through which the connection for the quartz crystal resonator is attached. The crystals are 2.54 cm in diameter and 0.33 mm thick and have a nominal resonant frequency of 5 MHz. The crystals were acquired from Maxtek, Inc., and are available in crystal electrode surfaces of gold, silver, platinum, and aluminum. For the studies reported here, gold crystal electrodes were used. The QCM measures deposition (i.e., an increase in mass) which occurs on overlapping sections of the two-sided electrodes. Thus, the device responds to deposition which occurs on the metal surface and does not respond to deposition on the exposed quartz.

The device is also equipped with a pressure transducer (Sensotec) to measure the absolute headspace pressure and a polarographic oxygen sensor (Ingold) to measure the headspace oxygen concentration. Previous studies have demonstrated the value of determining the oxidation characteristics of fuels and fuels with additives.[2,6] A personal computer is used to acquire data at 1 min intervals during the experimental run. The following data are recorded during a run: temperature, crystal frequency, headspace pressure, headspace oxygen concentration, and crystal damping voltage.

The reactor is charged with 60 mL of fuel, which is sparged with air for 1 h before each test. The reactor is then sealed, and the heater is started. All runs in this study were performed at 140 °C; heat-up time to this temperature is 40 ± 5 min. Most runs are conducted for 15 h, after which the heater is turned off and the reactor allowed to cool. Surface mass measurements can only be determined during the constant temperature (±0.2 °C) portion of an experimental run. The crystal frequency is converted to a surface mass measurement using the process described below.

The theory that relates the measured frequency changes to surface mass has been presented in detail elsewhere.[8] The frequency change of a crystal immersed in a liquid fuel can be due to two effects: the first results from changes in the surface mass density, the second is due to changes in the liquid density and viscosity. At constant temperature and relatively small extents of chemical conversion, the liquid properties remain constant and the frequency change can be related to surface deposition via the equation

$$\rho_s = -(2.21 \times 10^5 \text{ g/(cm}^2 \text{ s)})\frac{\Delta f}{f_0^2} \qquad (1)$$

where f_0 is the unperturbed resonant frequency, Δf is the change in resonant frequency, and ρ_s is the surface mass density (mass/area). The reproducibility of the mass deposition measurements on fuels is limited to ±20% for the QCM technique. The fuels studied and some of their properties are listed in Table 1. The fuels were acquired from the Propulsion Sciences and Advanced Concepts Division, Propulsion Directorate, Air Force Research Laboratory (AFRL), U.S. Air Force, Wright-Patterson AFB, OH, and are referred to by the AFRL-assigned accession number. Silylation agents were acquired from Pierce Chemical.

Table 1. Properties of Fuels Studied

fuel no. (type)	total sulfur (ppm)	copper (ppb)
F-2827 (Jet A)	763	<5
F-3119 (Jet A)	1000	7
F-2980 (Jet A)	614	<5
F-3084 (Jet A)	527	35
Exxsol D110 (aliphatic hydrocarbon solvent)	<3	<5

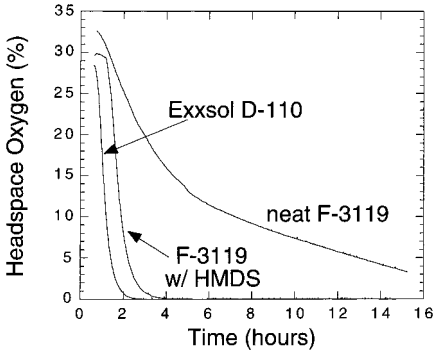

Figure 1. Plots of headspace oxygen for fuel F-3119 with and without HMDS, and Exxsol D-110.

Results and Discussion

Jet fuel is a complex mixture which is primarily composed of branched and straight-chain alkanes, cycloalkanes, and alkyl-substituted aromatics. In addition, various heteroatomic species may be present at relatively small concentrations, including but not limited to phenols, peroxides, alcohols, organic acids, sulfides, thiols, thiophenes, and amines. In the absence of these heteroatomic species, this hydrocarbon mixture oxidizes readily at elevated temperature via the classic hydrocarbon autoxidation mechanism. For example, a pure alkane, such as dodecane, or a highly refined petroleum fraction, such as Exxsol D-110 (as shown in Figure 1), will completely consume all available oxygen in the QCM system on the order of 1−2 h at 140 °C. But real jet fuels oxidize much more slowly and can require from 5 to more than 60 h to consume the available oxygen. These real fuels oxidize more slowly than pure hydrocarbons due to the presence of these heteroatomic species. These species slow oxidation by intercepting alkyl peroxy radicals and/or by decomposing alkyl hydroperoxides to nonradical products.[4,9] Thus, the removal of such species should result in a significant increase in the oxidation rate of the fuel. This effect is illustrated in the hydrotreatment process, which removes heteroatomic species and results in highly oxidizable fuel. In fact, synthetic antioxidants are generally added to hydrotreated fuels to prevent oxidation during storage. The same naturally occurring species which slow oxidation of fuel also play important roles in forming surface and bulk deposits upon fuel oxidation. Thus, a fuel which is treated to remove such heteroatomic species will oxidize rapidly but display reduced deposit formation.

Treating jet fuel with silylating agents results in the reaction of species with active hydrogens to form tri-

(6) Zabarnick, S.; Whitacre, S. D. *J. Eng. Gas Turbines Power* **1998**, *120*, 519−525.
(7) Zabarnick, S. *Ind. Eng. Chem. Res.* **1994**, *33*, 1348−1354.
(8) Martin, S. J.; Granstaff, V. E.; Frye, G. C. *Anal. Chem.* **1991**, *63*, 2272−2281.
(9) Zabarnick, S. *Energy Fuels* **1998**, *12*, 547−553.

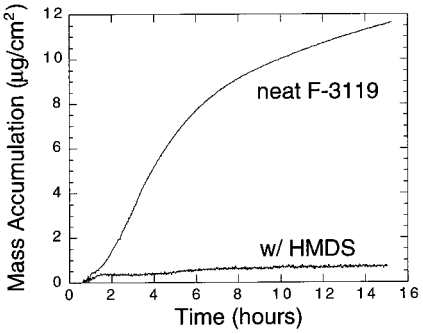

Figure 2. Plots of mass accumulation for fuel F-3119 with and without HMDS.

methylsilyl derivatives. For the case of an alkyl phenol, the following reaction occurs:

We convert a phenol with a reactive hydrogen to its trimethylsilyl derivative, which is much less reactive and does not contain an active hydrogen. The resulting compound is not reactive toward alkylperoxy radicals (relative to the original phenol) and, thus, does not interfere with the fuel autoxidation chain. Thus, the oxidation rate of the fuel will increase. Analogous reactions are also possible for other compounds with active hydrogens.

To explore the effect that silylation has on jet fuel, we added 1 mL of the silylation agent hexamethyldisilazane (HMDS) to 60 mL of a Jet A fuel, F-3119, and stressed this additized fuel in the QCM at 140 °C for 15 h. The resulting oxygen sensor and QCM deposition plots for the neat and additized fuel are shown in Figures 1 and 2. The headspace oxygen plot shows that HMDS causes a substantial increase in the oxidation rate of the fuel. The resulting oxygen decay is nearly as fast as a pure hydrocarbon solvent (an oxidation plot for Exxsol D-110 is shown for comparison in Figure 1). The deposition plot shows that HMDS causes a >90% decrease in deposition during the run. It is apparent that treatment of this fuel with HMDS results in significant removal of species which delay oxidation. In addition, removal of these species results in reduced deposition.

It is important to note that besides reacting with naturally occurring species in the fuel, the silylation agent, if present in excess, may also react with various autoxidation products and intermediates during the oxidation process. For example, hydroperoxides are common autoxidation products which can also behave as intermediates at higher temperatures. However, silylation of hydroperoxides during oxidation would likely result in a reduction in the observed oxidation rate, in contrast to the increase in oxidation rate measured here.

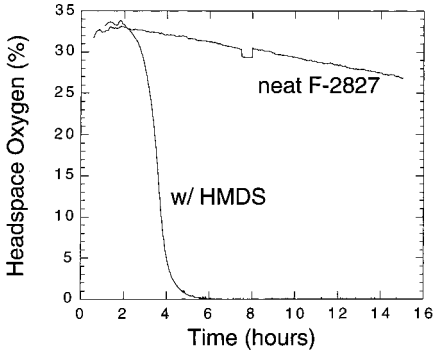

Figure 3. Plots of headspace oxygen for fuel F-2827 with and without HMDS.

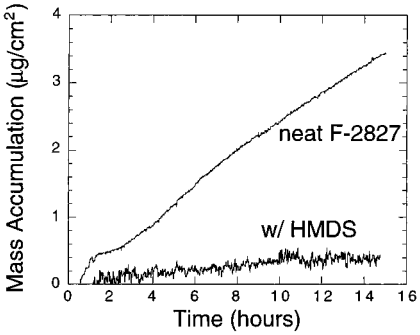

Figure 4. Plots of mass accumulation for fuel F-2827 with and without HMDS.

To demonstrate that the results shown in Figures 1 and 2 are not unique to the fuel used, we performed the identical experiment on a second Jet A fuel sample, F-2827. Oxidation and deposition plots for this fuel are shown in Figures 3 and 4. The plots show that the effects are observed over a range of fuels and are not limited to a single sample of fuel. Figure 3 shows that fuel F-2827 is a particularly slow oxidizing fuel, consuming only 19% of the available oxygen during the 15 h run. Addition of HMDS results in complete oxygen consumption in 5 h. In addition, as shown in Figure 4, deposition is reduced by 90%.

To investigate the chemical changes that occur in the fuel upon silylation treatment, we used gas chromatography with mass spectrometric detection (GC-MS) to monitor the relative amounts of phenols before and after treatment with silylation agent. Polar fuel species can be monitored by GC-MS after preconcentration of the polar fuel species via silica-gel solid-phase extraction with subsequent methanol back extraction.[10] This technique is particularly useful for identification of phenolic species in the fuel. Figure 5 shows GC-MS chromatograms of concentrated polar fractions of a Jet A fuel, F-2980. These are ion chromatograms of 135 amu, which is an ion indicative of the C3-alkylated phenols present. Thus, the chromatograms show the relative amount of C3-alkylated phenols. The top chromatogram is the neat, unstressed fuel; the middle chromatogram is the neat stressed fuel; and the bottom chromatogram is the stressed fuel with added HMDS (1 mL per 60 mL of fuel). The top and middle chromatograms show that the neat fuel contains C3-alkylated phenols and that their relative concentrations

(10) Schulz, W. D. *Prepr.—Am. Chem. Soc., Div. Pet. Chem.* **1992**, *37*, 477.

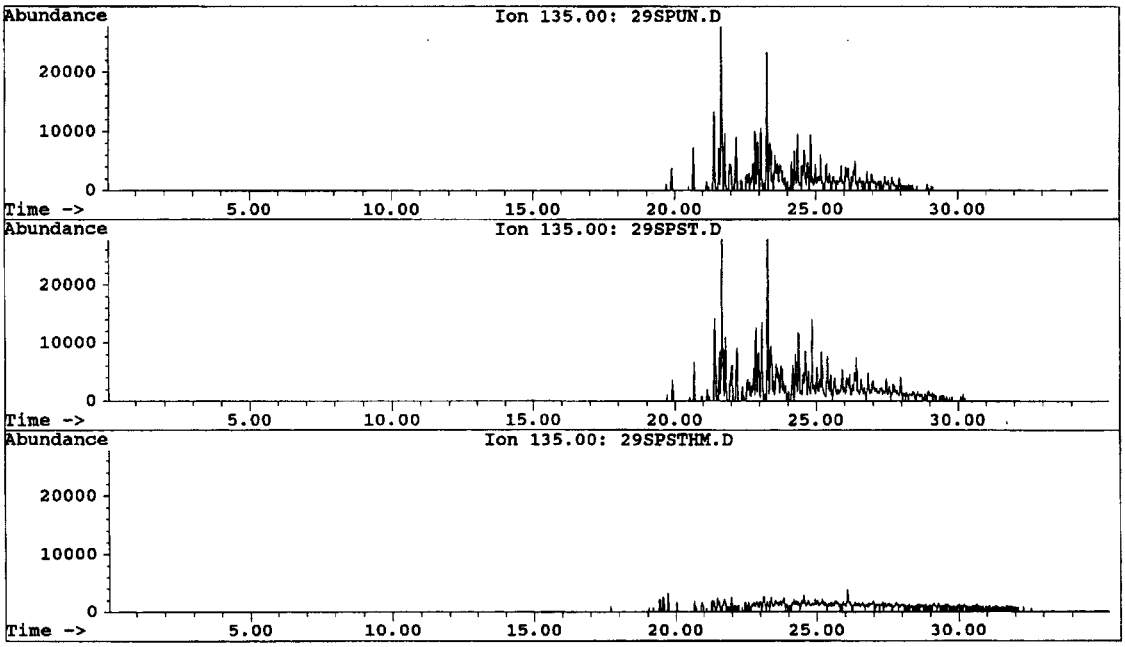

Figure 5. Ion chromatograms (135 amu) of F-2980 unstressed (top), thermally stressed (middle), and thermally stressed with HMDS (bottom).

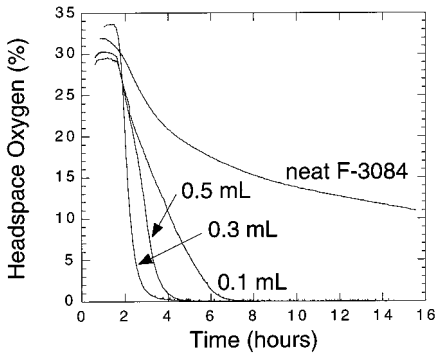

Figure 6. Plots of headspace oxygen for fuel F-3084 with various levels of added HMDS.

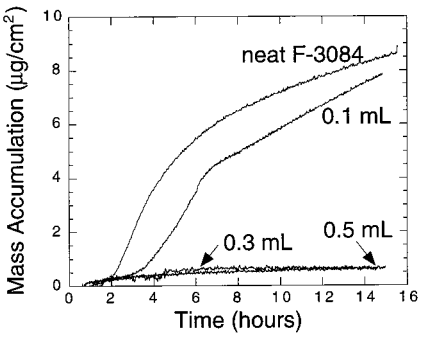

Figure 7. Plots of mass accumulation for fuel F-3084 with various levels of added HMDS.

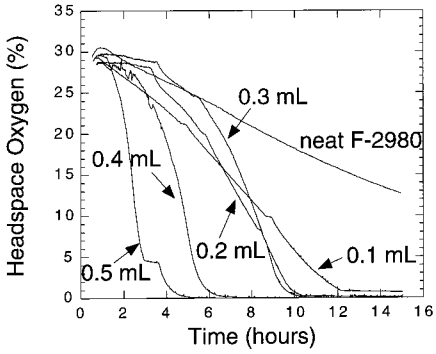

Figure 8. Plots of headspace oxygen for fuel F-2980 with various levels of added HMDS.

remain substantially the same after stressing. The bottom chromatogram shows that thermally stressing the fuel in the presence of HMDS results in substantial removal of these phenols, presumably by conversion to their silylated derivatives. These results are in agreement with the supposition that the silylation agent removes phenols, resulting in increasing oxidation rates.

The HMDS concentration employed in the above runs, 1.67 vol %, is quite high for use as a jet fuel additive, which are typically added at much lower quantities. Such high concentrations would probably result in such an additive being cost prohibitive for use in jet fuels. To explore the use of these additives at lower concentrations and to study the effect of concentration on the oxidation/deposition behavior, we studied the effect of concentration of HMDS on two jet fuels. The results are shown in Figures 6−9. HMDS was varied over the range 0.1−0.5 mL per 60 mL of fuel (0.167−0.833 vol %). Figure 6 shows that for fuel F-3084, 0.1 mL of added HMDS increases the oxidation rate significantly. Increasing the added HMDS up to 0.5 mL results in relatively minor increases in the oxidation rate above this. Figure 7 shows the resulting deposition plots for fuel F-3084. The addition of 0.1 mL of HMDS provides a relatively short delay in deposition, but at long times, deposition is similar to the unadditized fuel. Increasing the added HMDS to 0.3 or 0.5 mL results in significantly reduced deposition during the entire 15 h run. To explore the fuel dependency of this behavior, we performed a similar set of runs on fuel F-2980, as shown in Figures 8 and 9. The oxidation plots of Figure 8 show that 0.1−0.3 mL of added HMDS yield similar oxidation curves with moderate increases in the oxidation rate above the neat fuel. Adding 0.4 and 0.5 mL of additive results in larger increases in the oxidation rate. The deposition plots for this fuel, shown in Figure 9, display

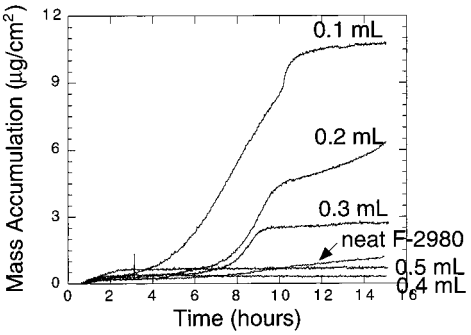

Figure 9. Plots of mass accumulation for fuel F-2980 with various levels of added HMDS.

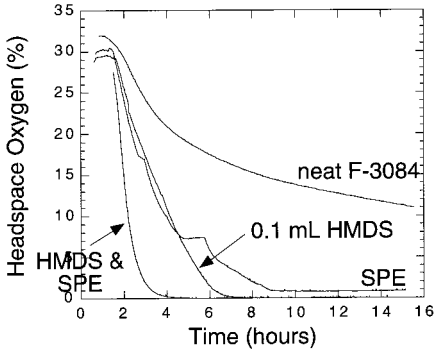

Figure 10. Plots of headspace oxygen for fuel F-3084 neat, with 0.1 mL of HMDS, and with 0.1 mL of HMDS and SPE treatment.

a very interesting behavior. Addition of 0.1−0.3 mL of HMDS actually results in increases in deposition above the neat fuel, while adding 0.4 and 0.5 mL results in deposition slightly below that of the neat fuel.

It is apparent from Figures 6−9 that the concentration dependence of the additive is quite fuel dependent. The additive needs to be added at or above 0.4 mL per 60 mL of fuel (0.833 vol %) to get its full effect in reducing deposition and increasing the oxidation rate under our test conditions. Fuel F-2980 shows increased deposition, above the neat fuel, at lower HMDS levels, while fuel F-3084 does not. Increasing the additive concentration results in increasing the oxidation rate in both fuels. It is apparent that the effect of the additive as a function of concentration is quite complex.

It is interesting to compare these results with another technique which removes heteroatomic species, solid-phase extraction (SPE) with silica gel. Of the heteroatomic species present, silica-gel SPE removes only those that have significant polarity. Previously, we demonstrated that SPE treatment reduces deposition significantly and also results in some increase in the observed oxidation rate.[7] In Figures 10 and 11 are shown plots which compare the effects of SPE and silylation on the oxidation characteristics of a single jet fuel, F-3084. In this study we pass 60 mL of fuel through a 1.0 g silica-gel SPE cartridge. The fuel which exits the cartridge contains much reduced levels of polar heteroatomic species. Figure 10 shows that the SPE treatment results in a substantial increase in the oxidation rate, while Figure 11 shows a substantial decrease in the deposition rate for this fuel. The figures show that SPE treatment yields oxidation rates which are similar to those produced from the addition of 0.1 mL of HMDS to the fuel, but the SPE treatment is

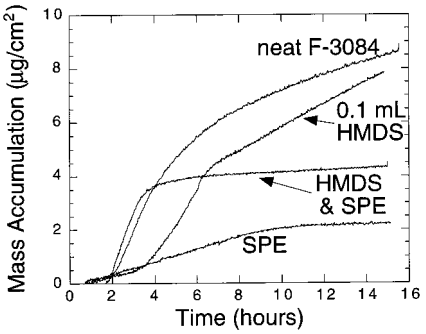

Figure 11. Plots of mass accumulation for fuel F-3084 neat, with 0.1 mL of HMDS, and with 0.1 mL of HMDS and SPE treatment.

substantially better at improving deposition than this level of HMDS. We previously demonstrated, in Figure 7, that 0.3−0.5 mL of added HMDS results in very low deposition levels. Also shown in Figures 10 and 11 are oxidation and deposition plots for fuel which was SPE treated and subsequently additized with 0.1 mL of HMDS. Figure 10 shows that the oxidation rate is increased above each of the individual treatments, but no synergism is apparent. The final deposition for the fuel which was treated with both SPE and HMDS is midway between the HMDS and SPE results (Figure 11). These similar observations of their effect on oxidation and deposition support the conclusion that SPE treatment and silylation both act in a similar manner, removing heteroatomic species which slow oxidation and increase deposition. The lack of synergism in delaying oxidation also supports the conclusion that these techniques act in similar ways, as complementary oxidation-delaying techniques often show synergistic behavior (e.g., peroxide decomposers and peroxy radical inhibitors).[9,11]

A variety of silylation reagents exist which display varying silylation selectivity, reactivity, side reactions, and character of reaction byproducts. In this way it may be possible to tailor the silylation process to meet the needs of the fuel application. For example while HMDS requires elevated temperatures (>50 °C) for reaction, silylation with *N*,*O*-bis(trimethylsilyl)acetamide (BSA) can be performed at room temperature. We, therefore, have the ability to control the time and/or temperature at which the silylation reaction occurs. The ability to remove phenols within aircraft fuel lines during the heating of the fuel in its transport through the fuel system may be quite useful. The presence of phenols can be desirable during fuel storage as they inhibit oxidation, but their presence is undesirable in fuel systems due to their contribution to fouling. By proper choice of a silylation additive, we may be able to design a fuel in which the silylation reaction occurs at a location of choice in the fuel system. Thus, the naturally occurring species which cause fuel to oxidize slowly will be present during fuel storage, where they will prevent detrimental storage oxidation, but these species will be removed by the silylation reactions when the fuel is heated within the aircraft fuel system. Thus, further studies of other silylation agents may be warranted to assess the time/temperature characteristics of their silylation reactions.

(11) Scott, G. *Chem. Ind.* **1963**, 271−281.

It is also interesting to consider that a variety of phenolic species may be present in the fuel. These include naturally occurring nonhindered phenols and also synthetic hindered phenols (such as 2,6 di-*tert*-butyl-4-methylphenol, BHT) that are added to prevent oxidation in storage. It is known that silylation of hindered phenols is more difficult than nonhindered phenols and can require elevated temperatures and extended periods for complete silylation.[12] We find that while nonhindered phenols are readily silylated at room temperature with BSA, hindered phenols such as BHT remain unsilylated. The same result is found at 140 °C with HMDS. This leads to the interesting possibility of being able to selectively remove the naturally occurring nonhindered phenols which promote deposition but leave the synthetic hindered phenols intact. Thus, we may be able to remove the negative impact of the naturally occurring phenols and at the same time keep the positive impact of the hindered phenols in preventing oxidation.

It is important to note that in addition to phenolic species, silylation agents are able to react with other species which contain active hydrogen atoms. These include sulfur, nitrogen, and other oxygen species. These species may also be involved in the autoxidation process whereby they increase deposition and slow oxidation. Thus, their removal by silylation would also show reduced deposition and an increased oxidation rate. In fact, Kauffman[5] has proposed a complex mechanism in which phenols, sulfur compounds, and basic nitrogen compounds act together to produce bulk and surface deposits. The present results indicate that phenolic species are major players in slowing oxidation, but the results do not preclude the participation of these other species.

The promise of silylation additives does not come without potential disadvantages. These include cost, water sensitivity, and problems due to product formation in combustors. Presently, silylation additives are relatively expensive when compared to common jet fuel additives, as they are produced in relatively small quantities for derivatization in chemical analysis. However, large-scale production of silylation agents would significantly reduce the cost. On the other hand, under the relatively high concentrations employed in the present work, silylation would still result in a relatively high additive cost. Silylation reagents react readily with water and humid air forming undesirable silanols. This may also result in the undesirable movement of water into the fuel from fuel tank water bottoms and humid air. Also, it is expected that silylating reagents and silylated products will be rapidly oxidized to silicon dioxide within the combustion chamber. This may have a negative effect on combustor and turbine materials depending on the physical form of the silicon dioxide product.

Another promising use of silylation in jet fuel is for the identification and study of deposit-promoting species. As mentioned previously, silylation agents can react with the heteroatomic species, such as phenols, which have been implicated in bulk and surface deposit formation. Silylation of these species will cause them to be much more amenable to chromatographic analysis and should improve our ability to identify them in the complex fuel matrix. In fact, silylation has recently been used to identify hydroperoxides in jet fuel.[13] Extraction of polar species via SPE or liquid−liquid extraction will allow preconcentration of these species and separation from the complex fuel matrix, and subsequent silylation will improve chromatographic separation and detectability. We believe that the identification and monitoring of deposit-promoting species via silylation will prove to be a very valuable tool in studying the mechanisms of deposit formation in jet fuels.

Conclusions

In this study we have explored the use of silylation agents as jet fuel additives for reducing oxidative deposition. Silylation agents react with the heteroatomic species, such as phenols, which have been implicated in deposit-producing mechanisms. Thus, they have the potential to chemically transform these species into relatively innocuous silylated products. In this work we have studied the effect that silylation agents have on jet fuel oxidation and deposition. We have shown that these additives result in an increased oxidation rate and substantially reduced deposition. These results show that silylation agents may be useful as jet fuel additives for preventing oxidative deposition in advanced aircraft fuels systems, including endothermic fuel systems. Silylation agents are also useful in identifying fuel components, particularly those detrimental to fuel thermal stability.

Acknowledgment. This work was supported by the Propulsion Sciences and Advanced Concepts Division, Propulsion Directorate, Air Force Research Laboratory, U.S. Air Force, Wright-Patterson AFB, OH, under Contract Nos. F33615-92-C-2207 and F33615-97-C-2719 with Mr. Charles Frayne as technical monitor.

EF980149K

(12) Perold, G. W. *J. Chromatogr.* **1984**, *291*, 365−367.
(13) Enqvist, J.; Ranta, E.; Enqvist, M. *Prepr. Pap.—Am. Chem. Soc., Div. Fuel Chem.* **1998**, *43*, 38−43.

J. Quantitation of Metal Deactivator Additive by Derivatization and Gas Chromatography-Mass Spectrometry

Quantitation of a Metal Deactivator Additive by Derivatization and Gas Chromatography–Mass Spectrometry

R.C. Striebich*, B. Grinstead, and **S. Zabarnick**
University of Dayton Research Institute, 300 College Park, Dayton, OH 45469-0140

Abstract

The quantitative analysis of phenolic and amine-containing petroleum additives can be challenging. One such compound—*N,N'*-disalicylidene-1,2-propanediamine, a common metal deactivator additive (MDA)—is thought to inhibit fuel oxidation catalyzed by metals both in the fuel and on surfaces. The ability to measure the concentration of MDA in storage stability tests, thermal-stressing studies, and field samples is important. Quantitating low concentrations of MDA can be difficult because of surface adsorptivity due to the phenol and amine functional groups. This paper describes the shortcomings of direct-injection gas chromatography–mass spectrometry to quantitate MDA as well as a solution to the analytical problem using the common silylation agent BSA to derivatize the MDA. Results demonstrate that the silylation technique is suitable for the determination of MDA concentrations in aviation fuel samples and suggests that the MDA may be readily determined in other petroleum products with a lower detection limit for MDA of 0.5 mg/L. Measurements conducted in heated batch reactors indicate that MDA concentration is reduced as hydrocarbon fuels are stressed. In addition, only free or available MDA is measured by this technique, not MDA that is complexed with metals.

Introduction

Metal deactivator additive (MDA) has been used for over sixty years to prevent metal catalyzed oxidation reactions in petroleum products (1). MDAs are thought to act in two ways: (*a*) by chelating (binding) dissolved metal ions (as shown in Figure 1) and (*b*) by passivating active sites on metal surfaces (2). Presently, the US Air Force allows refineries to add up to 5.7 mg/L of a metal deactivator solution (75% active ingredient) to JP-8 fuel to improve thermal stability (the tendency to resist deposit formation under conditions of elevated temperature). Recently, the US Air Force has been treating JP-8 fuel with an additive package that contains as one of its components *N,N'*-disalicylidene-1,2-propanediamine (in this study referred to as the MDA), at a treatment rate of 2.0 mg MDA per liter of fuel. The additive package JP-8+100 minimizes deposition when the fuel is used as a heat sink by high-performance aircraft. Because of its surface activity and reactivity, MDA may be reduced in concentration as the fuel is handled or thermally "stressed" (oxidized at the elevated temperatures experienced in flight). It is desirable to be able to measure MDA concentrations in JP-8+100 fuels to verify that the addition was made properly. Furthermore, it would be beneficial to be able to monitor MDA concentrations in thermal stressing and storage stability studies in order to understand the role MDA plays in these processes.

The goal of this work was to develop a simple technique to quantitate JP-8 specification levels of MDA (2.0–5.7 mg/L) without prior concentration in both stressed and unstressed fuels. In addition, this analysis needed to be capable of quantitating lower levels of MDA (0.1–2 mg/L) in stressed aviation fuels from thermal stability studies. Finally, an autosampling technique for analysis was desired using the most common type of autosampler for gas chromatography (GC) (i.e., automatic injection into conventional split/splitless injectors).

Several nonchromatographic techniques for measuring MDA are available (3–5). These techniques typically require an

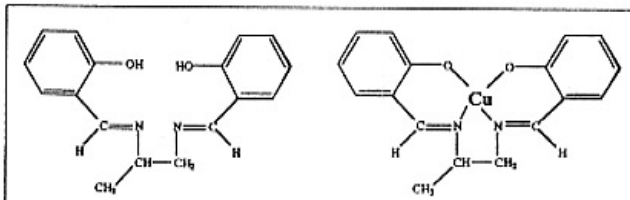

Figure 1. Chelation of copper by MDA.

* Author to whom correspondence should be addressed: email richs@snake.appl.wpafb.af.mil.

extraction of the metal deactivator from the fuel matrix, followed by spectrometric analysis. Many of these techniques do not work properly if the aviation fuel has a high polar content, low level of MDA, or yellow or brown color from thermal oxidation. The tests generally involve a large volume of fuel (10–100 mL) and aqueous extractions. These extractions may not be effective when powerful detergent/dispersant additives such as those used in the JP-8+100 package are present. Consequently, a chromatographic technique with high specificity, good detection limits, and small sample size is desired.

The two main obstacles to overcome in analyzing MDA by GC–MS are the adsorptive nature of the solute molecule and the complex matrix of the fuel. The surface adsorptivity of MDA was investigated by several chromatographic experiments described here as well as by inverse liquid chromatography experiments described elsewhere (6). The complex fuel matrix complexity was addressed mainly by programmed temperature GC, which separated the volatile components of the fuel matrix (less than approximately 226 amu) from the higher molecular weight MDA (282 amu) or its heavier derivatized product.

Surface adsorptivity of MDA

MDA (Figure 1) has a molecular weight of 282 g/mol and contains two amine and two hydroxyl groups. Because of the phenolic and amine functionalities, this compound is extremely adsorptive in both the liquid and gas phase. In liquid-phase adsorption work (conducted in an HPLC configuration), the dispersion and tailing of the solute zone was measured and compared to nonadsorptive solutes (6). The result of these studies demonstrated the importance of liquid-phase adsorption onto both glass and metal surfaces, and that MDA must be handled carefully in the laboratory to prevent adsorption to syringes, filters, sample vials, and other glass and metal surfaces. Gas-phase adsorption of phenolic and amine-containing compounds is well-documented for GC systems (7) and is a common concern for practicing chromatographers. The analysis of these types of compounds usually involves the deactivation of surfaces in order to obtain less adsorption and therefore better quantitation.

Derivatization techniques

The common derivatizing agent BSA (*N,O*-bis[trimethylsilyl]acetamide) was investigated to reduce the adsorptivity of MDA. This silylation reaction decreases the surface activity of phenolic substituents by replacing the phenolic hydrogens with the trimethylsilyl functionality (Figure 2). The decrease in surface activity inhibits adsorption processes that are problematic in low-concentration analyses.

Although there are many different types of silylation agents available, room-temperature silylation reactions with short reaction times were preferred for this application. Other silylation reactions using hexamethyldisilazane work well with phenolic analytes but must be heated to temperatures above 50°C for short periods of time (8,9). Derivatizing agents allow more-common chromatographic columns and conventional injectors and detectors to be used without having to incorporate "base-deactivated" or surface-passivated injector liners and wool. The resultant silylated MDA complex was much less adsorptive, thus allowing for GC splitless injection and quantitation without solid-phase extraction (SPE) preconcentration.

Experimental

Direct split injection

Initial measurement techniques were conducted using a straight-forward approach of split injection at 300°C of an unsilylated analyte into a silanized glass liner/silanized glass wool using a conventional DB-5 capillary column (0.25-mm i.d., 0.25-µm film thickness) with a flame ionization detector (FID). Other experiments were conducted using the same column and injector system with a Hewlett Packard (Palo Alto, CA) 5971 mass-selective detector (MSD). MSD experiments were generally conducted in the selected ion monitoring (SIM) mode for the 161- and 282-amu ions.

SPE and preconcentration with split/splitless injection

An alternative technique for the analysis of MDA was also used to increase detection limits and decrease matrix effects (coelution of trace compounds). Normal-phase SPE was used to separate MDA from its matrix. In this technique, each 1-g silica gel cartridge (Baker Chemical, Phillipsburg, NJ) used was treated with an initial wash of 5 mL of methanol, followed by 15 mL of heptane to condition the bed. The sample containing MDA in jet fuel or kerosene solvent was then added, followed by a 15-mL heptane wash to remove the nonpolar matrix. Finally, the MDA was eluted using 1 mL of methanol. After blowing to dryness in nitrogen, the residue was dissolved in toluene (200 µL), and this final solution was injected into the GC–MS system as previously described.

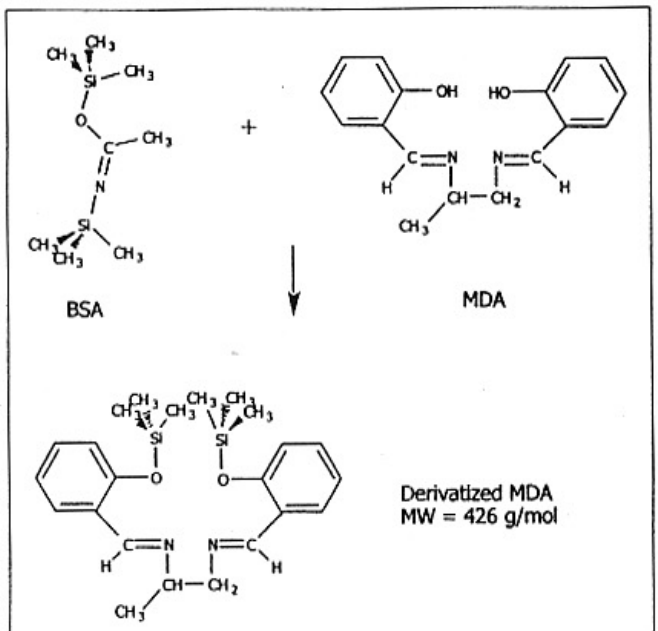

Figure 2. Silylation reagent BSA reacting with MDA to produce a nonadsorptive derivative.

Silylation and quantitative analysis

Standards were prepared by blending MDA (Octel America, Newark, DE) in standard kerosene (Aldrich Chemical, Milwaukee, WI) to produce a stock solution (400–600 mg/L) that was serially diluted to 10, 7, 5, 3, 1, and 0.5 mg/L in kerosene. A 200-µL aliquot of each standard was pipetted into glass vials with glass or plastic 250-µL inserts, to which 5 µL of BSA (Pierce Chemical, Rockford, IL) was added using a Hamilton 701-series syringe. Care was taken to minimize exposure of the BSA to atmospheric moisture, because BSA is highly reactive with water. Each solution was mixed for approximately 10 s on a vortex mixer and analyzed by GC–MS (Table I). Jet fuel samples were handled in a similar manner by pipetting 200 µL of each fuel into a GC vial/insert. In the case of thermally unstressed fuel samples, 5 µL of BSA was used to silylate the additive. Thermally stressed fuels from the Isothermal Oxidation Apparatus (IOA) contained more organic alcohols and acids and thus were spiked with 20 µL of BSA to insure that sufficient BSA was available to react with MDA. All samples were analyzed within one day of adding the derivatizing reagent.

The chromatographic column used was typically a 30-m, 0.25-mm-i.d., 0.25-µm film thickness HP-5 capillary column (Hewlett Packard), although almost any nonpolar column having a thermal stability greater than 300°C would be suitable. Thin-film columns (0.1-µm film thickness) may be more desirable for both resolution and analysis time. The mass-spectral patterns of the MDA and silylated MDA are shown in Figure 3. The 220- and 235-amu ions were chosen for quantitation because they were abundant in the silylated MDA but absent in the MDA. The retention time and ratio of the selected ions identified the derivatized MDA from interferences and various reaction products.

Results and Discussion

Direct split injection

Gas-solid adsorption clearly occurs during the analysis of MDA, as with many types of phenolic analytes in similar chromatographic systems (7). The direct analysis of MDA by FID systems for split injectors (clean borosilicate glass liner, silanized or deactivated glass wool, and conventional DB-5 column) is nonlinear with a lower detection limit of approximately 50–80 mg/L (Figure 4). Base deactivation of the injector liner, wool (Restek, Bellefonte, PA), and column (RTX-5 amine, Restek) resulted in a reduction of the detection limit by an order of magnitude, improvement in chromatographic peak shapes, and an increase in linearity.

These deactivation steps improved the analysis, but detection limits were still greater than specification levels (0–5.7 mg/L), presumably because of other surface-adsorptivity factors for MDA. Split injection gave an unexpected improvement in response as compared with splitless injection, indicating that adsorption effects continued to play a role despite our attempts at surface deactivation. Undeactivated surfaces in the ion source, column tips, and injector or detector components that were not surface passivated may have been

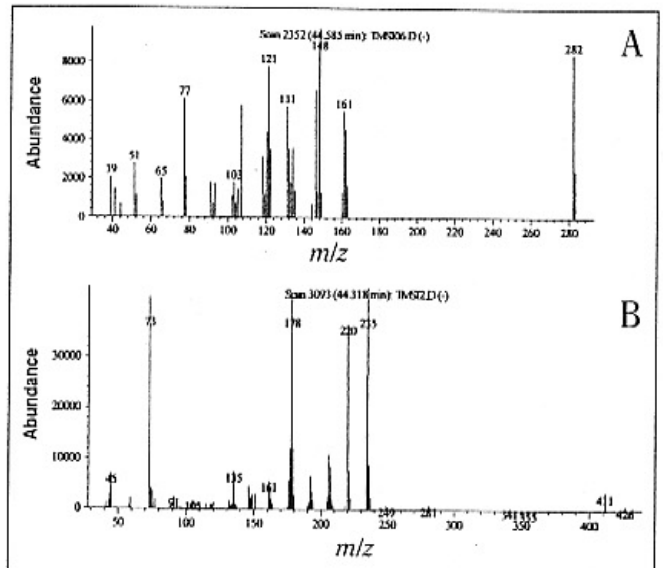

Figure 3. Mass-spectral patterns (70eV) for MDA (A) and derivatized MDA (B).

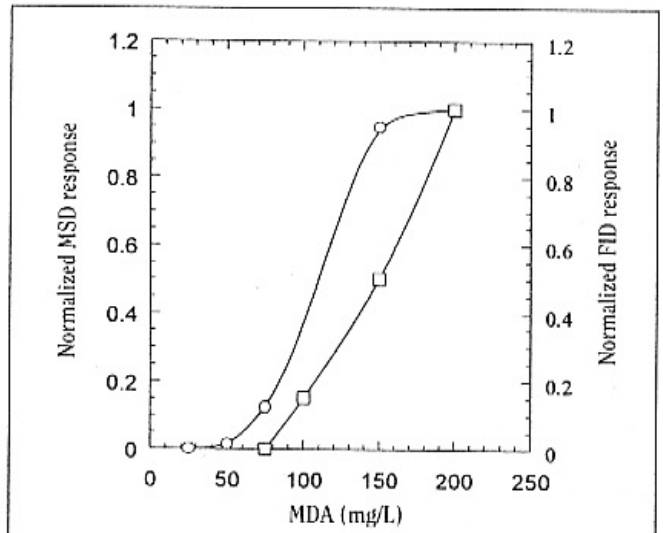

Figure 4. Early calibration work for MDA in nondeactivated chromatographic systems by direct injection: FID response (○) and MSD response (□).

Table I. GC–MS Conditions for Analysis of Silylated Jet Fuels

GC conditions	MS conditions
Splitless injection: 300°C	SIM: 220, 235 amu
Injection volume: 3 µL	Electron impact ionization: 70 eV
Initial temperature: 150°C (1-min hold)	Dwell time: 100 ms
Temperature program: 10°C/min	
Final temperature: 300°C (5-min hold)	
MS transfer line temperature: 280°C	

detrimental to system performance. "Cool" (ambient temperature) on-column injection was considered but was not desirable because of its limited autosampling capabilities with on-column syringes.

SPE with direct injection

Clearly, detection limits needed to be lowered in order to make this technique effective. SPE successfully increased the concentration of MDA and replaced the complex fuel matrix with the elution solvent methanol. In this work, a 10-mL sample of fuel was concentrated by a factor of 10, and the 1-mL sample was injected into the GC–MS system in SIM mode. The results were similar to previous direct-injection results in that low-level detection was still difficult (detection limits of 2 mg/L were typical). A split ratio of 10:1 provided more response than did splitless operation, presumably because sweeping of the solute through the glass injector liner was more efficient than the splitless process, which may increase contact time with glass or metal surfaces. Also, the accompanying solvent evaporation technique for the injection of the MDA became more time-consuming and tedious.

These steps created an improvement in the analysis, but detection limits were still not acceptable to measure at and below specification levels (2–6 mg/L). Split injection gave improved response as compared with splitless injection, indicating that perhaps adsorption effects continued to play a role in spite of surface deactivation.

Calibration results for derivatized MDA

MDA derivatized with BSA showed detection linearity between 0 and 10 mg/L and low detection limits (Figure 5) in duplicate analyses. The intercept for the curve is nonzero, indicating a lower detection limit of approximately 0.5 mg/L.

The lower detection limit of the derivatized MDA may be affected by the adsorption of MDA to the glass-vial insert and other surfaces to which the MDA was exposed before it was injected into the GC. If BSA is added to a 10-mg/L solution and the derivatized MDA is then serially diluted with reference kerosene to produce several solutions between 0 and 1 mg/L, the minimum detectable level is greatly improved (Figure 6). This observation is consistent with MDA being adsorbed to active sites in the glass vial that have high surface-to-volume ratios, affecting the lower-level standards more than higher-level standards. The use of plastic inserts did not improve the adsorption of MDA before it could be derivatized.

Table II. Precision and Accuracy of MDA Measurements Using Silylation with BSA

Known values (mg/L)	Measured response (mg/L)		
	Mean	Standard deviation	RSD
0.41	0.38	0.053	14%
2.5	2.5	0.11	4.3%
6.4	6.3	0.060	0.94%

Table III. Effects of Fuel Matrix on MDA Quantitation

Fuel ID	Fuel type	MDA added (mg/L)	MDA measured (mg/L)
POSF-2827	Jet A	2.0	2.8
POSF-2926	Jet A	2.0	2.4
POSF-2962	JP-5	2.0	2.5
POSF-2962	JP-5	6.0	6.0
POSF-2963	JP-5	2.0	2.2
POSF-2963	JP-5	6.0	5.0
POSF-2985	Jet A	2.0	2.0
POSF-3059	Jet A	2.0	2.5
POSF-3084	Jet A	2.0	2.8
POSF-3119	Jet A	2.0	2.7

Method repeatability

Replicate analyses ($n = 5$) were conducted for three levels of MDA in a reference kerosene. The solutions of MDA in kerosene were then spiked with the derivatizing agent and analyzed using the autosampling splitless injection. The results showed good agreement with spiked levels of MDA and reasonable standard deviations for replicate analyses (Table II). Low concentrations of MDA clearly have a higher relative standard deviation (RSD) because of the difficulty of insuring that all of the analyte is successfully transported to the chromatographic detector. Any glass or metal surface may adsorb a small amount of the analyte, making results less consistent. However, this level of RSD is typical of trace analyses at the sub-parts-per-million level, especially for such a surface-active compound.

Effect of fuel matrix on measurement

To explore the effect of the fuel matrix on the quantitation of MDA, a series of Jet-A and JP-5 aviation fuels were spiked with a known amount of MDA. These samples were treated with BSA, and duplicate measurements of each were used to quantitate the level of MDA (see Table III). No history of the origin of the fuel was available. Levels of MDA that may have already

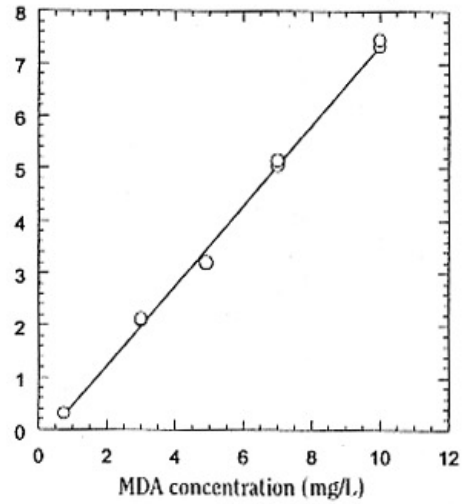

Figure 5. Typical calibration for derivatized MDA in a reference kerosene ($n = 2$).

existed in the fuel were not available.

All of the results obtained were greater than or equal to the amount added to the original fuel. We suspect that some of these fuels may have been doped with MDA at the refinery (up to 5.7 mg/L is allowable for Jet-A and 5.8 mg/L for JP-5). Because the history of each fuel was unknown, all unspiked or fresh-fuel samples were reanalyzed with BSA alone to detect low levels of MDA. With the exception of POSF-2962, all samples showed small amounts of MDA present (less than 0.5 mg/L). Attempts were made to quantitate between 0 and 1 mg/L, but results indicated nonlinearity in this range because of adsorption of the small amounts of MDA on surfaces. Further work needs to be conducted to improve the low-level accuracy (and precision) of this technique.

We suspect that MDA would not be silylated when chelated with a metal in solution. To test this hypothesis, 98-ppb copper, 60-ppb iron, and 14-ppb zinc were added to POSF-2962 and referred to as POSF-2963. Because the mass spectrometer was used to detect a specific mass at a specific retention time, MDA complexed with copper and silylated should not be detected at the same retention time as MDA not complexed with copper. The metal-containing fuel had approximately 1.0 ppm lower level of MDA, indicating that the MDA metal complex was not detected in this chromatographic arrangement (see Table III). In fact, the metal content of 172 ppb (the total for these three metals) would almost account for the 1.0 ppm difference, because 1 mol of each metal would complex with 1 mol of MDA and the mass ratio would be an approximate factor of 4.5 (for copper). These three metals alone account for 0.8 ppm of the MDA; other trace metals were not measured. Therefore, we concluded that the silylation technique is applicable only to uncomplexed or available MDA (i.e., MDA that has not already reacted with trace metals in the matrix).

Measurement of field samples for additive content

An additive package currently being developed for Air Force fuels (JP-8+100) is comprised of several additives including a detergent/dispersent, antioxidant, and MDA. Because the additive package is introduced in the field at the user level, measurements of the level of MDA could provide an important check on the techniques used to deliver and mix the additive package. Four samples were obtained from active air bases currently using the JP8+100 additive and were received in 1-gal metal cans. Results from the four samples indicated levels of MDA below the desired level of 2.0 mg/L. Again, MDA adsorptivity in holding, sampling, and analysis containers may have each had an effect in reducing the level of MDA for the chromatographic detector. Field samples may be more accurately measured by the addition of BSA to small samples taken from larger tanks in the field. These small samples could then be shipped to a laboratory for analysis. Using metal cans with high surface-to-volume ratios (compared to storage tanks) may deplete MDA as a result of adsorption or reaction with surface-bound water. Future work will address the possible deactivation of these surfaces so that field sampling of the additive package will be able to predict or indicate problems in the field.

Tracking additive concentration during stressing tests

The ability to measure MDA concentration as a function of time during fuel testing is of interest to fuel researchers. The time dependence of the MDA concentration can yield information about the chemical and physical mechanisms of MDA action as well as enable the optimization of the MDA concentration for a given system or fuel or both. Figure 7 shows that MDA concentration decreases as a function of time with simulated aircraft fuel-system stressing in an IOA (10). In these experiments, nitrogen was bubbled through the fuel as the fuel was heated to 180°C in an all-glass batch reactor. After reaching the desired temperature, air was introduced and the MDA level was measured as a function of time. The lack of metal exposure and low surface-to-volume ratio would preclude the explanation of the adsorption of MDA in reducing its concentration. Thermolysis (or a unimolecular decomposition) of MDA at 180°C is possible, although the reactor was

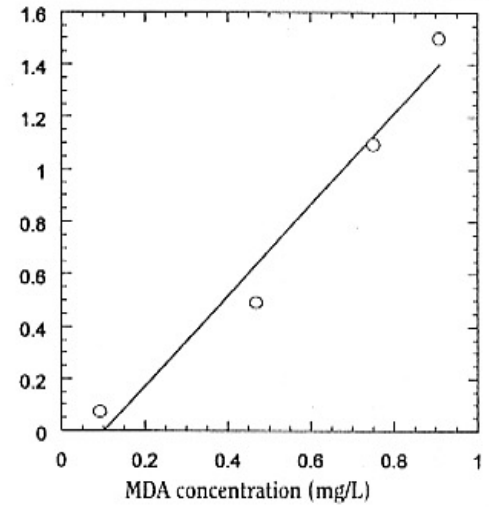

Figure 6. Calibration curve between 0 and 1 mg/L by dilution of the derivatized MDA.

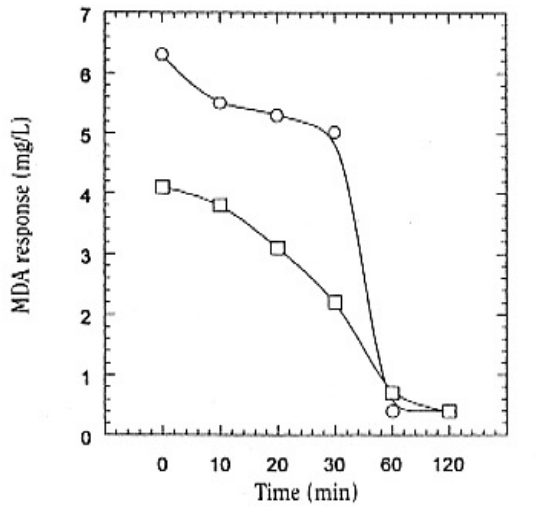

Figure 7. MDA reaction during thermal stressing of neat and copper-doped fuel in the IOA.

heated in a flowing stream of nitrogen as the system was heated. A significant amount of MDA would have degraded during the 60–90 min spent arriving at a thermal equilibrium if thermolysis was important. It would seem that bimolecular reactions involving the phenolic or amine functionality or both would be a more likely route of degradation for MDA. Previous work in a copper-doped fuel also observed MDA consumption during thermal oxidation at 140°C (11). MDA consumption below concentrations required to completely complex the copper resulted in substantial increases in the oxidation rate. It was surmised that MDA consumption could occur by the process of fuel peroxy radical extraction of one of MDA's phenolic hydrogens. In this study, the fuel containing 98-ppb copper showed a lower level of uncomplexed MDA initially, as was expected. Both experiments showed similar rates of decrease for uncomplexed MDA, indicating the probability of the same mechanism for MDA removal in both samples. Future experiments may include investigations of the ultimate fate of the MDA.

Conclusion

MDA can be successfully quantitated by GC–MS at jet-fuel specification concentrations by creating a trimethylsilyl derivative using BSA. The derivative circumvents the problems with accuracy, precision, and detectability of low levels (0–6 mg/L) of the highly adsorptive MDA molecule. Derivatization with BSA can be conducted at room temperature using extremely small samples (200 µL) with sensitivity sufficient to cover the specification range of the additive (2–6 mg/L). The technique has been applied with reasonable success to the evaluation of additive concentrations in JP-8+100 samples and the tracking of MDA concentrations in thermal-stressing studies.

Acknowledgments

This work was sponsored by the US Air Force, AFRL/PRSF, at Wright-Patterson AFB, Ohio under contract number F33615-97-C-2719. Mr. Charles Frayne was the technical monitor.

References

1. F.B. Downing, R.G. Clarkson, and C.J. Pederson. Suppression of metal catalysts in gasoline gum formation. *Oil and Gas Journal* **38:** 97–101 (1939).
2. J.A. Schreifels, R.E. Morris, N.H. Turner, R.L. Mowery, and S.M. Hues. Adsorption of a metal deactivator additive onto metal surfaces. *Energy and Fuels* **5:** 263–68 (1991).
3. DuPont petroleum laboratory test method, uncombined metal deactivator in gasoline and fuel oil. *Analytical Method G37-86.* E.I. DuPont DeNemors & Co., Wilmington, DE, 1986.
4. R.E. Kauffman. *Simple analytical techniques to determine the dispersant capacity and metal deactivator concentration of JP8+100 and other jet fuels,* 97-GT-77. Presented at the ASME-IGTI, Orlando, FL, June 1997.
5. W.D. Schulz. Analysis of jet fuel additives. *ACS Petroleum Division Preprints* **37:** 477–83 (1992).
6. R.C. Striebich, W.A. Rubey, and S.A. Anderson. Surface adsorption studies using inverse gas chromatography and inverse liquid chromatography. *ACS Petroleum Division Preprints* **39:** 64–66 (1994).
7. A.E. Pierce. *Silylation of Organic Compounds.* Pierce Chemical Company, Rockford, IL, 1968.
8. S. Zabarnick, M.S. Mick, R.C. Striebich, and R.R. Grinstead. Model studies of silylation agents as thermal oxidative jet fuel additives. *Energy and Fuels* **13(1):** 154–59 (1999).
9. M.S. Mick. M.S. Dissertation, University of Dayton, August 1996.
10. B. Grinstead and S. Zabarnick. Studies of jet fuel thermal stability, oxidation, and additives, using an isothermal oxidation apparatus equipped with an oxygen sensor. *Energy and Fuels* **13:** 756–760 (1999).
11. S. Zabarnick and S.D. Whitacre. Aspects of jet fuel oxidation. *J. Eng. Gas Turbines & Power* **120:** 519–25 (1998).

Manuscript accepted June 22, 2000.

K. One-Dimensional Simulations of Jet Fuel Thermal-Oxidative Degradation and Deposit Formation Within Cylindrical Passages

One-Dimensional Simulations of Jet Fuel Thermal-Oxidative Degradation and Deposit Formation Within Cylindrical Passages

J. S. Ervin
Mem. ASME

S. Zabarnick

T. F. Williams

University of Dayton Research Institute,
Dayton, OH 45469-0210

Flowing aviation fuel is used as a coolant in military aircraft. Dissolved O_2 reacts with the heated fuel to form undesirable surface deposits which disrupt the normal flow. For purposes of aircraft design, it is important to understand and predict jet fuel oxidation and the resulting surface deposition. Detailed multi-dimensional numerical simulations are useful in understanding interactions between the fluid dynamics and fuel chemistry. Unfortunately, the detailed simulation of an entire fuel system is impractical. One-dimensional and lumped parameter models of fluid dynamics and chemistry can provide the simultaneous simulation of all components which comprise a complex fuel system. In this work, a simplified one-dimensional model of jet fuel oxidation and surface deposition within cylindrical passages is developed. Both global and pseudo-detailed chemical kinetic mechanisms are used to model fuel oxidation, while a global chemistry model alone is used to model surface deposition. Dissolved O_2 concentration profiles and surface deposition rates are calculated for nearly isothermal and nonisothermal flow conditions. Flowing experiments are performed using straight-run jet fuels, and the predicted dissolved O_2 concentrations and surface deposition rates agree reasonably well with measurements over a wide range of temperature and flow conditions. The new model is computationally inexpensive and represents a practical alternative to detailed multi-dimensional calculations of the flow in cylindrical passages. [S0195-0738(00)01204-8]

Introduction

Jet fuel is circulated in high-performance military aircraft for cooling purposes before it is burned. Unfortunately, jet fuel degrades in the presence of heat and dissolved O_2 at relatively low temperatures (120–300°C) through numerous complex reactions forming insoluble particles and surface deposits. Surface deposits impair engine performance by disrupting the normal fuel flow through fuel system components. Insoluble particles may further react to form surface deposits or block fuel system filters. Moreover, the fouling of close-tolerance valves may lead to catastrophic failure. Thus, it is imperative for aircraft engine and fuel system designers to have a fundamental understanding of thermal-oxidative fuel degradation and a method for predicting the location and rate of deposit accumulation. Also, numerical simulations of fuel degradation can assist the interpretation of laboratory results and the design of aircraft fuel systems.

The thermal-oxidative degradation of jet fuels has been studied by experiment, and empirical correlations have largely been used to describe the experimental results [1]. Numerical simulations [2–4] of the fluid dynamics, heat transfer, and fuel chemistry are more general than empirical correlations of deposit formation which are limited to specific flow devices. The success of a computational approach depends on the development of a chemical kinetics model that can employ laboratory measurements as input to characterize a fuel and remains valid over a wide range of temperature, residence time, and flow properties. However, the development of chemical kinetic models is complicated by the fact that individual jet fuel samples possess a range of oxidation and deposition characteristics which results from varying source petroleum and refinery processing [5]. In addition, jet fuels consist not of a single compound, but are a complex hydrocarbon mixture whose behavior can be further complicated by the presence of additives and dissolved metals. Although the present understanding of fuel degradation processes is incomplete, the lack of comprehension is not fatal to the development of practical numerical models.

Previous studies which employed computational fluid dynamics have considered multi-dimensional flows [3,4]. However, solving coupled, multi-dimensional governing equations can be time-consuming for preliminary designs, requiring, for example, several hours of computational time for a single system component. It is not yet practical to simulate entire integrated aircraft fuel and thermal management systems in two or three dimensions. Thus, there is a need for the development of simple fuel degradation and surface deposition models which have computational times on the order of seconds and can be used in system simulations. Chin et al. [6] attempted simplified solutions using an approximate integral technique, but some assumptions used in representing the flow and temperature fields and the fuel properties are unclear. Deshpande et al. [7] used a one-dimensional analysis and a global kinetic mechanism consisting of three reactions, but the agreement with experimental measurements was unsatisfactory. The objective of this work is to develop a one-dimensional numerical model of thermal-oxidative deposit formation that retains a reasonable degree of fidelity with experimental measurement.

Numerical Model

The approach taken here avoids the computational complexities associated with multi-dimensions, but still retains the dominant physics and chemistry. As shown in the sectional view of Fig. 1,

Contributed by the Fuels and Combustion Technologies Division for publication in the JOURNAL OF ENERGY RESOURCES TECHNOLOGY. Manuscript received by the FACT Division, January 5, 2000; revised manuscript received September 19, 2000. Associate Technical Editor: A. Moussa.

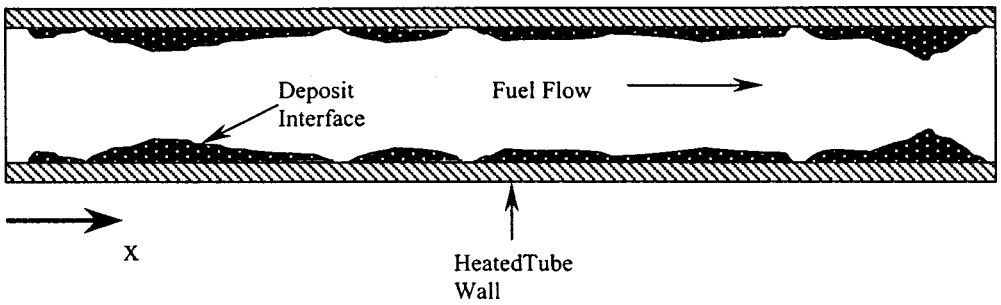

Fig. 1 Cross section of heated tube containing forming surface deposits

the flow within the cylindrical passage is bounded by the interface between the deposit and fuel. To capture the gradual growth of the deposit, time-dependent forms of the enthalpy equations, Eq. (1), and species, Eq. (2), are employed.

$$\frac{\partial(\rho A_c h)}{\partial t}+\frac{\partial(\rho u h A_c)}{\partial x}=h_{\text{conv}}\mathcal{P}(T_{\text{int}}-T)+\frac{\partial}{\partial x}\left(kA_c\frac{\partial T}{\partial x}\right) \quad (1)$$

In Eq. (1), ρ represents the fuel density, $\mathcal{P}$ is the tube internal perimeter, T_{int} is the deposit-fuel interface temperature, k is the fuel thermal conductivity, h_{conv} is the convection heat transfer coefficient, and A_c is the cross-sectional area within the tube through which the fuel passes. The variables h, u, and T are the enthalpy, velocity, and bulk temperature. Here, t and x represent time and the axial location within the tube. Since the wall of the fuel passage is thin relative to its length, the radial temperature profile within the tube-wall at any location along the tube length is assumed to be uniform. As carbonaceous deposits accumulate on the inner tube surface, the heat transfer from the metal wall to the fuel is reduced because the deposits offer conductive resistance to heat diffusion in the radial direction. Here, the heat conduction from the metal tube through the deposit is calculated assuming that the heat transfer rate in the radial direction is constant [8,9] for a given axial location along the tube and for a given time-step. It is also assumed that the rate of axial heat diffusion within the deposit is negligible. (A representative value of thermal conductivity for the deposit was selected to be 0.1 W/m°C [1].) Thus, the heat transfer between the deposit-fuel interface and the bulk fuel is known given the measured outer surface temperature along the tube length and the appropriate internal convective heat transfer correlation. For flow conditions present in aircraft fuel systems, the axial heat diffusion term is negligible (large Peclet number). However, axial diffusion terms are retained here for purposes of numerical stability in the finite difference solution. The chemical reactions which occur involve a mixture of dilute species. Thus, they do not significantly contribute to the heating of the liquid and are neglected in Eq. (1).

In Eq. (2), f_i is the mass fraction of the ith species, ω_i is the rate of production or removal of the ith species, and h_m is the mass transfer coefficient. The term $(\rho f_i)_{\text{int}}$ of Eq. (2) represents the concentration of the ith species existing at the deposit-fuel interface.

$$\frac{\partial(\rho A_c f_i)}{\partial t}+\frac{\partial(\rho A_c u f_i)}{\partial x}=h_m\mathcal{P}((\rho f_i)_{\text{int}}-\rho f_i)+\frac{\partial}{\partial x}\left(D_i A_c\frac{\partial(\rho f_i)}{\partial x}\right)+\omega_i A_c \quad (2)$$

In the present model, the fuel concentration is much greater than the fuel degradation products. As a consequence, the chemical mixture can be treated as a dilute solution of product species within a nondepleting fuel.

Multi-dimensional effects are accounted for in Eqs. (1) and (2) by using convective heat and mass transfer coefficients. It is assumed for simplicity that heat and mass are transported by similar processes. Thus, the mass transfer coefficient is obtained by substituting the Schmidt number, Sc, for the Prandtl number, Pr, and D_i for k in the appropriate convective heat transfer correlation [10]. Since the thermodynamic and transport properties for jet fuel vary strongly with temperature, property values used in Eqs. (1) and (2) come from curve fits obtained for JP-8 fuel [11]. In addition, pressures existing in aircraft fuel systems are large. Thus, the fuel remains in the liquid phase.

The species generation term of Eq. (2) arises from a selected chemical kinetic mechanism. Global chemical kinetic mechanisms have been used [2,9,12] to simplify complexities of thermal-oxidative chemistry and generally employ one reaction to represent fuel oxidation

$$\text{Fuel}+O_2\rightarrow\text{Products} \quad (3)$$

Although fuel oxidation involves many reactions, the underlying assumption of Eq. (3) is that the overall reaction of a mixture of compounds can be represented by one rate equation. This rate equation consists of a rate constant multiplied by concentrations having simple order dependence, as in Eq. (4)

$$-\frac{d[O_2]}{dt}=k[\text{RH}][O_2]^n \quad (4)$$

In Eq. (4), the fuel is represented by a single compound RH because it is extremely difficult to model the multitude of compounds present in jet fuel.

The global kinetic model of Table 1 has been used with reasonable success to simulate fouling in heated sections for a Jet A fuel sample [9]. In Table 1, RH represents the fuel, $\mathcal{P}$ is deposit-forming precursor, D_{bulk} represents bulk insolubles, and D_{int} is the surface deposit. The values of Arrhenius parameters come from a combination of theory, experiment and trial-and-error. The units for pre-exponentials in Table 1 do not correspond to bimolecular reactions because the concentrations of RH and F_s are assumed

Table 1 Global-kinetic model of Katta and Roquemore [3]

Bulk Fuel Reactions	Activation Energy (kcal/mol)	Pre-exponential Multiplier	Reaction Number
$RH + O_2 \rightarrow ROO^{\bullet}$	32	2.5×10^{13} (mole $m^{-3}s^{-1}$)	1)
$ROO^{\bullet} + RH \rightarrow$ Solubles	10	1×10^{4} (s^{-1})	2)
$ROO^{\bullet} + F_s \rightarrow \mathcal{P}$	15	8×10^{9} (s^{-1})	3)
$ROO^{\bullet} + RH \rightarrow D_{bulk}$	10	200 (s^{-1})	4)
$\mathcal{P} + RH \rightarrow$ Solubles	30	3.2×10^{12} (s^{-1})	5)
$D_{bulk} + RH \rightarrow 2D_{bulk}$	0.0	1×10^{-3} (s^{-1})	6)
Surface Reactions			
$O_2 + RH \rightarrow \mathcal{P}$	12	5.2×10^{-3} (ms^{-1})	7)
$\mathcal{P} \rightarrow D_{int}$	17	260 (ms^{-1})	8)
$D_{bulk} \rightarrow D_{int}$	10	0.8 (ms^{-1})	9)

constant (nondepleting) and, consequently, are viewed as part of the Arrhenius expression for reaction rate. (The Arrhenius expressions used have the form $k=A\exp[-E/\mathrm{RT}]$ in which E is the activation energy and R is the universal gas constant.) Reactions 1 through 6 are presumed to occur within the bulk fuel, and Reactions 7 through 9 are assumed to occur at the deposit-fuel interface. Reactions 8 and 9 represent the conversion of particles D_{bulk} and P to surface deposit, D_{int}.

In the mechanism of Table 1, different fuel samples are represented by having different concentrations of F_s. F_s designates a chemical species within the jet fuel that removes alkyl peroxy-free radicals from the auto-oxidation chain and is required for the formation of deposit precursor. Thus, F_s may represent phenols which are known to slow oxidation by the removal of alkyl peroxy free radicals. Ultimately, a chemical kinetics mechanism will be most useful if an analytical chemistry test could be used to determine an ''effective'' F_s concentration for individual jet fuel samples. Thus, an ''effective'' F_s concentration within the fuel could be measured in the laboratory and entered into the model to provide a method to predict the deposition properties of the fuel over a range of temperatures, residence times, and flow properties. The concentration of F_s in reaction 3 can be obtained indirectly using measurements of surface deposition [9]. To account for the variation in oxidative characteristics of different fuel sources, flowing tests which measure dissolved O_2 consumption over a range of flow conditions can provide the activation energy and pre-exponential multiplier of reaction 1.

The global kinetic mechanism of Table 1 was modified for use in the present work and appears in Table 2. The first five reactions of Table 2 are identical to those of Table 1. Calculations show that the contributions of reactions 6 and 9 (Table 1) to surface deposition are insignificant relative to those resulting from other reactions. Moreover, fundamental differences between species $\mathcal{P}$ and D_{bulk} of Table 1 are unclear. Thus, reactions 6 and 9 (Table 1) are eliminated in the current global mechanism. In addition, to improve the representation for dissolved O_2 consumption (particularly for long residence times), the activation energies and pre-exponential multipliers of reactions 1a and 6a were adjusted to fit experimental measurements of dissolved O_2. The remaining reactions of Table 2 were then determined by trial-and-error using experimental measurements of surface deposition. The large differences in pre-exponential multipliers and activation energies between bulk fuel reactions 3 and 4 (Table 1) and reactions 3a and 4a (Table 2) result primarily from changes in reactions 1a and 6a. Fluid dynamics and heat transfer strongly influence fuel chemistry, but the nature of this influence is not well understood [1]. For this reason, computations were performed using a set of flow and temperature conditions that are very different from those available in the current experiments. If a global mechanism can satisfactorily predict surface deposition and fuel oxidation under conditions very different from those used for calibration, a measure of generality may be demonstrated. In contrast to the conditions of our experiments, the experiments have been conducted in a near isothermal flowing test rig (NIFTR) [13] at lower temperatures and flow rates (0.5 mL/min and 0.125 mL/min at 185°C) in order to attain near-isothermal conditions in a minimum length of tube. In both kinds of experiments, the temperature of the copper block used to heat the tube and the flow rate are varied to produce different oxidation rates and residence times, respectively. The NIFTR experiments use a 81.3-cm-long heated tube, whereas the current experiments use a 45.8-cm-long heated tube. In the experiments performed here, the bulk fuel temperature increases along the entire heated tube length, never reaching the wall temperature. In contrast, in the NIFTR for a flow rate of 0.125 mL/min, the fuel temperature attains the tube wall temperature very near the flow entrance.

Table 2 Global-kinetic model used in one-dimensional simulations

Bulk Fuel Reactions	Activation Energy (kcal/mol)	Pre-exponential Multiplier	Reaction Number
$RH + O_2 \rightarrow ROO^{\bullet}$	40	1×10^{11} (mole $m^{-3}s^{-1}$)	1a)
$ROO^{\bullet} + RH \rightarrow$ Solubles	10	1×10^{4} (s^{-1})	2a)
$ROO^{\bullet} + F_s \rightarrow \mathcal{P}$	15	1×10^{14} (s^{-1})	3a)
$ROO^{\bullet} + RH \rightarrow D_{bulk}$	15	1.5×10^{14} (s^{-1})	4a)
$\mathcal{P} + RH \rightarrow$ Solubles	29	3×10^{11} (s^{-1})	5a)
Surface Reactions			
$O_2 + RH \rightarrow \mathcal{P}$	19	1×10^{3} (ms^{-1})	6a)
$\mathcal{P} \rightarrow D_{int}$	10	5×10^{-3} (ms^{-1})	7a)

Although more complex chemical kinetic mechanisms [14] of oxidation exist, the global mechanism of Table 2 was used for convenience in simulations of surface deposition. With regard to the first reaction of Table 2, the order, n, of Eq. (4) is assumed to change from zero order to first order when the dissolved O_2 concentration falls below 10 ppm. In general, a two-parameter representation for reaction 1 is insufficient over a very wide temperature range, particularly if naturally occurring antioxidants or antioxidant additives are present [15]. However within the temperature range (25–300°C) of the present experiments, it will be shown that a single set of Arrhenius parameters provides an acceptable prediction of fuel oxidation.

Surface deposition is a complex physical and chemical process that is understood even less than fuel oxidation. In the formation of a surface deposit, it is unknown if the deposit initiates from a nucleation process originating at the metal surface, from particle migration from within the bulk, or from a combination of surface nucleation and bulk particle adhesion. Moreover, it is unclear how particles nucleate and grow within the bulk fuel. Although global models for deposition disguise the complexities associated with surface phenomena, they remain useful engineering representations. The number of particles, $\mathcal{P}$, that adhere to a surface and transform into D_{int} depends on the sticking probability and the concentration gradient of $\mathcal{P}$. The sticking probability is defined as the probability that a particle reaching the wall will remain there and includes an Arrhenius-like dependence on the wall temperature [16]. It is reasonable to assume that the sticking probability would vary inversely with the shear stress at the deposit-fuel interface, τ_{int}. Thus, τ_{int} appears in the denominator of the right-hand side of Eq. (5) and is calculated from surface friction factors, Eq. (9). In two-dimensional computations, Katta et al. [9] have used the constant 0.7 for n of Eq. (5). In the present model, it was found that values of n near 0.1 resulted in predictions which follow more closely the measured surface deposition rates.

$$\frac{dD_{\mathrm{int}}}{dt}=\frac{c}{\tau_{\mathrm{int}}^{n}}\left[\frac{\rho^{\mathrm{int}}f_{\mathcal{P}}^{\mathrm{int}}}{\mathrm{MP}}\right]A_{7a}e^{-E_{7a}/\mathrm{RT}_{\mathrm{int}}} \tag{5}$$

In Eq. (5), c is a dimensionally correct constant of order unity, and MP is the molecular weight of the precursor species.

The precursor mass fraction at the deposit-fuel interface ($f_{\mathcal{P}}^{\mathrm{int}}$) must be known in order to use Eq. (2) to solve for the precursor concentration existing in the bulk flow. In addition, $f_{\mathcal{P}}^{\mathrm{int}}$ is required for calculation of the rate of deposit formation given by Eq. (5). (The concentration of $\mathcal{P}$ at the deposit-fuel interface equals the product of $f_{\mathcal{P}}^{\mathrm{int}}$ and ρ^{int}.) By balancing the rate of production of $f_{\mathcal{P}}^{\mathrm{int}}$ at the deposit-fuel interface with the rate of species transport between the fuel bulk and the wall and removal via reaction 7a, Eq. (6) may be derived

$$f_{\mathcal{P}}^{\mathrm{int}}=\frac{\dfrac{\mathrm{MP}}{\mathrm{MO}_2}A_{6a}\rho^{\mathrm{int}}f_{\mathrm{O}_2}^{\mathrm{int}}e^{-E_{6a}/\mathrm{RT}_{\mathrm{int}}}+h_m f_{\mathcal{P}}\rho}{\left[\dfrac{c}{\tau_{\mathrm{int}}^{n}}A_{7a}\rho^{\mathrm{int}}e^{-E_{7a}/\mathrm{RT}_{\mathrm{int}}}+h_m\rho^{\mathrm{int}}\right]} \tag{6}$$

In Eq. (6), MO_2 is the molecular weight of the dissolved O_2. Similarly, $f_{O_2}^{int}$ is given by a balance between the rate of O_2 consumption at the wall and the rate of transport to the deposit fuel interface

$$f_{O_2}^{int} = \frac{h_m f_{O_2} \rho}{[A_{6a} \rho^{int} e^{-E_{6a}/RT_{int}} + h_m \rho^{int}]} \tag{7}$$

It is important to know the pressure change across a fuel system component. Thus, for convenience, the steady form of the one-dimensional momentum equation, Eq. (8), is used in the present analysis for convenience. Quasi-steady use of this equation is reasonable provided that there is no large sudden change in the mass flow rate, in effect, no ''water hammer'' phenomena exist.

$$\frac{dP}{dx} = -\frac{m^2}{2\rho D A_c^2} F \tag{8}$$

In Eq. (8), P is pressure, D is the hydraulic diameter, F is the friction factor, and m is the mass flow rate. The friction factor is defined using the empirical correlation of Miller [17]

$$F = 0.25\left[\log\left(\frac{e/D}{3.7} + \frac{5.74}{\mathrm{Re}^{0.9}}\right)\right]^{-2} \tag{9}$$

where e is the absolute surface roughness and Re is the Reynolds number given by

$$\mathrm{Re} = \frac{4m}{\pi \mu D} \tag{10}$$

Here, μ is the dynamic viscosity. In the simulations performed here, the interior surfaces of the tubes were assumed to be smooth for simplicity.

Equations (1) and (2) are solved sequentially by finite difference solution using an iterative procedure which employs a relaxation technique. Upwinding was used for the convective terms, and the finite difference expressions in space and time are first-order accurate. The difference equations are solved implicitly such that large time steps may be used. After each time step, the geometry of the deposit-fuel interface may change, and the one-dimensional grid is reconstructed after every time step to account for changes in the solid boundary following the procedure of Katta and Roquemore [3]. From the calculated surface deposition rate, Ω, the latest radial location of the fuel-deposit interface is given by

$$r = r^o \sqrt{1 - \frac{2\Omega \Delta t}{\rho_{dep} r^o}} \tag{11}$$

In Eq. (11), ρ_{dep} is the deposit density and is treated as a constant. r^o represents the radius of the fuel-deposit interface at the previous time step.

In the present simulations, the volumetric flow rate at the tube inlet is known (0.125 mL/min to 16 mL/min), as is the inlet pressure (1000 psia) and temperature (25°C). The concentration of dissolved O_2 at the tube inlet was measured and used as a boundary condition for f_{O_2} (70 ppm). The mass fractions of the species produced in the reactions (ROO$^\bullet$, $\mathcal{P}$, D_{bulk}, and solubles) are zero at the flow inlet. For all simulations, the transport properties, enthalpy, and density at a given temperature arise from curve fits of Jet A fuel data [18].

An approach that is different from past global modeling of oxidation is to use several reactions which represent the dominant chemistry, rather than using hundreds of reactions as might be found in a detailed model, or a single oxidation reaction as found in previous global models. Zabarnick [14] and Ervin and Zabarnick [4] have referred to this approach as pseudo-detailed chemical kinetics and have used it to successfully explore the effects of two classes of antioxidants on fuel oxidation and in studies of the blending of fuels. To demonstrate the versatility of the present one-dimensional analysis, pseudo-detailed chemical kinetic modeling is used to simulate fuel oxidation using the mechanism of Table 3. This mechanism is based on the work of Zabarnick [14]. The Arrhenius parameters here were estimated by comparison with measured rate constants and from theory. The first reaction of Table 3 is assumed to occur by unimolecular decomposition of the initiating species, *I*. The first four reactions together with reaction 10 represent a simple chain mechanism for fuel oxidation. Reactions 5 through 9 represent the antioxidant chemistry associated with hindered phenol-like species (AH), and reactions 11 through 16 are associated with hydroperoxide decomposition which is believed to have an important role in accelerated O_2 consumption [19,20]. Reaction 17 represents the effects of hydroperoxide-decomposing species (SH). In this oxidation mechanism, there are no surface reactions listed. The effect of a metal surface in accelerating the oxidation rate is taken into account by reducing the value of the activation energy for the uni-

Table 3 Pseudo-detailed reaction mechanism for chemical kinetic modeling

Reaction	Arrhenius A-factor (mol, L, and s)	Activation Energy (kcal/mol)	Reaction No.
I→R$^\bullet$	1×10^{10}	0	(1)
R$^\bullet$ + O_2→$RO_2^\bullet$	3×10^9	0	(2)
$RO_2^\bullet$+RH→RO_2H + R$^\bullet$	3×10^9	12	(3)
$RO_2^\bullet$ + $RO_2^\bullet$→termination	3×10^9	0	(4)
$RO_2^\bullet$ + AH→ RO_2H + A$^\bullet$	3×10^9	5	(5)
$AO_2^\bullet$ + RH→AO_2H + R$^\bullet$	3×10^5	10	(6)
A$^\bullet$ + O_2→$AO_2^\bullet$	3×10^9	0	(7)
$AO_2^\bullet$ + AH→ AO_2H + A$^\bullet$	3×10^9	6	(8)
$AO_2^\bullet$ + $AO_2^\bullet$→products	3×10^9	0	(9)
R$^\bullet$ + R$^\bullet$ → R_2	3×10^9	0	(10)
RO_2H→ RO$^\bullet$ + $^\bullet$OH	1×10^{15}	37	(11)
RO$^\bullet$ + RH→ ROH+ R$^\bullet$	3×10^9	10	(12)
RO$^\bullet$→ $R_{prime}^\bullet$ + carbonyl	1×10^{16}	15	(13)
$^\bullet$OH + RH → H_2O + R$^\bullet$	3×10^9	10	(14)
RO$^\bullet$ + RO$^\bullet$ → termination	3×10^9	0	(15)
$R_{prime}^\bullet$ + RH → alkane + R$^\bullet$	3×10^9	10	(16)
RO_2H + SH → products	3×10^9	16	(17)

Table 4 Concentrations of species at tube inlet

Species	Initial Concentration (moles/liter)
I	4.0×10^{-8}
RH	4.7
AH	1.62×10^{-3}
SH	1.21×10^{-3}
O_2	1.8×10^{-3}
remaining species	0

molecular hydroperoxide decomposition reaction from 42 kcal/mol [14] to 37 kcal/mol [4]. Values of the variables required at the tube inlet are given in Table 4.

Experimental

Table 5 lists characteristics of the two Jet A fuel samples used in this work. In this work, Jet A fuel samples F2827 and F3119 are used. These straight-run fuels produce relatively low hydroperoxide concentrations and oxidize relatively slowly when heated in the presence of dissolved O_2.

The experimental apparatus is shown in Fig. 2 [4]. In a preconditioning tank, nitrogen and oxygen gases were bubbled through the fuel such that the dissolved oxygen concentration was nominally 70 ppm (normal air saturated value) as the fuel entered the heated block. Bulk dissolved O_2 levels were measured at the locations shown in Fig. 2 by means of a Hewlett Packard 5890 Series II gas chromatograph. To produce the desired thermal flow environment, a heated copper block and a second cooled copper block envelope the 316 stainless steel tubing (2.16-mm i.d. by 3.18-mm o.d.) through which the fuel passes. The electric power to each block (46 cm long with a 7.6-cm diameter) is controlled such that the tube wall temperature remains steady, and the tubing between the heated blocks is insulated. The cooled copper block has internal passages through which chilled water flows. Thermocouples are welded to the outer surface of the tubing to measure wall temperatures with an uncertainty of $\pm 2°C$. The tubes (ASTM grade A269/A213) are cleaned in an ultrasonic bath, rinsed with deionized water, and dried with flowing laboratory-grade nitrogen gas prior to use.

Fluid dynamics is an important element of fouling. In the present experiments, the volumetric flow rate was varied to show the effects of flow velocity on the observed surface deposition. Volumetric flow rates of 8 and 16 mL/min were used. The extent of fuel oxidation depends on both the residence time and the temperature field. As the fuel passes through several heated components in an aircraft, not all of the dissolved O_2 may be consumed because of large flow rates. Since dissolved O_2 is more readily consumed under conditions of high temperature and long residence times, the rate of O_2 consumption was increased by increasing the fuel temperature for a constant flow rate. The experiments with a flow rate of 16 mL/min were conducted for six-hour periods, and those with a flow rate of 8 mL/min were conducted for 12-h periods.

At the termination of an experiment, the tubes were rinsed with hexane, cut into 50-mm segments, and heated in a vacuum oven at 120°C for 1 h to remove fuel trapped in the deposits. A Leco (RC-412) multiphase carbon analyzer determined the mass of carbon on the tube segments. All tests were performed within the same week using neat fuel from the same batch.

Table 5 Characteristics of F2827 and F3119 Jet A fuels

	F2827	F3119
refinery treatment	Straight-run	---
total sulfur (ppm)	763	1000
mercaptan sulfur (%)	0.001	---
aromatics (vol %)	19	---
JFTOT breakpoint (°C)	266	failed
copper (ppb)	< 5	7
iron (ppb)	8	26
zinc (ppb)	<5	47

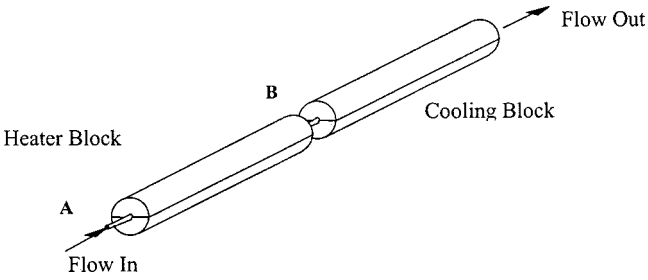

Fig. 2 Dissolved O_2 and fuel temperature measured at locations A and B

Results and Discussion

Temperature Simulations. Fluid dynamics and heat transfer strongly influence jet fuel oxidation which, in turn, affect the production of insoluble and soluble products. Thus, a numerical simulation must capture the flow and thermal physics with some fidelity in order to provide reasonable predictions of deposit accumulation. For this reason, computations were performed to assess the accuracy of the model by comparing predicted and measured temperatures at the exit of the heated tube. It has been observed [21] that temperature variations in a fluid flowing through a horizontal tube of small internal diameter can produce vortices that are superimposed on the main flow, and these vortices can significantly enhance the heat transfer. The surface deposition experiments are performed using inlet flow rates of 8 and 16 mL/min and, thus, the flow is anticipated to be laminar because the Reynolds numbers for these conditions are well below 2300. However, using axisymmetric finite difference simulations of the current flow conditions in a horizontal tube, Katta et al. [22] found that turbulent solutions (buoyancy forces acting radially were not included) for temperatures at the exit of the heated tube better approximated the measured temperatures than did laminar solutions. Moreover, they concluded that this flow regime was one of mixed natural and forced convection. In the present work, heat transfer correlations are used to represent multi-dimensional transport effects. The convective heat transfer coefficients used for flow rates below 40 mL/min come from the mixed convection heat transfer correlation of Oliver [23] for laminar flow in heated horizontal tubes

$$\mathrm{Nu}=1.75\left(\frac{\mu}{\mu_{\mathrm{int}}}\right)^{0.14}[\mathrm{Gz}+0.0083(\mathrm{GrPr})^{0.75}]^{1/3} \qquad (12)$$

In Eq. (12), Nu is the Nusselt number, Gz is the Graetz number, Gr is the Grashoff number, and Pr is the Prandtl number. In the present computations which used correlations, the transport properties were calculated using the latest bulk temperature at a given axial location along the tube.

Figure 3 shows measured and predicted outlet fuel temperatures of the present model together with the finite difference calculations of the enthalpy and Navier-Stokes equations [22]. Figure 3 shows that the current predictions for flow rates below 40 mL/min which incorporate buoyancy effects by means of Eq. (12) agree well with the measurements and, thus, support the assertion of Katta et al. [22] of the formation of streamwise vortices. The turbulent finite difference solution agrees with the measurements because buoyancy forces provide an early transition to turbulent flow. In Fig. 3, between 40 and 80 mL/min, neither Eq. (12) nor the finite difference turbulent calculations yield adequate predictions because the flow is believed to become fully three-dimensional. Between 40 and 80 mL/min, this complex flow tran-

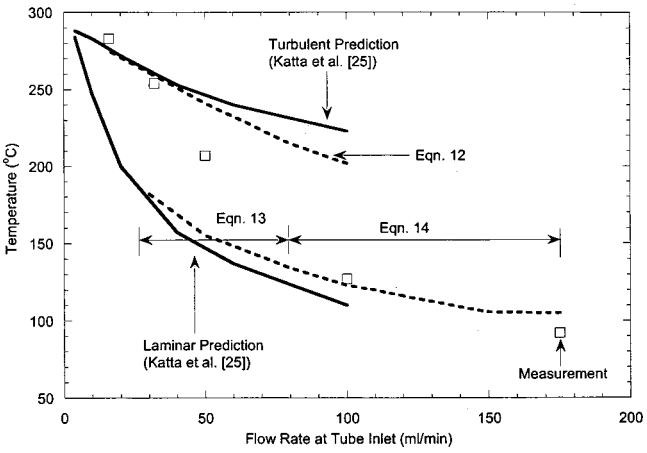

Fig. 3 Measured and predicted fuel temperatures at tube exit; 300°C block temperature

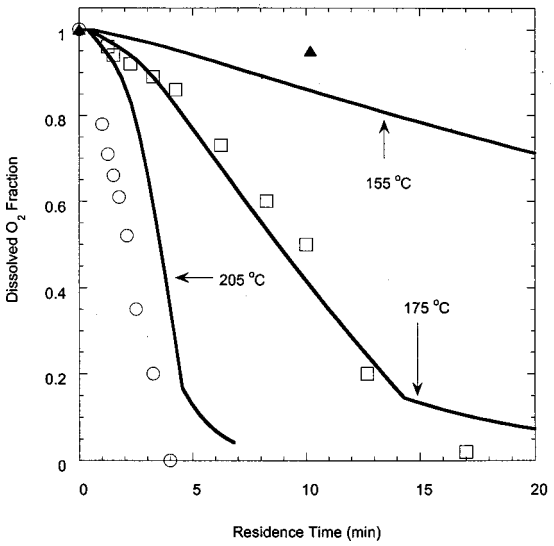

Fig. 4 Measured and predicted dissolved O_2 fractions for different tube wall temperatures. The curve is the current model prediction, and the symbols represent measurements obtained from NIFTR experiments [13] at a flow rate of 0.125 mL/min.

sitions to laminarlike flow because the measured temperatures begin to approach both the laminar finite difference prediction of Katta et al. [22] and the present computations which employed the laminar heat transfer correlation of Sieder and Tate [24]

$$\mathrm{Nu} = 1.86\left(\frac{\mathrm{Re\,Pr}\,D}{L}\right)^{1/3}\left(\frac{\mu}{\mu_{\mathrm{int}}}\right)^{0.14} \tag{13}$$

If desired, an alternative and more accurate heat transfer correlation could be developed for this flow regime. However, in the deposition experiments, the maximum flow rate was limited to 16 mL/min. As the flow rate increases beyond 80 mL/min, the Reynolds number approaches 2300, and the main flow transitions to turbulent flow. (In Fig. 3, 172 mL/min corresponds to Re~3900.) With mixed convection in small-diameter tubes, buoyancy-induced vortices are significant when the flow rate is low; they become less dominant as the main flow increases [21]. For laminar-turbulent transition and for fully turbulent flow, the heat transfer correlation of Gnielinski [25] has been used with reasonable success [21], and, thus, was used for simulations of the mixed laminar-turbulent and turbulent conditions.

$$\mathrm{Nu} = \frac{(F/8)(\mathrm{Re}-1000)\mathrm{Pr}}{1+12.7(F/8)^{1/2}(\mathrm{Pr}^{2/3}-1)} \tag{14}$$

In the Gnielinski correlation of Eq. (14), F is the friction factor within the tube and is given by Eq. (9). Figure 3 shows that the heat transfer correlations used in the present one-dimensional analysis provide reasonable solutions for the temperature of the fuel at the tube exit for flow rates between 80 and 175 mL/min.

Simulations of Dissolved O_2 Consumption. The consumption of dissolved O_2 is intimately tied to the formation of surface deposits, but the involved chemical and physical relationships are not well understood. Figure 4 shows predicted and measured dissolved O_2 fractions at the exit of a heated tube for fuel F2827 flowing at 0.125 mL/min (laminar flow-NIFTR conditions) through stainless-steel tubes [13] and for different imposed wall temperatures using the global chemical kinetic mechanism of Table 2. At a constant mass flow rate, any position along the tube may be directly related to the residence time through the average velocity which, in turn, can be found from the known inner tube diameter, mass flow rate, and fuel density. Thus, Fig. 4 shows the dissolved O_2 fraction as a function of residence time. In addition, Fig. 4 shows that as the tube wall temperature is increased from 155°C to 205°C, the residence time required for O_2 depletion decreases. Figure 5 shows measurements and predictions of dissolved O_2 consumption for conditions of the present experiments in which the imposed wall temperatures vary along the entire tube length. The predictions use the global chemical kinetic mechanism of Table 2 which was calibrated using fuel F2827 under the NIFTR conditions of Fig. 4. Figure 5 shows that the one-dimensional model predicts reasonably well the dissolved O_2 consumption of fuel F2827 under conditions that are very different from those used for model calibration.

To demonstrate that a more complex chemical kinetic mechanism may be used with the current one-dimensional model, the pseudo-detailed chemical kinetic mechanism for dissolved O_2 consumption of Table 3 was used. Concentrations for each species at the tube entrance were input to the numerical code along with species concentrations (O_2, AH, SH, RH, and I), tube wall temperature profile, and the grid resolution. With the activation energies and pre-exponential factors of Table 3, it is then possible to

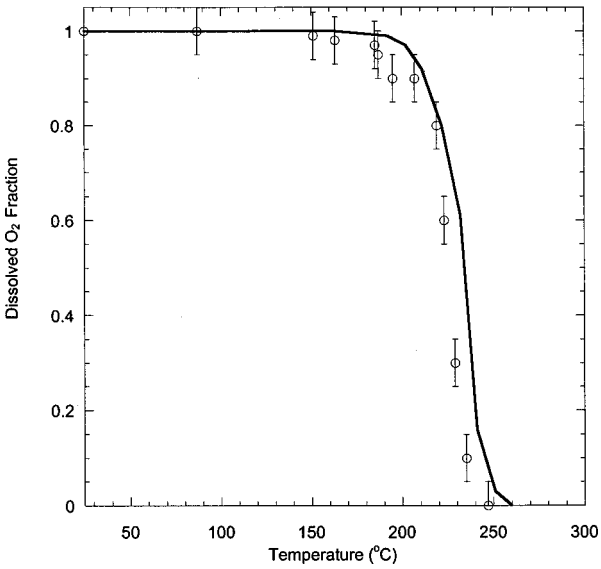

Fig. 5 Measured and predicted dissolved O_2 fractions for current experiments. The curve is the prediction of the current model, and the symbols represent measurements obtained from the current experiments at a flow rate of 16 mL/min using fuel F2827.

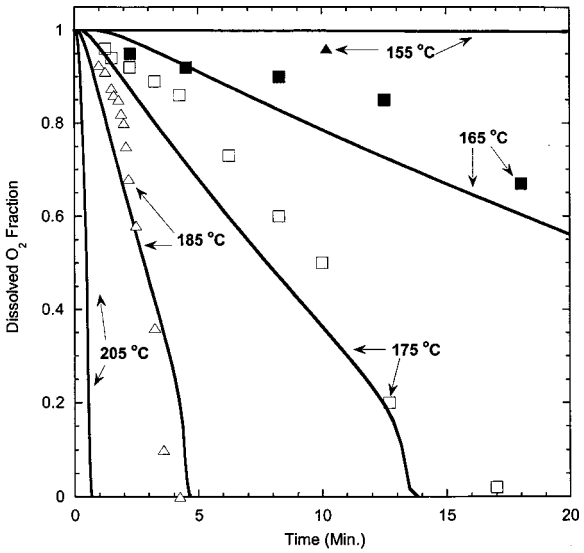

Fig. 6 Predicted and measured [13] dissolved O_2 removal for NIFTR experiments at a flow rate of 0.125 mL/min and fuel F2827. The curves are predicted values, and the symbols represent measurements.

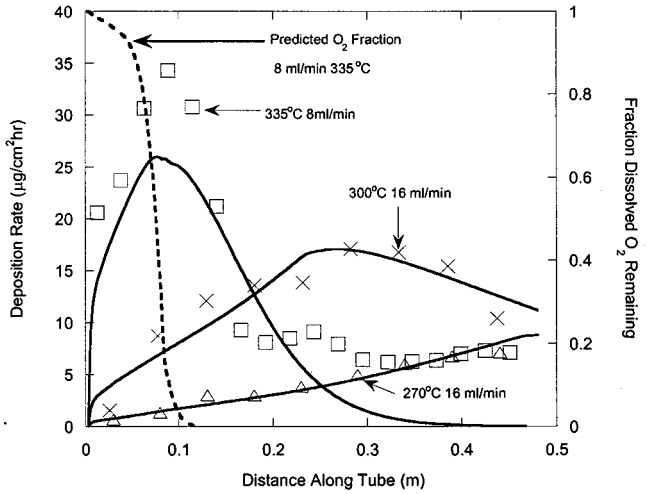

Fig. 7 Measured and predicted deposition rates along heated tube for fuel F2827 and copper block temperatures of 335°C (8 mL/min), 300°C (16 mL/min), and 270°C (16 mL/min). Predicted deposition rates are represented by the solid curves. In addition, the predicted fraction of dissolved O_2 remaining for conditions of a 335°C block temperature and flow rate of 8 mL/min is indicated by a dashed curve.

define different fuels in terms of their initial AH and SH concentrations. To provide the range of oxidation that a fuel may possess, the antioxidant AH, and the hydroperoxide decomposer, SH, can be modified for individual fuel samples. For the fuel F2827, AH and SH concentrations were chosen to match experimentally determined oxidation rates and hydroperoxide concentrations. The initial AH concentration was assumed to be 1.62×10^{-3} mol/L, which is a reasonable value for jet fuels, and the initial SH concentration was assumed to be 1.21×10^{-3} mol/L. For the same flow conditions as in Fig. 4 (0.125 mL/min), Fig. 6 shows measured and predicted dissolved O_2 fractions at the exit of a heated stainless-steel tube for fuel F2827 as a function of residence time. The initial AH and SH concentrations were adjusted to give an O_2 consumption history which followed the O_2 consumption at 185°C. O_2 consumption histories of F2827 at the other temperatures were predicted reasonably well using these initial concentrations of AH and SH. (It is mentioned in passing that differences between the dissolved O_2 fractions of Figs. 4 and 6 are due to substantial differences in the kinetic mechanisms.) Ultimately, this pseudo-detailed chemistry mechanism will be most useful if an analytical chemistry test could be used to determine ''effective'' AH and SH concentrations for individual jet fuel samples.

Simulations of Surface Deposition. It is important to vary the fuel temperature and residence time (flow rate) to demonstrate that the current global kinetics and transport models have a degree of generality in simulating surface deposition. For fuel F2827, Fig. 7 shows measured and predicted values of surface deposition rate along the heated tube length arising from block temperatures of 270°C and 300°C and a flow rate of 16 mL/min. In addition, Fig. 7 shows surface deposition rates for a higher block temperature of 335°C and a flow rate of 8 mL/min. A block temperature of 270°C (16 mL/min) produces an outlet fuel temperature of 241°C. Under this condition, the dissolved O_2 is not fully consumed and, as a consequence, the measured and predicted deposition rates essentially rise along the tube length, as does the fuel temperature. For a higher block temperature of 300°C (16 mL/min), the deposition rate increases over much of the tube and attains a maximum near 0.28 m. Measurements show that the dissolved O_2 is completely consumed at the tube exit. There the bulk fuel temperature is 275°C. For a block temperature of 300°C, the model predicts that the dissolved O_2 is depleted (not shown in Fig. 7) near the location where the deposition rate is a maximum, and this has been observed experimentally elsewhere [12]. In terms of the model, the surface deposition rate decreases as the dissolved O_2 concentration is depleted because the rate of production of precursor species is diminished. For a greater block temperature of 335°C (outlet fuel temperature of 310°C) and flow rate of 8 mL/min, Fig. 7 shows that the model predicts that the dissolved O_2 is entirely consumed early within the tube (near 0.1 m). Moreover, measurements indicate that the dissolved O_2 is depleted at the tube exit. In addition, the deposition rates along the tube prior to O_2 depletion are significantly greater than those observed for the other conditions. For this relatively high-temperature condition and long residence time, the predicted values of the deposition rate are lower than the measured rates along much of the tube length. However, the differences existing between the measurements and predictions are reasonable given the approximations involved in the global chemistry mechanism and the transport model. In further support of the model, the predicted location of the maximum deposition rate coincides with the actual location.

Under significantly different flow (0.125 and 0.5 mL/min) and temperature (185°C) conditions that are characteristic of the NIFTR, Fig. 8 shows measured [13,26] and predicted surface deposition rates for fuel F2827. In Fig. 8, the predicted deposition rates follow the measured values reasonably well. The predicted shapes of the deposition rate curves are similar to those of the measurements, and the peaks of the predicted curves lie near the locations of the peaks of the measured deposition rate curves for both flow rates. Thus, Fig. 8 shows that the Arrhenius multipliers determined from the current experiments using fuel F2827 satisfactorily predict surface deposition rates at much lower flow rates and temperatures. Under the conditions of Fig. 8, the dissolved O_2 is depleted before the fuel exits the heated tube. As might be expected from the behavior observed in Fig. 7, the locations of dissolved O_2 depletion are predicted to occur near the peaks in the deposition rates. It is interesting to note that a two-dimensional fluid dynamics computational model which incorporates the global mechanism of Table 1 [3] identical conditions and fuel predicts peaks in the surface deposition rates to occur at locations much further upstream of the maximum measured deposition rates. The global chemical kinetic and transport model presented

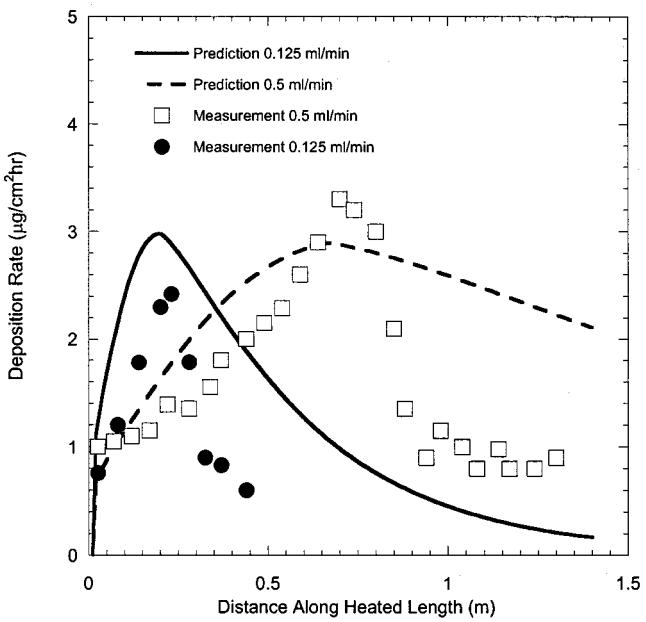

Fig. 8 Measured [13,26] and predicted surface deposition rates for NIFTR experiments

here appears to more accurately predict the location of the maximum surface deposition rate for these conditions.

In another test of the model, a different fuel, F3119, was used. Figure 9 shows measured and predicted surface deposition rates along the heated tube for a flow rate of 16 mL/min and a block temperature of 270°C (outlet fuel temperature of 241°C) for fuel F3119. In order for the current method to satisfactorily predict surface deposition rates for fuel F3119, the pre-exponential multiplier of the oxidation reaction and the concentration of species F_s were determined by calibration with experiment. Previous measurements of dissolved O_2 consumption show that fuel F3119 oxidizes more rapidly than fuel F2827, and a value of 2×10^{11} mole m^{-3} s^{-1} for the pre-exponential multiplier of the oxidation reaction (Table 2) sufficiently represents oxidation of F3119 over a range of temperatures. In the original calibration of the global mechanism of Table 2 using fuel F2827, F_s was taken as unity. In order for the measured and predicted surface deposition rates to agree for fuel F3119, F_s was adjusted to be 0.4 mol/L. Although not shown here, the simulations of oxidation and deposition for fuel F3119 agree well with measurements at other conditions. For similar flow and thermal conditions (block temperature of 270°C and flow rate of 16 mL/min), it is interesting to compare deposition rates for fuels F2827 (Fig. 7) and F3119 (Fig. 9). Figure 9 shows that the dissolved O_2 is depleted at the tube exit for fuel F3119, and there is a peak in the surface deposition rate. In contrast, a maximum in the surface deposition rate is not reached within the heated tube using fuel F2827 with this block temperature and flow rate (Fig. 7).

Limitations of the Model. Although the present model has many advantages, particularly in the modeling of the dynamics of an entire fuel system, the model has limitations:

1 For complex flow geometries in which two or three-dimensional effects are significant, the multidimensional fluid dynamics and heat transfer may not be adequately represented by a one-dimensional model.

2 Some understanding of the fluid dynamics must be known a priori such that the appropriate heat transfer correlations are chosen to provide realistic convective heat and mass transfer coefficients.

3 As the fuel passes through the heated tube, the deposits accumulate at the internal tube surface. With time, the axial thermal

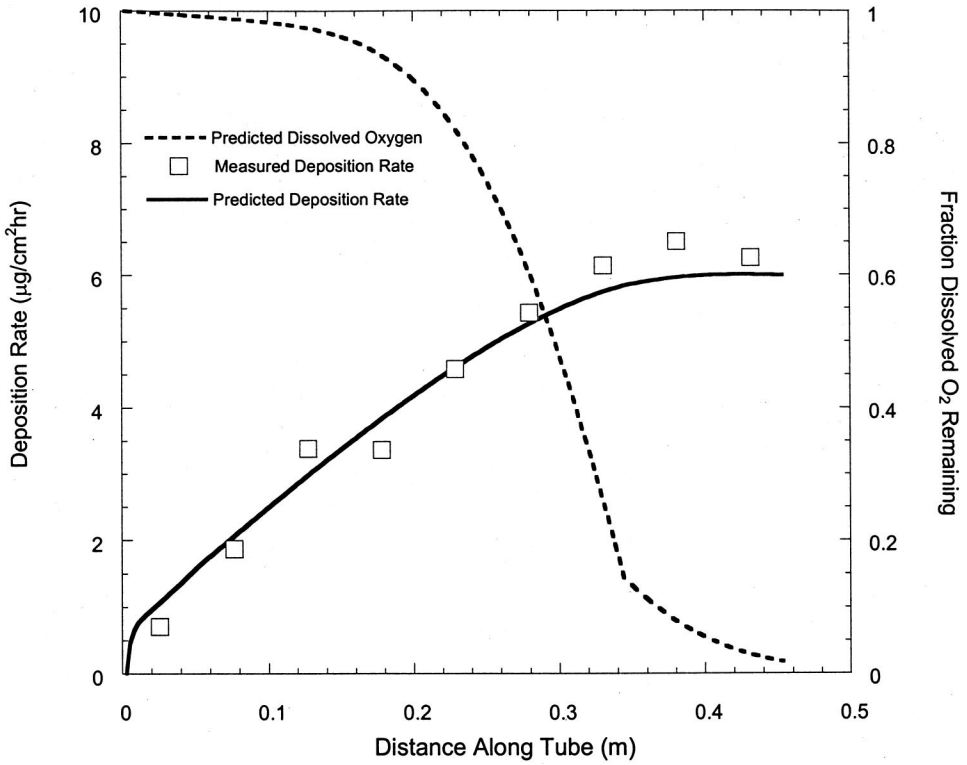

Fig. 9 Deposition rate along heated tube for fuel F3119, 270°C block temperature, and 16 mL/min flow rate

conduction through the deposit may become significant, and the assumption of radial conduction alone through the deposit becomes invalid.

Conclusions

In this study, a one-dimensional computational model of the fluid dynamics and thermal-oxidative chemistry for flowing jet fuel was developed. Because the model is one-dimensional, the numerical algorithm is simple and computationally inexpensive. Experiments were performed using a heat exchanger which simulated a complex thermal and flow environment. Dissolved O_2 consumption and surface deposition were measured for relatively slow oxidizing straight-run jet fuels. The predictions of the one-dimensional model compared well with the measurements. Because of the accuracy and simplicity of this model, it can assist in the simultaneous simulation of all fuel system components and, thus, will benefit aircraft designers.

Acknowledgments

This work was supported by the U.S. Air Force Research Laboratory, Propulsion Directorate, Propulsion Sciences and Advanced Concepts Division, Wright-Patterson Air Force Base, Ohio under Contract No. F33615-97-C-2719 (Technical Monitor: C.W. Frayne).

Nomenclature

A = pre-exponential multiplier, units vary
A_c = cross-sectional area within tube, m^2
AH = hindered phenol-like species
c = dimensionally correct constant in Eq. (5)
c_p = specific heat, J/kg K
D = hydraulic diameter, m
D_{bulk} = bulk insolubles
D_i = diffusion coefficient for ith species, L/(ms)
D_{int} = surface deposit
e = absolute surface roughness, m
E = activation energy, kcal/mole
f_i = mass fraction of ith species, dimensionless
f_i^{int} = mass fraction of ith species at deposit-fuel interface, dimensionless
F = friction factor, dimensionless
F_s = trace species required for formation of deposit precursor
g = gravitational acceleration, m/s^2
Gr = Grashoff no., $(g\beta(T_{\text{int}}-T)D^3\rho^2)/\mu^2$, dimensionless
Gz = Graetz no., $(\text{Re}\,\text{Pr}\,D)/L$, dimensionless
h = fuel enthalpy, J/kg
h_{conv} = convection heat transfer coefficient, $W/(m^2K)$
h_{m} = mass transfer coefficient, m/s
I = initiator species
k = fuel thermal conductivity, W/(mK); rate constant, units vary
L = tube length, characteristic length, m
M = mass flow rate, kg/s
MP = molecular weight of precursor species, g/mole
MO_2 = molecular weight of O_2, g/mole
n = reaction order Eq. (4); constant in Eq. (5), dimensionless
Nu = Nusselt no., $(h_{\text{con}}D)/k$, dimensionless
$\mathcal{P}$ = tube internal perimeter; deposit-forming precursor, m
Pr = Prandtl no., $c_p\mu/k$, dimensionless
P = pressure, kPa
r = radius of deposit-fuel interface, m
r^o = radius of deposit-fuel interface at previous time step, m
R = universal gas constant, kcal/(mole K)
Re = Reynolds no.; $\text{Re}=4m/\pi\mu D$, dimensionless
RH = fuel
ROO* = alkyl peroxy radical
SH = hydroperoxide-decomposing species
t = time, s
T = fuel temperature, K
T_{int} = deposit-fuel interface temperature, K
u = flow velocity, m/s
x = axial location within tube, m
ρ = fuel density, kg/m^3
ρ_{dep} = deposit density, kg/m^3
μ = dynamic viscosity, Ns/m^2
τ_{int} = shear stress at deposit-fuel interface, kPa
ω_i = rate of production or removal of ith species, $kg/(m^3s)$
Ω = deposition rate, $kg/(m^2s)$

Subscripts

int = deposit-fuel interface
dep = deposit
i = ith species
bulk = bulk fuel property

Superscript

int = deposit-fuel interface

References

[1] Hazlett, R. N., 1991, *Thermal Oxidative Stability of Aviation Turbine Fuels*, American Society for Testing and Materials, Philadelphia, PA.
[2] Krazinski, J. L., Vanka, S. P., Pearce, J. A., and Roquemore, W. M., 1992, ''Computational Fluid Dynamics and Chemistry Model for Jet Fuel Thermal Stability,'' ASME J. Eng. Gas Turbines Power, **114**, pp. 104–110.
[3] Katta, V. R., and Roquemore, W. M., 1993, ''Numerical Method for Simulating Fluid Dynamic & Heat Transfer Changes in Jet Engine Injector Feed Arm Due to Fouling,'' J. Thermophys. Heat Transfer, **7**, pp. 651–660.
[4] Ervin, J. S., and Zabarnick, S., 1998, ''Computational Fluid Dynamics Simulation of Jet Fuel Oxidation Incorporating Pseudo-Detailed Chemical Kinetics,'' Energy Fuels, **12**, pp. 344–352.
[5] Zabarnick, S., and Grinstead, R., 1994, ''Studies of Jet Fuel Additives Using the Quartz Crystal Microbalance & Pressure Monitoring at 140C,'' Ind. Eng. Chem. Res., **33**, pp. 2771–2777.
[6] Chin, J., Rizk, N., and Razdan, M., 1995, ''Engineering Model for Prediction of Deposit Rates in Heate Fuels,'' 31st AIAA/ASME/SAE/ASEE Joint Propulsion Conference and Exhibit, San Diego, CA.
[7] Despande, G. V., Michael, A. S., Solomon, P. R., and Malhotra, R., 1989, ''Modeling of the Thermal Stability of Aviation Fuels,'' 198th ACS National Meeting, Symposium on the Chemical Aspects of Hypersonic Propulsion, Miami FL.
[8] Arpaci, V. S., 1966, *Conduction Heat Transfer*, Addison-Wesley, Reading, MA.
[9] Katta, V. R., Jones, E. G., and Roquemore, W. M., 1993, ''Development of Global Chemistry Model for Jet-Fuel Thermal Stability Based on Observations from Static and Flowing Experiments,'' 81st AGARD Symposium on Fuels and Combustion Technology for Advanced Aircraft Engines, AGARD-CP-536, Paper No. PEP-19, Collifero, Italy.
[10] Chamra, L. M., and Webb, R. L., 1993, ''Effect of Particle Size and Size Distribution on Particulate Fouling in Enhanced Tubes,'' J. Enhanced Heat Transfer, **1**, pp. 65–75.
[11] Coordinating Research Council, 1983, *Handbook of Aviation Fuel Properties*, Atlanta, GA.
[12] Ervin, J. S., Williams, T. F., and Katta, V. R., 1996, ''Global Kinetic Modeling of Aviation Fuel Fouling in Cooled Regions in a Flowing System,'' Ind. Eng. Chem. Res., **35**, pp. 4028–4036.
[13] Jones, E. G., Balster, W. J., and Post, M. E., 1995, ''Degradation of A Jet Fuel In A Single-Pass Heat Exchanger,'' ASME J. Eng. Gas Turbines Power, **117**, pp. 125–131.
[14] Zabarnick, S., 1998, ''Pseudo-Detailed Chemical Kinetic Modeling of Antioxidant Chemistry for Jet Fuel Applications,'' Energy Fuels, **12**, pp. 547–553.
[15] Ervin, J. S., and Heneghan, S. P., 1998, ''The Meaning of Activation Energy and Reaction Order in Autoaccelerating Systems,'' ASME J. Eng. Gas Turbines Power, **120**, pp. 468–476.
[16] Epstein, N., 1986, *Heat Exchanger Sourcebook*, J. W. Pale, ed., Hemisphere, Washington DC.
[17] Miller, R. W., 1983, *Flow Measurement Engineering Handbook*, McGraw-Hill, New York, NY.
[18] Nixon, A. C., Ackerman, G. H., Faith, L. E., Henderson, H. T., Ritchie, A. W., Ryland, L. B., and Shryne, T. M., 1967, ''Vaporizing and Endothermic Fuels for Advanced Engine Application: Part III, Studies of Thermal and Catalytic Reactions, Thermal Stabilities, and Combustion Properties of Hydrocarbon Fuels,'' AFAPL-TR-67-114, 3, Wright-Patterson AFB, OH.
[19] Scott, G., 1963, ''Antioxidants,'' Chem. Ind., pp. 271–281.
[20] Zabarnick, S., 1993, ''Chemical Kinetic Modeling of Jet Fuel Autoxidation and Antioxidant Chemistry,'' Ind. Eng. Chem. Res., **32**, pp. 1012–1017.

[21] Kakac, S., Shah, R. K., and Aung, W., 1987, *Handbook of Single-Phase Convective Heat Transfer*, Wiley, New York, NY.
[22] Katta, V. R., Blust, J., Williams, T. F., and Martel, C. R., 1995, ''Role of Buoyancy in Fuel-Thermal-Stability Studies,'' J. Thermophys. Heat Transfer, **9**, pp. 159–168.
[23] Oliver, D. R., 1962, ''The Effect of Natural Convection on Viscous-Flow Heat Transfer in Horizontal Tubes,'' Chem. Eng. Sci., **17**, pp. 335–350.
[24] Sieder, E. N., and Tate, C. E., 1936, ''Heat Transfer and Pressure Drop of Liquids in Tubes,'' Ind. Eng. Chem., **28**, pp. 1429–1435.
[25] Gnielinski, V., 1976, ''New Equations for Heat and Mass Transfer in Turbulent Pipe Channel Flow,'' Int. Chem. Eng., **16**, pp. 359–368.
[26] L. P. Chin, V. R. Katta, and S. P. Heneghan, 1994, ''Computer Modeling of Deposits Formed in Jet Fuels,'' 207th ACS National Meeting, Symposium on Autooxidation of Distillate Fuels, San Diego, CA.

L. Studies of Jet Fuel Freezing by Differential Scanning Calorimetry

Studies of Jet Fuel Freezing by Differential Scanning Calorimetry

Steven Zabarnick* and Nikki Widmor

University of Dayton Research Institute and Department of Mechanical and Aerospace Engineering, 300 College Park, Dayton, Ohio 45409-0140

Received March 27, 2001

Differential scanning calorimetry (DSC) was used to study the freezing of jet fuel and the effect of cold flow improving additives. We find that the cooling (freezing) exotherm is a more useful diagnostic tool for this purpose than the heating (melting) endotherm. Jet fuels (Jet A, JP-8, and Jet A-1) display a strong exotherm upon cooling between −45 and −60 °C. By the study of mixtures composed of classes of jet fuel components (normal paraffins, isoparaffins, and aromatics), we find that the cooling exotherm is primarily due to the liquid−solid phase transition of the normal paraffins. Cold flow improving additives (e.g., pour point depressants) show only small effects on the DSC exotherm despite larger effects observed in cold flow devices. This indicates that these additives work primarily by affecting the habit of the *n*-alkane crystals. This change in crystal habit is supported by low-temperature microscopy studies.

Introduction

The operation of aircraft at high altitudes for long periods of time can subject jet fuel to extremely low temperatures. Such conditions result in greatly increased fuel viscosity and, at the most extreme conditions, partial solidification of the fuel. The U.S. Air Force uses the specialty fuel JPTS for the high altitude mission of the U-2 aircraft. JPTS exhibits a low freeze point and excellent high temperature thermal stability, but unfortunately is relatively expensive. Replacement of JPTS with the less expensive JP-8 fuel would be attractive for both economic and logistical reasons. This work is part of a program in which the Air Force is investigating the use of additives to improve both the cold flow and high temperature thermal stability properties of JP-8 fuel.[1]

Differential scanning calorimetry (DSC) is a well-known thermal analysis technique that can yield information on phase transitions such as transition temperatures and enthalpies.[2] It has been successfully employed to study wax formation in lubricating oils, crude oils, and diesel fuels.[3−6] To date, very little work has been performed using DSC to investigate the freezing of jet fuels. In this work, we investigate the use of DSC to study the liquid−solid phase transitions of jet fuels and the effect of various component mixtures on the DSC response. One objective is to study the utility of DSC in providing a rapid, low-cost technique for evaluation of cold flow improving additives for jet fuel. A second objective is to use DSC for fundamental studies of fuel crystallization and wax formation, and to provide fundamental parameters of fuel thermodynamics that are needed for the modeling of the fuel crystallization process.

Table 1. Select Properties of Fuels Studied

fuel designation	fuel type	wt % aromatics	wt % *n*-alkanes	freeze point (°C)	cloud point (°C)	pour point (°C)
POSF-3219	Jet A	18.3	22.1	−46.3	−50.9	−56.0
POSF-2827	Jet A	17.4	23.0	−43.4	−48.0	−52.5
POSF-3657	JPTS	NA	30.0	−53.8	−57.8	−64.5

Experimental Section

DSC data were acquired using a TA Instruments DSC 2920 equipped with a Liquid Nitrogen Cooling Accessory (LNCA). The LNCA directs a mixture of gaseous and liquid nitrogen to the sample chamber that permits thermal analysis data to be acquired at subambient temperatures. Typically, 20 μL of liquid fuel is sampled using a chromatographic syringe, injected into an open aluminum sample pan, and subsequently weighed. An empty aluminum pan is used for the reference. Most data were acquired at a cooling rate of 1 °C/min over the temperature range −45 to −65 °C.

Cloud point, pour point, and freeze point data were acquired using a Phase Technology PSA-70V Petroleum Analyzer, via ASTM D5773-95, D5949-96, and D5972-96, respectively. The pour point analyses were conducted at 1 °C intervals.

The jet fuels were obtained from the Fuels Branch (PRTG) of the Turbine Engine Division of the Propulsion Directorate of the Air Force Research Laboratory at Wright-Patterson AFB, Ohio. Cloud point, pour point, and freeze point data for the fuels studied are listed in Table 1. Norpar 13, Isopar M,

* Author to whom correspondence should be addressed. Phone/voice: (937) 255-3549. Fax: (937) 252-9917. E-mail: zabarnick@udri.udayton.edu.

(1) Ervin, J. S.; Zabarnick, S.; Binns, E.; Dieterle, G.; Davis, D.; Obringer, C. *Energy Fuels.* **1999**, *13*, 1246−1251.
(2) Wendlandt, W. W. *Thermal Analysis*; Wiley: New York, 1986.
(3) Noel, F. *Thermochim. Acta* **1972**, *4*, 377−392.
(4) Letoffe, J. M.; Claudy, P.; Garcin, M.; Volle, J. L. *Fuel* **1995**, *74*, 92−95.
(5) Aboul-Gheit, A. K.; Abd-el-Moghny, T.; Al-Eseimi, M. M. *Thermochim. Acta* **1997**, *306*, 127−130.
(6) Srivastava, S. P.; Tandon, R. S.; Verma, P. S.; Pandey, D. C.; Goyal, S. K. *Fuel* **1995**, *74*, 928−931.

10.1021/ef010074b CCC: $20.00
Published on Web 09/26/2001

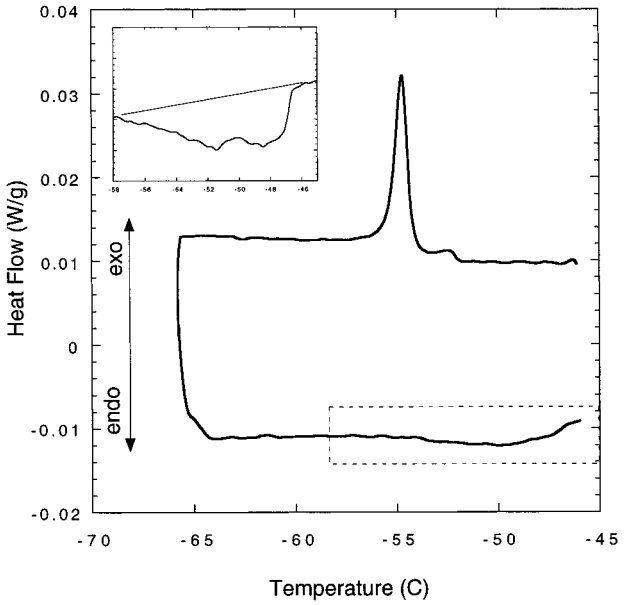

Figure 1. DSC curve for a Jet A fuel (POSF-3219) with cooling and heating rates of 1 °C/min. The inset shows the dotted area expanded to reveal the melting endotherm.

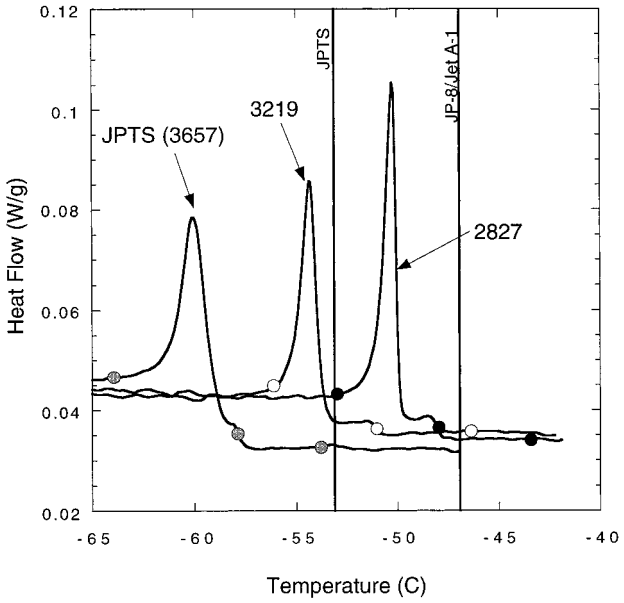

Figure 2. DSC cooling curves for three fuels. Also shown are pour (lowest temperature), cloud (intermediate temperature), and freeze points (highest temperature) for each fuel (POSF-2827 black circles, POSF-3219 open circles, and POSF-3657 {JPTS} gray circles). Also shown are vertical lines at −53 °C and −47 °C to represent the JPTS and JP-8/Jet A-1 freeze point specifications, respectively.

and Aromatic 200 were obtained from ExxonMobil. Select properties data for these solvents are shown in Table 2 in comparison with Jet A and JP-8 fuels. Dodecane (99+%) was obtained from Sigma-Aldrich and used without further purification.

Results and Discussion

Understanding Jet Fuel DSC Exotherms. Initial DSC scans on heating and cooling of jet fuel revealed liquid−solid phase transitions in the temperature range −45 to −60 °C. A typical cooling exotherm and heating endotherm are shown in Figure 1 for a Jet A fuel (POSF-3219). The figure shows that upon cooling from −45 to −65 °C a significant exothermic feature is observed near −55 °C. This is due to crystallization of at least some components which constitute the complex fuel mixture. Upon subsequent heating over the same temperature range, a broad, endothermic feature is noted, centered near −50 °C (see inset of Figure 1), which corresponds to the melting of the fuel components. It is apparent from the figure that the cooling exotherm is a more attractive feature to study due to its larger intensity and greater signal-to-noise ratio. Also, fuel cooling is more relevant to the processes of interest in aircraft fuel systems and for the study of additives. All subsequent work will concentrate on this exothermic feature obtained upon cooling.

If during the entire heating and cooling process thermal equilibrium could be assured, the heating and cooling DSC curves would look like mirror images. The observed narrow lower temperature cooling curve (obtained during freezing) and broad higher temperature heating curve (obtained during melting) are indications that supercooling of the fuel occurs during the cooling process.[7] Runs performed over a range of cooling rates also indicate that supercooling is present.[8] In these studies DSC curves were obtained at three cooling rates with and without an added pour-point depressing additive. The neat fuel displayed differences in location of the beginning of freezing exotherm, indicative of supercooling. The presence of the additive, which increases nucleation, greatly reduces this effect, which supports the presence of supercooling. Thermal lag between the fuel sample and the calorimeter heating block can also account for some of the temperature difference observed. Often, supercooling results in irreproducible freezing behavior due to the variations in availability of nucleation sites. In the present study of jet fuels and hydrocarbons, this irreproducibility was not observed. All DSC freezing curves could be reproduced within ±0.2 °C.

Figure 2 shows a comparison of the DSC exotherms for three different fuels: two Jet A fuels (POSF-3219 and POSF-2827) and a JPTS fuel (POSF-3657). Also shown in the figure are the measured freeze points, cloud points, and pour points for the three fuels. The figure shows that the main exotherm varies by almost 10 °C for these fuels. The cloud and pour points of each of the fuels bracket the DSC exotherm. The measured cloud points are found on the rising edge of the high temperature "shoulder" of each exotherm. The measured pour points are located on the low-temperature side of the exotherm, near where the exotherm returns to baseline. Presumably, this return to baseline indicates complete crystallization of the fuel components. The measured freeze points are 4−5 °C higher in temperature than the cloud points for each of the fuels studied.

(7) Moynihan, C. T.; Shahriari, M. R.; Bardakci, T. *Thermochim. Acta* **1982**, *52*, 131−141.

(8) Widmor, N.; Ervin, J. S.; Vangsness, M.; Zabarnick, S. Studies of Jet Fuel Freezing by Differential Scanning Calorimetry and Cold-Stage Microscopy. Presented at the ASME Turbo Expo 2001, New Orleans, 2001.

Table 2. Select Properties of Solvents Studied

solvent or fuel designation	composition	initial boiling point (°C)	dry point (°C)	flash point (°C)
Norpar 13	97 vol % min paraffins, primarily *n*-C_{12}, *n*-C_{13}, and *n*-C_{14}	221 min	248 max	93 min
Isopar M	0.05 wt % max aromatics	218 min	257 max	80.5 min
Aromatic 200	98.0 % min aromatics	230 min	293 max	95 min
Jet A	22 vol % max aromatics	205 max 10% recovered temperature	300 max	38 min
JP-8	25 vol % max aromatics	205 max 10% recovered temperature	300 max	38 min

The exotherm of the highest freezing fuel, POSF-2827, is centered near −50 °C with a freeze point near −43 °C. The POSF-3219 exotherm is centered near −55 °C and has a freeze point near −47 °C, which is just at the JP-8 specification limit. Thus, POSF-3219 is a "worst case" fuel for low-temperature JP-8 behavior, and it has been selected for subsequent additive studies. The JPTS fuel (POSF-3657) has an exotherm centered near −60 °C with a freeze point near −54 °C. This is a JPTS fuel that has a freeze point close to the JPTS freeze point specification (−53 °C) and, thus, is a relevant fuel to use as a goal of the additive program.

Figure 2 also shows that the freeze point temperatures are always several degrees higher than the main cooling exotherm. This is expected as the ASTM freeze point specification is actually a melting point measurement (measured as the temperature at which solid crystals completely disappear upon heating). Also, the cloud point measurements are near the initial part of the exotherm peak. This is also expected, as the cloud point is an indication of the beginning of the crystallization process upon cooling. The figure shows that to change a fuel which meets the minimum JP-8 freeze point specification to a JPTS fuel would require a decrease in the freezing exotherm of about 5 °C. Fortunately, changes in the location of the exotherm are not necessarily required because an additive that affects the crystal habit or structure could enable fuel to flow at low temperatures without changing the exotherm location.[7,9,10] Thus, a change in the temperature of the freezing exotherm and/or a change in the crystal properties are required.

Previous work on diesel fuels has shown that the long-chain normal alkanes are the species that crystallize at relatively high temperatures and form a flow resistant matrix with the liquid portions of fuel.[9] In diesel fuels, these *n*-alkanes are typically in the range C_{24} to C_{28}. Moynihan et al.[11] and Van Winkle et al.[12,13] showed that *n*-alkanes were significantly concentrated in solids separated from partially frozen JP-5 fuels. These workers also observed that the crystalline solids entrapped large amounts of liquid fuel. These studies suggest, that for the jet fuels studied here, the large normal alkanes are the first species to crystallize (i.e., *n*-C_{15} to *n*-C_{17}).

To employ the measured DSC curves for the study of jet fuel crystallization, we need to identify the species that cause the resulting exotherm. Jet fuels are primarily composed of the following species: normal alkanes, branched alkanes (i.e., isoalkanes), cycloalkanes (i.e., naphthenes), and aromatics. Table 3 lists heat of fusion values for selected compounds for each of these classes. The table shows that relatively large normal alkanes have heat of fusion values that are significantly larger than the other classes of species. Thus, one would expect that most of the exothermic response we have noted is due to normal alkane crystallization. To confirm this hypothesis, we have selected commercially available mixtures of three of these chemical classes for study in the DSC. ExxonMobil Norpar 13 was used to represent the normal alkanes, ExxonMobil Isopar M was used for the isoalkanes, and ExxonMobil Aromatic 200 was used for the aromatics. A suitable mixture of cycloalkanes could not be located. Each of these three mixtures has a distillation range whose midpoint is near that of jet fuel and thus should contain species that are representative of those found in jet fuel (Table 2).

Table 3. Enthalpy of Fusion Values for Fuel Compound Types[16]

chemical class	species	heat of fusion (kJ/mol)
normal alkanes	*n*-dodecane	36.6
	n-octadecane	61.4
branched alkanes	2,2,4,4-tetramethylpentane	9.8
cycloalkanes	methylcyclohexane	6.8
	ethylcyclohexane	8.3
	butylcyclohexane	14.2
	cyclooctane	2.4
aromatics	benzene	6.9
	o-xylene	13.6
	propylbenzene	9.3
	naphthalene	19.1

Figures 3−5 show DSC cooling curves for each of these mixtures. The Isopar M curve in Figure 3 shows no significant exotherm down to −65 °C. Experiments down below −100 °C showed a very small exotherm near −105 °C (not shown). Branched alkanes, such as contained in Isopar M, tend to have a more spherical molecular geometry than *n*-alkanes that minimizes the intermolecular attractive forces and thus minimizes the energy that is released upon formation of crystals at low temperature. This is also apparent from the heat of fusion values shown in Table 3. Figure 4 shows the DSC curve for the Aromatic 200 mixture. Aromatic 200 displays a somewhat narrow exotherm near −15 °C, with a broad baseline shift out to −50 °C. This curve appears to be the superposition of two types of transitions: a narrow crystallization transition and a broad glass transition. Aromatics are commonly found to display glass transitions in which an amorphous solid structure is formed, as opposed to a crystalline structure. This type of behavior is not observed in our jet

(9) Lewtas, K.; Tack, R. D.; Beiny, D. H. M.; Mullin, J. W. In *Advances in Industrial Crystallization*; Garside, J., Davey, R. J., Jones, A. G., Eds.; Butterworth Heinemann: Oxford, 1991; pp 166−179.

(10) Dunn, R. O.; Schockley, M. W.; Bagby, M. O. *J. Am. Oil Chem. Soc.* **1996**, *73*, 1719−1728.

(11) Moynihan, C. T.; Mossadegh, R.; Bruce, A. J. *Fuel* **1984**, *63*, 378−384.

(12) Van Winkle, T. L.; Affens, W. A.; Beal, E. J.; Mushrush, G. W.; Hazlett, R. N.; DeGuzman, J. *Fuel* **1987**, *66*, 890−896.

(13) Van Winkle, T. L.; Affens, W. A.; Beal, E. J.; Mushrush, G. W.; Hazlett, R. N.; DeGuzman, J. *Fuel* **1987**, *66*, 947−953.

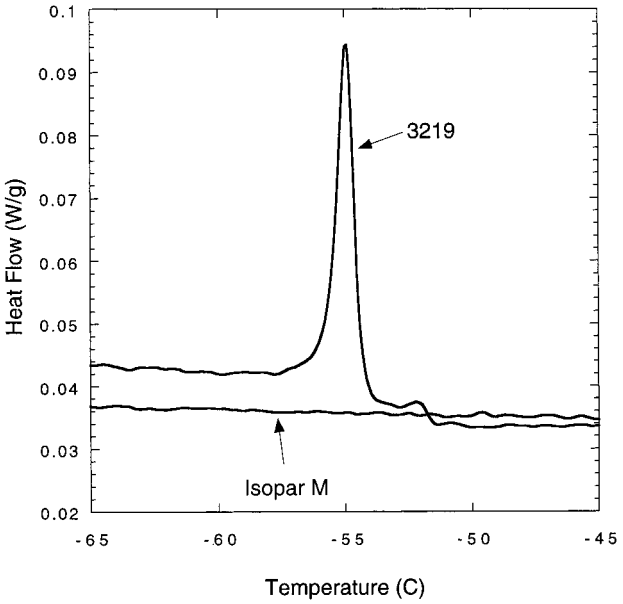

Figure 3. DSC cooling curves for Isopar M and a jet fuel.

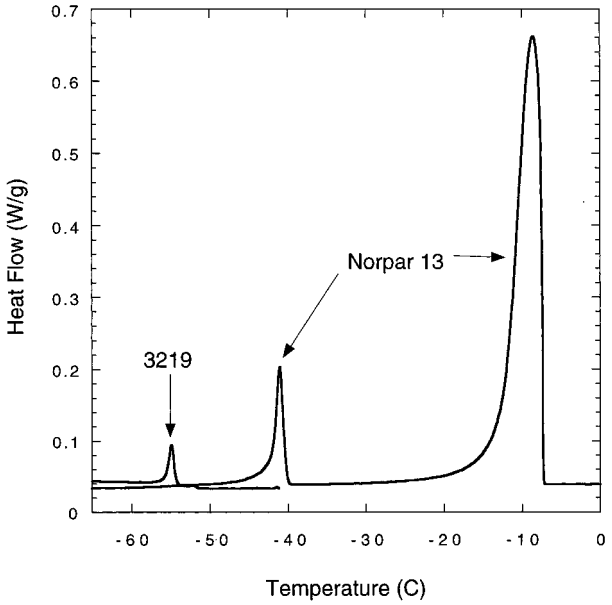

Figure 5. DSC curves for Norpar 13 and a jet fuel.

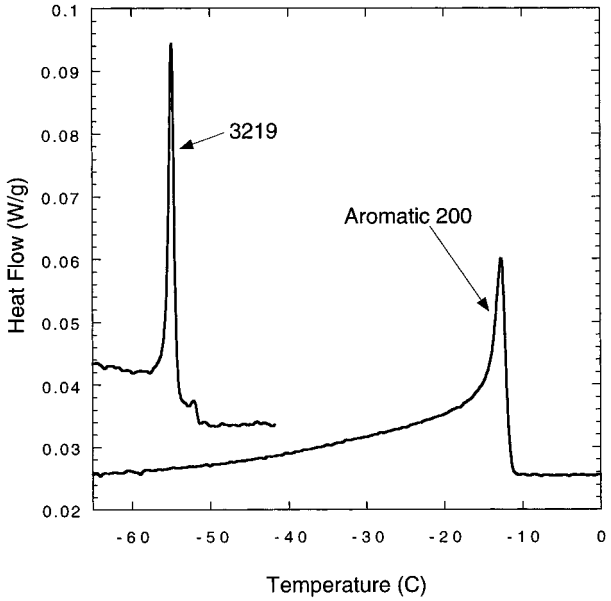

Figure 4. DSC curves of Aromatic 200 and a jet fuel.

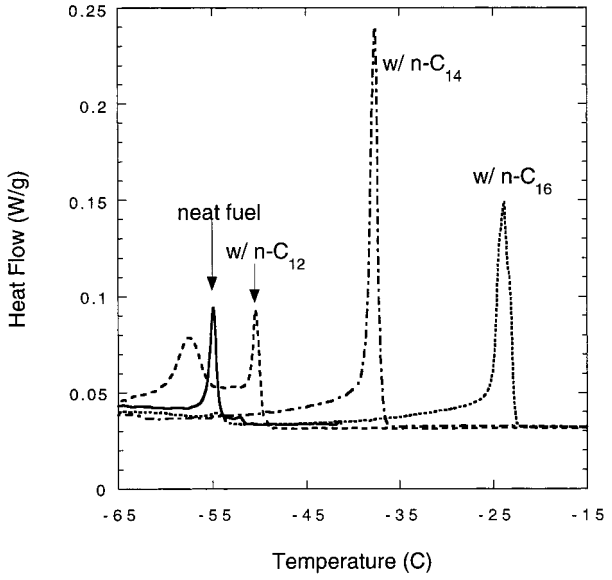

Figure 6. DSC curves for a Jet A fuel (POSF-3219) with 10% added alkane: neat fuel (solid line), with n-dodecane (dashed line), with n-tetradecane (dot−dashed line), and with n-hexadecane (dotted line).

fuel data. Also, the magnitude of the transition seen in Aromatic 200 is not large enough to account for the observed transition in jet fuel when one takes into account the approximate 15−20% aromatic composition of jet fuels (see Table 1). Figure 5 shows the DSC curve obtained for Norpar 13. Norpar 13 displays two very large transitions near −10 and −40 °C. It is well-known that odd carbon number normal alkanes display a solid−solid transition in addition to a liquid−solid transition.[14] Norpar 13, which consists mainly of *n*-C_{12}, *n*-C_{13}, and *n*-C_{14}, displays a solid−solid transition feature (near −40 °C) due to the large concentration of *n*-C_{13}. The main transition near −10 °C is the liquid−solid transition. It is apparent from comparison with the jet fuel exotherm that the Norpar 13 mixture yields an exotherm that is large enough to account for the feature observed in the jet fuel when considering the concentration of normal alkanes expected. Thus we conclude that the exothermic feature observed upon cooling of jet fuel is mainly due to the crystallization of the large normal alkanes present.

Studies of Mixtures of Fuel Components. To further our understanding of the DSC curves of jet fuel and to better understand the importance of the individual compound classes in the freezing process, we prepared a series of mixtures of fuel, the commercially available mixtures studied above, and pure compounds.

The primary feature observed via DSC upon the freezing of jet fuel is due to the crystallization of normal alkanes. By adding additional normal alkanes, we can study the effect of concentration and the interaction between the various normal alkanes present. In Figure 6 we show DSC curves obtained on mixtures of POSF-3219 jet fuel with 10% added n-dodecane, n-tetradecane,

(14) Turner, W. R. *Ind. Eng. Chem. Prod. Res. Dev.* **1971**, *10*, 238−260.

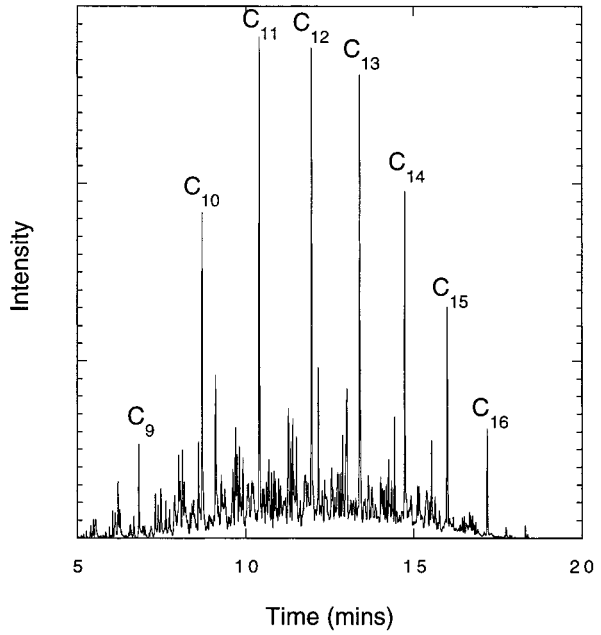

Figure 7. Chromatogram of fuel POSF-3219 showing normal alkane constituents.

and n-hexadecane. The chromatogram of Figure 7 shows that n-hexadecane is the largest normal alkane present in this fuel with a significant concentration. Thus, n-hexadecane is likely to be one of the major species involved in crystallization of this fuel. Figure 6 shows two significant changes that occur when 10% n-hexadecane is added to the fuel. In the first, a large exothermic feature is observed near −25 °C. Additionally, the exotherm near −55 °C, which was observed for the neat fuel, has been nearly completely eliminated. Interestingly, the elimination of the peak near −55 °C indicates that the species that were crystallizing at this temperature in the neat fuel are no longer freezing out at this temperature. These species now appear to be co-crystallizing with the n-hexadecane near −25 °C (the melting point of pure n-hexadecane is 18.2 °C). In binary systems, it is well-known that normal alkane species that are similar in carbon number form solid solutions, while those that are significantly different in size display eutectic behavior.[14] Figure 6 suggests the formation of a solid solution between the added n-hexadecane and the normal alkanes present in the fuel. The chromatogram of Figure 7 shows that the fuel contains normal alkanes over the range C_9 to C_{16}.

Figure 6 shows similar solid-solution behavior for n-tetradecane, which displays a large exotherm near −38 °C. In contrast, the behavior of n-dodecane is more indicative of a eutectic system (near complete insolubility of solids). Upon addition of n-dodecane, two exotherms are observed near −50 and −57 °C. Apparently, a portion of the n-dodecane crystallizes in this mixture at −50 °C with some of the larger *n*-alkanes. The remaining *n*-alkanes present crystallize separately, which results in a freezing exotherm that is slightly reduced (ca. 2 °C) from that of the neat fuel. The different behavior observed for n-dodecane, relative to the larger species n-tetradecane and n-hexadecane, is due to the relative size differences between these species and the normal alkanes present in the fuel. The figure indicates that the larger normal alkanes ($\geq C_{14}$) are more important in the freezing process that the smaller alkanes present in the fuel. These studies of adding normal alkanes have provided us insight into the behavior of these species in the complex fuel mixture.

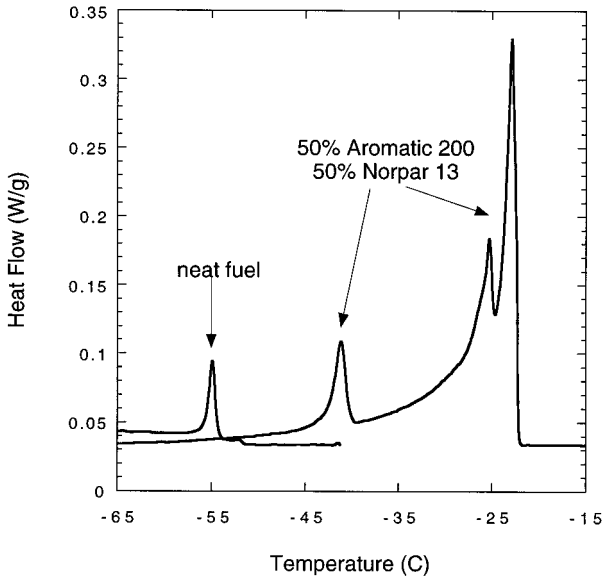

Figure 8. DSC curves for a mixture of 50% Aromatic 200 and 50% Norpar 13 compared with a jet fuel.

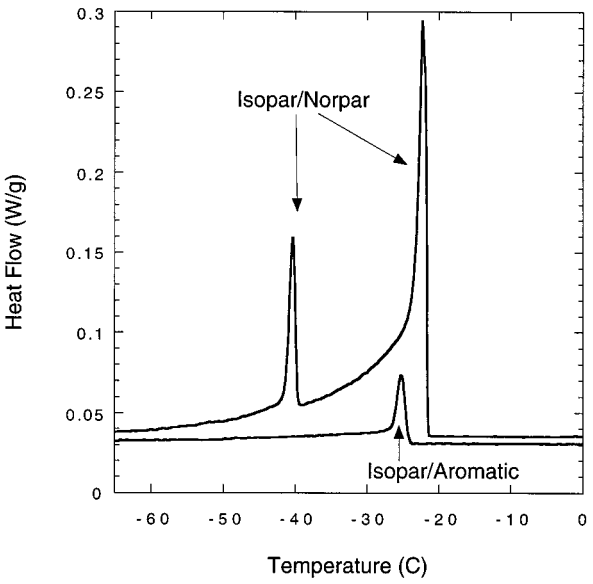

Figure 9. DSC curves for a mixtures of 50% Isopar M to 50% Norpar 13 and 50% Isopar to 50% Aromatic 200.

To understand the role that the various chemical classes present in the fuel have on freezing, we have prepared and studied mixtures of the commercially available chemical class solvents. These results are shown in Figures 8 and 9. Figure 8 shows the DSC curves for the freezing of a 50/50 mixture of Aromatic 200 and Norpar 13. By comparison with the neat Norpar 13 shown in Figure 5, we see that the presence of Aromatic 200 lowers the temperature of the solid−liquid transition of Norpar 13 from −9 to −23 °C. The temperature of the Norpar 13 solid−solid transition does not change from its location at −41 °C. The observation that the solid−solid transition does not move indicates that the odd normal alkane, *n*-tridecane, does not co-crystallize with Aromatic 200 components. That is, the

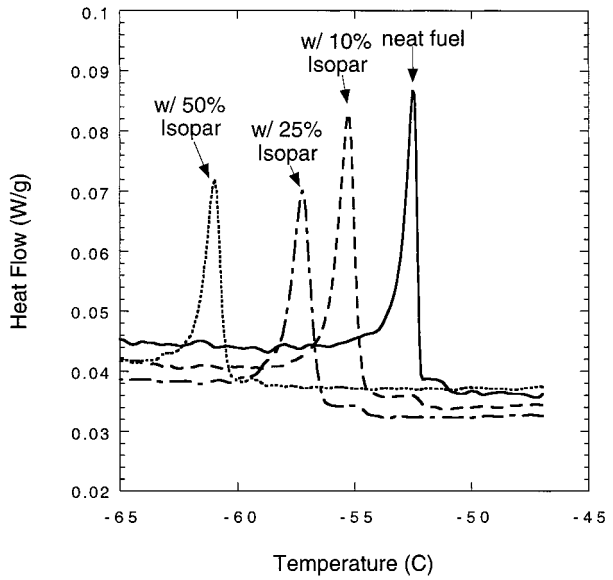

Figure 10. DSC curves for a Jet A fuel (POSF-3219) with various amounts of added Isopar M.

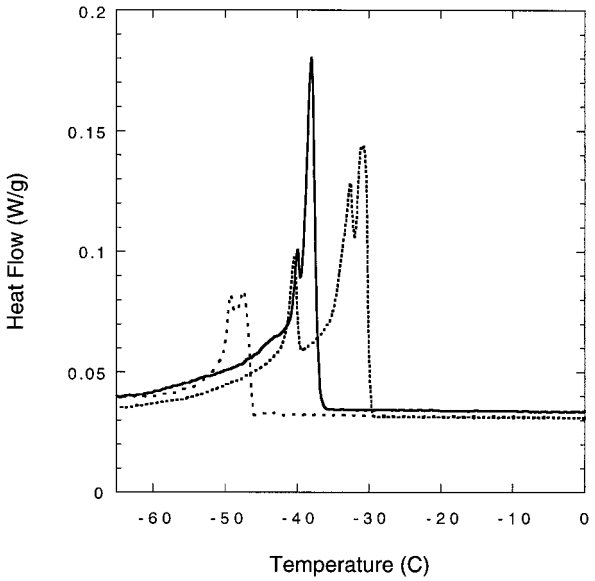

Figure 11. DSC curves for three mixtures of Aromatic 200/ Norpar 13/Isopar M; solid line 25/25/50; dotted line 33/33/33; dashed line, 12.5/12.5/75.

observation that the solid−solid transition temperature remains constant in the mixture shows that the solid *n*-tridecane molecules (and likely the other normal alkanes present) are present in the same microenvironment. The third peak observed in the figure near −25 °C is due to the freezing of the components in the Aromatic 200 fraction. This peak is shifted from its location at −13 °C in the neat solvent.

The results for 50/50 mixtures of Isopar M with Norpar 13 and Aromatic 200 are shown in Figure 9. As shown in Figure 3, Isopar M displays no crystallization behavior over the temperature range studied here. But, the presence of Isopar M in these other mixtures can modify their freezing and/or crystallization behavior. In the Isopar/Aromatic mixture, the exotherm due to Aromatic 200 is shifted from −13 °C in the neat solvent to −25 °C. Notice that this is the identical shift observed above in Norpar 13. In the Norpar/Isopar mixture, the liquid−solid transition moves from −9 °C in the neat solvent to −22 °C in the mixture, while the solid−solid transition remains near −41 °C. Again notice that these observations in the Norpar/Isopar mixture are the same as observed in Norpar/Aromatic mixture. Figures 8 and 9 show that the presence of Aromatic 200 or Isopar M have similar effects on the crystallization of Norpar 13 components, reducing their exotherm to near −23 °C. Also, the figures show that the presence of Isopar M or Norpar 13 have similar effects on the crystallization of Aromatic 200 components, reducing their exotherm to near −25 °C. These observations support the conclusion that there is little interaction between the components present in these mixtures, other than a dilution effect. This is in marked contrast to the strong interactions observed in Figure 6 when adding normal alkanes to jet fuel.

This observation of similar changes in exotherm temperatures upon dilution in these Norpar/Isopar/ Aromatic mixtures appears to indicate that these changes are due to colligative freezing point depression. To further investigate these observations, we have added various amounts of Isopar M to jet fuel as shown in Figure 10. The figure shows that adding 10, 25, and 50% Isopar M to fuel POSF-3219 reduces the freezing exotherm by 2.7, 4.7, and 8.5 °C, respectively. We can use average values for hydrocarbon freezing point depression cryoscopic constants listed in ASTM D1016-99 to estimate the expected colligative freezing point depression. For addition of 10% impurity to a hydrocarbon, the test method shows an expected freezing point depression of 2.8 °C. This value is very close to that measured for the addition of 10% Isopar. The cryoscopic constants listed in the test method are only good for hydrocarbons purities above 95%, so we have not used the greater dilution values.

The data indicate that addition of a noninteracting species to a fuel results in a colligative depression of the freeze point (Figure 10), while addition of a species that interacts with the *n*-alkane freezing process (such as additional more *n*-alkanes) can increase the freezing temperature of the mixture (Figure 6). These observations have important implications for the design of low freezing fuels. In particular, the data show that fuels with higher concentrations of branched alkanes relative to normal alkanes will exhibit better low-temperature properties. It is also important to reduce the size and concentration of the large normal alkanes as much as is feasible. The aromatic content appears to be less important in determining the freezing characteristics of a fuel than these other factors.

An obvious question now arises: if we mix the Norpar 13, Isopar M, and Aromatic 200, are we able to generate a mixture which displays low temperature behavior which is similar to jet fuel? The results are shown in Figure 11 for three mixtures in varying proportions. The mixture with the highest Isopar concentration displays the lowest freezing exotherm, as expected from the data above. The 33/33/33 mixture looks qualitatively very much like the 50/50 Aromatic/Norpar mixture shown in Figure 8, with the main exothermic feature being shifted to lower temperatures due to the presence of Isopar. The 25/25/50 mixture is further shifted to lower temperatures as a result of the higher concentration of Isopar. This mixture no longer displays a separate odd

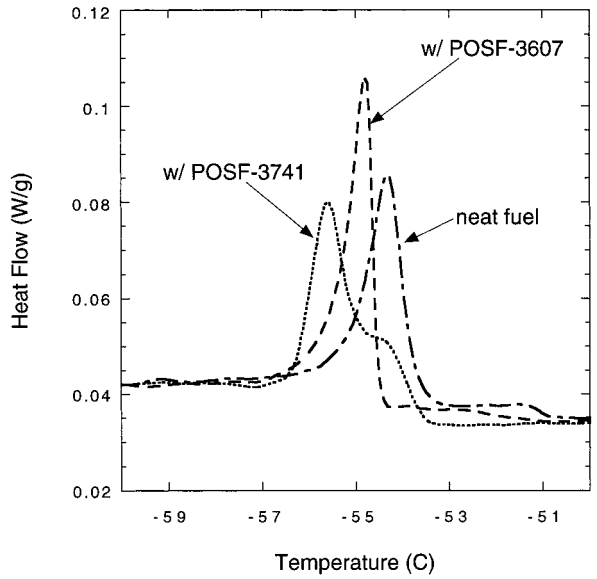

Figure 12. DSC curves for fuel POSF-3219 neat (solid line), with additive POSF-3607 (dotted line), and with additive POSF-3741 (dashed line).

n-alkane solid−solid transition as the main transition overlaps where it would occur (near −41 °C). The 12.5/12.5/75 mixture displays the lowest temperature freezing exotherm, which is near the feature of the POSF-2827 fuel (Figure 2). The exotherm displayed by this mixture is broader than that of the jet fuels and appears to consist of two overlapped peaks.

Unfortunately, the mixtures studied here lack the cycloalkanes that make a significant fraction of most jet fuels. Cycloalkane molecules tend to be much more spherical in geometry than normal alkanes, and thus likely behave more like the branched alkanes during the freezing process. The similar heats of fusion for these two classes of compounds, as shown in Figure 2, support this hypothesis. Thus, the inclusion of cycloalkanes to these mixtures would likely lower the temperature of freezing if the isoalkane concentration were not lowered also. To further elucidate the effect of cycloalkanes on fuel crystallization we performed a set of experiments in which we added three different cycloalkane species (methylcyclohexane, cyclooctane, and cyclodecane) to fuel 3219 and to a mixture of Norpar 13, Isopar M, and Aromatic 200. These results (not shown) indicate the methylcyclohexane behaves very much like the isoalkane mixture, lowering the temperature of the freezing exothermic feature. Cyclooctane and cyclodecane perturb the exotherms to a much greater extent. These larger cycloalkanes, with ring size greater than six carbons, are not likely present in jet fuels. Most cycloalkanes detected in jet fuels are alkyl substituted cyclohexanes, so the behavior of methylcyclohexane is likely more representative of the species present in real fuels.

Additive Studies. Now that we better understand the DSC response for jet fuel we can more readily use the instrument for assessing fuels and additives. Figure 12 shows the DSC curves obtained for two different cold flow additives in POSF-3219 fuel at 250 mg/L. The first additive, POSF-3607, showed excellent improvement in large scale cold flow testing, reducing fuel hold-up and increasing flow rate significantly at low temperatures.[1] On the other hand, the second additive, POSF-3741, was less satisfactory in the flow tests. These are both proprietary additives obtained from a major petroleum additive supplier. Both additives produce changes in the DSC exotherm, as shown in the figure. The changes observed in the DSC exotherms (1 to 2 °C shifts in the location of the exotherm peak) are quite small relative to the difference between the neat fuel and a JPTS (Figure 2). The excellent performance of additive POSF-3607 in the flow testing, and small changes in the DSC exotherm noted here, indicate that the additive works primarily by affecting the crystal morphology rather than by significantly changing the temperature at which crystallization occurs. Indeed, the DSC gives information on the latter process and cannot supply information on the former. To supplement the thermal analysis information supplied by DSC we have also used low temperature microscopy to supply information on crystal structure during fuel cooling.[15] These microscopy studies show that additive POSF-3607 does indeed affect the crystal habit. The presence of the additive results in more numerous and smaller crystals, which is the type of behavior expected of "pour point" type additives. These additives, which often consist of ethylene vinyl acetate copolymers, act by co-crystallizing with the normal alkanes. They contain a hydrocarbon backbone with protruding moieties. The protruding functional groups interfere with the alkane crystallization resulting in smaller crystals. The smaller crystals are more likely to allow flow through filters and small passageways in fuel systems.

Conclusions

We have shown that differential scanning calorimetry is a useful technique for the study of the freezing behavior of jet fuels. Upon cooling, the crystallization of large normal alkanes yields an exotherm due to the heat of fusion generated. Other fuel species, such as isoparaffins, naphthenes, and aromatics, do not contribute significantly to the signal. The addition of "pour point" additives results in only small changes in the measured exotherms despite large changes observed in cold flow devices. This observation indicates that the additives primarily act by altering the crystal structure and/or size.

Acknowledgment. This work was supported by the U.S. Air Force, Warner Robins Air Logistic Command, U-2 Special Programs Office, Robins Air Force Base, Warner Robins, Georgia, under Project No. 205 (Project Manager: Mr. Doug Hanlin) and the U.S. Air Force Research Laboratory, Propulsion Directorate, Propulsion Sciences and Advanced Concepts Division, Wright-Patterson Air Force Base, Ohio, under Contract No. F33615-97-C-2719 (Technical Monitor: R.W. Morris, Jr.). We thank Lt. Kirsten Wohlwend (USAF) for obtaining the freeze, pour, and cloud point data.

EF010074B

(15) Vangsness, M. D.; Zabarnick, S.; Widmor, N.; Ervin, J. S. *Prepr. Pap.—Am. Chem. Soc., Div Pet. Chem.* **2000**, *45*, 534−537.
(16) *CRC Handbook of Chemistry and Physics*, 74th ed.; CRC Publishing Co.: Boca Raton, FL, 1993.

M. Thermal Stability of Energetic Hydrocarbon Fuels for Use in Combined Cycle Engines

JOURNAL OF PROPULSION AND POWER
Vol. 17, No. 6, November–December 2001

Thermal Stability of Energetic Hydrocarbon Fuels for Use in Combined Cycle Engines

K. Wohlwend,* L. Q. Maurice,† and T. Edwards†
U.S. Air Force Research Laboratory, Wright–Patterson Air Force Base, Ohio 45433
R. C. Striebich‡ and M. Vangsness§
University of Dayton, Dayton, Ohio 45469-0132
and
A. S. Hill¶
University of Toledo, Toledo, Ohio 43606

Greater ease of use and higher density make energetic hydrocarbon fuels an attractive alternative to cryogenic fuels. The use of high-energy hydrocarbons in rocket and combined-cycle propulsion systems is being explored. In addition to its obvious use for propulsive purposes, fuel is used to cool system structures regeneratively to temperatures commensurate with presently available materials. Fuel thermal stability unfortunately limits the use of hydrocarbon fuels. In the present contribution, the thermal stability of RP-1, JP-10, and quadricyclane is assessed using a system for thermal diagnostic studies. It is found that, whereas JP-10 and RP-1 exhibit reasonable thermal stability, the highly strained quadricyclane rapidly degrades under high-pressure, condensed-phase thermal stress.

Introduction

CRYOGENIC propellants offer attractive performance advantages for launch vehicles.[1–4**] Liquid hydrogen (LH_2) and liquid oxygen (LO_2) are used in the high-efficiency main engines of the space shuttle, which has a high specific impulse I_{sp} rating of 455 s. Specific impulse is a measure of the thrust per mass flow rate of propellant at the nozzle; even small increases in specific impulse can have large potential benefits in the payload weight able to be placed into orbit. LH_2 and LO_2 also powered the upper stages of the Saturn lB and Saturn V rockets as well as the second stage of the Atlas/Centaur launch vehicle, the first U.S. LH_2/LO_2 rocket.** The RL-10 engines on the Centaur, a first-stage LH_2/LO_2 rocket, have an I_{sp} of 444 s. I_{sp} ratings for hydrocarbon rockets can be 30% less than I_{sp} values for cryogenic propellants. For example, the RP-1-fueled/LO_2 Atlas G/Centaur rocket has an I_{sp} of 257 s (Ref. 4).

Regrettably, significant operational disadvantages are also associated with the use of LH_2: its low density (71 kg/m^3) translates into large storage tanks, increasing the dry (unfueled) mass of the launch vehicle. Also, cryogenic propellants require considerable thermal insulation, thus further increasing the potential weight of the structure used to carry the propellant. Moreover, the additional logistics and safety concerns of cryogenic propellants and the high cost of LH_2 (70 times that of JP-8 on a volume basis) limit its use.[1] Despite these drawbacks, the high efficiency of LH_2/LO_2 makes these problems worth consideration when reaction time and storability are not critical.

Hydrocarbons, however, remain the fuel of choice for rapid response, storable systems. The advantages of energetic hydrocarbons over conventional JP-8 (aircraft) and RP-1 (rocket) fuels as well as cryogenic propellants are considerable and have been reviewed.[1–4] The higher density of liquid hydrocarbons, such as JP-8 (0.80 g/ml) and RP-1 (0.81 g/ml), over LH_2 (0.071 g/ml) provide a real incentive to consider the high-energy density materials. The higher energy densities of energetic hydrocarbons can overcome the lower I_{sp} values as compared to LH_2.

The higher energy content of high-energy hydrocarbons is a result of the high angle strain of the bonds in energetic compounds. Table 1 shows an example of how energy content (heat of combustion) for similar hydrocarbons increases with increased bond strain, normalized for carbon number. Cyclopropane, for example, with 60-deg bond angles, has a higher heat of combustion per CH_2 group than a straight chain alkane. High-energy density hydrocarbons such as quadricyclane (Fig. 1) feature total heats of combustion exceeding not only those of conventional rocket fuel (RP-1) (Fig. 2) but even moderately strained missile fuel (JP-10).

There exist a variety of other hydrocarbons that derive their high-energy density due to a compact molecular structure, such as aromatics or cycloalkanes, for example, cis–decalin, density = 0.897 g/ml. Other compounds such as cubane (C_8H_8), first synthesized in 1964, is both dense and strained.[5] Highly strained compounds were the only materials considered in this work because of their perceived thermal instability.

High-energy fuels may be used to cool system structures regeneratively to temperatures commensurate with presently available materials in combined-cycle engines. Thermal stability unfortunately limits the use of hydrocarbons as coolants.[1,6] Liquid-phase pyrolysis reactions have been shown to be indicative of a fuel's propensity to form undesirable deposits under thermal stress at high temperatures.[7,8] Whereas detailed gas-phase pyrolysis of energetic materials has enabled an understanding of strained-ring hydrocarbons decomposition pathways under combustion conditions,[9–12] study of the liquid-phase pyrolysis of these fuels has not been undertaken to date. Strained-ring hydrocarbon fuels have shown a propensity to soot,[3] and soot formation pathways have been shown to be analogous to pyrolytic deposition mechanisms in fuels systems.[8] Thus, the development of liquid-phase pyrolysis experiments is the logical foundation for beginning to assess the potential use of energetic hydrocarbons as coolants.

Table 2 shows some selected properties of hydrocarbons (also see Refs. 13 and 14).

Description of Experiment

The thermal stability of fuel is often characterized by the mass of deposits that a particular fuel forms under thermal stress. However,

Received 1 July 2000; revision received 20 July 2001; accepted for publication 6 August 2001.

*Fuels Chemist, Propulsion Directorate, Propulsion Sciences and Advanced Concepts Division, 1790 Loop Road North. Member AIAA.
†Fuels Chemist, Propulsion Directorate, Propulsion Sciences and Advanced Concepts Division, 1790 Loop Road North. Associate Fellow AIAA.
‡Research Engineer, Research Institute, Environmental Sciences, 300 College Park.
§Associate Research Physicist, Research Institute, Aerospace Mechanics Division, 300 College Park.
¶Research Assistant, Department of Chemical Engineering.
**See Web site URL:http://www.commkey.net/braeunig/space/propel.htm.

such measurements do not provide insight into the initiation chemistry of the deposition process. An understanding of deposition precursor processes is crucial to devising deposition mitigation techniques, as well as evaluating a candidate fuel's thermal stability.

In the present work, thermal decomposition is studied in a system for thermal diagnostic studies (STDS).[15] The STDS is a versatile system for investigating thermal degradation in the gaseous or condensed phase (Fig. 3). It requires only small volumes of reactants (~5 ml) and, therefore, is an ideal tool for evaluating synthesized, strained hydrocarbons. The STDS is capable of accurately controlling experimental variables such as residence time, temperature, reactive atmosphere, and pressure (supercritical conditions).

A membrane-diffusion solvent degasser was used to remove dissolved oxygen from the liquid reactant. Removing dissolved oxygen mitigated thermal-oxidative reactions, so that pyrolytic degradation could be examined without concern for oxygenated products acting as pyrolysis initiators or suppressors. A high-performance liquid chromatography (HPLC) pump delivered the liquid-phase material to the high-temperature reactor, with a backpressure regulator (500 psig) used downstream of the reactor to keep the material in the condensed phase, even at high temperature. Reactors were made using stainless-steel HPLC tubing with an internal diameter of 0.0254 cm, making exposures closer to near-isothermal conditions. Experiments consisted of exposing the reactant to high-temperature conditions and examining the decomposition of the reactant and products to determine reactant stability and speculate on the decomposition mechanism.

The thermal reaction compartment of the STDS is a gas chromatograph (GC) (Hewlett-Packard-5890A) with a separately controlled, high-temperature furnace inside. The high-temperature reactor is controlled isothermally at temperatures of between 200 and 650°C, with the GC oven around it held constant at 200°C for quantitative transport of reactants and products. Each experiment is completed at near-isothermal conditions, due to the small reactor and low flow rate of the reactants. High-pressure argon flows through the reactor while liquid flow is established and oxygen is removed by solvent degassing. When dissolved oxygen is fully removed, a high-pressure HPLC sampling valve switches the degassed liquid stream into the reactor leg, replacing the high-pressure argon gas. All experiments were conducted with a constant flow rate of 0.5 ml/min (laminar flow), giving a residence time of 1.8 s at 200°C. Backpressure regulators keep the system pressure at 34 atm. After the flow through, the high-temperature reactor is stabilized for 1 min, the decomposed reactant stream is sampled using a high-temperature, high-pressure sampling valve connected to a GC system (HP-5890). The GC is operated to separate and identify the thermal reaction products using a flame ionization detector. A 0.32-mm-i.d. Gas Pro column (Astec, Inc.) was used to separate the C_1–C_8 components of the sampled stream. A parallel 0.25-mm-i.d. DB-5 (J and W Scientific) capillary column was used in conjunction with a mass selective detector (HP-5970B) to help identify compounds of interest online.

Additional offline analyses were performed by GC–mass spectrometry (GC–MS). Once chromatographic samples are taken, valves are used to restore argon flow back through the reactor to reduce pyrolytic deposition and tube plugging.

Table 1 Hydrocarbon structure and stored energy

Hydrocarbon type	Molecular structure	Bond angle	Heat of combustion (per CH_2 group) kcal/mol
Open chain	—	109.5	157.4
Cyclohexane	⬡	109.5	157.4
Cyclopentane	⬠	108	158.7
Cyclobutane	□	90	164.0
Cyclopropane	△	60	166.6

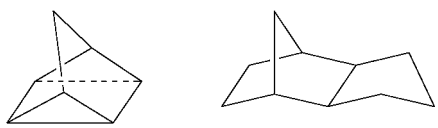

Quadricyclane

JP-10
exo-tetrahydro-dicyclopentadiene

Fig. 1 Chemical structure of pure hydrocarbons considered.

Results and Discussion

The decomposition profiles of the three reactants are shown in Fig. 4. Decomposition profiles are defined by percent of reactant remaining vs temperature as measured on the GC–MS. Clearly, quadricyclane degrades at much lower temperatures than either JP-10 or RP-1. JP-10 is more stable than quadricyclane, but appears to be less stable than RP-1. From the perspective of regenerative cooling using these hydrocarbons, it is important to consider parent

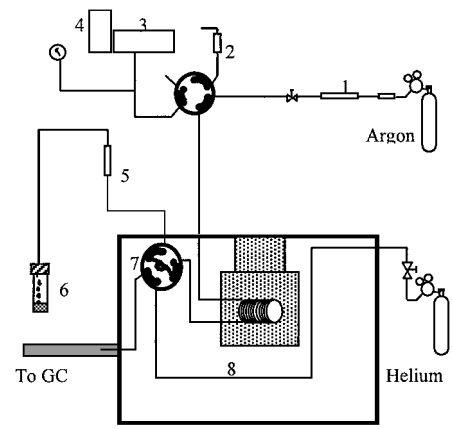

Fig. 3 STDS schematic: 1) check valve/filter, 2) restrictor, 3) HPLC pump, 4) solvent degasser, 5) backpressure regulator (500 psig), 6) sample collection, 7) sampling valve, and 8) furnace.

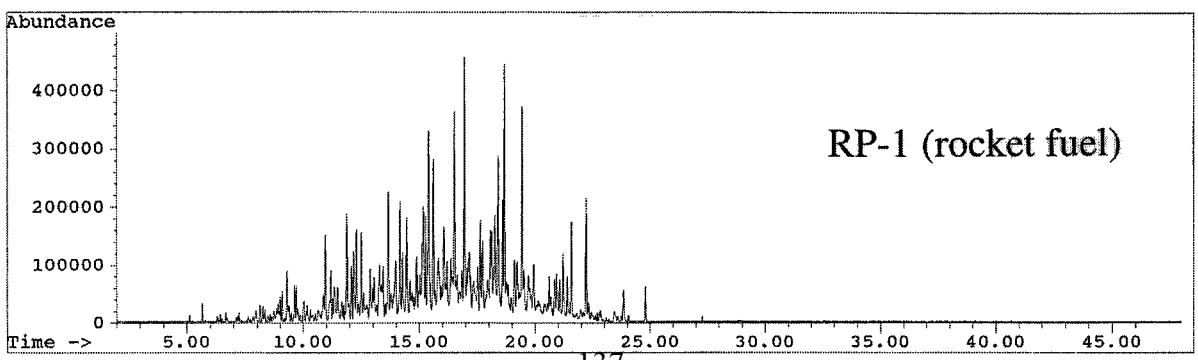

Fig. 2 RP-1 gas chromatogram.

Table 2 Selected properties of hydrocarbons[13,14]

Physical and chemical properties	JP-8	RP-1	JP-10	Quadricyclane	LH_2
Molecular weight	152	170.7	136	92	2.02
Molecular formula	$C_{10.9}H_{20.9}$	$C_{12.1}H_{23.42}$	$C_{10}H_{16}$	C_7H_8	H_2
Density, g/ml	0.80	0.81	0.95	0.98	0.071
Heat of combustion					
Btu/lb	18,494	18,600	18,130	19,061	49,900
kJ/mol	6,538	7,385	5,735	4,114	234
Boiling point, K (°F)	448–543 (347–518)	453–543 (354–518)	455 (360)	381 (226)	20 (−423)
Flash point, K (°F)	311 (100)	343 (158)	327 (130)	284 (52)	——

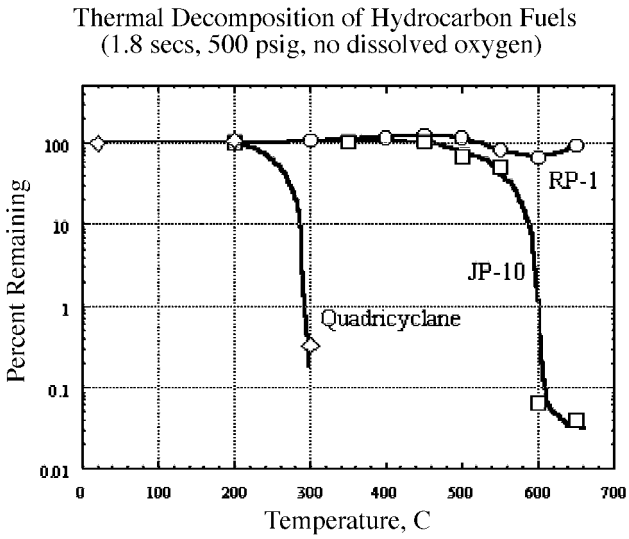

Fig. 4 RP-1, JP-10, and quadricyclane decomposition profiles.

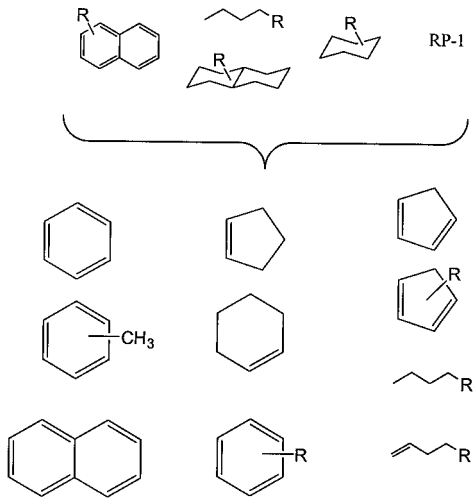

Fig. 5 RP-1 thermal decomposition products as determined by GC–MS.

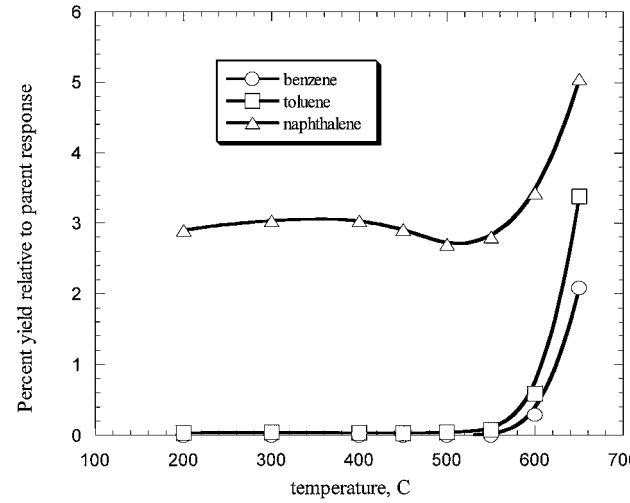

Fig. 6 Aromatic formation in RP-1 based on parent reponse to GC–MS detection at 200°C.

compound stability. If quadricyclane were used as a coolant and experienced temperatures above 200–300°C, some or all of the strain energy of the molecule would be lost because the quadricyclane would decompose before the combustor. Fuel system designers must consider the implications with regard to energy loss for a material to be used as a coolant and propellant.

The parent compound stability provides an indication of how much thermal stress a molecule may undergo before it degrades. After the molecule degrades, the products that form may indicate its propensity to form deposits[12] as well as to provide a possible decomposition mechanism as a function of temperature. Decomposition products for RP-1 are shown in Fig. 5, as determined by GC–MS results. The RP-1 parent material is composed of a wide range of compounds comprising primarily cycloparaffins and paraffins. A small amount of fragmentation is evident initially at 500°C. The RP-1 components experience more severe fragmentation at temperatures above 600°C. Product formation at 650°C appears from Fig. 4 to decrease (~95%) parent compound stability, but this response was difficult to determine accurately due to the complex nature of the RP-1. Cyclics and unsaturates dominate light product formation. Although RP-1 pyrolysis does not plug the reactor, the effluent turned yellow at 600°C and became even darker at 650°C. Higher temperature tests were not completed to avoid plugging the reactor. Benzene, toluene, and naphthalene formation occurred and became detectable between 600 and 650°C, as shown in Fig. 6. Single-ring and polycyclic aromatic hydrocarbon formation may be indicative of substantial parent compound degradation and subsequent molecular growth reactions to larger, more stable aromatic hydrocarbons. However, it must be noted that the RP-1 parent compounds may include small quantities (<3%) of aromatic compounds. As seen in Fig. 6, a small amount of naphthalene is already present in RP-1. No benzene or toluene were originally present in RP-1.

Decomposition products observed in JP-10 exposure are shown in Fig. 7, as determined by GC–MS. Because JP-10 is essentially a pure compound, its product distribution is more straightforward than is RP-1. JP-10 starts to fragment slightly at 450°C and decomposes readily by 600°C. The major decomposition products observed are cyclopentene and cyclopentadiene. Minor products include substituted cyclopentene and substituted cyclopentadiene. Tetrahydrodicyclo-pentadiene is also formed, possibly via JP-10 isomerization. Benzene, toluene, and naphthalene formation is observed between 550 and 600°C, as shown in Fig. 8. None of these

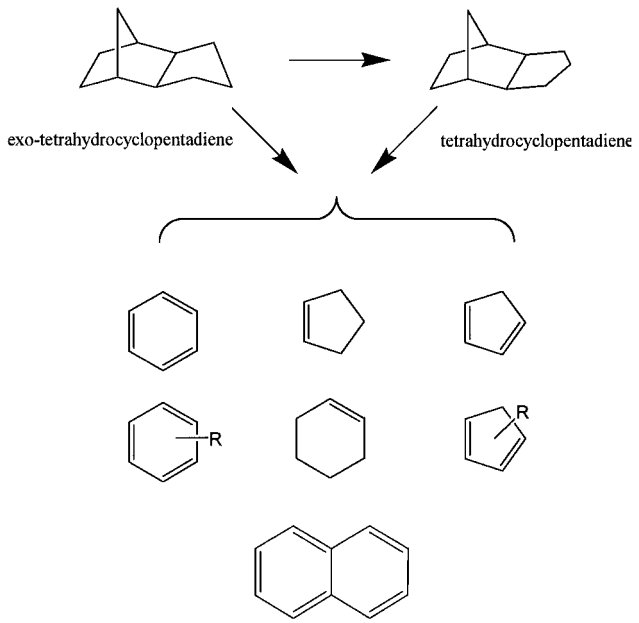

Fig. 7 JP-10 thermal decomposition products.

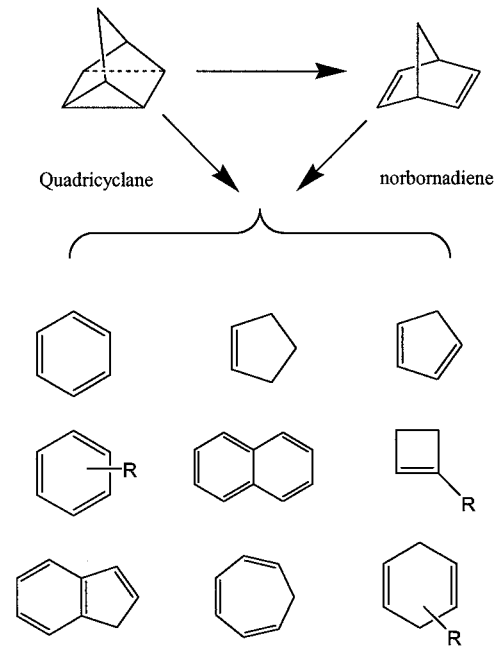

Fig. 9 Quadricyclane thermal decomposition pathways.

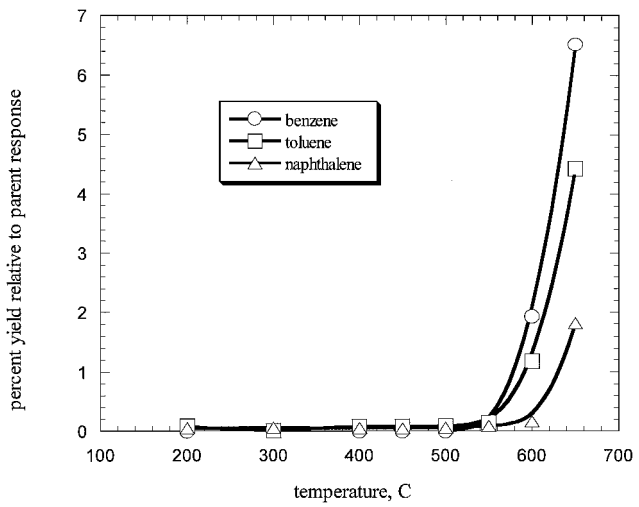

Fig. 8 Aromatic formation in JP-10 based on parent reponse to GC–MS detection at 200° C.

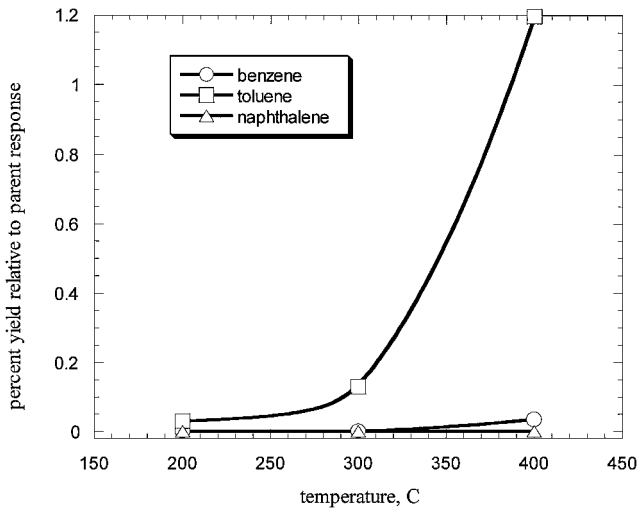

Fig. 10 Aromatic formation from quadricyclane based on parent reponse to GC–MS detection at 200° C.

compounds were present in the original JP-10. Because of the slightly lower temperatures at which initial fragmentation is observed for JP-10 when compared to RP-1, the former is considered slightly less stable. However, aromatic formation was more prevalent in RP-1 than observed for JP-10, probably due to the initial concentration of aromatic components in the RP-1. These aromatics may have acted as seed components to form the aromatic decomposition products. JP-10 degradation products did not plug the reactor, but the fuel became discolored at 600–650°C.

Because of its higher strain energy, quadricyclane was (predictably) more thermally unstable than either RP-1 or JP-10. Moreover, quadricyclane polymerized rapidly at 450°C, plugging the reactor tube. Quadricyclane isomerized to norbornadiene, even at temperatures below 300°C. The norbornadiene decomposition products indicate the eventual formation of aromatics, as shown in Fig. 9. Benzene and toluene formation is shown in Fig. 10; no naphthalene formation was observed at these lower (<450°C) temperatures. A small amount of toluene formation is observed at 200°C. The isomerization of quadricyclane to norbornadiene is consistent with observations in gas-phase studies.[10,11] Similar decomposition products are seen in both the gas-phase and condensed-phase studies. Because the reactor was plugged at such a low temperature, samples stressed to higher temperatures could not be collected. Polymerization-inhibiting additives may retard the decomposition process and will be studied in future work.

Conclusions

The thermal decomposition behavior of high-energy density hydrocarbons under condensed-phase high-temperature conditions was examined. These experiments examine conditions more typical of fuel systems for combined-cycle engines than do gas-phase experiments previously conducted.

Stability measurements performed in this study indicated that RP-1 was the most stable at the conditions investigated, followed closely by JP-10. Quadricyclane is the least stable, degrading at relatively low temperatures compared to JP-10 and RP-1. Once substantial pyrolysis is observed, aromatic formation increases are observed for all three reactants. JP-10 degradation leads to the formation of small amounts of benzene and toluene whereas RP-1 yielded higher formation of benzene and toluene, along with naphthalene. Quadricyclane features slight formation of benzene and toluene, but substantial polymerization, which leads to reactor plugging even at low temperatures. Apparently, quadricyclane would not be capable

of providing significant fuel system cooling (due to its thermal instability) if reaction times or temperatures were excessive. Product formation from the degradation of these reactants is helpful in speculating about the mechanism of decomposition and the propensity for deposition. The mitigation of undesirable pyrolytic deposition processes is predicated on the understanding of the inherent formation chemistry. Work to address pyrolytic deposition for strained hydrocarbons under condensed-phase high-temperature conditions is ongoing in our laboratory.

Acknowledgments

The financial support of the Air Force Research Laboratory Hypersonic Technology program is gratefully acknowledged. The authors would like to also thank Lockheed Martin for providing RP-1 and for their helpful discussions.

References

[1]Maurice, L. Q., Edwards, J. T., and Griffiths, J. F., "Liquid Hydrocarbon Fuels for Hypersonic Propulsion," edited by S. N. B. Murthy and E. T. Curran, AIAA Progress in Aeronautics and Astronautics, New York, 1999.

[2]Roy, G. D., "Straining for Long-Range Solutions," *Aerospace America*, Vol. 32, No. 8, 1994, pp. 33–35.

[3]Roy, G. D., "High Density Strained Hydrocarbon Fuels for Airbreathing Propulsion—II Combustion Characterization," *Proceedings of the International Symposium on Air Breathing Engines*, ISABE Paper 95-7098, Oct. 1995.

[4]Wagner, W. R., and Shoji, J. M., "Advanced Cooling Techniques for Future Space Transportation Systems," AIAA Paper 75-1247, Sept. 1975.

[5]Schmidt, M. W., Gordon, M. S., and Boatz, J. A., "Cubic Fuels?," *Journal of Quantum Chemistry*, Vol. 76, 2000, pp. 434–446.

[6]Edwards, T., and Atria, J., "Thermal Stability of High Temperature Fuels," American Society of Mechanical Engineers, ASME Paper 97-GT-143, June 1997.

[7]Stewart, J. F., Brezinsky, K., and Glassman, I., "Supercritical Pyrolysis of Methylcyclohexane," *ACS Petroleum Chemistry Division Preprints*, Vol. 43, No. 3, 1998, pp. 433–437.

[8]Maurice, L. Q., Striebich, R. C., and Edwards, T., "The Analogy of Cyclic Compound Formation in the Gas-Phase and Supercritical Fuel Systems of Hydrocarbon Fueled High Speed Vehicles," *ACS Petroleum Chemistry Division Preprints*, Vol. 43, No. 3, 1998, pp. 423–427.

[9]Weaver, D. P., Campbell, D. H., Wysong, I. J., Vaghjiani, G. L., Alfano, A., Wadsworth, D., and Ketsdever, A., "Combustion and Plumes," *Proceedings of the Air Force Office of Scientific Research AFOSR Contractor's Meeting*, Contractor's Meeting, 1996, pp. 29–33.

[10]Alfano, A. J., "Gas-Phase Pyrolysis Mechanism and Kinetics of 3–t–Butoxyquadricyclane," *International Journal of Chemical Kinetics*, Vol. 28, No. 7, 1996, pp. 481–487.

[11]Alfano, A. J., "Gas-Phase Pyrolysis Mechanism and Kinetics of 3–Chloroquadricyclane," *International Journal of Chemical Kinetics*, Vol. 29, No. 9, 1997, pp. 689–694.

[12]Taylor, P. H., and Rubey, W. A., "Evaluation of the Gas-Phase Thermal Decomposition Behavior of Future Jet Fuels," *Energy and Fuels*, Vol. 2, No. 6, 1988, pp. 723–728.

[13]*Handbook of Aviation Turbine Fuels Properties*, Coordinating Research Council, Document 530, Atlanta, GA, 1983, pp. 6–9.

[14]Edwards, T., and Marurice, L. Q., "Surrogate Mixtures to Represent Complex Aviation and Rocket Fuels," *Journal of Propulsion and Power*, Vol 17, No. 2, 2001, pp. 461–466.

[15]Striebich, R. C., and Rubey, W. A., "A System for Thermal Diagnostics Studies," *American Laboratory*, Vol. 22, No. 1, 1990, pp. 64–69.

N. Freezing of Jet Fuel within a Buoyancy-Driven Flow in a Rectangular Optical Cell

Freezing of Jet Fuel within a Buoyancy-Driven Flow in a Rectangular Optical Cell

D. L. Atkins* and J. S. Ervin

University of Dayton Research Institute, 300 College Park, Dayton, Ohio 45409-0140

Received April 19, 2001. Revised Manuscript Received June 27, 2001

JPTS, kerosene, Jet A, and additized Jet A samples were cooled below their freeze point temperatures in a rectangular, optical cell. Images and temperature data recorded during the solidification process provided information on crystal habit, crystallization behavior, and the influence of the buoyancy-driven flow on freezing. *n*-Alkane composition of the samples was determined. The Jet A sample contained the least *n*-alkane mass. The cooling of JPTS resulted in the least wax formation, while the cooling of kerosene yielded the greatest wax formation. The JPTS and kerosene samples exhibited similar crystallization behavior and crystal habits during cooling. Low-temperature additives modified the crystal habit of the Jet A fuel. Crystal shapes and sizes were recorded for use in future computational modeling.

Introduction

Aircraft operation in arctic regions or at high altitudes can expose jet fuel to temperatures below its freeze point temperature specification. Frozen fuel can be trapped within tanks or obstruct flow by blocking filters. Fuel freezing limits aircraft operational capabilities and, if unchecked, may result in the loss of aircraft and crew. The U. S. Air Force has previously developed a specialty jet fuel, JPTS, for low temperature use. Unfortunately, specialty fuels increase cost and logistical complexity, reducing their potential for both military and commercial applications. Commercial applications for jet fuel with improved low-temperature properties include high-altitude long-duration aircraft, which provide high-speed broadband Internet and cellular communication services[1] and trans-polar flights. Shorter trans-polar routes reduce flight time and save fuel but require increased artic ground operations. Therefore, there is a need to better understand the freezing of jet fuels for the safe and economical operation of aircraft at extreme low temperatures.

The solidification of jet fuel due to freezing involves complex molecular and continuum-level phenomena. The purpose of the present work is to gain an improved continuum-level understanding of the process of jet fuel freezing in a buoyancy-driven flow. Buoyancy-dominated flow is expected in aircraft fuel tanks. The freezing process is affected by fuel composition, fuel temperature and flow velocity. Jet fuel is a mixture of numerous hydrocarbons consisting primarily of *n*-alkanes, branched alkanes, cycloparaffins, olefins, and aromatics that vary with refinery source. Frozen jet fuel consists primarily of crystals composed of solid solutions of *n*-alkanes.[2] The crystal size and shape (habit) affects the freezing process and is influenced by several factors. Studies of diesel fuel have shown that additives can influence crystal habit.[3] The cooling rate can affect phase change kinetics and crystal habit. Phase change for a mixture takes place over a temperature range as species precipitate out of solution, altering the properties of the remaining liquid mixture. Also, because jet fuel freezing is not isothermal, crystalline structures may be porous and offer resistance to flow. Moreover, flow resistance depends on crystal shape and size.

Crystalline structures formed when jet fuel freezes are interlaced with liquid (as great as 80% by mass[4]), and similar structures have been referred to as mushy regions in studies involving the solidification of metal alloys.[5] Flow in mushy regions is analogous to flow in porous materials. The resistance to flow through the mushy region can be expressed in terms of an effective permeability. The permeability (K) represents the ease with which a fluid flows through the porous material. Darcy's law[6] relates permeability to the geometry of the porous structure, and different representations of the permeability have been used. The isotropic Koseny−Carman representation of permeability has been applied extensively in the study of metal alloy mushy regions and can be represented as:

$$K = d_s^2 \frac{(1 - \epsilon_s)^3}{c\epsilon_s^2} \quad (1)$$

where d_s is the characteristic diameter of the solid crystals, ϵ_s is the solid volume fraction, and c is the

* Corresponding author. Tel: (937) 252-8878. E-mail: datkinspe@aol.com.

(1) Iannotta, B. *Aerospace Am.* **2000**, *40*, 36−40.

(2) Van Winkle, T. L.; Affens, W. A.; Beal, E. J.; Mushrush, G. W.; Hazlett, R. N.; DeGuzman, J. *Fuel* 1**987**, *66*, 947−953.

(3) Lewtas, K.; Tack, R. D.; Beiny, D. H. M.; Mullin, J. W. In *Advances in Industrial Crystallization*; Garside, J., Davey, R. J., Jones, A. G., Ed.; Butterworth Heinemann: Oxford, 1991; pp 166−179.

(4) Moynihan, C. T.; Mossadegh, R.; Bruce, A. J. *Fuel* **1984**, *63*, 378−384.

(5) Beckermann, C.; Viskanta, R. *ASME Appl. Mech. Rev.* **1983**, *46*, 1−25.

(6) Collins, R. E. *Flow of Fluids through Porous Materials*; Reinhold Chemical Engineering Series: New York, 1961; pp 10−65.

10.1021/ef010098i CCC: $20.00
Published on Web 08/15/2001

Kozeny coefficient.[7] The Kozeny coefficient depends on crystal shape and may be determined from optical experiments using jet fuel. In addition, the characteristic diameter and solid volume fraction for jet fuel can be determined from images of fuel crystallization. Measurements of d_s, ϵ_s, and c of eq 1 may then be incorporated in the development of computational models for the simulation of the freezing of jet fuel.

Unfortunately, the extent of fundamental research on fuel freezing in a buoyancy-driven flow is limited. Jet fuel availability concerns spurred low-temperature fuel research in the late 1970s and early 1980s.[8] This led to the relaxation of the freeze point specification for Jet A-1 from 223.2 to 226.2 K and prompted further applied research related to operational issues. The applied studies did not provide the information needed to accurately model freezing fuel. For example, recorded images were not of sufficient resolution to distinguish between regions of liquid or solid fuel. In addition, complexities, such as structural members and free surfaces, obscured the understanding of the freezing process. Fundamental studies of freezing and solidification have generally been limited to single-compound or binary mixtures. For example, in a study involving a simple geometry, measurements of the solid area and temperatures were obtained for the melting and resolidification of pure *n*-octadecane about two cylinders.[9] In contrast, jet fuel is a complex hydrocarbon mixture for which simple phase relationships do not exist. Clearly, more fundamental research is needed to better understand the freezing of jet fuel.

The objective of this study is to gain insight into the freezing process by obtaining detailed images and temperature measurements of neat and additized jet fuel freezing within a two-dimensional, buoyancy-induced flow with imposed surface temperatures for a simple rectangular geometry. Recorded images assist in the understanding of how fluid dynamics influence phase change and how additives modify crystal habit. Moreover, images can provide information concerning the relative porosity of solidifying structures, characteristic dimensions of wax crystals, and relative areas of liquid and solid phases. These quantities may be used in the development of computational fluid dynamics models to better design aircraft fuel systems and predict the freezing behavior of jet fuel.

Experimental Section

A test apparatus was fabricated to view and record images of jet fuel freezing within a vessel with imposed surface temperatures. This optical freezing cell is shown in Figure 1. In aircraft, jet fuel is stored in various tank geometries; however, a rectangular geometry was chosen for convenience. The cell (88.9 mm × 38.1 mm × 44.5 mm) was fabricated from commercially available aluminum (6061) tubing that has a wall thickness of 6.4 mm. Aluminum was chosen due to its use in aircraft fuel tanks and its high thermal conductivity. The cell surface was sand blasted with glass beads (60−120 micron) to obtain a uniform finish. A cell depth of 44.5 mm

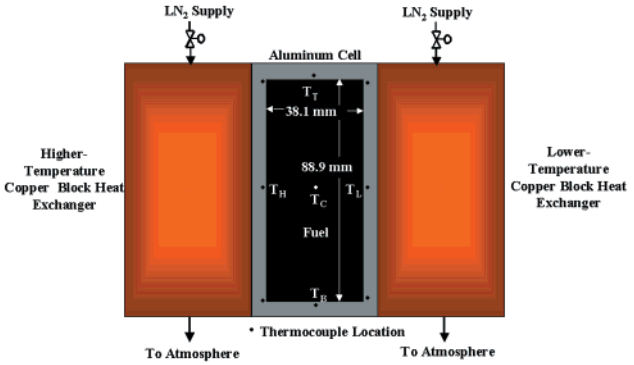

Figure 1. Schematic of low-temperature optical cell.

was sufficient to establish a two-dimensional flow by minimizing heat transfer end effects. Copper block heat exchangers are clamped to opposite vertical sides of the cell to impose the desired surface temperatures, and the resulting density differences drive the flow within the cell. The copper blocks (88.9 mm × 50.4 mm × 44.5 mm) were cut from bar stock, and two flow passages (12.7 mm diameter) were drilled through each block for the flow of liquid nitrogen. A mixing vane within each passage enhances heat transfer between the liquid nitrogen and copper surfaces.

Temperature control (within ±0.5 K) is accomplished by the use of cryogenic solenoid valves, which meter the flow of liquid nitrogen into the copper blocks. Calibrated (type T) thermocouples measure temperatures on the internal surfaces of the aluminum cell. Wells for thermocouples (5.6 mm deep) were drilled into the exterior aluminum walls. The thermocouples were calibrated (in the range 293.3−203.3 K) using a platinum resistance device as a standard. The estimated uncertainty in the temperature measurements is ±0.5 K. Figure 1 shows the locations of the nine thermocouples used to verify isothermal surface conditions and to control the experiment. In Figure 1, T_H represents the average of the three thermocouples located along the higher-temperature surface, midway from front to back. Likewise, T_L represents the average of the three thermocouples located along the lower-temperature surface. Surface temperatures were determined to be isothermal to within 1 K standard deviation. The temperature of the top and bottom surfaces is measured by a thermocouple placed at the center of each surface. In addition, a single thermocouple is located in the fuel sample at the center (T_C) of the optical cell. A digital data acquisition and control system records thermocouple readings at a rate of 1 Hz. Components of the system include a network interface (National Instruments, Fieldpoint FP-1001), thermocouple input module (National Instruments, Field Point FP-AI-100), an electronic relay module (National Instruments, Fieldpoint FP−FLY-420), and software (National Instruments, Lookout 4.0).

Quartz is used on the front and rear of the cell to allow for illumination and image collection. Figure 2 shows the cell with polycarbonate and quartz vacuum chambers located at the front and rear of the cell. The use of vacuum chambers eliminates frost accumulation (from ambient water vapor) on the quartz and minimizes heat transfer end effects. Heat transfer through the front and rear quartz was evaluated by measuring the liquid fuel temperature from front to back, along the bottom of the cell. The heat transfer through the front and rear viewing windows was assumed to be negligible since the temperature variation was always less than 0.5 K. Quartz was chosen for its strength and optical clarity, while polycarbonate plastic was chosen for its strength and low thermal conductivity. Figure 2 also shows the optical arrangement. An illumination source is placed at one end of the cell, while a camera is located at the other. Opal glass is used to uniformly diffuse the light source. Polarizing filters are placed immediately in front of each quartz vacuum chamber to

(7) Ni, J.; Incropera, F. P. *Int. J. Heat Mass Transfer*. **1995**, *38*, 1271−1284.
(8) Low-Temperature Behavior of Fuels in Simulated Aircraft Tanks, CRC Report No. 532, CRC Project No. CA-58-78.
(9) Sasaguchi, K.; Viskanta, R. *J. Energy Resources Technol.* **1989**, *111*, 43−49.

Table 1. Select Low-Temperature Properties of Fuels Studied and Comparison of Onset of Phase Change

fuel	freeze point (K)	cloud point (K)	pour point (K)	cell onset T_L (K)	DSC onset (K)
JPTS (F3775)	218.7	215.9	212.2	214.0	214.6
Kerosene (Fisher)	231.1	227.2	218.2	226.5	226.0
Jet A (F3219)	227.2	222.2	217.2	220.5	222.2
Jet A (F3219 additized with F3607)	227.2	222.3	208.3	218.5	221.2
Jet A (F3219 additized with F3741)	228.4	221.2	211.2	221.0	219.0

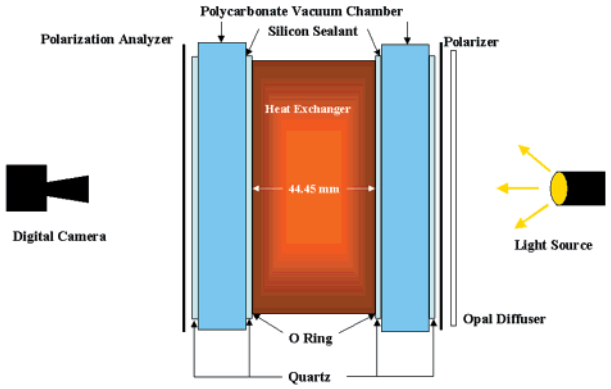

Figure 2. Side view of optical cell.

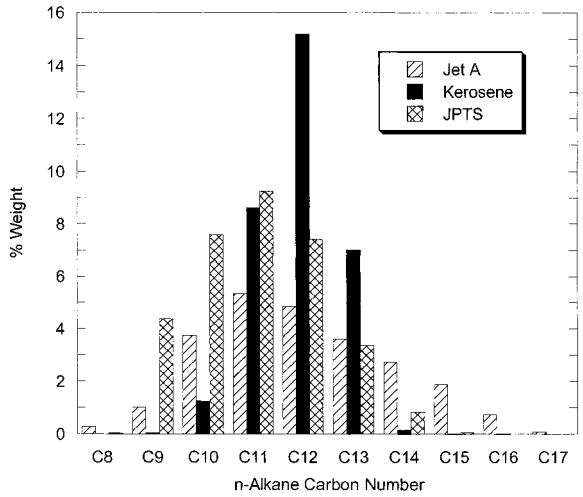

Figure 3. Distribution of *n*-Alkanes for neat fuels before freezing.

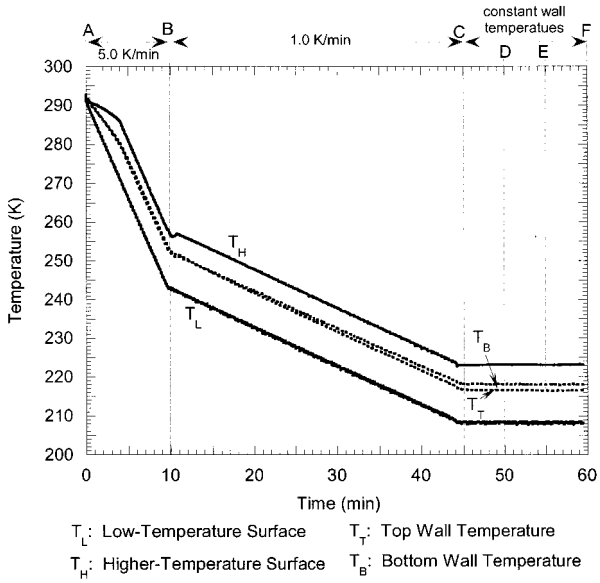

Figure 4. Optical cell surface temperatures.

improve contrast between the liquid and solid fuel. Cross polarization eliminates light transmittance through the liquid fuel. As the fuel solidifies, crystals rotate the polarization plane, allowing light to pass through the front polarization analyzer. Two camera systems are used to obtain images. A high-resolution digital camera (Sony DKC-ST5, 4 mega-pixel) equipped with a zoom lens (Sony VCL1205B) captures images from the direction normal to the viewing window. A video camera (Panasonic WV-CL352) equipped with a macro lens records magnified (10X) images of the crystal morphology.

The cell is gravity fed from an elevated reservoir until completely filled with fuel. A makeup fuel supply is maintained in the reservoir to allow for changes in fuel density (contraction) during cooling. The jet fuels were obtained from the Fuels Branch (PRTG) of the Turbine Engine Division of the Propulsion Directorate of the Air Force Research Laboratory at Wright-Patterson AFB, Ohio. Bottled kerosene was obtained from Fisher Scientific.

JPTS (F3775), a kerosene sample, Jet A (F3219), and Jet A samples additized with two proprietary low-temperature additives (F3607 and F3741) were selected for study. The kerosene was included since jet fuels are kerosene based, and it is readily available. Table 1 lists select low-temperature properties of the fuels and fuel-additive combinations studied. A single concentration of 2000 mg/L of each additive was studied. Before freezing, the samples were analyzed using gas chromatography to determine the *n*-alkane (weight) distribution (Figure 3). The JPTS sample consists of 33% *n*-alkanes ranging from C_9 to C_{14} and centered about C_{11}. The kerosene sample contains 32% *n*-alkanes, primarily from C_{10} to C_{13}. The Jet A sample has 24% *n*-alkanes in the range C_9 to C_{16} and centered about C_{12}. The kerosene possesses the narrowest *n*-alkane distribution while Jet A has the widest distribution. The Jet A sample has fewer total *n*-alkanes than the other fuels, but it has the greatest mass of long-chain *n*-alkanes (C_{15}−C_{17}). The JPTS sample does not contain C_{16} or C_{17} and has only trace amounts of C_{15}.

Each fuel was subjected to the surface temperatures shown in Figure 4. The cooling experiment was divided into three periods. For convenience, during the first period (Figure 4,A−B), the lower-temperature surface (T_L) was cooled rapidly from room temperature (293.2 K) at a rate of 5.0 K/min. This rate was used to provide a rapid cool to a temperature well above the highest freeze point temperature of the fuels studied (Table 1). Cooling rate has an affect on crystal habit, and thus, during the second period (Figure 4,B−C), the lower-temperature surface (T_L) was cooled from 243.2 to 208.2 K at a rate of 1.0 K/min. The actual cooling rate of fuel in aircraft fuel tanks is typically less than 1.0 K/min. To ensure freezing T_L was set at 208.2 K, which is less than the lowest pour point temperature of the fuels studied (Table 1), a 15 K temperature difference between the opposite vertical surfaces was maintained throughout the experiment to induce flow. Actual aircraft fuel tanks may experience surface temperature differences due to solar heating or other heat transfer mechanisms. The vertical surfaces were then maintained at constant temperatures (Figure 4,C−F) for a period of 15 min to allow for adequate fuel solidification. Top and bottom surface tem-

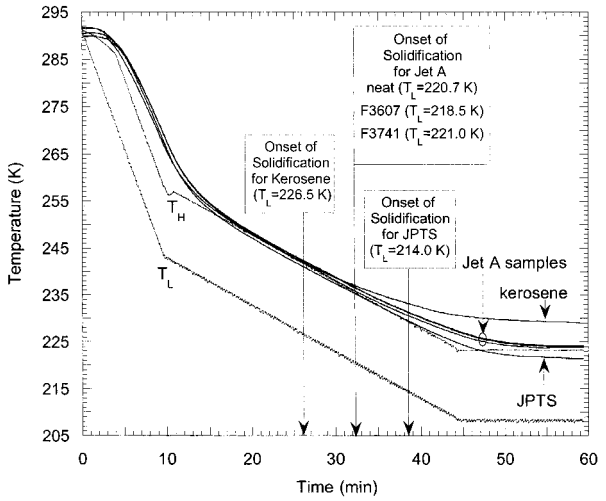

Figure 5. Temperature (T_C) at center of cell for all fuels.

peratures of the cell were not actively controlled, but were measured. Figure 4 shows that top and bottom surface temperatures are similar and fall between the imposed vertical surface temperatures. The top surface temperature deviates from that of the bottom starting at 240 K during cooling. It is believed that the deviation arises due to conduction heat transfer through supports located on the bottom of the cell.

Results and Discussion

Temperatures and images recorded during the freezing process provide information on crystal microstructure, crystallization behavior, liquid−solid volume fraction, and the influence of buoyancy-driven flow on phase change. Surface temperatures and the temperature at the center of the optical cell are presented for each fuel sample. In addition, images (Figures 6−15) were obtained for each fuel sample at the times and surface temperatures indicated in Figure 4 (times C, D, E and F).

Temperature Measurements. Figure 5 shows temperature readings at the center of the optical cell as well as the temperatures imposed on the vertical surfaces of the optical cell for all the fuel samples. The center temperature differs between samples due to the fact that the fuel samples possess different thermal and transport properties. Figure 5 shows the temperatures at which phase change was visually observed to begin on the lower-temperature surface for the JPTS, kerosene, and Jet A (neat and additized) samples. Figure 5 also shows that after phase change begins, the center temperatures begin to deviate from each other due to surface freezing and concomitant heat release due to crystallization. The kerosene sample deviates the greatest due to an earlier onset of phase change and higher heats of fusion (Figure 16) for the precipitating *n*-alkanes. In addition, Figure 5 indicates that during initial rapid cooling of the vertical surfaces (Figure 4,A−B), the cooling rate at the center of the cell is less than the imposed vertical surface cooling rate (5.0 K/min). Buoyancy-driven flow in the cell is complex, and time is required before the effects of the imposed surface condition fully penetrate to the cell center during rapid cooling. During the reduced cooling rate period (Figure 4,B−C), the temperature at the center of the optical cell begins to decrease at the same rate as the imposed rate well before phase change begins.

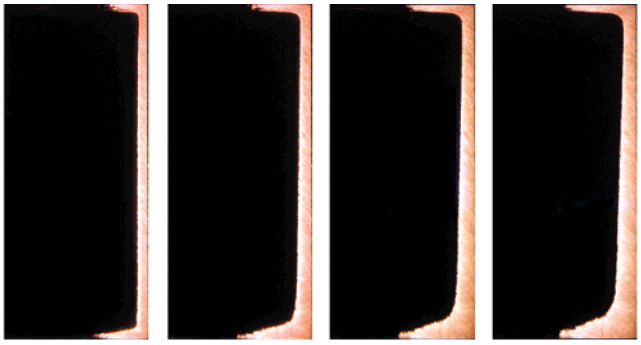

Figure 6. Freezing JPTS after (a) 45, (b) 50, (c) 55, and (d) 60 min of cooling in the optical cell. Times refer to those of Figure 4.

Optical Cell Images. Two-dimensional images obtained from the direction normal to the viewing window provide details of crystallization behavior, the relative areas of liquid and solid, the effect of flow, and crystal habit. For each sample, the amount of solidification is estimated from recorded images (magnification 10X) along with crystal size, shape, and spacing.

Figure 6 shows images of the JPTS sample freezing. In Figure 6, the right side of each image is the lower-temperature surface, and the left side is the higher-temperature surface. The surface temperatures for each image of the figure correspond to times C, D, E, and F shown in Figure 4. Figure 6a shows fuel that has begun to solidify after 45 min of cooling (Figure 4,A−C). The light region of Figure 6a is fuel that has solidified on the lower-temperature vertical surface and the top and bottom surfaces. The remaining area is liquid that appears dark due to the cross-polarization used. Figures 6a−d show that with increasing time, the crystallization front advances along the bottom and top of the cell from the lower-temperature vertical surface toward the higher-temperature vertical surface. After 60 min of cooling, the solidifying structure has advanced to the center of the top and bottom surfaces, and a profile of the solidified structure is visible. The profile extends uniformly from the front to the rear of the cell, indicating that heat transfer end effects are negligible and the buoyancy-driven flow field is fully two-dimensional. The images in Figure 6 suggest that the solidifying structure is comprised of long, thin crystals, adhered to the cell surfaces. The thickest portion of the solidifying structure is located at the bottom of the lower-temperature surface (Figure 6d).

Figure 7a shows the JPTS sample in the optical cell after 60 min of cooling with a (6.4 mm) uniform grid superimposed. The profile area of the stationary solidified fuel attached to the cell surfaces is estimated from this image to be 594 mm^2. From this area, it can be estimated that the solidifying structure occupies 18% of the optical cell volume. Figure 7b (10X magnification) reveals a porous structure of needlelike crystals, generally growing in the opposite direction of the heat transfer (normal to the cell surfaces). The needlelike crystals visible in Figure 7b have a characteristic width of 0.1 mm and reach lengths equivalent to the thickness of the solidifying structure (6 mm). Crystal spacing varies, but distances as great as 1 mm can be measured between crystals.

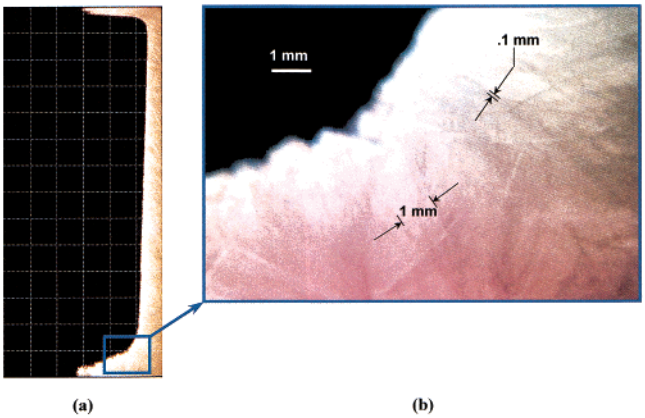

Figure 7. Frozen JPTS (a) 594 mm^2 of solidified fuel and (b) crystal habit after 60 min of cooling.

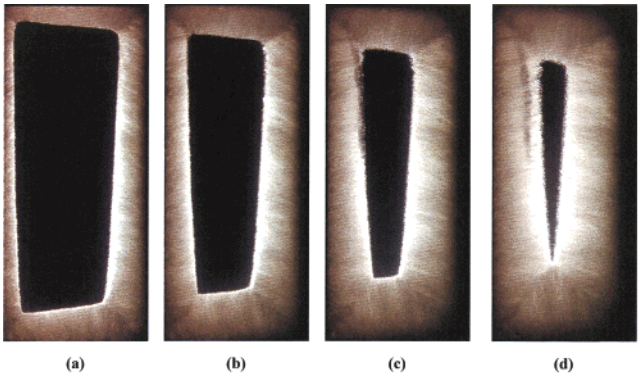

Figure 8. Freezing Kerosene after (a) 45, (b) 50, (c) 55, and (d) 60 min of cooling in the optical cell. Times refer to those of Figure 4.

Figure 8 shows images of freezing kerosene for the same period as the JPTS sample (Figure 4,C−F). Figure 8a shows that by the beginning of the constant wall temperature period (45 min of cooling), a significant amount of fuel has crystallized, and crystals cover all surfaces of the optical cell. After 60 min, the crystalline structure nearly fills the cell. The thickest part of the wax structure exceeds 20 mm, beyond the center of the cell. Figure 8d shows that near the vertical lower-temperature and bottom surfaces, much of the solidifying structure is dark and indiscernible from the liquid region. This implies that the crystal spacing of the solidifying structure is not uniform. The images in Figure 8 clearly show the solidifying structure is made up of long, thin crystals, similar to the JPTS sample. Additional crystallization behavior similar to the JPTS sample is the greater accumulation of solidified fuel at the bottom of the cell.

Figure 9a shows kerosene in the optical cell after 60 min of cooling (Figure 4,F) with a (6.4 mm) uniform grid superimposed. The solidifying structure occupies 93% of the optical cell volume, which is over 5 times greater than that of the JPTS sample. Figure 9b (10X magnification) shows solidified fuel after 45 min of cooling (Figure 4,C) and reveals long needlelike crystals similar to those observed for the JPTS sample. Figure 9 shows crystallization behavior that is similar to that of the JPTS sample: crystals attached to the cell surfaces, growing in the direction opposite that of heat transfer. The crystals shown in Figure 9b have a characteristic width of 1 mm and reach lengths equivalent to the thickness of the solidifying structure (22 mm). Where discernible, crystal spacing is consistent with the spacing found in the JPTS sample. In the dark, indiscernible regions of the solidifying structure crystal spacing cannot be determined.

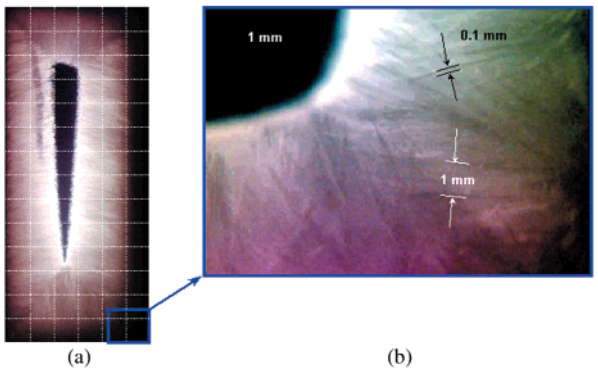

Figure 9. Frozen Kerosene (a) 3161 mm^2 of solidified fuel after 60 min of cooling and (b) crystal habit after 45 min of cooling.

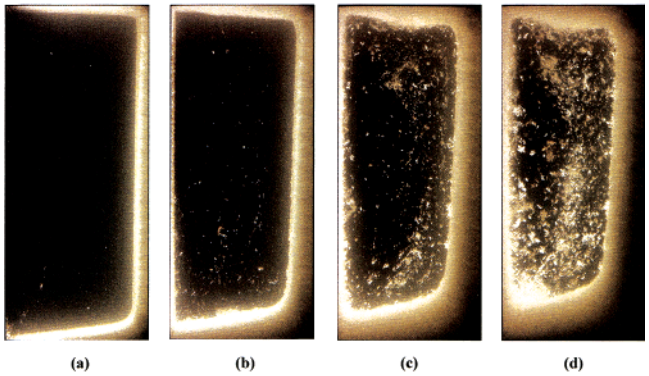

Figure 10. Freezing Jet A after (a) 45, (b) 50, (c) 55, and (d) 60 min of cooling in the optical cell. Times refer to those of Figure 4.

Figure 10 shows images of Jet A freezing while holding surface temperatures constant (Figure 4,C−F). Figure 10a shows that after 45 min, a crystalline structure covers the vertical lower-temperature surface and the top and bottom surfaces. It is obvious that Jet A crystal morphology is very different from either that of the kerosene or JPTS samples. Figure 10 shows that components of the fuel solidify and attach to the surfaces of the optical cell. In addition, crystals nucleate and drift within the liquid. As time progresses, the liquid fuel temperature falls below the cloud point throughout the cell, and the suspended crystals continue to grow. The crystals move with convective currents, becoming entangled with the surface-adhered crystalline structures. There, they pack and contribute to the growth of the adhered, larger structures. Thus, the buoyancy-induced flow creates a mechanism for growth of stationary crystalline structures. After 60 min, Figure 10d shows that all surfaces have adhering crystals with the greatest accumulation of solids at the bottom of the cell, as observed with the JPTS and kerosene samples. The thickness of the crystalline structure exceeds 12 mm along portions of the vertical lower-temperature and bottom surfaces. Areas of solidification adjacent to the cell surfaces are dark, similar to those of the kerosene sample.

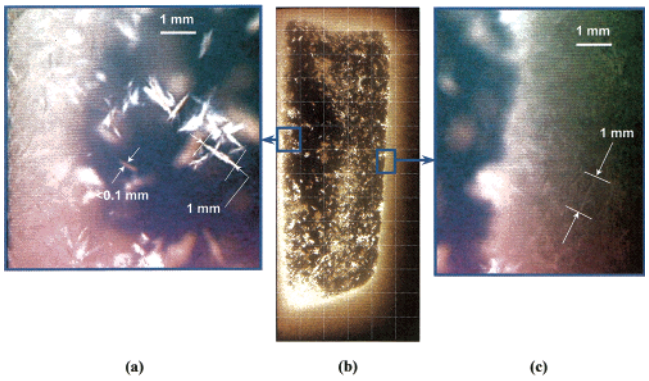

Figure 11. Frozen Jet A (a) crystal habit, (b) 1594 mm^2 of solidified fuel area, and (c) densely packed crystals after 60 min of cooling.

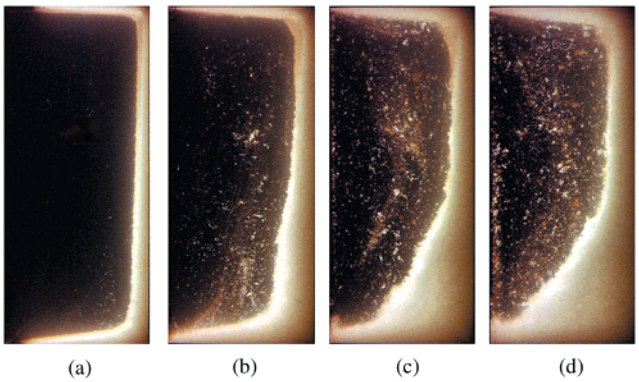

Figure 12. Freezing Jet A additized with F3607 after (a) 45, (b) 50, (c) 55, and (d) 60 min of cooling in the optical cell. Times refer to those of Figure 4.

Panels a and e of Figure 11 (10X magnification) reveal the neat Jet A sample crystal habit and the growth mechanism of the larger structures. Figure 11a shows migrating crystals becoming entangled with surface adhered structures. Figure 11c shows densely packed crystals that have adhered to the lower-temperature vertical surface with no identifiable spacing between crystals. Closer inspection of Figure 11c shows that the crystals are randomly oriented. Figure 11b shows Jet A in the optical cell after 60 min with a (6.4 mm) uniform grid superimposed. The area of wax solidification is more difficult to estimate than that for the other fuels since numerous suspended crystals are present in the liquid region. However, it is estimated from Figure 11b that the solidified fuel attached to the cell surfaces occupies 47% of the cell volume. Figure 11c shows the stationary crystalline structures to be made up of short, uniform platelike crystals, packed together randomly, accumulating in a direction opposite that of the heat transfer. As the solid fraction increases in the cell, the crystal interaction increases, causing packing and formation of larger, stationary solid structures. Figure 11a shows these crystals to be 0.1 mm thick and 1 mm in length. Figure 11c shows densely packed crystals in the dark region adjacent to the lower-temperature surface. It is believed that the dark regions in both the Jet A and kerosene samples are relatively nonporous solid structures.

Similarities in the growth of the stationary crystalline structures were observed for the fuel samples studied. The motion of the liquid fuel influences the local liquid temperature, which, in turn, affects the crystal growth rate and habit. The buoyancy-induced flow driven by the imposed surface temperatures affects the growth of solidifying structures. Large-scale liquid motion flows downward along the lower-temperature vertical surface (fuel density increases) and upward along the higher-temperature vertical surface (fuel density decreases) in a clockwise rotation. Thus, the minimum temperature of the flowing liquid is located near the bottom of the vertical lower-temperature surface. As observed in the present experiments, this region would be expected to have the greatest accumulation of solidified fuel.

Analysis of the fuel *n*-alkane compositions before freezing assists the understanding of crystallization behavior. JPTS is the present preferred low-temperature jet fuel. Yet, its crystallization behavior is similar to that of kerosene, which exhibited the greatest solidification volume. Figure 3 shows that the JPTS and kerosene samples have similar total masses of *n*-alkanes (32−33%). Compared with those in the kerosene sample, the *n*-alkanes in the JPTS sample are more widely distributed with a larger concentration of C_{10} and below, which may account for its lower freeze point temperature. The total *n*-alkane composition of the Jet A sample (24%) is significantly lower than the other two fuels. However, the freeze point of the Jet A sample is higher than that of the JPTS sample. Figure 3 reveals that the Jet A sample contains a greater mass of larger *n*-alkane species (C_{15}−C_{16}) than the JPTS sample, which may account for the higher freeze point temperature of the Jet A sample.

The crystallization behavior of the JPTS and kerosene samples (long, needlelike crystals, attached to the cell walls and growing in the direction opposite that of heat transfer) has been observed in metal alloy solidification and is referred to as columnar (constrained) dendritic solidification.[5] The nucleation of crystals in the liquid region, migration of crystals along convective currents, and crystal interaction and packing exhibited in the present study by Jet A freezing has also been observed in alloy solidification and is referred to equiaxed (unconstrained) crystallization.[5] Thus, the crystallization behavior of JPTS, kerosene, and Jet A is similar to that observed in metal alloy solidification. It is believed that numerical models used in the simulation of alloy solidification may also be extended to simulate the freezing of jet fuel. For modeling the freezing of jet fuel, the optical cell images provide estimates of d_s, ϵ_s, and c. As a first-order approximation, the Koseny−Carman model can be used to simulate flow through the porous, solid structures present in freezing jet fuel.

Additive Studies. The flow visualization studies described here are part of a larger research effort to develop additives which improve the low-temperature behavior of jet fuel. Additives modify freezing behavior by increasing *n*-alkane solubility, increasing nucleation, or limiting crystal size. Previous research involved the evaluation of the effectiveness of cold flow additives to reduce the amount of fuel trapped by the solidifying wax structure.[10] Proprietary additive F3607 was found to be effective, while additive F3741 was ineffective.

Figure 12 shows images of freezing Jet A additized with (2000 mg/L) F3607 in the period from 45 to 60 min (Figure 4,C−F). Figure 12d shows that there are a greater number of smaller crystals than were present

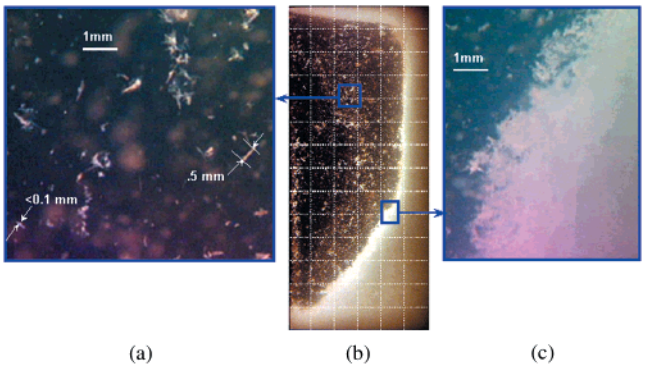

Figure 13. Frozen Jet A additized with F3607 (a) crystal habit, (b) 1361 mm^2 of solidified fuel and (c) migrating crystals after 60 min of cooling.

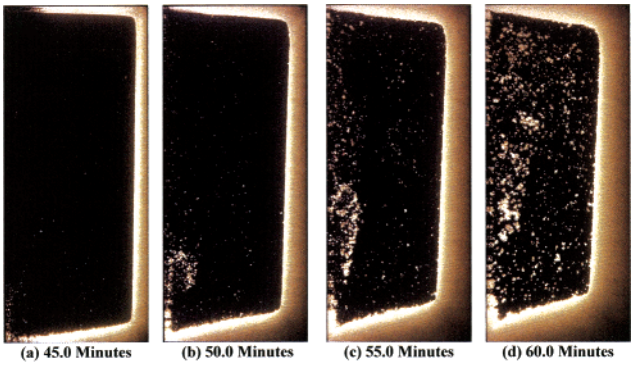

Figure 14. Freezing Jet A additized with F3741 after (a) 45, (b) 50, (c) 55, and (d) 60 min of cooling in the optical cell. Times refer to those of Figure 4.

in the neat Jet A sample (Figure 10d) for otherwise identical conditions. When compared to the neat Jet A sample (Figure 10), the crystals in the solidifying structure are neither as densely packed nor constrained to the cell surfaces. Figure 12 shows that the additive has significantly altered the crystal habit of Jet A, revealing why the additive was effective. The migrating equiaxed crystals do not densely pack, but flow to the bottom of the cell. Spacing between these crystals is difficult to determine from the images, however, the accumulated crystals are visually observed to shift with liquid fuel flow. Panels a and c of Figure 13 (10X magnification) reveal small, irregularly shaped crystals that do not densely pack. Also, the magnified images show the crystals are needlelike in shape as opposed to the platelike crystals observed in the solidifying neat Jet A. The length of these needlelike crystals (0.5 mm) is roughly half the length of the platelike neat Jet A crystals (1 mm), while the crystal thickness is similar (<0.1 mm). Figure 13b shows the optical cell at 60 min, and as with neat Jet A, the total area of wax solidification is difficult to estimate since numerous equiaxed crystals are present. The volume of the optical cell that the accumulated solidified fuel occupies is approximately 40%.

Figure 14 shows images of the Jet A sample additized with (2000 mg/L) F3741 freezing in the final period of cooling (Figure 4,C−F). The additive has altered the crystal habit of the neat Jet A sample, and there are

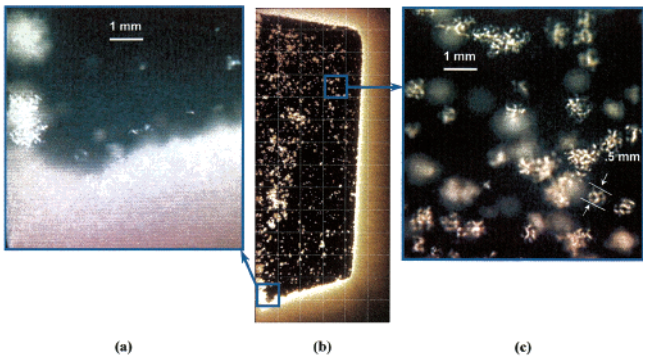

Figure 15. Frozen Jet A additized with F3741 (a) densely packing, (b) 1239 mm^2 of solidified fuel and (c) migrating crystals after 60 min of cooling.

fewer equiaxed crystals when compared to either the neat Jet A sample or the Jet A sample additized with F3607. Figure 14d shows that the solidifying structure is similar to that of the neat Jet A sample (Figure 10d). Panels a and c of Figure 15 (10X magnification) show solidification on the cell walls and reveals a crystal size (0.5 mm) smaller than that of the neat Jet A sample (1 mm) and of a more uniform size and shape. With additive F3741, the overall shape of the crystals is spherical. Figure 15b shows that the volume of the stationary solidifying structure (37%) is less than that of the neat Jet A sample.

The irregular shape of the crystals in the Jet A sample additized with the effective additive (F3607) may explain why the equiaxed crystals do not form larger, adhered structures. The crystals present in the Jet A sample additized with the ineffective additive (F3741) are similar to the noneutectic crystal shapes present in metal alloy solidification and have been referred to as equiaxed dendritic in studies of alloy solidification.[5]

Related Experiments. In related work using differential scanning calorimetry (DSC),[11] the onset of phase change was determined (Table 1) at a 1.0 K/min cooling rate for the fuels of the present work. Under the thermal conditions of the optical cell, the wall temperature at which crystallization initially becomes visible corresponds coincides well with the DSC measurements and with the measured cloud-point temperatures presented. This agreement among different studies supports the experimental method of the present work.

Figure 16 shows the DSC cooling curve measurements for the fuel samples of the present work. Additive F3607 has shifted the exothermic peak of Jet A to a lower temperature, but more importantly, the peak is narrower and greater in magnitude than the peak of the neat the Jet A fuel sample. This observation agrees with the optical cell images that show larger numbers of smaller crystals (Figure 12d), demonstrating that an effective habit-modifying additive increases nucleation rate. In addition, small, irregular shaped crystals are less likely to remain trapped in the fuel tank and more likely to form porous structures that allow flow. The improved flowability is evident by the significant reduction in pour point temperature shown in Table 1. Additive F3741 has shifted the exothermic peak of Jet

(10) Ervin, J. S.; Zabarnick, S.; Binns, E.; Dieterle, G.; Davis, D.; Obringer, C. *Energy Fuels* **1999**, *13*, 1246−1251.

(11) Ervin, J. S.; Widmor, N.; Zabarnick, S. *Studies of Jet Fuel Freezing by Differential Scanning Calorimetry and Cold-Stage Microscopy*; ASME Turbo Exposition, New Orleans, June 2001.

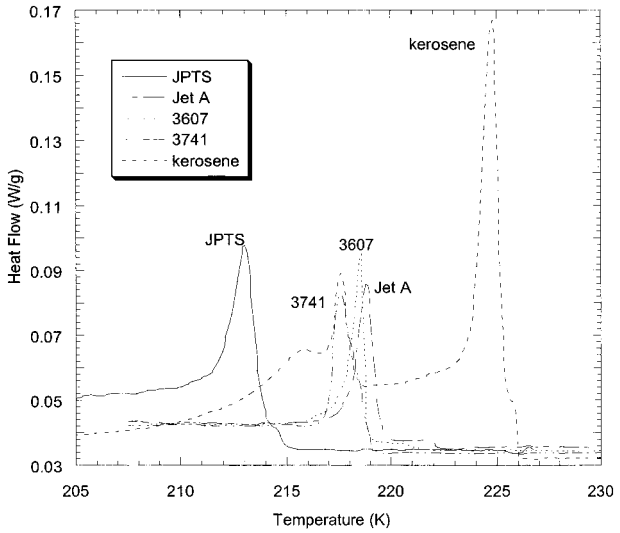

Figure 16. DSC heat of fusion measurements at 1.0 K/min cooling rate.

A to an even lower temperature than that produced by additive F3607, but the DSC exothermic peak is wider at the base and lower in magnitude than the neat Jet A peak. Also, the optical cell images show fewer numbers of crystals (Figure 14d) as compared to those of the neat Jet A sample (Figure 10d). Fewer crystals imply that the additive has not increased the nucleation rate. Interestingly, the ineffective additive did reduce the volume of the stationary solidifying structure, which may be the result of the onset of solidification occurring at a lower temperature. The optical cell in conjunction with the DSC indicates that the F3607 additive is effective at altering the crystal habit by producing small, irregularly shaped, loosely packed crystals, as opposed to reducing the temperature at which crystallization occurs.

Conclusions

Images of JPTS, kerosene, Jet A, and additized Jet A jet fuels freezing within a buoyancy-induced, two-dimensional flow, under well-defined thermal conditions, were obtained using an optical cell. Buoyancy-induced flow controlled the growth of the wax structures on the cell surfaces. In addition, the flow enhanced the growth of wax structures on cell surfaces for the Jet A sample by increasing crystal interaction. The effective additive did not substantially change the amount of wax formation, but changed crystal shape, size, and the packing density of crystals. Additives that create irregularly shaped, needlelike, smaller crystals are effective cold flow additives. Crystal structures resulting from effective cold flow additives, trapped in fuel tanks or filters in the fuel system, are permeable. The images captured provide sufficient resolution to estimate solid volume fractions and characteristic crystal sizes and shapes of the solidifying structures for future modeling of the freezing process in a buoyancy-driven flow. Jet fuel solidification due to freezing is similar to metal alloy solidification. Modeling the freezing of neat and additized jet fuel can be accomplished by the modification of the governing equations to include a permeability term.

The optical cell experiments suggest that jet fuels with a wide distribution of small *n*-alkane species ($<C_{14}$) may have desirable low temperature properties. In addition, additives that lower the temperature at which crystallization occurs may not necessarily reduce the mass of solidified fuel or reduce crystal size to enable flow through filters.

Acknowledgment. This work was supported by the U.S. Air Force, Warner Robins Air Logistic Command, U-2 Special Programs Office, Robins Air Force Base, Warner Robins, Georgia, under Project No. 205 (Project Manager: Doug Hanlin), and the U.S. Air Force Research Laboratory, Propulsion Directorate, Propulsion Sciences and Advanced Concepts Division, Wright-Patterson Air Force Base, Ohio, under Contract No. F33615-97-C-2719 (Technical Monitor C.W. Frayne). We would like to thank Rich Striebich for obtaining the gas chromatograph data, Nikki Widmor for obtaining the DSC data, and Lt. Kirsten Wohlwend (USAF) for obtaining the freeze, pour, and cloud point temperature data.

EF010098I

O. Suppression Behavior of Obstruction-Stabilized Pool Flames

Combust. Sci. and Tech., 2001, Vol. 163, pp. 107-130
Reprints available directly from the publisher
Photocopying permitted by license only

Suppression Behavior of Obstruction-Stabilized Pool Flames

FUMIAKI TAKAHASHI[a*], W. JOHN SCHMOLL[a], EDWARD A. STRADER[a] and VINCENT M. BELOVICH[b]

[a]*University of Dayton Research Institute 300 College Park Dayton, Ohio 45469 and* [b]*Air Force Research Laboratory Wright-Patterson Air Force Base, Ohio 45433*

(Received January 13, 2000; In final form October 18, 2000)

The suppression phenomena of a nonpremixed flame stabilized by a recirculation zone behind an obstruction in a combustion tunnel have been studied because of their relation to fires in aircraft engine nacelles, dry bays, and shipboard and ground-vehicle compartments. The JP-8 fuel was supplied as a liquid fuel pool, or a gaseous (methane or ethane) fuel issued from a flat porous plate, downstream of a backward-facing step or J-shape flange. The OH planar laser-induced fluorescence revealed a narrow, wrinkled diffusion flame zone that was deeply folded into the recirculation zone in response to the dynamic air entrainment and back-flow. Both transient and steady-state fire suppression limits were determined; by impulsively injecting a gaseous fire-extinguishing agent (nitrogen, CF_3Br, or C_2HF_5), or by continuously adding nitrogen, into the approaching airflow in the combustion tunnel. For high air velocities, the normalized critical agent mole fraction at suppression was a unique function of the agent injection period normalized by the effective mixing time in the recirculation zone, independent of types of fuels, agents, and obstacles. The extinction of the relatively low-strain-rate diffusion flame zone in the recirculation zone appears to determine the suppression limits of obstruction-stabilized flames.

INTRODUCTION

A fire-extinguishing agent, halon 1301 (bromotrifluoromethane, CF_3Br), has long been used to protect aircraft, ships, vehicles, and facilities because of its superior effectiveness (Grosshandler et al., 1994; Hamins et al, 1995). The United Nations (1994) Montreal Protocol ban on the production of halon 1301 due to its high ozone-depletion potential has prompted broad research into a

* Corresponding author. Present address: National Center for Microgravity Research on Fluids and Combustion, NASA Glenn Research Center, MS 500–115, 21000 Brookpark Road, Cleveland, OH 44135. E-mail: Fumiaki.Takahashi@grc.nasa.gov

search for replacement and alternative agents. The superior attributes of halon 1301 have not yet been matched by agents with acceptable levels of toxicity, ozone-depletion potential, and global warming potential. As halon 1301 is replaced with a possibly less effective agent, improvements to fire-suppression systems have become important to enhance their performance and efficient use of the agent. Fires in aircraft engine nacelles, dry bays, shipboard machinery space, or ground armored vehicle compartments often occur in a complex geometry under highly ventilated conditions. A recirculation zone behind clutter such as flanges, pipes, or steps provides conditions favorable for flame holding (Raghunandan and Yogesh, 1989; Rohmat et al., 1998), i.e., lower velocities, heat recycling to the flame stabilizing region; augmented heat transfer to condensed fuel surfaces; and enhanced mixing of fuel, air, and hot combustion products. In addition, the complex geometry also affects the dynamics of an agent entrained in the fire zone. Therefore, fluid mechanics and flame stability behind an obstruction may be a dominant factor affecting the performance of fire-suppression agents (Moussa, 1994).

Few results have been reported in the literature on the suppression of obstruction-stabilized nonpremixed flames. Hirst and Sutton (1961), Hirst et al (1976, 1977), and Dyer et al. (1977a, 1977b) studied baffle-stabilized kerosene pool fires in a wind tunnel and concluded that the most stable type of flame to be encountered in an aircraft engine fire is a liquid surface diffusion flame from a pool of fuel burning behind an obstruction in an airflow. For the suppression of baffle-stabilized JP-8 spray flames, Hamins et al. (1996) identified two crucial parameters; i.e., a characteristic mixing time in the recirculation zone and the critical agent concentration at suppression for long agent injection durations and derived a theoretical expression for the critical agent mole fraction as a function of the injection duration. In a previous paper (Takahashi et al., 2000), the authors reported for the first time the results of characteristic mixing time measurements using obstruction-stabilized methane flames and incorporated the results into the correlation between the critical mole fraction at suppression and the agent injection period.

The role of computational modeling and simulations of fire dynamics and suppression has gained importance in recent years as a result of progress in understanding of the subject phenomena and the rapid growth of computational capabilities. The fire and suppression models for cluttered compartments are currently under development (Gritzo et al., 1999; Tieszen and Lopez, 1999) with particular emphasis on the applications to fires in aircraft dry bays, fuel tanks, engine nacelles, ground vehicle crew and engine compartments, shipboard machinery, and occupied spaces, etc. Computational models must be validated and/or calibrated by experimental data to develop practical, credible engineering

tools for the design of efficient fire protection systems using the best available agents.

The objectives of this study are to gain a better understanding of the flame stabilization and suppression behavior of obstacle-stabilized nonpremixed flames and to obtain experimental data to set coefficients in fire-suppression submodels. The fire-suppression submodels will then be tested (Gritzo et al., 1999; Tieszen and Lopez, 1999) in a spectrum of applications to ensure applicability outside the narrow range of experimental data. In addition to the baseline suppression-limit data previously obtained (Takahashi et al., 2000) for step-stabilized methane flames using halon 1301, new results are reported in this paper using various types of fuels, fire-extinguishing agents, and obstructions. Furthermore, planar laser-induced fluorescence (PLIF) of hydroxyl (OH) radicals was used to characterize the spatial burning variations in the recirculation zone. An attempt is made to obtain a universal suppression-limit curve valid for various parameters and to extract physical insights into underlying mechanisms common in obstacle-stabilized flames.

EXPERIMENTAL TECHNIQUES

Experimental Apparatus

The fire-suppression test facility, described elsewhere (Takahashi et al., 2000), has been modified to accommodate specific requirements for a large volume of an inert-gas agent (nitrogen) and a liquid fuel (JP-8). Figure 1 shows the experimental apparatus, which consists of the fuel, air, and agent supply systems, a horizontal small-scale combustion tunnel (154-mm square cross-section, 77-cm length) with quartz windows. A water-cooled porous plate (150-mm square × 12.7-mm thickness, 316L stainless steel) is placed flush with the bottom surface of the test section downstream of an obstruction. The flow rate of a gaseous fuel (methane or ethane) is arbitrary set at 10 l/min (heat release: 5.45 kW and 9.73 kW for methane and ethane, respectively), which results in a low mean (upward) fuel velocity (0.7 cm/s) typical of pool flames. The obstructions used (see Fig. 1 inset), described in detail elsewhere (Takahashi et al., 2000), are a right-angle backward-facing step (height, h_s= 32 mm or 64 mm), a 45°-angle backward-facing step (h_s = 64 mm), and an inverted-J-shape flange (h_s = 64 mm; downstream overhang: 38-mm length × 13-mm height with 6-mm-radius corners). The angled step is used in consideration of a helical flow induced by the circumferential agent injection in the annular aircraft engine nacelle. The J-flange mimics mechanical strengthening members in the engine bay.

suppressants. For nitrogen, two sets of agent storage vessels and computer-controlled parallel solenoid valves are used, depending on the air flow condition: (1) for $U_{a0} = 7.1$ m/s, two connected vessels (2 × ~300 l or ~300 l + ~600 l) and up to eight valves (Peter Paul 72T10DCM, response time: ~12 ms); (2) for $U_{a0} = 10.8$ m/s, a large vessel (~3700 l) and eight valves (ASCO 8210G3).

The gaseous agent was injected impulsively into the airflow ~1 m upstream of the flame. Uniform agent dispersion into the airstream was achieved by injecting the agent perpendicular to the airflow in a reduced diameter (108 mm) section through up to 32 × 6.4-mm-dia. holes in four rows in a 25.4-mm-o.d. closed-end tube for $U_{a0} = 7.1$ m/s, or 30 × 9.5-mm-dia. holes in four rows in a 50.8-mm-o.d. closed-end tube for $U_{a0} = 10.8$ m/s. The mesh screens and a perforated plate downstream enhance further mixing. The schlieren visualization performed previously (Takahashi et al., 2000) for halon 1301 revealed fairly good agent dispersion and mixing in air. The agent temperature and pressure in the storage vessel are measured with a T-type (copper-constantan) thermocouple and a pressure transducer (Druck PTX-620). The amount of injected agent is controlled by varying the initial storage vessel pressure and the time period that the valve is open and is determined from the difference between the initial and final pressures and temperatures in the storage vessel using the ideal-gas equation of state. Because the sufficiently large storage volume results in a relatively small pressure drop during agent discharge and the valve response time is relatively short compared to the agent injection period, a constant agent discharge rate is assumed. Therefore, the mean volumetric agent concentration is determined by dividing the mean agent flow rate ([volume]/[injection period]) by the total (air and agent) flow rate.

The continuous nitrogen supply system for steady-state fire suppression experiments consists of high-pressure (up to 170 atmg) nitrogen vessels on a trailer, dome pressure regulators, a rupture disk, a calibrated critical flow nozzle (Flow-Dyne, throat dia.: 4.90 mm), a pressure transducer, and a T-type thermocouple. The mass flow rate of nitrogen is determined from the measured pressure and temperature upstream of the critical flow nozzle.

Flame Suppression Limit Measurements

The transient fire suppression limit experiment is conducted as follows. First, a stable flame is established for a fixed air velocity for a period of at least 20 min, and the agent is injected for a particular storage vessel pressure and injection period to determine whether or not the flame extinguishes. When extinguished, the flame is re-ignited using a propane-torch-assisted spark igniter equipped on the back wall of the test section. The agent injection test is repeated 20 or 50

times for halogenated agents or nitrogen, respectively, and the probability of suppression is determined by dividing the number of extinguishments by the total number of runs. Then either the storage vessel pressure (which determines agent concentration) or injection period is varied step-wise and the experiment is repeated. The suppression condition is confirmed at a probability of 90% chosen arbitrarily. The steady-state fire suppression limit experiment is conducted by gradually adding nitrogen into the air by maintaining the air flow rate constant until the flame extinguishes. The maximum relative error of the flame suppression limit was estimated as ±8% for pool flames with halogenated agents and ±4% and ±2% for gaseous flames with nitrogen for transient and steady-state measurements, respectively.

Planar Laser-induced Fluorescence Measurements

OH PLIF images are acquired to characterize the spatial burning variations without agent injection using a right-angle or 45°-angle backward-facing step at a mean inlet air velocity of 7.1 m/s. The OH PLIF system (Fig. 2), which is similar to that used by Donbar et al. (2000), consists of a pulsed Nd:YAG laser (Quanta Ray DCR-24–10), a dye laser (Spectra Physics PDL-2), a doubling crystal (Inrad Auto Tracker II), a harmonic separator (Inrad 752–104), and an intensified charge-coupled device camera (Princeton Instruments ICCD-576S/B, 576 × 384 pixels). OH fluorescence is obtained by tuning a Nd:YAG-pumped dye laser to the $R_1(8.5)$ transition of the $A^2\Sigma^+$-$X^2\Pi$ ($v' = 1$, $v'' = 0$) band ($\lambda = 281.34$ nm) and fluorescence from the A-X (1,1) and (0,0) bands ($\lambda = 306$–320 nm) is collected with a lens (UV Nikkor 105 mm/f4.5) and imaged onto a PI ICCD array. To improve the signal-to-noise ratio, each 2-by-2 pixel region is spatially averaged; thus the spatial resolution of each OH image is the area that is imaged on two pixels, or 0.65 mm.

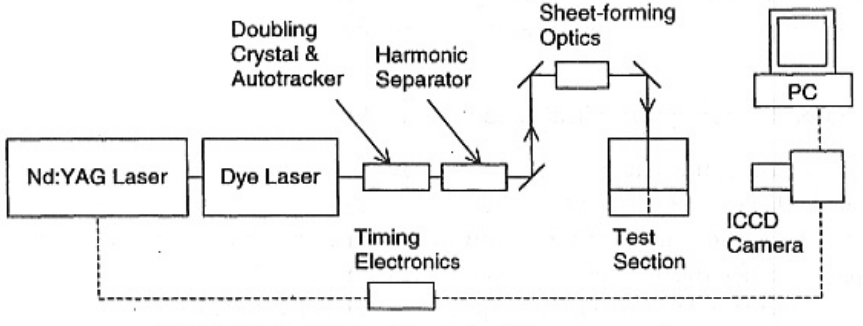

FIGURE 2 The OH Planar laser-induced fluorescence system

RESULTS AND DISCUSSION

Optical Observations

Figure 3 shows direct and schlieren photographs of methane flames stabilized behind a right-angle backward-facing step. In the previous paper (Takahashi et al., 2000), we reported two distinct flame stabilization and suppression regimes; i.e., (I) rim-attached and (II) wake-stabilized, depending on the mean air velocity. In regime I (Fig. 3a, $U_{a0} = 1.4$ m/s), a luminous (sooty), continuously wrinkled laminar flame zone was formed as a result of interactions of the diffusion flame zone and large-scale vortices evolved and developed in the free shear layer. In regime II (Fig. 3b, $U_{a0} = 7.1$ m/s), the flame zone in the shear layer detached and became a turbulent blue flame. Separate blue flame zones with sporadic yellow flashes were formed in the recirculation zone as a result of dynamic air entrainment. The regime-II flames are more likely to occur in highly ventilated fires.

Figure 3c shows the instantaneous schlieren photograph (partial view) of a regime-II flame ($U_{a0} = 7.1$ m/s) at the event of suppression by halon 1301. The agent was released into the airflow for duration of 0.25 s. Because the knife-edge of the schlieren system was placed vertical, the image showed the horizontal gradient of the refractive index field, which depended primarily on the density and, thus, the reciprocal of the temperature. In addition, the schlieren deflectometry was able to capture the wave of agent-laden airflow as a fine irregularity due to the agent's high molecular weight (149). In regime II, a detached turbulent flame was formed in the shear layer, where the small-scale turbulence coexisted with the large-scale vortices, and flame elements were also visualized as oblique dark zones in the recirculation zone. In Fig. 3c, the agent just arrived (at 0.145 s after injection) and the shear layer flame was already affected. Unfortunately, the location of the flame zone is somewhat ambiguous because schlieren imaging is a line-of-sight technique and the flame is not completely two-dimensional due to the three-dimensional nature of turbulent motions.

Figure 4 shows OH PLIF images of methane flames stabilized behind a right-angle backward-facing step, revealing spatial burning variations and the dynamic features of the flame zone in the shear layer and the recirculation zone in the wake of the step. In general, the OH radicals were contained in relatively narrow zones, indicative of wrinkled sheet-like diffusion flames. The broadened lower-intensity regions on lower left (fuel) side of the bright OH zones are thought to be scattering from soot particles (or polycyclic nuclear aromatic hydrocarbons) in fuel pyrolysis zones, which were observed as yellow flashes by the naked eye. Figure 4a shows the flame zone, which was stabilized (but not attached) by the step edges and developed in the shear layer. The flame was

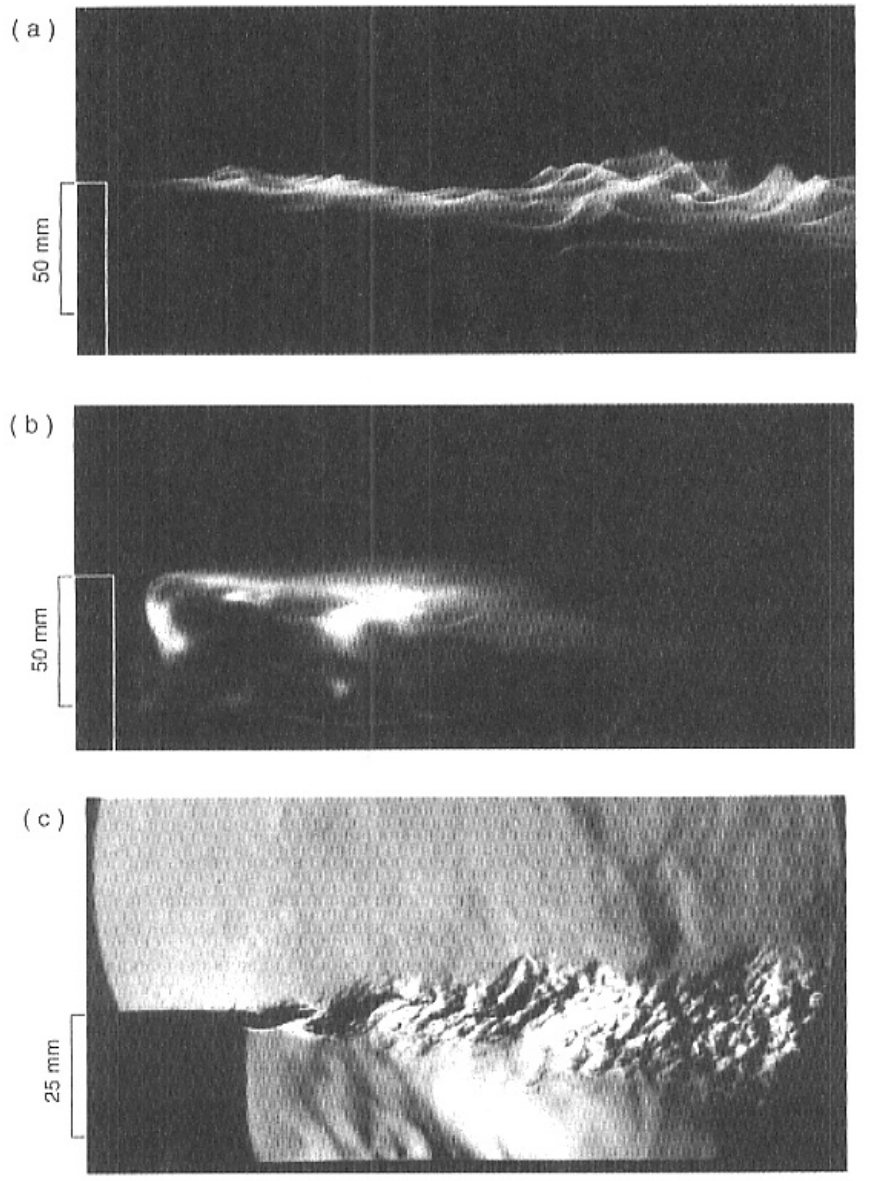

FIGURE 3 Photographs of methane flames stabilized behind a right-angle backward-facing step. Film: KODAK EPH-1600. (a) Direct time exposure (f5.6, 1/4000 s), $h_s = 64$ mm, $U_{a0} = 1.4$ m/s (Regime I); (b) direct time exposure (f1.4, 1/125 s), $h_s = 64$ mm, $U_{a0} = 7.1$ m/s (Regime II); (c) instantaneous (~1 μs) schlieren, $h_s = 32$ mm, $U_{a0} = 7.1$ m/s (Regime II) (See Color Plate III at the back of this issue)

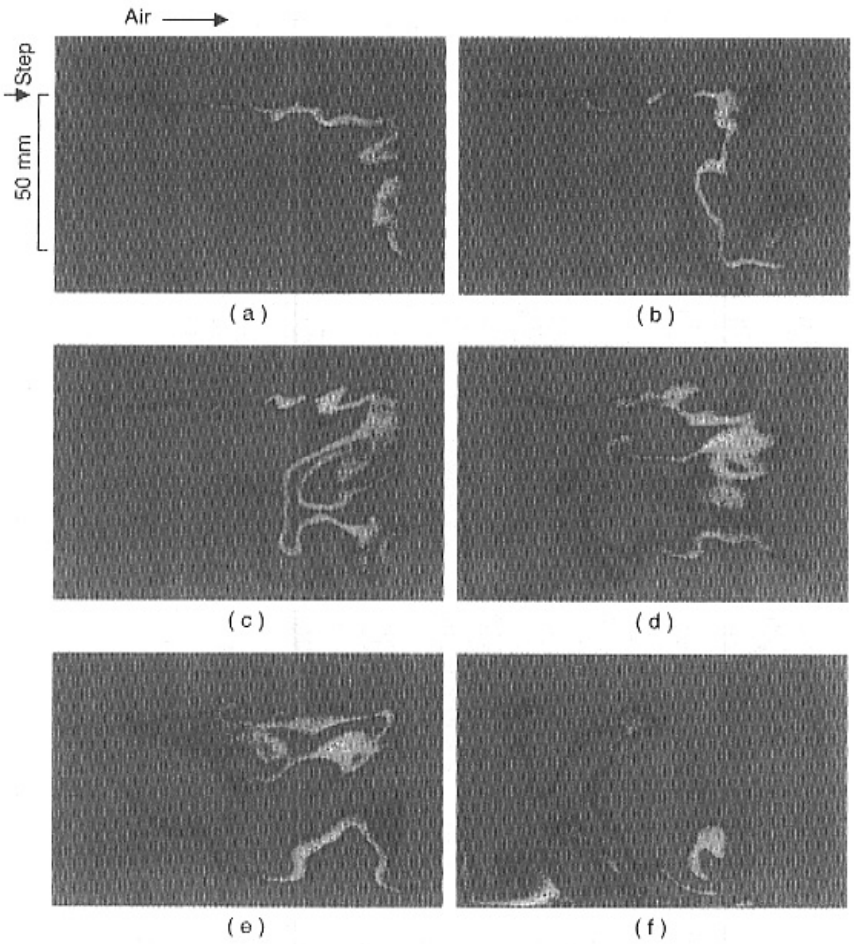

FIGURE 4 Instantaneous (10 ns) OH planar laser-induced fluorescence images of methane flames stabilized behind a right-angle backward-facing step. h_s= 64 mm, U_{a0} = 7.1 m/s (Regime II) (See Color Plate IV at the back of this issue)

wrinkled as a result of interactions with large-scale vortices evolved and developed in the shear layer. The local extinction, or separation, of the shear layer flame was obvious in Figs. 4b through 4d. Unlike visual observations of the flame by the naked eye, the behavior of the flame zone represented by the OH zones was totally dynamic. Although the images in Fig. 4 are not in an actual time sequence, general features of the dynamic behavior of the flame can be extracted. As a result of a back flow of air entrained into the recirculation zone,

the shear layer flame was folded along the fuel-air interface and penetrated deeply into the recirculation zone (Figs. 4a through 4e). A mushroom shaped vortex is evident in Fig. 4c. As the packet of fuel burning in the shear layer (the upper side in Fig. 4e) was consumed, only the flame in the recirculation zone remained momentarily (Fig. 4f). As the fresh fuel emerged and ignited behind the flame in the recirculation zone, a shear layer flame might redevelop (Fig. 4a) and repeat the oscillatory process.

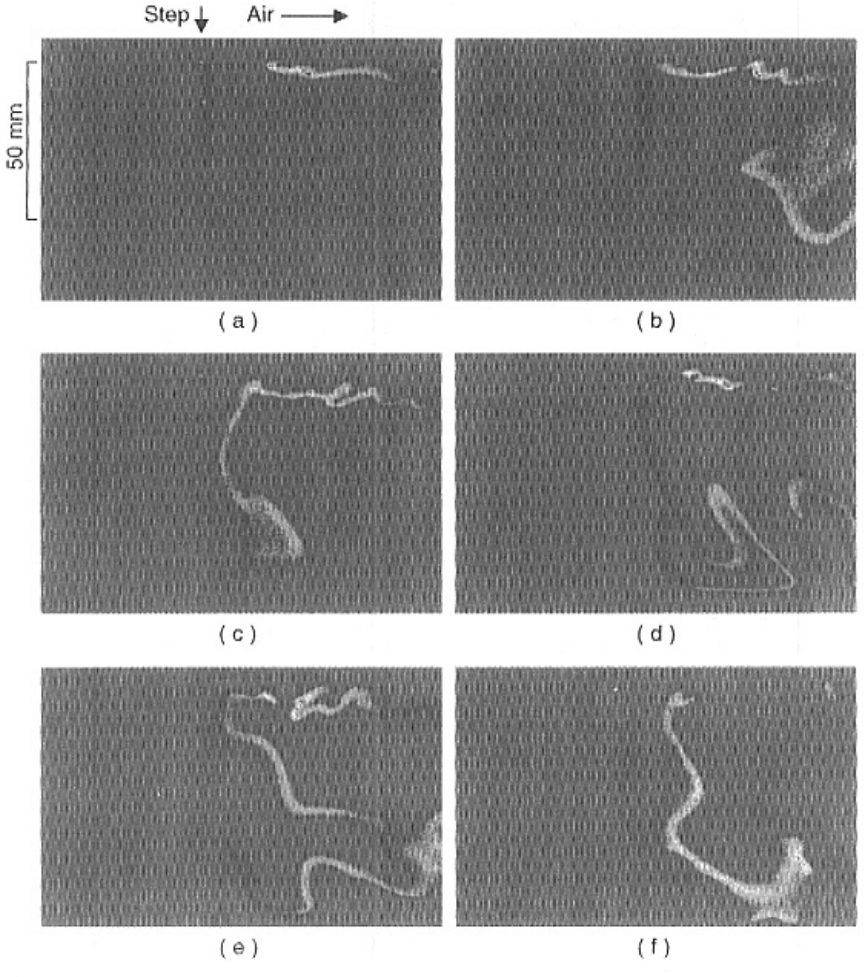

FIGURE 5 Instantaneous (10 ns) OH planar laser-induced fluorescence images of methane flames stabilized behind a 45°-angle backward-facing step. $h_s = 64$ mm, $U_{g0} = 7.1$ m/s (Regime II) (See Color Plate V at the back of this issue)

OH PLIF images in Fig. 5 revealed a feature peculiar to a 45°-angle step. Figures 5a and 5b show the shear layer flame and the flame folding phenomena described above. In addition to the dynamic behavior due to the back flow of the entrained air, the flame zone extended downward near the step (Figs. 5c through 5e) probably because air penetrated along the step wall toward the inside corner, where a counter-rotating recirculation zone was formed. As the local extinction of the shear layer flame spread, the flame near the wall remained (Fig. 5f). Although it is beyond the scope of this paper, the three-dimensional flow field measurement is needed to further investigate the peculiar flame dynamics.

Suppression Limits for Long Agent Injection Periods

The critical agent mole fractions in the oxidizer stream at suppression (X_c) were measured by the transient method at various agent injection periods (Δt) and the steady-state method. Figure 6 shows the probability of extinction (P_{ext}) of ethane flames as a function of the mole fraction of injected nitrogen in the oxidizer stream (X_{N_2}) for a sufficiently long injection period ($\Delta t = 2$ s) and $U_{a0} = 7.1$ m/s (regime II). Thus, for the transient method, the critical agent (nitrogen) mole fraction at suppression for long injection periods (X_∞) was determined at $P_{ext} = 0.9$ as 0.365 for ethane and, in the same manner, as 0.292 for methane. For the JP-8 pool flames, $X_\infty$was 0.04 and 0.087 for halon 1301 and HFC-125, respectively, for $\Delta t = 1$ s or 2 s and $U_{a0} = 7.1$ m/s. These X_∞values indicate that HFC-125 requires a volume factor of ~2, compared to halon 1301, as is consistent with the previous result (Hamins et al., 1994a).

By using the steady-state method, the critical nitrogen mole fraction at suppression of ethane flames was determined at $U_{a0} = 10.9$ m/s as 0.347, which corresponded to a value for the transient method of $P_{ext} = 0.5$ (Fig. 6). At higher nitrogen concentrations, the flame could not be sustained continuously even with repeated re-ignition by the igniter. It is reasonable that for the steady-state measurement, the flame suppression occurred at a nitrogen mole fraction less than the critical value at the transient suppression probability of $P_{ext} = 0.9$.

Although one would anticipate that the flame would blow out by increasing the airflow velocity with no agent added, baffle-stabilized flames are very stable. Hirst and Sutton (1961) showed that the extinction velocities of baffle-stabilized kerosene flames increased monotonically with increasing pressure (0.1–0.8 atm) and height of projection up to an optimum size of plate (~16 mm) and then decreased. The extinction velocity at 1 atm, extrapolated from their data for the plate height of 51 mm, would be over 40 m/s. Therefore, the present experimental conditions ($U_{a0} < 10.9$ m/s) must be substantially less than the extinction limit

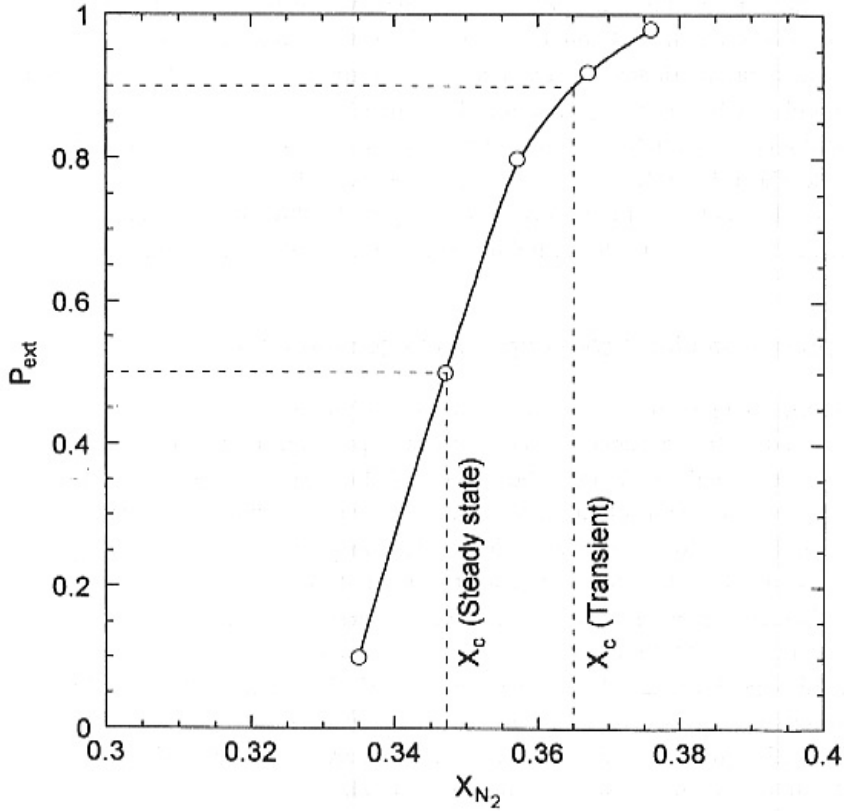

FIGURE 6 The probability of extinction of ethane flames as a function of the mole fraction of injected nitrogen in the oxidizer stream for a long injection period (Δt = 2 s). h_s = 64 mm, U_{a0} = 7.1 m/s (Regime II)

without agent, and thus, X_∞ measured here appears to be independent of the air velocity within the experimental range.

Table I compares the suppression limits for the present obstruction-stabilized flames with the extinction limit data in the literature obtained for various fuels by cup burners (Hirst and Booth, 1977; Bajpai, 1974; Sheinson et al., 1989; NFPA, 1994; Hamins et al., 1994a; Sakai et al, 1995; Saito et al., 1996; Moor et al., 1996; Babb et al., 1999), counterflow diffusion flames (Simmons and Wolfhard, 1957; Tsuji, 1982; Hamins et al., 1994b; Saso et al., 1996; Papas et al., 1996; Pitts and Blevins, 1999) turbulent spray flames (Hamins et al, 1994a, 1996), and baffle-stabilized pool fire (Dyer et al., 1977a). The former two are the

steady-state methods and the latter two are the transient methods, for which the X_c values for long injection periods (X_∞) are listed. Hence, Simmons and Wolfhard (1957) and Tsuji (1982) determined the limiting oxygen index (χ_{O_2}) using hemispherical and cylindrical counterflow diffusion flames, respectively. The limiting oxygen index is the mole fraction of oxygen in the oxidizer stream below which no flame can be stabilized irrespective of the stagnation velocity gradient (i.e., strain rate). Thus, Table I includes both the critical agent mole fractions and the limiting oxygen indices in the oxidizer stream at suppression. The conversion between the two quantities can be made using the relationship:

$$\chi_{O_2} = 0.2093(1 - X_c) \tag{1}$$

Although χ_{O_2} has been used for inert-gas agents, X_c is more distinguishable for halogenated agents, for which X_c is much smaller than unity and thus χ_{O_2} does not vary much.

For nitrogen as the agent, the X_c values for counterflow diffusion flames (0.32 – 0.336 for methane, 0.436 for ethane, 0.393 for propane), particularly by Simmons and Wolfhard (1957), were higher than those for present wake-stabilized (regime II) turbulent flames (0.292 for methane, 0.347 – 0.365 for ethane) and cup-burner flames (0.325 for propane). X_c's for heptane flames using cup burners by various investigators (0.30 – 0.336) were scattered around a value for relatively low strain-rate flat counterflow flames (0.31 for $a = 50\ s^{-1}$). The X_c values using hemispherical counterflow flames by Simmons and Wolfhard (1957) (0.362 for hexane, 0.36 for octane, and 0.357 for decane) were nearly the same and identical to that for a flat counterflow heptane flame at the lowest strain rate listed (0.36 for $a = 24\ s^{-1}$). As expected, the X_c value for the couterflow flame at a high strain rate (360 s^{-1}) was low (0.118). Interestingly, the baffle-stabilized kerosene pool fire resulted in the highest X_c value (0.38) among all fuels listed.

As reported in the previous paper (Takahashi et al., 2000), the critical agent mole fraction at suppression at long injection periods for rim-attached (regime I) and wake-stabilized (regime II) methane flames extinguished with halon 1301 was the same (0.025) and identical to that obtained in the counterflow diffusion flame (Papas et al., 1996). The critical agent mole fraction for step-stabilized JP-8 pool flames with halon 1301 (0.04) was higher than X_c's for JP-8 and heptane using cup burners (0.029 – 0.035) and counterflow flames (0.027 – 0.031) at relatively low strain rates (30 – 45 s^{-1}). The present result for step-stabilized JP-8 pool flames with HFC-125 (0.087) was identical to that for cup burners and among the scatter of the data (0.081 – 0.094) for both JP-8 and heptane using cup burners and counterflow flames. The value for turbulent spray flames (0.078), which might have lower flame stability, was slightly lower than the others. In

summary, a general trend in X_c's for various burner systems, flow conditions, and researchers, in a descending order is as follows:

$$\begin{aligned}\text{Hemispherical counterflow (cf)} \approx \text{flat cf } (a = 24\ \text{s}^{-1}) > &\text{step-stabilized} \\ \approx \text{cup burner} \approx \text{flat cf } (a = 30 - 50\ \text{s}^{-1}) \\ \approx \text{turbulent spray} > \text{flat cf } (a = 360\ \text{s}^{-1})\end{aligned}$$

Here, X_c's for step-stabilized flames might have a wide spread from the lowest (methane/nitrogen) to the highest (kerosene/nitrogen and JP-8/halon 1301) among each group probably because there were many uncontrolled variables affecting the extinction phenomena. Nevertheless, X_c's for the step-stabilized flames did not deviate much from the scattered data range for various burner systems with vastly different flow conditions. This result suggested that the suppression mechanism was essentially the same, except for the counterflow flames at high strain rates ($a \sim 360\ \text{s}^{-1}$), which were extinguished primarily by aerodynamic stretch.

Suppression Limit Dependency on Agent Injection Period

Figure 7 shows the critical agent mole fraction at suppression as a function of the agent injection period at different mean initial air velocities for methane, ethane (Fig. 7a), and JP-8 flames (Fig. 7b). In Fig. 7a, the critical agent (nitrogen) mole fractions remained constant at the X_∞ values (0.292 and 0.365 for methane and ethane, respectively) in the range of $0.5\ \text{s} < \Delta t < 2\ \text{s}$ and increased as Δt was decreased further. The experiment for short agent injection periods was limited by the volume of nitrogen storage vessel and the solenoid valve response time. Thus, minimum injection periods, below which the flame could not be extinguished even at high agent concentrations, could not be determined, unlike the case for methane with halon 1301 reported previously (Takahashi et al., 2000).

For the JP-8 pool flames (Fig. 7b), the dependencies of the critical agent mole fraction on the injection period were determined for various experimental parameters: the agent type, obstruction shape, height, and the mean air velocity. The general trends were the same as the previous results (Takahashi et al., 2000) for methane flames extinguished with halon 1301; the critical agent mole fraction at suppression increased as the injection period was decreased. Any parameter variation, which increases the characteristic mixing time, i.e., increased obstruction height or decreased air velocity, also increased X_c. For halon 1301, the theoretical suppression-limit curve (to be described later) for $\tau = 0.5$ s was just about passing the condition for the design criterion for the current halon fire-extinguishing system in the aircraft engine nacelle; i.e., a minimum agent concentration (about 6% by volume) must be maintained throughout the nacelle for a

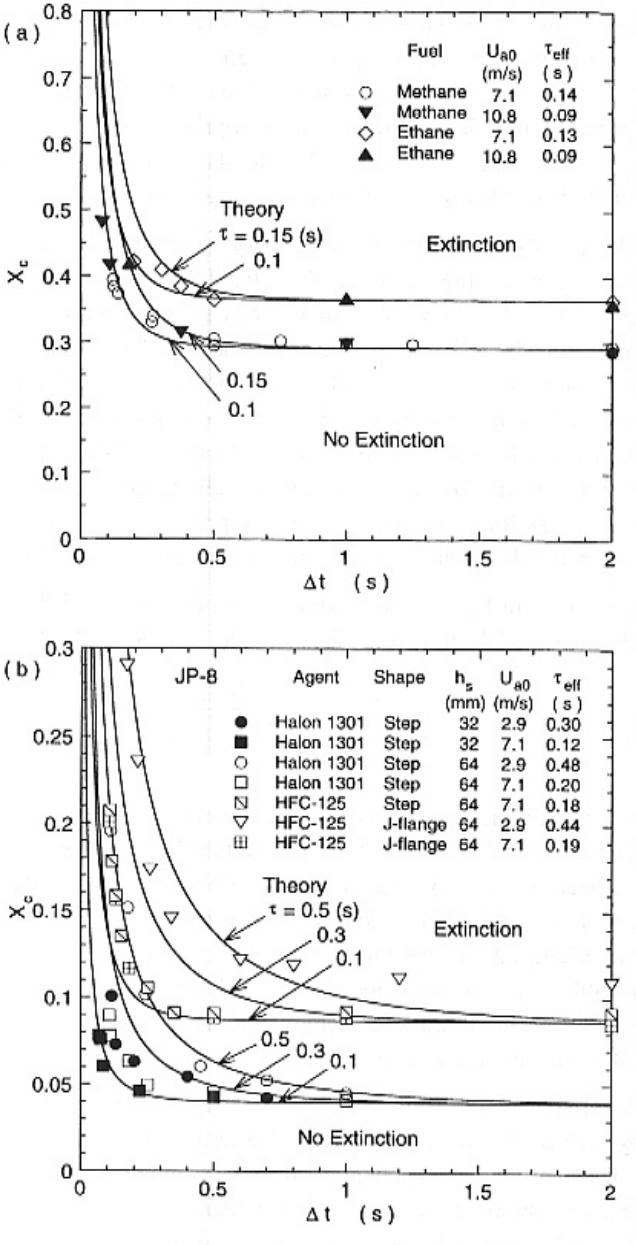

FIGURE 7 Measured critical agent mole fraction in the oxidizer stream at suppression and theoretical curves as a function of the agent injection period. (a) Agent: nitrogen; fuel: methane and ethane. Obstruction: right-angle backward-facing-step (h_s = 64 mm). (b) Agent: halon 1301, HFC-125; fuel: JP-8

minimum time interval (about 0.5 s) to ensure that the fire will be extinguished and not re-light. Thus, the obstruction-stabilized fires, in which the characteristic mixing time is greater than ~0.5 s (the upper-right side of the curve), may not be extinguished by a system whose performance does not exceed the current design criterion. Therefore, the physical time is inappropriate to be used for the design criterion because the suppression limits depend also on the characteristic mixing time, a function of the obstruction size and the flow velocity.

For HFC-125, no difference in the suppression limits for the step and J-flange were found at $U_{a0} = 7.1$ m/s, and the X_∞ value (0.087) was maintained in the range of $0.3 \text{ s} < \Delta t < 2$ s. At a lower air velocity ($U_{a0} = 2.9$ m/s, regime I $\rightarrow$ II transitional), X_c for HFC-125 decreased to 0.1 at $\Delta t = 2$ s but did not approach the minimum value. The similar trend of a higher minimum agent (HFC-125) mole fraction at a low air velocity was also observed by Hamins et al. (1996) for an axisymmetric baffle-stabilized JP-8 spray flame (0.078 and 0.10 at the air velocities of 7.5 m/s and 3.0 m/s, respectively). The critical agent mole fraction may further decrease for much longer injection periods, as was observed previously (Fig. 9c in Takahashi et al., 2000) for methane flames with halon 1301.

Theoretical curves in Fig. 7 were derived by Hamins et al. (1996) based on a phenomenological model for a well-stirred reactor developed by Longwell et al. (1953):

$$X_c = \frac{X_\infty}{1 - e^{(-\Delta t/\tau)}} \tag{2}$$

Hence, τ is the characteristic mixing time for entrainment into the recirculation zone. The measured values of X_∞ were used in the plot. For a long injection period, Eq. 2 becomes $X_c \approx X_\infty$, i.e., a minimum value (X_∞) is sufficient for the free stream mole fraction (X_c) to achieve X_∞ in the recirculation zone to extinguish the flame. Thus, X_∞ is theoretically the same as the steady-state conditions as listed in Table I. For a short injection period, large free stream agent mole fractions ($X_c > X_\infty$) were required to achieve the same condition in the recirculation zone within the available time.

The characteristic mixing time (τ_{exp}) was measured previously (Takahashi et al., 2000) by the sodium emission method (Winterfeld, 1965) as the reciprocal of the rate constant for the exponential turbulent material exchange process between the recirculation zone and the free stream. A linear correlation (Takahashi et al., 2000) was obtained for various obstructions (right-angle and 45°-angle backward-facing steps, baffle plate, and J-flange) as:

$$\tau_{exp} = 34.7(h_s/U_a^*) \tag{3}$$

TABLE I Comparisons of the Extinction Limit Data

Agent	*Fuel*	*Critical Agent Mole Fraction* X_c	*Limiting Oxygen Index*[a] χ_{O_2}	*Flame Configuration*[b]	*Researcher*
Nitrogen	Methane	0.292	0.148	Step-stabilized flame, transient	This study
	Methane	0.336	0.139	Counterflow flame, hemispherical	Simmons & Wolfhard (1957)
	Methane	0.32	0.143	Counterflow flame, cylindrical	Tsuji (1982)
	Methane	0.33	0.140	Counterflow flame, estimate	Pitts & Blevins (1999)
	Ethane	0.365	0.133	Step-stabilized flame, transient	This study
	Ethane	0.347	0.137	Step-stabilized flame, steady-state	This study
	Ethane	0.436	0.118	Counterflow flame, hemispherical	Simmons & Wolfhard (1957)
	Propane	0.393	0.127	Counterflow flame, hemispherical	Simmons & Wolfhard (1957)
	Propane	0.325	0.141	Cup burner	Hamins et al. (1994a)
	Hexane	0.362	0.1335	Counterflow flame, hemispherical	Simmons & Wolfhard (1957)
	Heptane	0.302	0.146	Cup burner	Hirst & Booth (1977)
	Heptane	0.30	0.147	Cup burner	Sheinson et al. (1989)
	Heptane	0.32	0.142	Cup burner	Hamins et al. (1994a)
	Heptane	0.30	0.147	Cup burner	Moore et al. (1996)
	Heptane	0.336	0.139	Cup burner	Sakai et al. (1995), Saito et al. (1996)
	Heptane	0.33	0.140	Cup burner	Babb et al. (1999)
	Heptane	0.31	0.144	Counterflow flame, flat, $a = 50\ s^{-1}$	Hamins et al. (1994a, 1994b)
	Heptane	0.118	0.185	Counterflow flame, flat, $a = 360\ s^{-1}$	Hamins et al. (1994a, 1994b)
	Heptane	0.36	0.134	Counterflow flame, flat, $a = 24\ s^{-1}$	Saso et al. (1996)
	Octane	0.360	0.134	Counterflow flame, hemispherical	Simmons & Wolfhard (1957)
	Decane	0.357	0.1345	Counterflow flame, hemispherical	Simmons & Wolfhard (1957)
	Kerosene	0.38	0.130	Baffle-stabilized pool fire	Dyer et al. (1977a)

Agent	*Fuel*	*Critical Agent Mole Fraction* X_c	*Limiting Oxygen Index*[a] χ_{O_2}	*Flame Configuration*[b]	*Researcher*
Halon 1301	Methane	0.025	0.204	Step-stabilized flame, transient	Takahashi et al. (2000)
	Methane	0.025	0.204	Counterflow flame, flat	Papas et al. (1996)
	JP-8	0.04	0.201	Step-stabilized flame, transient	This study
	JP-8	0.031	0.203	Cup burner	Hamins et al. (1994a)
	JP-8	0.027	0.204	Counterflow flame, flat, $a = 45\ s^{-1}$	Hamins et al. (1994a, 1994b)
	JP-8	0.033	0.202	Turbulent spray flame	Hamins et al. (1994a, 1996)
	Heptane	0.033	0.202	Cup burner	Bajpai (1974)
	Heptane	0.035	0.202	Cup burner	Hirst & Booth (1977)
	Heptane	0.031	0.203	Cup burner	Sheinson et al. (1989)
	Heptane	0.031	0.203	Cup burner	Hamins et al. (1994a)
	Heptane	0.029–0.035	0.202–0.203	Cup burner	NFPA (1994)
	Heptane	0.034	0.202	Cup burner	Sakai et al. (1995), Saito et al. (1996)
	Heptane	0.031	0.203	Counterflow flame, flat, $a = 45\ s^{-1}$	Hamins et al. (1994a, 1994b)
	Heptane	0.03	0.203	Counterflow flame, flat, $a = 30\ s^{-1}$	Saso et al. (1996)
HFC-125	JP-8	0.087	0.191	Step-stabilized flame, transient	This study
	JP-8	0.087	0.191	Cup burner	Hamins et al. (1994a)
	JP-8	0.083	0.192	Counterflow flame, flat, $a = 50\ s^{-1}$	Hamins et al. (1994a)
	JP-8	0.078	0.193	Turbulent spray flame	Hamins et al. (1994a, 1996)
	Heptane	0.081–0.094	0.190–0.192	Cup burner	NFPA (1994)
	Heptane	0.087	0.191	Cup burner	Hamins et al. (1994a)
	Heptane	0.085	0.192	Counterflow flame, flat, $a = 45\ s^{-1}$	Hamins et al. (1994a)

a. Converted from the critical agent mole fraction except for the values by Simmons & Wolfhard (1957) and Tsuji (1982).
b. a is the effective strain rate ($2V/L$; V: the injection velocity, L: the burner separation; Hamins et al., 1994b) for counterflow diffusion flames.

Because the definition of the characteristic mixing time is based on the time constant for the mathematical (exponential decay) function, it is reasonable to define further an effective mixing time for the specific physical phenomenon (suppression limit) as $\tau_{eff} = C\tau_{exp}$. The coefficient C was determined by plotting the data points in $(1 - X_\infty/X_c)$ vs. $\exp[-\Delta t/(\tau_{eff})]$ with various C values until the linear correlation gives a slope of unity (the equality of these variables). Figure 8 includes the previous data for methane flames extinguished with halon 1301 (Fig. 10 in Takahashi et al., 2000) as well as the present data (Fig. 7). In the previous paper (Takahashi et al., 2000), because of relatively low mole fraction of halon 1301 ($X_\infty = 0.025$) to extinguish methane flames, an increase in the flow velocity as a result of agent injection was neglected. However, because of substantial agent concentrations, particularly for nitrogen, the total (air and agent) effective mean velocity (U_t^*) was substituted into U_a^* to calculate τ_{exp} (Fig. 3) and then τ_{eff} for all data in this paper. From Fig. 8, the coefficient C was determined as 0.92, and thus,

$$\tau_{eff} = 0.92\tau_{exp} = 31.9(h_s/U_t^*) \tag{4}$$

τ_{eff} for each condition for the JP-8 flames is listed in Fig. 7.

Figure 8a indicates that the most data points scatter around the theoretical line within ±20% of X_∞. Figure 8b shows the critical agent mole fraction at suppression normalized by the minimum value (X_c/X_{∞}) vs. the agent injection period normalized by the effective mixing time in the recirculation zone ($\Delta t/\tau_{eff}$) with a theoretical curve (Eq. 2 with Eq. 4). The data points collapsed into a single curve independent of the agent and fuel types, the obstruction shape and height, and the mean inlet air velocity. The theoretical curve follows the data trend extremely well. It should be noted, however, that although Eq. 2 was originally derived based on the well-stirred reactor theory, it does not necessarily mean that the flame-flow phenomena in the recirculation zone resemble those in a well-stirred (premixed) reactor. OH PLIF observations rather revealed sheet-like wrinkled laminar diffusion flame zone at the interface of inhomogeneously stirred packets of the fuel and air. The theory worked well probably because the material exchange between the recirculation zone and free stream by the dynamic air entrainment might also be expressed, in a global sense, by the first-order differential equation (Eq. 1 in Takahashi et al., 2000).

The nondimensional representation of the results revealed that the critical agent mole fraction at suppression dramatically increased as the agent injection period decreased below the effective mixing time ($\Delta t/\tau_{eff} < 1$). Because the minimum agent mole fraction can be approximated by the value obtained by conventional steady-state methods (i.e., cup-burner flames or low-strain-rate counterflow diffusion flames) and the effective mixing time is correlated (Eq. 4)

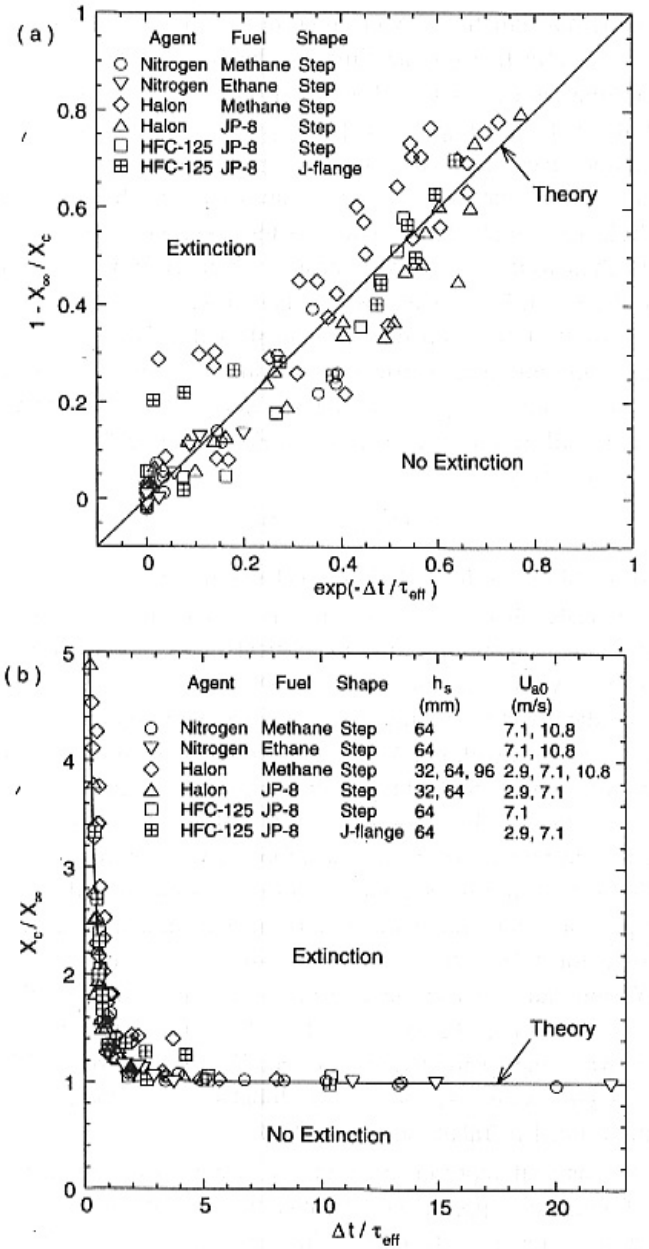

FIGURE 8 Nondimensional representations of the measured suppression limits and a theoretical curve for various agents, fuels, obstruction shapes, heights, and air velocities. (a) $(1 - X_\infty/X_c)$ vs. $\exp(-\Delta t/\tau_{eff})$; (b) X_c/X_∞ vs. $\Delta t/\tau_{eff}$

to the experimental conditions (the step height and effective total mean air velocity), the suppression limit of step-stabilized flames can be predicted theoretically within an error bar of approximately ±20%.

Suppression Mechanism

The extinction of diffusion flames is generally explained (Williams, 1974) by a critical Damköhler number (Da = τ_r/τ_c, τ_c: the chemical time and τ_r: the flow or diffusion time) below which extinction occurs. Thus, Da decreases either by decreasing τ_r or increasing τ_c. Increasing the velocity gradient (strain rate) across the flame zone decreases τ_r, thus leading to extinction by aerodynamic flame stretch. On the other hand, increasing the agent concentration decreases the flame temperature (thermal effects) and/or inhibits oxidation (chemical effects), thus increasing τ_c, thus resulting in extinction by thermochemical effects. Nitrogen and HFC-125 are thermal suppressants, and halon 1301 is considered to be primarily chemical suppressant. In the present experiments, the air velocities were substantially smaller than those for blowout conditions with no agent and X_∞ was independent of the airflow velocity as described earlier. Furthermore, the current results revealed that X_∞ was similar to the values obtained by the steady-state cup-burner or low-strain-rate counterflow diffusion flame and that suppression occurred if the agent injection period was long enough to increase the agent mole fraction in the recirculation zone to X_∞. In addition, even at high air velocities in regime II, freely moving (low strain rate) flame zones exist in the low-velocity recirculation zone in addition to the high-strain flame in the shear layer. Therefore, the suppression of obstruction-stabilized flames appears to occur by extinction of relatively low-strain-rate diffusion flames due to thermochemical causes. Although the experimental conditions of the data presented here are limited, the basic concept for suppression criterion obtained for a gaseous fuel using simple geometries must apply to liquid-fuel pool fires stabilized in more complex clutter configurations.

CONCLUSIONS

The suppression limits of nonpremixed flames of methane, ethane, and JP-8, stabilized by a backward-facing step or J-flange in an airstream were measured as the critical agent mole fraction at suppression as a function of the unsteady injection period of a gaseous fire-extinguishing agent (nitrogen, halon 1301, or HFC-125) for various obstruction heights and air velocities. The steady-state

suppression limit was also measured by continuously adding nitrogen into the approach airflow in the ethane flame. The minimum agent mole fraction at suppression obtained at long injection periods in the transient method (0.292 and 0.365 for methane and ethane, respectively, with nitrogen; 0.04 and 0.087 for JP-8 with halon 1301 and HFC-125, respectively) or by the steady-state method (0.347 for ethane with nitrogen) did not vary much from the values obtained by the conventional steady-state methods, i.e., cup burners or laminar, relatively low strain-rate counterflow diffusion flames. Furthermore, OH PLIF images revealed the narrow, wrinkled laminar flame zone, which freely move with the fuel-air interface in response to the dynamic air entrainment. Therefore, the suppression process must be controlled by thermochemical extinction of the relatively low-strain-rate flames in the low-speed recirculation zone even at high free-stream velocities.

The obstruction-stabilized JP-8 pool fire may not be extinguished with halon 1301 at the conditions specified by the design criterion (6% agent concentration for 0.5-s duration) for the current fire-extinguishing system in the aircraft engine nacelle. The physical time is inappropriate to be used for the design criterion; instead, the effective mixing time, determined as $\tau_{\text{eff}} = 31.9[h_s/U_t^*]$, is more relevant to the extinction condition and should be considered in establishing a criterion. The measured extinction-limit data points collapsed into a single curve when plotting the critical agent mole fraction at extinction normalized by its minimum value obtained at long injection periods as a function of the agent injection period normalized by the effective mixing (residence) time. The data trend can be predicted by a theoretical expression using the minimum agent mole fraction and the effective mixing time. The effect of obstruction on the extinction limits is significant only when the agent injection period is less than the effective mixing time. These physical understanding and prediction capability would simplify testing of future agents and shift the practical design problem to one of quantifying the local velocity and obstruction size in the most likely location for a pool fire.

Acknowledgements

This research is part of the Department of Defense's Next-Generation Fire Suppression Technology Program, funded by the DoD Strategic Environmental Research and Development Program, Sandia National Laboratories (SNL), Albuquerque, New Mexico, under Contract No. BF-3670, and the Air Force Research Laboratory, Propulsion Directorate, Propulsion Sciences and Advanced Concept Division, Wright-Patterson Air Force Base, Ohio, under Contract No. F33615–97-C-2719 (Technical Monitor: C. W. Frayne). The authors wish to acknowledge the assistance in conducting the PLIF experiment by Dr. Campbell

D. Carter of Innovative Scientific Solutions, Inc., stimulating discussions with Dr. Sheldon R. Tieszen, Ms. Amalia R. Lopez, and Dr. Louis A. Gritzo of SNL, and valuable inputs for realistic test conditions and geometries by Mr. Mark Kay and Dr. Glen Harper of The Boeing Company.

References

Babb, M., Gollahalli, S. R., and Sliepcevich, C. M. (1999). Extinguishment of liquid heptane and gaseous propane diffusion flames. *Journal of Propulsion and Power*, 15, 260–265.

Bajpai, S. N. (1974). An investigation of the extinction of diffusion flames by halons. *J. Fire and Flammability*, 5, 255.

Donbar, J. M., Driscoll, J. F., and Carter, C. D. (2000). Reaction zone structure in turbulent nonpremixed jet flames – from CH-OH PLIF Images. *Combustion and Flame*, 122, 1–19.

Dyer, J. H., Marjoram, M. J., and Simmons, R. F. (1977a). The extinction of fires in aircraft jet engines-Part III, Extinction of fires at low airflows. *Fire Technology*, 13, 126–138.

Dyer, J. H., Marjoram, M. J., and Simmons, R. F. (1977b). The extinction of fires in aircraft jet engines-Part IV, Extinction of fires by sprays of bromochlorodifluoromethane. *Fire Technology* 13, 223–230.

Gritzo, L. A., Tucker, J. R., Ash, L. (1999). Development of fire and suppression models for DoD vehicle compartments: background, objectives, and methodology. *Proceedings of the 9th Halon Options Technical Working Conference (HOTWC-99)*, Albuquerque, NM, pp. 34–44.

Grosshandler, W. L., Gann, R. G., and Pitts, W. M., Introduction (1994). Introduction. *Evaluation of Alternative In-Flight Fire Suppressants for Full-Scale Testing in Simulated Aircraft Engine Nacelles and Dry Bays (W. L. Grosshandler, R. G. Gann, and W. M. Pitts, Eds.)*, National Institute of Standards and Technology, NIST SP 861, pp. 1–12.

Hamins, A., Gmurczyk, G., Grosshandler, W., Rehwoldt, R. G., Vazquez, L., Cleary, T., Presser, C., and Seshadri, K. (1994a). Flame Suppression Effectiveness. *Evaluation of Alternative In-Flight Fire Suppressants for Full-Scale Testing in Simulated Aircraft Engine Nacelles and Dry Bays* (W. L. Grosshandler, R. G. Gann, and W. M. Pitts, Eds.), National Institute of Standards and Technology, NIST SP 861, pp. 345–465.

Hamins, A., Trees, D., Seshadri, K., and Chelliah, H. K. (1994b). Extinction of nonpremixed flames with halogenated fire suppressants. *Combustion and Flame*, 99, 221–230.

Hamins, A., Cleary, T., Borthwick, P., Gorchkov, N., McGrattan, K., Forney, G., Grosshandler, W., Presser, C., and Melton, L. (1995). Suppression of Engine Nacelle Fires. *Fire Suppression System Performance of Alternative Agents in Aircraft Engine and Dry Bay Laboratory Simulations* (R. G. Gann, Ed.), National Institute of Standards and Technology, NIST SP 890, Vol. II, pp. 1–199.

Hamins, A., Presser, C., and Melton, L. (1996). Suppression of a baffle-stabilized spray flame by halogenated agents. *Proceedings of The Combustion Institute*, 26, 1413–1420.

Hirst, R., and Booth, K., (1977). Measurements of flame-extinguishing concentrations. *Fire Technology*, 13, 4.

Hirst, R., Farenden, P. J., and Simmons, R. F. (1976). The extinction of fires in aircraft jet engines-Part I, Small-scale simulation of fires. *Fire Technology*, 12, 266–289.

Hirst, R., Farenden, P. J., and Simmons, R. F. (1977). The extinction of fires in aircraft jet engines-Part II, Full-scale fire tests. *Fire Technology*, 13, 59–67.

Hirst, R., and Sutton, D. (1961). The effect of reduced pressure and airflow on liquid surface diffusion flames. *Combustion and Flame*, 5, 319–330.

Longwell, J. P., Frost, E. E., and Weiss, M. A. (1953). Flame stability in bluff body recirculation zones. *Industrial and Engineering Chemistry*, 45, 1629–1633.

Moore, T. A., Weitz, C. A., and Tapscott, R. E. (1996). An update of NMERI cup-burner test results. *Proceedings of the 6th Halon Options Technical Working Conference (HOTWC-96)*,Albuquerque, NM, pp. 551–564.

Moussa, N. A. (1994). Effects of Clutter on Performance of Fire Suppression Agents in Aircraft Dry Bays and Engine Nacelles. Report prepared for Booz, Allen and Hamilton, Dayton, Ohio.

National Fire Protection Agency (1994). *Standard on Clean Agent Fire Extinguishing Systems*, NFPA 2001.

Papas, P., Fleming, J. W., and Sheinson, R. S. (1996). Extinction of non-premixed methane- and propane-air counterflow flames inhibited with CF_4, CF_3H and CF_3Br. *Proceedings of The Combustion Institute*, 26, 1405–1411.

Pitts, W. M., and Blevins, L. G. (1999). An investigation of extinguishment by thermal agents using detailed chemical modeling of opposed-flow diffusion flames. *Proceedings of the 9th Halon Options Technical Working Conference (HOTWC-99)*, Albuquerque, NM, pp. 145–156.

Raghunandan, B. N., and Yogesh, G. P. (1989). Recirculating flow over a burning surface-flame structure and heat transfer augmentation. *Proceedings of The Combustion Institute*, 22, 1501–1507.

Rohmat, T. A., Katoh, H., Obara, T., Yoshihashi, T., and Ohyagi, S. (1998). Diffusion flame stabilized on a porous plate in a parallel airstream. *AIAA J.* 36, 1945–1952.

Saito, N., Ogawa, Y., Saso, Y., and Sakai, R. (1996). Improvement on Reproducibility of Flame Extinguishing Concentration Measured by Cup Burner Method. Report of Fire Research Institute of Japan, No. 81, pp. 22–29.

Sakai, R., Saito, N., Saso, Y., Ogawa, Y., and Inoue, Y. (1995). Flame Extinguishing Concentrations of Halon Replacements for Flammable Liquids. Report of Fire Research Institute of Japan, No. 80, pp. 36–42.

Saso, Y., Saito, N., Liao, C., and Ogawa, Y. (1996). Extinction of counterflow diffusion flames with halon replacements. *Fire Safety Journal*, 26, 303–326.

Sheinson, R. S., Penner-Hahn, J. E., and Indritz, D. (1989). The physical and chemical action of fire suppressants. *Fire Safety Journal*, 15, 437–450.

Simmons, R. F., and Wolfhard, H. G. (1957). Some limiting oxygen concentrations for diffusion flames in air diluted with nitrogen. *Combustion and Flame*, 1, 155–161.

Takahashi, F., Schmoll, W. J., Strader, E. A., and Belovich, V. M. (2000). Suppression of a non-premixed flame stabilized by a backward-facing step. *Combustion and Flame*, 122, 105–116.

Tieszen, S. R., and Lopez, A. R. (1999). Issues in numerical simulation of fire suppression. *Proceedings of the 9th Halon Options Technical Working Conference (HOTWC-99)*, Albuquerque, NM, pp. 178–190.

Tsuji, H. (1982). Counter flow diffusion flames. *Prog. Energy Combust. Sci.*, 8, 93–119.

United Nations Environment Programme (UNEP) (1994). *Report of the Halon Fire Extinguishing Agents Technical Options Committee*.

Williams, F. A. (1974). A unified view of fire suppression. *Journal of Fire & Flammability*, 5, 54–63.

Winterfeld, G. (1965). On processes of turbulent exchange behind flame holders. *Proceedings of The Combustion Institute*, 10, 1265–1275.

P. A Time Scale Approach to Understanding Jet Fuel Combustion and Particulate Formation and Growth

A01-16870

AIAA 2001-1085
A Time Scale Approach to Understanding Jet Fuel Combustion and Particulate Formation and Growth

D. R. Ballal
University of Dayton
Dayton, OH
and
W. E. Harrison, III
Air Force Research Laboratory (AFRL/PRTG)
WPAFB, OH

39th AIAA Aerospace Sciences Meeting & Exhibit
8-11 January 2001 / Reno, NV

A Time Scale Approach to Understanding Jet Fuel Combustion and Particulate Formation and Growth

by

Dilip R. Ballal*
University of Dayton
Dayton, OH

William E. Harrison III
Air Force Research Lab. (AFRL/PRTG)
Wright-Patterson AFB, OH 45433

Abstract

Airborne particulates and aerosols are produced during combustion in a turbine engine. Particulates affect engine durability since particulate impingement causes pitting of turbine blades and carbon deposits can clog fuel injectors. Particulates cause respiratory aliments, haze that impairs visual range, serve as nucleation sites for condensation trails, and sites for chemical reactions that can lead to ozone depletion at high altitudes. For these reasons, the Fuels Branch of the Air Force Research Laboratory (AFRL/PRTG) at Wright-Patterson AFB Ohio is conducting research on fuel additives that would significantly decrease particulate emissions. To understand how fuel additives reduce particulate emissions, a fundamental understanding of particulate formation and growth is needed.

In this investigation, time scales of fuel combustion were calculated for a gas turbine combustor burning JP-8 fuel. The time scales ranged between 4.5 μs (elementary chemical reactions) to 10 ms (jet fuel thermal stressed oxidation time). Between these two extremes can be found time scales of ignition (60 μs) and microscale turbulent mixing (67 μs). These time scales were used in the fundamental analysis of particulate formation and growth.

An embryonic stage of particle formation is nuclei formation. The theory of homogeneous nucleation predicted the formation of stable nuclei in the size range 1.6 to 3 nm dia. containing 30 to 140 molecules respectively. As stable nuclei concentration increases, they collide and coalesce to form larger primary particles. Calculations predicted a primary particle size of 71 nm. Primary particles grow as a result of two key processes: heterogeneous chemical reaction condensation and turbulent coagulation. For the turbulent Kolmogoroff micro scale convection time of 67 μs in a typical gas turbine combustor, the rate of heterogeneous chemical reactions increased the primary particle size 13 percent to 80 nm diameter and turbulent coagulation grew it further 17 percent to a 94 nm diameter particle. In a combustion process, soot oxidation decreases particle size. Garo et al (1990) and Howard (1996) have measured particulates down to 50 nm in diameter. Thus, it remains to relate the predicted particulate formation and growth to the measured particulate size and emissions index (g/kg of fuel) from gas turbine engines and also to determine how jet fuel additives work to decrease the particulate size and number density.

*Fellow AIAA

Nomenclature

a_p	particle radius
A, B	surface area per unit volume of fluid, reactants
d_p	particle or drop diameter
D	diffusion coefficient
D_f	fractal dimension
I_n	nucleation rate
k	Boltzmann constant, reaction rate coefficient
l_p	mean free path
m	mass of particle or molecule
MW	molecular weight
n	concentration
N_p	number of primary particles in agglomerate
P	pressure
r	reaction rate
S	vapor saturation ratio, (S_T = turbulent burning velocity)
t	time
T	absolute temperature
u'	turbulent fluctuating velocity
v	particle volume
v_m	molecular volume, ($M/N_{av}\,\rho_p$)
x,y,z	direction coordinates

Greek alphabet

α	thermal diffusivity
β	collision frequency function
ε	turbulent eddy dissipation
ϕ	equivalence ratio, aerosol volumetric concentration
η_k	Kolmogoroff micro scale
λ_{eff}	evaporation coefficient
μ	dynamic viscosity
ν	kinematic viscosity, stoichiometric coefficient
ρ	density, (ρ_p = particle density)
σ	surface tension
τ	characteristic time

Introduction

The United States military uses between 15 – 20 billion liters (4 – 5 billion gallons) of jet fuel (JP-8 and JP-5) per year (Edwards et al. 2001), about 10 percent of the total jet fuel consumed in the U.S. The fleet average emission index for soot particulates has been estimated by the International Civil Aviation Organization (ICAO) to be approximately 0.04 g/kg of fuel burned, thus military aircraft produce approximately 600,000 kilograms of particulate emissions per year (Landau et al., 1994; Thompson, 1996) for a total of approximately 2.3×10^{30} particulates. The average size of the particulate is 50 nm and average density is 2 g/cm^3 (Howard 1996). Although there is some uncertainty in these estimates, they are consistent with the magnitude being used to estimate global emission from aircraft (Niedzwieki, 1998). Airborne particles pose both health and environmental risks. The National Ambient Air Quality Standards have a health based regulation (PM10) for particulate matter with $d_p < 10$ μm and there is growing evidence that this regulation is insufficient. The EPA is evaluating regulations for particulates << 2.5 μm (EPA Fact Sheet dated July 16, 1997). Since solid particulates in aircraft exhaust are sub-micron in size (Lefebvre 1999), aircraft emissions may be included in the enforcement legislation. Also, it is unclear at this point how the new legislation will affect the military aircraft. However, the total particulate emissions emitted by aircraft

at a base can lead to non-attainment of the overall air quality standards for the region where the base is located.

The specifications for military jet fuels were developed approximately 50 years ago and the sulfur level allowed in jet fuel then, as is now, is 0.3 weight percent, significantly higher than levels currently allowed in diesel fuel or gasoline. Jet fuels produced with 0.3 weight percent sulfur are extremely rare, however Henz and Robinson (1998) state that the median sulfur level for jet fuels is approximately 0.06 weight percent. As a result, military aircraft emit over 8.9×10^9 kilograms per year of sulfur oxides. Sulfur compounds have been linked to the generation of particulates in internal combustion engines and may play a role in the particulate emissions generated by turbine engines. Eliminating sulfur from jet fuels will decrease particulate and aerosol levels, but it will not entirely eliminate the particulate formation as research has shown that soot particles can form via other mechanisms.

Research conducted by the Fuels Branch of the Air Force Research Laboratory (AFRL/PRTG) at WPAFB, Ohio has found that additives can be blended with jet fuel to reduce the level of particulate emissions. The first evidence of this was found during the demonstration of the thermal stability improving additive "JP-8+100" in fighter aircraft. One could walk along the flight line and clearly identify those aircraft that had been using JP-8+100 for approximately 100 flight hours or more by the reduction of soot in the exhaust area (Fig. 1) (see Maurice et al 1999). Boeing, in collaboration with the Air Force and the University of Missouri at Rolla, was first to measure the reduction of particulates with JP-8+100 (Toepke 1999). These findings led to a series of initial experiments by AFRL researchers in a generic swirl stabilized single cup atmospheric combustion rig. Experiments confirmed the Boeing results for the "JP-8+100" additive and proved that other more highly tailored additives could reduce the particulate emissions by as much as 50 percent (Maurice et al. 1999). With careful development, new additives may be able to reduce particulate emissions by as much as 70 percent. During these experiments, it was realized that to understand how these additives were mitigating particulate formation, characteristic time scales of fuel combustion must be identified and fundamental mechanisms of particulate formation and growth analyzed.

Particulates are produced during the combustion process and grow in size in the combustor and the exhaust. The process of fuel delivery and combustion in most practical systems is dynamic in nature. As such, the competition between various processes as expressed by their rates or characteristic time scales dictate the outcome of fuel oxidation, combustion, particulate formation, and particulate oxidation in a practical combustion system.

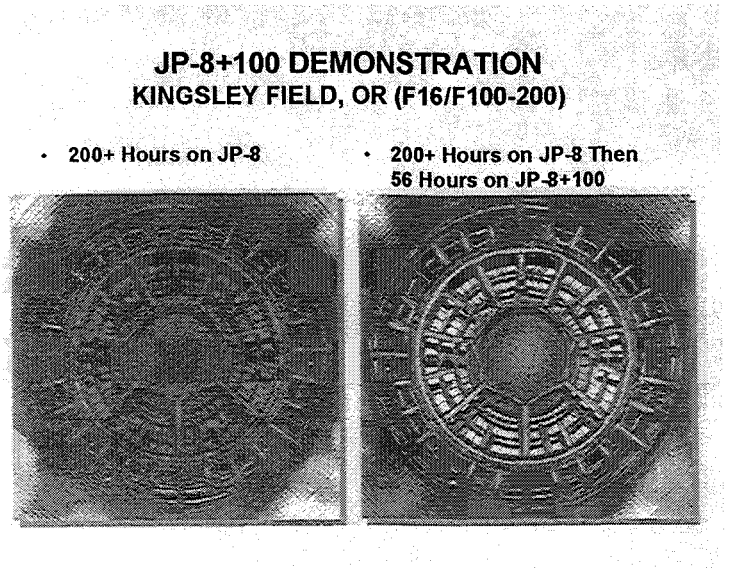

Fig. 1: Demonstration of reduced particulate emissions with JP-8+100 jet fuel additive.

In this paper, the time scales of fuel combustion processes are calculated for a typical gas turbine combustor operating condition. Next, analysis of particulate formation is presented and time scale-particulate formation relationship is discussed. Finally, initial theories of fuel additive interactions to reduce particulates are discussed.

Time Scale Estimation

In this investigation, time scales of fuel oxidation and combustion were calculated for a gas turbine combustor, 20 cm long, 15 cm diameter. and supplied with JP-8 liquid fuel. The following combustor operating conditions were used (Lefebvre 1999) unless otherwise specified: P = 20 atm, inlet T = 750K, mean velocity = 50 m/s, turbulence level = 30 percent, Kolmogoroff eddy size = 1 mm, integral scale = 15 mm, flame temp. = 2200K. In this combustor the flow residence time is 4-8 ms corresponding to a mean reference velocity range of 25-50 m/s. Table 1 summarizes the results of our calculations.

The time scales of fluid mechanics and combustion processes cover a very wide range. At one extreme is the slow oxidation of aviation jet fuel as it serves the function of a heat sink for engine components. In the engine fuel injector where jet fuel is heated to 435K at 100 atmospheres prior to combustion, the time scale is of the order of 10 ms. At the other extreme are elementary chemical reaction time scales as short as 4.5 μs. Between these two extremes can be found time scales of ignition (60 μs), microscale turbulent mixing and transport (67 μs), and combustor residence time (4 ms). Thus, a challenge lies in relating this large time span to mechanism of particulate formation.

Table 1: Typical Time Scales for Jet Fuel Oxidation and Combustion

A. Chemical Reactions
- CH_4 elementary reaction: 4.5 μs
- NO formation: 4.4 ms to 16 ms
- Global chemical reaction: 300 μs
- Soot formation: 2.5 ms

B. Turbulent Mixing
- Kolmogoroff scale convection: 67 μs
- Integral scale convection: 1 ms

C. Liquid Fuel Evaporation
- Spray evaporation: 3.3 ms (SMD = 50 μm)

D. Spark Ignition
- Optimum spark duration: 60 μs
- Flame kernel growth: 400 μs

E. GT Combustor

- Maximum convection time: 4 ms (50 m/s); 8 ms (25 m/s)

F. Jet Fuel Oxidation

- Jet fuel oxidation: 10.14 ms
- Soot oxidation in flame: 25 μs (1 μm dia.), 2.5 ms (10 μm dia.)
- CO oxidation: 31 μs (elementary); 170 μs (global)

Jet Fuel Oxidation Time

Jet fuel is used as a primary heat sink to cool aircraft subsystems and engines. As the fuel cools, it is thermally stressed causing gums, varnish and coke to form. (Heneghan et al. 1996.) A typical military engine with 13,600 kgf of thrust has a specific fuel consumption of 0.79 kg/hr/kgf thrust. Each of its 32 fuel injectors delivers 0.2 kg/s of JP-8 fuel to the combustor. The fuel line exposed to high temperature is 15.2 cm long and 0.46 cm i.d. Thus, the fuel residence time in the nozzle is 10.14 ms. Over this time, the jet fuel is at a temperature of 480 K (400F) or higher. Tests conducted at AFRL/PRTG demonstrate that over a 10 ms time interval, approximately 1 ppm of carbon deposition is produced in the JP-8 fuel. This thermally stressed fuel provides particulate precursors that may increase particulate formation and growth.

Fuel Evaporation Time

As the fuel injector atomizes the liquid fuel into fine droplets and injects them into the hot combustor surroundings, the droplets evaporate rapidly. By definition, the evaporation time is given by the relationship:

$$T_{evap} = D_o^2/\lambda_{eff}.$$

The effective evaporation coefficient, λ_{eff} takes into account both convective and transient heat-up effects at high pressure and temperature found in gas turbine combustors (Lefebvre, 1989). Thus, for a pressure of 20 atm., reaction temperature of 2200K, and spray-air relative velocity of 25 m/s, the droplet evaporation time is 13.3 ms and 3.32 ms for fuel spray SMD of 100 μm and 50 μm respectively. Thus, this time may be available for particulate formation within the droplet before it evaporates completely.

Fuel-Air Mixing Time

Large (integral) eddies in the turbulent flow convectively transport fuel-air mixture to different parts of the combustor and small (Kolmogoroff) eddies cause local molecular-level mixing of fuel and air. Thus, for a typical combustor, the integral convective mixing time scale L_y/u'. = 1 ms and the micro-mixing time scale η_k/u' = 67 μs. These mixing times are over an order of magnitude lower than fuel evaporation time.

Ignition Time

To ignite the fuel-air mixture in the most efficient manner, the spark energy is released into the mixture in as short a time as possible. Ballal and Lefebvre (1975) discovered that for turbulent flowing mixtures, the optimum spark duration for minimum ignition energy was 60 μs. The firing of spark into the combustible mixture initiates local ignition and formation of a spherical flame kernel. This flame kernel has to grow above a certain critical size so that the rate of heat released from the combustion of fresh mixture in its

spherical volume exceeds the rate of heat loss from its surface. Using the Ballal and Lefebvre (1977) formulation, the duration required to grow the spherical flame kernel to its critical size (or quench diameter) is called the quench time. For the pressure, temperature, and turbulent flow conditions within the combustor, the quench time is calculated to be 400 μs. Thus, the total ignition time scale is 460 μs.

Chemical Reaction Time

The combustion process can be analyzed at two levels: elementary and global. A characteristic chemical time, τ_{chem} may be defined as time required for the concentration of a reactant to decrease from its initial value to a value equal to *(1/e)* times the initial value. For a bimolecular reaction:

$$\tau_{chem} = \ln[e + (1-e)([A]_0/[B]_0)]/([B]_0 - [A]_0)k_{bimole}$$

An important elementary bimolecular reaction in the oxidation of methane is:

$$CH_4 + OH \rightarrow CH_3 + H_2O$$

with a rate coefficient:

$$k\ (cm^3/gmol\text{-}s) = 1.0\ 10^8\ T\ (K)^{1.6}\ \exp\ [-1570/T\ (K)]$$

For the pressure and temperature conditions in the combustor, the chemical reaction time for this reaction is calculated to be 4.5 μs. For methane-air global chemical reaction, Ballal and Lefebvre (1981) define:

$$\tau_{chem} = 15.6\ \alpha/[u'\ (S_T - 0.63\ u')].$$

This formula yields a global chemical reaction time = 300 μs.

Gaseous Pollutant Formation and Oxidation Time

CO Oxidation

Hydrocarbon combustion can be characterized as a two-step process: the first step involves the breakdown of fuel to CO and the second step is the oxidation of CO to CO_2. It is well known (Glassman 1996) that CO formation time is much shorter than the CO oxidation time. Thus, all efforts in controlling CO emissions are directed towards the enhancement of CO oxidation rather than attempting to inhibit its formation. The key reaction in the CO oxidation is:

$$CO + OH \rightarrow CO_2 + H$$

with the rate coefficient:

$$k\ (cm^3/gmol\text{-}s) = 4.76\ 10^7\ T\ (K)^{1.23}\ \exp\ [-35.2/T\ (K)]$$

For the pressure and temperature conditions in the combustor, the CO oxidation reaction time is calculated to be 31 μs. In practical combustors, using global kinetics, Vranos (1974) has calculated the CO oxidation time of 170 μs corresponding to a primary zone equivalence ratio of 0.8.

NOx Formation

The formation of species such as NO and NO_2 is a complex function of temperature, residence time, equivalence ratio and detailed chemical kinetic pathways, such as thermal, prompt, or N_2O-intermediate mechanism.

The thermal mechanism dominates at high-temperature (T> 1800K) over a range of equivalence ratios close to

stoichiometric, while the prompt mechanism is important in rich combustion. For very lean, low-temperature combustion process, the N_2O-intermediate mechanism plays an important role in the production of NO. This last mechanism is important in NO control strategies that involve lean premixed combustion, which are currently being explored by gas turbine designers for power generation. In the atmosphere, nitric oxide ultimately oxidizes to form nitrogen dioxide, which is important to the production of particulates, acid rain, and photochemical smog. The NO formation rate may be calculated as follows:

(i) The reaction:

$$CH + N_2 \rightarrow HCN + N$$

with the rate coefficient:

$$k\ (cm^3/gmol\text{-}s) = 2.86\ 10^8\ T\ (K)^{1.1}\ \exp\ [-10{,}267/T\ (K)]$$

is the rate-limiting step in the formation of N atom. For a fuel lean, low-temperature ($T \approx 1350K$) condition, the N atom formation time is 410 μs and for high-temperature ($T \approx 2200K$) condition, it is 20 μs.

(ii) Calculation of NO formation using the reactions:

$$N_2 + O \rightarrow NO + N$$

$$N + O_2 \rightarrow NO + O$$

can be made by using the rate expression:

$$d[NO]/dt = 2\ k_1\ [O]_{equil}\ [N_2]$$

where k_1 is the forward rate coefficient for the rate-limiting reaction:

$$N_2 + O \rightarrow NO + N$$

This calculation yields NO formation rate of 16 ms at 2200K and 4.4 ms at 2300K respectively.

(iii) The elementary reaction step that is responsible for forming NO_2 is:

$$NO + HO_2 \rightarrow NO_2 + OH$$

where the HO_2 radicals are formed in the relatively low-temperature regions. Thus, NO molecules from the high-temperature regions are transported by fluid mixing into the low-temperature HO_2-rich regions. Particulate nitrates may be formed by this gas phase oxidation of NO to NO_2. Also, nitric acid forms in the atmosphere by the reaction between NO_2 and hydroxyl radicals:

$$NO_2 + OH \rightarrow HNO_3.$$

Soot Formation

The formation and destruction of soot is an important feature of non-premixed and rich premixed combustion. Carbon particulate matter is a major constituent of the total particulate count and its emission is known to be a health hazard. Both the carbon particulate size and number density can aggravate pre-existing respiratory ailments and may contain adsorbed carcinogens. Soot is formed in flames over a limited range of temperatures (1300-1600K). The soot formation region is very narrow. It is generally agreed that soot formation is a four-step process: formation of precursor species, particulate inception, surface growth and agglomeration, and soot particle oxidation.

In the first step, polycyclic aromatic hydrocarbons (PAH) are thought to be important intermediates between the fuel molecule and the primary soot particle (Glassman, 1996). These PAHs have size range between 10 nm to 100 nm. The formation of ring structures and their growth via reactions with acetylene (C_2H_2) have been identified as important processes. Second, particulate inception involves the formation of very small particles of certain critical size (3K-10K atomic mass units) from growth by both chemical means (i.e. $2CO \rightarrow CO_2 + C$) and coagulation. This process transforms large molecules into particulates. Third, this primary soot particle exposed to pyrolyzing fuel vapor experiences surface growth and agglomeration. Fourth, and finally, soot particles are partially oxidized as they pass through excess (dilution) air zone in the combustor.

It is difficult to calculate and separate the time evolution of steps 1 to 3. Therefore, experimental data of Garo et al. (1990), as shown in Fig. 2, was used to estimate soot formation time of 2.5 ms in a laminar cylindrical methane-air diffusion flame. For the soot oxidation step four; it is assumed that the soot particle is spherical, above a temperature of 1830K and composed of pure carbon that oxidizes to CO via the most likely reaction:

$$2C + O_2 \rightarrow 2CO$$

For this reaction, the burning rate constant and time required to oxidize a soot particle (Glassman 1996) is calculated as 25 μs (1 μm dia.) to 2.5 ms (10 μm dia.).

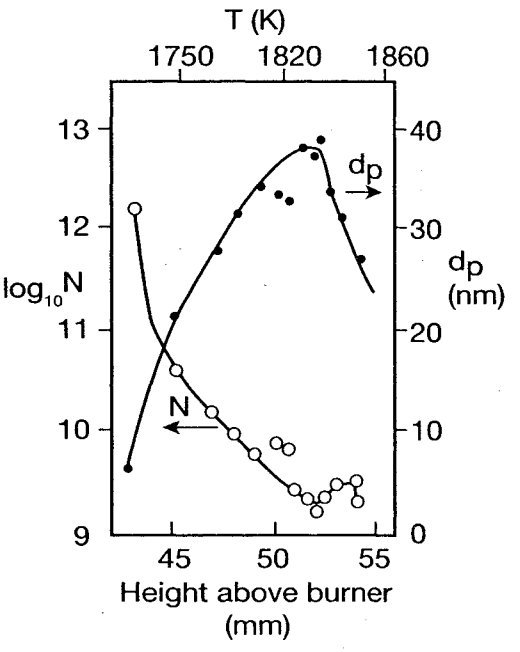

Fig. 2: Axial profiles of soot number density and mean particle size for a cylindrical methane/air diffusion flame (Garo et. al. 1990)

Analysis of Particulate Formation

Combustion-generated particulates are formed by disintegration of suspended solid particles (called foreign nuclei) in liquid fuel and/or by the conversion of clean fuel vapor-air mixture to particulate matter (no foreign nuclei) and /or by initial precursors generated by thermally stressing fuel. Conversion of clean fuel produces sub-micron particles. In a flowing combustible mixture, competition between various fluid dynamic, thermodynamics, and chemical kinetic processes dictates the net rate of particulate formation, growth, and emissions. Particulates range in 10 nm-500 nm size (Niedzwieki, 1999) and those formed within the combustor are soot, SO_2, radicals, and HCs. Particulates that are found in engine exhaust are H_2SO_4, HNO_3, and NO_x and

these are formed during the expansion of gases and post combustion reactions through the turbine and the exhaust nozzle. In practical combustion systems, particulate emission can be controlled by fuel-lean burning, high combustion efficiency, high temperature, and staged combustor geometry. Fig. 3 illustrates the key fundamental processes taking part in particulate formation and growth; each process is analyzed below.

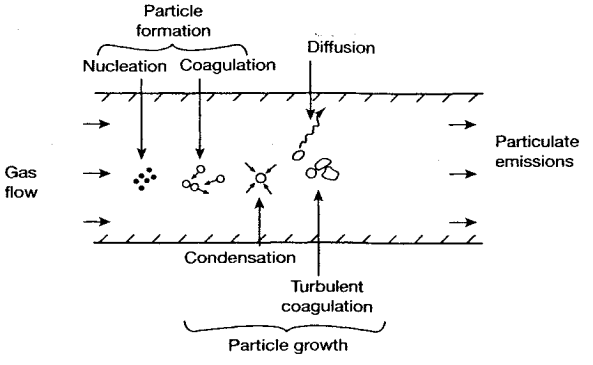

Fig. 3: Key processes in particulate formation and growth.

Nuclei Formation

An embryonic stage to particle formation is the formation of nuclei. Nuclei are molecular clusters that provide sites for the growth of matter into a particle and are formed by the process of condensation called homogeneous nucleation. The condensation nuclei are generated by the vapor itself.

Molecular clusters are always present even in an unsaturated gas. Because gas solubility decreases with increasing temperature, heating of liquid jet fuel causes (especially) the lighter fuel vapor fraction and oxygen to come out of solution. The vapor pressure of the gas is given by the fundamental thermodynamic expression:

$$\ln p_s = -\Delta H/RT + \text{const}$$

where ΔH is molar heat of vaporization and T is critical temperature. When the system becomes supersaturated, these clusters increase in concentration and pass through a critical size d_p^* by attachment of single molecules. The formation of stable nuclei relieves the super saturation in the gas. Because condensation nuclei are generated by vapor itself, this process is also known as self-nucleation.

Condensation of the product vapor to solid phase may also occur by rapid quenching due to sudden adiabatic expansion and/or mixing with cooler gases at a lower vapor concentration. This process produces the solid nuclei and is accompanied by the release of the latent heat of vaporization of the condensate. If only a single condensable species is formed by chemical reaction between fuel vapor and oxygen, it may condense by homogeneous nucleation in the absence of existing particles. Nuclei formed in this manner mix with fresh saturated and supersaturated gas and may serve as foreign nuclei.

Hirth and Pound (1963) and Friedlander (1978) describe the theory of condensation and nucleation. Stable nuclei grow due to condensation and disappear due to evaporation. Thus, the nucleation growth rate I_n (particles/cm^3 s) is:

I_n = condensation growth – evaporation loss

and is given as:

$$I_n = 2\,[p_1/(2\pi mkT)^{1/2}]\,(n_1\, v_m^{2/3})\,A \quad (1)$$

where:

$$A = [\sigma v_m^{2/3}]^{1/2} \exp [-16 \pi \sigma^3 v_m^2/3(kT)^3 (\ln S)^2]$$

Equation (1) shows the strong dependence of nucleation rate on saturation ratio S. The first term in this equation represents the monomer flux (molecules per unit area per unit time) and the second term is proportional to monomer surface area per unit volume of gas. Stable nuclei are not formed unless the saturation ratio $S > S_{crit}$. Using equation (1), characteristics of stable nuclei may be calculated for various organic vapors. Table 2 lists these values. The properties for toluene were obtained from Katz et al. (1975).

Table 2: Prediction of Stable Nuclei Size Using Homogeneous Nucleation Theory of Hirth and Pound (1963) (*current calculations)

Vapor	S_{crit}	d_n (nm)	N_{mol}
Methanol	1.8	1.58	32
Ethanol	2.3	2.84	128
Toluene*	5	3.2	140

It is observed that stable nuclei range between 1.6 nm to 3 nm dia. and contain 30 to 140 molecules respectively. (Note: When a large concentration of foreign nuclei is present and the super saturation is low, condensation takes place on the existing nuclei without the formation of new nuclei. This is called the heterogeneous condensation process resembling cloud formation in the atmosphere. Its effect on the growth of the nuclei is described later.)

Primary Particulate Formation

As stable nuclei concentration increases, they collide and initially coalesce to form large particles. These particles may be liquid or solid during the coalescence period. Coalescence ceases or slows significantly as particle size increases and/or the gases cool. These, so called individual (primary) particles, are much larger than the original condensation nuclei. If the average collision time between two particles is τ_c and coalescence time is τ_f, then as shown in Fig. 4, at high temperature, primary particles grow in size because particle coalescence occurs almost on contact, resulting in agglomerates of large particle number and small surface area. On the contrary, at low temperature, coalescence is slower than collisions, producing fractal-like agglomerates with high specific surface area.

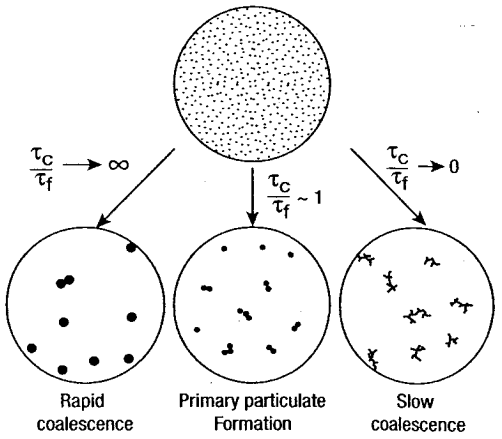

Fig. 4: Sketch illustrating competition between collision and coalescence processes and the emergence of primary particulate structure

In a combustion process that contains high concentration of ultra fine particles,

initially, $\tau_f << \tau_c$ and particles coalesce as fast as they collide. As coagulation proceeds and gas cools, both τ_f and τ_c increase. However, and depending upon the time-temperature history of the combustion process, at some point, $\tau_f > \tau_c$ i.e. collisions take place more rapidly than coalescence. When $\tau_f = \tau_c$, an optimum size of primary particle is reached. Ulrich (1971) states that the primary particle size is determined by the relative rates of particle collision and coalescence and this corresponds with the condition $\tau_c = \tau_f$. Now, Friedlander and Wu (1994) have shown that:

$$\tau_f = 3\ kTv/64\ \pi\ D\ \sigma\ v_m \qquad (2)$$

and

$$(3/\tau_c) = 0.5\ \alpha\ (6kT/\rho_p)^{1/2}\ (3/4\ \pi)^{1/6}\ \phi\ v^{-5/6} \quad (3)$$

Equating (2) and (3) and solving for average particle volume $v = (\pi/6)\ d_p^3$ yields the value of primary soot particle size as 71 nm. Because practical jet fuels such as JP-8 have highly complex molecular structure, physical and chemical properties of pure heptane were used in the above calculations. Also, the above analysis is based upon the use of a linear approximation for the decay with time of the area of a doublet:

$$da/dt = -\ (a-a_{sph})/\ \tau_f$$

Also, equation (3) for τ_c is based on assuming a free molecular regime.

Growth of Primary Particle

When high concentrations of particles are present in the flow, particles grow in size due to many mechanisms. In a highly turbulent practical combustion system, two key growth processes are heterogeneous condensation and turbulent coagulation.

Heterogeneous Condensation

In this mechanism, condensation of gas-phase chemical reactions takes place on the particle surface and it grows in size. The rate of heterogeneous condensation depends upon the exchange of mass and heat between the particle and the continuous phase. In the continuum range ($d_p >> l_p$) the condensation rate will be limited by gas-phase transport. In contrast, in the free molecular regime ($d_p << l_p$), the growth will be based upon molecular transport. Chemical reactions on the particle surface may also lead to particle growth if products of reaction accumulate on its surface. This mechanism is likely to be valid only if the particle surface is fresh and its catalytic activity high.

In a practical combustor burning fuel droplet spray, the most relevant gas-to-particle-conversion process is the droplet-phase chemical reaction. The same reaction takes place in all droplets, leading to the conversion of gas to particle phase. As fast as material is consumed by reaction in the droplet phase, it is replenished by transport from the gas. As shown below, the particle growth can be calculated by combining equations (4 to 6) to yield equation (7) and then, by integration to equation (8).

Rate of chemical reaction:

$$r = dn_i/\nu_l\ v\ dt \qquad (4)$$

Change in the droplet mass:

$$dm/dt = \rho_p\ dv/dt = \sum_l dm_i/dt \quad (5)$$

Rate of mass conversion by chemical reaction:

$$\sum_I dm_i/dt = (\sum_I MW_i\ \nu_I)\ v\ r \quad (6)$$

Hence,

$$dv/dt = v\ r\ (\sum_I MW_i\ \nu_I)/\rho_p \quad (7)$$

From equation (7), we can write:

$$d(d_p)/dt = k_v\ d_p$$

where

$$k_v = (\sum_I MW_i\ \nu_I)\ r/3\rho_p.$$

Integrating this equation from $d_p = d_{p0}$ at $t = 0$ gives:

$$(d_p/\ d_{p0}) = \exp\ (k_v\ t) \quad (8)$$

Equation (8) was used to calculate the primary soot particle growth for JP-8 droplets with a molecular weight MW = 152, droplet density ρ_p = 0.81 g/cc, stoichiometric coefficient ν_I = 1.33 (unimolecular conversion to CO), and the measured value of the reaction rate:

$r = 20.4 \exp (-79{,}800/RT)$ g/s.cm^3 atm

from Howard and Essenhigh (1967). Fig. 5 shows the results of our calculations. For the turbulent Kolmogoroff microscale convection time of 67 μs, chemical reactions will grow the primary particle size by 13 percent to a value of 1.13 x 71 nm = 80 nm.

Turbulent Coagulation

In industrial aerosol reactors, turbulent combustion systems, and atmosphere, turbulent coagulation almost always takes place. For particles large than a few microns, turbulent coagulation is important, especially at high turbulence levels. Coagulation can occur due to turbulent shear and turbulent inertial effects. Particle concentration in the flow N should be high so that the distances between colliding particles $N^{-1/3}$ << Kolmogoroff scale, η_k. Thus, for η_k = 1 mm, N >> 10^3 particles/cm^3.

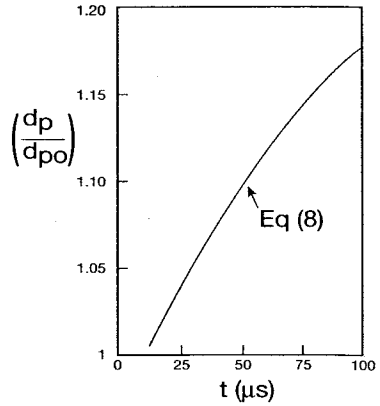

Fig. 5: Growth of primary particle with time due to heterogeneous condensation of gas-phase chemical reactions.

Smoluchowski (1917) developed the theory of Brownian coagulation and laminar shear. For particles smaller than 1 μm, Brownian collision is important and for larger particles, turbulent coagulation is dominant. When two particles collide, they coalesce instantaneously to form a third particle whose volume is equal to sum of the original two. In the Smoluchowski (1917) theory, a collision frequency function $\beta(v_i, v_j)$ represents the particle volume growth (cm^3/sec) per unit time. The collision frequency function $\beta(v_i, v_j)$ depends upon sizes of the colliding particles and flow properties such as temperature, pressure, and velocity. Equations for coagulation and their

solutions are reviewed by Williams and Loyalka (1991). Landgrebe and Pratsinis (1990) have developed numerical solutions. For turbulent shear coagulation:

$$\beta(v_i, v_j) = A\,(\varepsilon_d/\nu)^{1/2}\,(d_L)^3 \qquad (9)$$

In equation (9), d_L represents the average inter-particle distance. Saffman and Turner (1956) recommend the value for the constant A = 1.3.

We performed sample calculations using equation (9). For highly turbulent pipe flow, we used a value for $\varepsilon_d = 2 \times 10^4$ cm^2/sec^3 given by Laufer (1954). Also, we assumed a minimum particle concentration of $N = 10^3$ particles/cm^3. This calculation yielded value of:

$$\beta(v_i, v_j) = 3.8 \times 10^{-10}\ \text{cm}^3/\text{sec}$$

Thus, turbulent coagulation results in the growth of each particle volume by 3.8×10^{-10} cm^3/sec. Fig. 6 shows a plot of particle diameter growth as a function of residence time in and downstream of the combustor. It is observed that during

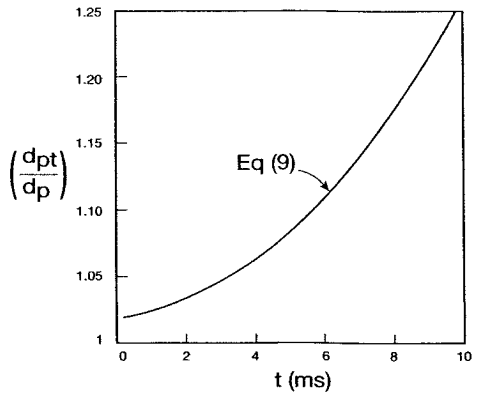

Fig. 6. Growth of primary particle with time due to turbulent coagulation.

the combustor residence time of 8 ms, the process of turbulent coagulation will cause a 80 nm diameter particle to grow by 17 percent in diameter (or 62% by volume) to a 94 nm diameter particle.

Agglomerate Formation

In the discussions presented above, it was assumed that particles are spherical, and colliding spherical particles coalesce instantaneously to form larger spherical particles. In practice, photographs of particulate emission samples and soot morphology show that particulates are clustered together as agglomerates that are non-spherical, non-rigid chain-like clusters. Fig. 7 shows different types of agglomerate structures that may be found in the scanning electron microphotographs of agglomerates.

An agglomerate may be composed of N_p primary particles, each with a radius a_{p0}. The characteristic radius of such an agglomerate structure is R. Agglomerate formation and computer simulation have been discussed by Meakin (1986). It was experimentally found that $N_p \propto R^{D_f}$, where D_f is called the fractal dimension and its value depends upon the details of the agglomerate formation process. For example, Fig. 7 shows that a reaction-limited aggregation (D_f = 3.0), involves repeated collisions and sticking between particles; as a result it produces the most compact particle-cluster agglomerate structure. In a diffusion-limited aggregation (D_f = 2.5), a primary particle serves as a well-defined center around which chain-like structures evolve. Finally, a cluster-cluster aggregate (D_f = 1.8) develops because of collision among agglomerates and it results in the most chain-like long structures without a well-defined center.

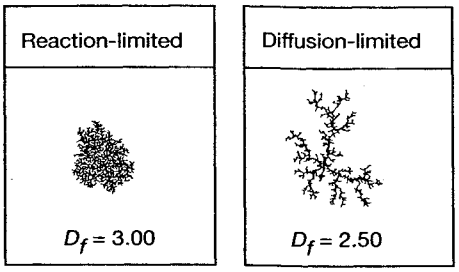

(a) Particle – Cluster Aggregation

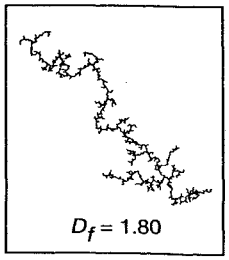

(b) Cluster – Cluster Aggregation

Fig. 7: Sketches illustrating different agglomerate structures observed in various modes and their corresponding fractal dimension.

For most practical applications, Wu and Friedlander (1993) recommend the following power law relationship for agglomerate size calculations:

$$N_p = A\,(R/\,a_{p0})^{D_f} \qquad (10)$$

In equation (10), value of the proportionality constant A = 1.43 for continuum regime and the fractal dimension D_f = 3.0 is most appropriate for agglomerate formation dominated by chemical reactions. As an example, for a 3 nm nuclei that grows to a 94 nm agglomerate, equation (10) yields a value of N_p = 43,990 particles per agglomerate.

Fig. 8 is a plot of time scales of different processes related to jet fuel combustion and particulate formation and growth that occur within an available combustor residence time of 8 ms. As shown, many of these processes occur in parallel and some in series. This illustrates the importance of time scales in the study of particulate formation and growth.

In summary, our fundamental work has provided insights into the mechanism of particulate formation and growth. Our estimates for the primary particulate size of 71 nm dia. and its growth to a size of 94 nm dia. compare favorably with the experimentally observed soot emissions of Garo et al (1990) and Howard (1996). Thus, four key factors appear to be responsible for the formation and growth of particulates.

Future Work

A long-term objective of this research is to formulate procedures for predicting the particulate emissions index (g/kg of fuel) from gas turbine engines and to determine how fuel additives reduce particulate emissions. To this end, the next step is to calculate particulate agglomerate concentration and oxidation in the post-combustor flow field.

Two other important products of gas-to-particle conversion are nitrates (discussed earlier) and sulfate particulates. Their formation and growth should be analyzed in the future. Sulfate particulates result from the atmospheric oxidation of SO_2 either by homogeneous gas phase reactions (≈100 nm dia. small particles) or by droplet-phase reactions (≈1 μm dia. large particles). Reaction with hydroxyl radical OH is thought to be

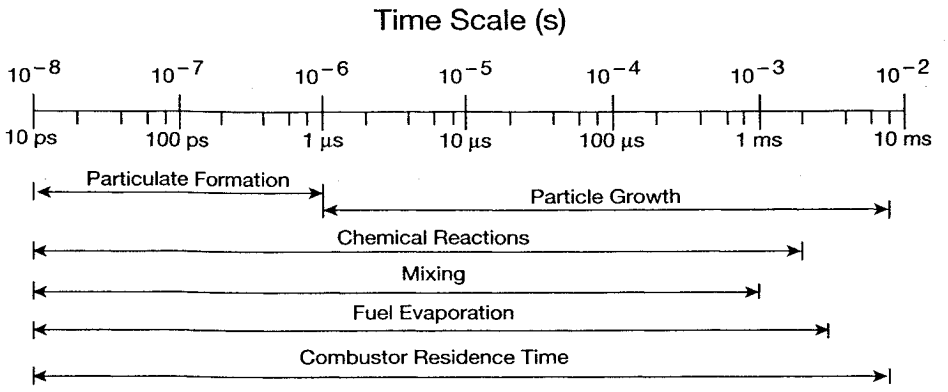

Fig 8: Summary of time scales of combustion, particulate formation and growth

the major gas-phase mechanism. Sulfates contribute heavily to visibility degradation and to the production of sulfuric acid.

Fuel additives have been shown to reduce particulate emissions level by 50% (Maurice et al. 1999). Additives may modify the critical saturation vapor pressure ratio S_{crit} of the fuel vapor and affect self-nucleation. Since the coalescence time $\tau_f \propto (D\ \sigma)^{-1}$ and collision time $\tau_c \propto v/(dv/dt)$, additives that alter values of diffusion coefficient, surface tension, or agglomerate structure will certainly affect primary particulate size and concentration. Finally, additives that affect the chemical reaction rate *r* and the fractal dimension D_f will significantly alter particle growth rate because of the strong (exponential and power law) dependence on these parameters. More data on particulate size, size distribution, and concentration density, with and without additives, are required to ascertain just how additives affect particle emissions.

Summary

1. Time scales of fuel oxidation and combustion cover a wide range. At one end are elementary chemical reaction time scales as short as 4.5 μs and at the other end are jet fuel oxidation times as long as 10 ms. Between these two extremes can be found time scales of ignition (60 μs), microscale turbulent mixing (67 μs), and combustor residence time (8 ms).

2. Four key processes are identified in the formation and growth of particles: nuclei formation, primary particulate formation, growth by heterogeneous condensation of chemical reactions, and growth by turbulent coagulation. Also, particle agglomeration is discussed.

3. An embryonic stage of particle formation is the formation of nuclei. A theory of homogeneous nucleation is discussed and stable nuclei size containing 30 to 140 molecules was estimated to be between 1.6 nm to 3 nm dia. respectively. The nuclei grow by collision and coalescence. An analysis shows that when $\tau_f = \tau_c$, an optimum

primary particle size is reached and this was estimated to be 71 nm.

4. The primary particle size grows 13 percent by the heterogeneous condensation of chemical reactions and an additional 17 percent in diameter by turbulent coagulation to a final size of 94 nm dia. within the available turbulent microscale time in the combustor.

5. A reaction-limited agglomerate (D_f = 3.0), involves repeated collisions and sticking between particles; as a result it produces the most compact particle-cluster agglomerate structure.

Our estimates of primary particulate size = 71 nm dia. are close to experimentally observed soot emissions of Garo et al. (1990) and Howard (1996).

Fuel additives may modify the key chemical reaction rates within the turbulent eddies to affect particulate emissions. Also, particulate oxidation significantly decreases size and number density. Thus, more data on particulate size, size distribution, and concentration density, with and without additives, are required to ascertain just how additives affect particle emissions and how procedures for predicting the particulate emissions index (g/kg of fuel) from gas turbine engines can be formulated.

References

- Ballal, D. R. and Lefebvre, A. H. (1975): Combust. Flame, Vol. 24, pp. 99-108.
- Ballal, D. R. and Lefebvre, A. H. (1977): Proc. R. Soc., London, Vol. 357, pp. 163-181.
- Ballal, D. R. and Lefebvre, A. H. (1981): Eighteenth Symposium (Int.) on Combustion, The Combustion Institute, Pittsburgh, PA.
- Edwards, T., Harrison, W. E, and Maurice, L. Q. (2001): AIAA Paper No. 2001-0498.
- Friedlander, S.K. (1978): Smoke, Dust, and Haze, Oxford University Press, New York, NY.
- Friedlander, S.K. and Wu, M.K. (1994): Phys. Rev. B, Vol. 49, pp. 3622-3627.
- Garo, A., Prado, G., and Lahaye, J. (1990): Combust. Flame, Vol. 79, pp 226-235.
- Glassman, I. (1996): Combustion, Academic Press, New York, NY
- Heneghan, S. P., Zabarnick, S., Ballal, D. R., and Harrison W. E. (1996): AIAA Paper No. 96-0403.
- Henz, K and Robinson, W. A, (1998): "Petroleum Quality Information System Jet Fuels Data 1997," Defense Energy Support Center (DESC).
- Hirth, J.P. and Pound, G.M. (1963): Condensation and Evaporation: Nucleation and Growth Kinetics, Macmillan, New York, NY.
- Howard, R. P. et. al. (1996): AEDC-TR-96-3.
- Howard, J.B. and Essenhigh, R.H. (1967): Eleventh Symposium (Int.) on Combustion, The Combustion Institute, Pittsburgh, PA., pp. 399-406.
- Katz, J.L., Scoppa, C.J., Kumar, N.G., and Mirabel, P. (1975): J. Chem. Phys., Vol. 62, pp. 448-454.
- Landau et al. (1994): NASA CR-4613.
- Landgrebe, J.L. and Pratsinis, S.E. (1990): J. Colloid Interface Sci., Vol. 139, pp. 63-74.
- Laufer, J. (1954): NACA Report 1174.
- Lefebvre, A. H. (1999): Gas Turbine Combustion, Taylor and Francis, Philadelphia, PA.

- Lefebvre, A. H. (1989): Atomization and Sprays, Hemisphere Publishing, New York, NY
- Maurice, L. Q., Corporan, E. Minus, D., Mantz, R., Edwards, T., Wolwend, K., and Harrison, W. E. (1999): AIAA-Paper No. 99-4916.
- Meakin, P. (1986): On Growth and Form, Edts. Stanley, H.E. and Ostrowsky, N., Martinus Nijhoff, Dordrecht, The Netherlands.
- Niedzwieki, R. (1999): NASA CP-1999-208918.
- Saffman, P., and Turner, J. (1956): J. Fluid Mech., Vol. 1, pp. 16-33.
- Smoluchowski, M. (1917): Z. Physik Chem., Vol. 92, pp. 129-136.
- Thompson, A. M. (1996): NASA RP-1385.
- Toepke, S. (1999): Boeing Company, Personal Correspondence.
- Ulrich, G.D. (1971): Comb. Sci. Tech., Vol. 4, pp. 47-58.
- Vranos, A. (1974): Combust. Flame, Vol. 22, pp. 253-262.
- Williams, M.M.R., and Loyalka, S.K. (1991): Aerosol Science Theory and Practice, Pergamon Press, Oxford, U.K.
- Wu, M.K., and Friedlander, S.K. (1993): J. Colloid Interface Sci., Vol. 159, pp. 246-255.

Q. Studies of Injection of Jet Fuel at Supercritical Conditions

Studies of Injection of Jet Fuel at Supercritical Conditions

Thammarat Doungthip, Jamie S. Ervin,* Theodore F. Williams, and Jarrod Bento

University of Dayton Research Institute, 300 College Park, Dayton, Ohio 45469-0210

At temperatures above 400 °C and at fuel system pressures, JP-8 and Jet A jet fuels exist as supercritical fluids. Fuel nozzles operating under conventional aircraft (subcritical) conditions atomize liquid fuel streams into droplets. The physical injection and mixing mechanisms associated with a nozzle operating under supercritical conditions are very different from those occurring under subcritical conditions. The current research examines the flow of fuel at supercritical conditions through a simple nozzle into a region that is also at supercritical conditions. Schlieren images of supercritical jet fuel exiting a simple nozzle into an optical chamber are presented. Computational fluid dynamics simulations of the flow were performed using *n*-decane as a surrogate fuel because it has a critical temperature and pressure similar to the pseudo critical temperature and pressure of the jet fuel sample used in the experiments. The results of the computational fluid dynamics simulations and the measurements obtained from the recorded images show that *n*-decane is a reasonable surrogate for Jet A fuel for predictions of the spreading angle and jet penetration length. Measurements and computation show that jet penetration and spreading angle are dependent on the fuel exit temperature and mass flow rate. In addition, it was found that the penetration depth of a supercritical jet into the optical chamber is less than that for a subcritical jet with the same fuel mass flow rate and pressure conditions.

Introduction

Fuel is the primary cooling medium in high-performance aircraft. Advanced aircraft are expected to have cooling demands which require jet fuel to exist at temperatures above the critical temperature before injection into the combustor. Thus, future gas turbine engines will require the injection of fuel existing at a supercritical thermodynamic state into an environment that is also above the critical point of the fuel. At temperatures above approximately 400 °C and at fuel system pressures, the primary fuel of the U.S. Air Force, JP-8, or jet fuels such as Jet A-1 and Jet A exist as a supercritical fluid with gaslike diffusivity and viscosity.[1] Under supercritical temperature conditions, pyrolytic reactions within heated jet fuel become dominant. Chemical changes, such as fuel pyrolysis, are controlled by physical characteristics of the fuel and the fuel system. The involved fluid dynamics and heat transfer vary during flight and change the location of maximum thermal gradients and maximum chemistry. Thus, it is important to understand the fundamental physical and chemical processes which occur for hydrocarbon fuels existing under supercritical conditions.

For purposes of combustion, fuel nozzles operating under conventional aircraft (subcritical) conditions atomize liquid fuel streams into small, uniformly sized droplets with the desired spray angle. Under supercritical conditions, the fuel exits the nozzle as a gaslike fluid rather than as a multitude of droplets, and there can be large variations in fuel density, specific heat, speed of sound, viscosity, and thermal conductivity.[2] Thus, the physical injection and mixing mechanisms associated with a nozzle operating under supercritical conditions are very different from those occurring under subcritical conditions. Previous research considered the injection of ethylene which was initially at supercritical conditions into a large chamber filled with nitrogen at constant temperature and subcritical pressures.[3,4] The goal was to examine the effects of transport properties near the critical point on shock structure, jet appearance, and flow choking. Others have studied the injection of liquid jets injected into supercritical conditions.[2,5−8] It is also desirable to conduct experiments in which a supercritical fluid is injected into surroundings under supercritical conditions. Knowledge of injection processes into surroundings at supercritical conditions is important because supercritical conditions will exist in the combustion chamber of advanced aircraft.[1] In some of their experiments, Chehroudi et al.[2] and Chen and Sui[8] injected fluids initially at supercritical conditions into surroundings that were also at supercritical pressures and temperatures (relative to the injected fluid). Chehroudi et al.[2] injected pure N_2, He, and O_2 into a high-pressure chamber containing either N_2, He, or mixtures of CO and N_2. Chen and Sui[8] studied the injection of SF_6 injected into a chamber filled with stagnant N_2 or CO_2 at high pressure. Much of their work focused on subcritical injection very near the critical point of SF_6. Unfortunately, there is little available in the literature concerning the injection of an initially supercritical hydrocarbon fuel into supercritical conditions.[9] The relatively high critical temperatures and pressures associated with common hydrocarbon fuels necessarily make injection studies at supercritical conditions difficult. Previous studies involving supercritical fluid injection largely consider studies of droplets and sprays. Studies involving jets of supercritical fluids are relatively rare and, thus, more research involving injection of supercritical fluids is needed.[2,9]

In the current work, Jet A fuel initially at supercritical conditions is injected into an environment with pressures and temperatures above the critical pressure

* To whom correspondence should be addressed. E-mail: jervin@engr.udayton.edu. Phone: 937-229-2998. Fax: 937-252-9917.

10.1021/ie0109915 CCC: $22.00
Published on Web 10/17/2002

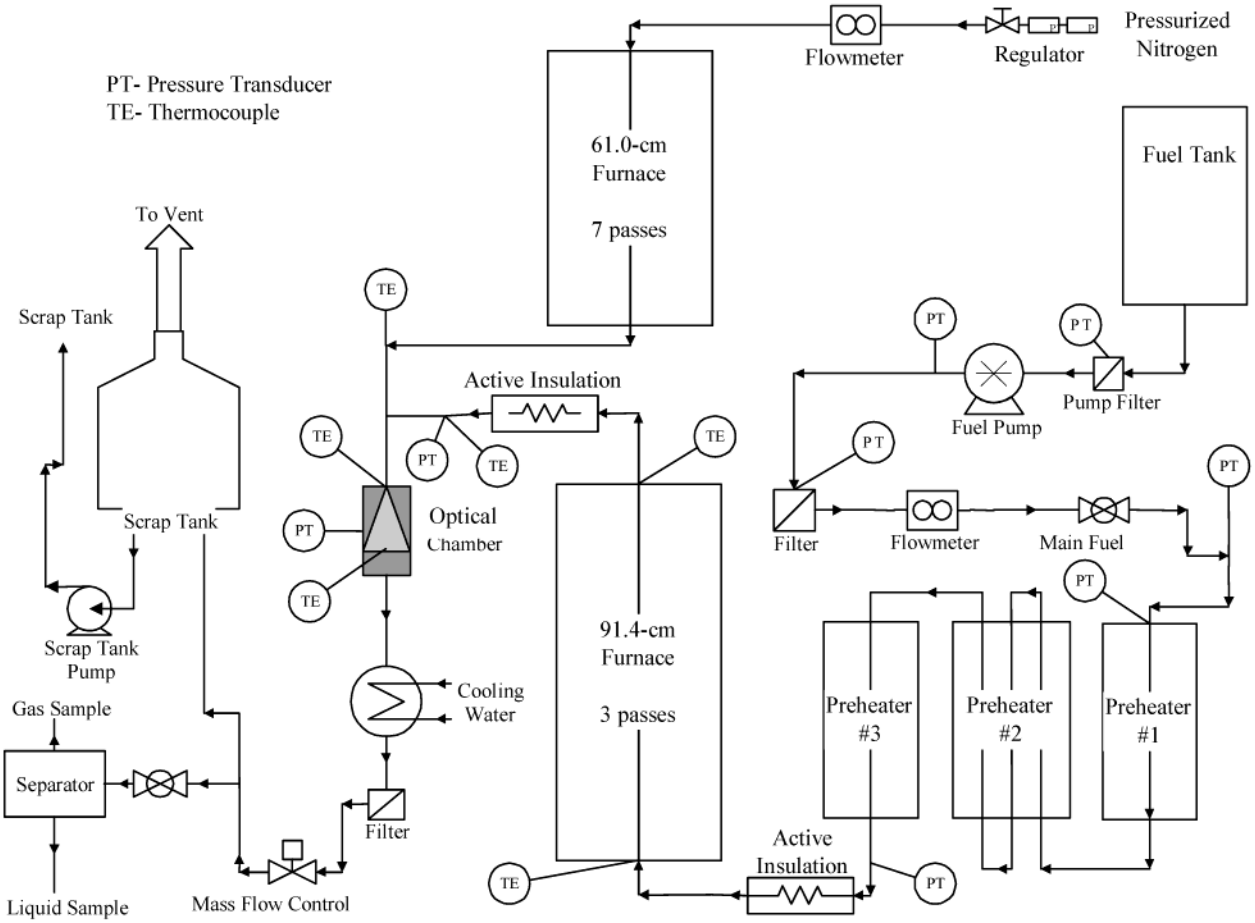

Figure 1. Schematic of the flow rig used to heat fuel.

Table 1. Characteristics of Jet A Fuel F3219

specific gravity at 15.6 °C	0.8109	flash point, °C	55
sulfur total, wt %	0.0321	aromatics, vol %	16.6
copper, ppb	$<5 \pm 5$	smoke point, mm	20
iron, ppb	$<10 \pm 5$	copper strip corrosion	1a
zinc, ppb	$<10 \pm 5$	JFTOT breakpoint, °C	285
freeze point, °C	−46		

and temperature of the fuel. In addition, the Jet A fuel is in coflow with N_2 gas. (In this work, supercritical refers to the critical condition of the fuel.) To better understand the mixing and injection processes, schlieren imaging is used. It is believed that these are the first images of supercritical jet fuel exiting a nozzle into a chamber which is also at supercritical conditions. Computational fluid dynamics simulations are performed using a simple surrogate fuel for purposes of comparison with the images of Jet A. The results of this work can be used to assist further development of computational models for engine designers to simulate fuel flowing through nozzles at supercritical conditions.

Experimental Section

Jet A fuel is similar to both JP-8 and Jet A-1 jet fuels, but Jet A has a higher freeze point temperature specification.[10] JP-8 is essentially Jet A-1 with three additives: a lubricity improver/corrosion inhibitor, an antistatic additive, and an icing inhibitor. In addition, Jet A and Jet A-1 are used as commercial aviation fuels. In this study, a Jet A fuel sample (designated as F3219 in Table 1) was additized and then injected into an optical chamber for purposes of flow visualization. Additives combined with the neat fuel include those given by MIL-T-83133D (JP-8 fuel specification) and a proprietary thermal stability additive (Betz Dearborn 8Q462) used in the JP-8+100 Program. This additive was found to reduce thermal-oxidative surface deposition significantly below that of the neat fuel in most fuel test devices.[11] Dissolved O_2 within heated jet fuel is responsible for thermal-oxidative fuel degradation and surface deposit formation. Because it was desired to eliminate surface deposition, gaseous N_2 was bubbled through the fuel to reduce the dissolved O_2 concentration within the fuel. A gas chromatograph verified that the dissolved O_2 concentration of the fuel before heating was less than 1 ppm (w/w) and, thus, ensured that minimal thermal-oxidative surface deposition would occur.

The fuel was heated in a flow rig (Figure 1) which uses two different types of heaters.[12] The first consists of a heated copper block. The block is comprised of two cylindrical halves which have a 7.62-cm diameter and a 45.7-cm length. The cylindrical pieces, when clamped together, form a near-interference fit about the stainless-steel tubing through which the fuel passes. Each half contains a 1500-W cartridge heater, and a thermocouple embedded within one of the halves provides a temperature signal to the controller for the cartridge heaters. The second kind of heater is a split-tube furnace (7980 W) that is mounted vertically and employs radiant heating. It has an active length of 61.0 cm and a 12.7-cm interior diameter. In addition, the furnace employs K-type thermocouples for control purposes. The pressure in the copper block and furnace was held near 2.7 MPa

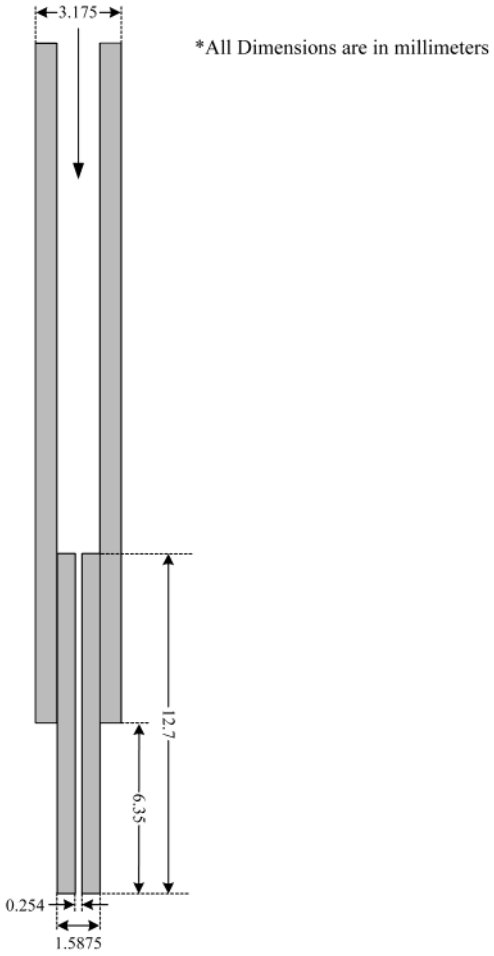

Figure 2. Nozzle used in flow visualization studies.

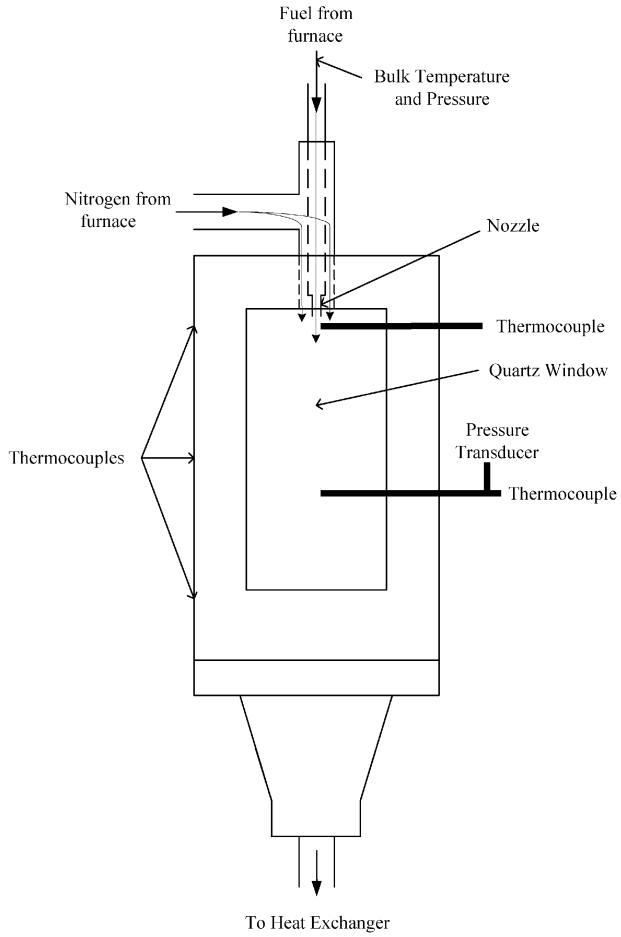

Figure 3. Optical chamber used in flow visualization experiments.

by the use of a pump and flow control valves such that the fuel entered the copper blocks as a liquid and transitioned to a supercritical fluid within the furnace. After passing through the heated block and furnace, the fuel flowed through a nozzle. The nozzle (Figure 2) consists of a (316) stainless-steel tube (12.7 mm length × 1.6 mm o.d. × 0.3 mm i.d.) welded to a larger tube. (The 3.2 mm o.d. × 1.4 mm i.d. fuel line tube was drilled to an i.d. of 1.6 mm and a depth of 6.35 mm to accommodate the smaller tube.) Fuel passed from the nozzle into the optical chamber (Figure 3) in (vertical downward) coaxial flow with heated N_2. The flowing N_2 (3.6 g/s) was heated by another furnace to produce a high nozzle wall temperature. In addition, for safety purposes the N_2 served to reduce the probability of ignition. Moreover, injected fuel in actual aircraft is often in coaxial flow with an air stream. The optical chamber has quartz windows (5.08 cm × 10.16 cm) on two sides for optical access and allows a maximum pressure of 3.45 MPa. Feed-throughs permit insertion of two type K thermocouples (1.5 mm diameter), and the pressure was measured using a pressure transducer. Thermocouples (20 gauge) welded to the outer surface of the chamber provided outer wall temperatures with an uncertainty of ±2 °C. The fuel mass flow rate was fixed at either 0.2 or 0.4 g/s. In these experiments, fuel and N_2 temperatures upstream of the nozzle, fuel and N_2 mixture temperatures below the nozzle, the chamber wall temperature, and fuel and N_2 flow rates were measured. Individual experiments were run for short times (~15 min) to minimize surface deposition.

A water-cooled heat exchanger reduces the temperature of the fuel to near ambient conditions after the fuel exits the test section. Cooling the fuel allows safe sample collection and extends the life of the tube downstream of the heat exchanger. Near the exit of the system, fuel is diverted to a gas/liquid separator. Separation allows gas product samples to be analyzed offline using a GC-FID/TCD system. The liquid portion of the stressed fuel is analyzed by conventional GC−MS techniques. Beyond the gas/liquid separator, the fuel exits to a scrap tank. In the experiments performed here, products of thermal cracking reactions were essentially immeasurable. Thus, it can be reasonably assumed that there was little pyrolysis of the fuel.

At supercritical conditions, fuel exiting the nozzle is visible neither to the naked eye nor to white light photography. For this reason, a schlieren optics arrangement (Figure 4) was used for flow visualization.[13] Light emanating from a xenon flash lamp passes through a condenser and focusing lens and is then redirected by a 45° flat mirror to a parabolic mirror (152.4-cm focal length × 15.2-cm diameter). The parabolic mirror then directs the parallel light rays through the test section. Other mirrors direct the detected light such that a knife edge blocks a portion of the light entering the camera. An image of the flow pattern is recorded using a CCD camera (Panasonic GPUS502, three interline transfer CCDs with 768 × 494 pixels) connected to a (Mitsubishi HSU770 SVHS) VCR. An image is captured using a frame grabber (Matrox

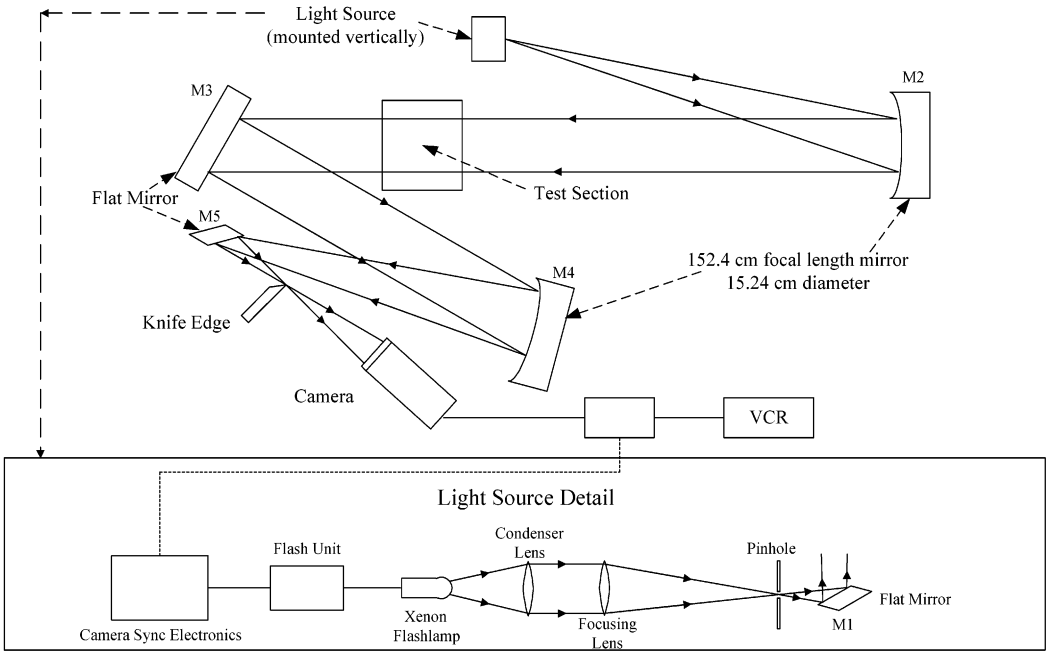

Figure 4. Schlieren optical arrangement.

Marvel G400) connected in series with the VCR. Two sequential images are averaged for each condition reported.

Numerical Model

Computational fluid dynamics simulations assist the interpretation of flow visualization studies and extend the study of phenomena for which experimental techniques are either unavailable or limited. To simulate the injection of supercritical fuel into a supercritical environment, the species, temperature, and velocity distributions were obtained by the finite volume solution of the species, enthalpy, Navier−Stokes, and turbulent energy equations. The time-dependent governing equations written in the cylindrical (z, r) coordinate system for axisymmetric flow are

$$\frac{\partial \rho}{\partial t} + \frac{\partial \rho u}{\partial z} + \frac{\partial \rho v}{\partial r} + \frac{\rho v}{r} = 0 \qquad (1)$$

$$\frac{\partial \rho \Phi}{\partial t} + \frac{\partial \rho u \Phi}{\partial z} + \frac{\partial \rho v \Phi}{\partial r} = \frac{\partial}{\partial z}\left(\Gamma^{\Phi}\frac{\partial \Phi}{\partial z}\right) + \frac{\partial}{\partial r}\left(\Gamma^{\Phi}\frac{\partial \Phi}{\partial r}\right) - \frac{\rho v \Phi}{r} + \frac{\Gamma^{\Phi}}{r}\frac{\partial \Phi}{\partial r} + S^{\Phi} \qquad (2)$$

Equation 1 is the continuity equation, and eq 2 represents the momentum, species, or energy equation depending on the variable represented by Φ. Table 2 lists the transport coefficients Γ^{Φ} and the source terms S^{Φ} of the governing equations. Buoyancy forces were included in the simulations, and the gravity vector is in the same direction as the flow from the nozzle. The fuel exiting the nozzle has Reynolds numbers (from 12 000 to 23 000) that are characteristic of turbulent jet flows (Re is defined as $\rho UD/\mu$). In contrast, the Reynolds number at the fuel nozzle exit of the nitrogen in coflow with the jet fuel was relatively low (on the order of 2000). The standard $k-\epsilon$ turbulence model[14] has been used previously in supercritical and transcritical studies to provide reasonable predictions of the evolution of an O_2 jet.[15] In preliminary work here, there were negligible differences between calculations of the spreading angle, jet length, and velocities which used the standard $k-\epsilon$ turbulence model and those which employed the low Reynolds number $k-\epsilon$ model of Chien.[16] In addition, it was found that calculations which used the low Reynolds number $k-\epsilon$ turbulence model required only half the computational time used by the standard $k-\epsilon$ model. Thus, in this physical arrangement which involved simultaneously occurring high and low Reynolds number flows, a low Reynolds number $k-\epsilon$ model was used in all of the calculations presented. Because the fuel (Re of 12 000−23 000 at the location where the fuel is injected into the optical chamber) and N_2 flows are turbulent, the rate of turbulent mass transport is several orders of magnitude greater than that of the concentration-driven (molecular-diffusive) mass transport. Thus, a constant Schmidt number of unity was used for simplicity. Values of the constants used in the model of turbulent species transport are listed in Table 2 and in the Nomenclature section.

Table 2. Source Terms and Transport Coefficients Appearing in Equations 1 and 2[a]

Φ	Γ^{Φ}	S^{Φ}
u	$\mu + \mu_t$	$-\frac{\partial p}{\partial z} + \frac{\partial}{\partial z}\left(\Gamma^{u}\frac{\partial u}{\partial z}\right) + \frac{\partial}{\partial r}\left(\Gamma^{u}\frac{\partial v}{\partial z}\right) + \frac{\Gamma^{u}}{r}\frac{\partial v}{\partial z} + \rho g$
v	$\mu + \mu_t$	$-\frac{\partial p}{\partial r} + \frac{\partial}{\partial z}\left(\Gamma^{v}\frac{\partial u}{\partial r}\right) + \frac{\partial}{\partial r}\left(\Gamma^{v}\frac{\partial v}{\partial r}\right) + \frac{\Gamma^{v}}{r}\frac{\partial v}{\partial r} - 2\Gamma^{v}\frac{v}{r^2}$
k	$\mu + \frac{\mu_t}{\sigma_k}$	$G - \rho\epsilon$
ϵ	$\mu + \frac{\mu_t}{\sigma_\epsilon}$	$C_1 G\frac{\epsilon}{k} - C_2\rho\frac{\epsilon^2}{k}$
h	$\frac{k}{c_p} + \frac{\mu_t}{\sigma_\epsilon}$	0
Y_i	$\rho D_i + \frac{\mu_t}{\sigma_{Y_i}}$	$\dot{\omega}_i$

[a] Here $G = \mu_t[2\{(\partial u/\partial z)^2 + (\partial v/\partial r)^2 + (v/r)^2\} + (\partial v/\partial z + \partial u/\partial r)^2]$, where $\mu_t = C_\mu \rho k^2/\epsilon$, $C_1 = 1.47$, $C_2 = 1.92$, $C_\mu = 0.09$, $\sigma_k = 1.0$, $\sigma_\epsilon = 1.3$, $\sigma_h = 1.0$, and $\sigma_{Y_i} = 1.0$.

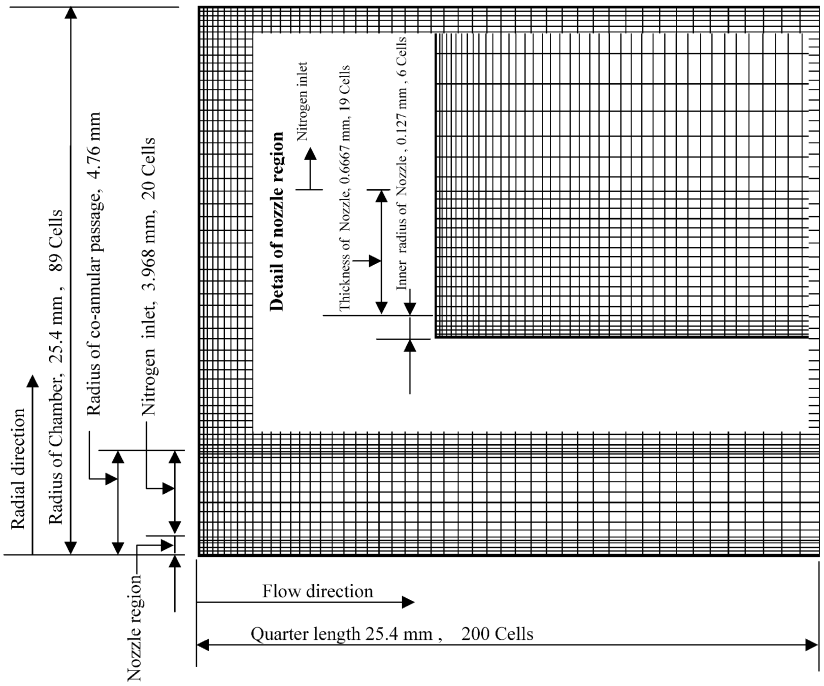

Figure 5. Computational grid.

The governing equations were solved sequentially using the commercially available CFD-ACE computational fluid dynamics code.[17] Convective terms were represented by a second-order accurate upwind scheme, and a version of the SIMPLEC algorithm was used in the solution procedure.[17] The grid system of Figure 5 which contains 89 cells in the radial direction and 200 cells in the axial direction is used in most simulations. Because the nozzle i.d. (0.3 mm) is significantly smaller than either the chamber width (50.8 mm) or length (101.6 mm), it was assumed that the flow near the chamber walls does not significantly affect the flow near the nozzle outlet. Thus, the rectangular shape of the actual chamber was (as a first-order approximation) adequately represented by a two-dimensional axisymmetric (structured) grid. Because the behavior of the fuel jet near the nozzle exit is of primary interest, the length of the computational grid is one-fourth of the chamber length (25.4 mm). The length in the radial direction of the computational grid is 25.4 mm. Computational cells are clustered within the shear layer between the N_2 and fuel. In other regions, the orthogonal grid system has expanding cell sizes in both z and r directions. Near the walls, the first cell was located at a $y+$ distance of less than 5.

Large gradients in temperature, velocity, or species are not expected in the far field away from the fuel and N_2 jets under the present flow conditions. From the physical arrangement, the greatest changes in the flow variables are expected to be near the co-annular passage (Figure 5). Thus, a grid study was performed in which the grid density was increased in the fuel nozzle (from 6 to 12 cells), the region where the *n*-decane and N_2 are mixed (from 19 to 38 cells), and the N_2 inlet (from 20 to 40 cells). In addition, the total number of cells in the axial (main flow direction) direction was increased (from 200 to 300 cells). The computational grid of Figure 5 was refined differently in different regions because of the grid nonuniformity. Solutions for species, temperature, and velocities changed little (less than 2%) with the use of the fine grid. In addition, the differences between the calculated spreading angles and penetration depths resulting from use of the coarse and fine grids were immeasurable. Thus, to have a more practical computational time, the coarse grid was used for the calculations presented in this work.

With regard to boundary conditions, the flow has zero velocity at solid surfaces. At the upper boundary of the grid (Figure 5), the velocity profiles of the entering nitrogen and fuel are assumed to be uniform for simplicity. Entering fuel and nitrogen temperatures, as well as the wall temperatures, were obtained from the experiments and are used as boundary conditions. In addition, the measured pressure level at the inlet was known. Along the bottom of the grid (Figure 5), an outflow boundary condition which employs a simple extrapolation procedure[17] is used to determine the unknown variables there. The calculations were initiated with a uniform flow of N_2 everywhere, and then the fuel flow is switched on. After the residuals were reduced below 4 orders of magnitude from their maximum value, the solution was considered to be converged.

Jet fuel is a complex mixture of a multitude of hydrocarbon species. For purposes of simulating the fluid dynamics involving a jet fuel, it is reasonable to use a simple representative fuel. Here, *n*-decane was selected as a surrogate fuel because it has a critical temperature and pressure ($T_c = 344.55 \pm 0.6$ °C and $P_c = 2.11 \pm 0.05$ MPa)[18] similar to the pseudo critical temperature and pressure of the selected Jet A sample. The pseudo critical temperature and pressure for this fuel sample were estimated ($T_c = 368$ °C and $P_c = 1.96$ MPa) using correlations described elsewhere.[19] Edwards and Maurice suggest that a single-component surrogate fuel that has a critical temperature near the pseudo critical temperature of a selected jet fuel can be used to adequately represent the actual jet fuel in simulations of nonreacting flows (which do not have liquid-to-vapor phase changes).[10] The commercial solver was modified to calculate supercritical thermodynamic and transport properties of mixtures of *n*-decane and N_2 as a function of the local pressure and temperature within the

Table 3. Properties of *n*-Decane/Nitrogen Mixtures for Different Temperatures, Pressures, and Mole Fractions Calculated Using SUPERTRAPP

temperature (K)	pressure (MPa)	$C_{10}H_{22}$ mole fraction	N_2 mole fraction	density (kg/m^3)	c_p (kJ/kg K)	μ ($\times 10^{-6}$ N·s/m^2)	k ($\times 10^{-2}$ W/m·K)
713	3.08	1	0	107.20	3.52	16.74	5.33
725	2.65	0.75	0.25	55.10	3.14	16.34	4.30
735	2.65	0.5	0.5	37.50	2.90	18.66	3.63
745	2.65	0.25	0.75	23.90	2.47	23.16	3.49

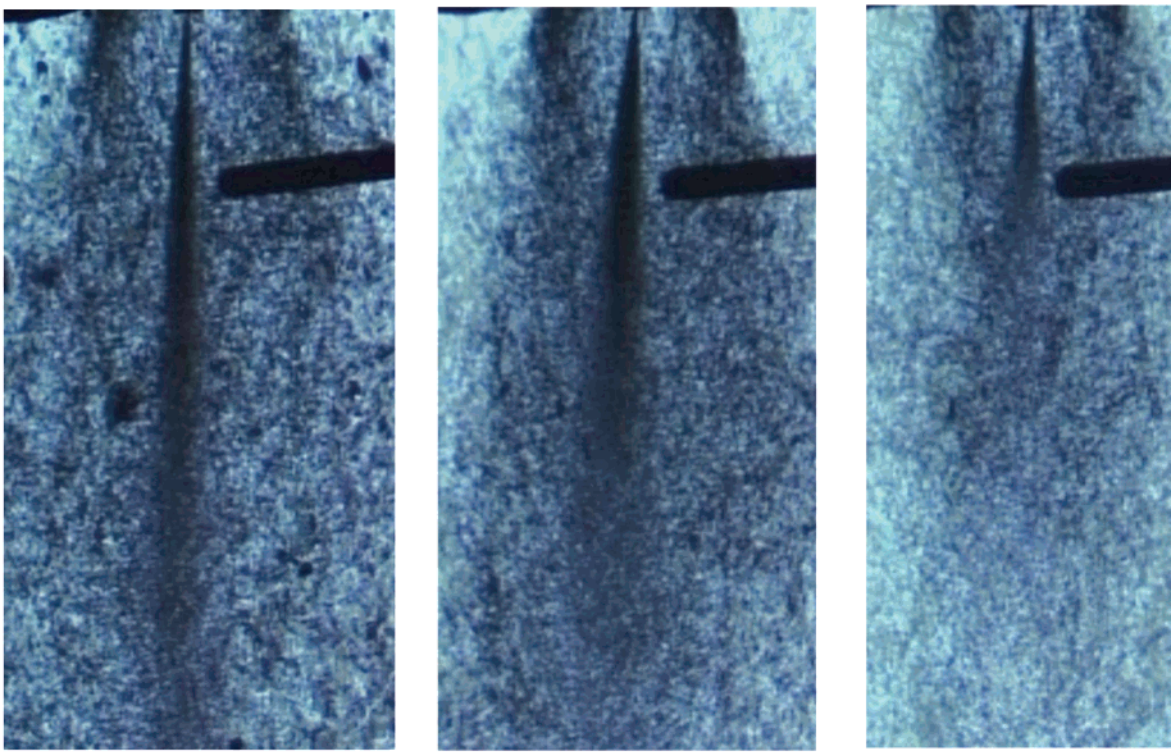

Figure 6. Effect of different jet fuel injection temperatures (fuel mass flow rate = 0.2 g/s and P_{ch} = 2.65 MPa): (a) 266 °C; (b) 325 °C; (c) 441 °C.

computational cells using SUPERTRAPP FORTRAN subroutines. With SUPERTRAPP, the phase compositions were calculated using the Peng−Robinson equation of state,[20] and the properties were determined by a NIST extended corresponding states model which uses propane as a reference fluid.[21] SUPERTRAPP is known to provide well-behaved thermodynamic properties near the critical point.[21] Table 3 shows representative values of thermodynamic and transport properties for mixtures of N_2 and *n*-decane for temperatures and pressures for which *n*-decane is a supercritical fluid.

Results and Discussion

Effects of Varying the Nozzle Exit Temperature. For a constant supercritical pressure, as the temperature of the fuel is increased above the effective critical temperature, the fuel transitions from liquid to supercritical fluid. From a fundamental perspective, it is important to study the effects of varying the nozzle exit temperature on the resulting flow. Figure 6 shows jet images under conditions of a fuel mass flow rate of 0.2 g/s and a chamber pressure of 2.65 MPa. In addition, Figure 6 shows the fuel jet in coflow with heated N_2 for three different fuel-nozzle exit temperatures. The fuel jet appears as a dark region emanating from the fuel tube, and the nitrogen jet is the larger structure about the fuel jet. The dark solid object that protrudes into the flow from the right side of each image is a thermocouple (1.5-mm diameter). In Figure 6a, the temperature of the fuel at the nozzle exit is 266 °C, and later it

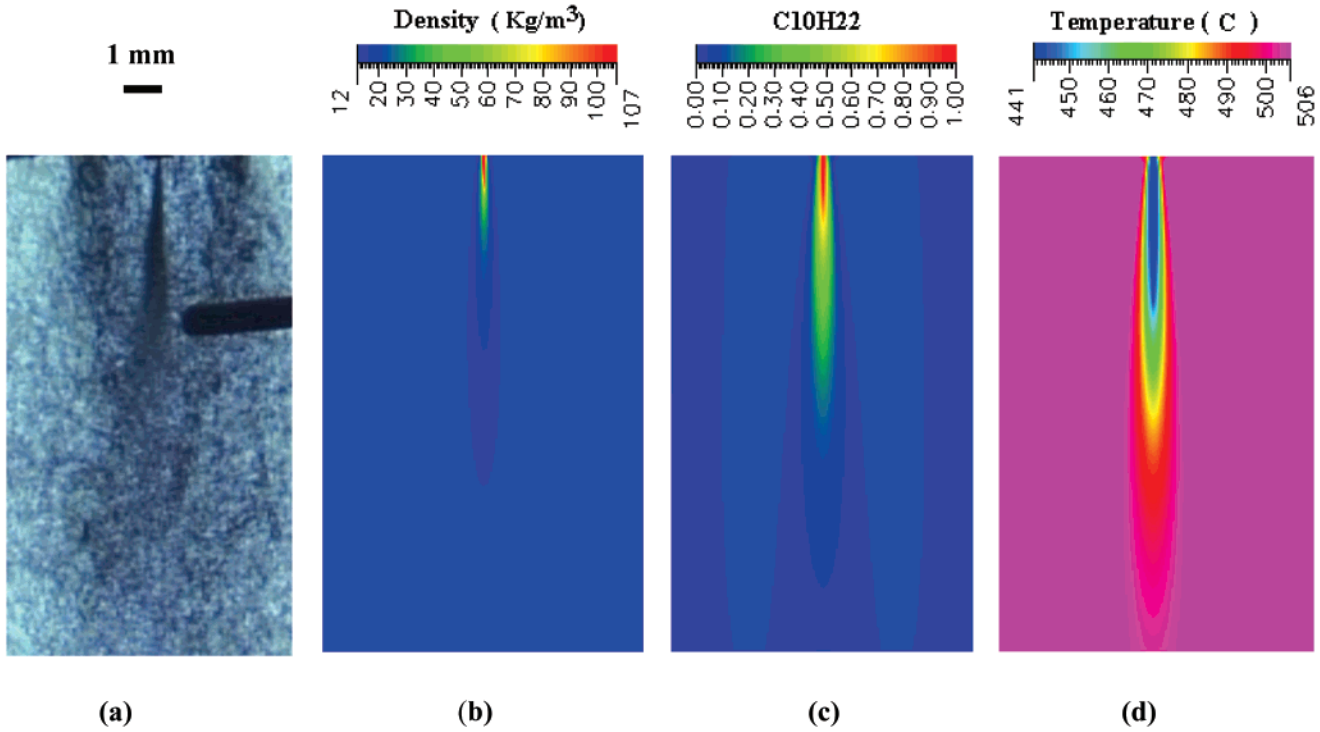

Figure 7. Jet fuel or *n*-decane at supercritical conditions in coflow with N_2. Fuel mass flow rate of 0.2 g/s, inlet nozzle temperature of 441 °C, and pressure of 2.65 MPa ($T_r = 1.11$ and $P_r = 1.35$). (a) Schlieren image of jet fuel and N_2 (scale above image for reference). (b) Predicted density (kg/m^3) of *n*-decane and N_2 mixture. (c) Predicted mass fraction of *n*-decane. (d) Predicted temperature (°C).

is increased to 441 °C (Figure 6c). Figure 6a shows the injection of fuel (*Re* of 12 800) initially at 266 °C as it flows into the chamber and field of view. In addition, the N_2 (*Re* of 2000) that heats the nozzle is at a temperature of 500 °C. At a temperature of 266 °C and a pressure of 2.65 MPa ($P_r = 1.35$ and $T_r = 0.84$), the major components of the fuel exist as a compressed liquid mixture (subcritical condition).[22] Figure 6a shows that the length of the fuel jet, measured from the nozzle exit to a location where the fuel is visually indistinguishable from the N_2, is 5.7 cm. With the nozzle exit fuel temperature increased to 325 °C ($P_r = 1.35$ and $T_r = 0.93$) and an exit N_2 temperature of 502 °C (*Re* of 2000), Figure 6b shows the injection of subcritical fuel into the chamber (*Re* of 16 400). From Figure 6b, the length of the fuel jet measured from the nozzle exit to a location where the fuel is visually indistinguishable from the N_2 is 3.5 cm. For the same pressure conditions as in Figure 6a but at a greater temperature of 325 °C (Figure 6b), both the surface tension and heat of vaporization of the fuel are diminished below values at 266 °C. In addition, the evaporation rate increases with decreasing surface tension and heat of vaporization. Thus, because of greater evaporation rates and more rapid entrainment of N_2, the fuel jet of Figure 6b (spreading angle of 4.5 ± 0.5° and nozzle exit temperature of 325 °C) widens more rapidly than that of Figure 6a (spreading angle of 3.0 ± 0.5° and nozzle exit temperature of 266 °C) for a given axial location along the centerline of the fuel jet. Moreover, the more rapid evaporation and enhanced mixing of the fuel in Figure 6b prevent the fuel from penetrating as far into the chamber as in Figure 6a. The nozzle exit temperature is 441 °C in Figure 6c, and the temperature (506 °C) of the flowing N_2 is similar to that of Figure 6a,b. At 2.65 MPa and 441 °C ($P_r = 1.35$ and $T_r = 1.11$), the fuel is a supercritical fluid upon entering the nozzle and the optical chamber.

For a given pressure, the density and viscosity of a hydrocarbon fuel may vary strongly with temperature. Thus, for a fixed mass flow rate and pressure, the Reynolds numbers of the fuel in Figure 6a−c increase rapidly with temperature. Upon comparison of images a−c of Figure 6, it is observed that the length of the fuel jet decreases as the injected fuel transitions from compressed liquid to supercritical fluid. The decrease in the jet length implies that the fuel and nitrogen are mixed faster than under subcritical conditions. Under supercritical conditions, the surface tension of the fuel vanishes, and the mixing process does not involve evaporation. Moreover, a supercritical fluid generally has a greater diffusivity and a lower viscosity than a liquid. Together with zero surface tension, these transport characteristics contribute to the relatively more rapid mixing of the supercritical fuel. Thus, the mixing process between the fuel and nitrogen occurs more rapidly for fuel at supercritical conditions and results in less penetration into the chamber than for liquid fuel. The observation that the penetration depth decreases with increasing fuel temperature at supercritical conditions is important for the design of future combustors. Admittedly, the design of gas turbine combustors is complex and depends on many factors. However, a reduced penetration depth implies a reduced mixing time for the fuel jet for otherwise identical circumstances.

Passing through the nozzle, jet fuel is heated by N_2 flowing over the nozzle exterior. Upon exiting the nozzle at supercritical conditions, the fuel expands into the chamber, forming a gaslike turbulent jet. Within the fuel jet, the fluctuating transverse velocity component enhances transport of unmixed fuel from the core region of the jet to the surrounding fluid. Understanding the mixing dynamics of Jet A and N_2 is complicated by differences in molecular weight, velocity, and temperature. Figure 7 shows a schlieren image of Jet A fuel

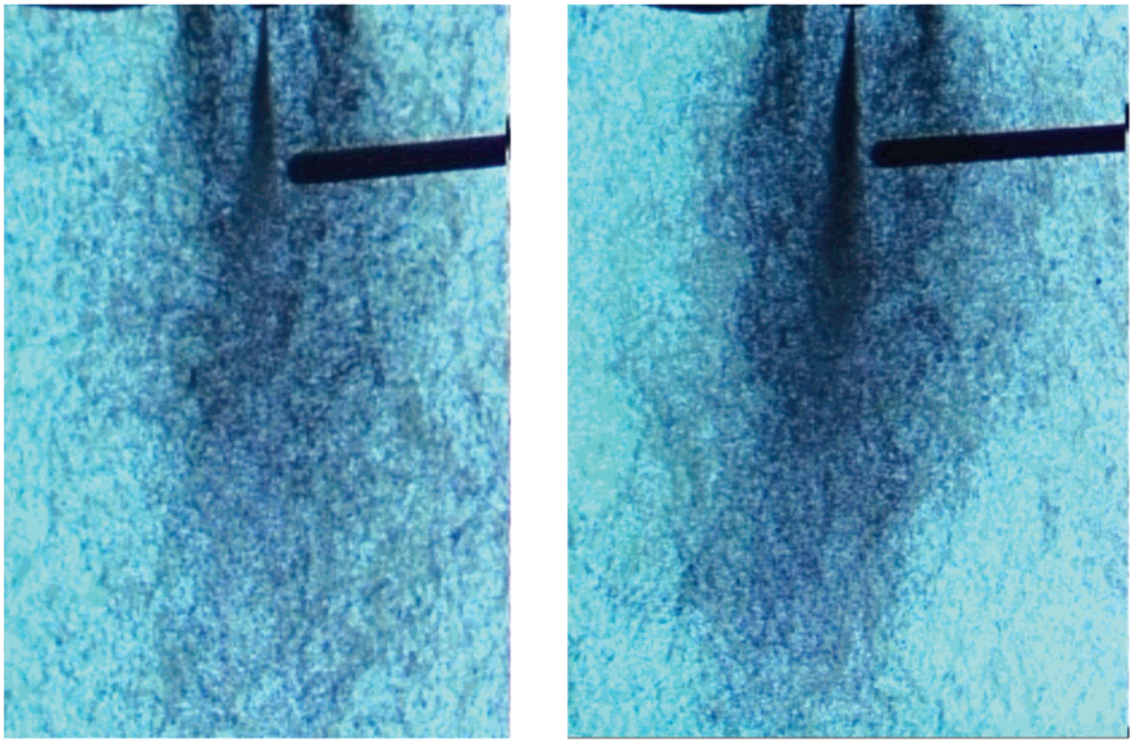

Figure 8. Effect of jet fuel mass flow rate. (a) Mass flow rate of 0.2 g/s, nozzle exit temperature of 441 °C ($T_r = 1.11$ and $P_r = 1.35$). N_2 temperature of 508 °C. (b) Mass flow rate of 0.4 g/s, nozzle exit temperature of 405 °C ($T_r = 1.06$ and $P_r = 1.35$). N_2 temperature of 588 °C.

and N_2 at supercritical conditions (Figure 7a; fuel mass flow rate of 0.2 g/s, exit nozzle temperature of 441 °C, and pressure of 2.65 MPa) together with plots of predicted density (Figure 7b), mass fraction of *n*-decane (Figure 7c), and temperature (Figure 7d). Figure 7a (same as Figure 6c) shows that the fuel jet becomes indistinguishable from the N_2 at a location 7.5 mm ($Z/D = 30$, where Z is the distance along the jet centerline below the nozzle and D is the nozzle i.d.) below the fuel nozzle. For nonisothermal cold-into-hot jets, similar Z/D have been observed elsewhere.[2,23] In addition, Figure 7b shows that axial and radial density gradients have become negligible 7.5 mm below the nozzle. Because schlieren imaging is sensitive to density gradient, images a and b of Figure 7 support one another in defining a value for the jet length (7.5 mm). This agreement also shows that it is reasonable to use a simple fuel such as *n*-decane in numerical simulations of the heat transfer and transport phenomena of a more complex Jet A fuel. At this location 7.5 mm from the nozzle, Figure 7c shows that the mass fraction is less than 0.2. Moreover, Figure 7d shows that the low-temperature (blue) core region of the fuel jet persists for 7.5 mm beyond the nozzle exit. Figure 7d also shows that the temperature of the N_2 away from the fuel jet is nearly uniform. This uniformity indicates that heat loss from the chamber walls to the ambient has little effect on the temperature distribution near the fuel jet.

Effects of Varying the Mass Flow Rate. The schlieren images of Figure 8a,b show the effects of increasing the jet fuel mass flow rate from 0.2 to 0.4 g/s for conditions of similar reduced temperatures. Figure 8a shows that the length of the Jet A jet which has the lower mass flow rate of 0.2 g/s (nozzle exit temperature of 441 °C; $T_r = 1.11$) is 7.5 mm. Figure 8b shows that, with a mass flow rate of 0.4 g/s (nozzle exit temperature of 405 °C; $T_r = 1.06$), the length of the Jet A jet increases to 15 cm. In addition, images a and b of Figure 8 show that the spreading angle increases from 3.5° to 5.0° when the mass flow rate increases from 0.2 to 0.4 g/s. However, understanding the influence of mass flow rate on the penetration of the fuel jet into the chamber is complicated by the coupled effects of fuel temperature and velocity. The results of numerical simulations assist the understanding of the influence of the mass flow rate on jet penetration and jet growth rate and are described below.

Jet Growth Rate. The fluctuating transverse velocity component of the *n*-decane jet enhances mixing of fuel from the jet core region with the surrounding N_2 within a mixing layer. The mixing layer grows outward as the heated jet extends further into the chamber. The growth of the mixing layer has been described in terms of an initial jet spreading angle.[24] In Figure 9, the jet spreading angle is measured from the nozzle centerline to a tangent line drawn along the outer portion of the jet mixing layer. The spreading angle of the Jet A jet in the schlieren image of Figure 9a is 3.5 ± 0.5°, and the spreading angle determined from the calculated density plot for *n*-decane in Figure 9b is 3.0 ± 0.5°. Here, the calculated density field resulting from the use of *n*-decane (nozzle exit temperature 441 °C and N_2 temperature of 506 °C) provides a reasonable prediction of the spreading angle of the supercritical Jet A jet. In addition, Table 4 shows that the spreading angles determined from schlieren images at other conditions compare well with those obtained by numerical simulation.

To confirm the numerical simulations of the coflow of *n*-decane and N_2 jets, predictions of the mean fuel mass fraction along the jet centerline are compared to

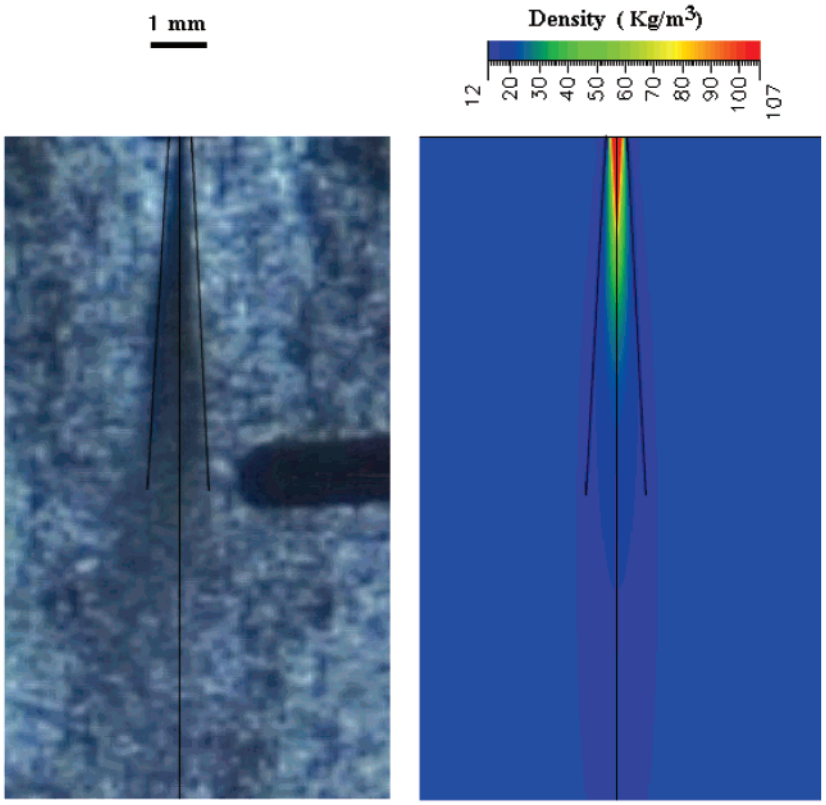

Figure 9. Measured (3.5°) and predicted (3.0°) spreading angle for jet fuel and surrogate fuel, *n*-decane.

Table 4. Predicted and Measured Spreading Angles and Jet Lengths (Chamber Pressure of 2.65 MPa)

mass flow rate (g/s)	exit temp (°C)		spreading angle (deg) (uncertainty ± 0.5°)		jet length (mm)	
	jet fuel	N_2	measd	pred	measd	pred
0.2	393	510	3.5	3.0	12.0	15.0
0.2	441	506	3.5	3.0	7.5	9.0
0.2	465	588	3.5	3.0	6.0	7.0
0.4	405	588	5.0	4.5	15.0	18.0
0.4	424	590	5.0	4.5	12.0	14.0
0.4	465	590	5.0	4.5	8.0	9.0

values predicted by a semiempirical correlation. Time-averaged concentration measurements along the centerlines of variable-density, axisymmetric, turbulent jets formed by the flow of a faster moving gas into a slow coflow of a second gas have been performed by Pitts.[23] Pitts found that eq 3 described his time-averaged

$$Y_o/Y_m = (K_c Z)/r_\epsilon + (\rho_\infty/\rho_o - 1)K \qquad (3)$$

measurements of the jet mass fraction along the centerline, Y_m.[23,25] In eq 3, Y_o is the time-averaged mass fraction at the nozzle exit, ρ_∞ is the density of the external, slow-moving gas, ρ_o is the density of the faster moving jet at the nozzle exit, Z is the distance from the nozzle exit along the jet centerline, and both K and K_c are constants. The effective radius, r_ϵ, is defined as $r_\epsilon = r_o(\rho_o/\rho_\infty)^{1/2}$, and r_o is the radius of the jet nozzle. (In this discussion, $Y_o = 1$.) Following Pitts, values of $K = -0.5$ and $K_c = 0.114$ have been assumed, and values for the global density ratio are from Figure 7b.[23] If our numerical simulations of Y_o/Y_m within the *n*-decane jet are reasonable, they should follow the predictions of eq 3. Figure 10 shows predictions of Y_o/Y_m for several different jet/coflow pairs as a function of Z/r_o using eq 3 and values from Pitts.[23] The use of several different

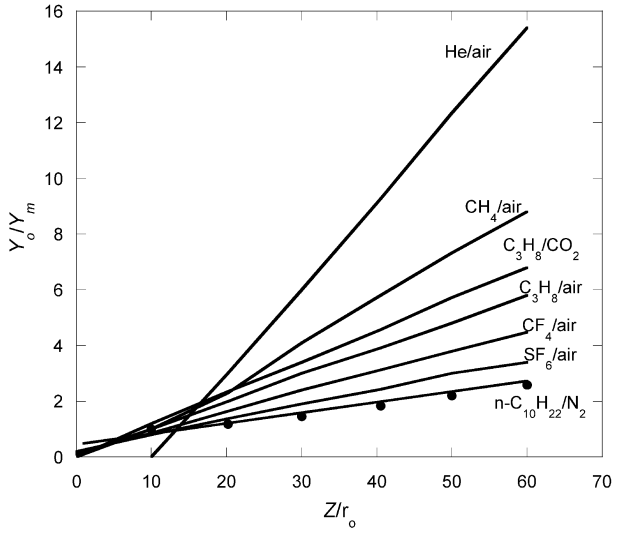

Figure 10. Reciprocal of the mass fraction for different gas pairs. The lines represent the correlation given by eq 3. The solid circles are predictions resulting from the present computational fluid dynamics simulations.

jet/coflow pairs demonstrates the wide applicability of eq 3. In addition, Figure 10 includes predictions of Y_o/Y_m for the *n*-decane/N_2 coflow pair from both the use of eq 3 and the present numerical simulations. The solid circular symbols near the *n*-decane/N_2 curve represent Y_o/Y_m values derived from the current numerical simulations which involve the Reynolds-averaged turbulence equations. Figure 10 shows that there is good agreement between the empirical correlation (eq 3) and the present simulations.

Downstream from the flow development region (>5−10 diameters) one dimensionless length scale will specify time-averaged concentrations for jet coflow pairs.[23] It

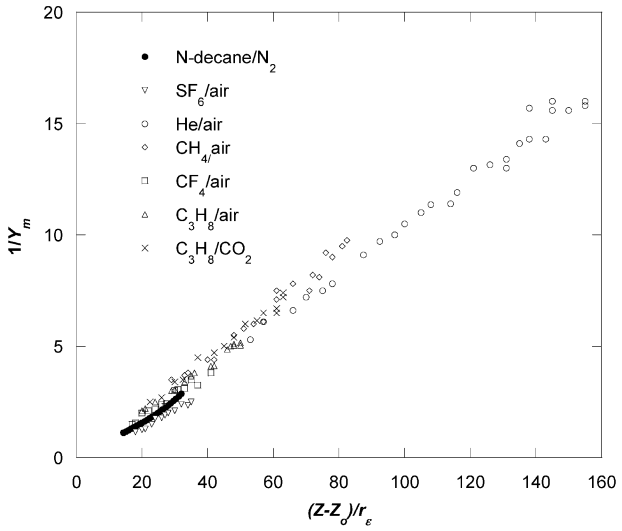

Figure 11. Reciprocal of the measured time-averaged mass fraction along the gaseous jet centerline for different gas pairs in coflow as a function of dimensionless distance from the virtual origin of the jet.[22] Here, $r_\epsilon = r_o(\rho_o/\rho_\infty)^{1/2}$. In addition, values obtained by computational fluid dynamics simulations for *n*-decane and N_2 are shown.

has been suggested that the reciprocal of the time-averaged mass fraction along a gaseous jet centerline scales with the following relationship: [23,25]

$$\frac{Y_o}{Y_m} = K_c\left(\frac{Z - Z_o}{r_\epsilon}\right) \tag{4}$$

In eq 4, Z_o is the virtual origin of the jet. (This is the point where the jet centerline intersects a line drawn tangent to the jet exterior. Here, Y_o is unity, and Z_o is negative.) Several experimental studies (isothermal and nonisothermal) support the scaling representation of eq 4 for axisymmetric jets where the coflowing gases have different densities but the downstream density asymptotically becomes constant.[25] Figure 11 shows $1/Y_m$ plotted against $(Z - Z_o)/r_\epsilon$ for the present *n*-decane and N_2 computational fluid dynamics calculations together with measured values for six jet/coflow gas pairs from Pitts.[23] Figure 11 shows that the jet/coflow pairs partially collapse onto a single curve, and this collapse indicates a degree of similarity. Similarity is useful in the fundamental understanding of the fluid dynamics of simple flows. Moreover, the observation that the numerical predictions for *n*-decane and N_2 tend to fall on a curve common to other coflow pairs provides additional validation of the present calculations.

Conclusions

Schlieren images of supercritical jet fuel exiting from a simple nozzle into a supercritical environment were obtained. The jet penetration depth, spreading angle, and phase behavior vary with fuel temperature and mass flow rate, which, in turn, can vary considerably during an aircraft mission. The observations that the penetration depth decreases with increasing fuel temperature at supercritical conditions and that the spreading angle increases with increasing mass flow rate are important for the design of future combustors.

Numerical simulations which used *n*-decane as a surrogate fuel for purposes of calculating the jet spreading angle and length agreed reasonably well with the measurements. In addition, the numerical predictions of the jet centerline fuel mass fraction agreed well with established correlations. Thus, *n*-decane or a similar hydrocarbon surrogate fuel can be used for calculations of the heat transfer and fluid dynamics of nonreacting supercritical jet fuel which has a similar critical temperature and pressure.

Acknowledgment

This work was supported by the U.S. Air Force, Fuels Branch, Propulsion Directorate, Air Force Research Laboratory, Wright-Patterson AFB, OH, under Contract No. F33615-97-C-2719.

Nomenclature

C_1 = constant = 1.47
C_2 = constant = 1.92
C_μ = constant = 0.09
D = tube diameter, m
D_i = diffusion coefficient of the *i*th species, m^2/s
$G = \mu_t[2\{(\partial u/\partial z)^2 + (\partial v/\partial r)^2 + (v/r)^2\} + (\partial v/\partial z + \partial u/\partial r)^2]$
g = gravitational acceleration, m/s^2
h = enthalpy, kJ/kg
k = thermal conductivity, W/m·K; turbulent kinetic energy, kJ/kg
K = constant in eq 3
K_c = constant in eq 4
p = pressure, MPa
P_{ch} = chamber pressure, MPa
r = radial coordinate, m
r_o = radius of the jet nozzle, m
r_ϵ = effective radius, m
S^Φ = source term
u = axial velocity component, m/s
u_τ = friction velocity, $(\tau_\omega/\rho)^{1/2}$, m/s
U = mean velocity, m/s
v = radial velocity component, m/s
$\dot{\omega}$ = rate of production of the *i*th species, kg/m^3·s
y = normal distance from the wall, m
Y_i = mass fraction of the *i*th species
Y_o = time-averaged mass fraction at the nozzle exit
Y_m = time-averaged mass fraction along the jet centerline
$y+$ = dimensionless distance from the wall, $\rho y u_\tau/\mu$
z = axial coordinate, m
Z = distance from the nozzle exit along the jet centerline, m
Z_o = virtual origin of the jet, m
Φ = assigned variable in eqs 1 and 2
Γ^Φ = transport coefficient
ϵ = dissipation rate, kJ/kg·s
ρ = density, kg/m^3
ρ_∞ = density of external, slow-moving gas, kg/m^3
ρ_o = density of faster-moving fuel at the nozzle exit, kg/m^3
σ_k = constant = 1.0
σ_ϵ = constant = 1.3
σ_h = constant = 1.0
σ_{Y_i} = constant = 1.0
τ_w = wall shear stress, N/m^2
μ = absolute viscosity, N·s/m^2
μ_t = turbulent viscosity, $C_\mu\rho k^2/\epsilon$, N·s/m

Literature Cited

(1) Edwards, T.; Zabarnick, S. Supercritical Fuel Deposition Mechanisms. *Ind. Eng. Chem. Res.* **1993**, *32*, 3117.

(2) Chehroudi, B.; Talley, D.; Coy, E. Initial Growth Rate and Visual Characteristics of Round Jet into a Sub- to Supercritical Environment of Relevance to Rocket, Gas Turbine, and Diesel

Engines. 37th AIAA Aerospace Sciences Meeting and Exhibit, Reno, NV, Jan 1999; Paper AIAA 99-0206.

(3) Wu, P.; Chen, T. H.; Nejad, A. S.; Carter, C. D. Injection of Supercritical Ethylene in Nitrogen. *J. Propul. Power* **1996**, *12*, 770.

(4) Wu, P. K.; Shahnam, M.; Kirkendall, K. A.; Carter, C. D.; Nejad, A. S. Expansion and Mixing Processes of Underexpanded Supercritical Fuel Jets into Superheated Conditions. *J. Propul. Power* **1999**, *15*, 642.

(5) Newman, J. A.; Brzustowski, T. A. Behavior of a Liquid Jet Near the Thermodynamic Critical Region. *AIAA J.* **1971**, *9*, 1595.

(6) Woodward, R. D.; Talley, D. G. Raman Imaging of Transcritical Cryogenic Propellants. 34th AIAA Aerospace Sciences Meeting and Exhibit, Reno, NV, Jan 1996; Paper AIAA 96-0468.

(7) Mayer, W.; Ivancic, B.; Schik, A.; Hornung, U. Propellant atomization in LOX/GH2 rocket combustors. 34th AIAA/ASME/SAE/ASEE Joint Propulsion Conference & Exhibit, Cleveland, OH, Jul 1998; Paper AIAA 98-3685.

(8) Chen, L. D.; Sui, P. C. Atomization During the Injection of Supercritical Fluid into High-Pressure Environment. 1994 IUTAM on Droplets and Sprays, Taiwan, Dec 1994.

(9) Bellan, J. Supercritical (and Subcritical) Fluid Behavior and Modeling: Drops, Streams, Shear and Mixing Layers, and Jets and Sprays. *Prog. Energy Combust. Sci.* **2000**, *26*, 329.

(10) Edwards, T.; Maurice, L. Q.Surrogate Mixtures To Represent Complex Aviation and Rocket Fuels. *J. Propul. Power* **2001**, *17*, 461.

(11) Heneghan, S. P.; Zabarnick, S.; Ballal, D. R.; Harrison, W. E., III. JP-8+100: The Development of High-Thermal Stability Jet Fuel. *J. Energy Resour. Technol.* **1996**, *118*, 170.

(12) Ervin, J. S.; Williams, T. F.; Hartman, G. Effect of Test Period on the Rate of Fouling in a Complex Flowing System. *Prepr.—Am. Chem. Soc., Div. Pet. Chem.* **1998**, *43*, 373.

(13) Eckert, E. R.; Goldstein, R. J. *Measurements in Heat Transfer*; Hemisphere: Washington, DC, 1976.

(14) Launder, B. E.; Spalding, D. B. The Numerical Computation of Turbulent Flows. *Comput. Methods Appl. Mech. Eng.* **1974**, *3*, 269.

(15) Ivancic, B.; Mayer, W.; Krulle, G.; Bruggeman, D. Experimental and Numerical Investigation of Time and Length Scales in LOX/GH_2—Rocket Combustors. 35th AIAA/ASME/SAE/ASEE Joint Propulsion Conference and Exhibit, Los Angeles, CA, Jun 1999; Paper AIAA 99-2211.

(16) Chien, K. Y. Predictions of Channel and Boundary Layer Flows with a Low-Reynolds Number Turbulence Model. *AIAA J.* **1982**, *20*, 33.

(17) CFD Research Corp. *CFD-ACE Theory Manual Version 5.0*; CFD Research Corp.: Huntsville, AL, 1998.

(18) Ambrose, D.; Tsonopoulos, C. Vapor—Liquid Critical Properties of Elements and Compounds. 2. Normal Alkanes. *J. Chem. Eng. Data* **1995**, *40*, 531.

(19) Yu, J.; Eser, S. Determination of Critical Properties. *Ind. Eng. Chem. Res.* **1995**, *34*, 404.

(20) Peng, D. Y.; Robinson, D. B. A New Two-Constant Equation of State. *Ind. Eng. Chem. Fundam.* **1976**, *15*, 59.

(21) Ely, J. F.; Huber, M. L. NIST Standard Reference Database 4—NIST Thermophysical Properties of Hydrocarbon Mixtures, Feb 1990.

(22) Nixon, A. C.; Ackerman, G. H.; Faith, L. E.; Henderson, H. T.; Ritchie, A. W.; Ryland, L. B.; Shryne, T. M. *Vaporizing and Endothermic Fuels for Advanced Engine Applications: Part III, Studies of Thermal and Catalytic Reactions, Thermal Stability, and Combustion Properties of Hydrocarbon Fuels (AFAPL-TR-67-114)*; Air Force Propulsion Laboratory: Wright-Patterson Air Force Base, OH, 1967.

(23) Pitts, W. M. Effects of Global Density Ratio on the Centerline Mixing Behavior of Axisymmetric Turbulent Jets. *Experiments in Fluids* **1991**, *11*, 125.

(24) Abramovich, G. N. *The Theory of Turbulent Jets;* MIT Press: Cambridge, MA, 1963.

(25) Pitts, W. M. *Effects of Global Density and Reynolds Number Variations on Mixing in Turbulent, Axisymmetric Jets*; Report No. NBSIR 86-3340; National Bureau of Standards: Washington, DC, Mar 1986.

Received for review December 7, 2001
Revised manuscript received August 19, 2002
Accepted August 27, 2002

IE0109915

R. Studies of Urea Treatment on the Low Temperature Properties of Jet Fuel

Studies of Urea Treatment on the Low-Temperature Properties of Jet Fuel

Steven Zabarnick,* Nikki Widmor, and Marlin Vangsness

University of Dayton Research Institute and Department of Mechanical and Aerospace Engineering, 300 College Park, Dayton, Ohio 45469-0116

Received May 28, 2002

Studies were conducted to investigate the use of urea treatment for improving the low-temperature properties of jet fuel. In particular, we utilized differential scanning calorimetry (DSC), cold-stage microscopy, and ASTM freeze, cloud, and pour-point testing to characterize the changes in the fuel that occur upon urea treatment. We also used gas chromatography (GC) to study both the qualitative and quantitative changes that occur in the chemical constituents of the fuel. These studies show that urea treatment in the presence of an activator species, such as methanol, is quite selective and effective at removing long chain *n*-alkanes. The resulting fuel shows a substantial decrease in crystal formation observed via DSC and cold-stage microscopy. The fuel also displays a significant reduction in the measured pour and cloud points. Some of the practical issues in using urea treatment for jet fuel are also discussed.

Introduction

The operation of aircraft at high altitudes for long periods of time can subject jet fuel to extremely low temperatures. Such conditions can result in greatly increased fuel viscosity and, at the most extreme conditions, partial solidification of the fuel. Fuel crystallization makes a portion of the fuel unavailable for propulsion, and in the most extreme situation can result in catastrophic fuel system failure. To prevent fuel system problems at low temperatures, the U.S. Air Force uses the specialty fuel JPTS (MIL-DTL-25524E) for high-altitude reconnaissance aircraft. JPTS is specially refined to exhibit a low freeze point and excellent high-temperature thermal stability, but unfortunately is relatively expensive. Replacement of JPTS with the less expensive JP-8 fuel would be attractive for both economic and logistical reasons. As a result, the U.S. Air Force is investigating the use of additives to improve both the cold-flow and high-temperature thermal stability properties of JP-8 fuel. Reduction in high-temperature thermal oxidative deposition can be affected by addition of the JP-8+100 additive package.[1] Pour-point-improving additives, such as ethylene vinyl-acetate (EVA) copolymers, show promise in improving cold flow properties of JP-8 to allow operation at the low temperatures for which JPTS was designed.[2,3] More recently, other proprietary copolymer classes have shown the ability to reduce the temperature of fuel crystallization and provide even lower temperature useability.[4] The resulting fuel with improved low- and high-temperature properties would be called JP-8+100LT.

Alternatively, fuel-processing techniques can be employed to improve the low-temperature properties of jet fuel. Reducing the concentration of higher molecular weight species, which lowers the freeze point, can be affected by changing the distillation range for these fuels, but this option is costly and is used in the production of JPTS. Postprocessing techniques, in which the high molecular weight normal alkanes (i.e., wax) are removed, offer the potential to be effective and less expensive for the relatively small volume of fuel required to replace JPTS. More specifically, three types of processes have been developed for the dewaxing of petroleum products: (1) low-temperature solvent dewaxing,[5] (2) catalytic dewaxing using zeolites,[6] and (3) urea treatment.[7−9] Solvent dewaxing involves dilution in a ketone solvent, chilling of the solution, filtration of wax crystals, and product recovery. Catalytic dewaxing is used commercially in the dewaxing of diesel and lubricating oil base stocks and involves the selective cracking of high melting waxy, *n*-paraffinic components in the oil.[6] The urea process is a low-temperature technique in which urea selectively reacts with long chain normal alkanes to form solid "inclusion compounds," which are also referred to as "adducts." These

* Corresponding author.

(1) Heneghan, S. P.; Zabarnick, S.; Ballal, D. R.; Harrison, W. E. *J. Energy Res. Technol.* **1996**, *118*, 170−179.

(2) Ervin, J. S.; Zabarnick, S.; Binns, E.; Dieterle, G.; Davis, D.; Obringer, C. *Energy Fuels* **1999**, *13*, 1246−1251.

(3) Zabarnick, S.; Widmor, N. *Energy Fuels* **2001**, *15*, 1447−1453.

(4) Zabarnick, S.; Vangsness, M. *Prepr. Pap.—Am. Chem. Soc., Div. Pet. Chem.* **2002**, *47*, 243−246.

(5) Taylor, R. J.; McCormack, A. J.; Nero, V. P. *Prepr. Pap.—Am. Chem. Soc., Div. Pet. Chem.* **1992**, *37*, 1337−1346.

(6) Sivansanker, S.; Ramaswamy, A. V.; Ratnasamy, P. *Appl. Catal. A: Gen.* **1996**, *138*, 369−379.

(7) Hoppe, A. In *Advances in Petroleum Chemistry and Refining*; McKetta, J. J., Ed.; Interscience Publishers: New York, 1964; Vol. 8, pp 193−234.

(8) McLaughlin, R. L. In *The Chemistry of Petroleum Hydrocarbons*; Brooks, B. T., Boord, C. E., Stewart, S. S., Schmerling, L., Eds.; Reinhold Publishing: New York, 1954; Vol. 1, pp 241−274.

(9) Takemoto, K.; Sonoda, N. In *Inclusion Compounds*; Atwood, J. L., Davies, J. E. D., MacNicol, D. D., Eds.; Academic Press: London, 1984; Vol. 2, pp 47−67.

10.1021/ef020116b CCC: $22.00
Published on Web 10/22/2002

adducts are then easily separated from the liquid fuel. In commercial operation, the urea can be regenerated for reuse and the *n*-paraffins recovered.

Bengen[10] is usually credited with discovery of the process in which *n*-alkanes form adducts with urea. Although linear unbranched alkanes readily form adducts, branched hydrocarbons may also form inclusions compounds, provided the molecule contains a sufficiently long linear chain.[7] The tendency for adduct formation and the thermal stability of the urea adducts increase with the molecular weight of the species. Thus, the long chain *n*-alkanes that have been implicated in wax formation in petroleum products may be selectively removed via urea treatment. Hoppe[7] details the commercial urea treatment processes that have been implemented in the past in the U.S., the former Soviet Union, France, and Germany for the production of low wax oils.

To date, no specific work has focused on the study of the urea treatment process for the treatment of jet fuels (i.e., kerosene-based aviation turbine fuels). These fuels typically have much lower wax concentrations than the oils produced in commercial urea dewaxing processes,[7] and must remain fluid to much lower temperatures (ASTM freeze point maximums: Jet A, −40 °C; Jet A-1 and JP-8, −47 °C; and JPTS, −53 °C). The reduced wax concentration and reduced solid formation temperatures may result in greater challenges in using the urea process for jet fuels. In this work, we investigate the use of urea treatment for improving the low-temperature properties of jet fuel. In particular, we utilize differential scanning calorimetry (DSC), cold-stage optical microscopy, and ASTM freeze, cloud, and pour-point testing to characterize the changes in the fuel that occur upon urea treatment. We also use gas chromatography (GC) to study the qualitative and quantitative changes that occur in the chemical constituents of the fuel upon processing. A series of tests are performed to optimize the urea treatment process and the practical implications for the use of the technique are discussed.

Experimental Section

All urea/fuel treatments were conducted at room temperature (23 ± 2 °C). Fuel, urea, and methanol (when used) were mixed in glass bottles and stirred, using a magnetic stirrer for the stated reaction times. After treatment, fuel samples were removed from the mixture via a chromatographic syringe. The fuels (Jet A sample 3219 and JPTS sample 3657) were acquired from the Fuels Branch, Propulsion Directorate, of the Air Force Research Laboratory, Wright-Patterson AFB, OH. Methanol and urea were acquired from Aldrich and used without further purification.

DSC data was acquired using a TA Instruments DSC 2920 calorimeter equipped with a Liquid Nitrogen Cooling Accessory (LNCA). The LNCA directs a mixture of gaseous and liquid nitrogen to the sample chamber, which permits thermal analysis data to be acquired at subambient temperatures. Typically, 20 μL (approximately 16 mg) of liquid fuel is sampled using a chromatographic syringe, injected into a preweighed open aluminum sample pan, and subsequently weighed. An empty aluminum pan is used for the reference. Most data were acquired at a cooling rate of 1 °C/min over the temperature range −45 to −65 °C.

Low-temperature microscopy information was acquired with an Olympus BX50 optical microscope with phase contrast and polarization optics. Most images were recorded through the 10× objective with crossed polarization optics and recorded with a Kodak DS120 megapixel digital camera. The sample was loaded onto a microscope slide with an elevated cover slip. The sample size was approximately 20 μL. The slide was placed on the cold plate of a Linkam heating/cooling stage, which isolates it from ambient conditions with insulation and a nitrogen purge. Using liquid nitrogen as the coolant, the sample was brought to −45 °C at a rate of 30 °C/min and held for 5 min. The sample was then cooled at a slower rate (typically 0.25 °C/min) below −65 °C while the crystallization state was recorded.

Cloud point, pour point, and freeze point data were acquired using a Phase Technology PSA-70V Petroleum Analyzer, via ASTM D5773-95, D5949-96, and D5972-96, respectively. The pour point analyses were conducted at 1 °C intervals.

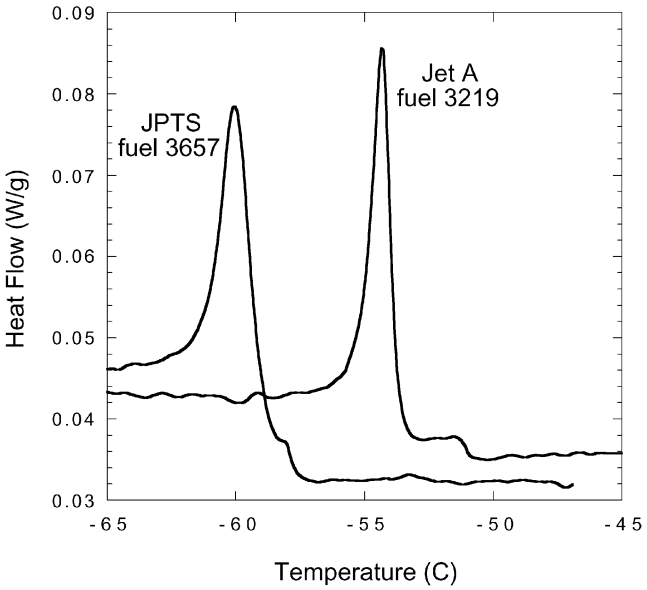

Figure 1. DSC cooling exotherms of two fuels: JPTS fuel 3657 and Jet A fuel 3219.

Results and Discussion

DSC Studies. In previous work, we have shown that the DSC exotherm obtained upon the cooling of jet fuel is an indication of fuel solidification that results from the crystallization of the largest normal alkanes present.[3] A recent study has shown that the formation of as little as 0.5−1 wt % of solid *n*-alkanes is enough to completely gel jet fuel.[11] In the present work, we use DSC to evaluate the effect of urea treatment on the freezing of jet fuel. In Figure 1, we have plotted DSC curves for two jet fuels: a Jet A fuel (3219) and a JPTS fuel (3657). Table 1 shows the measured freeze, cloud, and pour points of these two fuels (note: only freeze point is a specification requirement for jet fuels). The table shows that the Jet A fuel (3219) has a freeze point (−46.3 °C) which is slightly outside the JP-8 freeze point specification (−47 °C maximum). The JPTS fuel (3657) has a freeze point (−53.8 °C) that is just within the JPTS specification (−53 °C max), although most other JPTS samples studied in our laboratory have lower (by 1 to 6 °C) freeze points.[4] Thus, this Jet A fuel is a potential candidate as a "worst-case fuel" for improving low-temperature properties. The JPTS fuel is considered a

(10) Bengen, F. German Pat. 869,070, 1940, assigned to Badische Anilin-und Soda-Fabrik, A. G.

(11) Coutinho, J. A. P.; Mirante, F.; Ribeiro, J. C.; Sansot, J. M.; Daridon, J. L. *Fuel* **2002**, *81*, 963−967.

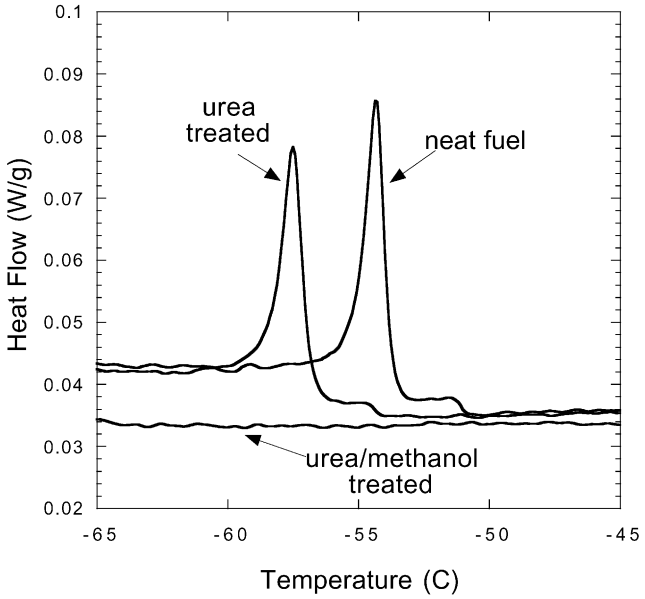

Figure 2. DSC curves for a neat fuel (Jet A 3219), after urea treatment, and after urea/methanol treatment.

Table 1. Pour, Cloud, and Freeze Points of Urea-Treated Fuel as a Function of the Amount of Urea, Amount of Methanol, and Time

urea treatment conditions	pour point (°C)	cloud point (°C)	freeze point (°C)
untreated Jet A Fuel (3219)	−56	−50.9	−46.3
1 h, 1% methanol			
1% urea	−55	−50.3	−46.9
5% urea	−56	−52.9	−47.9
25% urea	−66	−59.3	−56.1
25% urea, 1% methanol			
1 hour	−66	−59.3	na
2 hours	−70	−61.3	−58.1
3 hours	−69	−60.8	na
4 hours	−69	−62.3	na
25% urea, 3 hours			
0% methanol	−56	−49.4	na
1% methanol	−69	−60.8	na
2% methanol	−70	−59.6	na
JPTS Fuel (3657)	−64	−57.8	−53.8

fuel that has low-temperature properties that are a minimum goal of the program. Thus, we would like to see a treatment process or additive treatment that changes the low-temperature properties of the 3219 fuel to at least as good as that of 3657 fuel. Figure 1 shows the exotherms obtained upon cooling these fuels. The JPTS fuel exhibits an exotherm with a peak that occurs at a lower temperature by 5.8 °C. Also, the table shows that the JPTS fuel has lower freeze, cloud, and pour points by 7.5, 6.9, and 8 °C, respectively. Thus, a successful treatment process should improve these properties by at least 6 to 8 °C. It is important to note that the flowability and pumpability of the fuel in the aircraft tanks and fuel system at operational temperatures determines the usability of a fuel, rather than the above listed fuel properties. In a separate study, we examined the effect of temperature and candidate cold flow additives on fuel viscosity;[4] however, viscosity measurements were not performed in the present study.

Figure 2 shows the DSC curves obtained before and after urea treatment of the Jet A fuel. Ten grams of urea was added to 20 mL of fuel, and the mixture was stirred for 24 h. The figure shows that treatment with urea alone resulted in a shift of the freezing exotherm to lower temperatures by 3 °C. This outcome, while encouraging, results from a relatively long treatment, which would be impractical for production of significant quantities of fuel. Previous work has shown that added solvents can greatly accelerate the adduct formation process in oils.[7] It is believed that these so-called "urea solvents" accelerate the "reaction" by improving the ability of the crystalline urea to dissolve into the liquid mixture, allowing increased contact between urea and the adductable species present. These solvents are also known as "activators." Common activators include water, low molecular weight alcohols, and various mixtures of the two.

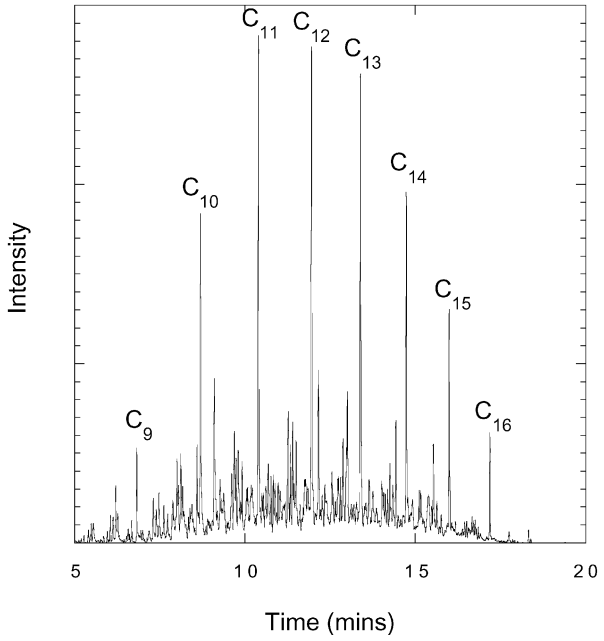

Figure 3. Chromatogram of fuel 3219 showing normal alkanes.

Methanol is one of the low molecular weight alcohols thought to act as an activator species in the urea process.[7] The presence of methanol is thought to increase the solubility of urea in the fuel, which results in a more complete urea/alkane reaction and faster reaction times. Also shown in Figure 2 is the DSC curve for fuel treated with a mixture of urea and methanol. The above procedure was repeated with the addition of 1 mL of methanol. The figure shows that the urea/methanol treatment eliminates the freezing exotherm out below −65 °C, providing a shift in the exotherm peak by more than 10 °C. This shows that the urea/methanol treatment has the potential to produce fuel that has improved low-temperature properties beyond that of in-specification JPTS (see Figure 1 for comparison).

To confirm that the improved low-temperature behavior is due to the removal of normal alkanes, as expected from previous studies, and to study the selectivity of the process for various size alkanes, we used gas chromatography (GC) to measure the change in concentration of the normal alkanes upon urea treatment. Figure 3 shows a chromatogram of the 3219 fuel, which shows that this fuel contains normal alkanes primarily in the range C_9 to C_{16}, with only very small amounts of C_{17} (<0.05 mol %). Figure 4 shows the percent decrease in concentration of these normal

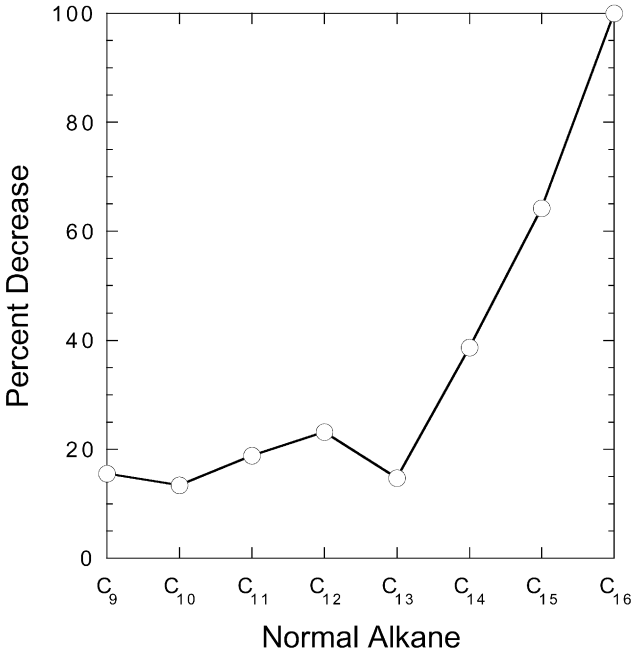

Figure 4. Plot of percent decrease of various normal alkanes after urea/methanol treatment.

alkanes after the urea/methanol treatment described above. The smaller alkanes, C_9 to C_{13}, are decreased by 10 to 25%. The larger normal alkanes ($\geq C_{14}$) are removed to the greatest extent, with essentially 100% removal of *n*-C_{16}. This shows that the urea/methanol treatment process is selective toward the larger normal alkanes present in jet fuel. This selectivity toward long-chain *n*-alkanes is quite desirable, as these species have been implicated as being the first species to crystallize upon the cooling of these fuels.[12,13] The initial crystallization of these species causes fuel clouding, which at lower temperatures and/or longer times, results in fuel gelation and the inhibition of fuel flow. A primary benefit of the urea adduction process is in this selectivity toward removal of the species that form solids (relatively large normal alkanes), while being much less likely to react with other fuel species, such as aromatics, branched alkanes, and cycloalkanes (naphthenes). Also, the process significantly lowers the measured freeze, cloud, and pour points (see below), while the use of cold-flow-improving additives has not demonstrated significant changes in all of these properties.[2,4]

Effect of Changing Urea Treatment Process Variables. We have attempted to optimize the room temperature urea treatment of jet fuel by varying the amount of added urea, the treatment reaction time, and the amount of added methanol activator species. Pour point, cloud point, and freeze point data for fuels treated under these varying conditions are reported in Table 1. Corresponding DSC curves for these fuels are shown in Figures 5−7. Initially, the amount of added urea was varied over the range 1 to 25% for reaction times of 1 h and 1% added methanol. Figure 5 shows that treatment with 1% urea does not significantly change the location of the DSC endotherm. Increasing the amount of added urea to 5% and 25% does show substantial changes in the peak location, with a decrease in temperature of over 9 °C for the peak location for the 25% urea case. The measured pour, cloud, and freeze points shown in Table 1 also show that the 25% urea case yields the largest decreases of 9 °C, 9.0 °C, and 9.2 °C, respectively, which are in good agreement with change observed in the DSC exotherm peak. Above 25% urea, it becomes very difficult to sample the fuel from the urea/methanol slurry that is created, so these levels were not further investigated.

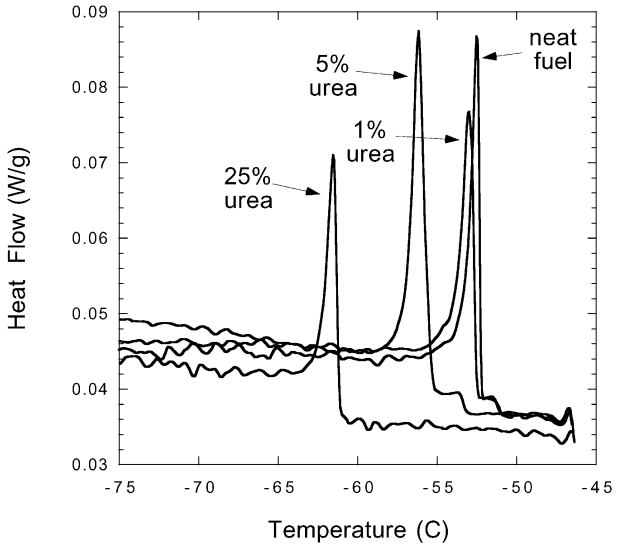

Figure 5. DSC curves for urea treatment at various levels of urea (all treatments performed at 1% methanol for 1 h).

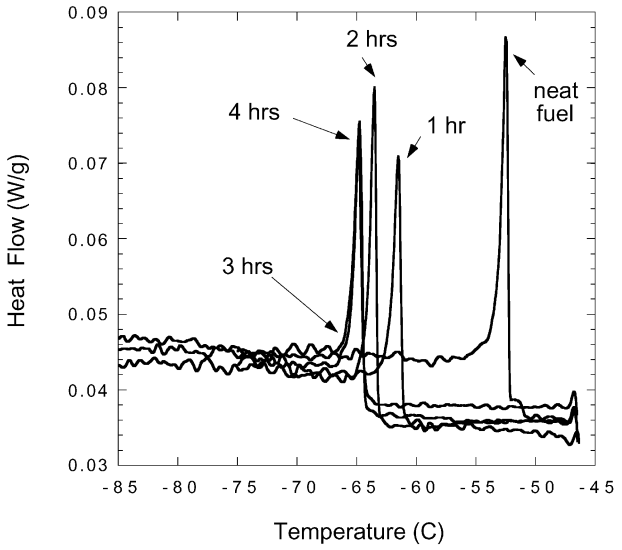

Figure 6. DSC curves for various urea treatment reaction times (all performed at 25% urea and 1% methanol).

Reaction time was varied over the range 1 to 4 h for fuel with 25% urea (optimized urea concentration) and 1% methanol. We demonstrate in Figure 6 that a 1 h reaction time lowers the temperature of the peak of the DSC endotherm from −52.4 °C for the untreated fuel to −61.4 °C. Much smaller decreases in temperature for the location of the peak are seen in increasing the reaction time to 2 and 3 h, demonstrating that most of the removal of normal alkanes is nearly complete in the first hour. No additional shift in the peak is seen in going from 3 to 4 h. The measured pour- and cloud-point

(12) Van Winkle, T. L.; Affens, W. A.; Beal, E. J.; Mushrush, G. W.; Hazlett, R. N.; DeGuzman, J. *Fuel* **1987**, *66*, 890−896.
(13) Van Winkle, T. L.; Affens, W. A.; Beal, E. J.; Mushrush, G. W.; Hazlett, R. N.; DeGuzman, J. *Fuel* **1987**, *66*, 947−953.

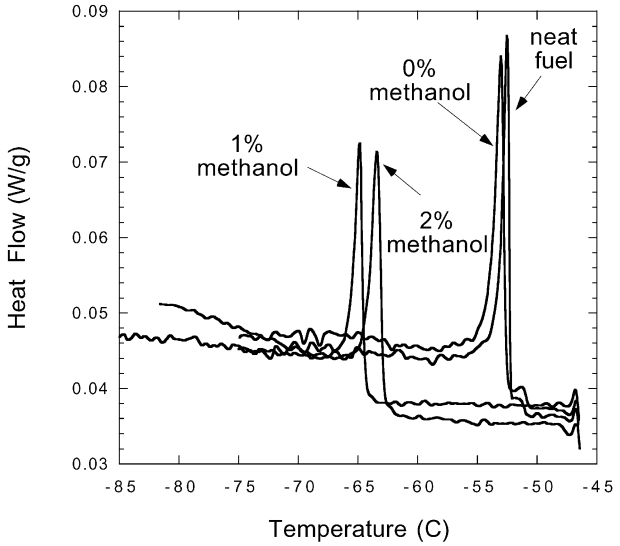

Figure 7. DSC curves for urea treatment at various levels of the methanol activator (all performed at 25% urea for 3 h).

data show that reaction times longer than 1 h are preferred, but the scatter in the data makes choosing the best time difficult.

Next we varied the amount of added methanol activator over the range 0 to 2% for treatment with 25% urea (optimized urea concentration) for 3 h (optimized reaction time). DSC endotherms for these treatments are shown in Figure 7. With no methanol present there is little change in the endotherm location. A substantial decrease is seen at 1% methanol, but the addition of 2% methanol provides no additional benefit. The pour and cloud point data also agree that no additional benefit is observed at 2% methanol. This preliminary attempt at optimizing the reaction time, urea amount, and methanol amount shows that the optimum parameters are a reaction time of 3 h with 25% urea and 1% methanol, providing a decrease in temperature of the peak of the DSC exotherm of 12.5 °C below that of the untreated fuel. This near-optimum treatment yields decreases in the pour and cloud points of 13 °C and 9.9 °C, respectively.

Hoppe[7] reported on a batch process used in the early 1960s for production of low wax white oil for medical use in which the pour point was lowered from −4 °C to −18 °C. This was the first large-scale urea dewaxing plant with a capacity of 900 kg per day. Interestingly, the process employed activated crystalline urea (activated with 1−2% methanol), 20% urea based on feed, and a reaction time of 1 h at ambient temperature. These parameters (levels of urea, methanol, and reaction time) are quite similar to the optimized parameters obtained in the present jet fuel work. The main difference is their use of shorter reaction times (1 vs 3 h). As shown above, most of the reaction is complete in 1 h, and therefore using this shorter reaction time can increase the amount of fuel treated in a given facility by a factor of 3, relative to using a 3-h reaction time.

Cold-Stage Microscopy. To further explore the effect of urea adduction on the freezing of jet fuels, we used a cold-stage microscope to generate images of the crystals that form upon cooling. Images taken at various temperatures for the neat Jet A fuel (3219) and the urea-treated fuel are shown in Figures 8 and 9, respectively. A cooling rate of 0.25 °C/min was employed.

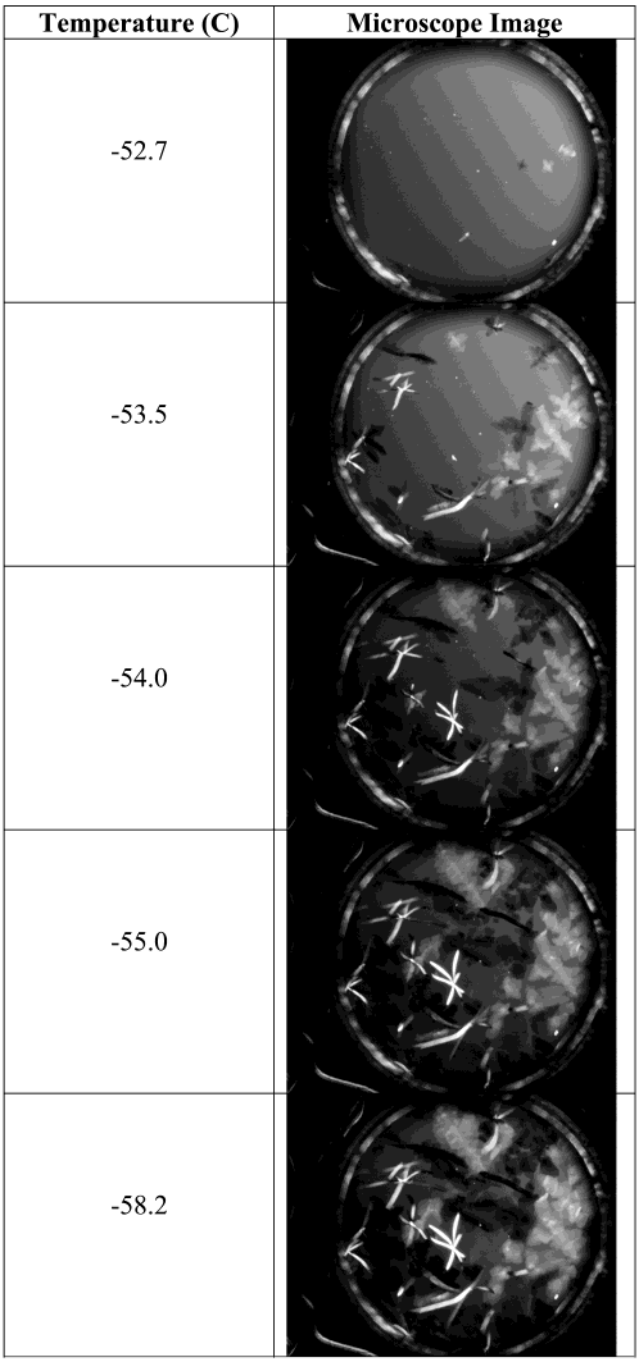

Figure 8. Cold-stage microscope images of the freezing of fuel 3219 at 0.25 °C/min. The circular aperture shown is 1.5 mm in diameter.

Figure 8 shows that at −52.7 °C a few small crystals are beginning to form, which compares well with the measured cloud point (−50.9 °C). As the temperature is lowered, further crystal growth is observed, as well as the formation of additional new crystals. Two primary types of crystals are observed in the neat fuel images: flat platelike crystals and dendritic crystals. Flat platelike crystals have been implicated in plugging the filters that are used in aircraft fuel systems.[14] Near the measured pour point (−56 °C) the field of view displays an intermingling mass of many crystals. Figure 9 shows that the early crystallization is delayed

(14) Lewtas, K.; Tack, R. D.; Beiny, D. H. M.; Mullin, J. W. In *Advances in Industrial Crystallization*; Garside, J., Davey, R. J., Jones, A. G., Eds.; Butterworth Heinemann: Oxford, 1991; pp 166−179.

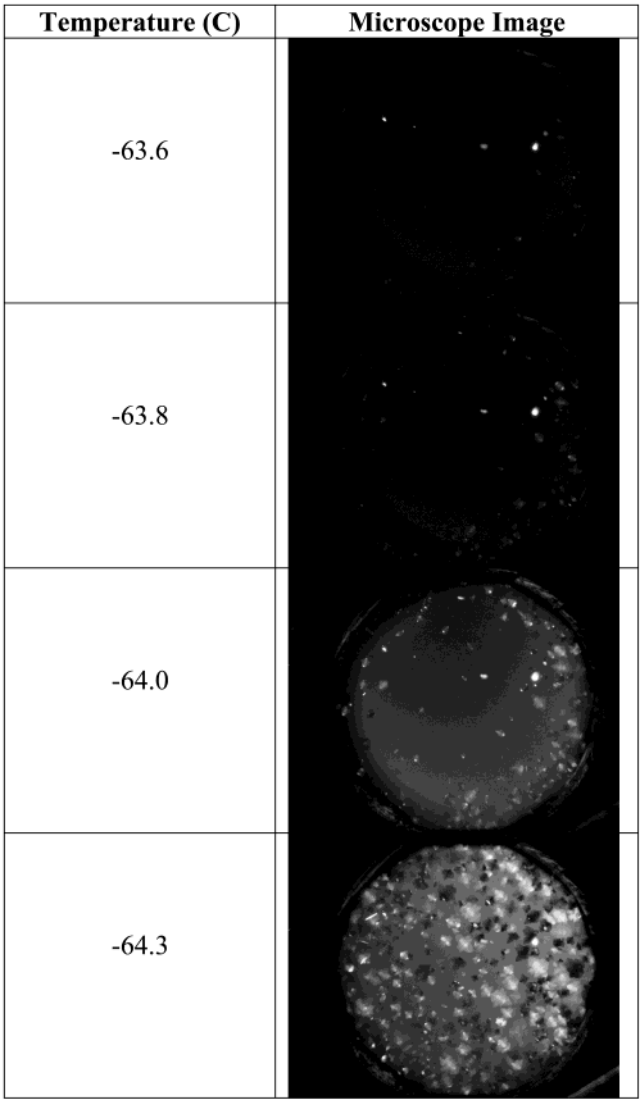

Figure 9. Cold-stage microscope images of the freezing of urea-treated fuel 3219 at 0.25 °C/min. The circular aperture shown is 1.5 mm in diameter. The fuel was treated with 25% urea, 1% methanol, for 4 h.

to −63.6 °C by the urea process. In addition, as the temperature is lowered the crystal habit is affected, with smaller crystals being produced. The dendritic crystals are no longer observed, and the flat platelike crystals are much smaller in size. This urea-treated fuel displays a cloud point of −62.3 °C and a pour point of −69 °C.

The cold-stage microscope images show that near the cloud point only a small number of very small crystals are observed, while near the pour point a tangle of a large number of crystals has formed. The urea treatment process significantly lowers the temperature at which the initial crystal formation is observed. It also changes the crystal habit, resulting in smaller crystals. Fortunately, both of these effects are desirable in a low-temperature fuel. The lower temperature of crystal formation will permit fuel system operation at reduced temperatures, while the smaller crystal size will reduce plugging of fuel system filter and close tolerance valves and passageways.

Practical Issues. The economic viability of the urea dewaxing process for the production of JPTS has not been studied in this paper; however, the significant improvement in low-temperature behavior observed shows that the benefits that can be obtained are substantial. The economic viability of the technique is limited by the low production of JPTS relative to other fuels, such as JP-8. In government fiscal year 2000, only 3.04 million gallons of JPTS were purchased in contrast to 2.7 billion gallons of JP-8 fuel.[15,16] On the other hand, the Air Force presently pays a premium price for JPTS (FY 2001, $3.25/gal) relative to that of JP-8 (FY 2001, $1.01/gal), due to the economy of scale of JP-8 production, as well as increased shipping and logistical costs for JPTS. Thus, a margin exists where the increased production costs of a urea treated fuel can be covered by increased fuel costs (above that of JP-8), while still allowing costs below that of JPTS.

Our laboratory urea treatment procedure did not include many of the procedures which would be included in a refinery process including: separation of the urea adduct from the fuel, decomposition of the adduct and regeneration of urea, and recovery of solvents and wax. These processes further complicate an analysis of the viability of the overall process for production of low-freezing jet fuel. The urea process would also need to be evaluated in comparison to the benefits of using cold flow improving additives, as in the present path of the JP-8+100LT program. In addition, we have not evaluated the implications of dissolved urea that cannot be removed from the fuel on other fuel properties, such as combustion.

Conclusions

We have studied the use of urea treatment for the production of jet fuel with improved low-temperature characteristics. This room temperature process is able to significantly improve the freeze, cloud, and pour points of jet fuels with relatively short treatment times. The addition of methanol to the treatment process significantly shortens the reaction time required. Gas chromatographic analyses of the normal alkanes species present in the fuel before and after treatment show that there is substantial removal of the largest normal alkane species. DSC and low-temperature microscopy measurements demonstrate that the treatment process lowers the temperature at which fuel crystallization begins. The microscopic studies also show that the crystal habit of the initial crystals which form upon cooling change substantially. Further studies need to be performed to evaluate the economic benefits of using the process to produce low-freezing fuel relative to the presently used refinery processes and the additive techniques being developed.

Acknowledgment. This work was supported by the U.S. Air Force, Warner Robins Air Logistic Command, U-2 Special Programs Office, Robins Air Force Base, Warner Robins, Georgia, and the U.S. Air Force Research Laboratory, Propulsion Directorate, Propulsion Sciences and Advanced Concepts Division, Wright-Patterson Air Force Base, Ohio, under Contract No. F33615-97-C-2719. We thank Dr. Matt DeWitt for reviewing the paper prior to submission and providing helpful comments.

EF020116B

(15) *Defense Energy Support Center Fact Book 2001*; Defense Energy Support Center, 2001.

(16) Simms, C. G. Thesis, Air Force Institue of Technology, 2001.

S. Combustion Particulates Mitigation Investigation Using a Well-Stirred Reactor

AIAA 2002-3723

Combustion Particulates Mitigation Investigation Using a Well-Stirred Reactor

S. D. Stouffer and R. C. Striebich
University of Dayton Research Institute
Dayton, OH

C. W. Frayne and J. Zelina
Air Force Research Laboratory
Wright-Patterson AFB, OH

38th Joint Propulsion Conference & Exhibit
7-10 July 2002
Indianapolis, Indiana

COMBUSTION PARTICULATES MITIGATION INVESTIGATION USING A WELL-STIRRED REACTOR

S. Stouffer*, R. C. Striebich
University of Dayton Research Institute
Dayton, OH

C. W. Frayne*, J. Zelina**
Air Force Research Laboratory
WPAFB, OH 45433

*Member AIAA **Senior Member AIAA

ABSTRACT

Combustion generated particulates can increase exhaust plume visibility and maintenance costs in gas turbine engines. Research is being conducted to determine particulate formation chemical mechanisms, understand precursors to particulate formation, and identify mitigation strategies. This paper describes a robust well-stirred reactor (WSR) combustion rig and facility that was constructed to study particulate formation. Preliminary experimental tests of particulate formation from premixed fuel-rich ($2.6>\phi>1.8$) ethylene/air mixtures have been completed. Multiple measurement techniques were used in the investigation including smoke measurement, particle counting, carbon burn-off and GC-MS analysis. Information gained from these investigations is used to provide details for combustion models of pollutant formation, kinetics, and particle formation and destruction. Particulate samples were collected from the plug flow region downstream of the WSR and it was found that the smoke number results for ethylene compared well with previous data from the literature. Lower particle counts and smoke numbers were observed as the reactor residence time was decreased suggesting that increased mixing or reduced time at elevated temperatures for soot formation was responsible for decrease in soot formation. The effect of using the oxygenated fuel additive, ethanol, as an additive to the ethylene was also examined and it was found that ethanol increased soot production compared to neat ethylene fuel.

NOMENCLATURE

EI	= emissions index (gm/kg fuel)
CPC	= condensation particle counter
GC-MS	= gas chromatograph- mass spectrometry
m_a	= air mass flow rate (kg/s)
m_f	= fuel mass flow rate (kg/s)
P	= pressure (kPa)
PAH	= polycyclic aromatic hydrocarbon
PFR	= plug flow reactor
T_a	= adiabatic flame temperature (K)
T_f	= reactor temperature (K)
T_o	= inlet temperature (K)
SN	= smoke number
V	= reactor volume (ml)
WSR	= well-stirred reactor

Symbols

ϕ	= equivalence ratio
ρ	= density (kg/m^3)
τ	= residence time

INTRODUCTION

Due to increased infrared exhaust plume visibility and maintenance costs associated with combustion generated particulates for gas turbine powered aircraft, several research groups are conducting experiments to understand particle formation and mitigation strategies. Fundamental studies are underway that use simplified combustion rigs to study the chemistry of particulate formation, investigate fuel additives to reduce particle formation, develop detailed models to predict soot formation, and identify mitigation strategies[1-5]. In addition, gas turbine engine manufacturers have developed empirical-type models to predict soot formation in their combustion chambers[6-8]. The ultimate goal of both of these efforts is to develop a detailed model to predict soot formation that can capture the chemistry and physics involved in the soot generation process.

One such facility used to investigate particulate formation is the Well-Stirred Reactor (WSR) facility.

Located at Wright-Patterson AFB, OH, the WSR was developed to perform fuel effect research for gas turbine combustor emissions and particulates, to investigate particulate formation mechanisms and identify fuel additives to mitigate particulate formation. A WSR provides a controlled research combustor configuration to study these effects. In an effort to develop a sooting model, sampling techniques, particulate measurement and fuel additization schemes were explored while using the WSR to burn pre-mixed gaseous ethylene/air and ethylene/ethanol/air mixtures. Modifications were made to develop a rugged, high temperature reactor that operates stably at high equivalence ratios ($1.8 < \phi < 2.6$), which allows measurement of particulates in a range of conditions from soot inception to heavy sooting. This program focuses on the development of an additive for JP-5 and JP-8 fuels that will reduce both the particulate mass emissions index EI(m) and particulate number density by 70%. Future collaborative efforts with NIST will involve developing a Polycyclic Aromatic Hydrocarbon (PAH) injection system and to test candidate PAH mitigation additives for liquid fuels.

In this paper, we describe the design of the WSR, experiments to calibrate the rig and to verify the temperatures in the reactor and stack (PFR), evaluation of gaseous combustion emissions (THC, O_2, NOx, CO, CO_2) within the reactor and characterization of particulate and soot samples as affected by the variation of residence time and inlet air temperatures. During the initial checkout of the facility, an exploratory study of the rich stability limits was conducted for the WSR with methane fuel.

A study of the effect of using ethanol as an ethylene additive to reduce particulate carbon formation was conducted while particulate samples were collected from the PFR, downstream of the WSR, on both paper and quartz filters. The samples acquired on the paper filters were analyzed using the SAE ARP1179[9] procedure to determine the smoke number based on reflected light from the samples. The quartz filters were analyzed using carbon burn-off and a GC-MS system.

As these preliminary sooting investigations were commencing, another reactor configuration was designed, using an Inconel jet ring. This was installed within a silicon carbide reactor, which is more resistant to thermal cracking than the previous zirconia-oxide design. Also, fibrous zirconia-oxide, used as ceramic stack insulation was found to shed particles and this was replaced with an Inconel stack. The previous WSR was built and operated to study lean blowout and emissions of CO, unburned hydrocarbons, and NO_X over a wide range of residence time and fuel-air ratios. The present work extends the previous research to cover a wider envelop of tests comprising the fuel-rich operation of gas turbine combustors at different residence times.[2-3]

In this work, we present preliminary experimental results of a WSR operating under fuel-rich conditions to investigate particulate and soot emissions.

EXPERIMENTAL APPARATUS

Test Facility

A facility schematic (Fig. 1) identifies components and instrumentation used for operation of the rig and analytical assessment of the WSR. The air system is capable of flowing 1680g/min main air, at temperatures up to 433°K; it is mixed with fuel entering the WSR through a jet ring injector inside the reactor. Air and gaseous fuel flow rates are measured and controlled using Brooks thermal mass flow controllers. Afterburner air, at 600 g/min, is available for combustion of excess fuel when operating at $\Phi > 1$. The gaseous fuel system is capable of flowing up to 50 g/min methane, or 70 g/min ethylene. The nitrogen supply can flow 580 g/min, its primary use is for diluting the reactants. Emissions analyzing equipment is available for on-line measurement of CO, CO_2, NO_x, O_2, and unburned hydrocarbons within the reactor. A circulating oil heater is used to heat emissions and particulates probes to 420°K. Thermocouples are located in the air line, WSR jet ring, inlet, reactor, housing and stack, and transducers are installed to indicate reactor pressure. Temperatures were measured in the toroidal and plug flow regions using 0.2 mm-diameter type-B thermocouples. Control of air and gaseous fuel flow, temperature, pressure and emissions indication is accomplished using National Instruments hardware and Labview software. The software also incorporates routines for performing exhaust gas emissions calculations of fuel-to-air ratios. The calculations were verified by comparison with measured gaseous fuel and air flows under steady state reactor conditions. A software programmed strip chart recorder facilitates assessment and analysis of the temperature and emissions measurements. For additive studies the liquid additive is metered using ISCO 500D syringe pumps, before flowing into the heated cross-stream of air.

An automated fail-safe retractable spark ignitor is used to initiate combustion within the reactor. A bellows seal is installed on the ignitor, sealing the housing holding the reactor chamber. This enables the reactor to maintain a positive pressure of up to 4.2 kPa above atmospheric pressure while running.

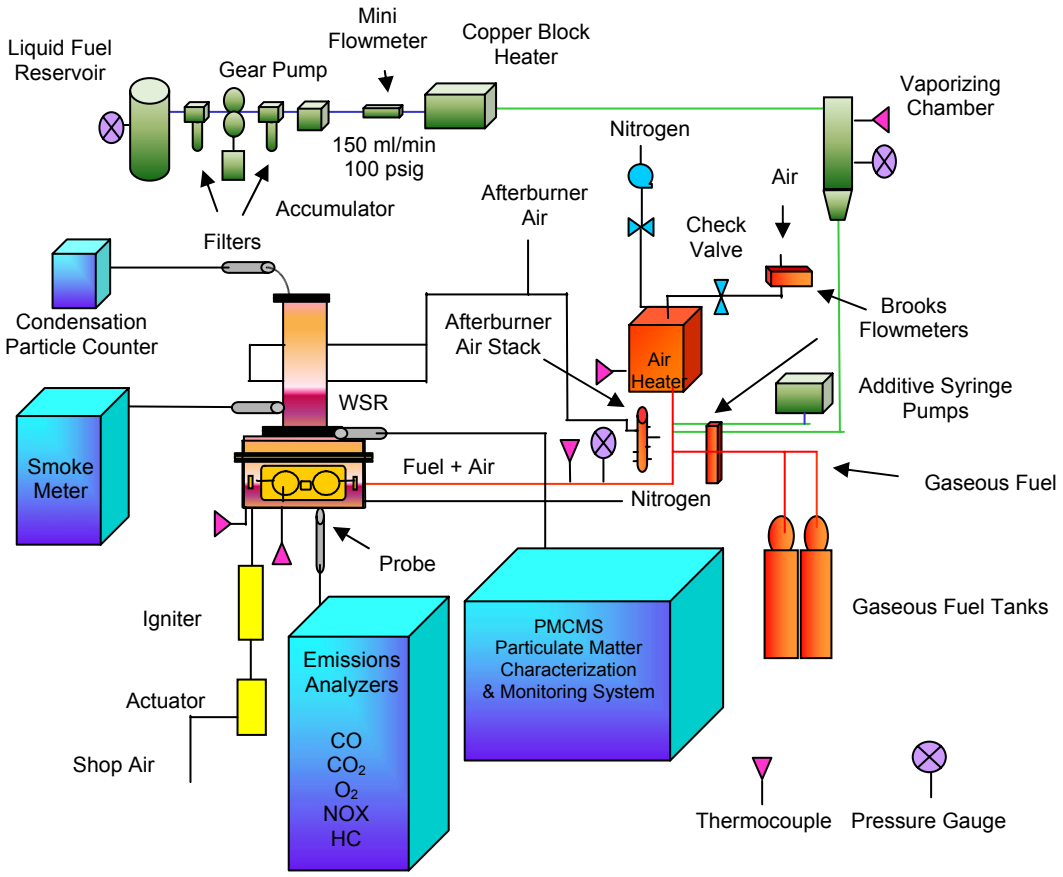

Figure 1: WSR Facility Schematic

Well-Stirred Reactor Design

A 250-ml toroidal WSR (Fig. 2), as designed by Nenniger et al.[10] and modified by Zelina[11], was used for initial experiments burning a premixed methane-air mixture. A reactor cast of zirconia oxide ceramic was used for tests operating near stoichiometric because this ceramic performed better at higher temperatures due to its higher melting point. The WSR was placed inside an insulated housing that was assembled to a PFR stack containing fibrous zirconia-oxide ceramic insulation (Fig. 3). Initial particulate measurement tests revealed that the stack material was shedding particles, and it was replaced with an Inconel stack.

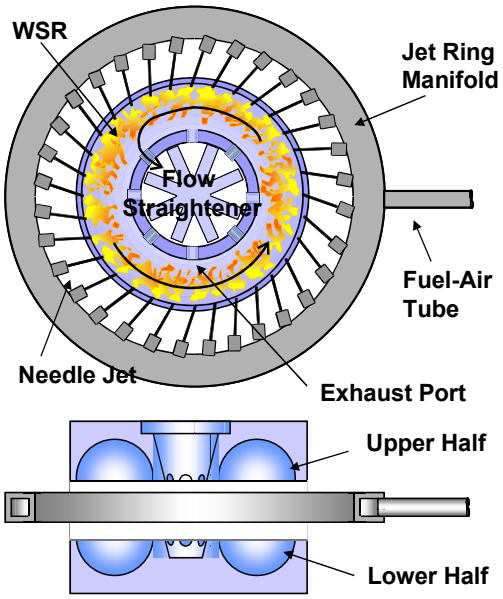

Figure 2: Schematic of WSR Design.

An improved WSR design, using an Inconel jet ring was installed within a silicon carbide reactor with spring-loaded reactor sections. This configuration, using the modified jet ring with 48 fuel/air jets (Fig. 4), and silicon carbide reactor (Fig. 5), which is more resistant to thermal cracking than zirconia-oxide was successfully tested, then used for the majority of the sooting experiments. The improved design provides a separate cooling flow of nitrogen on the outside of the jet ring to lower the temperature to avoid autoignition in the jet ring. The new design allows the fast detection of thermal-mechanical cracking problems and rapid replacement and re-assembly of ceramic reactor parts.

Figure 3: WSR Inside Housing Section, Attached to PFR Stack, Burning Premixed Methane-Air.

Figure 4: Inconel Jet Ring Containing 48 Fuel-Air Jets.

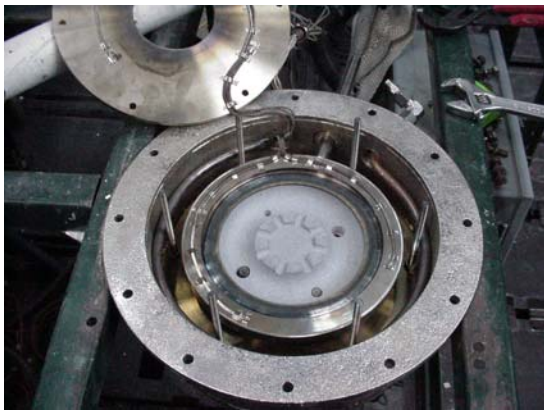

Figure 5: Jet Ring Atop Bottom Half of Silicon Carbide Reactor, Mounted in Housing.

Experimental Sampling Techniques

Soot samples were collected from the plug flow region 25 cm downstream of the WSR on paper or quartz filters by drawing the exhaust gas collected in the probe through the filters. The gas sample was first pulled through a 25 cm-long oil-cooled probe with an inside diameter of 0.47 cm. The probe was cooled to 150°C by circulating oil through the outer jacket. The gas then passed through an electrically heated (constant surface temperature of 150°C) 2-meter long sample line before passing into a Roseco engine smoke emissions sampler.

The volume of the sample gas collected for each test was 7.08 liters. Each sample required 30-60 seconds to collect. The samples acquired on the paper filters (Whatman #4) were analyzed using the SAE ARP1179 procedure to determine the smoke number based on reflected light from the samples:

$$SN = 100\left(1 - \frac{R_s}{R_W}\right)$$

where: R_s = Reflectance of the stained filter
R_w = Reflectance of the unstained filter

The samples acquired on the quartz filters (Whatman type-QMA) were analyzed by measuring the amount of carbon burned off in a LECO carbon analyzer. The total carbon analyzer measures the carbon mass deposited on the filter by measuring the CO_2 produced while increasing the temperature of the filter in an oven in the presence of excess oxygen. An advantage of the carbon analyzer is that any inorganic deposits on the filter, caused by erosion of the reactor materials will be ignored in the analysis.

In addition to the carbon burn-off analysis the quartz filter samples were also studied using GC-MS analysis to determine the PAH content. The PAH's were thermally desorbed from the sample before passing into the GC and a targeted analysis for 12 separate species listed in Table 1 was conducted for the filters.

Table 1. PAH Species Considered in the GC-MS Analysis

Acenaphthylene
Acenaphthene
Fluorene
Anthracene
Fluoranthene
Pyrene
Benz [a] anthracene
Benzo [k] fluoranthene
Benzo [a] pyrene
Indeno [1,2,3-cd] pyrene
Dibenz [a,h] anthracene
Benzo [ghi] perylene

During the experiments, it was found that soot accumulating on the reactor thermocouple lowered the apparent combustion temperature by increasing the thermal resistance between the thermocouple and the flame. Localized air injection, upon the thermocouple, was used to eliminate the soot accumulation and to obtain accurate temperature measurements in the sooty reactor environment.

Particulate and Emissions Measurement Instrumentation

The particulate instrumentation system is composed of a TSI 3022 condensation particle counter (CPC) and a sampling system using a vacuum pump to control sample flow through a 12g/min flow meter and transmitter. This combination of Brooks flow meters is used to set accurate dilution air flows to the particulate sampling probe. The CPC and sampling system are configured to adapt to the PMCMS (Particulate-Matter Chemical Characterization and Monitoring System) that can be used to evaluate particulate species and PAH. The particle number density was determined using the CPC sampling from the stack of the WSR. A short stack configuration was used to minimize the PFR region for obtaining particulate, smoke and soot measurements close to the reactor while the exhaust was still unmixed and hot (Fig. 6).

The emissions system consists of a 150°C oil cooled emissions probe and a 150°C heated sampling line that is 6.1 m. long. The hot sample enters an Alpha Laval chiller, which provides the main sampling pump, condenses water vapor from the gas sample and sets the sample flow to the emissions analyzers. This dry sample is routed to a VIG model FID 20 total hydrocarbon analyzer and a series of Horiba analyzers composed of a model MPA-510 oxygen analyzer, model VIA-510 CO, model VIA-510 CO_2 and model CLA-510 SS NO_X. The analyzers are calibrated before each test using 2% certified standard gases and often spanned for verification of ~3% accuracy during the tests, using several calibration gas mixtures to check drift and maintain linearity.

Figure 6: WSR Short Stack Configuration.

TEST CONDITIONS

The air flow for the experiments ranged from 180 to 390 g/min with an inlet temperature that ranged from 290 K to 420 K. The fuel/air equivalence ratio,ϕ, ranged from 1.7-1.95 for methane/air and 1.8 to 2.6 in the ethylene/air experiments. The gage pressure of the reactor increased with increasing flow rate and temperature and was less than 4.2 kPa above the ambient pressure for all of the experiments. The average residence time in the reactor, τ, which was calculated using: $\tau=\rho V/(m_a+m_f)$, ranged between 5.0 and 12 ms for the experiment.

EXPERIMENTAL RESULTS

Initial tests were conducted with methane/air and ethylene/air mixtures in the zirconia reactor with an air flow rate of 240 g/min, which corresponds to a reactor residence time of 9.6 ms. The smoke number results for these tests are shown in Figure 7. The soot inception limit, defined as the equivalence ratio at which the smoke number begins to increase as the equivalence ratio increases, was determined to be 1.7 for methane/air. The smoke number for methane slowly increased linearly as ϕ was increased between the inception limit and the rich blow-off limit of ϕ=1.95. The smoke number for ethylene/air combustion increased non-linearly with a rapid increase between ϕ=2, and ϕ=2.2, and a soot inception point of ϕ=1.9. The results for ethylene-air also compare well with previous data from Takahashi et al.[12] which was acquired in a similar WSR under approximately the same operating conditions.

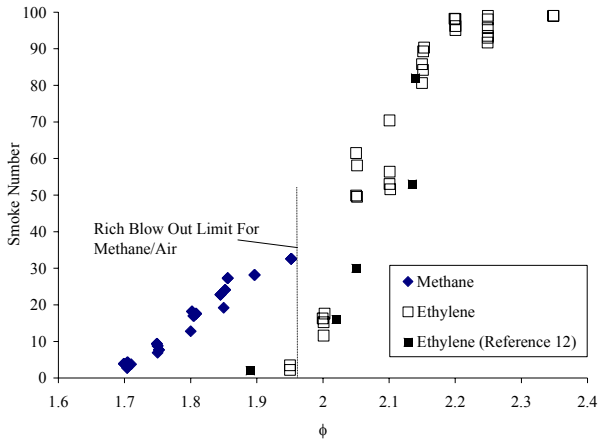

Figure 7: Smoke Number vs. Equivalence Ratio for Methane-Air and Ethylene-Air Mixtures.

The effective equivalence ratio, Ψ, which is defined as the equivalence ratio calculated assuming that the only combustion products are H_2O and CO, was calculated at the soot inception point for the two fuels. Takahashi et al.[12] previously examined the soot threshold for ethylene, propane, and toluene, at similar residence times to the present study and found that the effective equivalence ratio, Ψ, at the soot inception limit was approximately 1.25 for all three fuels. The effective equivalence ratio at the soot inception limit for methane/air, and ethylene/air was found to be 1.275 and 1.26 respectively, which is in agreement with the results from Takahashi et al.[12].

The effect of using ethanol as an additive was examined by adding ethanol in mass fractions of 15 and 30 % of the total fuel mass to the ethylene. The smoke number results are plotted in Figure 8 as a function of the total equivalence ratio based on the combined fuel. The mixed fuel corresponds to mass fractions of ethanol fuel with 5.3% and 10.5% oxygen content by mass. The ethanol-ethylene mixtures produced more soot than the neat ethylene-air mixtures. It is thought that a major reason for the increase in soot production with oxygenated additive is because the reactor temperature is decreased by the lower reaction enthalpy of the ethanol.

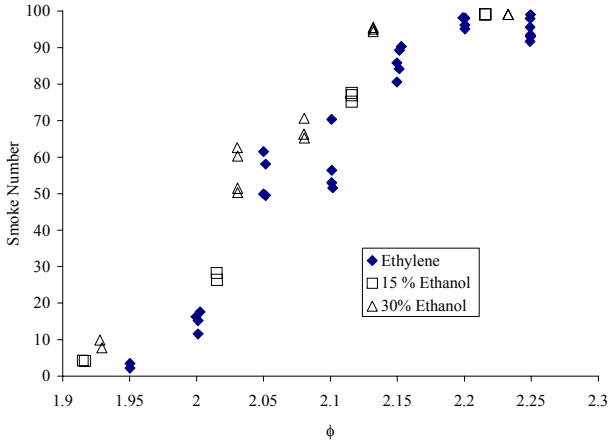

Figure 8: Smoke Number vs. Equivalence Ratio for Ethylene-Air and Ethylene-Ethanol-Air Mixtures.

A limited number of quartz filter samples were analyzed using a targeted GC-MS analysis to measure the concentration of 12 separate PAH species. The results of the total PAH concentration measured on the filter are shown in Figure 9 plotted against the equivalence ratio. The total concentration of PAH increased as the equivalence ratio increased. Of the PAH species considered, pyrene was generally the species present in the highest mass concentration.

Particulate samples were obtained on Whatman Type-QMA Quartz filters for the determination of Carbon mass. During early experiments the filters were weighed before and after sample collection using a balance with a resolution of +/-0.1 g. The same filters were then analyzed using the carbon burn-off technique. As shown in Figure 10 the filter mass gain

compared well with the carbon mass measured during burn-off.

Figure 11 shows the total carbon burn-off results for the ethylene-air cases in the zirconia-oxide reactor an air flow rate of 240 g/min (residence time ≈9.6 ms). The carbon burn-off mass increased by a factor of over 1000 as the equivalence ratio increased from 1.95 to 2.35. The most rapid increase in carbon mass occurred between ϕ =1.95 and 2.15, with a slower increase in the carbon deposition with increasing ϕ at higher equivalence ratios.

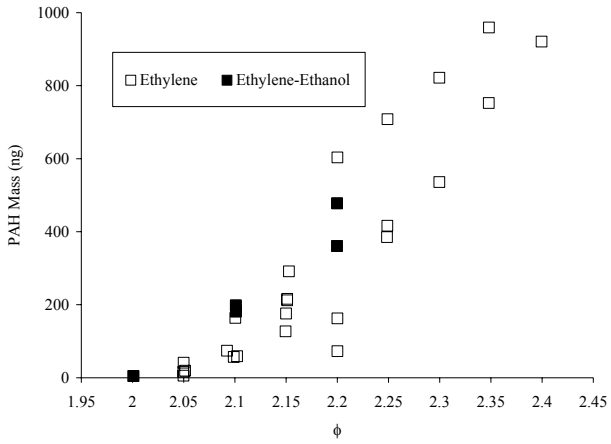

Figure 9: Total PAH Content Measured GC-MS.

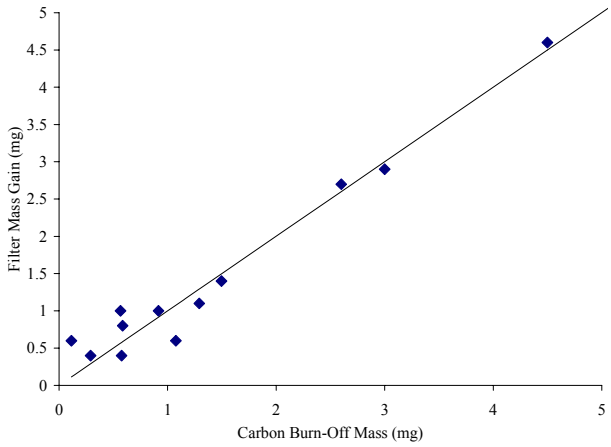

Figure 10: Comparison of Filter Mass Gain vs. Carbon Burn-Off

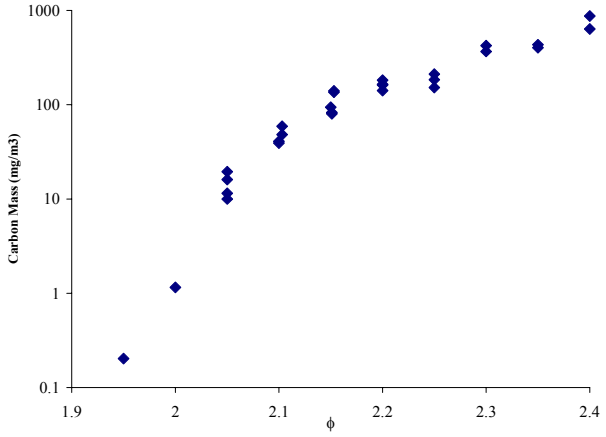

Figure 11: The Carbon Burn-off Mass for Ethylene-Air Combustion (Residence Time ≈ 10 ms).

In addition to determining the total carbon present on the filter, the carbon burn-off analysis can provide qualitative information on chemical content of the filter sample. During the analysis the oven temperature is steadily increased while the relative carbon count is recorded along with the temperature. The total integrated area under the carbon count curve is equal to the total carbon mass deposited on the filter while the shape of the carbon burn-off curve is indicative of the type of carbon compounds present in the filter.

Figure 12 shows the relative carbon count vs. temperature of three filters along with corresponding photographs of the filters before the carbon analysis was conducted. The equivalence ratio of the reactor was 1.9, 2.0, and 2.1 for samples A, B, and C, respectively. As the equivalence ratio increased, the total carbon mass deposited on the filter, indicated by the integrated area under the carbon count-temperature curve increased dramatically between samples A and C. Note that the vertical scale for the three samples increases as ϕ increases. As the equivalence ratio was increased the distribution of the carbon burn-off vs. temperature can be seen to shift to increasing temperatures. The low temperature region of the carbon vs. temperature curve is due to the presence of volatile PAH while the higher temperature region of the curve is indicative of carbonaceous soot. The three samples show the progression of soot formation with increasing ϕ from incipient soot formation at ϕ=1.9, to increasing content of less volatile PAH's at

ϕ= 2.0, to the formation of carbonaceous soot for the ϕ= 2.1 case.

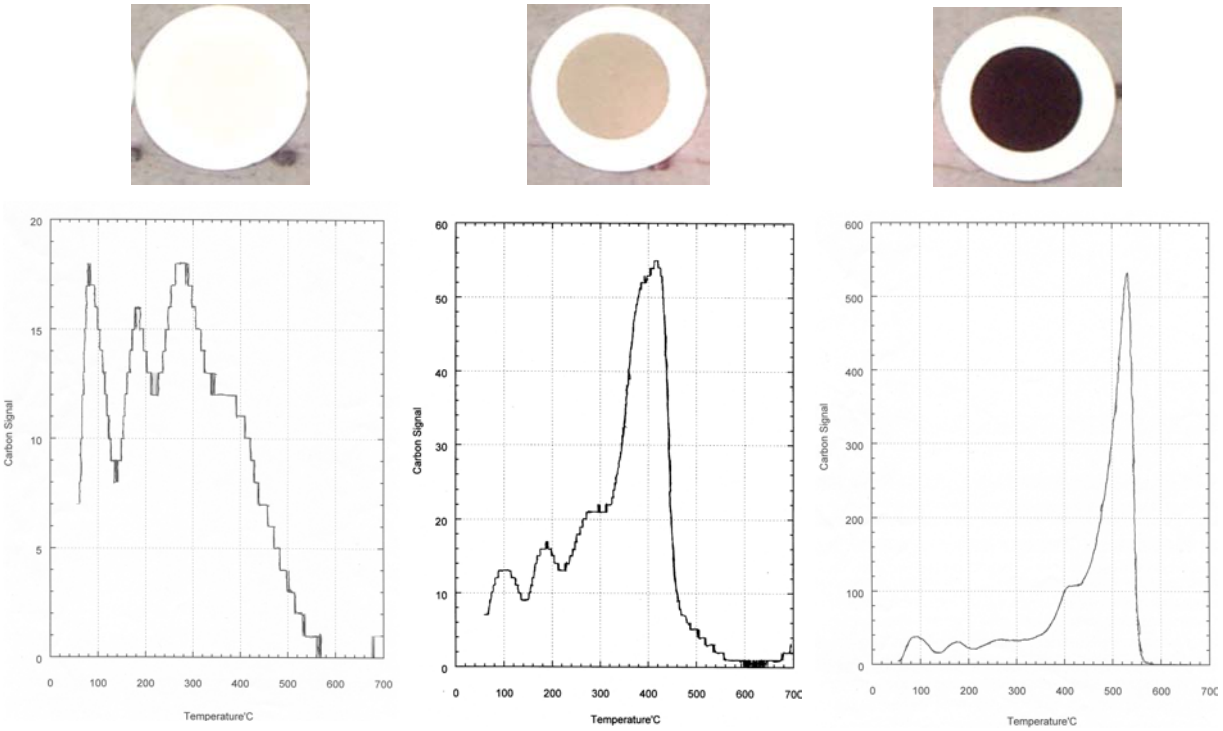

Figure 12: Carbon Burn-off vs. Temperature and Photographs of the Corresponding Filters before Analysis. Residence time =11 ms.

As shown in the photographs in Figure 12 the filter samples became darker as ϕ increased corresponding to the increasing carbon mass on the filters. In addition, the color of the filter samples was also observed to change as ϕ increased, from light crème for ϕ = 1.9, to tan-colored at ϕ = 2.0, and black at ϕ = 2.1. Therefore, the filter color and shade is in qualitative agreement with the carbon burn-off vs. temperature graphs.

Particle counting tests were conducted in the silicon carbide reactor equipped with either of two Inconel stacks in an effort to minimize false counts due to reactor or stack erosion. The height of the sampling point was 15.8 cm above the reactor for the short stack configuration and 69.2 cm above the reactor for the tall stack configuration.

The reactor was initially operated at lean equivalence ratios with higher temperatures than those expected in the fuel rich tests to determine if background particles were being generated from reactor erosion. It was found that the particle number produced under lean and hot conditions were two orders of magnitude lower than the background count of room air. Therefore, the particles measured under rich conditions were all assumed to be combustion-generated.

Figure 13 shows the total particle number density measured by a condensation particle counter (CPC) for ethylene-air mixtures vs. the equivalence ratio. The upper limit of the particle count was limited to $5x10^8$ particles/cc by the upper saturation limit of the CPC ($1x10^7$ particles/cc) and the maximum dilution ratio (98% dilution) used in the experiments. The results show that the total particulate number density increased exponentially at both flow rates and both stack locations as the equivalence ratio increased. For cases with the lowest flow rate (210 g/min) the particulate number density increased as the stack length increased, while there was no significant increase in the particulate number density for the high flow case (330 g/min) along the stack length. The particle number density measured at the top of the tall stack

configuration was found to be over two orders of magnitude lower for the higher flow rate case than for the low flow rate case. It is thought that the larger number of particles formed in the low flow rate case is due to the lower turbulent mixing and the longer residence time in which particles can be formed.

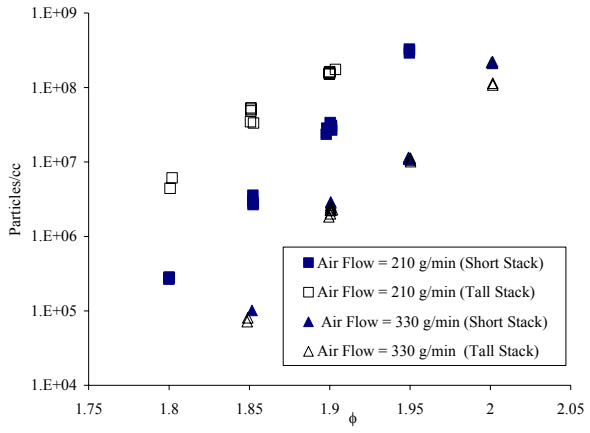

Figure 13: The Particle Number Density vs. Equivalence Ratio for Ethylene-Air Mixtures.

Preliminary measurements of the particle size distribution, made by placing a TSI 3080 electrostatic classifier before the CNC, showed that the median particle size was smaller than the 15 nm for both flow rates. Further determination of the particle size distribution will be the subject of future research.

The effect of residence time and temperature on the soot production at a single equivalence ratio was determined by measuring the smoke number for a series of tests at different inlet temperatures and flow rates at the same ϕ (ϕ=2). The samples were acquired from the side of the tall stack at a height of 15.8 cm above the reactor. The results in Figure 14 show that the smoke number drops with an increase in the inlet temperature and a decrease in the residence time. It is thought that the decrease in particulate mass with shorter residence times is due a combination of the increased turbulent mixing associated with the higher mass flows and the decreased time at elevated temperatures required for the formation of soot.

Figure 15 shows the smoke number vs. ϕ for the silicon carbide reactor at a fixed air flow rate (330 g/min) over a large range of equivalence ratios. Two sets of data corresponding to two different ring cooling nitrogen flow rates are plotted. Recall that the ring cooling is necessary in the new design to reduce the temperature of the gas in the ring to a level low enough to avoid auto ignition in the jet ring and the subsequent destruction of the ring. The cooling of the ring has the secondary effect that the outside of the reactor is also cooled.

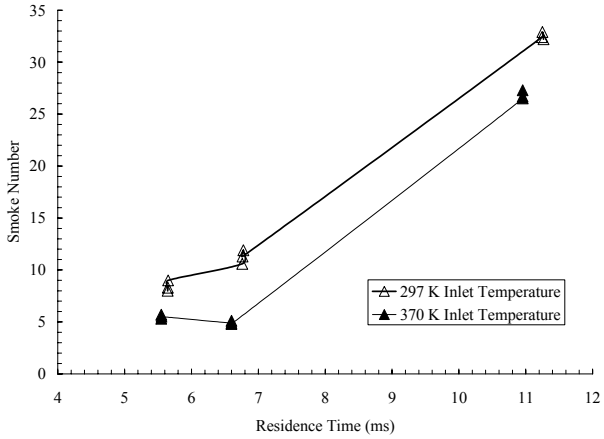

Figure 14: The Effect of Residence Time and Temperature on the Smoke Number (ϕ=2).

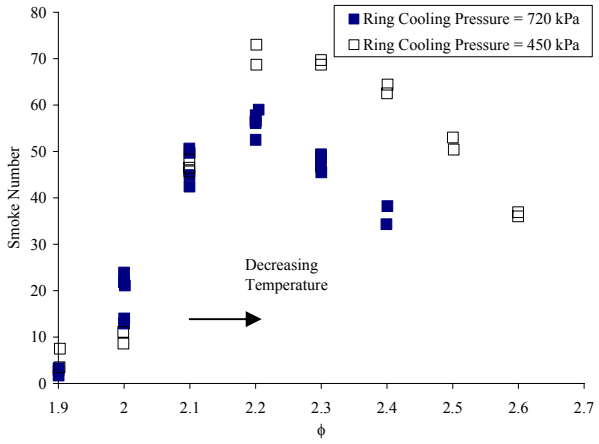

Figure 15: Smoke Number vs. Equivalence Ratio for Ethylene-air (Air Flow = 330 g/min).

Rather than continuously increasing as ϕ increased, the smoke number initially increases between ϕ = 1.9 and 2.3 and starts to decrease as ϕ is increased further. Note that the soot produced is higher for the case which has the lowest cooling of the injector ring. Although there is more un-reacted fuel available for the formation of soot at the higher equivalence ratios, it is thought that the soot produced drops because of the decreased temperatures, and thus slower chemical reaction times. This is consistent with the result that the soot level is highest for the cases with the least cooling for equivalence ratios above 2.3.

The gaseous emission data measured at the same location in the stack where the particulate is gathered is shown in Figure 16. The oxygen consumption and CO production is highest for the case with the lowest cooling of the jet ring.

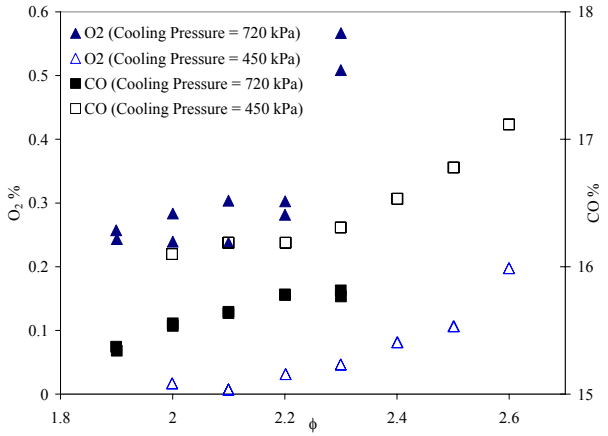

Figure 16: Oxygen Consumption and CO Production for Ethylene-Air (Air flow = 330 g/min).

The same smoke number data from Figure 15 was re-plotted vs. the reactor temperature and is plotted in Figure 17. The peak sooting was observed to occur between 1560°K and 1620°K for both cooling levels. The results imply that at low equivalence ratios (high temperatures) the effects that lower the reactor temperature (such as lower inlet temperature or lower energy additives) tend to increase the soot levels, while the opposite may be true at higher equivalence ratios. These results show similar trends as found in recent experiments at elevated pressure conditions burning a variety of hydrocarbon-air mixtures[13].

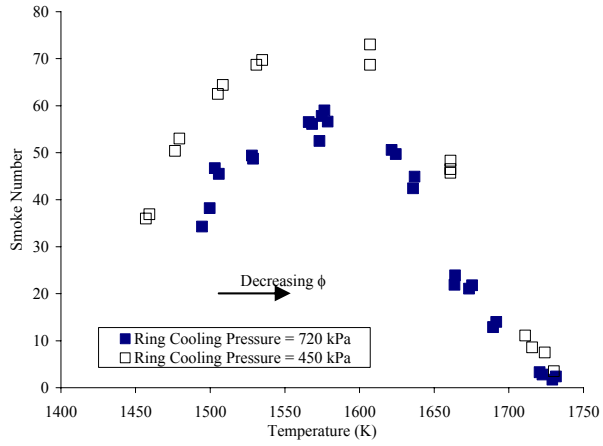

Figure 17: Smoke number vs. Temperature for Ethylene-Air (Air flow = 330 g/min).

SUMMARY AND CONCLUSIONS

A robust, multi-use WSR rig and facility was constructed to study particulate formation in hydrocarbon-air combustion systems. Preliminary experimental results from tests with the WSR operating on fuel-rich mixtures of ethylene-air, methane-air, and ethylene-ethanol fuel mixtures to investigate particulate emissions were completed. Several measurement techniques were investigated, including on-line smoke measurement, carbon burn-off, CNC particle counter, and off-line GC-MS analysis of PAH. It was found that:

1. Soot inception point in the WSR tests agreed well with historical values, with this limit occurring at effective equivalence ratios of 1.25.

2. Ethanol addition increased soot production compared to neat ethylene-air mixtures.

3. High concentrations of PAH's were found which increased as ϕ increased in the reactor. Pyrene was found in the highest concentrations for the conditions tested.

4. Excellent agreement in filter weight measurements and carbon burn-off techniques suggest the validity of using burn-off to determine amount of carbon and give qualitative indications of the types of carbon containing species.

5. Lower particle counts and lower smoke numbers were found at lower reactor residence time, suggesting that mixing or lack of time at temperature is responsible for this trend.

6. A maximum soot limit is reached at ϕ ~ 2.2 or T = 1600 K, with trends similar to historic data. The soot production decrease at higher equivalence ratios is due to inadequate temperature for hydrocarbon-soot reactions, as indicated by the decreased O_2 consumption.

FUTURE RESEARCH PLANS

The present results indicate that because the injector ring cooling has the undesirable result of also decreasing the reactor temperature, it is planned to reduce the cooling required by using thermal barrier coating on inside surfaces of the jet ring to reduce the cooling requirements.

It is planned to use the PMCMS (Particulate-Matter Chemical Characterization and Monitoring System) to evaluate the chemical constituents of the soot as a function of the soot size.

The capability to vaporize liquid fuels will soon be available, so that vaporized liquid fuels such as heptane and JP8 can be examined.

ACKNOWLEGEMENTS

The authors would like to thank Dr. Mel Roquemore for his enlightening discussions on combustion and soot formation and support of this research. The authors are also grateful for the contributions of the following personnel: Mr. Mike Arstingstall for his assistance with rig set-up, fabrication, assembly and test of the WSR. Mr. Edward Strader for design and assembly of the fuel/air controls system. Mr. David Brooks and Dr. Matt Dewitt for the LECO analysis. Mr. Tom McCray and Ron Britton for their support on the instrumentation and data acquisition, and Amy Lynch for her help with the filter samples. The first two authors gratefully acknowledge the support of the Air Force through contract F33615-97-C-2719.

REFERENCES

1. Ballal D. R., and Harrison, W. E., "A Time Scale Approach to Understanding Jet Fuel Combustion and Particulate Formation and Growth," AIAA-2001-1085.

2. Blevins, L. G., Mulholland, G. W., Benner, B. A., and Steel, E. B., "Morphology and Chemistry of Aircraft Engine Soot," Presented at the 2002 Spring Technical Meeting, Western States Section, The Combustion Institute, San Diego, CA March 25-26, 2002.

3. Appel, J., Bockhorn, H., and Frenlach, M., "Kinetic Modeling of Soot Formation with Detailed Chemistry and Physics: Laminar Premixed Flames of C2 Hydrocarbons," Combustion and Flame 121:122-136, 2000.

4. Violi, A., D'Anna, A., D'Alessio, A., "Modeling of Particulate Formation in Combustion and Pyrolisis," Chemical Engineering Science 54: 3433-3442, 1999.

5. Shurupov, S. V., "Particulate Carbon Formation From Hydrocarbon Mixtures," Experimental Thermal and Fluid Science 21: 26-32, 2000.

6. Popovitchea, O. B., Persiantseva, N.,M., Trukhin, M. E., Shonija, N. K., Buriko, Y. Y., Starik, A. M., Demirdjian, B., and Suzanne, J., "Experimental Characterization of Aircraft Combustor Soot: Microstructure, Surface Area, Porosity, and Water Adsorption," Phys. Chem. Chem. Phys., 2: 4421-4426, 2000.

7. Brocklehurst, H. T., Pridden, C. H., Moss, J. B., "Soot Predictions Within an Aero Gas Turbine Combustion Chamber," ASME 97-GT-148.

8. Tolpadi, A. K., Danis, A. M., Mongia, H. C., and Lindstedt R. P., "Soot Modeling in Gas Turbine Combustors," ASME 97-GT-149.

9. Society of Automotive Engineers (SAE), 1997, Aerospace Recommended Practice, "Aircraft Gas Turbine Engine Exhaust Smoke Measurement," *ARP 1179 Rev. C.*

10. Nenniger, J. E., Kridiotis, A., Chomiak, J., Longwell, J. P., and Sarofim, A. F., 1984, "Characterization of a Toroidal Well Stirred Reactor," *Twentieth Symposium (International) on Combustion,* The Combustion Institute, pp. 473-479.

11. Zelina, J., "Combustion Studies in a Well-Stirred Reactor," Ph.D. Thesis, *University of Dayton, Dayton, OH 1995*.

12. Takahashi, F., Blust, J.W., Zelina, J., Striebich, R., and Frayne, C. W., "Soot Threshold Measurements Using a Well-Stirred Reactor", Eastern States Section Meeting, The Combustion Institute, Oct 16-18, 1995.

13. Bauerle, S., Karasevich, Y., Slavov, S., Tanke, D., Tappe, M., Thienel, T., and Wagner, H. G., "Soot Formation at Elevated Pressures and Carbon Concentrations in Hydrocarbon Pyrolysis," Twenty-Fifth Symposium (International) on Combustion, The Combustion Institute, pp. 627-634, 1994.

T. Studies of Jet Fuel Freezing by Differential Scanning Calorimetry and Cold-Stage Microscopy

N. Widmor

J. S. Ervin

S. Zabarnick

M. Vangness

Mechanical Engineering Department,
University of Dayton,
300 College Park,
Dayton, OH 45469-0210

Studies of Jet Fuel Freezing by Differential Scanning Calorimetry and Cold-Stage Microscopy

Aircraft which fly at high altitude or encounter extremely cold environments have the potential for fuel freezing and, consequently, catastrophic failure of the fuel system. Thus, it is important to study the freezing of hydrocarbon jet fuels. In the current work, a differential scanning calorimeter is used to study thermal characteristics and phase transitions of freezing jet fuel. In addition, a cold-stage microscope is used to record images of the resulting crystalline microstructure. A kinetic representation for the freezing of jet fuel is presented. Kinetic mechanisms that describe the liquid-to-solid phase transformation in fuels are necessary for the development of computational fluid dynamics models that can be used by aircraft designers. [DOI: 10.1115/1.1492836]

Introduction

Operation of aircraft at high altitude for long periods subjects jet fuel to low temperatures. These conditions increase the fuel viscosity and, thus, limit the ability of the fuel to flow. Moreover, prolonged exposure to low temperatures can cause the fuel to solidify. The U.S. Air Force uses a specialty fuel, JPTS, which not only has a low freeze-point temperature, but also has excellent thermal-oxidative stability properties. Unfortunately, JPTS has logistical disadvantages and is more costly than JP-8, the primary jet fuel of the U.S. Air Force ([1]). The thermal-oxidative stability characteristics of JP-8 have been addressed by the JP-8 + 100 additive package. However, the low-temperature properties of JP-8 have gone unstudied until recently ([1]). In addition, commercial aircraft makers and commercial airlines desire to avoid fuel freezing under severe environmental conditions. Thus, there is both military and commercial interest in low-temperature jet fuel research.

With jet fuel at low temperatures, paraffin crystallization can cause line or filter blockage. An economical alternative to the use of specialty fuels is the employment of relatively inexpensive fuel additives. Additives which enhance the low-temperature behavior of jet fuels have not been used previously in aircraft. Thus, there is a need to increase our fundamental understanding of how newly developed additives influence the freezing of jet fuel.

There have been numerous low-temperature studies ([2–4]) of diesel fuels, crude oils, and lubricating oils which have used differential scanning calorimetry (DSC) alone or in combination with microscopy. In contrast, there have been relatively few such studies of the freezing of jet fuel. Moreover, it is believed that the present work is one of the first investigations ([5]) to examine the freezing of jet fuel using a DSC in combination with a cold-stage microscope. The DSC measures the heat flow from (to) a material as it is cooled (heated) and can indicate phase transition temperatures and determine thermodynamic properties such as specific heat and heat of fusion. Such properties are important for numerical simulation of the phase-change dynamics. The cold-stage microscope cools the fuel and simultaneously provides images of the fuel microstructure that assist the interpretation of DSC measurements.

The understanding of the freezing of jet fuels is complicated by the fact that individual jet fuel samples possess a range of freezing characteristics that results from the varying source petroleum and refinery processing. In addition, jet fuels consist not of a single compound, but are a complex hydrocarbon mixture whose behavior can be further complicated by the presence of additives. The effects of changing concentrations of species that continuously precipitate from solution during the freezing process makes the phase-change process more difficult to understand. In addition, the growth of precipitating structures in hydrocarbon fuels depends strongly on the cooling rate. The DSC has been used in previous research ([6]) of the freezing of hydrocarbon blends to indicate the relative degree of freezing with respect to temperature and cooling rate. A semi-empirical kinetic model for nonisothermal crystallization of binary, isomorphous mixtures was developed, and it was believed that this model could be extended to multicomponent mixtures. Similar techniques involving the DSC are used here for jet fuel. In the current work, the use of a semi-empirical kinetic representation for the freezing of jet fuel is considered. Kinetic mechanisms are necessary for the development of computational fluid dynamics models that can be used in aircraft design. Additives alter the behavior of fuels, and the DSC is also used to analyze the effects of additives on jet fuel freezing. The combination of the DSC and microscope not only increase the understanding of hydrocarbon freezing processes but also assist the screening of low-temperature additives.

Experimental

For the differential scanning calorimetry (DSC) studies (TA Instruments, DSC 2920) performed here, open aluminum pans were used for both the sample and reference. The DSC measures the temperature difference between the sample and reference pans and reports the heat flow from the sample. A syringe is used to fill the sample pan (20 μl), and the mass is recorded. A liquid nitrogen cooling accessory (LNCA) cools the sample to a prescribed temperature and allows it to equilibrate above temperatures expected for fuel freezing. The sample is then further cooled at a prescribed rate over a given temperature range. (The same process can be conducted for melting.) At the relatively low temperatures of this study, the maximum cooling rate of the DSC is limited to 5.0 K/min. The reproducibility of the temperature measurement of the DSC is within 0.2 K.

A cold-stage microscope system is used to obtain crystal growth images during the freezing process. Here, the microscope (Olympus BX50) incorporates phase contrast and cross-polarization optics. A 10X objective lens is used together with a digital camera (Sony DKS). The sample (20 μL) is placed on a microscope slide with an elevated cover slip, and the slide resides

Contributed by the International Gas Turbine Institute (IGTI) of THE AMERICAN SOCIETY OF MECHANICAL ENGINEERS for publication in the ASME JOURNAL OF ENGINEERING FOR GAS TURBINES AND POWER. Paper presented at the International Gas Turbine and Aeroengine Congress and Exhibition, New Orleans, LA, June 4–7, 2001; Paper 2001-GT-378. Manuscript received by IGTI, Dec. 2000, final revision, Mar. 2001. Associate Editor: R. Natole.

Table 1 Freeze point, cloud point, and pour point data

Fuel	Freeze Point Temperature (K)	Cloud Point Temperature (K)	Pour Point Temperature (K)
F2827	229.8	225.2	220.2
F3219	226.9	222.3	217.2
F3775	218.7	215.9	212.2

on the cold stage (Linkam) that cools the fuel. Using liquid nitrogen as the coolant, the sample is cooled at the same rate as the DSC while images of the fuel are recorded. Two Jet A fuel samples (F2827 and F3219) and one JPTS fuel sample (F3775) are used in these experiments.

Cloud point, pour point, and freeze point temperatures were measured using a Phase Technology Series 70V Petroleum Analyzer (using ASTM D5773-95, D5949-96, and DD5972-96, respectively). The pour point measurements were obtained at 1 K intervals, and appear in Table 1. It is important to note that the ASTM freeze point temperature is the measured temperature at which the last solid crystals vanish during *heating*. Thus, the freeze point temperature is actually a *melting* temperature.

Kinetics of Fuel Crystallization. Fuel freezing in aircraft fuel systems is generally a nonisothermal process. Moreover, the cooling rate is believed to strongly influence crystal growth and the resulting microstructure of the precipitating phase. Hammami and Mehrotra [6] performed studies of nonisothermal crystallization involving binary mixtures of even and odd-numbered normal-alkanes. In their analysis, they combined Eq. (1) from the theory of Ozawa [7]

$$x_r = \frac{x(T)}{x_\infty} = 1 - \exp\left(\frac{-\chi(T)}{|\lambda|^m}\right) \tag{1}$$

with a semi-empirical expression for the crystallization function, $\chi(T)$, defined as

$$\chi(T) = C_1 (T_m^0 - T)^{m+1} \exp\left(\frac{-C_2}{T(T_m^0 - T)^2}\right). \tag{2}$$

In Eq. (1), x_r is the relative crystallinity, x_∞ is the crystallinity at the termination of the crystallization process, x is the crystallinity at temperature T (K), and λ is the constant cooling rate (K/min). With regard to Eq. (2), Hammami and Mehrotra [6] represented C_1 as a constant that is not strongly temperature dependent and C_2 as a constant associated with the free energy of nucleation. In addition, T_m^0 (K) represents the measured equilibrium melting temperature. From preliminary work, we have found T_m^0 to be well defined and reproducible, and this observation is supported by experiments conducted elsewhere ([8]) using crystalline polymers. The melting point, rather than the temperature associated with the inception of paraffin crystals, is often assumed to be a more accurate measure of the equilibrium solid-liquid coexistence temperature ([6]). Equation (2) was derived ([9]) assuming homogeneous crystallization and one-dimensional crystal growth. Hammami and Mehrotra [6], combined Eqs. (1) and (2) with a set of mixing rules to model the crystallization kinetics of a binary, isomorphous mixture. Moreover, they believed that their model could be extended to a multicomponent isomorphous mixture. The current work presents an extension of their model to represent the kinetics of crystallization of normal alkanes from freezing jet fuel samples.

DSC measurements provide plots of crystallization exotherms for jet fuel samples. The exotherms can be integrated ([6]) with respect to temperature and can provide values of the relative crystallinity, $x_r(T)$:

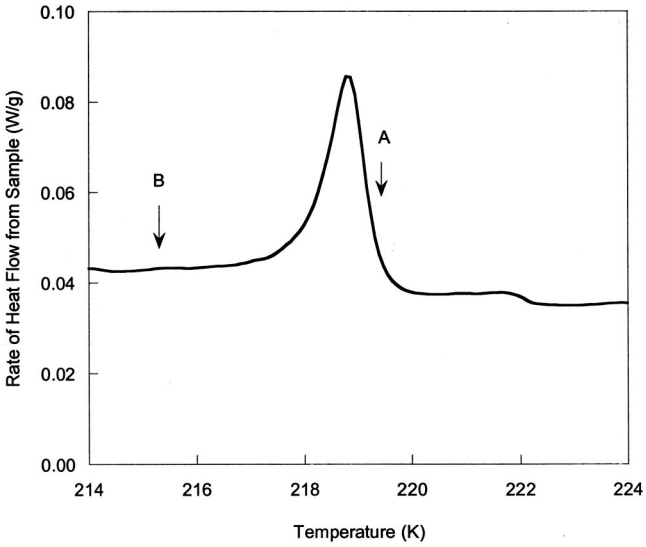

Fig. 1 Jet A (F3219) exotherm measured by differential scanning calorimetry (DSC) at a 1.0 K/min cooling rate. Indicated locations along the curve correspond to images of Fig. 2.

$$x_r = \frac{\int_{T_S}^{T} \left(\frac{dQ}{dt}\right) dT}{\int_{T_S}^{T_\infty} \left(\frac{dQ}{dT}\right) dT}. \tag{3}$$

In Eq. (3), T_s (K) is the temperature associated with the initiation of crystal formation and T_∞ (K) represents the temperature at which crystal formation is complete. Thus, x_r represents the extent of completion of the crystallization process during freezing. In the current work, exotherms and values of x_r (Eq. (3)) were generated using cooling rates of 0.25, 0.5, 1.0, 2.5, and 5.0 K/min.

Results and Discussion

DSC Exotherms for Jet Fuels. Figure 1 shows DSC measurements of the rate of heat evolution together with the fuel temperature from a cooled Jet A fuel sample (F3219). Below 228 K, the jet fuel of Fig. 1 was cooled at a constant rate of 1.0 K/min. Locations along the cooling rate-temperature curve are assigned letters which correspond to the microscope images of Fig. 2. Moving from right-to-left as the fuel cools, the exotherm begins to rise above the baseline as crystals begin to form in the fuel. Consequently, Fig. 2(*a*) shows the appearance of initial fuel crystals. The crystals of Fig. 2(*a*) are largely in the shape of plates, and the formation of similarly shaped wax plates have been observed in studies of the freezing of diesel fuels ([10]). In addition to the plates, Fig. 2(*a*) shows that there are a few ''ribbon-shaped'' crystals. Relatively large normal alkanes have heat of fusion values that are significantly larger than other classes of fuel species (iso-alkanes, cyclo-alkanes, and aromatics). As a consequence, it is believed that most of the exothermic response is due to normal alkane crystallization, and we expect that the large normal alkanes in the jet fuel will crystallize first (n-C_{16} to n-C_{18}) ([5]). Figure 1 shows that the large peak in the exotherm is centered near 219 K. When the cooling curve of Fig. 1 returns to the baseline, the freezing process is considered complete. After the exotherm returns to the baseline, Fig. 2(*b*) (location B Fig. 1) shows that crystals are generally larger than those imaged at the higher temperature of Fig. 2(*a*) (location A Fig. 1). In addition, Fig. 2(*b*) shows that the crystal population increases at the lower temperature (location B Fig. 1).

As jet fuels come from a variety of refinery sources, they may have different low-temperature characteristics. Thus, it is impor-

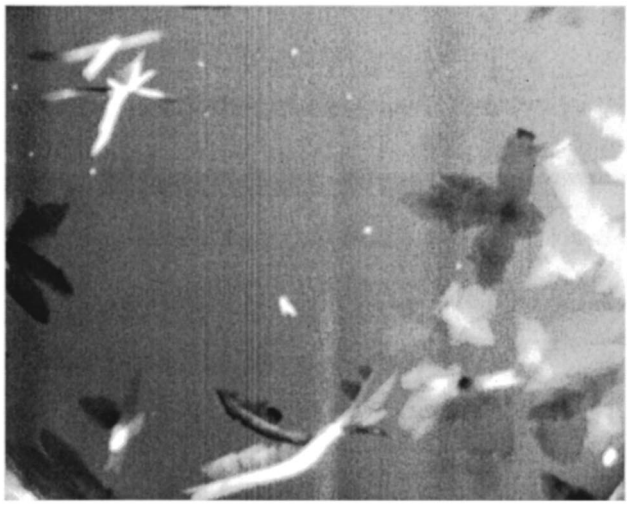

(*a*)

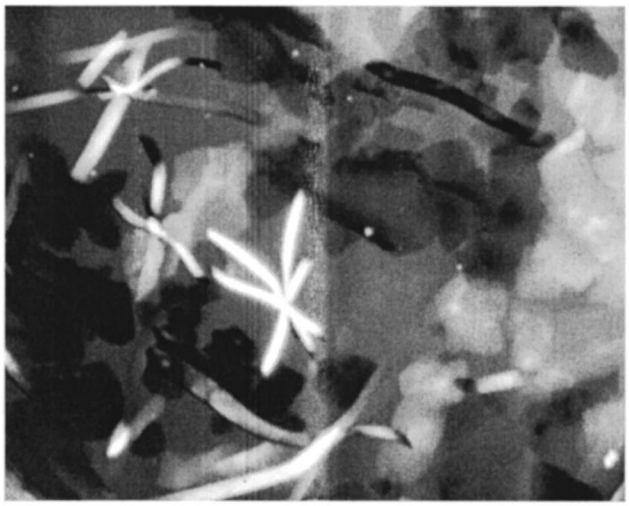

(*b*)

Fig. 2 Images of fuel crystals forming using cold-stage microscopy with a cooling rate of 1.0 K/min. (*a*) and (*b*) correspond to points on the curve of Fig. 1 (magnification 40×).

tant to study different jet fuel samples. Figure 3 shows DSC curves (cooling rate of 1.0 K/min) for two Jet A fuel samples (F3219 and F2827) and one sample of JPTS (F3775). The large JPTS peak (A3) is located at a lower temperature than that of the Jet A peaks (A1 and A2). JPTS fuel is designed for high altitude, low temperature flight, and its freeze point specification is 6 K lower than that of Jet A. Thus, the location of the JPTS exothermic peak relative to the Jet A samples is expected. The ''shoulders'' (labeled B1–B3) at the base of the peaks correspond to the measured cloud point temperatures (temperatures where crystallization begins, Table 1) of the fuel samples. Beyond the cloud point temperature, the heat flow curve reaches a maximum, and the fuel sample continues to solidify. On the low-temperature side of the exothermic peak, the measured pour points (Table 1) are located where the exotherm returns to the baseline. The heat flow curve of fuel F2827 is centered near 223 K with a freeze point near 230 K. For fuel F3219, the large exothermic peak is located near 218 K and has a freeze point temperature near 226 K, which is just at the JP-8 specification limit. Thus, F3219 is a ''worst case'' fuel for JP-8 low-temperature behavior and is being used in the fuel additive studies. Figure 3 shows three symbols on the

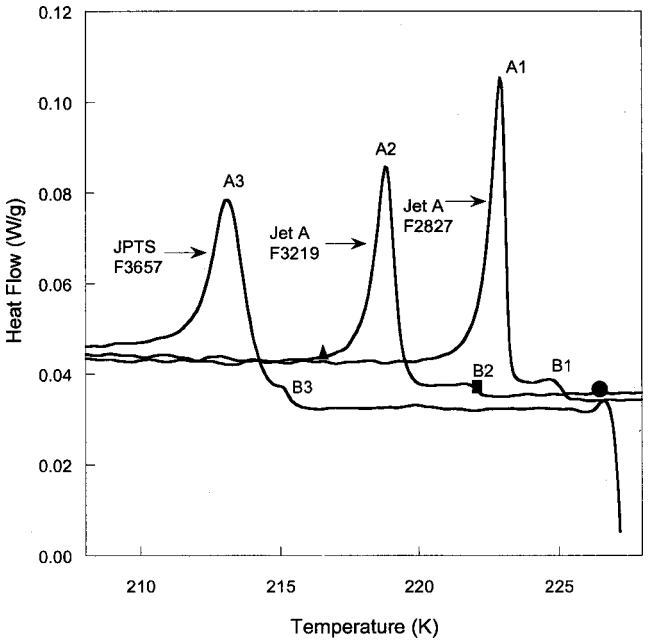

Fig. 3 Differential scanning calorimetry (DSC) measurements for three fuel samples at a cooling rate of 1 K/min

F3219 curve to further clarify the concepts of freeze point (circle), cloud point (rectangle), and pour point (triangle).

Kinetics of Liquid-Solid Phase Transformation. Figure 4 shows calculated and measured values of the relative freezing fraction for the JPTS (F3775) fuel sample for cooling rates between 0.5 K/min and 5.0 K/min. A more satisfactory fit of the kinetic expression of Eqs. (1) and (2) was obtained by introducing another variable, n, to replace the exponent, $m+1$, on term $(T_m^0 - T)$ of Eq. (2). The added complexity of replacing $m+1$ in Eq. (2) with n is reasonable because Eqs. (1) and (2) were originally intended for use in relatively simple binary n-alkane mixtures rather than in more complex mixtures like jet fuel. (The variable m was otherwise retained in Eq. (1).) The new variable n was used in all nonlinear regression analyses that were performed using commercially available software (Table Curve 3D, Jandel Scientific) that employs the Levenburg-Marquardt procedure ([11]).

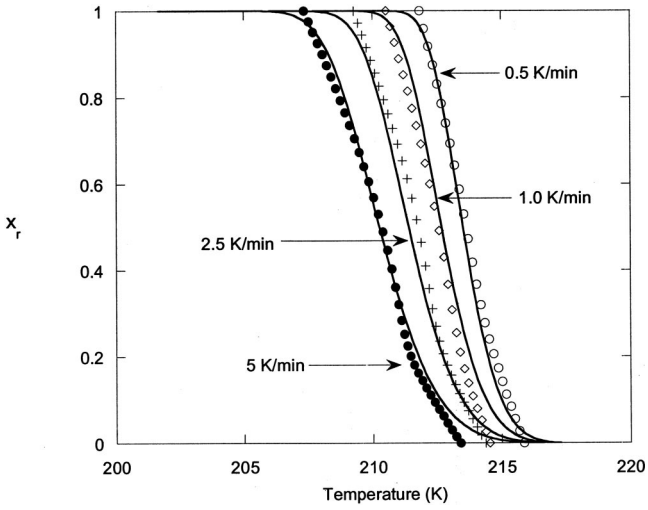

Fig. 4 Predicted and measured relative freezing fraction for JPTS (F3775) with different cooling rates

Table 2 Parameters obtained by nonlinear regression and used in Eqs. (1) and (2)

Fuel	C_1	C_2	m	n
JPTS	1.67904×10-6	22870.4	1.20197	6.35765
Jet A (F3219)	2.24352×10-4	10.8435	0.834486	4.28286

Figure 4 shows that the nonlinear fit (Table 2) of Eqs. (2) and (3) provides a reasonable description of the freezing process of JPTS for cooling rates between 0.5 and 5.0 K/min.

Locations along the temperature axis ($x_r=0$) of Fig. 4 essentially represent the initiation of fuel crystallization. Figure 4 shows that as the cooling rate is increased from 0.5 K/min to 5.0 K/min, the measured temperature at which freezing begins is shifted to lower temperatures. The kinetic model overpredicts the temperature of freezing, and the overprediction is greatest for the cooling rate of 5.0 K/min. However, the model does reflect the downward shift in freezing initiation temperatures as the cooling rate is increased. The shift in freezing initiation to lower temperatures is believed to be a consequence of supercooling of the fuel. Hydrocarbon mixtures which contain larger n-alkane species ($C_{25}-C_{50}$) and are supercooled show a similar shift in temperature as the cooling rate is increased ([6]). In a different experiment ([12]), detailed images of this JPTS jet fuel (F3775) freezing under conditions of a two-dimensional buoyancy-induced flow with imposed surface temperatures were obtained. Freezing began on a cooled aluminum test surface (cooling rate of 1 K/min) at 215.1 K (±0.5 K). Moreover, Fig. 4 shows that at a cooling rate of 1.0 K/min that the JPTS fuel begins to freeze in the DSC experiment at 214.6 K. Thus, with the same cooling rate, the temperature at which the freezing of JPTS begins is essentially the same in two different experiments. The agreement of initial crystallization temperatures between essentially nonflowing (DSC) and flowing experiments illustrates the potential for using DSC measurements to develop correlations that can be used in numerical simulations to predict phase-change behavior over a range of flow conditions. In computational fluid dynamics simulations of the freezing of jet fuel, it is desirable to incorporate the effects of supercooling. The values given in Table 2 correspond to the constants of Eqs. (1) and (2), which can be incorporated within future computational simulations in which x_r is a progress variable and supercooling behavior can be represented. Numerical simulations will assist in the interpretation of experiments and the design of fuel systems that have a wide range of flow and cooling conditions.

Figure 5 shows the calculated and measured relative freezing fraction for the Jet A (F3219) fuel sample. As with Fig. 4 (JPTS fuel) for each cooling rate, the fit of Eq. (1) is better near $x_r=1$ than that near crystal initiation ($x_r=0$). With the values listed in Table 2 for this fuel, Eq. (1) overpredicts the temperature of the onset of freezing, and the difference between measurement and prediction increases with increasing cooling rate. Although the present kinetic model overpredicts the temperature of crystal initiation, the discrepancy is not fatal. This kinetic representation still provides a reasonable representation for x_r beyond crystal initiation and can be used in numerical simulations of fuel freezing. In the experiment ([12]) used for the visualization of the freezing of flowing Jet A fuel (F3219), freezing begins on the aluminum test surface (cooling rate of 1 K/min) at 220.5 K (±0.5 K). At a cooling rate of 1.0 K/min, Fig. 5 shows that the Jet A fuel (F3219) initially freezes in the DSC experiment at 221.6 K. As in the case of the JPTS fuel (Fig. 4), two different experiments indicate that the onset of crystallization for this Jet A fuel (cooling rate of 1 K/min) occurs near 221 K. The measurement of similar temperatures occurring at the initiation of crystal formation corroborates each experimental technique. Moreover, Fig. 4 and 5 together underscore the importance of supercooling in the freezing of jet fuels.

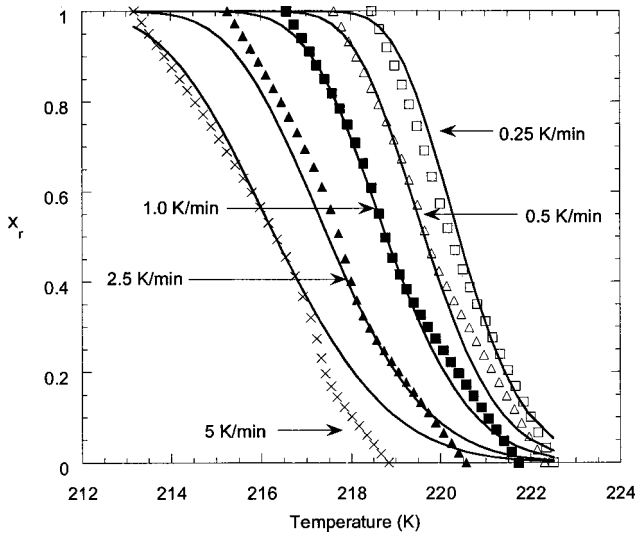

Fig. 5 Predicted and measured relative freezing fraction for Jet A (F3219) with different cooling rates

Additive Studies. The rate at which a hydrocarbon mixture is cooled affects the nucleation rate of normal alkanes from solution. In addition, the rate of change in local concentrations of species precipitating from solution can influence the local transport properties and crystal growth. Additives have been used to modify nucleation and growth processes of freezing diesel fuel. Flow improver additives such as ethylene vinyl acetate copolymers cocrystallize with normal alkanes and have protruding functional groups that interfere with incorporation of free normal alkanes found in diesel fuels. Consequently, smaller crystals result. It is desirable to form numerous small crystals that do not block fuel system filters or flow passages. In addition, flow improver additives are often designed to create multitudes of nuclei to which precipitating wax molecules attach and form crystals. The cooling rate has an important influence on crystal formation in hydrocarbon fuels and, thus, could have an effect on the behavior of low-temperature additives. As a consequence, DSC studies were performed in which the cooling rates of both neat fuel and fuel containing an additive were varied. In large-scale experiments ([1]), the proprietary additive 3607 greatly improved the low-temperature characteristics of fuel F3219 and was selected for this study.

Figure 6 shows values of an effective specific heat for a neat Jet A fuel (F3219) which includes heat of fusion contributions for cooling rates of 1.0 K/min, 2.5 K/min, and 5.0 K/min. Figure 6 shows that as the cooling rate is increased from 1.0 K/min to 5.0 K/min, the large peak in the neat fuel trace shifts from 218.5 K to 217.2 K. In contrast, Fig. 7 shows that the large peak associated with the fuel containing additive 3607 shifts less than 1 K (from 218.3 K to 217.6 K) as the cooling rate is increased from 1.0 K/min to 5.0 K/min. In addition, Fig. 7 shows that there is a more rapid rise and narrower width in the large peaks when contrasted with those of Fig. 6. The more rapid rise in the specific heat values of Fig. 7 implies a faster nucleation rate at a given temperature for the additized fuel. When contrasted with Fig. 6 at the lowest cooling rate, Fig. 7 shows that the additive acts to slightly depress the temperature at which crystallization begins. As the cooling rate increases, Fig. 7 shows that the additive reduces the level of supercooling that can be achieved before crystal nucleation begins. Presumably, the additive becomes a source for heterogeneous crystal nucleation. Figure 7 shows that the behavior of cold flow additives varies with cooling rate in a manner that is not well understood.

The small changes in the DSC exotherms shown here indicate that the additive works primarily by altering crystal morphology

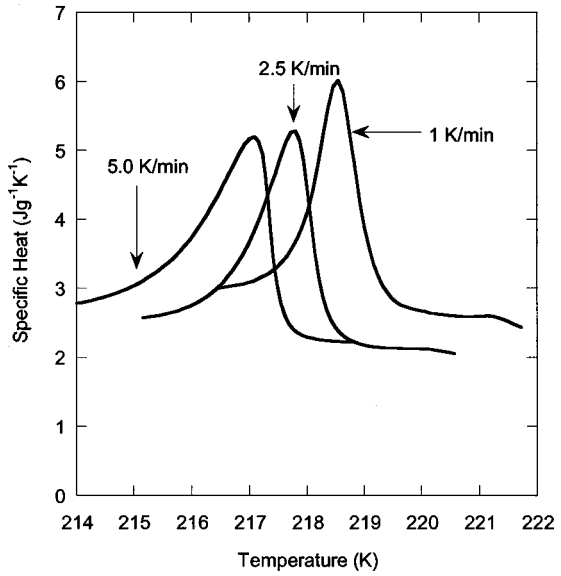

Fig. 6 Measured specific heats for neat Jet A fuel (F3219) and different cooling rates

rather than by significantly changing the temperature at which crystallization begins. To supplement the thermal analysis provided by DSC measurements, we have also used low-temperature microscopy to observe changes in crystal structure during cooling. Figure 8 shows images of the fuel (near 219 K) containing additive 3607 and cooled at a rate of 1.0 K/min. The presence of the additive results in numerous ''long and narrow'' crystals rather than the plate-like crystals of the neat fuel of Fig. 2. The formation of numerous, narrow crystals is the type of behavior expected from ''pour point'' type additives.

Conclusions

In the current work, the DSC was used to detect phase transitions in the cooling of jet fuels. In addition, the DSC demonstrated differences in the low-temperature characteristics of two Jet A fuel samples and a JPTS fuel. By varying the cooling rate over a large range, the effect of supercooling on crystallization within jet fuel was shown to be important. In addition, correlations for liquid-to-solid phase-change kinetics were developed.

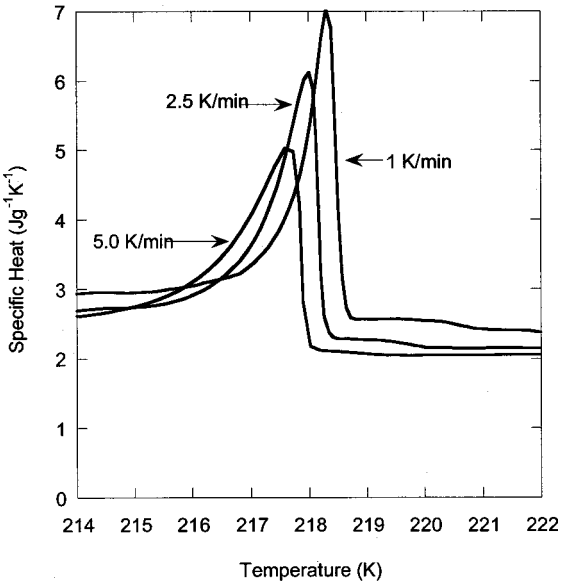

Fig. 7 Measured specific heats for additized Jet A fuel (F3219) and different cooling rates

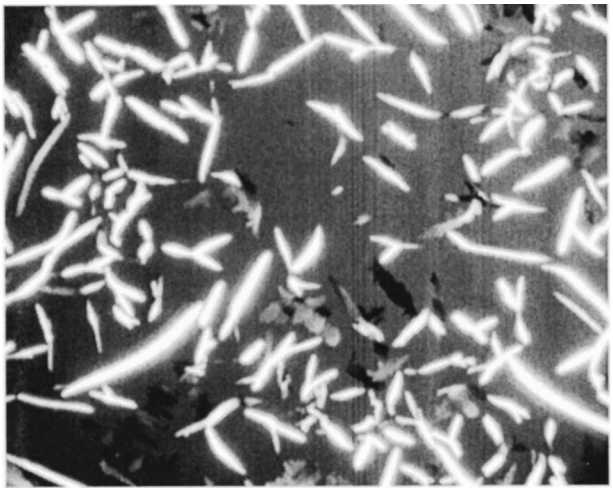

Fig. 8 Images of crystals forming from Jet A containing additive 3607 using cold-stage microscopy with a cooling rate of 1.0 K/min (magnification 40×)

The DSC is a useful instrument in the study of the freezing of jet fuel. The DSC can be used to develop kinetic models of fuel crystal formation and growth and can provide specific heat measurements. Both kinetic growth models and specific heat measurements are important for the development of engineering computational fluid dynamics models. The cold-stage microscope provides information concerning crystal morphology that varies with cooling rate and can also be used in future numerical simulations that involve multiphase flows.

Acknowledgments

This work was supported by the U.S. Air Force, Warner Robins Air Logistic Command, U-2 Special Programs Office, Robins Air Force Base, Warner Robins, Georgia, under Project No. 205 (Project Manager: Capt. Bernard Frank) and the U.S. Air Force Research Laboratory, Propulsion Directorate, Propulsion Sciences and Advanced Concepts Division, Wright-Patterson Air Force Base, Ohio, under Contract No. F33615-97-C-2719.

Nomenclature

C_1 = constant in Eq. (2)
C_2 = constant in Eq. (1)
dQ/dT = differential heat transfer rate (W)
m = exponent used in Eq. (1) and (2)
n = exponent used in nonlinear regression
T = temperature (K)
T_m^0 = measured equilibrium melting temperature (K)
T_S = crystal formation initiation temperature (K)
x_r = relative crystallinity (dimensionless)
$x(T)$ = crystallization as function of temperature (dimensionless)
x_∞ = crystallinity at termination of crystallization process (dimensionless)
λ = cooling rate (K/min.)

References

[1] Ervin, J. S., Zabarnick, S., Binns, E., Dieterle, G., Davis, D., and Obringer, C., 1999, ''Investigation of the Use of JP-8+100 With Cold Flow Enhancer Additives as a Low-Cost Replacement for JPTS,'' Energy Fuels, **13**, pp. 1246–1251.

[2] Noel, F., 1972, ''Thermal Analysis of Lubricating Oils,'' Thermochim. Acta, **4**, pp. 377–392.

[3] Letoffe, J. M., Claudy, P., Garcin, M., and Volle, J. L., 1995, ''Crude Oils: Characterization of Waxes Precipitated on Cooling by D.S.C. and Thermomicroscopy,'' Fuel, **74**, pp. 92–95.
[4] Aboul-Gheit, A. K., Abd-el-Moghny, T., and Al-Eseimi, M. M., 1997, ''Characterization of Oils by Differential Scanning Calorimetry,'' Thermochim. Acta, **306**, pp. 127–130.
[5] Zabarnick, S., and Widmor, N., 2001, ''Studies of Jet Fuel Freezing By Differential Scanning Calorimetry,'' Energy & Fuels, **15**, pp. 1447–1453.
[6] Hammami, A., and Mehrotra, A. K., 1996, ''Non-Isothermal Crystallization Kinetics of Binary Mixtures on N-Alkanes: Ideal Eutectic and Isomorphous Systems,'' Fuel, **75**, pp. 500–508.
[7] Ozawa, T., ''Kinetics of Non-isothermal Crystallization,'' Polymer, **12**, pp. 150–158.
[8] Roberts, D. E., and Mandelkern, L. J., 1955, ''Thermodynamics of Crystallization in High Polymers: Natural Rubber,'' J. Am. Chem. Soc., **77**, pp. 781–786.
[9] Hammami, A., and Mehrotra, A. K., 1992, ''Non-isothermal Crystallization Kinetics of n-Paraffins With Chain Lengths Between Thirty and Fifty,'' Thermochim. Acta, **211**, pp. 137–153.
[10] Lewtas, K., Tack, R. D., Beiny, D., and Mullin, J., 1991, ''Wax Crystallization in Diesel Fuel: Habit Modification and the Growth of n-Alkane Crystals,'' *Advances in Industrial Crystallization*, Butterworth Heinemann, Oxford, UK.
[11] Bevington, P. R., 1969, *Data Reduction and Error Analysis for the Physical Sciences*, McGraw-Hill, New York.
[12] Atkins, D., and Ervin, J. S., 2001, ''Freezing of Jet Fuel Within a Buoyancy-Driven Flow in a Rectangular Optical Cell,'' Energy & Fuels, **15**, pp. 1233–1240.

U. Surface Deposition within Treated and Untreated Stainless Steel Tubes Resulting from Thermal-Oxidative and Pyrolytic Degradation of Jet Fuel

Surface Deposition within Treated and Untreated Stainless Steel Tubes Resulting from Thermal-Oxidative and Pyrolytic Degradation of Jet Fuel

Jamie S. Ervin,* Thomas A. Ward, Theodore F. Williams, and Jarrod Bento

University of Dayton Research Institute, Dayton, Ohio 45469-0210

Received August 12, 2002

Flow experiments using heated Jet-A fuel and additives were performed to study the effects of treated surfaces on surface deposition. The experimental apparatus was designed to view deposition due to both thermal oxidative and pyrolytic degradation of the fuel. Carbon burnoff and scanning electron microscopy were used to examine the deposits. To understand the effect of fuel temperature on surface deposition, computational fluid dynamics was used to calculate the two-dimensional temperature profile within the tube. Three kinds of experiments were performed. In the first kind, the dissolved O_2 consumption of heated fuel is measured on different surface types over a range of temperatures. It is found that use of treated tubes significantly delays oxidation of the fuel. In the second kind, the treated length of tubing is progressively increased which varies the characteristics of the thermal-oxidative deposits formed. In the third type of experiment, pyrolytic surface deposition in either fully treated or untreated tubes is studied. It is found that the treated surface significantly reduced the formation of surface deposits for both thermal oxidative and pyrolytic degradation mechanisms. Moreover, it was found that the chemical reactions resulting in pyrolytic deposition on the untreated surface are more sensitive to pressure level than those causing pyrolytic deposition on the treated surface.

Introduction

Jet fuel is used in military aircraft for purposes of cooling before it is burned in the combustor. As fuel flows through the fuel system, trace species within the heated fuel react with dissolved O_2 to form surface deposits. At relatively higher fuel temperatures, the dissolved O_2 is depleted, and pyrolytic chemistry becomes dominant (at temperatures greater than ∼450 °C). Pyrolytic reactions change the composition of the major fuel species and, like thermal-oxidative reactions, produce surface deposits and other undesirable products. Under conditions of either thermal-oxidative or pyrolytic reactions, surface deposits collect on surfaces within valves and impede flow through metal passages. Since surface deposits have the potential to cause catastrophic failure of an aircraft fuel system, it is important to study the influence of the surface on deposition occurring under conditions of both thermal-oxidative and pyrolytic fuel degradation.

It has been observed that the surface material over which heated fuel flows can strongly influence thermal-oxidative chemistry.[1] For example, in flowing experiments with Jet-A fuels, Jones[2] found that the rate of fuel oxidation within treated stainless steel tubes was slower than that within untreated stainless steel tubes. The surface treatment involved the chemical vapor deposition of a proprietary silica-based layer (Silcosteel[3]). A passivating layer, which prevents active sites on a stainless steel surface from contacting fuel, would be expected to result in a slower rate of dissolved O_2 consumption. Moreover, reduction of the consumption of dissolved O_2 decreases the potential for surface deposition. In a high-temperature study (pyrolytic conditions) involving the flow of heated jet fuel over a range of surface materials (nickel, SS 316, SS 304, Silcosteel, and glass), it was found, using temperature-programmed oxidation analysis and scanning electron microscopy on the deposits, that different surface materials resulted in deposits of varying character.[4] Silcosteel-treated surfaces, which are presumed to be less active than stainless steel surfaces containing nickel, were observed to reduce carbon deposition.

Although past research has suggested that surface treatment may be used to reduce surface deposition, the influence of the surface material on deposition in thermal-oxidative and pyrolytic fuel degradation is not well understood. One theory for thermal oxidative degradation is that particles form in the bulk of the fuel, migrate to heated walls, and then adhere there to form surface deposits. Other possibilities for surface deposit formation are that deposits are initiated at the heated surface with little contribution from particles in the bulk flow or that surface deposition results from contributions from both adhering bulk particles and deposits formed only at the wall. A further complication in

* Corresponding author. E-mail: jervin@engr.udayton.edu.

(1) Hazlett, R. N. *Thermal Oxidation Stability of Aviation Turbine Fuels*; American Society for Testing and Materials: Philadelphia, 1991; pp 116−120.

(2) Jones, E. G.; Balster, W. J.; Pickard J. M. *Trans. ASME, J. Eng. Gas Turbines Power* **1996**, *118*, 286−291.

(3) Silcosteel tubing, Restek Corporation, Bellefonte, PA.

(4) Altin, O.; Eser, S. *Ind. Eng. Chem. Res.* **2001**, *40*, 596−603.

10.1021/ef020180t CCC: $25.00
Published on Web 03/25/2003

Table 1. Description of Experiments

	experiment		
	1	2	3
	dissolved O_2 consumption for different surfaces	thermal-oxidative surface deposition	pyrolytic surface deposition
interior tube surface	fully treated or untreated	varying starting lengths of treated tube	fully treated or untreated
duration of experiment (h)	24	24	4 & 8
flow rate (mL/min)	20	20	32
pressure (MPa)	4.5	4.5	3.89, 5.27 or 6.31
Reynolds number range	120−3,730	120−3,730	193−27,200
residence time (s)	11−1st furnace 7−2nd furnace	11−1st furnace 7−2nd furnace	5−1st furnace 2−2nd furnace

Table 2. Characteristics of Neat Jet-A Fuel F3219

characteristic	value
JFTOT breakpoint, °C (°F)	285 (545)
sulfur, total, wt %	0.0321
aromatics, vol %	16.6
hydrogen content, mass %	13.6
copper	$<5 \pm 5$ ppb
iron	$<10 \pm 5$ ppb
zinc	$<10 \pm 5$ ppb
specific gravity @ 60 °F	0.8109

understanding how the wall influences fuel degradation is that the composition of the surface contacting the fuel changes as deposits accumulate. Moreover, the influence of pressure (particularly high pressures) on pyrolytic deposition for surfaces of different composition has gone relatively unexplored. The understanding of how pressure influences deposition is especially important for fuel nozzles where the pressure may change substantially.

To assist the understanding of the influence of a stainless steel surface (316) and a passivated surface (Silcosteel) on thermal-oxidative and pyrolytic deposition, three kinds of flowing, heated tube experiments (Table 1) are carried out using jet fuel. In the first kind, the heated surface is either stainless steel (316) or is treated. The goal is to measure the dissolved O_2 consumption of heated fuel on different surface types over a range of temperatures. In the second kind of experiment, the length of treated tubing relative to stainless steel tubing is progressively increased with the intention of affecting the measured O_2 consumption and, in turn, thermal-oxidative surface deposition. In the third type of experiment, the entire flow path consists of either stainless steel or treated tube, and surface deposits formed by fuel pyrolysis is the objective. In addition, the influence of pressure on surface deposition is studied. Carbon burnoff analysis provides a relative measure of the deposit mass, and scanning electron microscopy (SEM) provides visual characteristics of the surface deposits. Understanding the behavior of fuel degradation in the presence of different surfaces is important because the U.S. Air Force is exploring different methods of increasing the thermal stability temperature limit of JP-8 jet fuel by 225 °F (JP-8+225) and greater (JP-900).

Experimental Section

Table 2 lists characteristics of the Jet-A fuel sample (Air Force designation F3219) used. Fuel F3219 produces relatively low hydroperoxide concentrations and oxidizes relatively slowly when heated. Samples of neat F3219 fuel (fuel A) and

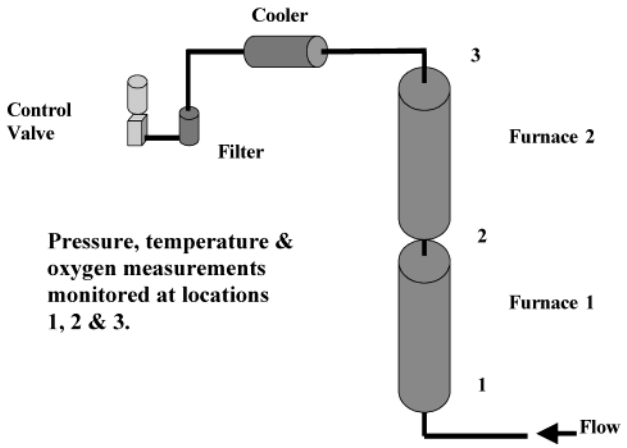

Figure 1. Flow apparatus for thermal-oxidative fuel degradation experiments. Carbon measurements from tubing in Furnace 1 & 2.

F3219 fuel with additives (fuel B) were used. The additives in fuel B include those given by MIL-T-83133D and a proprietary thermal stability additive (Betz Dearborn 8Q462) used in the JP-8+100 Program.

Since the surface material influences the rate of fuel oxidation, it is important to study fuel oxidation using tubes that have different interior surfaces. In the current experiments, the fuel flows through either untreated tubing (316 stainless steel, 2.16-mm i.d. × 3.18-mm o.d., ASTM grade A269/A213, surface roughness of 8−15 micro inches) or tubing with a surface treatment. The surface treatment involves the chemical vapor deposition of a proprietary silica-based layer (Silcosteel) that has a thickness of approximately 10 000 Å The layer was suspected to be inert relative to stainless steel tubing and, thus, was selected to reduce the catalytic influence of the stainless steel tube surfaces on dissolved O_2 consumption. Thermocouples (20 gage) are welded to the outer surface of the tubing to provide the tube wall temperatures with an uncertainty of ± 2 °C. The bulk fuel temperature at the exit of the heated tube was also measured (uncertainty of ± 5 °C). After each test, the tubing was cut into 5 cm sections, rinsed with hexane, vacuum-dried at 120 °C for 2 h, and analyzed by carbon burnoff. The uncertainty in the surface deposition measurement is estimated to be ±3% from replicate experiments. In addition, some sections were analyzed using an Amray AMR 1600 SEM.

Each experiment was conducted using a flow rig (Figure 1) that simulates a complex thermal and flow environment. The two furnaces of Figure 1 are mounted vertically in series. With this arrangement, there is buoyancy-assisted flow that reduces the probability of secondary flow patterns and, thus, makes the flow well-defined and easier to understand. The first furnace (12.7 cm i.d. and 11.5 kW) has a total heated length of 91.4 cm, and the second furnace (12.7 cm i.d. and 8 kW) has a total heated length of 61 cm. The tubing passes through the center of the ovens and is secured to the oven base plate

Table 3. Complex Jet-A Surrogate Composition Used in CFD Simulation[10]

compound	chemical formula	chemical group	mole fraction
dodecane	$C_{12}H_{26}$	paraffins	0.154
tetradecane	$C_{14}H_{30}$	paraffins	0.101
decane	$C_{10}H_{22}$	paraffins	0.134
hexane	C_6H_{14}	paraffins	0.132
n-octane	C_8H_{18}	paraffins	0.053
methylcyclohexane	C_7H_{14}	naphthenes	0.067
ethylcyclohexane	C_8H_{16}	naphthenes	0.060
m-xylene	C_8H_{10}	aromatics	0.070
butylbenzene	$C_{10}H_{14}$	aromatics	0.167
1-methylnaphthalene	$C_{11}H_{14}$	naphthalenes	0.062

and thermally isolated with a ceramic standoff. To compensate for thermal expansion, a constant 5-pound tensile load is applied by means of a thermally insulated spring to the top end of the tube. The section between the furnaces (30 cm long) is insulated. Table 1 shows additional experimental details for the three kinds of experiments performed. Bulk dissolved O_2 levels were measured on-line at locations indicated in Figure 1 by means of a modified gas chromatograph[5] (uncertainty less than ±1% of the measured value). The dissolved O_2 concentration at the flow inlet was 70 ppm w/w (air saturated value). For all deposition experiments, the measurable dissolved O_2 was entirely consumed in the first furnace.

Numerical Simulations

To understand the effect of fuel temperature on surface deposition, computational fluid dynamics (CFD) was used to simulate the turbulent flow and calculate the temperature profile within the tube. A method employing the Navier−Stokes, turbulent energy, and enthalpy equations was used.[6] A turbulent model was used because there is a rapid transition from laminar to turbulent flow as the fuel is heated (Table 1). Therefore, the flow is turbulent for most of the length of the reactor. The fluid motion inside the tube was assumed to be axisymmetric and steady. The governing equations written in the cylindrical (z, r) coordinate system for axisymmetric flow are the following:

$$\frac{\partial \rho u}{\partial z} + \frac{\partial \rho v}{\partial r} + \frac{\rho v}{r} = 0 \quad (1)$$

$$\frac{\partial \rho u \Phi}{\partial z} + \frac{\partial \rho v \Phi}{\partial r} = \frac{\partial}{\partial z}\left(\Gamma^{\Phi}\frac{\partial \Phi}{\partial z}\right) + \frac{\partial}{\partial r}\left(\Gamma^{\Phi}\frac{\partial \Phi}{\partial r}\right) - \frac{\rho v \Phi}{r} + \frac{\Gamma^{\Phi}}{r}\frac{\partial \Phi}{\partial r} + S^{\Phi} \quad (2)$$

Equation 1 is the continuity equation, and eq 2 represents the momentum or energy equation depending on the variable, Φ. Here ρ is the mixture density and u and v are the axial and radial velocity components, respectively. Table 4 lists the transport coefficients Γ^{Φ} and the source terms S^{Φ} of the governing equations. The governing equations are discretized utilizing a second-order central-differencing scheme everywhere, except where the local Peclet number becomes greater than two in which case a first-order upwind scheme is used. Wall functions were used to determine the flow variables near the wall.[7] Buoyancy forces are included in the simulations, with the gravity vector in the opposite direction of the flow. The flow was set to zero velocity at the tube wall. Since surface deposition here is thin, it was assumed to have a negligible effect on heat transfer and was not modeled. Wall temperatures were represented by curve fits of the thermocouple measurements. Additionally, the inlet velocity and temperature profile of the fuel were assumed to be uniform for simplicity. The inlet temperature was 20 °C and the measured pressure (Table 1) was used. When the velocity, pressure, turbulent kinetic energy, turbulent dissipation, and enthalpy global error residuals were all reduced below 4 orders of magnitude from their maximum values, the solution was considered to be converged.

Table 4. Source Terms and Transport Coefficients Appearing in Equations 1,2

Φ	Γ^{Φ}	S^{Φ}
u	$\mu + \mu_t$	$-\frac{\partial p}{\partial z} + \frac{\partial}{\partial z}\left(\Gamma^{u}\frac{\partial u}{\partial z}\right) + \frac{\partial}{\partial r}\left(\Gamma^{u}\frac{\partial v}{\partial z}\right) + \frac{\Gamma^{u}}{r}\frac{\partial v}{\partial z} + \rho g$
v	$\mu + \mu_t$	$-\frac{\partial p}{\partial r} + \frac{\partial}{\partial z}\left(\Gamma^{v}\frac{\partial u}{\partial r}\right) + \frac{\partial}{\partial r}\left(\Gamma^{v}\frac{\partial v}{\partial r}\right) + \frac{\Gamma^{v}}{r}\frac{\partial v}{\partial r} - 2\Gamma^{v}\frac{v}{r^2}$
k	$\mu + \frac{\mu_t}{\sigma_k}$	$G - \rho\varepsilon$[a]
ε	$\mu + \frac{\mu_t}{\sigma_\varepsilon}$	$C_1 G\frac{\varepsilon}{k} - C_2\rho\frac{\varepsilon^2}{k}$ (C_1=1.47, C_2=1.92)
h	$\frac{\kappa}{c_p} + \frac{\mu_t}{\sigma_\varepsilon}$	0

[a] $G = \mu_t\left[2\left\{\left(\frac{\partial u}{\partial z}\right)^2 + \left(\frac{\partial v}{\partial r}\right)^2 + \left(\frac{v}{r}\right)^2\right\} + \left(\frac{\partial v}{\partial z} + \frac{\partial u}{\partial r}\right)^2\right]$

The grid structure used in the simulations. The grid of Figure 2b has a nonuniform spacing between the two furnaces in order to decrease the computational run time while maintaining a finer grid spacing representing the second furnace (pyrolysis region), which was of primary interest in the third set of experiments. Simulations of the flow and temperatures were performed using different grid densities ($z \times r$): 80 × 12, 160 × 15, 160 × 20, and 200 × 25. The maximum difference in calculated bulk fuel temperature between the 160 × 15 and 200 × 25 grid densities was only 3%, which occurred over a small distance (0.2 m) near the tube inlet. For the remainder of the tube, the difference in calculated bulk temperatures was less than 1%. Thus, only small improvements in accuracy can be gained by increasing the grid density beyond 200 × 25. The execution time on a 2.2 GHz Pentium 4 computer for the 200 × 25 grid was one week. Further increasing the grid density beyond 200 × 25 has a high computational cost for a nearly negligible gain in accuracy. Figures 3 and 4 show the simulated bulk fuel temperatures along the heated tube using a 200 × 25 grid for the three sets of experiments. In addition, Figures 3 and 4 show that the calculated bulk temperature at the exit of each furnace agrees reasonably well with the measured fuel temperature.

The thermodynamic and transport properties of the fuel were calculated at every grid point (Figures 2a and

(5) Rubey, W. A.; Striebich, R. C.; Tissandier, M. D.; Tirey, D. A.; Anderson, S. D. *J. Chromatogr. Sci.* **1995**, *33*, 433−437.

(6) Katta, V. R.; Roquemore, W. M. *J. Thermophys. Heat Transfer* **1993**, *7*, 651−660.

(7) Launder, B. E.; Spalding, D. B. *Comput. Methods Appl. Mech. Eng.* **1974**, *3*, 269−289.

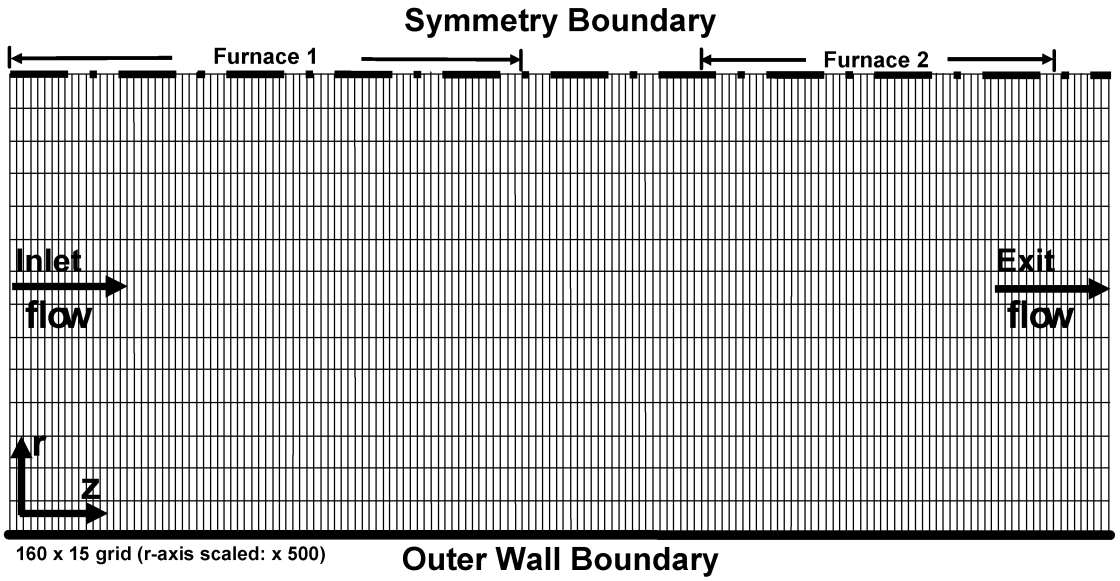

Figure 2. CFD grids used in flow simulations.

2b) by incorporating SUPERTRAPP subroutines.[8] SUPERTRAPP performs phase equilibrium calculations with the Peng−Robinson equation of state,[9] and transport properties are calculated with an extended corresponding states model. SUPERTRAPP provides well-behaved thermodynamic properties near the critical point and in the supercritical regime. Since jet fuel is a complex mixture of hydrocarbons, surrogate fuels were examined to simplify the CFD simulations. Simple surrogates allow quicker computer run times but do not exactly have the same properties of a real jet fuel. To determine a reasonable surrogate, simulations were performed using *n*-decane, *n*-dodecane, and a multicomponent mixture (Table 3).[10] All three surrogates have critical temperatures and pressures similar to the pseudo-critical temperature and pressure ($T_c \approx 410$ °C, $P_c \approx 2.34$ MPa) of the selected Jet-A sample.

Figure 3 shows the calculated temperature profile of Experiments 1 and 2; and Figure 4 shows the calculated temperature profile of Experiment 3. In Figures 3 and 4, the calculated bulk fuel temperatures among the surrogate fuels span a maximum difference of 10% (located along 0.2−0.35 m in the first furnace). At locations beyond 0.6 m, the maximum difference in calculated temperatures is less than 3%. All simulations predict furnace-outlet bulk temperatures within the experimental error (±5%) of the measured values. It has been observed previously that single-component *n*-alkanes can correctly represent the single-phase heat transfer behavior of jet fuels.[11] Provided the critical temperature and pressures are similar, the calculations of Figures 3

(8) Ely, J. F.; Huber, M. L. *NIST Standard Reference Database 4—NIST Thermophysical Properties of Hydrocarbon Mixtures Database (SUPERTRAPP), Version 3.0*; U.S. Department of Commerce, Gaithersburg, MD, 1999.

(9) Peng, D.; Robinson, D. B. *Ind. Eng. Chem. Fundam.* **1976**, *15*, 59−64.

(10) Schulz, W. D. *Prepr. Pap.−Am. Chem. Soc., Div. Pet. Chem.* **1991**, *37*, 303−392.

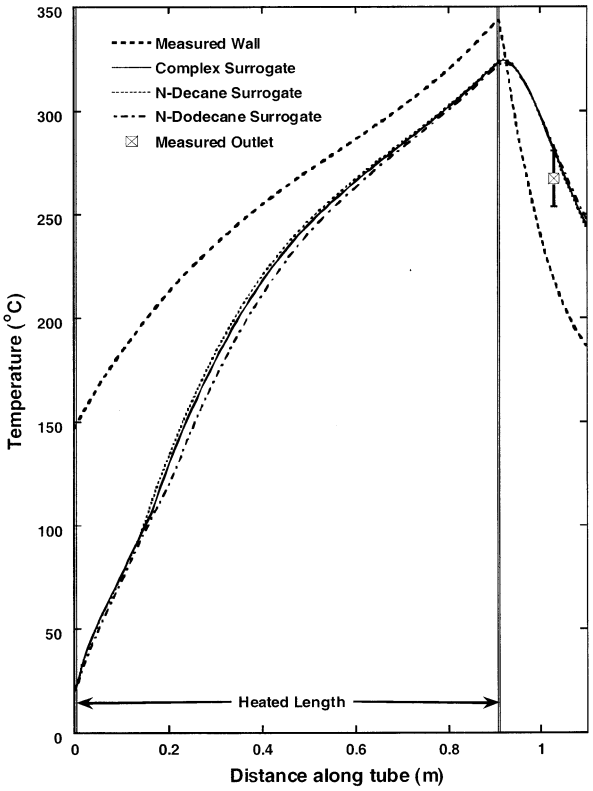

Figure 3. Simulated bulk fuel temperature profiles (Experiments 1 and 2, Table 1).

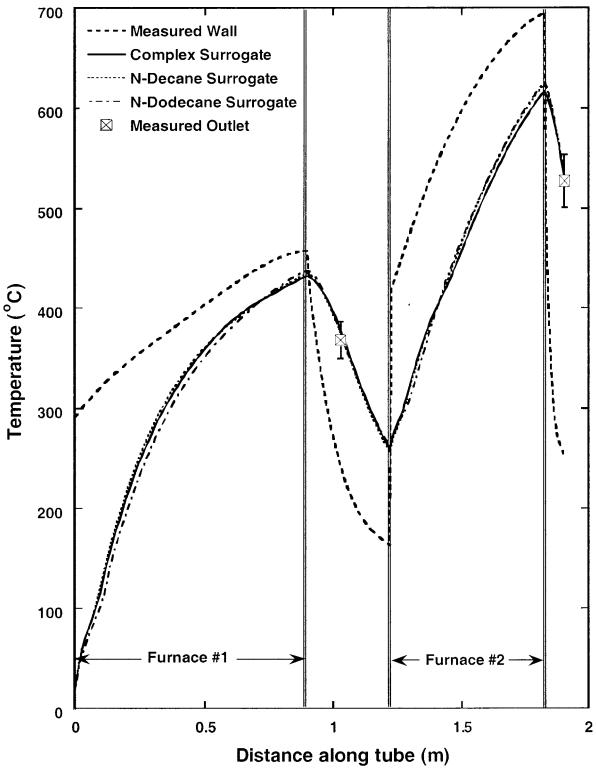

Figure 4. Simulated bulk fuel temperature profiles (Experiment 3, Table 1).

and 4 support the observation that a single-component *n*-alkane can reasonably approximate the heat transfer for a jet fuel for smooth property transitions between a compressed liquid and supercritical fluid.

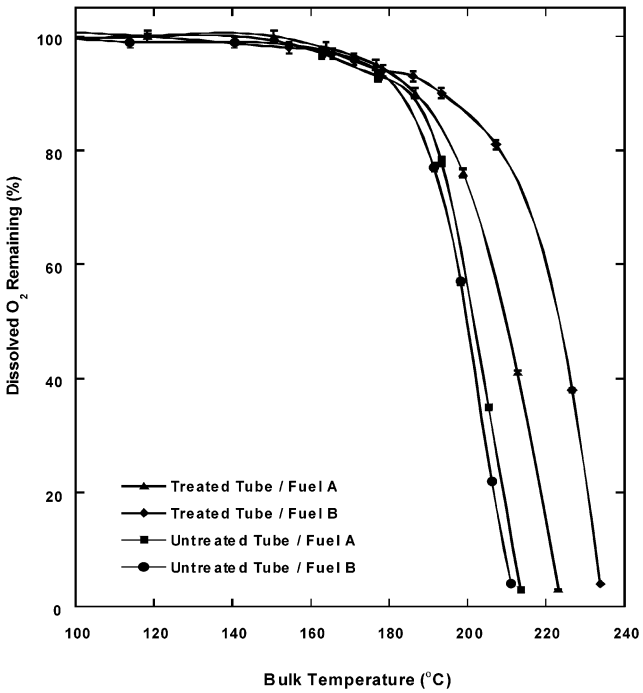

Figure 5. Fraction of dissolved O_2 remaining at the end of the heated tube for treated and untreated tubes and for fuel A (neat Jet-A) and fuel B (Jet-A with additives) (for 20 mL/min flow rate).

Results and Discussion

Fuel Oxidation Studies. Studies of fuel oxidation are necessary for the understanding of surface deposition. In this particular experiment, only the phenomenon occurring in the first furnace was of interest (Figure 2a). To characterize how dissolved O_2 is consumed for the fuel sample used here, the wall temperature of the first furnace was increased while the flow rate was held at 20 mL/min. As the wall temperature was increased, the bulk temperature of the flowing fuel at the outlet of the heated tube rose. Figure 5 shows the fraction of dissolved O_2 remaining for both fuels A and B for different surface materials. Figure 5 shows that the dissolved O_2 in fuel A, which flows through a treated tube, is completely consumed at an outlet bulk temperature of 224 °C. Complete conversion of the dissolved O_2 in fuel B, also flowing through a treated tube, does not occur until 233 °C. This delay in oxidation is not surprising as the additive package in fuel B contains an antioxidant that is believed to reduce the rate of fuel oxidation by reacting with alkyl-peroxy free radicals. In addition, MDA is included in the additive package, which is believed to chelate dissolved metals and act to reduce the rate of oxidation. For the untreated tube, Figure 5 shows that the consumption of dissolved O_2 within fuel A appears to be delayed longer than that for fuel B in the stainless steel tube. (However differences between these two O_2 consumption curves are insignificant because of the uncertainty in the outlet bulk fuel temperature measurements and the sensitivity of the dissolved O_2 measurement.) Although not proven here, a plausible explanation for the accelerated dissolved O_2 consumption with the stainless steel surface

(11) Edwards, T.; Maurice, L. Q. *J. Propul. Power* **2001**, *17*, 461–466.

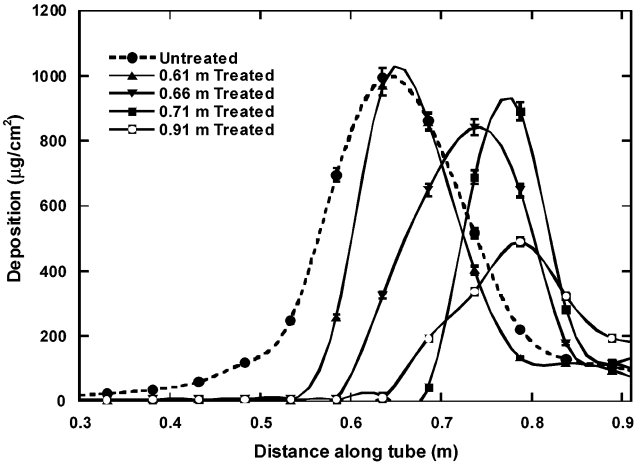

Figure 6. Surface deposition along the heated tube after 24 h (flow rate of 20 mL/min, reaching a maximum fuel temperature of 350 °C). Varying treated lengths of interior surface using fuel A (neat Jet-A).

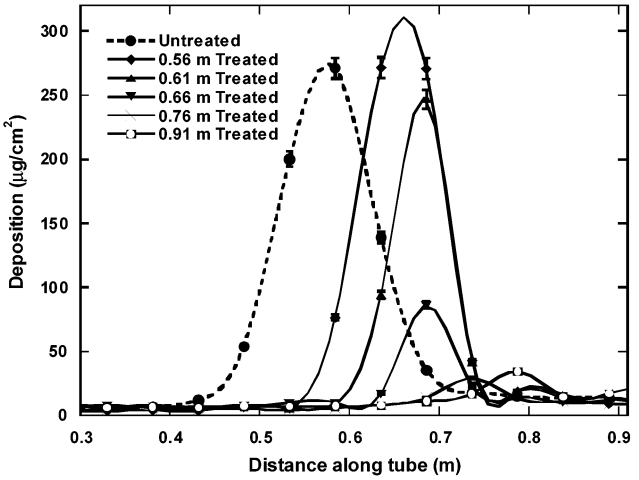

Figure 7. Surface deposition along the heated tube after 24 h (flow rate of 20 mL/min, reaching a maximum fuel temperature of 350 °C). Varying treated lengths of interior surface using fuel B (Jet-A with additives).

(relative to that of the treated surface) is that the stainless steel surface has numerous active sites that take part in the catalyzed thermal dissociation of alkyl-hydroperoxides. The free radicals, RO• and •OH, resulting from alkyl-hydroperoxide dissociation reactions contribute to the propagation and acceleration of the oxidation chain.[12] Walling[13] has described such metal-catalyzed dissociation reactions of hydroperoxides. In contrast, similar active sites are not available on the treated tube and, thus, the oxidation rate would be expected to be slower for treated tubes, as shown in Figure 5.

Figure 5 shows that the treated tube in combination with the additive package is more effective in delaying fuel oxidation than the stainless steel surface in the presence of either fuel A or B. In addition, it is known that the presence of metal surfaces inhibits the reaction of fuel antioxidants with alkyl-peroxy free radicals.[14] Thus, the delayed oxidation occurring with the combination of treated tube and additive package relative to that of the stainless steel tube might be expected.

Deposition Studies in Which the Length of the Treated Tube Is Varied. To better understand the influence of the wall material on thermal-oxidative surface deposition, the length of the heated Silcosteel region upstream from the untreated tube was progressively increased in a series of experiments. In the final experiment the entire heated section within the first furnace was treated (91 cm). Figure 6 shows measured surface deposition along the heated tube (of Furnace 1) with a flow rate of 20 mL/min for a period of 24 h for each successive test. For each 5 cm section, the carbon measurement is divided by the interior surface area for that section. Figure 6 shows that significant deposition in the untreated tube begins near 35 cm and peaks near 61 cm. At the location where surface deposition begins to rise (35 cm), the wall temperature is ~245 °C and the calculated bulk temperature is ~200 °C. Figure 5 shows that under these conditions the bulk fuel is rapidly oxidizing. The numerical simulations show that the temperature near the wall is greater than the bulk temperature. Thus, the dissolved O_2 fraction near the wall is less than the measured bulk dissolved O_2 fraction of Figure 5. At locations beyond 43 cm (Figure 5), the bulk fuel temperature is greater than 225 °C and the dissolved O_2 is fully consumed. Once the dissolved O_2 is depleted, deposit-forming species essentially no longer form and the deposit precursor species are depleted from the liquid phase. Thus, all of the deposition peaks in Figure 6 occur downstream from the location where dissolved O_2 is fully consumed. Figure 6 also shows that as more length of tube is treated, the surface deposition is delayed beyond the treated length of the tube. When the heated length of the tube is fully treated (91 cm), there is a significant reduction in the total deposit (~500 μg/cm^2). Figure 6 shows that treating the tube surface inhibits surface reactions and possible physical attachment mechanisms responsible for deposit formation otherwise occurring on the stainless steel. These results show that the inhibition of chemical reactions at the tube surface (by treating it with an inert surface) significantly reduces thermo-oxidative surface deposits.

A similar set of experiments was also performed with fuel B. As with the experiments using fuel A (Figure 6), the length of heated treated tube upstream of the untreated tube was progressively increased until the entire tube within the first furnace was treated. A comparison of the deposition on the untreated surfaces in Figures 6 and 7 shows that the proprietary additive package (containing detergent-dispersants) in fuel B significantly reduces surface deposition relative to that of fuel A. Figure 7 shows that, for fuel B flowing through an untreated tube, there is a reduction of the deposition peak (to approximately 700 μg/cm^2) and a shift of the peak downstream relative to that of fuel A (Figure 6). Figure 7 shows that the rise in deposition on the untreated tube begins near 43 cm and peaks near 56 cm. Figure 5 shows that, under these conditions, the bulk fuel B is rapidly oxidizing and most of the dissolved O_2 is gone (similarly observed with fuel A flowing through the untreated tube). Figure 7 (as in Figure 6) shows that as more length of tube is treated, the surface deposition is delayed beyond the treated length of the

(12) Zabarnick, S. *Energy Fuels* **1998**, *12*, 547−553.
(13) Walling, C. *Free Radicals in Solution*; John Wiley and Sons: New York, 1957; p 427.
(14) Downing, F. B.; Clarkson, R. G.; Pedersen, C. J. *Oil Gas J.* **1939**, *38*, 97−101.

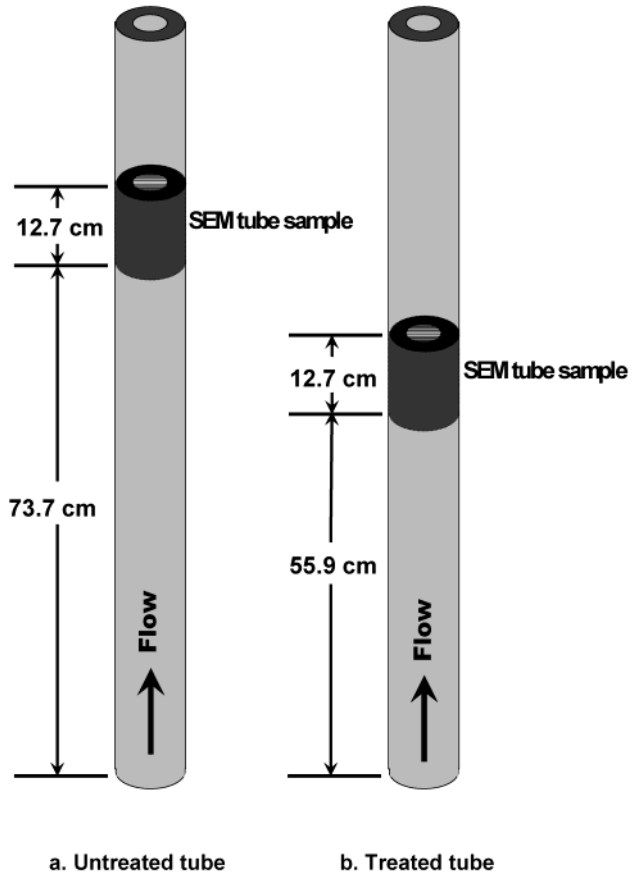

Figure 8. SEM analysis tube sample sections.

tube. When the heated length of the tube is fully treated (91 cm), the deposition nearly vanishes. Figure 7 shows that the use of the surface treatment together with the additive decreases the surface deposition below that of what either method acting alone is capable of doing. Thus, there is synergistic reduction in surface deposition when both additives and surface treatment are used.

The microstructure of thermal-oxidative deposits was studied by examining SEM images of the surface deposits. Knowledge of the surface deposit microstructure assists the understanding of how deposits are formed. Figure 8 shows the location where tubes were sectioned for SEM analysis. Both of these 12.7 cm sections come from locations of maximum thermal-oxidative deposition following 24 h of exposure to heated, flowing neat Jet-A fuel. Figures 9 and 10 are digitized images of the inner surface of the sections. (For reference, the white bar at the bottom of the figures represents a length of 100 μm.) For reference, Figures 9a and 10a show the microstructure of the treated and untreated surfaces before testing. The untreated surface has larger nonuniform surface structures than those of the treated surface. Figure 9b shows that, after heated jet fuel flows over the untreated surface for 24 h, the original underlying wall microstructure is no longer visible after the experiment. In addition, Figure 9b shows that some of the structures composed of microspheres are as large as 70 μm in diameter. Similar large microsphere structures have been observed in previous flowing studies[16−18] of thermal-oxidative deposition on

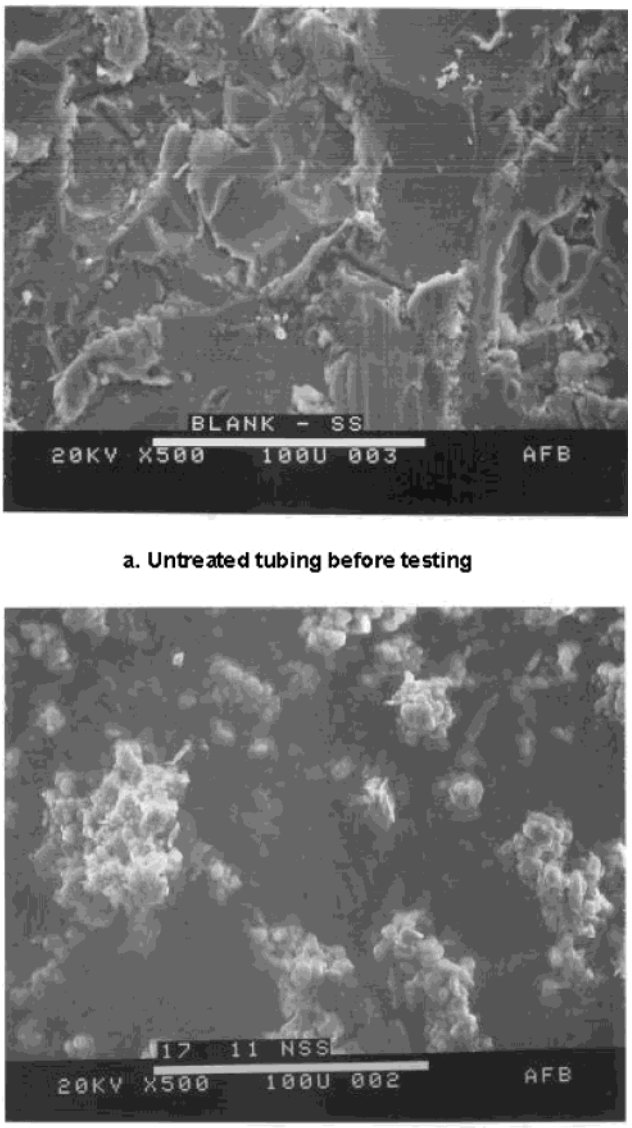

Figure 9. SEM micrograph of interior of untreated, stainless steel tubing for varying times at the peak deposition location. (The white bar length at the bottom of the image equals 100 μm.)

stainless steel surfaces. The large microspheres are formed from smaller nearly spherical particles which accumulate on the surface in randomly packed structures, which become fused together near the heated surface. Schirmer[18] reported the appearance of similar spherical particles in the same size range in a variety of Air Force and commercial flow rigs for fuels heated near 175−205 °C. It has been observed that initial small particles may form on a thin incipient polymolecular film attached to the stainless steel surface. This film has been analyzed using Auger spectroscopy in a study[17] in which the stainless steel surface was exposed for different periods of time to heated flowing jet fuel. It has been proposed that the large porous structures

(15) Jones, E. G.; Balster, W. J.; Rubey, W. A. *Prepr. Pap.—Am. Chem. Soc., Div. Pet. Chem.* **1995**, *40*, 655−659.

(16) Ervin, J. S.; Williams, T. F. *Ind. Eng. Chem. Res.* **1996**, *35*, 899−904.

(17) Ervin, J. S.; Heneghan, S. P.; Martel, C. R.; Williams, T. F. *Trans. ASME, J. Eng. Gas Turbines Power* **1996**, *118*, 278−285.

(18) Schirmer, R. M. Morphology of Deposits in Aircraft and Fuel Systems. Presented at the SAE National Air Transportation Conference, New York, April 1970. Paper 700258.

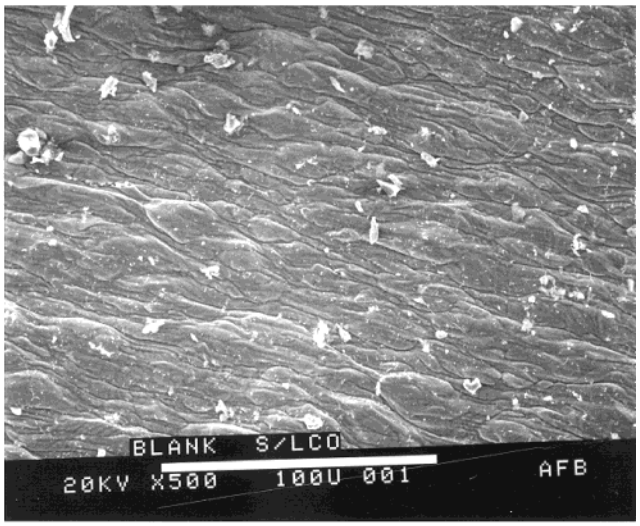

a. Treated tubing before testing

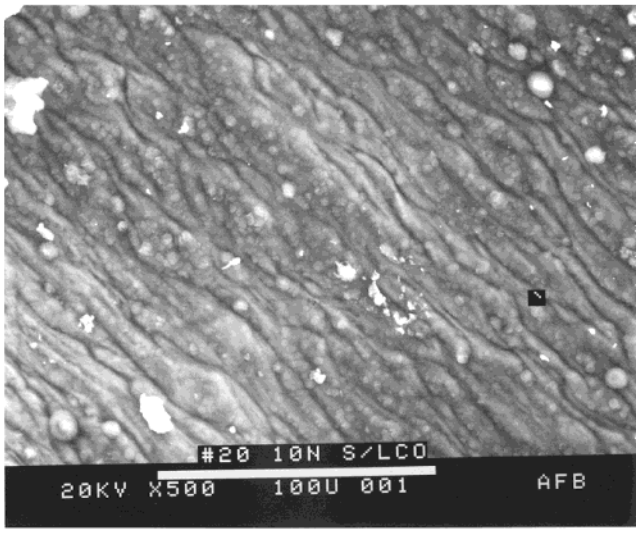

b. Treated tubing after 24 hours

Figure 10. SEM micrograph of the interior of treated tubing for varying times at the peak deposition location. (The white bar length at the bottom of the image equals 100 μm.)

(observed in Figure 9) grow by trapping fuel.[17] Thick deposits have been observed to reduce the rate of fuel oxidation.[15] However, the deposits formed under the conditions of the present experiments are thin and nonuniform, and a decrease in the over-all oxidation rate was not measured. Thus, the influence of the surface treatment (especially with fuel additives) is more dominant than a reduction in surface activity due to surface deposition. For the increasing lengths of treated tube (Figures 6 and 7), the dissolved O_2 was always depleted, and the deposition peak shifted downstream and to lower values.

In Figure 10b, the topography of the underlying tube surface can still be distinguished and numerous spherical particles attached to the silica surface are also observable. The aggregate carbon structures are much smaller (less than 10 μm in diameter) than those observed on the stainless steel surface. The structure of the surface deposit on the treated tube (Figure 10b) consists of spherical particles, but the particles on the treated surface are less numerous than those observed on the more active stainless steel surface. Figure 10b shows that the surface treatment changes the large-scale structure of the deposit relative to the deposit formed on stainless steel. Moreover, Figure 10b shows that the treated surface inhibits deposition resulting in less accumulation of microspheres as supported by Figures 6 and 7.

In a related work (which used a Jet-A fuel) Jones[15] also found that the deposition rate on (Silcosteel) treated surfaces was generally lower and occurred at longer residence times than deposition rates associated with stainless steel surfaces. Jones assumed that the use of detergent-dispersant additives affected particle size, solubility, and (together with the treated surface) adherence of insolubles to the heated surfaces. Both Jones[15] and this work show that the combination of using treated tubing and fuel B (with the proprietary additives) act synergistically to decrease the deposition rate.

As fuel flows through an aircraft fuel system, it encounters different wall temperatures. Previously, using a complex flowing system with initially clean tubes, we found that surface deposition on stainless steel tubes rapidly decreases with a reduction in wall temperature although the bulk fuel temperature may be greater than the (upstream) wall temperature associated with significant surface deposition.[16] Thus, a deposition profile along the tube that follows the wall temperature suggests the relative importance of the surface reactions in the formation of surface deposits. We believe that surface reactions play a strong role in both oxidation and surface deposition reactions. In the current work, Figures 6 and 7 show that the deposition preferentially occurs on the stainless steel surface which contains relatively active constituents such as chromium, iron, and nickel rather than on the less active silica surface.

Pyrolytic Deposition Studies. Because of the relatively low temperatures in the first furnace, thermal-oxidative surface deposition occurs there. As the fuel flows through the second furnace, pyrolytic reactions become dominant at greater wall temperatures (~650 °C), and deposition due to pyrolysis reactions begins. Pyrolytic surface deposition will be an important concern for future flow passages that may be heated to temperatures beyond the pseudocritical point of a jet fuel. Thus, another goal of this research is to study the effects of pressure and surface material on pyrolytic surface deposition.

Figure 11a shows measured surface deposition (after a 4-h period) along the untreated tube for pressures that are above the pseudocritical pressure of the fuel. (For reference, Figure 4 shows the measured wall temperature along the heated tube in the second furnace.) Figure 11a shows that there is a peak in surface deposition at an axial location of 1.75 m. Figure 11b shows measured surface deposition along the treated tube which peaks at 1.88 m. A comparison of Figures 11a and 11b shows that surface deposition resulting from pyrolysis is greater for the untreated surfaces than for the treated surfaces for otherwise identical conditions. Altin and Eser[4] have likewise observed catalytic activity associated with stainless steel surfaces and the acceleration of surface deposition relative to that of tubes treated with Silcosteel using temperature-pro-

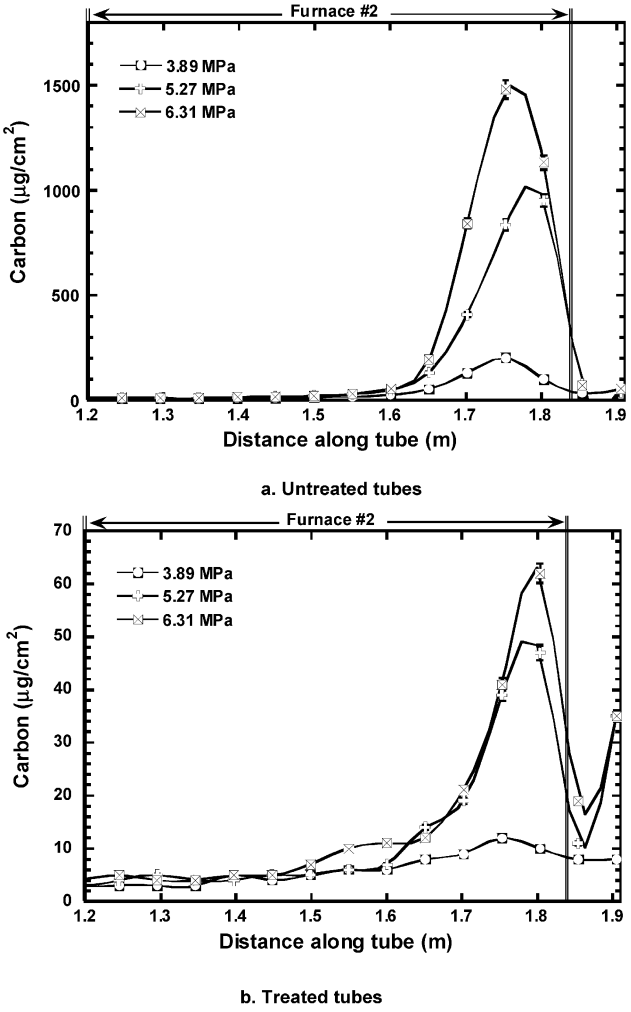

Figure 11. Pyrolytic surface deposition for different pressures.

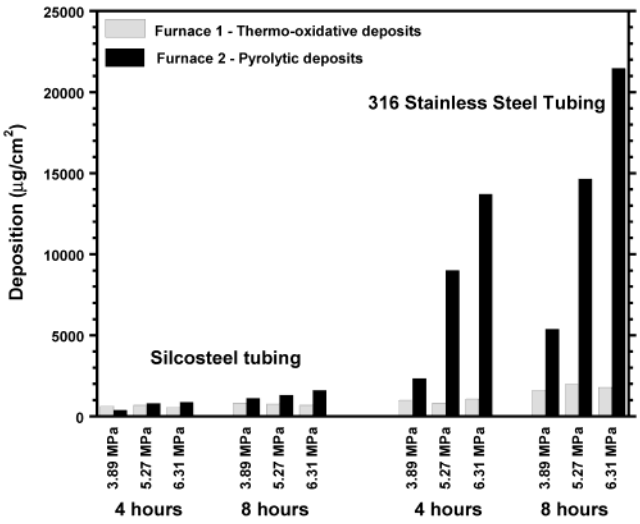

Figure 12. Influence of pressure on total thermal-oxidative and pyrolytic deposition.

grammed oxidation analysis and SEM for JP-8 flowing in heated 316 stainless steel tubes (1 mL/min for 5 h, temperatures up to 813 K, and 500 psi).

For four and 8-h periods, Figure 12 shows total surface deposition for both treated and untreated tubes in the first and second furnaces. For pressure levels of 3.89, 5.27, and 6.31 MPa, Figure 12 shows that pressure essentially does not influence thermal-oxidative deposition for either untreated or treated tubes. For elementary reactions occurring in a liquid solvent, the liquid is essentially incompressible, and pressure changes on the order of several kilobars are required to significantly affect the rate constant. Thus, pressure is not expected to influence surface deposition resulting from thermal-oxidative chemistry that occurs within a liquid solution. Figure 12 shows that surface deposition in the pyrolytic regime increases with increasing pressure level for both treated and untreated tubes. Within the higher temperature furnace, the fuel transitions to a supercritical fluid. In general, the molecular collision frequency is higher in a supercritical fluid than in a liquid. Therefore the reaction rate of a supercritical fluid will be greater than that of a liquid.

Figure 12 shows that treated tubes generally have lower rates of surface deposition than do the stainless steel tubes for both thermal-oxidative and pyrolytic forms of surface deposition. Moreover, as the system pressure is increased from 3.89 to 6.31 MPa, Figures 11 and 12 show that the total pyrolytic surface deposition within the stainless steel tubes is several times greater than that of the treated tubes. Thus, Figures 11 and 12 show that the chemical reactions, which result in pyrolytic deposition on the stainless steel surface, are much more sensitive to pressure level than those causing pyrolytic deposition on a relatively inert surface. The sensitivity to pressure of pyrolytic reactions on stainless steel is important to the designers of future aircraft who have to consider the use of valves and nozzles which necessarily involve large pressure changes.

Conclusions

The three kinds of flow experiments presented here yielded promising results on the use of treated surfaces alone or in combination with fuel additive packages to reduce thermal-oxidative and pyrolytic surface deposition. In the first kind of experiment, it was shown that fuel additives could be used to reduce the rate of fuel oxidation, thereby delaying and reducing the formation of thermal-oxidative deposits. When used in combination with tube surface treatment the oxidation rate is further delayed. In the second kind of experiment, as the treated portion of the heated tube is progressively increased, the surface deposition peak progressively moves downstream and is reduced. These effects are most pronounced when the additive package is also added. These results indicate that chemical reactions occurring at the tube surface are important in the formation of surface deposits. In the third type of experiment, the effects of surface treatment and pressure on pyrolytic surface deposition are studied. Experiments with the inert surface treatment had much less surface deposition than untreated tubes. Also the formation of pyrolytic deposition was less sensitive to pressure on treated tubes relative to untreated stainless steel tubes. Furthermore, the combination of using fuel with additives in treated tubes appears to have a synergistic effect in reducing thermal-oxidative surface deposition. The combination of additives and surface treatment shows great potential in significantly reducing the formation of surface deposition in the fuel flow pathways of advanced aircraft.

Nomenclature

ASTM	American Society for Testing and Materials
C_1	constant = 1.47
C_2	constant = 1.92
C_μ	constant = 0.09
CFD	computational fluid dynamics
D	tube diameter, m
D_i	diffusion coefficient of ith species
G	$\mu_t\left[2\left\{\left(\frac{\partial u}{\partial z}\right)^2+\left(\frac{\partial v}{\partial r}\right)^2+\left(\frac{v}{r}\right)^2\right\}+\left(\frac{\partial v}{\partial z}+\frac{\partial u}{\partial r}\right)^2\right]$
g	gravitational acceleration, m/s^2
h	enthalpy, kJ/kg
k	turbulent kinetic energy, kJ/kg
JFTOT	jet fuel thermal oxidation tester
MDA	metal deactivator additive
P	pressure, MPa
r	radial coordinate
SEM	scanning electron microscope
S^Φ	source term
u	axial velocity component, m/s
u_τ	friction velocity, $(\tau_\omega/\rho)^{1/2}$, m/s
v	radial velocity component, m/s
z	axial coordinate
Φ	assigned variable in eqs 1,2
Γ^Φ	transport coefficient
ϵ	dissipation rate
κ	thermal conductivity, W/m-K
ρ	density, kg/m^3
σ_k	constant = 1.0
σ_ϵ	constant = 1.3
σ_h	constant = 1.0
τ_w	μ absolute viscosity wall shear stress, N/m^2
μ_t	turbulent viscosity, $C_\mu\rho k^2/\epsilon$

Acknowledgment. This work was supported by the Dayton Area Graduate Studies Institute and the U.S. Air Force, Air Force Research Laboratory, Propulsion Directorate, Turbine Engines Division, Fuels Branch, Wright-Patterson AFB, OH, under contract F33615-97-C-2719.

EF020180T

V. Particulate Matter and Polycyclic Aromatic Hydrocarbon Determination Using a Well-Stirred Reactor

41st Aerospace Sciences Meeting and Exhibit
6-9 January 2003, Reno, Nevada

AIAA 2003-664

PARTICULATE MATTER AND POLYCYCLIC AROMATIC HYDROCARBON DETERMINATION USING A WELL-STIRRED REACTOR

R. F. Reich[1], S. D. Stouffer[2*], V. R. Katta[3], H. T. Mayfield[4], C. W. Frayne[1*], and J. Zelina[1**]

Air Force Research Laboratory[1]
Wright-Patterson AFB, OH

University of Dayton Research Institute[2]
Dayton, OH

Innovative Scientific Solutions, Inc.[3]
Dayton, OH

Air Force Research Laboratory[4]
Tyndall AFB, FL

*Member AIAA **Senior Member AIAA

ABSTRACT

Combustion generated particulates from gas turbine combustors can cause adverse effects on engine maintenance costs, plume visibility and the environment. Research is being conducted to provide understanding of the mechanisms of soot formation and identify mitigation strategies. A cooled well-stirred reactor (WSR), which simulates the primary zone of a gas turbine combustor, is used in the current study. Experiments have been completed with premixed, fuel-rich ($1.9 < \phi < 2.6$) ethylene-air and ethylene-ethanol-air mixtures. Multiple physical characteristics, including particle number density, particle size distribution, total carbon mass, and (polycyclic aromatic hydrocarbon) PAH content, were used to quantify the soot. A unique instrument, the Particulate Matter Characterization and Monitoring System (PMCMS), was used for the determination of the particle size distribution, and the chemical characterization of the soot and gaseous emissions. The results of the study showed that the benzene concentration in the gas phase increased monotonically with equivalence ratio while the pyrene was shown to correlate with the soot content. The results suggest that pyrene and other PAH species can be used to predict the soot formation for more complex combustion systems. For the conditions of the present study, the addition of ethanol to ethylene was shown to lower soot production compared to pure ethylene.

NOMENCLATURE

CNC	= condensation nuclei counter
GC/MS	= gas chromatograph/mass spectrometer
ICP-MS	= inductively coupled plasma mass spectrometer
RDMA	= radial differential mobility analyzer
m_a	= air mass flow rate (kg/s)
m_f	= fuel mass flow rate (kg/s)
MSVI	= multi-stage virtual impactor
PAH	= polycyclic aromatic hydrocarbon
PFR	= plug flow reactor
PM	= particulate matter
PMCMS	= Particulate Matter Characterization and Monitoring System
R_s	= reflectance of the stained filter
R_w	= reflectance of the unstained filter
SN	= smoke number
T_a	= adiabatic flame temperature (K)
T_f	= reactor temperature (K)
T_o	= inlet temperature (K)
THC	= total hydrocarbons
UNICORN	= UNsteady Ignition and COmbustion with ReactioNs
V	= reactor volume (mL)
WSR	= well-stirred reactor

Symbols

ϕ	= equivalence ratio
ρ	= density (kg/m^3)
τ	= residence time (ms)

INTRODUCTION

The accepted process of soot formation (Figure 1) demonstrates the reaction path to soot by which a portion of fuel is broken into unsaturated radicals and intermediates during combustion. These are known as soot precursors, which then react to form small polycyclic aromatic hydrocarbons (PAH). The growth of PAH continues through further reactions and by collisions and nucleation with each other forming larger PAH, becoming incipient soot particles. These particles continue to grow by processes of surface growth, condensation and coalescence, and through reactions with acetylene and smaller PAH, forming particulate matter (PM) < 50 nm in aerodynamic diameter, referred to as primary soot particles. Primary particles collide and coagulate forming PM ranging in size from hundreds of nanometers to microns. Oxidation continues throughout the combustion process, concurrently and within all stages of PM formation, consuming PAH, the growth species and soot particles comprising PM. Oxidation reactions occur by highly reactive radical species containing OH and oxygen atoms, forming primary combustion products, CO_2, H_2O, CO, NOx, unburned total hydrocarbons (THC) and smoke, an aerosol containing soot.

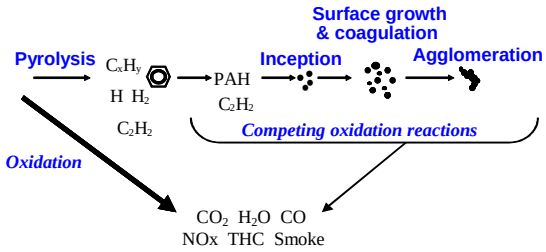

Figure 1: PM Formation Process

To investigate the reduction of PAH and PM due to oxygenates, ethylene fuel (C_2H_4) and ethanol (C_2H_5OH), as an additive, were burned in the Air Force Research Laboratory's Well-Stirred Reactor (WSR)[1-3], while samples were collected from the effluent and analyzed using the Particulate Matter Characterization and Monitoring System (PMCMS)[4]. This study was particularly well-suited for the WSR, which simulates the combustion process in the primary zone of a gas turbine combustor, while eliminating the effects of fuel atomization, evaporation, and mixing processes, and continues the work that was presented in Stouffer et al.[5].

The determination of the PAH and PM generated by the WSR is significant because fundamental information can be evaluated using the PMCMS, before particle inception occurs and after primary particle coagulation into PM. The PMCMS analyses were compared with a predictive model of PAH using UNsteady Ignition and COmbustion using ReactioNs (UNICORN)[6] code which provides quantification and identification of single and multi- ring aromatic hydrocarbons generated in a perfectly stirred reactor.

PM quantification is compared to analyses determined from captured soot and smoke stains, providing further verification of this useful approach and methodology for assessing the validity of experimental and computational results. These results are important for further investigations to determine particulate formation mechanisms, to develop combustion models of pollutant formation and to identify fuel additives to reduce particulate formation.

EXPERIMENTAL APPARATUS

Well-Stirred Reactor

A toroidal-shaped WSR research combustor with a volume of 250 mL was used for the study. A cross section of the reactor and jet ring is shown in Figure 2. The design is a modification of an earlier WSR design by Nenniger[1] and Zelina[2] and features an Inconel jet ring with 48 fuel/air jets. The upper and lower halves of the toroidal reactor are cast from silicon carbide. Silicon carbide was used because of its resistance to thermal cracking. The ceramic reactor is contained inside a steel housing, and has a 2-inch diameter stack connected to the exhaust port which forms the plug flow reactor (PFR) section. The jet ring is cooled by nitrogen impingement cooling to avoid autoignition of the fuel-air mixture within the jet ring manifold.

The two fuels used in the current study were neat ethylene and an ethylene-ethanol mixture with 5% of the fuel mass from the oxygen in the ethanol (14.4% ethanol by mass). With these fuels the WSR operates stably at high equivalence ratios ($1.8 < \phi < 2.6$), which allows measurement of PAH, particulates and smoke in a range of conditions from soot inception through the formation of carbonaceous soot.

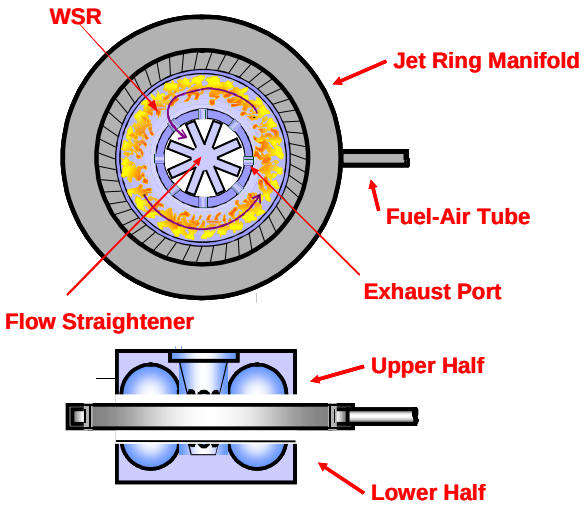

Figure 2: Schematic of WSR Design

Figure 3 is a photograph of the WSR rig during operation which also shows a sampling probe penetrating the exhaust stack, entering the plug flow region above the reactor. Gaseous emissions and smoke were drawn from the PFR section. A port at the bottom of the housing permits probe access to the reactor for obtaining emissions and smoke samples.

Figure 3: WSR Test Rig Burning Ethylene

Experimental Sampling Techniques

Soot samples were collected on filters from both the plug flow region 16 cm downstream of the WSR and from the inside of the toroidal WSR volume on paper or quartz filters by drawing the exhaust gas collected in the probe through the filters. The gas sample was first pulled through a 25 cm-long oil-cooled probe with an inside diameter of 0.47 cm. The probe was cooled to 150°C by circulating oil through the outer jacket. The gas then passed through an electrically heated (constant surface temperature of 150°C) 2-meter long sample line before passing into a Roseco engine smoke emissions sampler.

The volume of the sample gas collected for each test was 7.08 liters. Each sample required 30-60 seconds to collect. The samples acquired on the paper filters (Whatman #4) were analyzed using the SAE ARP1179 procedure[7] to determine the smoke number based on reflected light from the samples:

$$SN = 100\left(1 - \frac{R_s}{R_w}\right)$$

where: R_s= Reflectance of the stained filter
R_w= Reflectance of the unstained filter

The samples acquired on the quartz filters (Whatman type-QMA) were analyzed to determine carbon burn-off in a LECO carbon analyzer. The total carbon analyzer measures the carbon mass deposited on the filter by measuring the CO_2 produced while increasing the temperature of the filter in an oven in the presence of excess oxygen. An advantage of the carbon analyzer is that any inorganic deposits on the filter, caused by erosion of the reactor materials will be ignored in the analysis.

In addition to the carbon burn-off analysis, the quartz filter samples were also analyzed using gas chromatograph/mass spectrometry (GC/MS) Chromatoprobe[8] (Figure 4) analysis to determine the PAH content of the soot. This was performed by placing a 2-mg sample cut from the soot stained quartz filter into the sample vial inside the Chromatoprobe shown in Figure 5. The Chromatoprobe was then inserted into the temperature programmable injector (Figure 6) of the GC/MS, which was rapidly ramped in temperature (150°C/min) from 40 to 320°C. This resulted in the PAH's being thermally desorbed from the quartz filter paper and sequentially injected into the GC/MS for separation and detection.

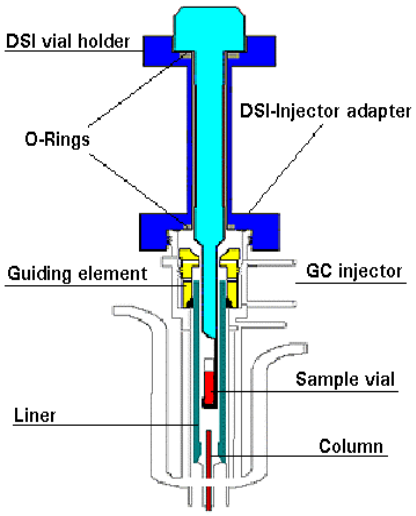

Figure 4: Varian Chromatoprobe

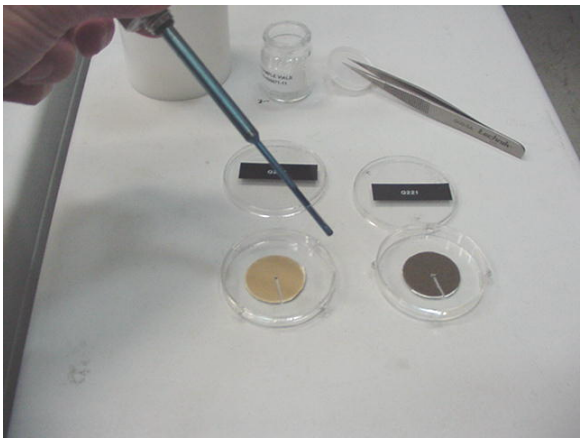

Figure 5: Chromatoprobe Sample

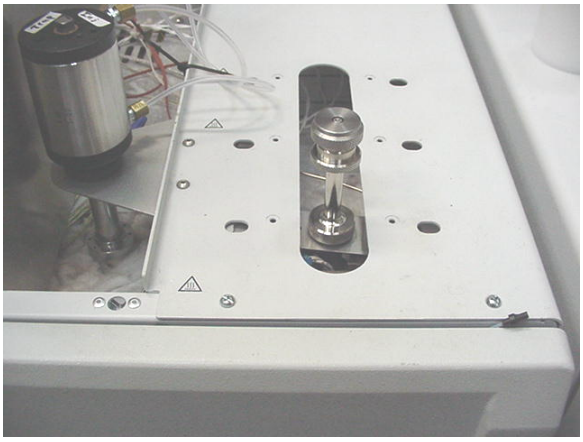

Figure 6: Chromatoprobe in GC/MS

Seventeen different PAH's identified during the Chromatoprobe analysis are listed in Table 1. Also listed are the target ions for each PAH, which are the most abundant ions from the mass spectrum of each PAH used for detection, along with the retention time, which is the time that the PAH is retained on the GC column before detected by the mass spectrometer. The retention time can be used to distinguish between PAH's with the same target ion.

Table 1. PAH Species Identified in the GC/MS Chromatoprobe Analysis

PAH	Target Ion (m/z)	Retention Time (min)
Naphthalene	128	5.367
Acenaphthylene	152	8.191
Acenaphthene	153	8.460
Fluorene	166	9.262
Phenanthrene	178	10.733
Anthracene	178	10.811
1,4-Diphenylbutadiyne	202	12.350
Fluoranthene	202	12.600
Pyrene	202	12.921
Benz [a] anthracene	228	14.899
Chrysene	228	14.951
Benzo [b] fluoranthene	252	16.809
Benzo [k] fluoranthene	252	16.846
Benzo [a] pyrene	252	17.344
Indeno [1,2,3-cd] pyrene	276	19.237
Dibenz [a,h] anthracene	278	19.653
Benzo [g,h,i] perylene	276	19.817

Emissions from the reactor section of the WSR were passed through a quartz filter to remove particulates and then trapped in a 250-mL gas sampling bulb. Gas samples were directly injected into the GC/MS for qualitative and quantitative analysis of combustion gas species. Seven trace combustion gas species were targeted for analysis and are shown in Table 2 along with their corresponding target ions and retention times.

Table 2. Combustion Gas Species Considered in the GC/MS Gas Analysis

Gas Species	Target Ion (m/z)	Retention Time (min)
1,3-Cyclopentadiene	66	0.400
Benzene	78	0.604
Toluene	91	1.094
Ethylbenzene	91	2.164
Phenylacetylene	102	2.485
Styrene	104	2.769
Naphthalene	128	7.980

Particulate and Emissions Measurement Instrumentation

The particulate instrumentation system is composed of a TSI 3022 condensation nuclei counter (CNC) and a sampling system using a vacuum pump to control sample flow through a 10 L/min flow meter and transmitter. This combination of Brooks flow meters is used to set accurate dilution air flows to the particulate sampling probe. The CNC and sampling system are configured to adapt to the PMCMS, shown in Figure 7, used to evaluate particulate species and PAH.

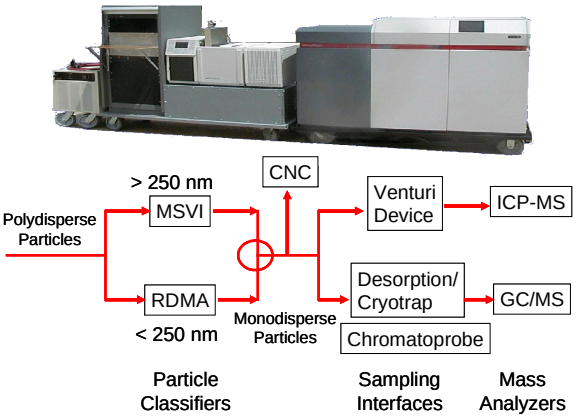

Figure 7: PMCMS and Schematic

Particle size below 250 nm was characterized using the Radial Differential Mobility Analyzer (RDMA)[9] within the PMCMS, shown in Figure 8.

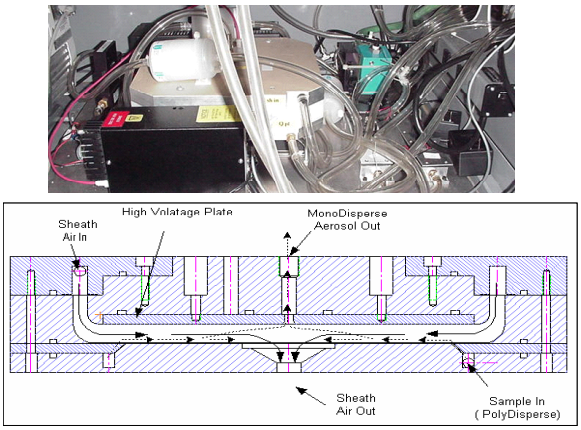

Figure 8: RDMA

Particle sizing is achieved by charging a polydisperse stream of aerosols and passing the stream through a well defined electric field. Charged particles within the aerosol will follow predetermined trajectories. The RDMA is designed to extract aerosols that follow one predetermined trajectory, while discarding all others. The particle number density was determined using the CNC sampling from the PFR in the WSR. A short stack configuration was used to minimize the PFR region for obtaining particulate, smoke and soot measurements close to the reactor. The sample from the PFR was extracted from a region 7 cm upstream of the PFR exit to capture the rich exhaust products before they could react with the ambient air.

The emissions system consists of a 150°C oil-cooled emissions probe and a 150°C heated sampling line that is 6.1 m long. The sample stream is then split into two streams. The first stream directly enters a flame ionization detector total hydrocarbon analyzer, while the second stream enters an Alpha Laval chiller, which provides the main sampling pump, condenses water vapor from the gas sample and sets the sample flow for the CO, CO_2, O_2 and NO_x analyzers. The analyzers are calibrated before each test using 2% certified standard gases and often spanned for verification of ~3% accuracy during the tests, using several calibration gas mixtures to check drift and maintain linearity.

TEST CONDITIONS

The air flow for the experiments was set at a constant 240 g/min with an inlet temperature set at 392 +/- 5K. The fuel/air equivalence ratio, ϕ, ranged from 1.9 to 2.6 for both fuels. The pressure inside the reactor section ranged from 1.1 to 1.7 kPa above the

ambient pressure for all of the experiments. The average residence time in the reactor, τ, which was calculated using: $\tau=\rho V/(m_a+m_f)$, was 9.7 +/- 0.3 ms for the experiment.

The gas temperature inside the reactor (uncorrected for the effects of radiation) ranged from 1480 to 1725 K. The temperatures are significantly lower than the adiabatic flame temperatures because of heat loss through the high-conductivity silicon carbide reactor walls to the nitrogen flow that is used to cool the jet ring.

EXPERIMENTAL RESULTS

The particle size distributions sampled from the plug flow region of the reactor are shown in Figure 9 for both the neat ethylene and the ethylene-ethanol mixtures over a range of ϕ from 2.0 to 2.6. The ethylene-ethanol mixture was shown to reduce particle concentration at all ϕ compared to the neat ethylene fuel. The highest particle concentrations for ethylene and the ethylene-ethanol were measured at ϕ = 2.4 and ϕ = 2.3, respectively.

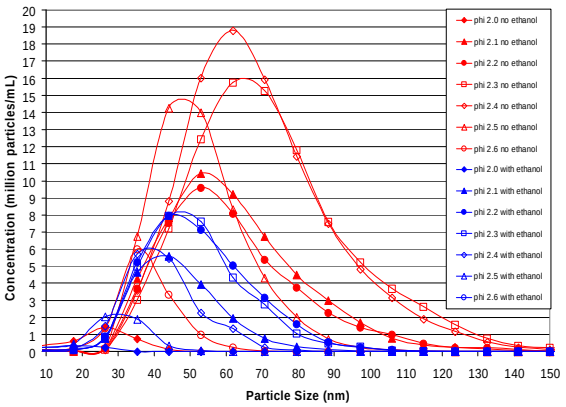

Figure 9: Particle Size Distribution

The diameter of the peak particle concentration for the size distributions is shown in Figure 10. The peak particle size increases as ϕ is increased from 1.9 to 2.3 for both fuels. As ϕ is further increased the peak particle size decreases. The ethylene-ethanol fuel resulted in smaller peak particle sizes compared to the ethylene fuel over the entire range of test conditions.

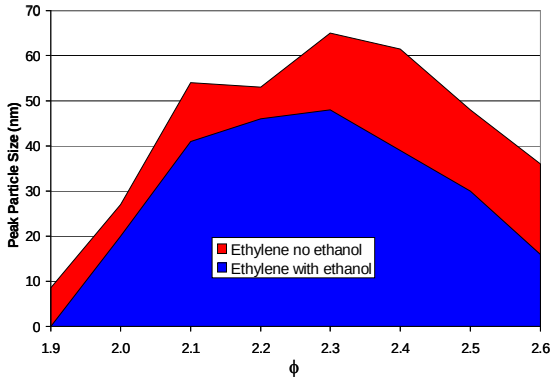

Figure 10: Peak Particle Size

The total particle concentration was calculated by integrating the area under the particle distribution curves for each ϕ, shown in Figure 11. The addition of ethanol resulted in a reduction in the total particle concentration measured over the entire range of ϕ tested. The bottom half of Figure 11 shows the stained quartz filters after the samples were acquired for both the neat ethylene fuel (top row) and ethylene-ethanol mixtures (bottom row) in order of increasing ϕ from left to right. The filter stains for both fuels are darker as ϕ is increased from 1.9 to 2.2 and then lightens as ϕ is further increased. For all ϕ the stains are darker for the ethylene fuel than they are for the ethylene-ethanol fuel.

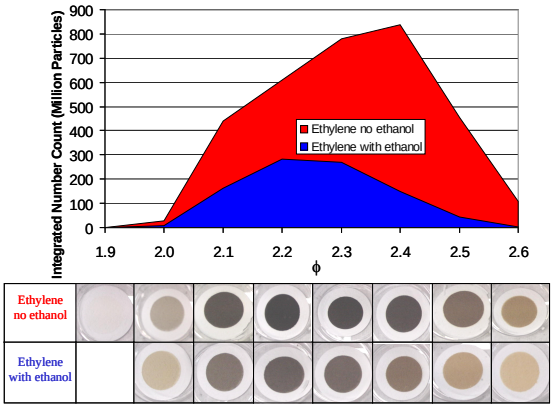

Figure 11: Total Particle Count (Top) and Corresponding Images of Filters from the Plug Flow Region (Bottom)

The GC/MS chromatogram resulting from direct injection of 500 µL of gas sampled from the WSR for a typical test is shown in Figure 12. Benzene was the most concentrated gaseous species detected followed by 1,3-cyclopentadiene and a series of other soot

precursors, whose structures are shown in the figure. These results were similar to those found by Lam et al.[10], where benzene was measured in highest concentration, followed by phenylacetylene, naphthalene, toluene and styrene. The mass chromatogram was magnified 100 times from 10.0-14.0 minutes to show the presence of trace PAH's in this range.

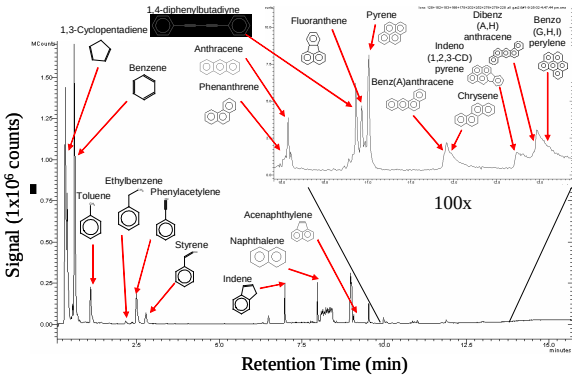

Figure 12: GC/MS Gas Analysis from WSR

A calibration curve was prepared for benzene by injecting 500 µL aliquots of benzene vapor at varying concentrations from a static dilution bottle. The mass of benzene per 500 µL sampled from the WSR is plotted for each ϕ, shown in Figure 13. The concentration of benzene increases linearly with increasing ϕ. The addition of ethanol resulted in no change in benzene content. All other gaseous soot precursors detected indicated a similar trend as benzene.

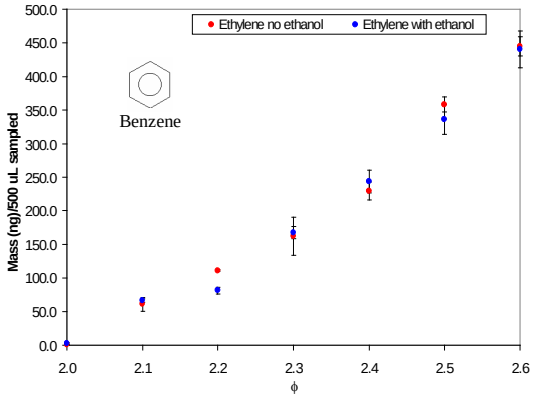

Figure 13: Benzene Concentration Sampled from the WSR

Figure 14 shows the smoke number measured from filter samples extracted from both the reactor and the plug flow section. For both fuels, the smoke number initially increases between ϕ = 1.9 and 2.2-2.3, and starts to decrease as ϕ is increased further. Although there is more fuel available for the formation of soot at higher ϕ, it is thought that the soot production is reduced due to decreasing temperatures and thus slower chemical reaction times. Note that the smoke number measured in both the reactor section and the plug flow regions are approximately equal for the same fuel at the same reactor conditions for ϕ < 2.4. As the fuel flow is further increased, the smoke number is seen to be lower in the reactor section than it is in the PFR.

The addition of ethanol results in a reduced smoke number for all ϕ measured, with the greatest reduction shown at ϕ = 2.2 and 2.3. This trend is different from the one observed previously in the study by Stouffer et al.[5] where the addition of ethanol was seen to slightly increase the soot production. However, it should be noted that the temperature inside the reactor in the previous study was higher (by approximately 110°C) than the reactor temperature in the current study because lower thermal conductivity ceramics were used for the wall materials in the previous study. It is thought that the combustion temperatures significantly affect the soot production mechanism.

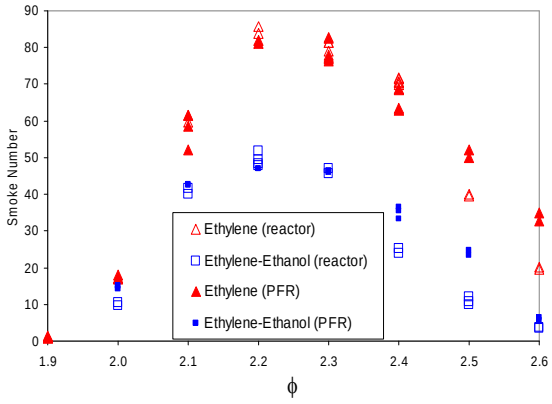

Figure 14: Smoke Number Results

Figure 15 shows total carbon analysis of the quartz filter samples extracted from both the reactor section and the plug flow sections of the WSR. The overall shape of the integrated carbon mass plot shown in Figure 15 shows trends similar to those shown for the smoke number plots in Figure 14. A significant difference is that there was an increase in the total carbon mass between the reactor and the plug flow section. The addition of ethanol decreases the

amount of carbon deposited on the quartz filters for all ϕ measured.

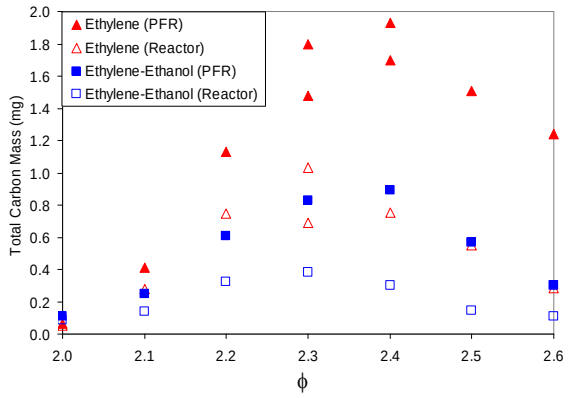

Figure 15: Total Carbon Mass

The relative carbon count plotted with increasing temperature for three equivalence ratios (ϕ = 2.1, ϕ = 2.3, and ϕ = 2.6) are shown in Figures 16A, 16B, and 16C, respectively, along with corresponding photographs of the filters before the carbon analysis was conducted. These figures show two distinct peaks, a low temperature peak located between 120 and 160°C, and a high temperature peak located between 450 and 560°C. The sample for the highest equivalence ratio (ϕ = 2.6 in Figure 16C) has the highest carbon content in the low temperature region and the filter stain is beige-colored while the high temperature carbon peak is highest for the ϕ = 2.3 case, shown in Figure 16B, which shows a much darker filter stain. It is thought that the low temperature peak is due to the presence of PAH's while the high temperature peak is due to the presence of carbonaceous soot.

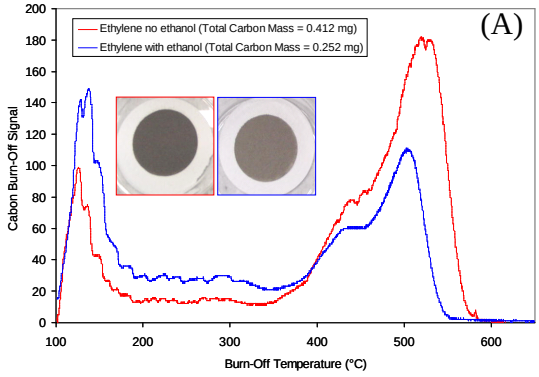

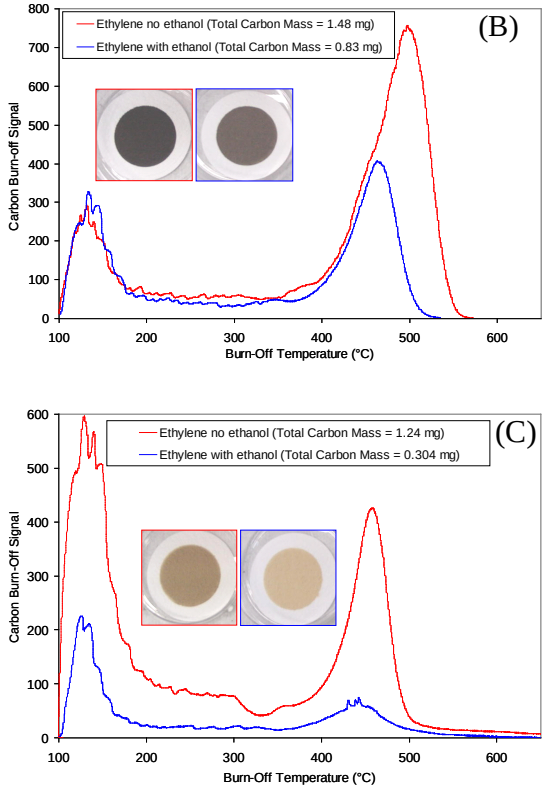

Figure 16: Carbon Vs. Filter Temperature, A (ϕ = 2.1), B (ϕ = 2.3), and C (ϕ = 2.6)

The chromatogram in Figure 17 was obtained from the GC/MS Chromatoprobe analysis of the particulate matter deposited on the quartz filters. Pyrene which is a known soot precursor was shown to be the most concentrated PAH detected and correlates well with total PAH content. Similar results were found by Lam et al.[10], where they saw large concentrations of acenaphthene, pyrene, and phenanthrene in the WSR plug-flow section.

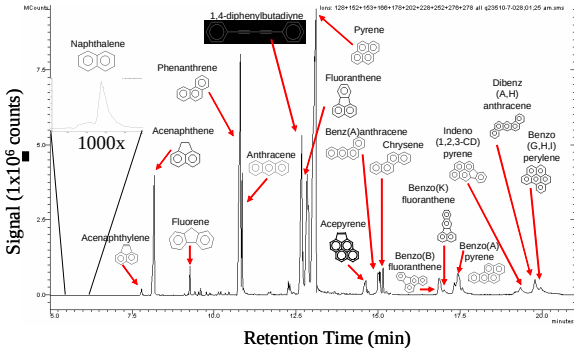

Figure 17: GC/MS Chromatogram of Species Thermally-Desorbed from Filter Samples

Pyrene concentration was determined from Chromatoprobe GC/MS analysis of quartz filters sampled at equivalence ratios (ϕ = 2.0 to 2.6). The concentration curve, Figure 18, follows a similar trend as the curve for total particle counts in Figure 11, indicating a relationship between pyrene and soot production - worthy of further examination. The addition of ethanol reduces the amount of pyrene deposited on the filters for ϕ > 2.2.

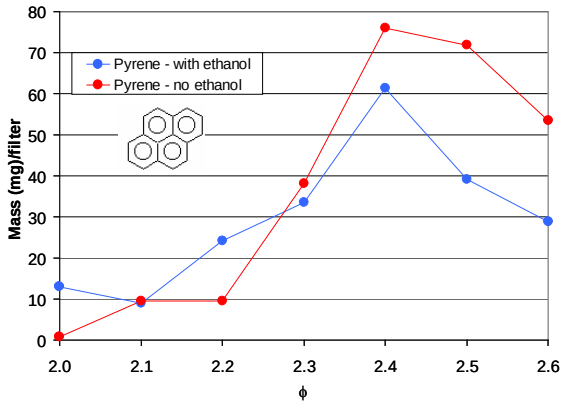

Figure 18: Pyrene Concentration

MODELING OF WSR FLOW

A time-dependent, axisymmetric mathematical model known as UNICORN[6,11] is developed to simulate the PAH's growth in unsteady flames. It solves for u- and v-momentum equations, continuity, and enthalpy- and species-conservation equations on a staggered-grid system. A detailed chemical-kinetics model of Wang and Frenklach[12] is incorporated in UNICORN for the investigation of PAH formation in acetylene and ethylene flames. It consists of 99 species and 1066 elementary-reaction steps. Thermo-physical properties such as enthalpy, viscosity, thermal conductivity, and binary molecular diffusion of all the species are calculated from the polynomial curve fits developed for the temperature range 300 – 5000 K. Molecular diffusion is assumed to be of the binary-diffusion type, and the diffusion velocity of a species is calculated using Fick's law and the effective-diffusion coefficient of that species in the mixture. A simple radiation model based on optically thin-media assumption was incorporated into the energy equation. Only radiation from CH_4, CO, CO_2, and H_2O was considered in the present study[13].

The finite-difference forms of the momentum equations are obtained using an implicit QUICKEST scheme, and those of the species and energy equations are obtained using a hybrid scheme of upwind and central differencing[11]. At every time-step, the pressure field is accurately calculated by solving all the pressure Poisson equations simultaneously and utilizing the LU (Lower and Upper diagonal) matrix-decomposition technique.

The WSR flow was modeled by assuming it as uniformly (in cross section) reacting gas flowing through a tube having a diameter and length of 51 and 150 mm, respectively. The formation of flame in the swirl section is highly three-dimensional and is not modeled in the present study, even though, it is believed to have significant influence on the generation of certain PAH species. These assumptions forced the model to make use of the prescribed temperature profile as input condition. The temperature distribution for each case along the length of the straight section of the WSR is constructed from the measurements made in the swirl section. A temperature drop of 100 K was assumed between the swirl and probe (150 mm) locations. Steady state calculations are performed for each case and the results are compared with the measurements in Figure 19.

The model predicts the CO concentration well, and over predicts the concentrations of stable species such as CO_2 (Figure 19A). As the model proved to predict CO_2 reasonably well in other systems such as burner-stabilized flames[14], the discrepancy noted in the present work could be attributed to the assumptions made in for the WSR flow. A good comparison between the predictions and measurements is obtained for benzene and acenaphthylene (Figure 19B). Note, samples of benzene were extracted from the reactor in gas phase while that of acenaphthylene were obtained in solid phase. On the other hand, the model seems to under predict the concentrations of heavier PAH species (Figure 19C). It is known that the inception of PAH species starts in the low temperature (~1200 K) region on the fuel side. Since the present model for WSR completely ignores the flame formation in the swirl section, prediction of lower amounts of PAH's should be expected.

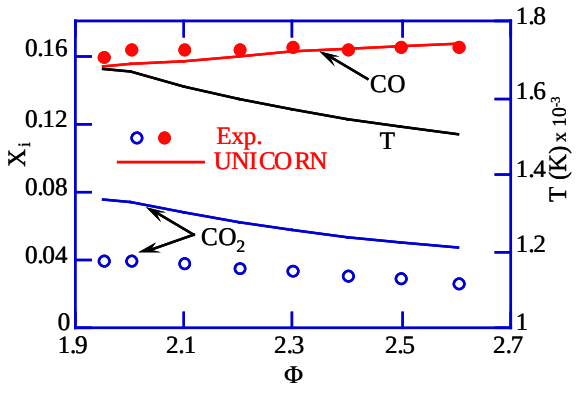

(A)

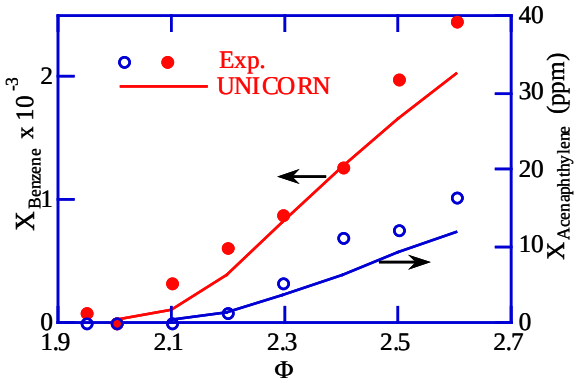

(B)

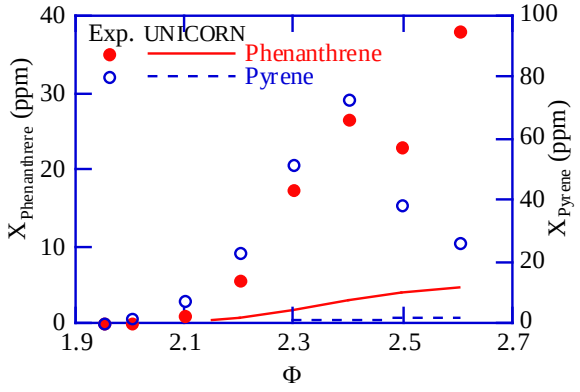

(C)

Figure 19: Predicted and Measured Species concentrations for Ethylene-Air Mixtures (A) Major species, (B) Benzene and Acenaphthylene, (C) Phenanthrene and Pyrene.

SUMMARY AND CONCLUSIONS

Experimental results from fuel-rich ethylene-air and ethylene-ethanol-air mixtures, where ethanol (5% of mixture) was used as a particulate reducing additive, were obtained using a WSR research combustor.

It was found that:

1. The PMCMS is capable of measuring particle size, particle distribution, and detailed chemical analysis of combustion products.
2. Particle count was reduced by 60% and peak particle size was reduced by 30% with ethanol addition to ethylene-air mixtures.
3. Large concentrations of benzene were found in the WSR, which increased linearly with increasing equivalence ratio. The benzene concentration was independent of additive addition.
4. A maximum 40% decrease in smoke number was observed with ethanol addition, with the maximum reduction occuring at $2.3 < \phi < 2.6$.
5. Carbon analysis of filter samples indicated two distinct carbon burn-off peaks attributed to PAH and carbonaceous soot deposits. These peaks shift in magnitude and temperature depending on the stoichiometry.
6. Pyrene was found to be a major PAH species, which correlates well with soot production.
7. These results suggest that pyrene, benzene and other PAH's can be used to predict soot formation in modeling and simulation routines for more complex practical combustion systems.

FUTURE RESEARCH PLANS

The WSR has been modified with the capability to vaporize heavier-hydrocarbon fuels such as heptane, toluene and JP-8 jet fuel. These pure compounds and practical fuels will be tested with various fuel additives to investigate soot mitigation processes. Long-term plans include the ability to predict soot formation in practical combustion systems by using detailed chemistry of soot precursors and the analysis of particle chemical content as a function of particle size.

ACKNOWLEGEMENTS

The authors are grateful for the contributions of the following personnel: Mr. Mike Arstingstall for his assistance with rig set-up, fabrication, assembly and test of the WSR, Mr. Richard Striebich for his assistance with the Chromatoprobe analysis, Mr. Ed Strader for assembly and set-up of the PMCMS, Dr. Matt Dewitt and Mr. David Brooks for the carbon burn-off analysis. The second author gratefully acknowledges the support of the Air Force through contract #F33615-97-C-2719.

REFERENCES

1. Nenniger, J. E., Kridiotis, A., Chomiak, J., Longwell, J. P., and Sarofim, A. F., "Characterization of a Toroidal Well Stirred Reactor," Twentieth Symposium (International) on Combustion, The Combustion Institute, pp. 473-479, 1984.

2. Zelina, J., "Combustion Studies in a Well-Stirred Reactor," Ph.D. Thesis, University of Dayton, Dayton, OH, 1995.

3. Zelina J. and Ballal, D. R., "Combustion Studies in a Well Stirred Reactor," AIAA Paper No. 94-0114, 1994.

4. "Development of a Particulate Matter On-Line Real Time Physical and Chemical Characterization and Monitoring System (PMCMS)," Final Report, SBIR Phase II, Contract No. F08637-99-C-6001, Deposition Research Laboratory Inc. Document No. 063001-01, 30 June 2001.

5. Stouffer, S. D., Streibich, R. C., Frayne, C. W., and Zelina, J., "Combustion Particulates Mitigation Investigations in a Well-Stirred Reactor," Paper No. AIAA 2002-3723, 38th Joint Propulsion Conference, 2002.

6. Roquemore, W. M. and Katta, V. R., "Role of Flow Visualization in the Development of UNICORN," *Journal of Visualization*, 2:257, 2000.

7. Society of Automotive Engineers (SAE), Aerospace Recommended Practice, "Aircraft Gas Turbine Engine Exhaust Smoke Measurement," *ARP 1179 Rev. C*, 1997.

8. Klosterman, J. R., Striebich, R. C. and Rubey, W. A., "Direct Thermal Desorption of Combustion Residues by GC-MS," Pittcon Paper No. 1034, New Orleans, LA, 5-8 March 2001.

9. Olson, D. D., Reed, X. B., and Whitefield, P. D., "The Design and Characterization of the Radial Differential Mobility Analyzer," Opportunity for Undergraduate Research Experience Final Report, University of Missouri-Rolla, 1998.

10. Lam, F. W., Howard, J. B., and Longwell, J. P., "The Behavior of Polycyclic Aromatic Hydrocarbons During the Early Stages of Soot Formation," Twenty-Second Symposium (International) on Combustion, The Combustion Institute, pp. 323-332, 1988.

11. Katta, V. R., Goss, L. P., and Roquemore, W. M., "Numerical Investigations of Transitional H_2/N_2 Jet Diffusion Flames," *AIAA Journal*, Vol. 32, No. 1, pp. 84-94, 1994.

12. Wang, H., and Frenklach, M., "A Detailed Kinetic Modeling Study of Aromatic Formation in Laminar Premixed Acetylene and Ethylene Flames," *Combustion and Flame*, Vol. 110, No. 1, p.173, 1997.

13. Annon., Computational Submodels, International Workshop on Measurement and Computation of Turbulent Nonpremixed Flames., http://www.ca.sandia.gov/tdf/Workshop/Submodels.html, 2001.

14. Katta, V. R., Blevins, L. G., and Roquemore, W. M., "PAH Formation in an Inverse Flame," AIAA Paper No. 2003-0666, Reno, NV, 6-9 January 2003.

W. Class- and Structure-Specific Separation, Analysis, and Identification Techniques for the Characterization of the Sulfur Components of JP-8 Aviation Fuel

Class- and Structure-Specific Separation, Analysis, and Identification Techniques for the Characterization of the Sulfur Components of JP-8 Aviation Fuel

Dirk D. Link,* John P. Baltrus, and Kurt S. Rothenberger

U.S. Department of Energy, National Energy Technology Laboratory, 626 Cochrans Mill Road, P.O. Box 10940, Pittsburgh, Pennsylvania 15236

Paul Zandhuis

NETL Site Support Contractor, Parsons Project Services, Inc., P.O. Box 618, South Park, Pennsylvania 15129

Donald K. Minus

Air Force Research Laboratory, Propulsion Directorate, Wright−Patterson Air Force Base, WPAFB, Ohio 45433-7103

Richard C. Striebich

University of Dayton Research Institute, Dayton, Ohio 45469-0132

Received April 4, 2003. Revised Manuscript Received June 25, 2003

Methods have been described for separating the sulfur content of aviation fuels into chemical classes for identification and quantitation. These separation methods simplified the fuel matrix, which allowed non-element-specific detection methods, such as mass spectrometry (MS), to be used for sulfur detection. These matrix simplification methods also enhanced the ability of element-specific detection methods, such as atomic emission detection (AED), to identify sulfur species that are present in the fuel. Separation of a model fuel mixture, as well as several representative aviation fuels, was performed using several different methods, including class-specific chemical oxidation methods that used iodine and another that used hydrogen peroxide, and a polarity-based separation that used a polar high-pressure liquid chromatography (HPLC) column. Following separation, sulfur concentration was quantified into "reactive" and "non-reactive" classes, on the basis of the ease of transformation of the species, using chemical oxidation procedures, which also relates to the tendency for the species to undergo typical hydrodesulfurization reactions with hydrogen. These two classes were broken down further, with sulfur compounds being classified as thiol, sulfides and disulfides, thiophenes, benzothiophenes, or dibenzothiophenes. The separation and identification methods proved to be robust and transferable; the results from two independent laboratories were in good agreement. Sulfur in the jet fuels tested in this study appeared mainly as thiols, sulfides, and disulfides, as determined by gas chromotography−atomic emission detection (GC−AED), following the chemical oxidation procedures. Of the refractory sulfur compounds, benzothiophenes comprised the majority, as determined by GC−MS following the (HPLC) fractionations. Thiophenes and dibenzothiophenes contributed minor amounts to the total concentration of refractory sulfur compounds. Two main components of the benzothiophene class were identified to be 2,3-dimethyl benzothiophene and 2,3,7-trimethyl benzothiophene.

Introduction

The sulfur content of distillate fuels continues to come under more stringent regulation by the U. S. Environmental Protection Agency (EPA) and other environmental regulatory agencies worldwide. Of primary concern is the sulfur poisoning of advanced automotive catalysts that are used to reduce emissions of pollutant hydrocarbons, carbon monoxide, and nitrogen oxides from gasoline- and diesel-fueled vehicles. Sulfur emissions from the combustion of a wide range of distillate fuels also present environmental concerns, because they contribute to acid rain.[1−8] Tier II sulfur regulations

* Author to whom correspondence should be addressed. E-mail: dlink@netl.doe.gov.

(1) Mossner, S. G.; Wise, S. A. *Anal. Chem.* **1999**, *71*, 58−69.
(2) Sinninghe Damste, J. S.; Van Dalen, A. C. K.; de Leeuw, J. W.; Schenck, P. A. *J. Chromatogr. A* **1988**, *435*, 435−452.
(3) Lee, M. L.; Willey, C.; Castle, R. N.; White, C. M. *Proceedings of the Fourth International Symposium on Polynuclear Aromatic Hydrocarbons*; Battelle Press: Columbus, OH, 1979; pp 59−73.

10.1021/ef0300747
Published on Web 07/26/2003

mandate that sulfur levels in gasoline be reduced from the current level of 300 ppm to 30 ppm by 2004, whereas sulfur levels in on-road diesel fuel must be reduced from 500 ppm to 15 ppm by 2006.[9−11]

The next transportation fuel that may likely be subjected to more-stringent sulfur regulations is aviation fuel, which currently has a total sulfur limit of 3000 ppm. Anticipation of lower limits for sulfur in aviation fuels has raised several concerns, with respect to how the fuel will behave under the high stresses that the fuel typically encounters, as well as the performance of engines that are powered by this fuel. In advanced aircraft that are used in military applications, jet fuel is used as a heat-exchange fluid to cool the airframe, engines, and avionics. Under the stress of high temperature, jet fuel can form oxidative deposits as the fuel thermally degrades. These carbonaceous deposits can decrease fuel flow, which, in turn, can lead to severe degradation of aircraft performance, loss of airframe subsystems, and even catastrophic failure of jet engines. Previous research has shown that the formation of thermal deposits is greatly affected by the sulfur concentration of the fuel.[12−14] Other fuel characteristics, such as lubricity and storage stability, are also dramatically affected by the amount of sulfur in the fuel, in both positive and negative ways.[15]

Simultaneous with jet engine development, the chemical composition of petroleum-derived jet fuels has been studied in an attempt to understand how the chemical composition of the fuel affects engine performance. As a result of those studies, the formation of deposits in jet fuels under thermal stress has been associated with the presence of reactive sulfur species such as thiols, sulfides, and disulfides. Just as deposit formation can be attributed to certain classes of sulfur compounds, the ease of removal of sulfur compounds from distillate fuels is also class dependent. For example, under certain conditions for hydrodesulfurization, the most reactive and easiest-to-remove classes of sulfur compounds are thiols, sulfides, and disulfides; compounds such as substituted benzothiophenes and dibenzothiophenes are more difficult to remove.[1,3,6,16−18] Therefore, it may be practical to alter fuel performance by targeting the removal of certain classes of sulfur compounds.

Before conducting additional studies to link the structure and reactivity of sulfur compounds in jet fuel, methods must be developed for determining the concentrations of individual classes of sulfur compounds, along with further identification of the individual components that comprise these classes. The methods must be robust enough to determine trace levels of sulfur components within a large hydrocarbon matrix. Although methods currently exist for measuring the total sulfur and thiol/mercaptan sulfur concentration of distillate fuels, routine methods for measuring the total nonreactive and reactive sulfur species in those fuels may be more informative. Although regulatory requirements only necessitate quantification of the total amount of sulfur present, it is clear that speciated sulfur information is necessary for a better understanding of the fuel properties and performance characteristics.

The analysis of sulfur in aviation fuel and other transportation fuels has been performed with both specific and universal detectors. The use of gas chromatography (GC) with sulfur-specific detectors, such as atomic emission detection (AED) and flame photometric detection (FPD), as well as the Hall detector, is well documented for isolation of individual sulfur components in distillate fuels.[1,7,19−23] Sulfur-specific detection allows for simplification of the fuel chromatogram by detection of only the hydrocarbons that contain sulfur. However, assignment of the peaks in the sulfur chromatogram to individual sulfur-containing species is still complicated and laborious, because it necessitates a comparison of the retention times of hundreds of sulfur compound peaks with those of known standards of appropriate purity. If the matrix effects from the hydrocarbon sample can be eliminated by other means, it may be more convenient to use a universal detection method, such as mass spectrometry (MS), to identify unknown sample components.[24,25] Separating the target analytes from the matrix also may enhance the capabilities of the other detectors.

Giddings[26] and others involved in multidimensional separations recognized that separation power need not be limited to one technique. Liquid chromatography−gas chromatography (LC−GC), supercritical fluid extraction−gas chromatography (SFE−GC), and other sample preparation techniques that are combined with GC are appropriate and powerful applications of multidimensional separations.[27] The work described herein includes a preseparation procedure that uses high-pressure liquid chromatography (HPLC) to isolate some of the important sulfur-containing species in jet fuels for mass spectral interpretation. The work also includes other wet chemical methods for class-specific separation and quantitation of sulfur species in jet fuels. The recovery of sulfur compounds from these wet chemical

(4) Ma, X.; Sakanishi, K.; Isoda, T.; Mochida, I. *Fuel* **1997**, *76*, 329−339.
(5) Ma, X.; Sun, L.; Yin, Z.; Song, C. *Prepr. Pap.—Am. Chem. Soc., Div. Fuel Chem.* **2001**, *46*, 648−649.
(6) Lamure-Meille, V.; Schulz, E.; Lemaire, M.; Vrinat, M. *Appl. Catal. A* **1995**, *131*, 143−157.
(7) Bradley, C.; Schiller, D. J. *Anal. Chem.* **1986**, *58*, 3017−3021.
(8) Andersson, J. T. *J. Chromatogr. A* **1986**, *354*, 83−98.
(9) *Fed. Regist.* **1997**, *62*, 37337.
(10) *Fed. Regist.* **1999**, *64*, 26055.
(11) *Fed. Regist.* **2000**, *65*, 6698−6869.
(12) Taylor, W. F. *Ind. Eng. Chem. Res.* **1968**, *7*, 198−202.
(13) Taylor, W. F. *Ind. Eng. Chem. Res.* **1974**, *13*, 133−138.
(14) Kauffman, R. E. *J. Eng. Gas Turb. Power* **1997**, *119*, 322−327.
(15) Mushrush, G. W.; Beal, E. J.; Slone, E.; Hardy, D. R. *Energy Fuels* **1996**, *10*, 504−508.
(16) Shafi, R.; Hutchings, G. J. *Catal. Today* **2000**, *59*, 423−442.
(17) Knudsen, K. G.; Cooper, B. H.; Topsoe, H. *Appl. Catal. A* **1999**, *189*, 205−215.
(18) Stumpf, A.; Tolvaj, K.; Juhasz, M. *J. Chromatogr. A* **1998**, *819*, 67−74.
(19) Ronkainen, P.; Denslow, J.; Leppanen, O. *J. Chromatogr. Sci.* **1973**, *11*, 384−390.
(20) Andersson, J. T.; Schmid, B. *J. Chromatogr. A* **1995**, *693*, 325−338.
(21) Albro, T. G.; Dreifuss, P. A.; Wormsbecher, R. F. *J. High Resolut. Chromatogr.* **1993**, *16*, 13−17.
(22) Depauw, G. A.; Froment, G. F. *J. Chromatogr. A* **1997**, *761*, 231−247.
(23) Quimby, B. D.; Giarrocco, V.; Sullivan, J. J.; McCleary, K. A. *J. High Resolut. Chromatogr.* **1992**, *15*, 705−709.
(24) Anderson, S.; Garver, J.; Rubey, W. A.; Striebich, R. C.; Grinstead, R. Presented at the 17th International Symposium on Capillary Chromatography and Electrophoresis, Wintergreen, VA, 1995.
(25) Rubey, W. A.; Striebich, R. C.; Dellinger, B. Presented at the 20th International Symposium on Capillary Chromatography, Riva del Garda, Italy, 1998.
(26) Giddings, J. C. *Anal. Chem.* **1984**, *56*, 1258A.
(27) Herschfeld, T. *Anal. Chem.* **1980**, *52*, 298A−312A.

Table 1. Conditions Used for Sulfur-Specific Analysis of Class-Separated Samples by GC−AED

	laboratory 1	laboratory 2
column	DB-1701 (Supelco); 30 m, 0.32 mm i.d., 1.0 μm df; 14% cyanopropylphenyl, 86% dimethylpolysiloxane	Rtx-1 (Restek); 30 m, 0.32 mm i.d., 4.0 μm df; 100% dimethylpolysiloxane
inlet	helium carrier, 17 psi head pressure (constant), 280 °C inlet temperature;1 μL injection volume, 20:1 split ratio	
oven	40 °C for 1 min, 40 °C to 250 °C @ 2.0 °C/min	
detector	sulfur emission, 181 nm; transfer line, 280 °C makeup gas, 100 mL/min; cavity temperature, 280 °C	

methods was explored, and potential losses of target species during the oxidation steps were identified. In addition, standards bracketing and the retention times of standard sulfur compounds are used to identify the major components of jet fuels, as measured by GC−AED. The standards bracketing method allows a higher degree of accuracy for class determinations than a simple subtraction of "before and after" sulfur chromatograms. Simple subtraction of full chromatograms would introduce significant errors in sulfur determinations, because oxidized sulfur species that are not completely removed by the chemical process would appear in the chromatogram, which would bias the results.

The advantages of these methods include the ability to separate the sulfur components in a jet fuel (JP-8) on the basis of structural class and/or ring number, allowing both sulfur-specific and universal detection methods to be used. The methods also allow the identification of several of the major individual sulfur compounds within these classes. This work provides a more comprehensive collection of methods for initially elucidating the identity and concentration of sulfur compounds that are present in jet fuel, to enable future studies that will link the sulfur-compound structure to fuel properties and reactivity.

Experimental Section

Samples. The samples used in this study were various Jet A and Jet A-1 fuels that have undergone different degrees of hydrotreatment. Therefore, the fuels are representative of jet fuels that may be encountered under actual scenarios, with sulfur concentrations ranging from high sulfur concentrations (>1300 ppm) to lower sulfur concentrations (<400 ppm). A standard reference material—SRM 1616a, sulfur in kerosene (NIST, Gaithersburg, MD)—was used to verify calibration.

A model mixture of sulfur compounds in fuel was prepared by spiking known amounts of several pure sulfur-containing compounds into a zero-sulfur kerosene. The mixture contained thiols, sulfides, disulfides, thiophenes, and benzothiophenes at a relatively low total sulfur level of ~165 μg/mL (see Table 4, presented later in this work). A portion of this mixture was diluted in zero-sulfur kerosene to yield a second standard that had a total sulfur content of ~83 μg/mL. These standard mixtures were used to evaluate the completeness of removal of the target species by the class-selective oxidation procedures.

Wet Chemical Class Separations. To characterize specific classes of sulfur compounds in the fuel samples, a procedure by Stumpf et al. was utilized.[18] The method was slightly modified to include retention indices, to distinguish the sulfur classes. In this procedure, sulfur class type is determined by oxidizing the reactive sulfur species, thiols, sulfides, and disulfides, followed by analysis of the sulfur-containing compounds by GC−AED. Thiols in the fuel are selectively oxidized with iodine, and subsequent phase separation leaves the original sulfides and thiophenic compounds untouched. Hydrogen peroxide selectively oxidizes the thiols, sulfides, and disulfides to form sulfonic acids and sulfones, which are removed by phase separation, leaving the thiophenic compounds unreacted.

Briefly, for the iodine oxidation, 3 mL of each fuel was mixed with 3 mL of iodine solution (0.32 g of I_2 in 8 mL of acetone). After periodic shaking for 10 min at room temperature, 2 mL of sodium thiosulfate solution (0.8 g of $Na_2S_2O_3$ in 10 mL of 0.05 M NaOH) was added. Phases were separated, and the fuel layer was washed four times with 2-mL portions of 18 MΩ·cm water. For the peroxide oxidation, 3 mL of 30% H_2O_2 was added to 3 mL of the fuel, along with 1 mL of acetic acid and 1 mL of acetone. The mixture was maintained at 60 °C for 1 h and was vigorously shaken periodically. Phases were separated, and the fuel layer was washed four times with 2-mL portions of 18 MΩ·cm water. More specific procedural details are available in the literature.[18]

Sulfur analyses of raw fuels and oxidized fractions were conducted in two different laboratories. One laboratory used a Hewlett−Packard model HP-5890 gas chromatograph that was equipped with an auto-sampler (Agilent, model 7673 ALS) that was coupled to an atomic emission detector (Agilent, model 2350A). The other laboratory used an Agilent model 6890A gas chromatograph with an Agilent model 7683 ALS auto-sampler, coupled to an Agilent model 2350A atomic emission detector. The details for chromatographic separation and emission detection are given in Table 1.

For instrument calibration, a three-component standard mixture was prepared by dissolving three different sulfur compounds, each at different concentrations, in sulfur-free kerosene (Fisher Scientific). Portions of this three-component mixture were further diluted with sulfur-free kerosene to create two additional calibration mixtures. Each mixture was injected, thus performing external calibration for a range of nine different sulfur concentrations using only three injections. This technique has been previously described and verified.[28] All calibration mixtures, standard reference materials, and fuel samples were injected and analyzed according to the details given in Table 1.

Standards Bracketing Method. The retention information gained from hydrocarbon standards was used to segment the different sulfur-containing classes that are present in the fuels. To determine their retention times, the following bracketing standard compounds were injected into the GC−AED system: benzene, naphthalene, phenanthrene, and chrysene. Conditions were as given in Table 1, except that, unlike the sulfur analyses, the carbon 179 emission line was monitored by AED to detect the elution of these standards.

HPLC Fractionation. The HPLC system (Agilent, model 1100) used a normal-phase cyano-column (Zorbax-CN, Agilent Technologies), along with detectors for diode-array detection (DAD) and refractive index detection (RID) used in series. Experimental details for the HPLC fractionation procedure are described in Table 2. Aviation fuels were first diluted to 100:1 in hexane and injected into the chromatographic system. Using a mobile phase of *n*-hexane (Fisher Scientific), the complex mixtures were separated into compound classes on the basis of polarity. These compound classes were detected by DAD and RID measurement at low concentrations for chromatographic resolution. After retention times for the classes had been established, subsequent separations were conducted by manual

(28) Link, D. D.; Baltrus, J. P.; Rothenberger, K. S.; Zandhuis, P.; Striebich, R. C.; Minus, D. M. *J. Chromatogr. Sci.* **2002**, *40*, 500−504.

Table 2. Instrumental Conditions for HPLC Fractionations and GC−MS Analysis

HPLC separation conditions		GC−MS analysis conditions	
mobile phase	*n*-hexane	carrier gas	He
column	Zorbax-CN (Agilent), 4.6 mm × 15 cm	column	HP-1 (Agilent), 30 m × 0.25 mm i.d.
flow rate	0.5 mL/min	film thickness	0.25 μm
temperature	25 °C	injector	280 °C, splitless
fraction collection	manual	solvent delay	5.0 min
injection volume	40 μL	oven	40 °C (2 min) to 280 °C (3 min) at 5 °C/min

Table 3. List of Organo-sulfur Compounds Injected as Part of the Study to Identify Sulfur Compounds by Matching Retention Times[a]

compound class	thiophene	benzothiophene	dibenzothiophene
parent compound	thiophene	benzothiophene	*dibenzothiophene*
alkyl constituent	3-methyl	2-methyl	3-methyl
		3-methyl	2,4,6-trimethyl
		2,3-dimethyl	1,2,3,4-tetrahydro
		2,5-dimethyl	1,2,3,4,4a,4b-hexahydro
		3,7-dimethyl	
		3,5-dimethyl	
		7-ethyl	
		2-ethyl	
		2,3,7-trimethyl	
		2,5,7-trimethyl	
		2-ethyl-7-methyl	
		2-ethyl-5-methyl	
		2-propyl	
		2,3,4,7-tetramethyl	
		2-ethyl-5,7-dimethyl	
		2-propyl-7-ethyl	
		2,7-diethyl	

[a] Identified compounds are shown in italics.

collection of fractions from more-concentrated samples (20:1 dilution) without using the RI detector, which had high dead volume and caused significant peak dispersion.

The success of the fractionation was evaluated using the raw collected samples in *n*-hexane. Samples were not concentrated by evaporation, because of the potential to lose a high concentration of volatile alkyl benzenes in the aromatic fraction of the sample. To determine which fractions contained a majority of the sulfur compounds, portions of each of the collected fractions were analyzed for sulfur content by GC−AED. The "diaromatics" fraction (i.e., the fraction that contained primarily substituted naphthalenes) was found to contain the majority of sulfur compounds. A concentrated sample of this fraction was subsequently prepared by performing 10 injections on the HPLC separation system, accumulating each target fraction, and finally concentrating the fraction by solvent evaporation. Finally, a high-resolution GC−MS system (Agilent Technologies, model 6890-5973) was used to analyze concentrated collections of the "diaromatics" fraction to determine structural information about the individual sulfur compounds that were contained in the fuel. Conditions for the high-resolution GC−MS analysis are shown in Table 2.

Identification by Comparison with Known Samples. Raw jet fuel samples were analyzed by GC−AED (using the Agilent Technologies model 6890 gas chromatograph, with the Agilent Technologies model 7683 autosampler, coupled to an Agilent Technologies model 2350A atomic emission detector) and by GC−MS (using the Agilent Technologies model 6890 gas chromatograph and the Agilent Technologies model 5973 mass spectrometer). The study had, at its disposal, a supply of more than 250 individual sulfur compounds. After a preliminary evaluation of the class-separation results, it was determined that the major individual sulfur-containing constituents were benzothiophenes. Therefore, individual samples of various benzothiophenes, covering many of the one-carbon-(C1), two-carbon- (C2), and three-carbon-(C3) substituted benzothiophenes, were chosen for comparison to the chromatograms of the jet fuel. In addition, several other compounds within the thiophene and dibenzothiophene classes were injected. A listing of many of the sulfur compounds injected as part of this identification study is given in Table 3. These standards were typically dissolved in a solvent such as isooctane or toluene, at concentration levels in the range of 5−200 μg/mL. The retention times and detector response for the pure compounds were compared to the retention times of the sulfur components in the jet fuel chromatograms.

Analysis of Total Sulfur in Fuels. In addition to the aforementioned methods for determining class-specific sulfur concentrations, the total sulfur concentrations in selected fuels were determined. Several analytical methods were used for total sulfur determinations, including traditional analysis by GC−AED, as well as "fast" GC−AED,[28,29] and UV fluorescence (using ASTM Method D5453) by an independent laboratory.[30]

Results and Discussion

Class Separation of Sulfur Compounds in Jet Fuels. The sulfur components were placed in classes based on a combination of their response to oxidation reactions and a chromatographic peak bracketing routine. All the sulfur components that were oxidized by iodine were classified as thiols. The components that were not oxidized by iodine but were oxidized by hydrogen peroxide were classified as sulfides or disulfides. This combined group of oxidizable components was broadly designated as being "reactive" sulfur species. The sulfur components that were not oxidized by either iodine or hydrogen peroxide were classified as either thiophenes, benzothiophenes, or dibenzothiophenes, and, as a group, these components were broadly designated as being "nonreactive" sulfur species. Figure 1 compares the GC−AED sulfur chromatograms of a

(29) Link, D. D.; Baltrus, J. P.; Rothenberger, K. S.; Minus, D. K.; Striebich, R. C. Presented at the Pittsburgh Conference on Analytical Chemistry and Applied Spectroscopy, New Orleans, LA, 2002.

(30) Dahnke, K. F.; Maholland, L. S. *Analysis of Fuels by ASTM D5453, Report to DOE/NETL*; Phillips Petroleum Co., Analytical Sciences Group: Bartlesville, OK, 2002; p 2.

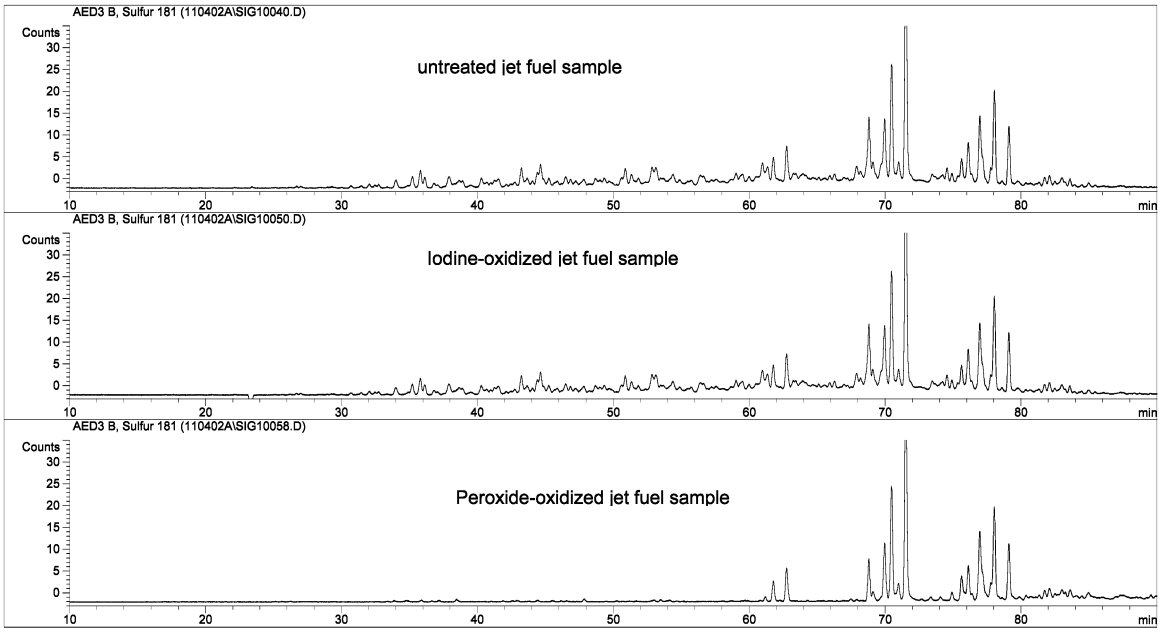

Figure 1. GC−AED sulfur chromatograms of an untreated sample of a representative jet fuel, an iodine-oxidized sample of the jet fuel, and a peroxide-oxidized sample of the jet fuel.

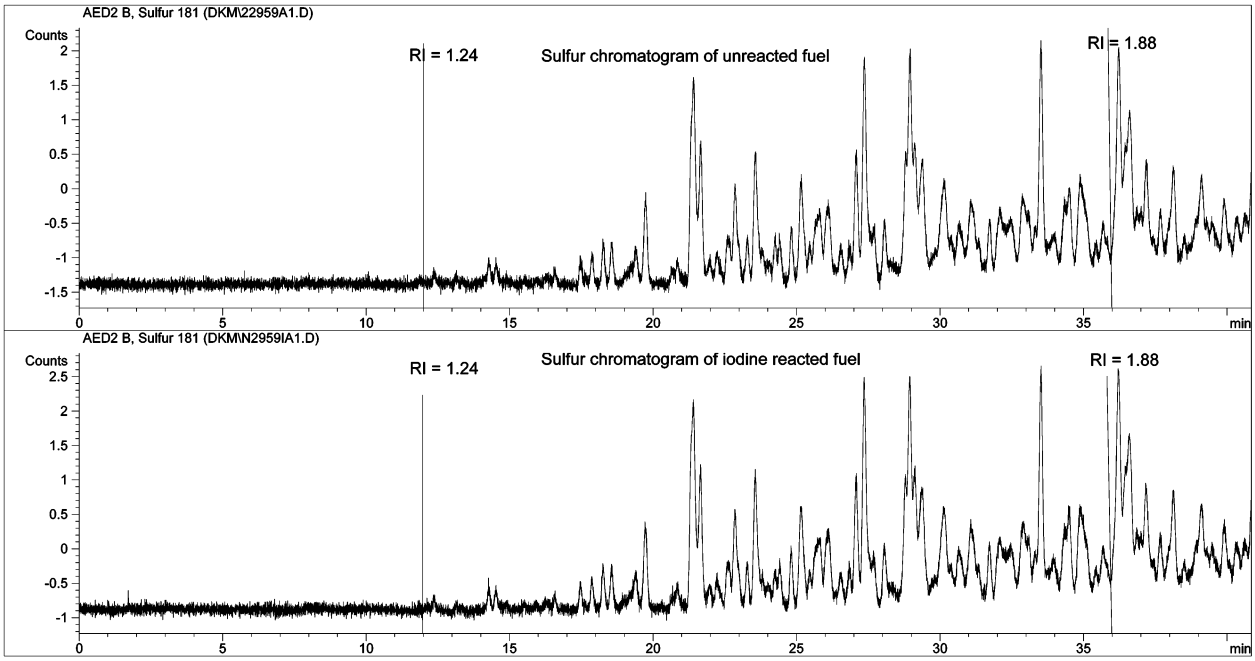

Figure 2. GC−AED sulfur chromatograms of the unreacted sample of jet fuel and the iodine-oxidized sample.

representative jet fuel sample with those of the iodine-oxidized and hydrogen peroxide-oxidized fuel samples.

For quantification of individual classes of sulfur species, the sulfur species were separated using segmented regions of the AED chromatograms that were based on the retention time of aromatic standards. Benzene was defined as having a retention index of RI = 1, naphthalene had a RI value of 2, phenanthrene had a RI value of 3, and chrysene had a RI value of 4. The concentration of thiols was determined by measuring the concentration of sulfur species with RI values of <1.88 units in the unreacted fuel, then subtracting from that the concentration of sulfur species with retention indices of <1.88 units in the iodine-oxidized fuel sample. An RI value of 1.88 was chosen because experimental results showed extraneous peaks in the sulfur chromatogram of the iodine-oxidized samples that eluted after this RI value. Prior studies showed that thiols are the only species that were oxidized by iodine; therefore, the reduction in sulfur species observed in the iodine-oxidized fuel sample is attributed exclusively to the loss of thiol species. Figure 2 shows the AED chromatograms of the unreacted fuel and iodine-oxidized fuel sample, expanded about the region of RI = 1.88 units, to highlight the loss of thiol species. For the jet fuels tested in this study, the concentrations of thiols present were expected to be low; thus, the differences between the sulfur response for the untreated fuel and that of the iodine-oxidized fraction are slight.

Because thiols, sulfides, and disulfides are all oxidized by hydrogen peroxide, subtracting the concentration of

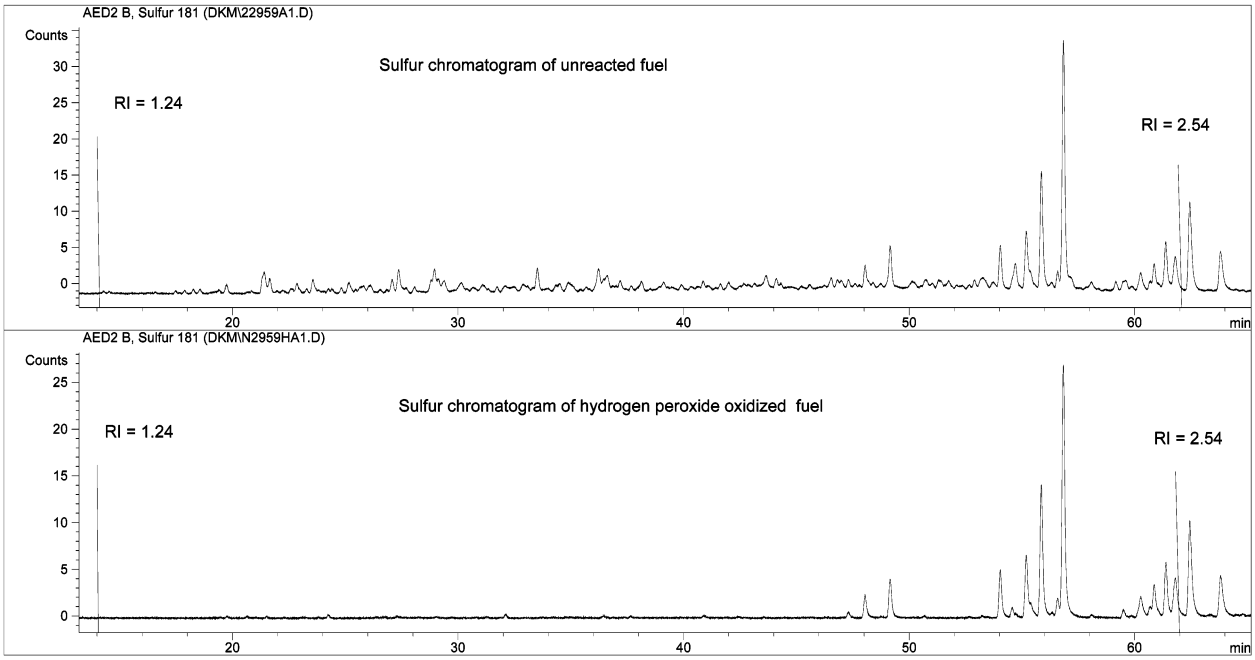

Figure 3. GC−AED sulfur chromatograms of the unreacted sample of jet fuel and the hydrogen peroxide-oxidized sample.

sulfur species with an RI value of <2.54 units in the hydrogen peroxide-oxidized fuel sample from the concentration of sulfur species within the same RI range in the unreacted fuel gave the combined concentration of the "reactive" sulfur species. To determine the concentration of the sulfide and disulfide fraction, the concentration of thiols, which was determined by the iodine oxidation, was subtracted from the concentration of "reactive" sulfur. The resulting concentration was classified as that of the sulfide and disulfide species. Figure 3 shows the AED chromatograms of the unreacted fuel and the hydrogen peroxide-oxidized fuel sample, expanded about the region of RI = 2.54 units, to highlight the loss of thiol, sulfide, and disulfide species. The large difference in sulfur response illustrates the large concentration of "reactive" sulfur compounds contained in this fuel.

The concentration of thiophenes was determined by measuring the combined concentration of sulfur species in the hydrogen peroxide-oxidized fuels with an RI value of <2.00 units, because thiophenes were the only sulfur species in this RI range that remained following hydrogen peroxide oxidation. The concentration of benzothiophenes was determined by measuring the combined concentration of sulfur species in the hydrogen peroxide-oxidized fuels with RI values of >2.00 units and <2.66 units. The concentration of dibenzothiophenes was determined by measuring the combined concentration of sulfur species in the unreacted fuel with RI values of >2.66 units and <3.54 units. The unreacted fuel chromatogram was used for dibenzothiophene quantitation, because the oxidized samples contain transformed sulfur species, such as sulfoxides and sulfones, which elute later in the chromatogram of oxidized fuels and could produce artificially high results for the dibenzothiophene concentration. Although oxidized sulfur species may be present in fuel, this peak bracketing routine may not be appropriate for their trace-level determination. These polar species would likely be partially removed by partitioning into the aqueous oxidation solutions. Any remaining oxidized sulfur species would elute at retention times that correspond to benzothiophenes and dibenzothiophenes; however, their emission would be masked by the emission from the benzothiophenes and dibenzothiophenes, which would likely be present at much-higher concentrations.

To determine the transferability of the oxidation and peak grouping routine, the method was tested by a second laboratory using a different column for GC separation (as shown in Table 1). Because the separation was altered, retention times that correspond to the chosen RI values needed to be determined for the different column. To transfer the RI values to different separation conditions, retention times that corresponded to the specified RI values were determined. The bracket time was calculated according to the following equation:

$$\frac{rt_{bracket} - rt_{prevRI}}{rt_{nextRI} - rt_{prevRI}} = RI_{bracket} - RI_{prev}$$

where $rt_{bracket}$ is the desired retention time being calculated, rt_{prevRI} the retention time for the aromatic bracket standard that elutes prior to the desired retention index, rt_{nextRI} the retention time for the aromatic bracket standard that elutes after the desired retention index, $RI_{bracket}$ the desired retention index, and RI_{prev} the retention index for the aromatic bracket standard that elutes prior to the desired retention index. For the model DB-1701 column, benzene eluted at 4.0 min, whereas naphthalene eluted at 40.1 min; therefore, a bracket RI value of 1.88 corresponded to a retention time of 35.8 min. For the model Rtx-1 column, benzene and naphthalene eluted at 9.7 and 53.1 min, respectively; therefore, a retention time of 47.9 min corresponded to a bracket RI value of 1.88.

Spiked Sulfur Mixture Study. Jet fuels typically contain low levels of thiol species; thus, it was difficult to establish the effectiveness of the method for removal of this particular species. Therefore, a model fuel

Table 4. Recovery of Spiked Analytes from the Selective Oxidation of a Model Jet-Fuel Mixture

compound class	original concentration[a]	I_2-oxidized concentration	percent recovery	H_2O_2-oxidized concentration	percent recovery
		Fuel Containing 165.7 μg Total Sulfur/mL			
thiol	52.7 ± 0.32	nd[b]		nd[b]	
sulfide/disulfide	69.1 ± 0.41	60.6 ± 0.26	87.7 ± 0.65	nd[b]	
thiophene	17.1 ± 0.11	15.9 ± 0.09	93.5 ± 0.81	15.5 ± 0.12	90.6 ± 0.91
benzothiophene	26.8 ± 0.44	31.0 ± 0.12	115 ± 1.9	23.8 ± 0.08	89.0 ± 1.5
		Fuel Containing 83.6 μg Total Sulfur/mL			
thiol	26.4 ± 0.25	nd[b]		nd[b]	
sulfide/disulfide	34.4 ± 0.31	29.6 ± 0.12	85.9 ± 0.85	nd[b]	
thiophene	8.69 ± 0.103	8.05 ± 0.012	92.7 ± 1.1	7.73 ± 0.039	88.9 ± 1.1
benzothiophene	14.1 ± 0.04	16.0 ± 0.05	113 ± 0.5	11.8 ± 0.10	83.6 ± 0.75

[a] Concentrations expressed as μg sulfur/mL ± standard deviation; $n \geq 2$. [b] nd indicates that the species concentration was not detected, because of complete removal of the chromatographic peak of the target species.

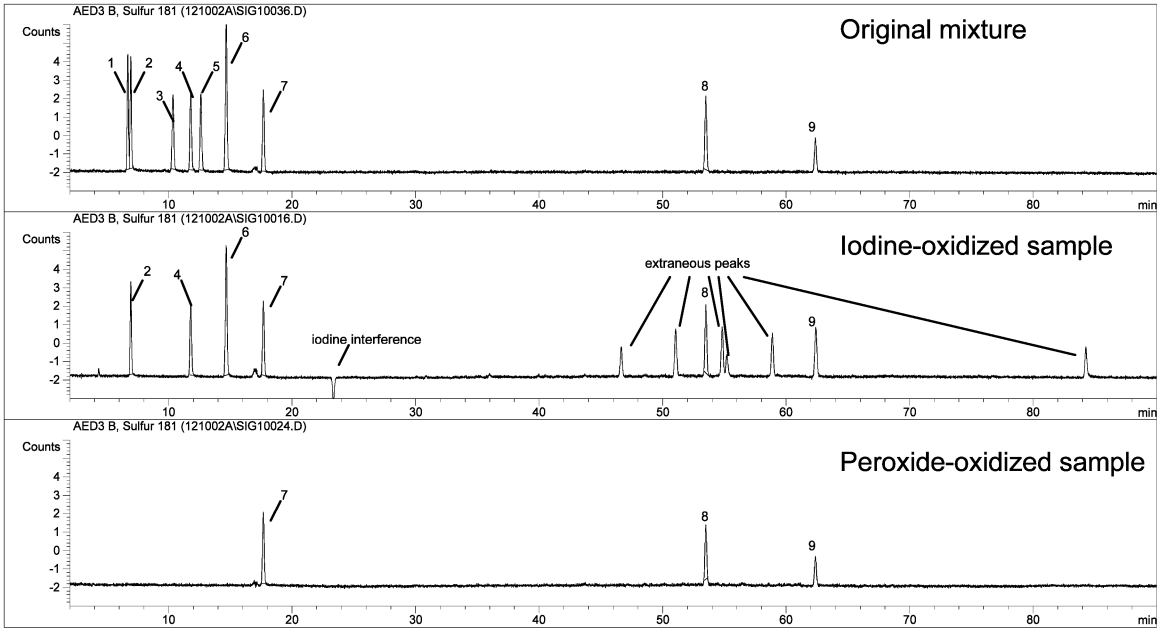

Figure 4. Sulfur chromatograms for the analysis of a model compound mixture, an iodine-oxidized sample, and a peroxide-oxidized sample, illustrating the removal of target classes by each oxidation procedure. Peak identities are as follows: 1, 1-propane thiol; 2, ethyl methyl sulfide; 3, 2-methyl-1-propane thiol; 4, diethyl sulfide; 5, 1-butane thiol; 6, methyl disulfide; 7, 3-methyl thiophene; 8, benzothiophene; and 9, 5-methyl benzothiophene.

mixture was prepared to test the ability of the method to selectively remove target classes of sulfur species at two different sulfur concentration levels. Using this model mixture, analytical parameters such as efficiency of removal, selectivity of oxidation, and sensitivity of the determination could be evaluated. Table 4 contains data regarding the removal and recovery of certain target fractions. Note the complete removal of thiols following the iodine oxidation procedure, as well as the complete removal of thiols, sulfides, and disulfides by the hydrogen peroxide oxidation procedure.

In addition to quantitative data, chromatographic evidence for the effectiveness of the oxidation procedure is shown in Figure 4. This figure shows the sulfur chromatogram for the original model fuel mixture, as well as those of the iodine-oxidized fuel mixture and the peroxide-oxidized fuel mixture. Complete removal of the three thiols was demonstrated by the iodine oxidation procedure, whereas other species remained in the mixture. For the peroxide-oxidized fraction, complete removal of thiols, sulfides, and disulfides was achieved, without the removal of thiophenes or benzothiophenes. It is important to note that the spiked thiol species appear at much shorter retention times than the region where a response to sulfur emission is observed for samples of jet fuel that have been tested (shown in Figure 1). This observation indicates that these jet fuels do not contain significant quantities of thiols. Moreover, the overlay shows the rationale for choosing the end-point for thiol elution at a RI value of 1.88. The iodine oxidation procedure converts thiols to more-polar sulfur compounds that elute after a RI value of 1.88. These compounds apparently are not completely removed via phase separation and washing. To minimize the introduction of positive bias, these extraneous peaks that result from the iodine oxidation procedure are excluded from the region of thiol quantification.

There were slight losses of thiophenes and benzothiophenes, as a result of the oxidation procedures. Although the magnitude of the losses is relatively small, they are repeatable. These losses may occur as a result of the processing of solutions during the oxidation procedure, because thiophenes and benzothiophenes are adsorptive and could be lost at each sample transfer step.[31] Loss of these species because of volatilization is

(31) Striebich, R. C.; Rubey, W. A.; Anderson, S. D. *Prepr.—Am. Chem. Soc., Div. Pet. Chem.* **1994**, *39*, 64−66.

Table 5a. Concentration of Sulfur,[a] As Determined by Sulfur Class-Separation Procedure by Independent Laboratories for Several Representative Jet Fuels

sample		thiols	thiols, sulfides, and disulfides	thiophenes	benzothiophenes	dibenzothiophenes
2827	Lab 1	19.2 ± 22.4	382 ± 46	6.4 ± 0.1	123 ± 26	56.8 ± 19.2
	Lab 2	2.0 ± 4.0	320 ± 12	12.8 ± 4.0	110 ± 5	118 ± 5
2926	Lab 1	3.2 ± 13	300 ± 28	nd[b]	46.4 ± 3.2	33.6 ± 6.4
	Lab 2	2.4 ± 2.1	236 ± 7	6.3 ± 2.1	58.9 ± 4.6	84.1 ± 2.9
2959	Lab 1	6.4 ± 14.4	832 ± 64	21.6 ± 4.8	422 ± 46	37.6 ± 1.6
	Lab 2	7.6 ± 10.0	793 ± 31	23.9 ± 1.0	513 ± 2.0	74.0 ± 2.2
3084	Lab 1	0.1 ± 9.6	343 ± 27	4.8 ± 1.6	114 ± 16	57.6 ± 4.0
	Lab 2	1.34 ± 5.84	323 ± 15	10.4 ± 2.5	124 ± 4	98.6 ± 2.1
3166	Lab 1	nd[b]	402 ± 34	8.0 ± 1.6	163 ± 2	55.2 ± 5.6
	Lab 2	1.14 ± 3.40	360 ± 8	14.2 ± 0.1	178 ± 2	97.4 ± 1.5

[a] Concentrations expressed as μg sulfur/mL ± standard deviation; $n \geq 2$. [b] nd indicates that the presence of this analyte was not detected using this method.

Table 5b. Total Concentration[a] of Sulfur in Fuels, Determined by Summation of Class Fractions, GC−AED Analysis of Untreated Fuel, and UV Fluorescence

sample	Sum of Fractions		GC−AED of Untreated Fuel		UV fluorescence of untreated fuel
	Lab 1	Lab 2	Lab 1	Lab 2	
2827	588 ± 60	560 ± 14	514 ± 6	667 ± 18	640 ± 10
2926	383 ± 32	385 ± 9	425 ± 28	465 ± 9	392 ± 8
2959	1319 ± 81	1404 ± 32	1307 ± 62	1428 ± 38	1307 ± 7
3084	519 ± 33	556 ± 16	559 ± 15	598 ± 17	543 ± 1
3166	626 ± 38	651 ± 8	673 ± 27	703 ± 10	652 ± 5

[a] Concentrations expressed as μg sulfur/mL ± standard deviation; $n \geq 2$.

also possible, especially when working with solutions at elevated temperatures, as in the hydrogen peroxide oxidation procedure. Further evidence that the losses are physical in nature is the absence of additional peaks in the target region of the sulfur chromatogram of the peroxide-oxidized mixture, indicating that additional sulfur species are not created during the oxidation procedure. The evaluation of the spiked mixture allowed us to conclude that the published method quantitatively removes the target species but may be susceptible to a slight loss of supposedly unreacted species. To our knowledge, this is the first time that the occurrence of losses using the published procedure[18] have been identified and quantified.

Table 5a shows a listing of the results for sulfur class separation and quantification for several representative fuels using the method that has been described. Table 5b compares the results obtained for total sulfur concentration by summing the fractions, as well as results of direct analysis of the untreated fuel by alternative methods. As the tables show, the summed results for the class-selective determinations are in agreement with the results for total sulfur concentration as determined by several different analytical techniques, showing good performance for the class-selective determinations. As mentioned previously, concentrations of thiols in hydrotreated fuels are expected to be low, so determinations using this method are more difficult as the level of thiols decreases. Regardless, note that consistent results are achieved for class determinations for independent laboratories using different chromatographic equipment, demonstrating that the selective oxidation and peak bracketing routine is transferable to different laboratories, using different chromatographic separation procedures.

Some interesting trends can be observed from the class-specific determinations. In all the fuels tested, the thiols, sulfides, and disulfides contribute more than 50% of the total sulfur concentration. This contribution seems to be independent of the total sulfur concentration of the fuel, because the fuel with the lowest sulfur concentration (sample 2926, with a total sulfur concentration of ~400 ppm) and the fuel with the highest sulfur concentration (sample 2959, with a total sulfur concentration of ~1300 ppm) both were composed of more than 60% thiols, sulfides, and disulfides. For the refractory sulfur compounds, the benzothiophene fraction was the majority, followed by dibenzothiophene, with thiophenes contributing less than 5% of the total sulfur in each jet fuel that was tested.

HPLC Class Fractionation. For additional speciation of the sulfur content in the fuel, the HPLC fractionation procedure isolated the fuel sample into the following different structural classes: saturates, single-ring compounds, double-ring compounds, and triple-ring compounds.[32] Ordinarily, the fuel matrix is too complex to use a nonselective detector, such as a mass spectrometer, to obtain good spectra for sulfur compounds. However, fractionation of the fuel into structural classes simplifies the matrix and allows GC−MS to be used as an effective tool for the detection and identification of various sulfur compounds in each fraction of the fuel.

The response of a refractive index detector was used to monitor the polarity separation of the compound classes in a typical kerosene-cut aviation fuel. The normal-phase HPLC separation proved to be a fast (<10 min) and convenient way to fractionate the sample of interest primarily into saturates, aromatics, and diaromatics fractions. GC−MS was used to confirm the initial measurements of the RID value and to evaluate the ability of the fractionation procedure to separate the desired fractions from each other accurately. The chromatogram for the neat fuel and the chromatograms for the saturates, aromatics, and diaromatics fractions are shown in Figure 5a, b, c, and d, respectively. Note that

(32) Striebich, R. C.; Rubey, W. A.; Klosterman, J. R.; Balster, L. M. T. Presented at the 23rd International Symposium on Capillary Chromatography and Electrophoresis, Las Vegas, NV, 2001.

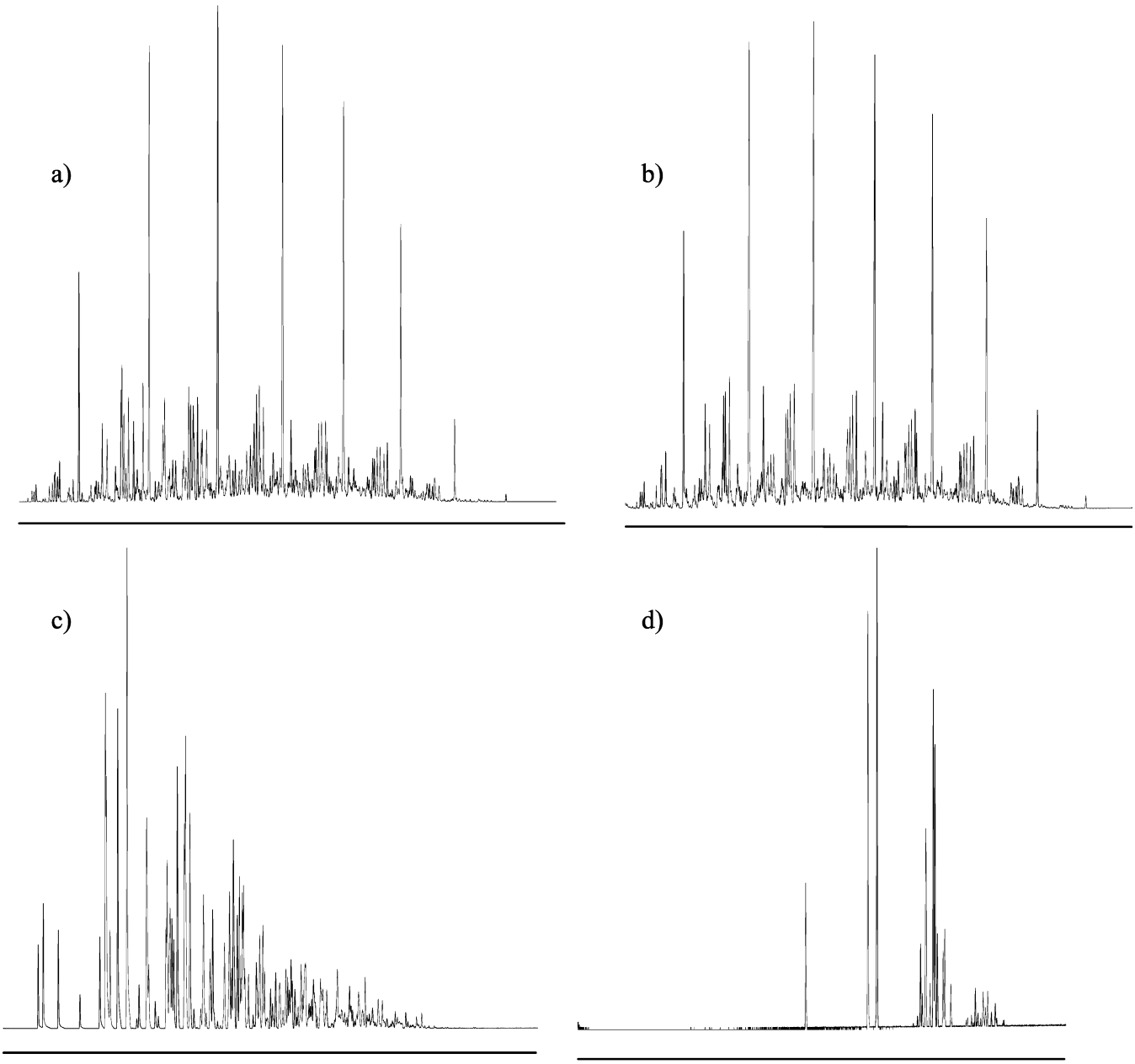

Figure 5. GC−MS chromatograms of (a) the raw fuel, (b) the HPLC fractionated saturates, (c) mono-aromatics, and (d) di-aromatics.

the figures are presented on dramatically different scales. Had identical scales been used, the chromatograms for the aromatic and diaromatic fractions would be obscured, because the saturates fraction comprises more than 75% of the fuel.

Carryover among the fractions was not observed, even between the saturates fraction and the aromatics fraction, even though the saturates fraction comprises more than 75% of the fuel matrix. Additional evidence for the robustness of the fractionation method is provided by the appearance of saturated dicycloalkanes (decalins) in the saturates fraction, whereas the unsaturated cycloalkanes (tetralins) were identified in the aromatics fraction. Further characterization of the fractions showed that the aromatic fraction consisted of C2- through C7-substituted benzenes primarily, whereas the diaromatics fraction contained naphthalene and C1- through C3-substituted naphthalenes. The polarity-sensitive normal phase fractionation procedure was determined to have separated the classes of compounds in the fuel correctly.

To determine which of the fuel fractions contained the highest concentration of sulfur compounds, each fraction from a high-sulfur jet fuel was analyzed for sulfur via GC−AED. This sulfur-specific detector responds only to the sulfur compounds in the fuels, thus allowing determination of the distribution of sulfur-containing compounds among the HPLC-fractionated samples. The sulfur-specific chromatograms for each of these fractions are shown in Figure 6.

GC−MS scans were performed on the fractionated fuels, and then extracted ion chromatographs were obtained from the scans. Even though hydrocarbon species still comprised a majority of the fractionated matrixes, the fractionation procedure simplified the matrix enough to identify sulfur-containing species. A majority of the sulfur-containing compounds were present

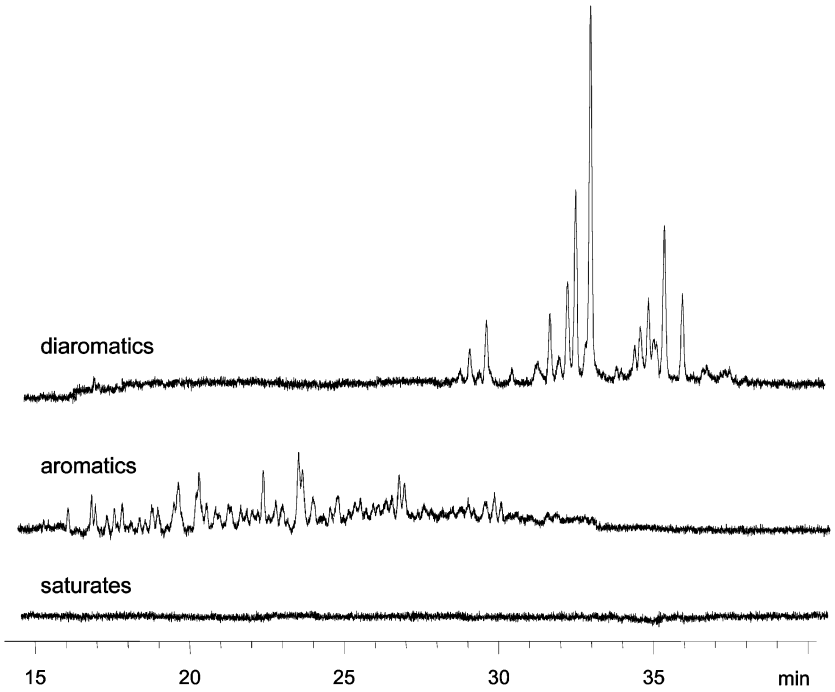

Figure 6. GC−AED sulfur chromatograms of the saturates, the aromatics, and the diaromatics following fractionation of the jet fuel by HPLC. All the extracted chromatograms are on the same scale.

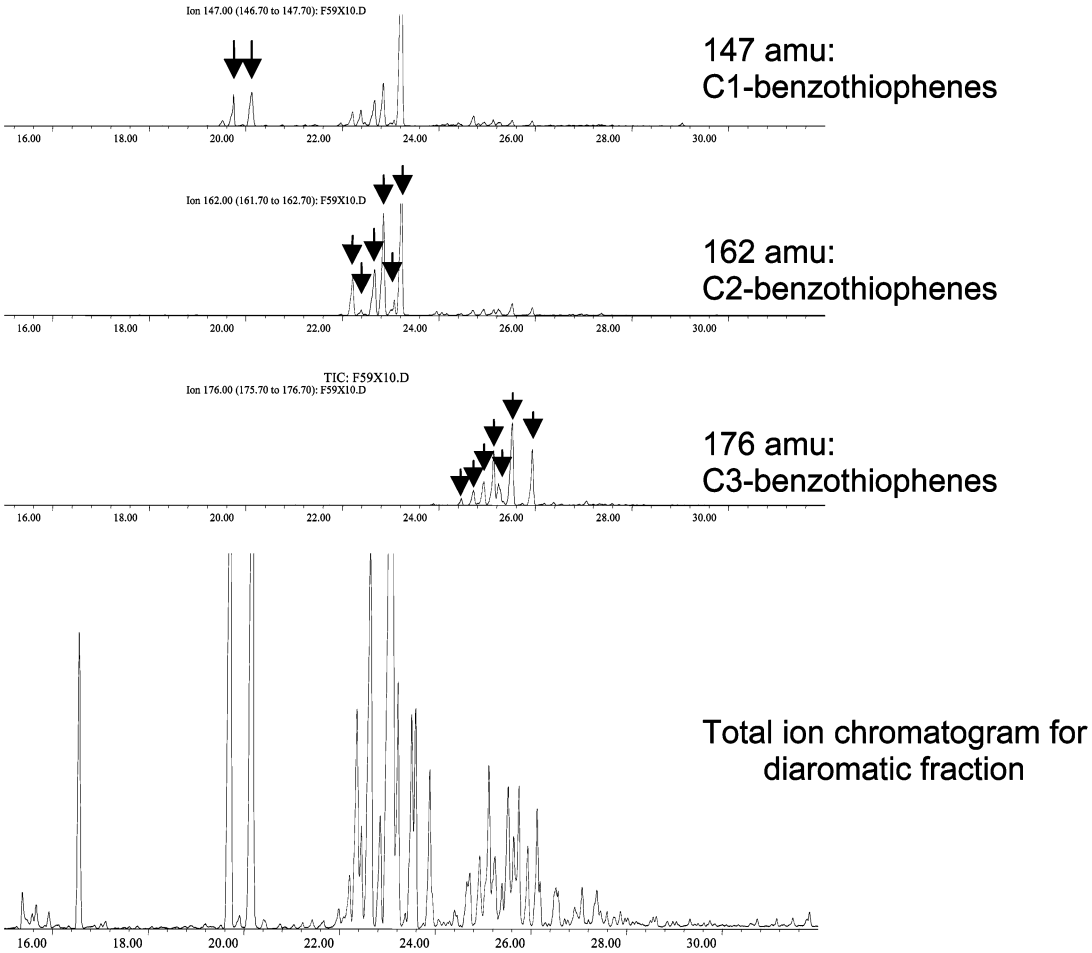

Figure 7. GC−MS analysis and identification of the sulfur components of the two-ring fraction of the jet fuel, as isolated by the HPLC fractionation procedure.

in the diaromatics fraction, as shown in Figure 6. Using masses that are indicative of specific groups of sulfur-containing compounds, group-specific identifications were made within each fractionated sample. This is shown in Figure 7, which identifies most of these sulfur compounds in the diaromatics fraction as alkyl-substi-

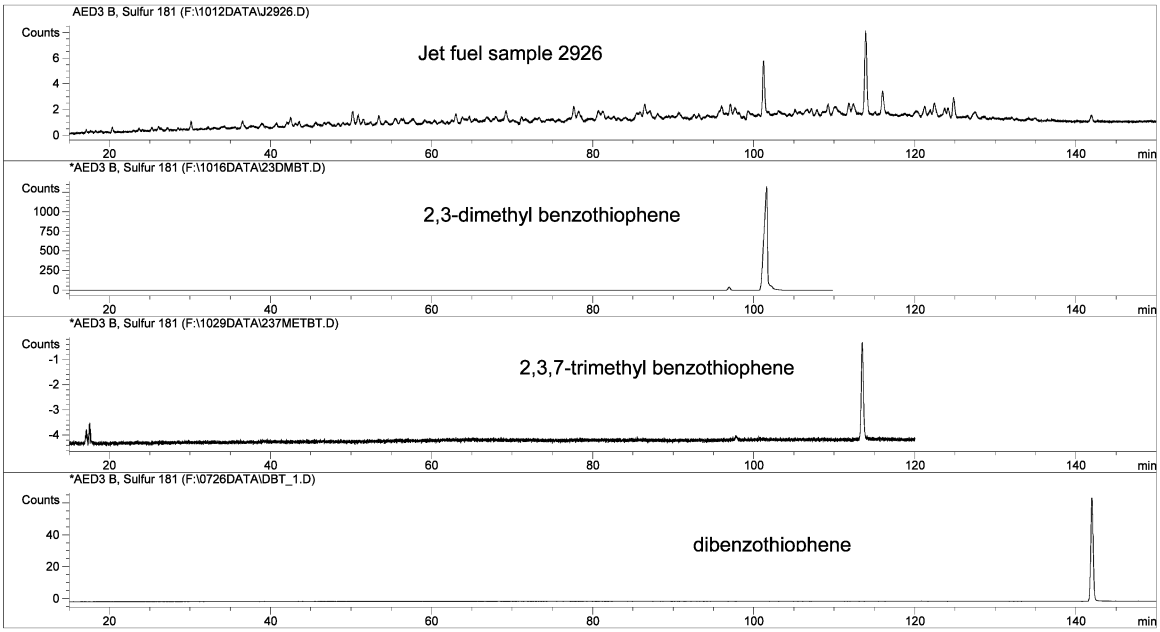

Figure 8. GC−AED sulfur chromatograms showing the identification of several sulfur-containing compounds in jet fuel by retention time matching.

tuted benzothiophenes. The fractionation step has the advantage of cleaning up the matrix prior to analysis, which allows for more-definitive identification of the trace amounts of sulfur-containing compounds in the bulk hydrocarbon matrix by mass spectrometric detection.

Identification of Individual Sulfur Constituents. Following the intensive separation of classes of sulfur compounds in the fuels, it was our goal to identify the individual compounds that comprised a majority of the classes. To do this, GC−AED sulfur chromatograms for jet fuels were compared to the results for solutions that contained a single sulfur compound. Identifications using this method were based on retention time matching. The major constituents of the alkyl-benzothiophene structures (C1, C2, and C3), and the major dibenzothiophene, were identified. Figure 8 shows the sulfur chromatogram of a representative jet fuel sample, as well as those of several components that were identified in the fuel: 2,3-dimethylbenzothiophene, 2,3,7-trimethylbenzothiophene, and dibenzothiophene. These identifications agree with other reports of sulfur compounds that are present in other fractions of hydrotreated fuels.[4,5,22,33]

Conclusions

This work has demonstrated effective techniques for separating aviation fuels into class-specific fractions to simplify the analysis of sulfur in the fuel and to quantify the reactive and nonreactive sulfur species in the fuel. Using these methods, fuels have been separated on the basis of the reactivity of the sulfur class, and on the basis of polarity and ring structure. The separation methods allowed a non-element-specific detection technique to be used, despite a large amount of matrix interference from the fuel. In addition, the separation methods increased the effectiveness of sulfur-specific methods such as gas chromatography−atomic emission detection (GC−AED).

Of the suite of sulfur-containing compounds in fuels, the thiols, sulfides, and disulfides are most reactive and were quantified by oxidation with either iodine or hydrogen peroxide, followed by the subtraction of bracketed regions of sulfur-specific chromatograms of the original fuel and the oxidized fuel. The least-reactive compounds—the thiophenes, benzothiophenes, and dibenzothiophenes—were also quantified by this bracketing and subtraction technique. However, the potential for losses of these compounds has been identified. The fuels tested in this study showed that reactive sulfur accounts for more than half of the sulfur concentration, which suggests that even a simple oxidation with hydrogen peroxide may greatly improve the fuel characteristics.

Using a high-pressure liquid chromatography fractionation technique, non-element-specific detection was used to establish that the class of fuel that contains the majority of sulfur is the diaromatics portion. Within this portion, sulfur exists primarily as alkyl-benzothiophenes, as determined by gas chromatography−mass spectroscopy, with individual contributors that are identified by GC−AED as being 2,3-dimethylbenzothiophene, 2,3,7-trimethylbenzothiophene, and dibenzothiophene.

Acknowledgment. Reference in this paper to any specific commercial product, process, or service is to facilitate understanding and does not necessarily imply its endorsement or favoring by the United States Department of Energy.

EF0300747

(33) Ma, X.; Sakanishi, K.; Mochida, I. *Ind. Eng. Chem. Res.* **1996**, *35*, 2487−2494.

X. Thermal Decomposition of High Energy Density Materials at High Pressure and Temperature

ELSEVIER

J. Anal. Appl. Pyrolysis 70 (2003) 339–352

JOURNAL of ANALYTICAL and APPLIED PYROLYSIS

www.elsevier.com/locate/jaap

Thermal decomposition of high-energy density materials at high pressure and temperature

R.C. Striebich [a,*], J. Lawrence [b,1]

[a] *University of Dayton Research Institute (UDRI), KL102, 300 College Park, Dayton, OH 45469-0132, USA*

[b] *AFRL/PRTG, Propulsion and Power Directorate, Air Force Research Laboratory, 1790 Loop Road N., Wright-Patterson Air Force Base, OH 45433-7103, USA*

Received 19 September 2002; accepted 5 November 2002

Abstract

High-energy density materials (HEDMs) are being investigated for use as propellants in rocket, air-breathing, and combined-cycle applications. These types of materials may be attractive alternatives to conventional propellants because of their high heat of combustion, density, and high strain energy. Because advanced propulsion systems may operate at very high pressure and temperature (>25 atm and temperatures exceeding 500 °C), the thermal decomposition of individual HEDMs is of interest to future fuel system designers. A laboratory-scale flow reactor was used to subject small amounts (approximately 1 ml) of deoxygenated HEDM to controlled conditions of temperature and residence-time-at-temperature at constant pressure (34 atm) in the liquid or supercritical phase. The reactor was 316 stainless steel HPLC tubing. Using an in-line analytical system, as well as off-line chromatographic analysis of products, the thermal stability of the parent material, as well as the thermal fragmentation products of each HEDM was measured. Some of the candidate materials tested (dimethyl-2-azidoethylamine (DAMEZ), quadricyclane, and bicyclopropylidene (BCP)) showed only marginal thermal stability with major decomposition occurring before 400 °C (~ 3 s residence time). Other candidate materials (JP-10, RP-1, RG-1, RJ-6, and RJ-7) showed excellent thermal stability: little decomposition even at 600 °C. Results show the pyrolytic stability of candidate materials relative to each other, and provided insights to the mechanisms of thermal decomposition for specific fuel candidates.

* Corresponding author. Tel.: +1-937-229-2846.

E-mail addresses: richs@snake.appl.wpafb.af.mil (R.C. Striebich), janine.lawrence@wpafb.af.mil (J. Lawrence).

[1] Tel.: +1-937-255-5345.

PII: S0165-2370(02)00181-X

Keywords: Bicyclopropylidene; Quadricyclane; RP-1; Rockets; Missiles; Fuels

1. Introduction

The US Air Force recently has begun to focus more attention on operating in space. As space missions continue to become more and more ambitious, the costs associated with space access must decrease. One way to reduce the infrastructure and expense needed to access space is to replace conventional rocket technology with high-speed aircraft technology. As one form of a reusable launch vehicle (RLV), high-speed aircraft may provide a cost-effective alternative for space missions. In this scenario, there is great interest in developing advanced propellants to be used in either dual-stage-to-orbit applications or combined-cycle applications of an RLV. Aircraft propellants, still the primary coolant of choice, will be thermally stressed like never before to cool the outer skin of the vehicle, which heats as it travels at supersonic speeds. Avionic devices and engines also need to be cooled by the fuel as they also generate significant amounts of heat [1]. Thus, it is important for the propellants not to degrade as they are used in this cooling role.

As space access continues to evolve, propellant research has become an ''enabling'' technology [2]. There is significant interest in developing high-energy density materials (HEDMs), such as strained hydrocarbon fuels, to replace conventional hydrocarbon rocket fuels (RP-1, i.e., ''rocket propulsion-1'') and aircraft fuels (JP-8, i.e., ''jet propulsion-8'') in order to provide improved payload mass and gross takeoff mass [2,3]. HEDMs may include both materials that are compacted due to their bond strain in addition to materials which are dense because of their specific gravity. The strained hydrocarbon fuels have high heat of combustion and densities compared with JP-10 (a current missile fuel) and can readily be incorporated into very high-speed applications with high energy requirements. One significant hurdle for hydrocarbon fuels in high-speed applications is that these fuels may be used to regeneratively cool system structures; unfortunately, candidate HEDMs may or may not be thermally stable at these temperatures and pressures. Currently, most aircraft and hydrocarbon rocket systems such as Atlas II, Atlas III, and Delta II use regenerative-cooled systems.

Another way to increase the performance of hydrocarbon-fueled rockets is to increase the combustion pressure; however, increased pressure results in an increase in the wall heat flux. The coolant, which in most cases is the fuel, must be able to adsorb the additional heat load due to an increase in pressure. However, regenerative cooling is only effective when the coolant temperature remains below its thermal decomposition or ''coking'' temperature. Commonly used materials, such as stainless steel or nickel, have wall-temperature limitations of approximately 870 °C. The maximum wall temperature allowed with the current rocket fuel RP-1 is approximately 450 °C. Energetic materials that degrade at temperatures below 450 °C may be less capable of effective cooling of surfaces and may also provide fuel system

control issues upon delivery to the combustor. Lowering the combustion pressure to accommodate materials with a low coking temperature will lower the efficiency and performance of the craft. Also, future high-speed rockets and aircraft have higher performance and temperature goals than current systems and may need an alternative coolant.

This contribution describes a laboratory study to investigate the thermal degradation of HEDMs under controlled conditions of temperature, pressure, and residence time. In addition, product formation from the decomposition of HEDMs was investigated to provide insight as to the mechanism of decomposition, as well as to understand the composition of the ultimate fuel to be delivered to the combustor for propulsion.

2. Experimental

2.1. Materials investigated

In this work, several HEDMs were examined including current high-density missile fuels, thermally stable aircraft fuels, conventional rocket fuels, and candidate materials not currently in use. The chemical structures of the pure compounds and complex mixtures are provided (see Table 1), as well as their corresponding densities and specific impulse (I_{sp}) values. I_{sp} is defined as the thrust per mass flow rate of

Table 1
HEDMs: structure and properties

MATERIAL	STRUCTURE	DENSITY (G/CM^3)	ISP (S)
Bicyclopropylidene (BCP)		0.85	312
AFRL-1	proprietary	0.78	311.1
Quadricyclane		0.98	306.8
1,7 Octadi-yne	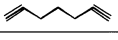	0.82	306
Dimethyl-2-azidoethylamine (2-DAMEZ)	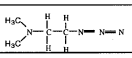	0.93	304.3
Russian Coolant	Mostly octane	0.70	303.5
RP-1	Mostly paraffins & cycloparaffins	0.81	300.1
RG-1	Mostly isoparaffins & cycloparaffins	0.84	299.5
JP-10		0.94	297.4
RJ-7	Mostly strained cyclopentadienes	1.01	296.7
RJ-6	 + JP-10	1.02	296.3

propellant at the nozzle. Small increases in I_{sp} value correspond to increases in the amount of payload a vehicle will be able to deliver to orbit.

2.2. Experimental apparatus

The system for thermal diagnostic studies (STDS) is a well-characterized flow system for studying the thermal degradation of materials in the gaseous or condensed phases [4,5]. Only small amounts of reactants are required, making this technique ideal for screening the thermal stability of novel, synthesized, toxic, or expensive fuel candidates. A schematic view of the system is shown in Fig. 1. An 83.8 cm length of stainless steel liquid chromatography tubing (Alltech Associates, 0.254 mm ID) is enclosed in an independently controlled high-temperature furnace. This furnace is surrounded by a gas chromatograph (Hewlett Packard 5890A), which acts as a preheater and effluent transfer line heater. The system operates at 500 psig in order to maintain liquid phase or supercritical (single phase) conditions. Removal of

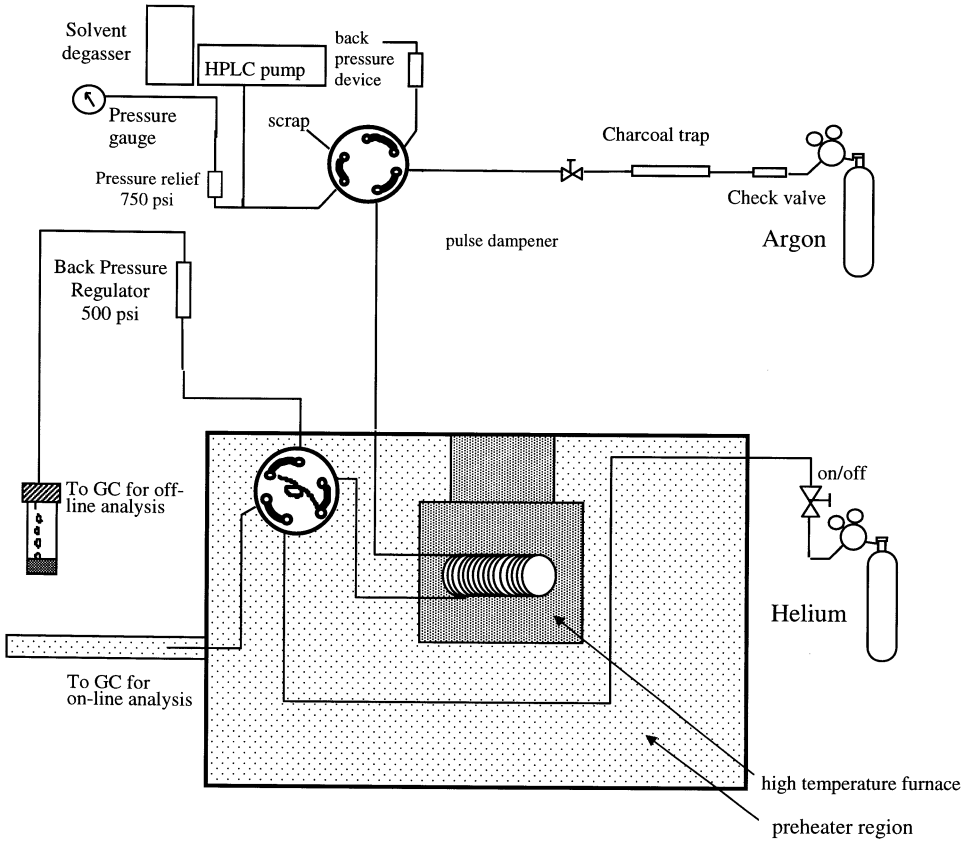

Fig. 1. Schematic view of the reactor system used for thermal decomposition studies of rocket fuel candidates.

dissolved oxygen suppresses thermal–oxidative reactions in favor of strictly pyrolytic degradation. A solvent degasser (Uniflows DG3310) removes any dissolved oxygen (< 1 ppm) from the reactant liquid stream. A high-pressure pump (SSI, Inc.) is used to deliver the liquid reactant at 0.5 ml min^{-1} through the HPLC tubing reactor. While the liquid flow is deoxygenated, high-pressure argon flows through the reactor. A high-pressure switching valve injects the liquid into the reactor and diverts the argon flow to vent. Once steady-state liquid flow is established, a liquid effluent sample is collected and analyzed off-line. Another high-pressure sampling valve injects the liquid directly into a GC via a sample loop and heated transfer line for online analysis. A 0.32 mm ID GasPro GSC (Astec Separation Technologies, Inc.) ''Porous-Layer Open Tubular'' (PLOT) column was used to perform the separation of C1–C8 components of the liquid stream using a flame ionization detector. A 0.25 mm ID DB-5 (J & W Scientific) capillary column in conjunction with a mass selective detector (Hewlett Packard 5970B) was used to identify heavier components than C8.

Off-line effluent analysis was performed in addition to the on-line analysis so that more directed and specific analyses were possible (e.g., trace analysis of products). A gas chromatography–mass spectrometry (GC–MS) method (Hewlett Packard 5971) was used to evaluate the levels of thermal degradation of the reactants and the concentration of products. In these analyses, a HP-1 (Hewlett Packard) 25 m, 0.25 mm in internal diameter, 0.5 μm in film thickness column was used in conjunction with an autosampler. The oven temperature was held at 50 °C for 3 min followed by a 5 °C min^{-1} ramp to a final temperature of 280 °C, which was held for 5 min. A scanning rate of 1.6 scans s^{-1} was established to scan a mass range 12–350 amu. A split flow of 50 ml min^{-1} was used to determine the percent of the parent compound remaining after stressing. Analysis of trace product formation was performed with lower split flows.

Prior to thermal stressing, all HEDMs were diluted by a factor of 100:1 in normal dodecane with the exception of bicyclopropylidene (BCP), which was diluted in toluene due to its insolubility in dodecane. Dilution was necessary because some of the materials were selectively synthesized and only available in small quantities. Also, the unknown toxicity of these materials and their decomposition products made dilution a safer alternative than reacting with pure components. Normal dodecane, however, is a hydrocarbon found in both RP-1 and RG-1. Therefore, RP-1 and RG-1 were diluted in octane to allow for a more accurate assessment of parent compound decomposition.

Thermal degradation of each material was analyzed at furnace temperatures between 100 and 600 °C. The preheater oven was held constant at 100 °C for a furnace temperature of 100 °C, and 200 °C for furnace temperatures above 200 °C. Near isothermal conditions were obtained for at least 67% of the reactor with reactor residence times between 1 and 5 s. Heat transfer and fluid-mechanical modeling of temperature and flow profiles in the reactor were conducted [6]. The flow rate of liquid was held constant at 0.5 ml min^{-1} through the reactor, which resulted in the residence time changes as a function of temperature.

Residence times for each solvent were calculated by assuming a constant heat flux across the tube [6]. A finite difference method was used to calculate the temperature of the fuel at 1 in. intervals for the initial one-third of the reactor tube length. Once the temperature of the fuel was calculated, a corresponding residence time was obtained for each section based on the density, mass flow rate, and the cross-sectional area of the tube. The last two-third of the tube was assumed to be isothermal and one residence time was obtained for that section. The temperature profile along the reactor tube was verified by computation modeling. Cumulative residence times were calculated for each solvent at each reactor temperature and are provided in Table 2.

3. Results and discussion

In the following sections, the thermal degradation of the parent compound BCP is discussed as an example of this thermal decomposition methodology, followed by inter-comparisons of all the parent compound decomposition profiles and their respective decomposition pathways.

3.1. Thermal decomposition of BCP

The thermal decomposition results for BCP are of interest to rocket system designers because of BCP's high strain energy and high I_{sp} value. BCP was subjected to increasing temperatures to develop a thermal decomposition profile under condensed phase pyrolysis conditions. The concentration of the parent material was measured with effectively no change in the dodecane solvent concentration. BCP was observed to be moderately stable with less than 20% decomposition occurring below 300 °C. However, at 400 °C, only 3% of BCP was left remaining. Fig. 2 shows the chromatograms associated with these experiments. As the parent material degraded, decomposition products are formed and increased the concentration as the parent compound decomposes and the temperature is raised. Fig. 3 shows the thermal decomposition profile of the BCP under condensed phase pyrolysis

Table 2
Residence time calculations

Temperature (°C)	Residence time (s)		
	Dodecane	Toluene	Octane
100	4.75	4.72	4.68
200	4.27	4.16	4.07
300	3.71	3.25	3.09
400	2.89	1.06	1.45
500	1.67	0.88	1.14
600	1.33	0.78	0.96

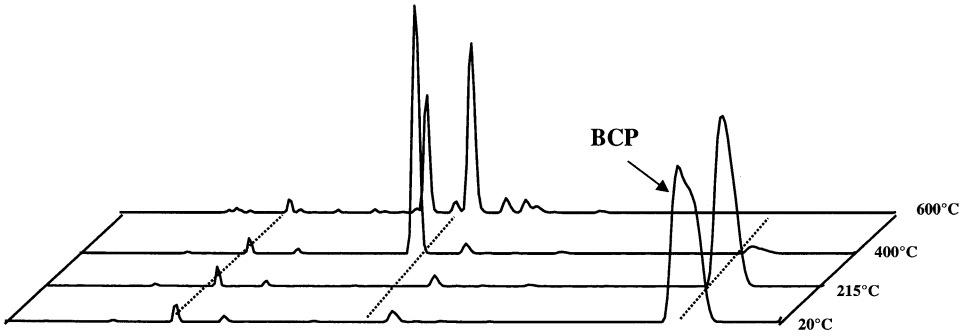

Fig. 2. Chromatographic representation of pyrolytic degradation of BCP and formation of products at increasing temperature.

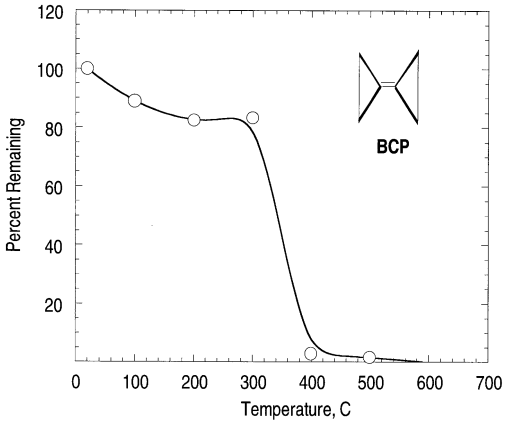

Fig. 3. Thermal decomposition profile for the pyrolysis of BCP at 500 psig for temperatures between 100 and 600 °C.

conditions. There was an apparent change in the rate of decomposition of BCP after 400 °C which may be due to the formation of more stable isomers of BCP with similar mass spectral patterns and retention times by GC–MS. In addition, the changing rate of decomposition may be due to the shorter residence time at higher temperature (see Table 2) since these experiments were not operated at constant residence time.

Although strained ring compounds may provide increases in energy content for combustion, it may not be desirable to thermally decompose the strained rings until the material is introduced to the combustion system. The strained energy may be lost in heating the fuel delivery system rather than in the combustor, where the additional energy could be harnessed to propel the vehicle. In the case of BCP, the data here indicate that if temperatures above 300 °C and 3 s residence time are reached in the fuel system, thermal decomposition may occur, changing significantly the physical and chemical properties of the coolant/propellant in the fuel system. Thus, it is

important to understand the thermal decomposition of a rocket fuel candidate with regard to its time–temperature history within a fuel system. It may be desirable to know the thermal decomposition temperature accurately, so that thermal management settings for maximum recycle temperatures and residence times may be tuned for particular fuels and high-energy candidates.

3.2. Thermal decomposition of other HEDMs

Other HEDMs can be classified in terms of their parent stability, relative to each other as shown in Fig. 4. Clearly, the strained ring compounds such as BCP, AFRL-1, and quadricyclane (with or without the additive) have low decomposition temperatures compared with some of the other more stable compounds such as JP-10 (Fig. 4). The cycloparaffinic materials such as JP-10, RP-1, RG-1, RJ-6, and RJ-7 (Fig. 5) have higher thermal stability than the strained hydrocarbons, with no appreciable decomposition even at 600 °C. Complex mixtures were evaluated by summing the major parent compounds to determine the stability. JP-10 has been shown to be particularly stable even in the gas phase [7].

By examining the shape of the decomposition profiles, HEDMs can be ranked according to their inherent thermal decomposition limits. AFRL-1, a proprietary chemical, and 1,7-octadi-yne are relatively unstable as compared to the current missile and rocket fuels. However, both thermal decomposition temperatures are 300 °C higher than quadricyclane. The Russian coolant, composed of mostly octane, also exhibits much higher thermal stability over the strained ring compounds. JP-10 and RP-1 exhibited the highest thermal stability of all the materials tested. RG-1 is very similar to RP-1 but contains none of the stable short-

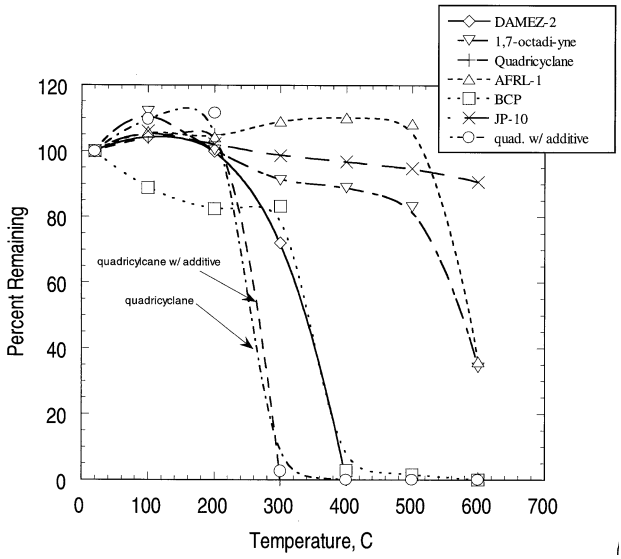

Fig. 4. Thermal decomposition of relatively unstable HEDMs at high pressure and temperature.

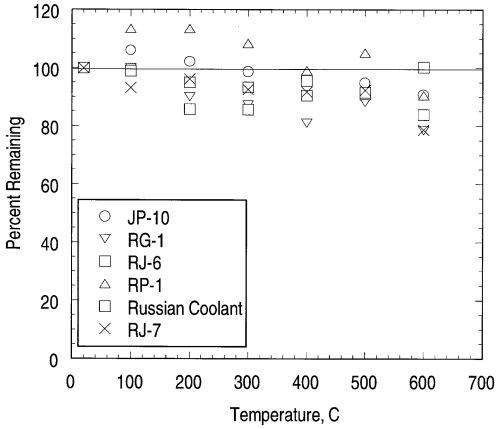

Fig. 5. Relative stability of stable HEDMs as a function of temperature; pressure = 500 psig.

chain alkyl-aromatics; therefore, one would suspect that RG-1 would be slightly less stable than RP-1 which seems to be the case according to Fig. 5. RJ-6 and RJ-7 are slightly lower in overall thermal stability than RP-1 and JP-10.

The additive used in quadricyclane does not appreciably affect the decomposition temperature of quadricyclane under pyrolysis conditions. Perhaps this proprietary additive is an additive for oxidation protection or a detergent additive used to solubilize decomposition products. In any case, this method of ranking decomposition may be a reasonable way to distinguish protection from oxidation reactions versus additives for protection from pyrolysis. Pyrolysis additives which are effective will shift the decomposition curves to a higher temperature.

Quadricyclane is particularly unstable, with significant decomposition occurring in this compound at 200 °C; the pyrolytic decomposition of quadricyclane is complete at a temperature of 300 °C at these residence times. The decomposition characteristics of substituted quadricyclane have been previously described for both gas phase [8,9] and condensed phase [2] reactions. Quadricyclane is known to isomerize to norbornadiene at temperatures as low as 200 °C; the norbornadiene then continues to react to form more stable products at higher temperatures [8,9]. In these experiments, we consider an isomerized product to be a reaction product even though it may have many of the same physical properties as the parent compound. Quadricyclane then continues to react to its final end products.

Dimethyl-2-azidoethylamine (DAMEZ) is slightly more stable than quadricyclane in that the compound begins to decompose at a temperature of approximately 300 °C and is completely decomposed by 400 °C. It is not a strained ring compound like the other materials but does contain unstable nitrogen–nitrogen bonds which readily fragment. The parent compound was clear in color and soluble in the dodecane solvent but the decomposition products were not. Polar amine compounds (brown in color) were observed on the sides of the collecting vial indicating incompatibility with non-polar organic solvents and possible polymerization reactions as the amines react with each other.

Thus, knowledge of the thermal decomposition in the condensed phase gives a good indication of the ability of a fuel to accept thermal stress as it is used in a system. In general, strained ring compounds appear more likely to fragment at lower temperatures followed by straight chain alkanes and then cycloparaffins. One notable exception from this trend was JP-10, which although contains a bridged carbon structure and is strained to a degree, yet has a high degree of thermal stability as compared with the other compounds. The mixtures containing cycloparaffins were the most stable compounds—RG-1, for example, is mostly cycloalkane and therefore stable in comparison to the strained compounds.

3.3. Product formation in high-energy density candidates

Although the high-energy density candidates were examined as dilute mixtures in a solvent, it was possible to observe compounds of decomposition of the less stable HEDM and speculate on their mechanisms of decomposition. Some of the materials, which are chemically similar to straight chain hydrocarbons (such as 1,7-octadi-yne), were difficult to distinguish thermal decomposition products from the thermal decomposition products occurring from dodecane at high temperature. Normal dodecane was also tested at temperature in order to distinguish the solvent decomposition products from solute decomposition products. A summary of the product formation for HEDMs chosen is provided in Table 3.

3.3.1. Product formation from the decomposition of BCP

In this example, BCP formed a variety of products which could be identified as shown in Fig. 6. There was an isomerization of the original BCP molecule to form the substituted spiropentane compound. This intermediate may have further decomposed to form the substituted cyclobutane molecule and the unsaturated straight chain structure by cleavage and rearrangement. This mechanism seems consistent with a mechanism for BCP decomposition described in the literature [10] for low temperature (210 °C) and long residence time (1 h). This mechanism suggests that the carbon–carbon bond of one of the cyclopropane groups was broken to form a bi-radical, which then formed a second cyclopropyl group [10]. As the temperature increased to 500 °C and above, the spiropentane intermediate reacts to form unsaturated non-cyclic compounds such as 2-hexen-4-yne or isomer, or alternatively, the cyclic compound formed from two cyclopropyl groups fragmenting: 1,2-bis-methylene-cyclobutane. Several heavier compounds (possible polymers with cyclopropyl or cyclobutyl fragments) were observed but could not be identified.

3.3.2. Quadricyclane

Quadricyclane has been studied under similar conditions to determine product formation in the condensed phase [2], as well as in the gas phase [8,9]. The condensed phase experiments described previously [2] show results for the thermal stability of pure component quadricyclane (not diluted) similar to those for diluted quadricyclane shown here. Quadricyclane readily isomerizes to norbornadiene even at temperatures of 200–300 °C. The norbornadiene intermediate is itself unstable at

Table 3
Relative product formation for six of the HEDMs

Reactants	Products (600 °C)	Relative yield
Quadricyclane	Norbornadiene	XXX
	Cyclopentadiene	XX
	Cycloheptatriene	XX
	Toluene	X
	Benzene	X
BCP	Methylene spiropentane	XXX
	2-Hexen-4-yne	XX
	1,2-Bis-methylene-cyclobutane	XX
	Other BCP isomers	X
JP-10	Alkenes, alkanes	XXX
	Cyclohexene	X
	Dimethylcyclopentadiene	X
DAMEZ	Tetramethyl methanediamine	XXX
	Dimethyl methaneamine	XX
	Trimethyl amine	XX
	Dimethyl amino propane nitrile	X
	Unknown substituted amine	X
1,7-Octadi-yne	Alkanes	XXX
	Alkenes	XXX
	Cyclopentene	XX
	3-Penten-1-yne	X
	Ethenylmethylene cyclopropane	X
	Alkylbenzenes	X
	Toluene	X
	Methyltetralin	X

X = low, XX = moderate, and XXX = high.

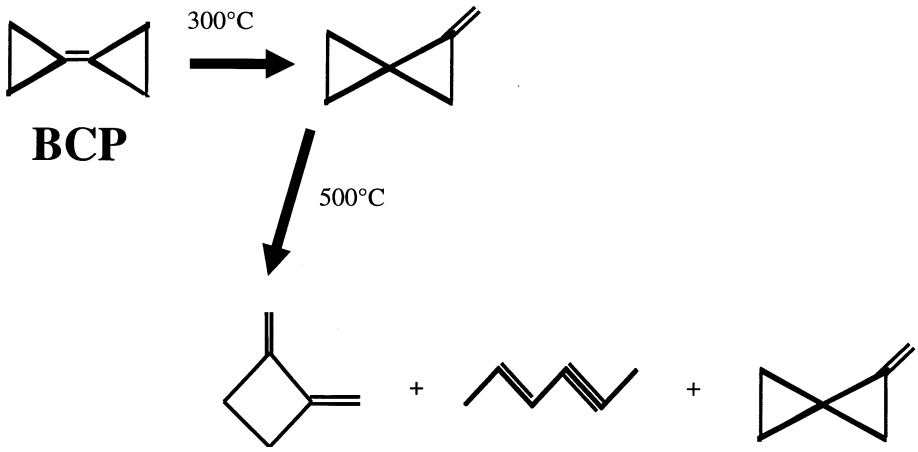

Fig. 6. Product formation from the decomposition of BCP.

temperatures greater than 300 °C; it fragments and rearranges to form the cyclopentadiene, cycloheptatriene, and aromatics (benzene and toluene). This cyclization and formation of unsaturates may be intermediates for the formation of aromatics (benzene and toluene) at higher temperature.

3.3.3. JP-10

JP-10 was the most stable of all of the compounds tested, which was surprising since the structure of JP-10 includes a bridged carbon atom. Since JP-10 was stable and did not decompose, it formed only a small amount of products, which included alkanes, alkenes, cycloalkenes, cyclopentadienes, and alkylbenzenes. JP-10 would probably be an excellent high-energy density candidate from a pyrolytic stability standpoint because it would not degrade until it experienced high temperatures in the combustor.

3.3.4. DAMEZ

This unusual compound tended to degrade into nitrogen-containing species such as amines and cyano-containing compounds. As was discussed earlier, these compounds that formed were largely insoluble in non-polar solvents. A major product of degradation was N,N,N',N'-tetramethyldiaminomethane with somewhat lesser yields of substituted amines such as trimethylamine at relatively low temperatures (400–500 °C). If used as a pure compound, DAMEZ would likely be able to solubilize its own reaction products. However, as in these experiments, if DAMEZ is used in conjunction with a non-polar solvent or fuel, mixture incompatibility may occur. This would create extreme types of problems in fuel systems as these materials have a propensity to foul surfaces and interfere with the operation of valves and control devices, as well as plugging orifices and other passages.

3.3.5. 1,7-Octadi-yne

A great deal of information exists on the pyrolysis of straight chain hydrocarbons. Alkanes generally fragment beta to the terminal carbon atom, and so they form radicals which react to produce a lower molecular weight 1-alkene or alkane. The 1,7-octadi-yne behaved in a similar manner, but because of its initial unsaturation, had a tendency to form a high amount of unsaturates and aromatics indicative of cyclization reactions. Major products included substituted cyclopentanes, substituted cyclohexenes, and toluene as an ultimate aromatic product at temperatures as low as 600 °C.

3.3.6. RG-1 and RP-1

RG-1 was a mixture of substituted decalins and other cycloparaffins with very little normal or branched alkane content. RP-1 also has high cycloparaffin content but also contains small amounts of normal alkanes. Both these fuels are currently being used for rocket applications; RG-1 is specified for Russian rocket applications and RP-1 is specification fuel for rockets from the US. The high cycloparaffin content of both these materials gives good thermal stability characteristics. Products

observed were cracked alkanes and alkenes, followed by unsaturation and cyclization to form aromatic compounds.

3.3.7. RJ-6 and RJ-7

The stability of these fuels is similar to the JP-10 in spite of the fact that there is significant strain energy in the RJ-6 structure (see Table 1). The stability of the material makes it difficult to determine the products of thermal decomposition that would form, but the products that were observed were similar to those formed from JP-10—alkanes, alkenes, cycloalkanes, and cycloalkenes.

4. Conclusions and recommendations

Due to their low thermal stability, some HEDMs are not appropriate candidates for some applications, as they will form significant amounts of degradation products at elevated temperatures. As a class, cycloparaffins provide more stability at high temperature and pressure than do strained hydrocarbons, even though the latter are more desirable from the standpoint of energy content for propulsive purposes. Thermal stability issues may be important considerations for HEDMs, since energy released in the fuel delivery system (instead of in the combustor) may be potentially undesirable. Since the candidate materials are being synthesized in small quantities, this research provides an approach for evaluating thermal stability of very small samples of the potential energetic material. By examining the thermal stability of the parent material, as well as the mechanism of degradation and identity of products of degradation, fuel system designers will obtain preliminary information as to the suitability of the fuel in the overall system.

Acknowledgements

This work was sponsored by the US Air Force, AFRL/PRTG, at Wright-Patterson AFB, Ohio, under contract number F33615-97-C-2719. Mr. Robert Morris was the technical monitor. The authors gratefully acknowledge the useful discussions and suggestions from Dr. Tim Edwards, Dr. Lourdes Maurice, Dr. Steve Zabarnick, and AFRL/PR personnel from Edwards AFB and Wright-Patterson AFB.

References

[1] B. Palaszewski, L. Ianovski, P. Carrick, J. Propulsion Power 14 (5) (1998) 641–648.
[2] K. Wohlwend, L. Maurice, T. Edwards, M. Vangness, R. Striebich, A. Hill, J. Propulsion Power 17 (6) (2001) 1258–1262.
[3] G.D. Roy, Aerospace America 32 (8) (1994) 33–35.
[4] W.A. Rubey, R.A. Grant, Am. Inst. Phys. 59 (2) (1988) 265–269.

[5] R.C. Striebich, W.A. Rubey, A condensed phase test cell assembly for the system for thermal diagnostic studies (STDS), Wright Laboratory Technical Report WE-TR-92-2040, 1992.
[6] J. Thornberg, Simulations of flowing supercritical *n*-decane, MS Thesis, Air Force Institute of Technology, 1998.
[7] P.H. Taylor, W.A. Rubey, Energy and Fuels 2 (1988) 723–728.
[8] A.J. Alfono, Int. J. Chem. Kinet. 29 (9) (1997) 689–694.
[9] A.J. Alfono, Int. J. Chem. Kinet. 28 (7) (1996) 481–487.
[10] P. Le Perchec, J.M. Conia, Tetrahedron Lett. 19 (1970) 1567–1588.

Y. Lists of UDRI Publications, Patents, Presentations, Honors and Awards Obtained during the Contract Period

AWARDS, PUBLICATIONS, AND PRESENTATIONS
(October 1997 to September 2003)

Honors and Awards

1. M. J. DeWitt (2003): Session Chair, 28th Annual Dayton-Cincinnati, AIAA Aerospace Sciences Symposium, Dayton, OH, March.

2. S. Zabarnick (2003): 2002 Outstanding Engineer and Scientist Award, Affiliate Societies Council of the Engineering and Science Foundation of Dayton, Dayton, OH

3. D. R. Ballal (2003): Chairman, ASME-IGTI Board of Directors, American Society of Mechanical Engineers, New York, NY.

4. J. Ervin (2002): Outstanding Research Award, School of Engineering, The University of Dayton, Dayton, OH, September.

5. UDRI Fuels and Combustion Group (2002): Partners with AFRL Researchers in AFOSR Star Team Award in Fuels & Combustion Research, September. (Note: S. Zabarnick and J. Ervin of UD were included in a photograph with AFRL researchers.)

6. M. J. DeWitt (2002): Session Chair, 38th AIAA/ASME/SAE/ASEE Joint Propulsion Conference and Exhibit, Indianapolis, IN July.

7. K. Straley, R. C. Striebich, and J. Klosterman (2002): Best Paper Award, AIAA Aerospace Sciences Symposium, Dayton, OH, March.

8. D. R. Ballal (2002): ASME-IGTI Aircraft Engine Technology Award, June.

9. M. DeWitt (2002): Session Chair, 27th Annual Dayton-Cincinnati AIAA Aerospace Sciences Symposium, Dayton, OH, March.

10. S. Zabarnick (2002): Session Chair, 27th Annual Dayton-Cincinnati AIAA Aerospace Sciences Symposium, Dayton, OH, March.

11. J. Ervin (2002): Full Professor, MAE Department, The University of Dayton, Dayton, OH, January.

12. D. R. Ballal (2001): Visiting Professor, Cranfield University, Cranfield, U.K., July.

13. J. Ervin (2001): Service Award, AIAA Dayton-Cincinnati Section, Dayton, OH, May.

14. J. Ervin (2001): Sigma Xi Research Award, The University of Dayton, Dayton, OH, March.

15. D. Davis (2001): Technician of the Year, University of Dayton Research Institute, March.

16. S. Zabarnick (2001): Session Chair, 26th Annual Dayton-Cincinnati AIAA Aerospace Sciences Symposium, March.

17. D. R. Ballal (2000): AIAA Distinguished Lecturer, Ohio Aerospace Institute, Cleveland, OH December.

18. D. R. Ballal (2000): Distinguished Faculty Seminar, "Gas Turbine Technology-Current Progress and Future Challenges," University of California, Berkeley, CA, November.

19. D. R. Ballal (2000): Invited Seminar, "Formation and Emissions of Combustion-Generated Pollutants," University of Washington, Seattle, WA. October.

20. S. Zabarnick (2000): Associate Professor, MAE Department, The University of Dayton, Dayton, OH, August.

21. D. R. Ballal (2000): AIAA "Propellants and Combustion National Award," Presented at AIAA/ASME/SAE/ASEE Joint Propulsion Conference, Huntsville, AL, July.

22. D. R. Ballal (2000): Chair of Conferences, 46th ASME Gas Turbine Congress and Exposition, New Orleans, LA, July.

23. D. R. Ballal (2000): Whittle-Von Ohain Memorial Lecture, Cranfield University, Cranfield, England, July.

24. D. R. Ballal (2000): Hans von Ohain Memorial Lecture, Dept. of Physics, University of Gottingen, Gottingen, Germany, May.

25. S. Zabarnick (2000): Session Chair, 25th Annual Dayton-Cincinnati AIAA Aerospace Sciences Symposium, March.

26. J. Ervin (2000): Session Chair, 25th Annual Dayton-Cincinnati AIAA Aerospace Sciences Symposium, March.

27. D. R. Ballal (1999): Review Chairman, 45th ASME Gas Turbine Congress and Exposition, Munich, Germany.

28. D. R. Ballal (1999): Hans von Ohain Distinguished Professor, The University of Dayton, Dayton, OH.

29. S. Zabarnick (1999): Session Chair, ASME Turbo Expo '99, Indianapolis, IN.

30. F. Takahashi (1999): Session Chair, 37th AIAA Aerospace Sciences Meeting and Exhibit, Reno, NV.

31. F. Takahashi (1999): Session Chair, 35th AIAA/ASME/SAE/ASEE Joint Propulsion Conference & Exhibit, Los Angeles, CA.

32. D. R. Ballal (1999): External Examiner for Doctoral Candidates, University of Washington, Seattle, WA.

33. F. Takahashi (1999): Invited Lecture, Department of Mechanical and Aerospace Engineering, Case Western Reserve University, Cleveland, OH.

34. S. Zabarnick (1998): Wohlleben-Hochwalt Outstanding Professional Research Award, University of Dayton, Dayton, OH.

35. D. R. Ballal (1998): Member, Board of Directors, ASME- International Gas Turbine Institute (IGTI), Atlanta, GA

36. F. Takahashi (1998): Session Chair, 34th AIAA/ASME/SAE/ASEE Joint Propulsion Conference & Exhibit, Cleveland, OH.

37. D. R. Ballal (1998): Member, NASA Panel on Combustion R & D, NASA HQ, Washington, D.C.

38. M.S. Mick and S. Zabarnick (1998): Best Paper Award, 23rd AIAA Mini-Symposium, Dayton, OH.

39. D. R. Ballal (1997): Member, Board of Directors, Central States Section, The Combustion Institute, Pittsburgh, PA.

Patents

1. S. Zabarnick, S.P. Heneghan, and M.S. Mick (2002): U.S. Patent 6,475,252B1, “Stabilizing Additive for the Prevention of Oxidation and Peroxide Formation.”

Journal Publications

1. J. S. Ervin, T. F. Williams, S. P. Heneghan, and S. Zabarnick, "The Effects of Dissolved Oxygen Concentration, Fractional Oxygen Consumption, and Additives on JP-8 Thermal Stability," *Transactions of ASME, Journal of Engineering for Gas Turbines and Power*, Vol. 119, pp. 822-829, November 1997.

2. J. S. Ervin and S. Zabarnick, "Computational Fluid Dynamics Simulation of Jet Fuel Oxidation Incorporating Pseudo-Detailed Chemical Kinetics," *Energy and Fuels*, Vol. 12, pp. 344-352, March 1998.

3. J. S. Ervin and S. Zabarnick, "Numerical Simulation of Jet Fuel Oxidation & Fluid Dynamics," *Proceedings of 6th (Int.) Conference on Stability & Handling of Liquid Fuels*, Vol. 1, pp. 385-402, October 1997.

4. S. Zabarnick, S. D. Whitacre, M. S. Mick, and J. S. Ervin, "Studies of Jet Fuel Oxidation Using Oxygen Monitoring and Chemical Kinetic Modeling," *Proceedings of 6th (Int.) Conference on Stability & Handling of Liquid Fuels*, Vol. 1, pp. 363-383, October 1997.

5. S. D. Anderson, W. A. Rubey, and R. C. Striebich, "Measurement of Dissolved and Total Water Content in Advanced Turbine Engine Fuels with a Gas-Liquid Chromatographic Technique," *Proceedings of 6th (Int.) Conference on Stability & Handling of Liquid Fuels*, Vol. 1, pp. 103-112, October 1997.

6. F. Takahashi, W. J. Schmoll, and V. R. Katta, "Attachment Mechanisms of Diffusion Flames," *Proceedings of 27th Symposium (Int.) on Combustion*, The Combustion Institute, 1998, pp. 675-684.

7. S. Zabarnick, "Pseudo-Detailed Chemical Kinetic Modeling of Antioxidant Chemistry for Jet Fuel Applications," *Energy and Fuels*, Vol. 12, pp. 547-553, 1998.

8. S. Zabarnick and S. D. Whitacre, "Aspects of Jet Fuel Oxidation," *Transactions of ASME, Journal of Engineering for Gas Turbines and Power*, Vol. 120, pp. 519-525, 1998.

9. S. Zabarnick, M. S. Mick, R. C. Striebich, R. R. Grinstead, and S. P. Heneghan, "Studies of Silylation Agents as Thermal-Oxidative Jet Fuel Additives," *Preprints of Symposia, Division of Fuel Chemistry, American Chemical Society*, Vol. 43, No. 1, pp. 64-68, 1998.

10. R. C. Striebich, R. R. Grinstead, and S. Zabarnick, "Analytical Separation and Quantification of Specification Levels of MDA in Aviation Fuels, *Preprints of Symposia, Division of Fuel Chemistry, American Chemical Society*, Vol. 43, No. 1, pp. 94-98, 1998.

11. J. S. Ervin and S. P. Heneghan, "The Meaning of Activation Energy and Reaction Order in Autocorrelating Systems," *Transactions of ASME, Journal of Engineering for Gas Turbines and Power*, Vol. 120, pp. 468-476, July 1998.

12. S. P. Heneghan and W. E. Harrison III, "JP-8+100: The Development of High Thermal Stability Jet Fuel," *Proceedings of the 6th International Conference on Stability & Handling*

of Liquid Fuels, Ed. H. N. Giles, US Department of Energy, Washington DC, Vol. 1, pp. 271-283, 1998.

13. S. P. Heneghan and M. D. Vangsness, "Additive Stability in JP-8-Metal Alloy Systems at Elevated Temperatures," *Proceedings of the 6th International Conference on Stability & Handling of Liquid Fuels*, Ed. H. N. Giles, US Department of Energy, Washington DC, Vol. 1, pp. 285-293, 1998.

14. D. H. Kalt, "The Effect of Detergent/Dispersant on Aircraft Materials," *Proceedings of the 6th International Conference on Stability & Handling of Liquid Fuels*, Ed. H. N. Giles, US Department of Energy, Washington DC, Vol. 1, pp. 251-269, 1998.

15. F. Takahashi and V. R. Katta, "A Role of Chemical Kinetics in the Simulation of the Reaction Kernel of Methane Jet Diffusion Flames," Paper No. AJTE 99-6190, *Proceedings of the 15th ASME/JSME Thermal Engineering Joint Conference*, San Diego, CA, 1998.

16. S. Zabarnick, M. S. Mick, R. C. Striebich, and R. R. Grinstead, "Model Studies of Silylation Agents as Thermal-Oxidative Jet Fuel Additives," *Energy and Fuels*, Vol. 13, pp. 154-159, 1999.

17. S. Zabarnick, E.G. Jones, S. Anderson, "The Measurement of Antioxidant Performance in Aviation Turbine Fuel Using the Quartz Crystal Microbalance and Near Isothermal Flowing Test Rig," *Proceedings of the 6th International Conference on Stability & Handling of Liquid Fuels*, Ed. H. N. Giles, US Department of Energy, Washington DC, Vol. 1, p. 989, 1998.

18. S. Zabarnick and M.S. Mick, "Studies of Hydroperoxide Decomposing Species for Inhibiting Oxidation in Jet Fuels," PREPRINTS, Division of Petroleum Chemistry, American Chemical Society, Vol. 43, pp. 349-352, 1998.

19. J.S. Ervin, T.F. Williams, and G. Hartman, "Effect of Test Period on the Rate of Fouling in a Complex Flowing System," PREPRINTS, Division of Petroleum Chemistry, American Chemical Society, Vol. 43, pp. 373-377, 1998.

20. R.C. Striebich and W.A.Rubey, "High-Pressure High Temperature Pyrolysis Reactions in the Condensed Phase with In-Line Chemical Analysis," PREPRINTS, Division of Petroleum Chemistry, American Chemical Society, Vol. 43, pp. 378-381, 1998.

21. L.Q. Maurice and R.C. Striebich, "Cyclic Species Formation in the Fuel Systems of High-Speed Vehicles, "PREPRINTS, Division of Petroleum Chemistry, American Chemical Society, Vol. 43, pp. 423-427, 1998.

22. D.T. Wickham, J.V. Atria, J.R. Engel, B.D. Hitch, M.E. Karpuk, R.C. Striebich, "Formation of Carbonaceous Deposits in a Model Jet Fuel under Pyrolysis Conditions," PREPRINTS, Division of Petroleum Chemistry, American Chemical Society, Vol. 43, pp. 428-432, 1998.

23. W.A. Rubey, R.C. Striebich, S.D. Anderson, "Various Instrumental Aspects of Analyzing Water in Jet Fuel by Gas-Liquid Chromatography," PREPRINTS, Division of Petroleum Chemistry, American Chemical Society, Vol. 43, pp. 471-474, 1998.

24. J. W. Blust, D. R. Ballal, and G. J. Sturgess, “Fuel Effects on Lean Blowout and Emissions from a Well-Stirred Reactor,” *AIAA Journal of Propulsion and Power*, Vol. 15, pp. 216-223, 1999.

25. S. Zabarnick and M. S. Mick, “Inhibition of Jet Fuel Oxidation by Addition of Hydroperoxide Decomposing Species,” Industrial & Engineering Chemistry Research, Vol. 38, pp. 3557-3563, Sept. 1999.

26. B. Grinstead and S. Zabarnick, “Studies of Jet Fuel Thermal Stability, Oxidation, and Additives Using an Isothermal Oxidation Apparatus Equipped with Oxygen Sensor,” Energy and Fuels, Vol. 13, pp. 756-760, 1999.

27. F. Takahashi, W. J. Schmoll, E. Strader, and V. M. Belovich, “Suppression Behavior of Obstruction-Stabilized Pool Flames,” Combustion Science and Tech. Vol 163, pp. 107-130, 2001

28. F. Takahashi and V. R. Katta, “Chemical Kinetic Structure of the Reaction Kernel of Methane Jet Diffusion Flames,” Combustion Science and Technology, Vol. 155, pp. 243-279, 2000

29. J. S. Ervin, S. Zabarnick, K. E. Binns, G. Dieterle, and C. Obringer, “Investigation of the Use of JP-8+100 with Cold Flow Enhancer Additives as a Low-Cost Replacement for JPTS,” *Energy and Fuels*, Vol. 13, pp. 1246-1251, (1999).

30. J.S. Ervin, S. Zabarnick, E. Binns, G. Dieterle, D. Davis, and C. Obringer, “Effect of Jet Fuel Additives on Low-Temperature Fluidity and Tank Hold-Up,” Proceedings of the 14th Intl. Symp. on Airbreathing Engines, Florence, Italy, September 1999.

31. L. Q. Maurice, E. Corporan, W. E. Harrison, D. Minus, R. Mantz, T. Edwards, R. C. Striebich, S. Sidhu, J. Graham, B. Hitch, D. Wickham, and M. Karpur, “Controlled Chemically Reacting Fuels: A New Beginning,” Proceedings of the 14th Intl. Symp. on Airbreathing Engines, Florence , Italy, September 1999.

32. J.S. Ervin, S. Zabarnick, and T.F. Williams, "One-Dimensional Simulations of Jet Fuel Thermal-Oxidative Degradation and Deposit Formation Within Cylindrical Passages," *Transactions of ASME, Journal of Energy Resource Technology*, Vol. 122, No. 4, pp. 229-238, December 2000.

33. R. C. Striebich, B. Grinstead, and S. Zabarnick, “Quantitation of Metal Deactivator Additive by Derivatization and Gas Chromatography-Mass Spectrometry,” *Journal of Chromatographic Science*, Vol. 38, pp. 393-398, 2000.

34. M. D. Vangsness, S. Zabarnick, N. Widmore, and J. S. Ervin, “Jet Fuel Crystallization at Low Temperatures,” PREPRINT, Division of Petroleum Chemistry, American Chemical Society, Vol. 45, pp. 534-537, 2000.

35. K. Wohlwend, S. Zabarnick, K. E. Binns, and B. Grinstead, "Thermal Stability Testing of the Baker Flo-XS Pipeline Drag Reducing Additive," PREPRINT, Division of Petroleum Chemistry, American Chemical Society, Vol. 45, pp. 501-504, 2000.

36. S. Zabarnick, "Investigation of Fuel Additives for a JP-8+225 Jet Fuel Using the Quartz Crystal Microbalance," PREPRINTS, Division of Petroleum Chemistry, American Chemical Society, Vol. 45, pp. 501-504, 2000.

37. D. L. Atkins, J. S. Ervin, M. Vangsness, and C. Obringer, "Flow Visualization of the Freezing of Jet Fuel," Proceedings of the 7th International Conference on Stability and Handling of Liquid Fuels, Graz, Austria, Vol. 2, pp. 841-856, 2001.

38. J. S. Ervin, T. F. Williams, J. Bento, and T. Doungthip, "Studies of Jet Fuel Thermal Stability and Flow Characteristics within a Nozzle Under Supercritical Conditions," Preprint, Div. Of Petroleum Chemistry, American Chemical Society, pp. 538-541, 2000.

39. C. A. Obringer, J. S. Ervin, S. Zabarnick, and K. E. Binns, "Development of a Low Temperature Jet Fuel," Proceedings of the 7th International Conference on Stability and Handling of Liquid Fuels, Graz, Austria, Vol. 2, pp. 633-646, 2001.

40. S. Zabarnick, N. Widmor, J. S. Ervin, and C. Obringer, "Studies of Jet Fuel Freezing and Cold Flow Improving Additives by Differential Scanning Calorimetry," Proceedings of the 7th International Conference on Stability and Handling of Liquid Fuels, Graz, Austria, Vol. 2, pp. 719-730, 2001.

41. S. Zabarnick and N. Widmor, "Studies of Jet Fuel Freezing by Differential Scanning Calorimetry," Energy and Fuels, Vol. 15, pp. 1447-1453, 2001

42. J. S. Ervin, N. Widmor, S. Zabarnick, and M. Vangsness, "Studies of Jet Fuel Freezing by Differential Scanning Calorimetry and Cold-Stage Microscopy," Transactions of ASME, *Journal of Engineering for Gas Turbines and Power*, Vol. 125, pp. 34-39, 2003.

43. D. R. Ballal and J. Zelina, "Assessment of Gas Turbine Combustor Performance and Emissions Using a Well-Stirred Reactor," ISABE-2001-1065, Proceedings of International Society for Air Breathing Engines (ISABE), Bangalore, India, 2001.

44. D. L. Atkins and J. S. Ervin, "Flow Visualization of the Freezing of Aviation Fuel," *Energy and Fuels*, Vol. 15, pp. 1233-1240, 2001.

45. D. L. Atkins and J. S. Ervin, "Simulation of the Freezing of Jet Fuel," Proceedings of NATO AVT Symposium on Heat Transfer and Cooling in Propulsion and Power Systems, Loen, Norway, May 2001.

46. T. Doungthip, J. S. Ervin, T. F. Williams, and J. Bento, "Studies of Injection of Jet Fuel at Supercritical Conditions," Industrial and Engineering Chemistry Research, Vol. 41, pp. 5856-5866, 2002.

47. K. Wohlwend, L. Q. Maurice, T. Edwards, R. C. Striebich, M. Vangsness, and A. S. Hill, "Thermal Stability of Energetic Hydrocarbon Fuels for Use in Combined Cycle Engines," AIAA J. of Propulsion & Power, Vol. 17, No. 6, Nov. 2001.

48. J. S. Ervin, T. F. Williams, T. Ward, and J. Bento, "Surface Deposition within Treated and Untreated Stainless-Steel Tubes Resulting from Thermal-Oxidative and Pyrolytic Degradation of Jet Fuel," *Energy and Fuels*, Vol. 17, pp. 577-586, 2003.

49. S. Zabarnick, and N. Widmor, "Studies of Urea Treatment on the Low Temperature Properties of Jet Fuel," *Energy and Fuels*, Vol. 16, pp. 1565-1570, 2002.

50. L. M. T. Balster, S. Zabarnick, and R. C. Striebich, "Predicting the Fouling Tendency of a Thermally Stressed Jet Fuel by High Performance Liquid Chromatography (HPLC) Analysis," *Prepr.-Am. Chem. Soc., Div Pet. Chem.,* Vol. 47, pp. 161-164, 2002.

51. M. W. Badger, S. Zabarnick, and G. R. Wilson, "Selection of Prototype Thermally Stable Jet Fuels. 2. Quartz Crystal Microbalance Tests for Thermal-Oxidative Stability," *Prepr.-Am. Chem. Soc., Div Pet. Chem.,* Vol. 47, pp. 170-173, 2002.

52. M. J. DeWitt, and S. Zabarnick, "Development and Evaluation of Additives to Inhibit Oxidative Deposition of Jet Fuels," *Prepr.-Am. Chem. Soc., Div Pet. Chem.,* Vol. 47, pp. 183-186, 2002.

53. T. Doungthip, J. S. Ervin, T. Ward, T. Williams, and S. Zabarnick, "Surface Deposition Within Treated and Untreated Stainless-Steel Tubes Resulting from Thermal-Oxidative Degradation of Jet Fuel," *Prepr.-Am. Chem. Soc., Div Pet. Chem.,* Vol. 47, pp. 204-207, 2002.

54. D. D. Link, D. K. Minus, R. C. Striebich, K. S. Rothenberger, and J. P. Baltrus, "The Analysis of Total Sulfur and Speciated Sulfur Compounds in Aviation Turbine Fuel," *Prepr.-Am. Chem. Soc., Div Pet. Chem.,* Vol. 47, pp. 212-215, 2002.

55. R. C. Striebich, "Fast Gas Chromatography for Middle-Distillate Aviation Turbine Fuels," *Prepr.-Am. Chem. Soc., Div Pet. Chem.,* Vol. 47, pp. 219-222, 2002.

56. S. Zabarnick, R. C. Striebich, K. Straley, and L. M. T. Balster, "Solid-Phase Extraction Analysis of Polar Species in Jet Fuel," *Prepr.-Am. Chem. Soc., Div Pet. Chem.,* Vol. 47, pp. 223-226, 2002.

57. S. M. Rozenzhak, R. C. Striebich, and C. E. Bunker, "Development of a High-Speed Jet-Fuel Diagnostic System Using Gas Chromatography and Principal Component Analysis," *Prepr.-Am. Chem. Soc., Div Pet. Chem.,* Vol. 47, pp. 227-230, 2002.

58. N. Widmor, J. S. Ervin, and S. Zabarnick, "Properties of Jet Fuels At Low Temperature and the Effect of Additives," *Prepr.-Am. Chem. Soc., Div Pet. Chem.,* Vol. 47, pp. 239-242, 2002.

59. S. Zabarnick, and M. Vangsness, “Properties of Jet Fuels At Low Temperature and the Effect of Additives,” *Prepr.-Am. Chem. Soc., Div Pet. Chem.,* Vol. 47, pp. 243-246, 2002.

60. E. Corporan, M. J. DeWitt, and M. Wagner, “Evaluation of Soot Particulate Mitigation Additives in a T63 Engine,” Proceedings of the International Conference on Air Quality III, Arlington, VA, September, 2002.

61. D. D. Link, J. P. Baltrus, K. S. Rothenberger, P. Zandhuis, D. Minus, and R. C. Striebich, “Rapid Determination of Total Sulfur in Fuels using Gas Chromatography with Atomic Emissions Detection,” Journal of Chromatographic Science, Vol. 40, pp. 500-504, 2002.

62. N. Kuprowicz, J. S. Ervin, and S. Zabarnick, “Modeling the Liquid Phase Oxidation of Hydrocarbons over a Range of Temperatures and Dissolved Oxygen Concentrations with Pseudo-Detailed Chemical Kinetics,” submitted to Industrial and Engineering Chemistry Research, December 2002.

63. D. R. Ballal, M. J. DeWitt, E. Corporan, and W. E. Harrison III, “Particulate Loading and Radiation in Gas Turbine Combustors,” AIAA Paper No. 2003-0337.

64. E. Corporan, M. J. Dewitt, and M. Wagner, “Evaluation of Soot Particulate Mitigation Additives in a T63 Engine,” submitted to Fuel processing Technology, March 2003.

65. L. Balster, “Fouling Tendency—Jet Fuels,” submitted for publication in the Encyclopedia of Petroleum Engineering, April 2003.

66. L. Balster, “Fouling Tendency—An Overview,” submitted for publication in the Encyclopedia of Petroleum Engineering, April 2003.

Presentations

1. V. J. Van Griethuysen and J.S.Ervin, "Modeling the F-22 Fuel System Test Rig," Presented at the JANNAF Meeting, West Palm Beach FL, October 1997

2. V. M. Belovich and F. Takahashi, "Suppressing Fires Stabilized Behind Clutter," Third Annual Strategic Environmental Research and Development Program (SERDP) Symposium, Washington D.C., December 1997.

3. R. C. Striebich, R. R. Grinstead, and S. Zabarnick, "Analytical Separation and Quantitation of Specification Levels of MDA in Aviation Fuels," American Chemical Society Meeting, Dallas, TX, March 1998.

4. M. Mick and S. Zabarnick, "Jet Fuel Oxidation: Peroxy Radical Inhibition and Peroxide Decomposition," Presented at the 23rd AIAA Mini-Symposium, Dayton OH, April 1998.

5. R. Grinstead, R. Striebich, and S. Zabarnick, "The Quantification of MDA in Aviation Fuels Using a Silylation Agent," Presented at the 23rd AIAA Mini-Symposium, Dayton OH, April 1998.

6. S. Zabarnick, E. G. Jones, and S. D. Anderson, "The Measurement of Antioxidant Performance in Aviation Turbine Fuel Using the Quartz Crystal Microbalance and Near Isothermal Test Rig," Sixth (Int.) Conference on Stability and Handling of Liquid Fuels, Vancouver, B.C., Canada, October 1997.

7. V. Acosta and J. S. Ervin, "Modeling the Advanced Reduced Scale Fuel System Simulator," 23rd AIAA Mini-Symposium, Dayton, OH, April 1998.

8. V. M. Belovich and F. Takahashi, "Suppressing Fires Stabilized Behind Clutter," 23rd AIAA Mini-Symposium, Dayton, OH, April 1998.

9. F. Takahashi, W. J. Schmoll, and V. R. Katta, "How is a Diffusion Flame Stabilized?" 23rd AIAA Mini-Symposium, Dayton, OH, April 1998.

10. F. Takahashi, W. J. Schmoll, and V. Belovich, "Extinction of Bluff-Body Stabilized Diffusion Flames," Central States Section Meeting, The Combustion Institute, Lexington, KY, May 1998.

11. V. Belovich and F. Takahashi, "Stabilization of Flames," Next generation Fire Suppression Technology Program, Annual Research Meeting, Rockville, MD, June 1998.

12. F. Takahashi, W. J. Schmoll, and V. Belovich, "Suppression of Bluff-Body Stabilized Diffusion Flames," AIAA Paper No. 98-3529, 34th AIAA/ASME/SAE/ASEE Joint Propulsion Conference and Exhibit, Cleveland, OH, July 1998.

13. V. M. Belovich, F. Takahashi, and W. J. Schmoll, "Suppressing Fires Stabilized Behind Clutter," 26th International Conference on Fire Safety, Columbus, OH, July 1998.

14. F. Takahashi, "Numerical Simulations of Methane Diffusion Flames," Workshop on Suppression of Bluff-Body Stabilized Pool Fires, National Institute of Standards and Technology, Gaithersburg, MD, June 1998.

15. J. S. Ervin, T. F. Williams, and G. J. Hartman, "Flowing Studies of JP-8+100 Jet Fuel at Supercritical Conditions," AIAA Paper No. 98-3760, 34th AIAA/ASME/SAE/ASEE Joint Propulsion Conference and Exhibit, Cleveland, OH, July 1998.

16. G. L. Dieterle and K. E. Binns, "Evaluation of JP-8+100 Additives in Large Laboratory Test Systems," AIAA Paper No. 98-3531, 34th AIAA/ASME/SAE/ASEE Joint Propulsion Conference and Exhibit, Cleveland, OH, July 1998.

17. D. H. Kalt, "The Effect of Detergent/Dispersant on Aircraft Materials," International Filteration Conference, Southwest Research Institute, San Antonio, TX, April 1998.

18. L. Q. Maurice, T. Edwards, and R. C. Striebich, "Formation of Cyclic Compounds in the Fuel Systems of Hydrocarbon High Speed Vehicles," AIAA Paper No. 98-3534, 34th AIAA/ASME/SAE/ASEE Joint Propulsion Conference and Exhibit, Cleveland, OH, July 1998.

19. S. Zabarnick and M.S. Mick, "Studies of Hydroperoxide Decomposing Species for Inhibiting Oxidation in Jet Fuels," Symposium on Structure of Jet Fuel V, Division of Petroleum Chemistry, 216th National Meeting, American Chemical Society, Boston, MA, August 23-27, 1998.

20. J.S. Ervin, T.F. Williams, and G. Hartman, "Effect of Test Period on the Rate of Fouling in a Complex Flowing System," Symposium on Structure of Jet Fuel V, Division of Petroleum Chemistry, 216th National Meeting, American Chemical Society, Boston, MA, August 23-27, 1998.

21. R.C. Striebich and W.A.Rubey, "High-Pressure High Temperature Pyrolysis Reactions in the Condensed Phase with In-Line Chemical Analysis," Symposium on Structure of Jet Fuel V, Division of Petroleum Chemistry, 216th National Meeting, American Chemical Society, Boston, MA, August 23-27, 1998.

22. L.Q. Maurice and R.C. Striebich, "Cyclic Species Formation in the Fuel Systems of High-Speed Vehicles," Symposium on Structure of Jet Fuel V, Division of Petroleum Chemistry, 216th National Meeting, American Chemical Society, Boston, MA, August 23-27, 1998.

23. D.T. Wickham, J.V. Atria, J.R. Engel, B.D. Hitch, M.E. Karpuk, R.C. Striebich, "Formation of Carbonaceous Deposits in a Model Jet Fuel under Pyrolysis Conditions," Symposium on Structure of Jet Fuel V, Division of Petroleum Chemistry, 216th National Meeting, American Chemical Society, Boston, MA, August 23-27, 1998.

24. W.A. Rubey, R.C. Striebich, S.D. Anderson, "Various Instrumental Aspects of Analyzing Water in Jet Fuel by Gas-Liquid Chromatography," Symposium on Structure of Jet Fuel V, Division of Petroleum Chemistry, 216th National Meeting, American Chemical Society, Boston, MA, August 23-27, 1998.

25. Takahashi, F., Vangsness, M. D., Durbin, M. D., and Schmoll, W. J., "Turbulence Structure of Swirling Hydrogen Jet Diffusion Flames," Poster Session at the Third International Workshop on Measurement and Calculation of Turbulent Nonpremixed Flames, Boulder, Colorado, July 30-August 1, 1998.

26. Takahashi, F., W. J. Schmoll, and Katta, V. R., "Attachment Mechanisms of Diffusion Flames," Twenty-Seventh Symposium (International) on Combustion, Boulder, Colorado, August 2-7, 1998.

27. Takahashi, F., Schmoll, W. J., and Belovich, V. M., "Suppression of Bluff-Body Stabilized Model Fires," Poster Session at the Twenty-Seventh International Symposium on Combustion, Boulder, Colorado, August 2-7, 1998.

28. Takahashi, F., Schmoll, W. J., and Belovich, V. M., "Suppression of Bluff-Body Stabilized Pool Fires," AIAA Paper No. 99-0327, 37th Aerospace Sciences Meeting and Exhibits, Reno, NV. January 11-14, 1999.

29. F. Takahashi, W. J. Schmoll, E. Strader, and V. M. Belovich, "Effects of Obstruction on Fire Suppression Efficiency," Proceedings of 9th Halon Options Technical Working Conference (HOTWC-99), Albuquerque, NM, April (1999)

30. F. Takahashi and V. R. Katta, "Role of Chemical Kinetics in the Simulation of the Reaction Kernel of Methane Jet Diffusion Flames," Proceedings of 5th ASME/JSME Joint Thermal Engineering Conference, San Diego, CA, Paper No. AJTE99-6190, March (1999)

31. Takahashi, F., Schmoll, W. J., and Belovich, V. M., "Stabilization and Suppression of a Diffusion Flame Behind a Step," Proceedings of Joint U.S. Sections Meeting of the Combustion Institute, Washington, D.C. March 1999.

32. S. P. Heneghan and C. W. Frayne, "Propagation of Errors Analysis for Emissions Analyzer Data," AIAA Dayton-Cincinnati Section Aerospace Sciences Symposium, April 1999.

33. S. Zabarnick, M.S. Mick, R.C. Striebich, R.R. Grinstead, and S.P. Heneghan, "Studies of Silylation Agents as Thermal-Oxidative Jet Fuel Additives," Presented at the 215th American Chemical Society National Meeting, Dallas, TX, March 30, 1998.

34. R. C. Striebich and W. A. Rubey, "High Pressure High-Temperature Pyrolysis Reactions in Condensed Phase with in-line Chemical Analysis," ACS Division of Petroleum Chemistry preprints, Vol. 43, No. 3, pp. 378-381, July 1998.

35. D. T. Wickham, J. R. Engel, M. E. Karpuk, J. V. Atria, B. D. Hitch, and R. C. Striebich, "Formation of Carbonaceous Deposits in a Model Jet Fuel under Pyrolysis Conditions," ACS Division of Petroleum Chemistry preprints, Vol. 43, No. 3, pp. 428-432, July 1998.

36. W. A. Rubey, R. C. Striebich, and S. D. Anderson, "Various Instrumental Aspects of Analyzing Water in Jet Fuel by Gas-Liquid Chromatography," ACS Division of Petroleum Chemistry preprints, Vol. 43, No. 3, pp. 378-381, July 1998.

37. R. C. Striebich, M. D. Vangsness, L. Q. Maurice, T. Edwards, K. Wohlwend, and A. S. Hill, "Thermal Decomposition of Energetic Fuel Candidates," AIAA Dayton-Cincinnati Section Aerospace Sciences Symposium, April 1999.

38. W. A. Rubey, R. C. Striebich, and J. V. Ryan, "Analysis of Trace-Level Organic Combustion Process Emissions Using Novel Multidimensional Gas Chromatography-Mass Spectrometry (MDGC-MS) Procedures," presented at the 18th (Int.) Conference On Incineration and Thermal Technologies, Orlando, May 1999.

39. R. C. Striebich and W. A. Rubey, "Formation of Aromatic Pyrolysis Products from Condensed Phase High Temperature High Pressure Reaction," Presented at PittCon, Orlando, March 1999.

40. J. Bento, J.S. Ervin, T.F. Williams, and G. Hartman, "Fouling of a Nozzle from Jet Fuel Flowing Under Supercritical Conditions," AIAA Dayton-Cincinnati Section Aerospace Sciences Symposium, April 1999.

41. S. Buerger and J.S. Ervin, "System Level Model for a High-Speed Aircraft Fuel System," Ohio Space Grant Consortium, Cleveland, April 1999.

42. J.S. Ervin, "System Level Modeling with EASY5," HYSET Workshop, W. Palm Beach Fl., January 1999.

43. J. Ervin, S. Zabarnick, E. Binns, G. Dieterle, D. Davis, and C. Obringer, "The Development of JP-8 as a Replacement Fuel for JPTS Jet Fuel," JANNAF Meeting, W. Palm Beach Fl., October 1999.

44. C. Obringer, J. Ervin, S. Zabarnick, E. Binns, G. Dieterle, and D. Davis, "Low-Temperature Additives for Jet Fuel," Coordinating Research Council, Washington D.C., May 1999.

45. K.E. Binns, and G.L. Dieterle, "High Temperature Stability of JP-8+100 and Other Fuels," ASME Paper No. 99-GT-107, June 1999.

46. R. C. Striebich, L. Q. Maurice, and T. Edwards, " Formation of Cyclic Compounds in Cracking Reactions for Hydrocarbon-Fueled High Speed Vehicles," ASME paper No. 99-GT-136, June 1999.

47. J. S. Ervin, S. Zabarnick, D. Davis, K. E. Binns, G. Dieterle, and C. Obringer, "Effect of Cold Flow Additives on Aviation Fuel Fluidity and Tank Hold-Up," 34th Intersociety Energy Conversion Engineering Conference, Vancouver, BC. Canada, August 1999.

48. F. Takahashi, W. J. Schmoll, E. A. Strader, and V. M. Belovich, "Effects of Obstruction on Fire Suppression Efficiency," Proceedings of the 9th Halon Options Technical Working Conference, Albuquerque, NM, April 1999.

49. F. Takahashi and V. R. Katta, "Stability-Limit Predictions of Methane Jet Diffusion Flames," 35th AIAA/ASME/SAE/ASEE Joint Propulsion Conference, Los Angeles, CA, June 1999.

50. T. F. Williams, E. Corporan, and D. K. Minus, “Studies of Decalin as a Suppressor of Pyrolytic Deposits in JP-8+100,” 35th AIAA/ASME/SAE/ASEE Joint Propulsion Conference, Los Angeles, CA, June 1999.

51. J.S. Ervin, S. Zabarnick, E. Binns, G. Dieterle, C. Obringer, and K.Wohlwend, "Effect of Cold Flow Additives on Jet Fuel Fluidity and Fuel Solidification," International Mechanical Engineering Conference & Exposition, Nashville, TN, November 1999.

52. Takahashi, F. and Belovich, V. M., “Suppression of Step-Stabilized Diffusion Flames in Air Vehicles,” Twenty-Eighth International Conference on Fire Safety, Columbus, OH, July 1999

53. R. C. Striebich, L. Q. Maurice, and T. Edwards, “Formation of Cyclic Compounds in Cracking Reactions for Hydrocarbon-Fueled High Speed Vehicles,” ASME Paper 99-GT-136, Indianapolis, IN

54. L. Q. Maurice, T. Edwards, and R.C. Striebich, “Formation of Cyclic Compounds in the Fuel System of Hydrocarbon-Fueled High Speed Vehicles,” AIAA No. 98-3534, Cleveland, OH

55. E. Corporan, L. Q. Maurice, D. K. Minus, R. C. Striebich, and S. Zabarnick, “Thermal Stability and Heat Sink Assessment of a Russian Fuel,” Proceedings of JANNAF Combustion Subcommittee, Airbreathing Propulsion Subcommittee and Propulsion Systems Hazards Subcommittee Joint Conference, Cocoa Beach, FL, October 1999.

56. M. Kennedy, M. Vangsness, and J. S. Ervin, “Fundamental Studies of the Freezing of Jet Fuels,” 25th Annual Dayton-Cincinnati AIAA Aerospace Sciences Symposium, March 2000.

57. J. Thornburg and J. S. Ervin, “Simulations of Flowing Supercritical n-Decane,” 25th Annual Dayton-Cincinnati AIAA Aerospace Sciences Symposium, March 2000.

58. J. S. Ervin, T. F. Williams, J. Bento, and T. Doungthip, “Studies of Jet Fuel Thermal Stability and Flow Characteristics within a Nozzle Under Supercritical Conditions,” Symposium on Structure of Jet Fuels VI, Div. Of Petroleum Chemistry, 220th National Meeting, American Chemical Society, Washington, DC, August 2000.

59. S. Zabarnick, “Investigation of Fuel additives for a JP-8+225 Jet Fuel Using the Quartz Crystal Microbalance,” Symposium on Structure of Jet Fuels VI, Div. Of Petroleum Chemistry, 220th National Meeting, American Chemical Society, Washington, DC, August 2000.

60. J. S. Ervin, D. Atkins, and M. D. Vangsness, “Flow Visualization of Freezing of Jet Fuel,” The 7th International Conference on Stability and Handling of Liquid Fuels, Graz, Austria, 2000.

61. S. Zabarnick, N. Widmor, J. S. Ervin, and C. Obringer, “Studies of Jet Fuel Freezing and Cold Flow Improving Additives by Differential Scanning Calorimetry,” IASH 2000, The 7th International Conference on Stability and Handling of Liquid Fuels, Graz, Austria, September 24-29, 2000.

62. C. A. Obringer, J. S. Ervin, and S. Zabarnick, "Development of a Low Temperature JP-8+100 Fuel," IASH 2000, The 7th International Conference on Stability and Handling of Liquid Fuels, Graz, Austria, 2000.

63. M. D. Vangsness, S. Zabarnick, N. Widmor, "Jet Fuel Crystallization at Low Temperatures," 220th American Chemical Society National Meeting, Washington, D.C., August 20-24, 2000.

64. K. Wohlwend, S. Zabarnick, K. E. Binns, and B. Grinstead, "Thermal Stability Testing of the Baker Flo-XS Pipeline Drag Reducing Additive," 220th American Chemical Society National Meeting, Washington, D.C., August 20-24, 2000.

65. S. Zabarnick, "Investigation of Fuel Additives for a JP-8+225 Jet Fuel Using the Quartz Crystal Microbalance," 220th American Chemical Society National Meeting, Washington, D.C., August 20-24, 2000.

66. J. S. Ervin, N. Widmor, S. Zabarnick, and M. Vangsness, "Studies of Jet Fuel Freezing by Differential Scanning Calorimetry and Cold Stage Microscope," ASME Turbo Expo. 2001, ASME-IGTI, New Orleans, LA, June 4-7, 2001.

67. D. R. Ballal D. R. and W. E. Harrison III, "A Time Scale Approach to Understanding Jet Fuel Combustion and Particulate Formation and Growth," AIAA 2001-1085, 39th AIAA Aerospace Sciences Meeting, Reno, NV, January 8-11, 2001.

68. K. Wohlwend, C. Obringer, and S. Zabarnick, "Freeze and Pour-Point Studies of Jet Fuel and Cold Flow Improving Additives," 26th Annual Dayton-Cincinnati AIAA Aerospace Sciences Symposium, March.

69. N. Widmor, J. S. Ervin, S. Zabarnick, and M. Vangsness, "Studies of Jet Fuel Freezing by Differential Scanning Calorimetry and Cold-Stage Microscopy," 26th Annual Dayton-Cincinnati AIAA Aerospace Sciences Symposium, March.

70. D. Atkins and J. S. Ervin, "Studies of Freezing of Jet Fuel in an Optical Cell," 26th Annual Dayton-Cincinnati AIAA Aerospace Sciences Symposium, March.

71. J. S. Ervin, S. Zabarnick, M. Vangsness, G. Dieterle, K. E. Binns, and C. Obringer, "Evaluation of Cold Flow Additives for use in JP-8+100," Paper No. AIAA-2001-3709, 37th AIAA/ASME/SAE/ASEE Joint Propulsion Conference, Salt Lake City, UT, 8-11 July 2001.

72. N. Kuprowicz, J. S. Ervin, and S. Zabarnick, "Simulations of Thermal-Oxidative Degradation Incorporating Pseudo-Detailed Chemistry," Paper No. AIAA-2001-3708, 37th AIAA/ASME/SAE/ASEE Joint Propulsion Conference, Salt Lake City, UT, 8-11 July 2001.

73. R. Striebich, W. A. Rubey, J. R. Klosterman, and L. M. T. Balster, "HPLC Pre separation with HRGC: A Comparison to MDGC," International Symposium on Capillary Chromatography and Electrophoresis, Las Vegas, NV, May 2001.

74. R. Striebich, J. R. Kolsterman, and W. A. Rubey, "MDGC of Aviation Fuels and Related Materials," Poster Presentation at Pittcon 2001, New Orleans, LA, March 2001.

75. S.D. Stouffer, R. C. Striebich, C.W. Frayne, and J. Zelina (2002): Combustion Particulates Mitigation Investigation Using a Well-Stirred Reactor," AIAA Paper No. 2002-3723, 38th Joint Propulsion Conference, 7-10 July, Indianapolis, IN

76. L. Balster, S. Zabarnick, and R. Striebich, "A High-Performance Liquid Chromatography Method for Predicting Surface Deposition Behavior of Thermally Stressed Jet Fuels," Presented at the 27th Annual Dayton-Cincinnati AIAA Aerospace Sciences Symposium, Dayton, OH, March 2002.

77. D. Goller, S. Zabarnick, and J. Ervin, "The Use of a Differential Scanning Calorimeter to Study Freezing of Jet Fuels," Presented at the 27th Annual Dayton-Cincinnati AIAA Aerospace Sciences Symposium, Dayton, OH, March 2002.

78. M. DeWitt and E. Corporan, "Analytical Capabilities for Measuring Particulate Mass Concentration and Qualifying/Identifying PAH Emissions," Presented at SERDP Review meeting, WPAFB, OH, March 2002.

79. M. DeWitt, S. Zabarnick, and D. Brooks, "Development and Evaluation of Additives to Inhibit Oxidative Deposition of Jet Fuels at Elevated Temperatures," Presented at CRC Aviation Meeting, Washington, D.C. April 2002.

80. T. Ward, J.S. Ervin, and R. Striebich, "Flow and Chemical Kinetics Simulations of Endothermic Fuels," Presented at the 27th Annual Dayton-Cincinnati AIAA Aerospace Sciences Symposium, Dayton, OH, March 2002.

81. T. Doungthip and J.S. Ervin, "Studies of Surface Effects on Jet Fuel Thermal-Oxidative Degradation," Presented at the 27th Annual Dayton-Cincinnati AIAA Aerospace Sciences Symposium, Dayton, OH, March 2002.

82. L. M. T. Balster, S. Zabarnick, and R. C. Striebich, "Predicting the Fouling Tendency of a Thermally Stressed Jet Fuel by High Performance Liquid Chromatography (HPLC) Analysis," Presented at the American Chemical Society 224th National Meeting, Boston, MA, August 2002.

83. M. W. Badger, S. Zabarnick, and G. R. Wilson, "Selection of Prototype Thermally Stable Jet Fuels: Quartz Crystal Microbalance Tests for Thermal-Oxidative Stability," Presented at the American Chemical Society 224th National Meeting, Boston, MA, August 2002.

84. M. J. DeWitt and S. Zabarnick, "Development and Evaluation of Additives to Inhibit Oxidative Deposition of Jet Fuels," Presented at the American Chemical Society 224th National Meeting, Boston, MA, August 2002.

85. T. Doungthip, J. S. Ervin, T. Ward, T. Williams, and S. Zabarnick, "Surface Deposition Within Treated and Untreated Stainless-Steel Tubes Resulting from Thermal-Oxidative Degradation of Jet Fuel," Presented at the American Chemical Society 224th National Meeting, Boston, MA, August 2002.

86. D. D. Link, D. K. Minus, R. C. Striebich, K. S. Rothenberger, and J. P. Baltrus, "The Analysis of Total Sulfur and Speciated Sulfur Compounds in Aviation Turbine Fuel," Presented at the American Chemical Society 224th National Meeting, Boston, MA, August 2002.

87. R. C. Striebich, "Fast Gas Chromatography for Middle-Distillate Aviation Turbine Fuels," Presented at the American Chemical Society 224th National Meeting, Boston, MA, August 2002.

88. S. Zabarnick, R. C. Striebich, K. Straley, and L. M. T. Balster, "Solid-Phase Extraction Analysis of Polar Species in Jet Fuel," Presented at the American Chemical Society 224th National Meeting, Boston, MA, August 2002.

89. S. M. Rozenzhak, R. C. Striebich, and C. E. Bunker, "Development of a High-Speed Jet-Fuel Diagnostic System Using Gas Chromatography and Principal Component Analysis," Presented at the American Chemical Society 224th National Meeting, Boston, MA, August 2002.

90. N. Widmor, J. S. Ervin, and S. Zabarnick, "Properties of Jet Fuels At Low Temperature and the Effect of Additives," Presented at the American Chemical Society 224th National Meeting, Boston, MA, August 2002.

91. S. Zabarnick and M. Vangsness, "Properties of Jet Fuels At Low Temperature and the Effect of Additives," Presented at the American Chemical Society 224th National Meeting, Boston, MA, August 2002.

92. E. Strobel, T. Biddle, D. Minus, S. Zabarnick, L. Balster, and E. Binns, "Thermal Stability Tests Performed on Refined Power II Flow Improver," Presented at the CRC Aviation Fuels Meeting, Alexandria, VA, May 2002.

93. E. Corporan, M. J. DeWitt, and M. Wagner, "Evaluation of Soot Particulate Mitigation Additives in a T63 Engine," Presented at the International Conference on Air Quality III, Arlington, VA, September, 2002.

94. M. Vangsness, "Polarization Microscopy Study of Jet Fuel Crystallization," Proceedings of International Microscopy Conference, Montreal, Quebec, Canada, October 2002.

95. D. R. Ballal, M. J. DeWitt, E. Corporan, and W. E. Harrison III, "Particulate Loading and Radiation in Gas Turbine Combustors," Presented at the 41st AIAA Aerospace Sciences Meeting and Exhibit, Reno, NV, January 2003.

96. J. Ervin, " Influence of Heat Transfer and Flow on Oxidation and Deposition, " Jet Fuel Thermal Stability Workshop, National Composites Center, Dayton, OH, December 2002.

97. S. Zabarnick, " Jet Fuel Oxidation and Deposition Chemistry Overview," Jet Fuel Thermal Stability Workshop, National Composites Center, Dayton, OH, December 2002.

98. L. Balster, S. Zabarnick, and R. Striebich, “HPLC Methods for Fuel Analysis,” Presented at the 28th Annual Dayton-Cincinnati, AIAA Aerospace Sciences Symposium, Dayton, OH, March 2003.

99. M. J. DeWitt, L. Shafer, and S. Zabarnick, “Development of Methodologies to Minimize the Oxidative Deposits of Jet Fuels,” Presented at the CRC Aviation Fuels Meeting, Alexandria, VA, April 2003.

100. L. G. Blevins, K. A. Jensen, R. A. Ristau, N. Y. C. Yang, C. W. Frayne, R. C. Striebich, M. J. DeWitt, S. D. Stouffer, E. J. Lee, R. A. Fletcher, J. M. Oran, J. M. Conny, and G. W. Mulholland, “Soot Inception in a Well Stirred Reactor,” Paper No. F-14, Proceedings of the Third Joint Meeting of the U.S. Sections of the Combustion Institute, Chicago, IL, March 2003.

101. T. Litzinger, R. Santora, M. Colket, D. Liscinsky, K. McNesby, R. Reich, C. Frayne, D. Phelps, S. Sidhu, and S. Stouffer, “Reduction of Particulate Matter Emissions from Burners. Part 1: Effects of Ethanol,” Poster PH-9, Third Joint Meeting of the U.S. Sections of the Combustion Institute, Chicago, IL, March 2003.

102. R. Reich, C. Frayne, J. Zelina, H. Mayfield, S. Stouffer and V. Katta, “Particulate Matter and Polycyclic Aromatic Hydrocarbon Determination Using a Well-Stirred Reactor,” AIAA Paper No. 2003-0664, 2003.

Technical Reports

1. D. H. Kalt and S. P. Heneghan, “Materials-Fuels Interaction Tests-Design, Results, and Analysis,” UDR-TR-1998-00073, June 1998.

2. D. H. Kalt, S. Zabarnick, S. D. Anderson, and P. D. Liberio, “Fuel and Fuel System Materials Compatibility Test program for the JP-8+100 Fuel Additive—Vol 1: BetzDearborn Spec.Aid 8Q462 Thermal Stability Additive Package,” Air Force Research Laboratory Technical Report, in press, 1999.

3. S. Zabarnick, G. L. Dieterle, S. P. Heneghan, W. A. Rubey, T. F. Williams, D. R. Ballal, J. S. Ervin, D. H. Kalt, R. C. Striebich, K. E. Binns, R. R. Grinstead, R. E. Kauffman, and M. D. Vangsness, “Combustion and Heat Transfer; Vol. 1: Advanced Jet Fuels Studies,” Air Force Research Laboratory, AFRL-PR-WP-TR-1998-2067, 1998.

4. S. Zabarnick, G. L. Dieterle, S. P. Heneghan, W. A. Rubey, T. F. Williams, D. R. Ballal, J. S. Ervin, D. H. Kalt, R. C. Striebich, K. E. Binns, R. R. Grinstead, R. E. Kauffman, and M. D. Vangsness, “Combustion and Heat Transfer; Vol. 2: Advanced Jet Fuels Data Sets,” Air Force Research Laboratory, AFRL-PR-WP-TR-1998-2068, 1998.

5. D. R. Ballal, D. Pestian, M. D. Vangsness, F. Takahashi, W. J. Schmoll, and R. Striebich, “Combustion and Heat Transfer; Vol. 3: Combustion Studies,” Air Force Research Laboratory, AFRL-PR-WP-TR-1998-2101, 1998.

6. D. R. Ballal, D. Pestian, M. D. Vangsness, F. Takahashi, W. J. Schmoll, and R. Striebich, “Combustion and Heat Transfer; Vol. 4: Combustion Data Sets,” Air Force Research Laboratory, AFRL-PR-WP-TR-1998-2102, 1998.

7. F. Takahashi, “Suppression and Characterization of Bluff-Body Stabilized Flames,” UDRI Report No. UDR-TR-1999-00088, November 1999.

8. J.S. Ervin, E. Binns, S. Zabarnick, G. Dieterle, D. Davis, C. Obringer, and K. Wohlwend, "Low-Temperature Experimental Simulations of the Global Hawk Fuel Tank," UDR-TR-1999-00001, October 1999.

9. C. Obringer, M. D. Vangsness, and D. R. Ballal, “Ignition of Jet-A Fuel Vapor by the Breakdown of Aircraft Fuel Gauge Terminal Strip Deposits,” NTSB Technical Report, January 2000.

10. K. E. Binns, G. Dieterle, and D. Davis, “Extended Duration Thermal Stability Tests of Copper Doped JP-5,” UDR-TR-2001-00022, February 2001.

11. R.W. Morris, D. Minus, S. Zabarnick, L. Balster, K. E. Binns, G. Dieterle, and T. Biddle, “Protocol of Test Methods for Evaluating High Heat Sink Fuel Thermal Stability Additives for Aviation Turbine Fuel: JP-8+100,” Technical Report No. AFRL-PR-WP-TR-2002-2037, Propulsion Directorate, Air Force Research Laboratory, September 2002.